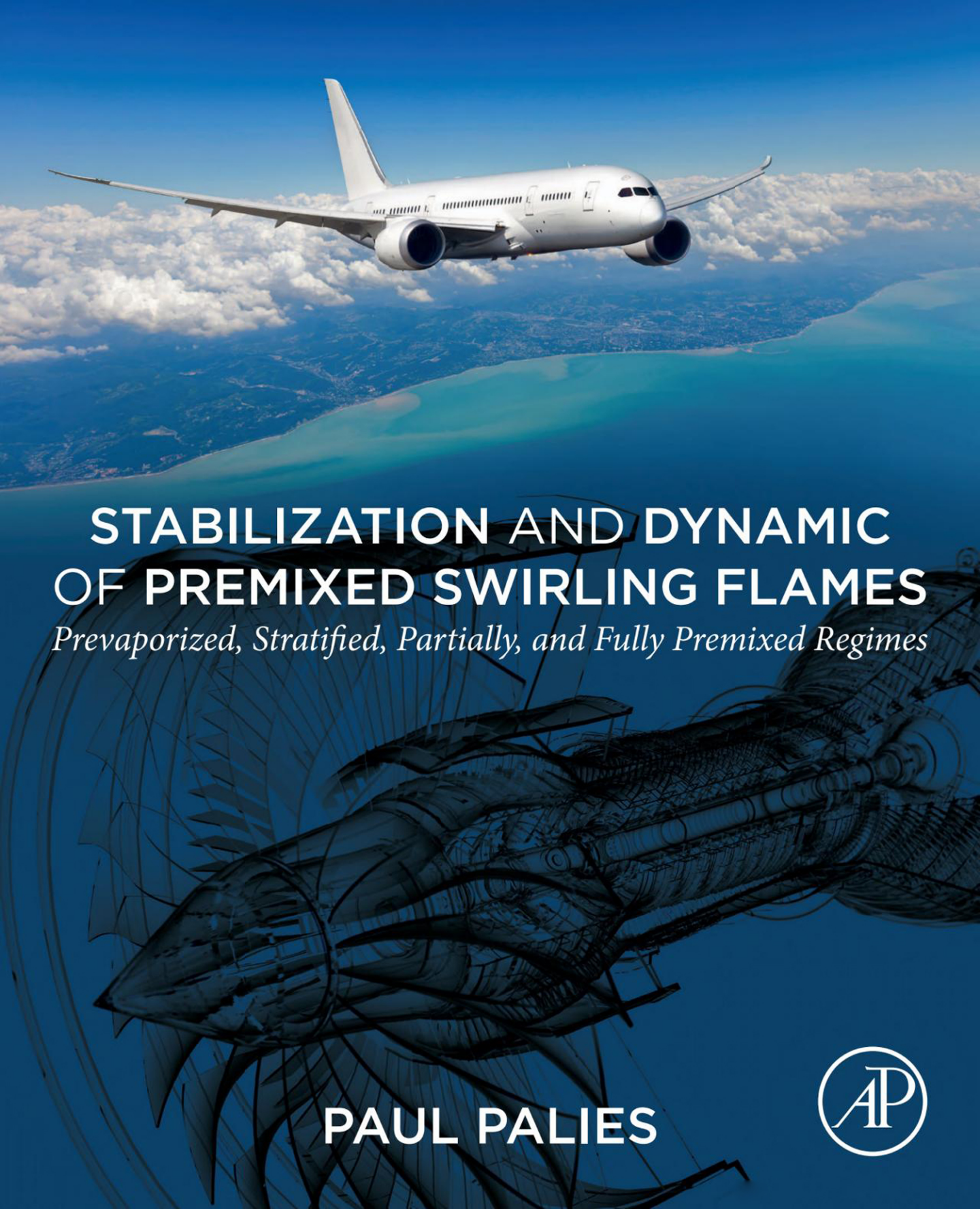

STABILIZATION AND DYNAMIC OF PREMIXED SWIRLING FLAMES

Prevaporized, Stratified, Partially, and Fully Premixed Regimes

PAUL PALIES

STABILIZATION AND DYNAMIC OF PREMIXED SWIRLING FLAMES

STABILIZATION AND DYNAMIC OF PREMIXED SWIRLING FLAMES

Prevaporized, Stratified, Partially, and Fully Premixed Regimes

PAUL PALIES
Principal Scientist
CFDRC
Huntsville, AL, United States

ACADEMIC PRESS
An imprint of Elsevier

Academic Press is an imprint of Elsevier
125 London Wall, London EC2Y 5AS, United Kingdom
525 B Street, Suite 1650, San Diego, CA 92101, United States
50 Hampshire Street, 5th Floor, Cambridge, MA 02139, United States
The Boulevard, Langford Lane, Kidlington, Oxford OX5 1GB, United Kingdom

Notices

Knowledge and best practice in this field are constantly changing. As new research and experience broaden our understanding, changes in research methods, professional practices, or medical treatment may become necessary.

Practitioners and researchers must always rely on their own experience and knowledge in evaluating and using any information, methods, compounds, or experiments described herein. In using such information or methods they should be mindful of their own safety and the safety of others, including parties for whom they have a professional responsibility.

To the fullest extent of the law, neither the Publisher nor the authors, contributors, or editors, assume any liability for any injury and/or damage to persons or property as a matter of products liability, negligence or otherwise, or from any use or operation of any methods, products, instructions, or ideas contained in the material herein.

Library of Congress Cataloging-in-Publication Data
A catalog record for this book is available from the Library of Congress

British Library Cataloguing-in-Publication Data
A catalogue record for this book is available from the British Library

ISBN: 978-0-12-819996-1

Publisher: Matthew Deans
Acquisitions Editor: Carrie Bolger
Editorial Project Manager: Isabella Silva
Production Project Manager: Poulouse Joseph
Designer: Matthew Limbert

Typeset by VTeX

To my family.

Contents

Preface

The present book is at the crossroads of aeronautical propulsion science and engineering. It attempts to bridge the gap between the fields of combustion and combustor design in a compact manner yet giving a comprehensive overview of the state of the art and of the current challenges. This book is to a large extent on premixed swirled combustion and on future design of premixed swirl-stabilized combustors. In that respect, this book is written for the following audience: students in the field of aeronautical engineering and researchers and engineers in university, public, and private research laboratories. The book covers introductory and state of the art topics and also significant recent research work by the author on premixed swirling flames, their physical understanding, and their modeling. This book presents and summarizes elements of a decade of work in the field.

The author is grateful to his advisors, peers, and colleagues whom he has learned from, interacted with, discussed with, elaborated with, encouraged, mentored, argued with, and discovered with on the topics related to this book at various levels.

The present book includes some elements of recent works funded by AFRL and NASA: (i) by the US Air Force Small Business Technology Transfer (STTR) program under contract number FA8650-17-C-2036 and (ii) by the NASA SBIR program under contract number 80NSSC18P1886 Phase I. Computational resources supporting elements of this work were provided by the NASA High-End Computing (HEC) Program through the NASA Advanced SuperComputing (NAS) Division of the Ames Research Center and by DoD HPCMP HPC Systems.

The author is thankful to his previous and present affiliations: CNRS ECP EM2C Laboratory, the United Technologies Research Center, and CFD Research Corporation. The author wishes to thank the Agence Nationale de la Recherche, DoE, NASA GRC, and AFRL for previous and ongoing research activities on unsteady combustion. The Elsevier team is gratefully thanked for the entire process of the publication of this book. The reviewers of the book's proposal are sincerely thanked for their comments and feedback.

Introduction

The industrial energy and transport technologies, including gas turbine engines, are directly linked to the current and future worldwide economic needs and climate requirements. As the passenger transport capacity and electricity capacity demands are increasing, and because the constraints on global warming/climate change are becoming more important, there is a requirement for better-designed and improved technologies.

The gas turbine engine relies on swirl-stabilized combustion, which consequently has a key role in this context. For example, operating a gas turbine engine with hydrogen can enable carbon emission-free electricity generation and propulsion technologies. Such technologies have been documented in the literature, see Brewer [1], Guynn and Olson [2], Council et al. [3], Khandelwal et al. [4]. For the future development of these systems, we will need to address various technological and scientific challenges in the energy and transport sectors. Some of these challenges are sector-specific, and some are common to both sectors. The pollutant emission reduction challenge is shared by both sectors, but the treatment of the emissions can be very different due to the weight and size constraints of land-based gas turbines and aircraft gas turbine engines. The noise footprint is also important in the transport sector for airports located close to cities. Other important challenges of these technologies include aircraft speed, fuel burn, transportation safety, the increase of data, and knowledge generation. Some of these challenges are specifically discussed below.

Aeronautics plays a key role in the worldwide transportation of passengers, particularly over long distances where rail transport is no feasible option. It has been and will be the preferred mode of transportation to cross oceans and cover long distances. The forecast of future global passengers traveling with aircraft is sketched in Fig. 0.1. This forecast indicates a global trend that the number of passengers using aircraft transport will approximately double between 2020 and 2040. This will require an increase of the number of aircraft and jet engines. Nowadays, this trend drives (i) a significant manufacturing momentum for turbofan engines and (ii) the development of future technologies that will fulfill the next generation of requirements from organizations' regulations. Some of these requirements are detailed below.

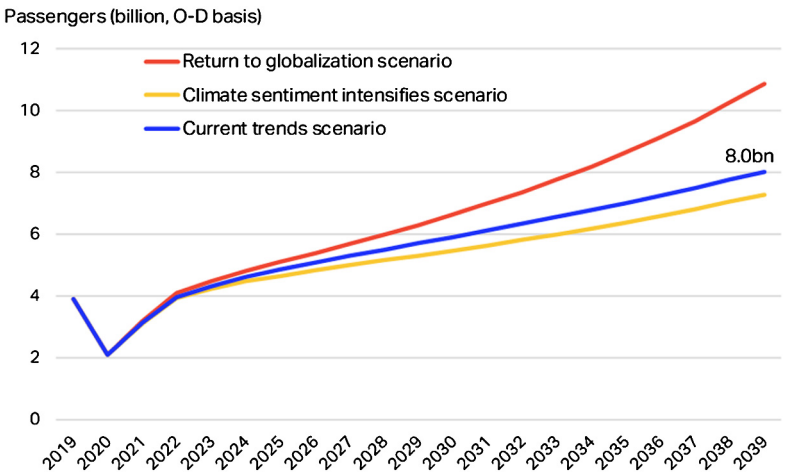

Figure 0.1 Global passengers forecast. International Air Transport Association data forecast of global passengers (in billions). Source: Permission from IATA Economics.

In the energy sector, the gas turbine engine plays an important role in the generation of electricity and heat. As the global demand for electricity is increasing, see Fig. 0.2, this technology will also play a key role in the near future.

The aeronautics field and the energy sector share the gas turbine engine, with requirements specific to each application. The gas turbine engine is also found in various other applications, such as propelling ships. The energy and transport industries face many outstanding technical challenges driven by environmental, economical, and geopolitical constraints. Some of these challenges are summarized next.

Environmental footprint

Since the increases in awareness of global warming and its consequences, the USA have signed multiple international treaties with the ultimate goal of reducing greenhouse gas (GHG) emissions, including CO_2, N_2O, and CH_4. The Kyoto Protocol is the international reference agreement that sets targets in terms of reducing GHG emissions. Since its entry into force on 16 February 2005, signatory countries that have ratified the text have undertaken efforts to reduce their emissions by 5% from 1990 levels during the period 2008 to 2012. To achieve this reduction, the ambition was to increase the energy expenditure linked to renewable energies. In 2004, 17% of the world's primary energy produced was derived from renewable sources, see REN21 [5]. Europe has set the

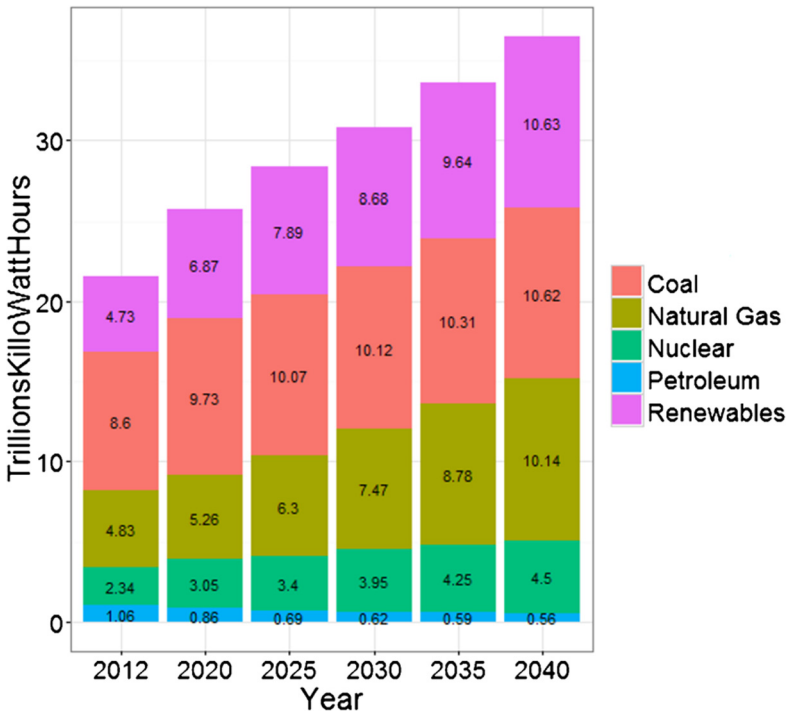

Figure 0.2 Electricity production projection. Current and future projection of electricity production per source. Source: US Energy Information Administration (2014).

goal to derive 20% of its primary energy from renewable sources by 2020.

The 2015 United Nations Climate Change Conference, COP21, held in Paris, France, from 30 November to 12 December 2015 led to the Paris Agreement. This agreement states an overall objective to maintain the global temperature increase well below 2°C above preindustrial levels and to pursue efforts to limit the temperature increase to 1.5°C. One of the major consequences of the Paris Agreement is the targeted reduction of emissions "so as to achieve a balance between anthropogenic emissions by sources and removals by sinks of greenhouse gases in the second half of this century." Two types of actions are defined by the Paris Agreement: (i) to reduce GHG emissions to the balance point between emission and sequestration and (ii) to increase sequestration of GHG emissions. It is important to recall the predicted use of combustion in electricity generation in the future, see the electricity production in Fig. 0.2. This graphic indicates the major role of combustion of coal, natural gas, and petroleum in the future of electricity gener-

ation. Therefore, the development and use of technologies aiming at reducing or suppressing pollutant emissions will have a strong impact and will support reaching the targeted COP21 goals.

In this general context, it is important to improve combustion technologies by enhancing system efficiencies and reducing the environmental impact in terms of emissions. It is known that conversion of hydrocarbon fuels into burned products generates GHGs like CO_2 and pollutants like unburned hydrocarbons HC, nitric oxides NO_x, and carbon monoxide CO. Amongst other harmful consequences, nitric oxides NO_x and unburned hydrocarbons are major contributors to the formation of smog and the production of near-ground level ozone. There are two ways to reduce those emissions: reduce their formation or eliminate their emission. It is also important to distinguish between emissions from ground gas turbines and jet engines, as the former can be sequestrated or undergo posttreatment, while the latter cannot.

As indicated in the previous section, combustion is utilized in many technological applications for the generation of electricity, for the production of heat, and for transport, especially in automotive transportation and aeronautics. In Tab. 0.1, the major sources of energy for transport and electricity production are summarized. The table lists the energy and transport sources, their areas of use, the category of energy conversion, the percentage of use as of 2014, and the major pro and con of each source. From this table, one can see that combustion is the key contributor with an accumulated 91.4% at the worldwide level for both transport and energy production. This number demonstrates the importance of the combustion discipline. While the main advantages of combustion are its range of operability and its range of use, its main disadvantage is the associated emission of combustion products, including CO_2 and NO_x.

The NASA Glenn Research Center (GRC) leads the effort in aeronautics to minimize the impact of aircraft transportation in terms of pollutant emissions to satisfy the future Federal Aviation Administration (FAA) requirements on emissions. The International Civil Aviation Organization (ICAO), through its Committee on Aviation Environmental Protection, has established international certification limits, see ICAO [6] and Chang et al. [7] for nitrogen oxide (NO_x) emission regulations for jet engines. The FAA enforces these standards through engine certification. The history of the ICAO NO_x regulations is presented in Fig. 0.3. This graphic shows the past accomplishments and the future requirements.

The contribution of the combustion of fossil fuels to the total energy demand at the worldwide level is significant. The other contributors to the total energy are renewable and nuclear en-

Table 0.1 Main advantages/disadvantages of energy and propulsion sources. Percentages were obtained from the International Energy Agency, 2014.

Source	Oil	Natural gas	Coal	Hydro	GSW	Nuclear	Biofuels
Area	Transport Automotive Aeronautical	Elec.	Elec.	Elec.	Elec.	Elec. Elec. Elec.	Transport
Category	Comb.[a]	Comb.	Comb.	Renew.[b]	Renew.	Nuclear	Comb.
Use (%)	31.3	21.2	28.6	2.4	1.4	4.8	10.3
Pros	Range	Range	Range	Unlimited	Unlimited	Cost	Emission
Cons	CO_2/NO_x	CO_2/NO_x	CO_2/NO_x	GWD	GWD	Waste	CO_2/NO_x

[a] Combustion.
[b] Renewable.

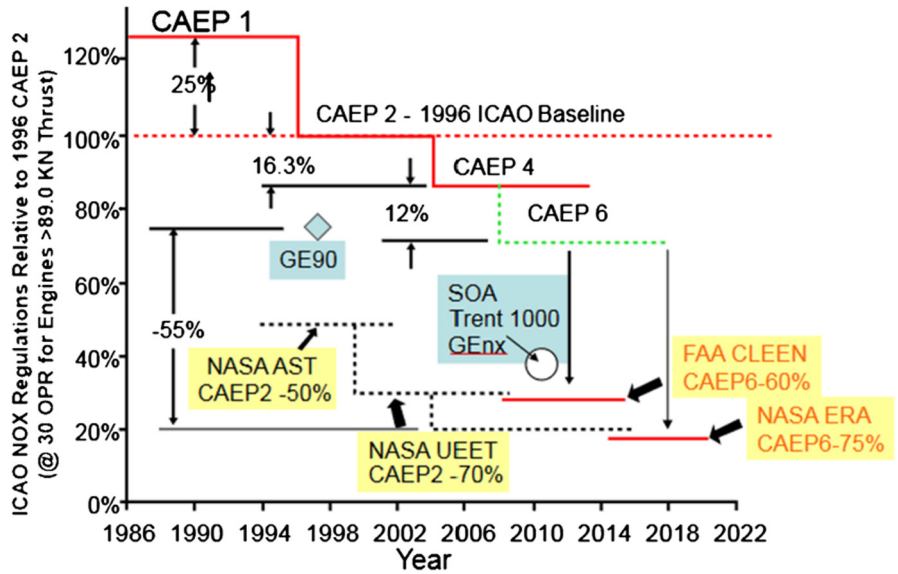

Figure 0.3 History of ICAO NO_x regulations for jet engines. History of ICAO NO_x regulations for engines and NASA program goals. Source: NASA from Chang et al. [7].

ergy. While each type of energy source follows a quasilinear growth since 1972 as a function of time, the slopes are different for different energy sources and thus modify the global percentage of each energy source a little. While the absolute contribution of renewable energy is increasing, its relative contribution remains stable

as a function of time. Combustion also shows a consistent relative contribution.

Primary energy sources are transformed through energy conversion processes to more convenient forms of energy that can directly be used by society, such as electrical energy, refined fuels, or synthetic fuels. In the field of energetics, these forms are called energy carriers, and they correspond to the concept of "secondary energy" in energy statistics. The ton of oil equivalent (toe) is a unit of energy defined as the amount of energy released by burning one ton of crude oil. It is approximately 42 GJ or 11 630 kWh. The worldwide electricity production by source of energy shows that the contribution from combustion is significant with respect to all other sources.

It is interesting to recall that most of the energy used in transportation is extracted from oil and transformed into mechanical energy through combustion. It is also worthwhile to remember that on a worldwide basis, 91% of the primary energy is delivered by combustion systems. In these applications, and in particular in high performance systems used in propulsion such as jet engines or energy conversion, combustion can interact with the acoustics of the system, leading to multiple types of instabilities. This phenomenon combines the complexities of combustion and those related to acoustics and unsteady fluid motions, giving rise to a wide range of challenges. Some of these are the subject of the present book and will be described and reviewed in detail.

Acoustic footprint

The acoustic footprint of aircraft is an important aspect to consider. Multiple sources of noise from the airplane, see Hubbard [8], induce the footprint around an airport, see the book of Zaporozhets et al. [9] on the regulation and standards for aircraft noise. These sources include the airframe noise, which is the noise due to the aerodynamic interaction between the air and the aircraft, including the wings, the landing gear, and the flaps. Other sources are the noise release near the jet of the engine, near the fan, and from the core, including turbomachinery and combustion noise. This latter is directly relevant to the present review and is usually referred to as core or engine noise, see the reviews by Dowling and Mahmoudi [10] for premixed combustion and by Ihme [11]. In Fig. 0.4, a breakdown of the noise into separate components of a typical engine with 1992-level technology during take-off and approach to landing indicates the large role of the engine noise.

Regulations around airports with respect to aircraft noise have been a priority for a long time. This is reflected by aircraft noise

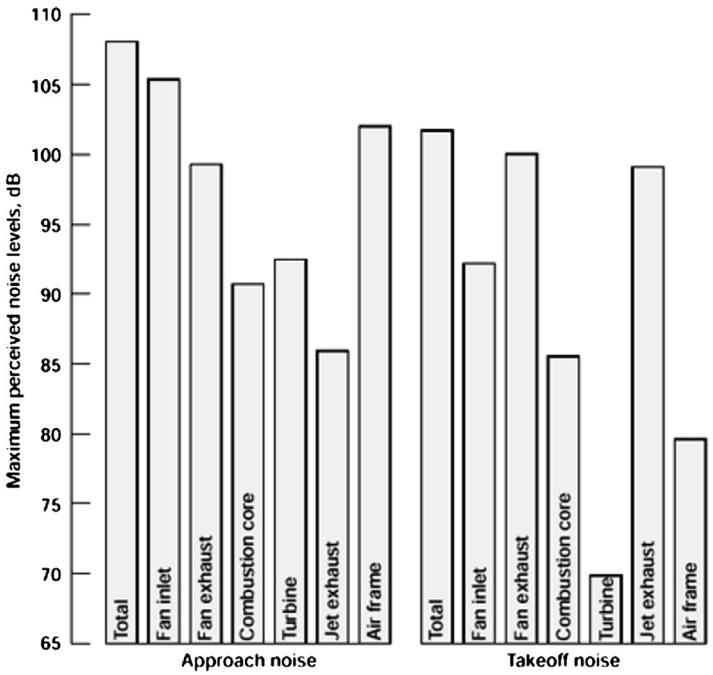

Figure 0.4 Aircraft noise distribution histogram. Maximum perceived noise level in dB. The representation of the noise distribution components for typical aircraft with 1992-level technology during take-off (right) and approach to landing (left) indicates the large part played by engine noise. Source: Figure taken from NASA.

standards and regulations from agencies such as the FAA, the European Aviation Safety Agency (EASA), and the International Civil Aviation Organization (ICAO). The FAA sets stages while the ICAO sets chapters, these two expressions corresponding to noise standards that must be met for airworthiness certification.

Economical and technical challenges

Economical and technical challenges are intrinsically linked. Sustained growth in aircraft transport will be achieved in the upcoming decades if transport speed is increased, fuel consumption is decreased, and the footprint is decreased, while the cost remains competitive with respect to other types of transports, such as trains. Indeed, this latter has shown continuous speed improvements; the fastest train circulating as of today, the Shanghai Maglev train, reaches 430 $\mathrm{km\,h^{-1}}$, while demonstration tests with the French TGV have been carried out at 575 $\mathrm{km\,h^{-1}}$, and existing projects such as the Hyperloop are targeting travel speeds near Mach 1. This is an important aspect, considering the fact that

where railways can compete, domestic flights transport a significant part of the total number of passengers. For example, in the USA in 2016, 77% of nearly one billion aircraft passengers traveled by domestic flights according to the Bureau of Transportation Statistics.

To reduce the environmental and acoustic footprints in order to meet the current and future pollutant emission and noise standards, and to be competitive with other transport markets, outstanding technical challenges need to be overcome. While a complete list of these challenges is beyond the scope of the present book, we can point out the ones directly linked to pollutant emission and acoustic footprint reductions, the increase in transport speed, and fuel burn reductions. Any progress in these four fields will have a tremendous impact on aeronautics.

1

The combustor

1 Overall principle of the gas turbine engine

1.1 Generalities and overall description

This section describes the principle of the gas turbine engine. The main goal of the gas turbine engine is to provide momentum to the fluid at rest to generate power or propulsion. Indeed, in the laboratory frame of reference and considering cruise conditions: for an aircraft engine or nominal conditions for a stationary gas turbine, the air is at rest upstream the engine. The momentum is transferred firstly to the air at rest by the rotating inlet fan and secondly to the ambient air by the exhaust jet. These two momentum exchanges are the two sources of thrust for current commercial subsonic turbofans (the thrust from the fan is dominant). The goal of the gas turbine engine is therefore to generate these two sources of momentum: fan rotation and exhaust jet. To achieve this goal, the turbofan engine has two distinct and linked flow paths: the so-called cold air flow path (also referred to as bypass flow), where the fan driven by the turbine transmits its momentum, and the so-called hot air flow path (also referred as core flow) due to the combustion inside the combustor, where the engine core transmits its momentum. The core is responsible for the rotation of the fan and induces the exhaust jet as well.

The main modules of the gas turbine engine are sketched in Fig. 1.1. The operation of the gas turbine engine and its components are now described. The description begins by considering the initial start of a typical engine, which corresponds to two simultaneous actions: (i) the ignition of the fresh gases in the combustor and (ii) the rotation of the core turbomachinery to enable the correct mass flow within the core, providing the upstream flame front flowfield. These two actions are respectively carried out with (i) a combustor igniter device and (ii) an electrical starter motor. Once the starting phase is finished, combustion is established within the combustor and the rotating parts of the core and the fan rotation are synchronized. The chemical energy of the fuel is converted to thermal energy within the combustion chamber. The thermal energy is converted to kinetic energy through two processes: the pressure expansion throughout the turbine and the change of fluid density from combustion. This kinetic energy en-

Stabilization and Dynamic of Premixed Swirling Flames
https://doi.org/10.1016/B978-0-12-819996-1.00009-3

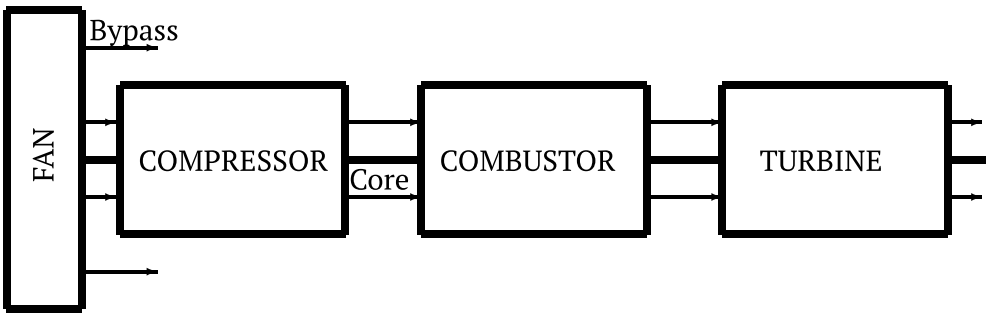

Figure 1.1 Schematic of the main modules of the gas turbine engine. The main modules of the gas turbine engine are sketched: the fan, the compressor, the combustor, and the turbine. The two main flow paths are also outlined: the cold air flow path through the fan (bypass flow stream) and the hot air flow path through the turbomachinery core (core flow stream). These two streams induce the total thrust of an aircraft's engine.

trains the turbine rotors through the viscous and pressure forces, and transfers momentum to the exhaust jet. The turbine also entrains the compressor rotor stages linked by a central shaft. The exhaust jet induces the second source of thrust. This description is further detailed in this chapter.

Within each gas turbine engine, a set of nearly 20 combustion sectors and injectors are distributed along the azimuth. Most recent annular combustors do not have walls separating these sectors. At least one swirling flame is located in each of these combustion sectors (depending on the concept, sometimes more than one). Swirl-stabilized combustion systems are part of most of the combustion-based devices generating electricity or thrust. In that perspective, any improvements to such systems can have tremendous impact. Both transform the chemical energy of the fuel into kinetic energy. This kinetic energy is used to entrain an alternator in the first case or to generate momentum in the second case. While these two applications have key common features, they also differ strongly. The most important differences include (i) the size and weight constraints for jet engines compared with ground-based operated gas turbines and (ii) the operating envelope and associated flow perturbations that are different. Two typical commercial turbofan engines are given in Fig. 1.2 and Fig. 1.3. Fig. 1.2 shows a CFM International from General Electric (GE) and Safran Aircraft Engines (SAE) turbofan CFM56-3 engine longitudinal cutaway describing the location of the engine's modules. Fig. 1.3 shows a Pratt and Whitney PW4000-94 turbofan engine with superimposed station numbers used to identify longitudinal location in such engines. The station numbering varies between engines and manufacturers. In Fig. 1.3, the far upstream flow con-

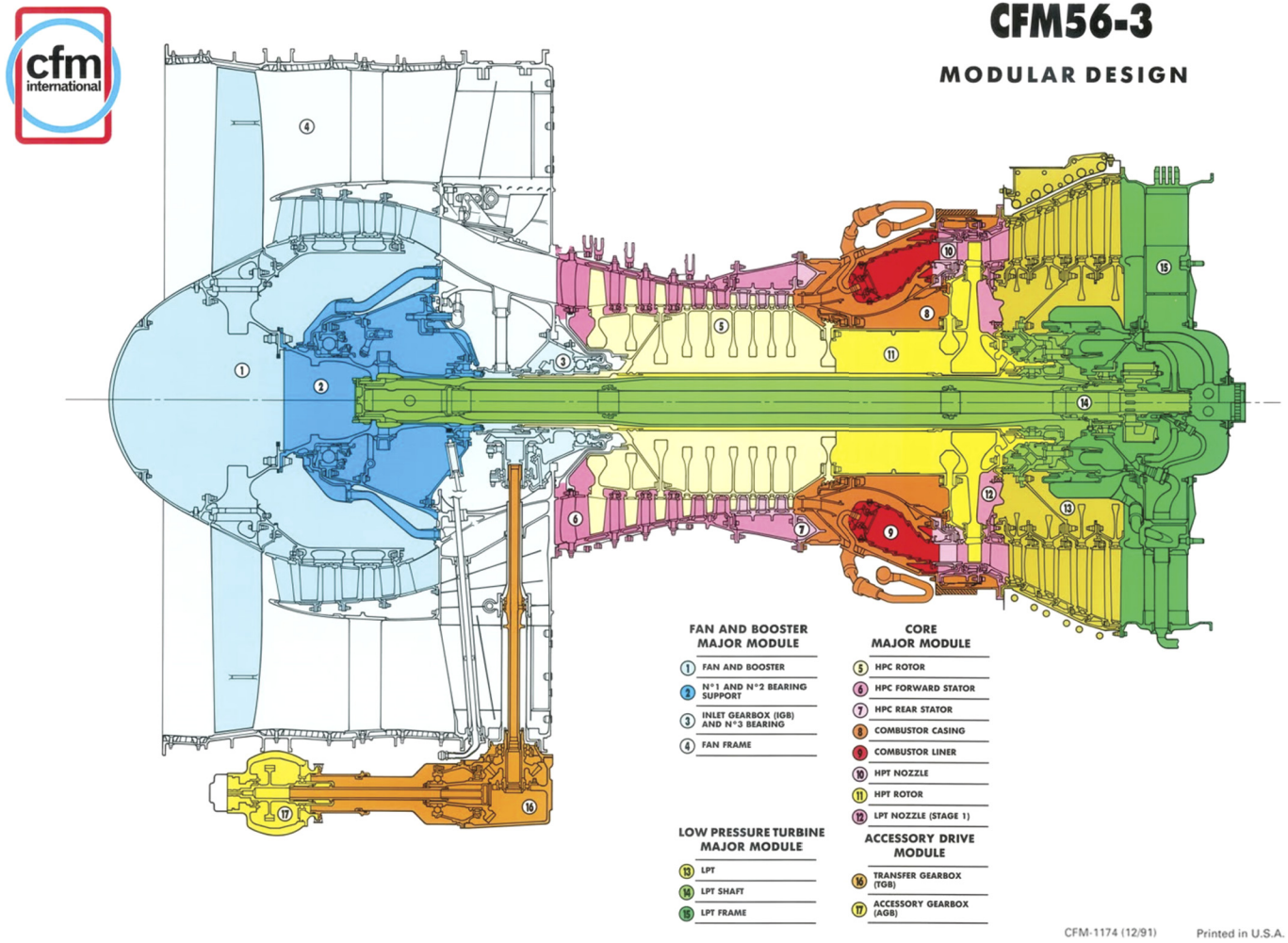

Figure 1.2 CFM International (GE and SAE) turbofan CFM56-3 engine. Turbofan engine longitudinal cutaway describing the location of the engine's modules. Source: Reproduced with permission from CFM International. CFM56 engines are a product of CFM International, a 50/50 joint company between GE and SAE.

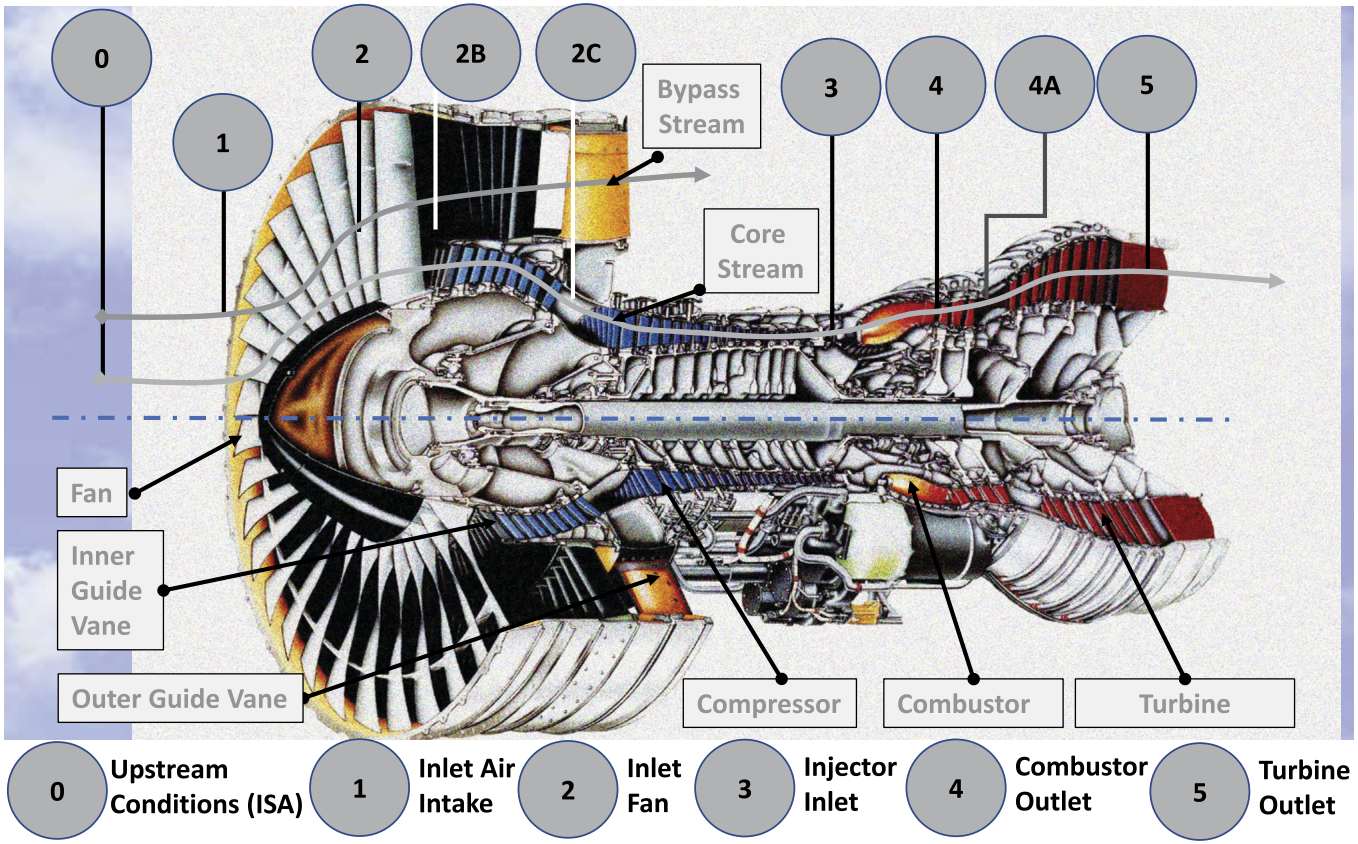

Figure 1.3 Pratt and Whitney PW4000-94 Turbofan engine. Illustration of the station numbers used in identifying longitudinal locations in an engine. Source: From A. Staroselsky, T. J. Martin, B. Cassenti, Transient Thermal Analysis and Viscoplastic Damage Model for Life Prediction of Turbine Components, J. Eng. Gas Turbines Power. Apr 2015, 137(4): 042501. Used with permission from ASME.

ditions are referred to as station 0, the station in the immediate vicinity of the air intake inlet, also called diffusor, is named station 1, and inside the diffusor upstream of the fan, the station number is 2. Downstream of the fan, the station is referred to as 2B. Station 2C is located at the exit of the low pressure compressor (LPC) and prior to the high pressure compressor (HPC). Station 3 is situated at the HPC outlet or injector/diffusor inlet, depending on the nomenclature. Station 4 is located at the end of the combustion chamber and at the inlet of the high pressure turbine (HPT). The stations downstream the HPT and the low pressure turbine (LPT) are marked 4A and 5, respectively. The station numbers are important because they are used for performance evaluation and various engine descriptions.

1.1.1 Propulsion versus power generation

Propulsion and power generation systems both rely on the gas turbine engine. In the first case, the engine is used to rotate a fan (turbofan) or a propeller (turboprop), or to generate a jet (turbojet). These systems induce a thrust, inducing vehicle motion. In the latter case, the engine is used to rotate a shaft that entrains an electricity generator.

Propulsion systems

In aeronautics, the propulsion system plays a major role in the range that can be covered by a given aircraft during initial and final instants t_0 and t_T, respectively. This range is known as the Breguet range and is written

$$\text{Range} = V \times \frac{L}{D} \times \frac{T}{\dot{m}_f g} \times \ln \frac{W_0}{W_T}, \tag{1.1}$$

where V is the constant aircraft velocity at cruise speed, L and D are the lift and drag forces on the aircraft, T is the engine's thrust, $\dot{m}_f$ is the total fuel mass flow rate of the engine, and g is the gravity constant. This equation is obtained by considering the rate of change of the overall weight W of the aircraft as being equal to the fuel weight consumption during cruise flight. This equation involves three main parameter groups: the aerodynamics of the aircraft through the ratio L/D, the propulsion/combustion system through $T/\dot{m}_f g$, and the mechanical structure of the aircraft through its overall weight W. The second group can be expressed as a function of the specific fuel consumption defined by the ratio of the fuel mass flow rate $\dot{m}_f$ to the thrust T.

The thrust definition of an engine is now introduced. The calculation of the thrust in an engine is conducted by considering

a fluid control volume encompassing the engine. On that control volume, by assuming steady flow, the conservation of mass and momentum in the axial direction of motion lead to the following formula for the thrust T:

$$T = \dot{m}_a[(1 + \Phi_g s_a)V_e - V] + A_e(p_e - p_a), \tag{1.2}$$

where Φ_g is the global equivalence ratio (i.e., the equivalence ratio based on the total air mass flow inside the turbomachinery core), s_a is the stoichiometric ratio, and V_e and p_e are the flow speed and pressure at the exhaust of the engine, respectively. The ambient pressure is p_a.

The other important characterization of the propulsion systems is based on the efficiencies. The efficiency reflects the reduction of power at the output of a system (for a given input) or in each of its components. The overall efficiency of a given system is consequently the product of the efficiencies of its components. In addition to the components' and modules' efficiencies, the performance of gas turbine engines is characterized by two major efficiencies, called the propulsive η_p and thermal (or thermodynamic) η_{th} efficiencies. They are now described for a single-stream turbojet engine. These two efficiencies have been used to compare engine performances and analyze past and future trends in aviation history. Their product leads to the overall efficiency η defined as the ratio of the thrust power (product of thrust T and flight velocity V) to the thermal power (equal to the product of the fuel mass flow rate $\dot{m}_f$ and the heat of reaction Δh_f of the fuel considered), such that

$$\eta = \frac{TV}{\dot{m}_f \Delta h_f}. \tag{1.3}$$

The propulsive efficiency writes as the ratio of the thrust power to the power transmitted to the exhaust air stream:

$$\eta_p = \frac{TV/\dot{m}_a}{(1 + \Phi_g s_a)V_e^2/2 - V^2/2}. \tag{1.4}$$

The propulsive efficiency is an estimation of the power lost in the exhaust/plume of the engine. Indeed, not the entire exhaust jet dynamics participates in jet propulsion, but only some particular terms of the governing equations. A way to increase the propulsive efficiency is thus to reduce fluid motion in the directions orthogonal to the flight direction, by avoiding fluctuations in those directions. This long-term goal could be enabled by coupled magnetohydrodynamic simulations or plasma-fluid dynamics interactions modeling. The thermal efficiency writes as the ratio of the output

Table 1.1 Aircraft and engine features plus key performances at cruise (C) and take-off (TO) conditions. Orders of magnitude.

	Range [km]	Thrust T [kN]	sfc [g s^{-1} kN^{-1}]	η_p [1]	η_{th} [1]	Mass[a] [kg]	Length [m]
Turbojet (F135, M88)	2200	150 (TO)	22[b] (C)			27 000	15.6
Turboprop (A400M)	8900	100 (TO)	6 (C)			141 000	45.0
Turbofan (A320, PW1000G)	6300	120 (TO)	16 (C)	0.7 (C)	0.5	79 000	37.6

[a] Maximum take-off weight.
[b] Without afterburner.

power transmitted to the air stream to the input engine thermal power:

$$\eta_{th} = \frac{(1+\Phi_g s_a)V_e^2/2 - V^2/2}{\dot{m}_f \Delta h_f}. \tag{1.5}$$

While the propulsive efficiency concerns the exhaust jet dynamics, the thermal efficiency is directly linked to the combustor, the combustion processes, and, importantly, to the combustor dilution jet for future premixed combustors.

The propulsive, thermal, and overall efficiencies, the thrust, the specific fuel consumption, and the Breguet range are key engine performance parameters. Table 1.1 lists typical aircraft and engine features plus performance parameters.

In order to complete the overall description of the gas turbine engine, it is important to introduce the model of the reference international standard atmosphere (ISA) and the typical mission envelope of a subsonic aircraft equipped with turbofan engines. The ISA is a static atmospheric model describing the evolution of the static pressure, temperature, and density as a function of the altitude. It is widely used in aeronautics to calculate aircraft and engine performances. The International Organization for Standardization (ISO) publishes the ISA as an international ISO standard. The International Civil Aviation Organization (ICAO) uses the same atmospheric model. Computed results for temperature, pressure, and density with this model are displayed in Fig. 1.4 from

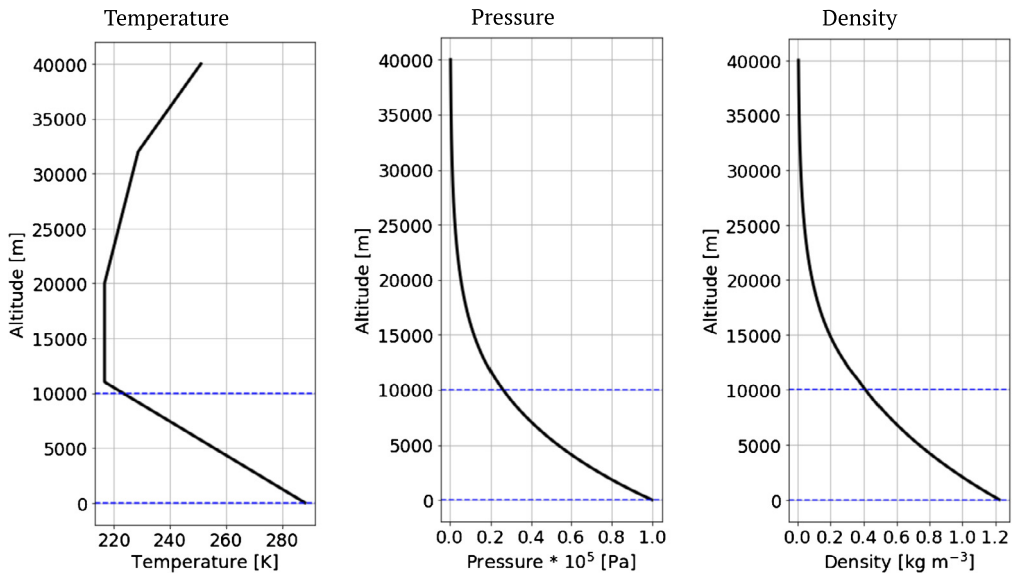

Figure 1.4 International standard atmosphere (ISA). Evolution of temperature, pressure, and density in the ISA. The horizontal lines correspond to the altitudes at sea level (0 m) and cruise flight (10 000 m) for a standard commercial aircraft.

sea level to 40 000 m altitude. The ISA is defined up to 100 km altitude.

The jet engine operating conditions are intrinsically linked to the performance requirements for a given aircraft at specific operating points on the trajectory (mission envelope) for that aircraft. The operating point can correspond to various positions along the flight envelope: taxi, take-off, climb, cruise, descent, approach, or landing conditions. These various positions along the trajectory are illustrated in Fig. 1.5. These different phases of flights are documented in detail by the ICAO safety regulations, see Organization [12], and include hundreds of possible flight phases. An intermediate level description between the presentation of Fig. 1.5 and the ICAO taxonomy is given in Penner et al. [13]. Three aircrafts engines configurations are given in Figure 1.6.

Power generation systems

In the case of a land-based gas turbine engine, the upstream conditions of the engines are atmospheric conditions. The mission envelope in that case is an operational envelope which depends on the required electricity power output. Some of the performance metrics presented in the previous section still apply,

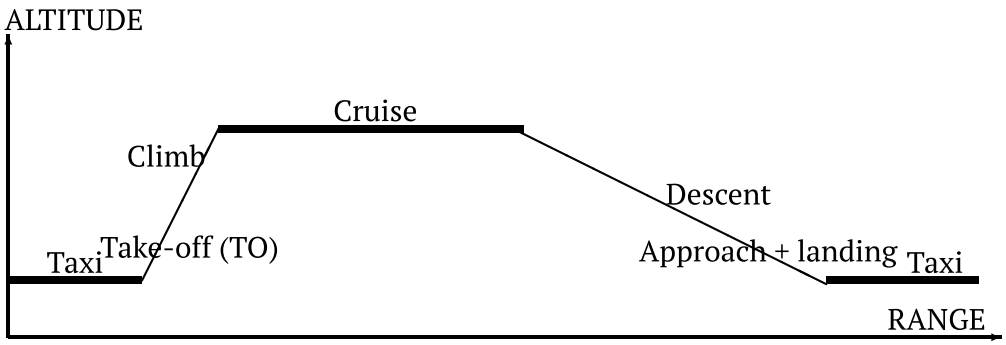

Figure 1.5 Schematic of the aircraft flight phases. The main phases of flight include taxi, take-off, climb, cruise, and descent.

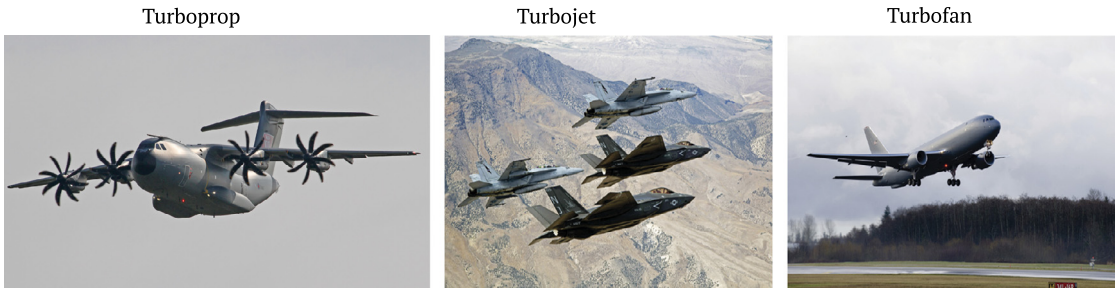

Figure 1.6 Three aircraft engine configurations. There are three main types of engines: the turboprop (propeller), the turbojet (jet), and the turbofan (fan + jet).

while others have to be adapted to consider as output the shaft power instead of the thrust.

1.1.2 Turboprop

A turboprop is a gas turbine engine where the power generated by the combustion of the fuel is used to rotate a propeller. The propeller momentum created is subsequently the only thrust source of the aircraft propelled. Turboprop engines equip a wide range of aircraft, from the single-engine land class to the multi-engine oversea class.

1.1.3 Turbojet

A turbojet is a gas turbine engine where the power generated by the combustion of the fuel is used to create a gaseous jet. This generated jet is the only source of thrust on these types of engines. Turbojet engines are mostly used on fighter aircraft. A specific feature of that type of aircraft is the addition of an additional combus-

tion chamber downstream of the turbine, the so-called augmenter or reheat combustor. In that region of the engine, additional fuel is burned to generate additional thrust.

1.1.4 Turbofan

The turbofan is the pillar of commercial aviation. Most commercial aircraft are equipped with these types of engines, and they are consequently responsible for a large economic activity worldwide. The turbofan can be seen as the trade-off between the turboprop and the turbojet. Indeed, the turbofan has two sources of thrusts: the fan (bypass stream) and the jet (core stream). For a turbofan engine, the thrust is produced by these different streams. As a consequence, Eq. (1.2) is rewritten as

$$T = \dot{m}_{aC}[(1 + \Phi_g s_a)V_{eC} - V] + \dot{m}_{aB}(V_{eB} - V), \tag{1.6}$$

where the subscripts B and C correspond to bypass and core air flow streams, respectively. Assuming the fuel to air ratio (FAR) negligible ($\Phi_g = \mathrm{FAR}/s_a$), and assuming an unchoked exhaust nozzle such as for turbofans ($\mathrm{p}_e = \mathrm{p}_a$), one can obtain the following expression for the propulsive efficiency:

$$\eta_p = \frac{2V[V_{eC} + \beta V_{eB} - (1 + \beta)V]}{V_{eC}^2 + \beta V_{eB}^2 - (1 + \beta)V^2}, \tag{1.7}$$

where β is the bypass ratio of the turbofan engine, defined as $\beta = \dot{m}_B/\dot{m}_C$, the ratio of air flowing between the bypass and the core flow paths. The thermal or thermodynamic efficiency writes within the same assumptions as

$$\eta_{th} = \frac{V_{eC}^2 + \beta V_{eB}^2 - (1 + \beta)V^2}{2\Phi_g s_a \Delta h_f}. \tag{1.8}$$

A summary of performances taken from the literature for two turbofan engines is given in Tab. 1.2. The table lists the take-off maximum thrust, the bypass ratio, the overall pressure ratio (OPR $= \mathrm{P}_3/\mathrm{P}_0$), the fan diameter, the engine mass and length, the engine staging configuration, and modules' rotational speeds, along with the combustor architecture.

1.1.5 Turboshaft and land-based gas turbine

Turboshafts are gas turbine engines that are used to rotate a shaft, which can for example be used to propel a ship or a set of helicopter blades. Land-based gas turbine engines are turboshafts that are used to entrain an electrical generator. These gas turbines

Table 1.2 Comparison of CFM LEAP (GE and SAE) versus PW GTF engines. Both engines are equipped with the A320 NEO.

	LEAP-1A	PW1100G GTF
Max thrust (TO)	155.7 kN	147.3 kN
Bypass ratio (β)	11	12.5
Overall pressure ratio (OPR)	40	50
Fan diameter	1980 mm	2200 mm
Length	3328 mm	3401 mm
Mass	3 t	3 t
Engine staging configuration	1 + 3 + 10 + 2 + 7	1 + G + 3 + 8 + 2 + 3
Fan - LPC - HPC - HPT - LPT		
Rotational speeds	4000 4000 20 000	4500 13 500 20 000
FAN - LPC - HPT		
Combustor	TAPS II (LPP[a])	TALON-X (RQL)

[a] With dilution holes.

have various sizes and weights, delivering low to high power. They have limited constraints (except for helicopters) on the space requirements compared with aircraft engines, and their efficiency can be consequently increased. This is for example carried out by utilizing the heat exiting from the turbine to generate steam through a steam generator which is used to power a steam turbine. This scheme of operation is called a combined cycle configuration.

1.2 Component/module technology descriptions

The present section focuses on the description of the component (module) technologies of the fan, the compressor, the combustor, the turbine, and the exhaust nozzle. It is important to discuss those modules because several of those are directly responsible for the upstream flow that will be seen by the flame front, and they also drive the flow that is exiting the combustor. In other words, understanding the flowfield is important (i) for the modeling and the physical description of the combustion chamber reacting swirling flow and (ii) for the understanding and description of the flowfield leaving the combustor, the latter impacting the thermal efficiency and the kinetic energy imparted to the turbine. Each stage of the compressor or the turbine is composed

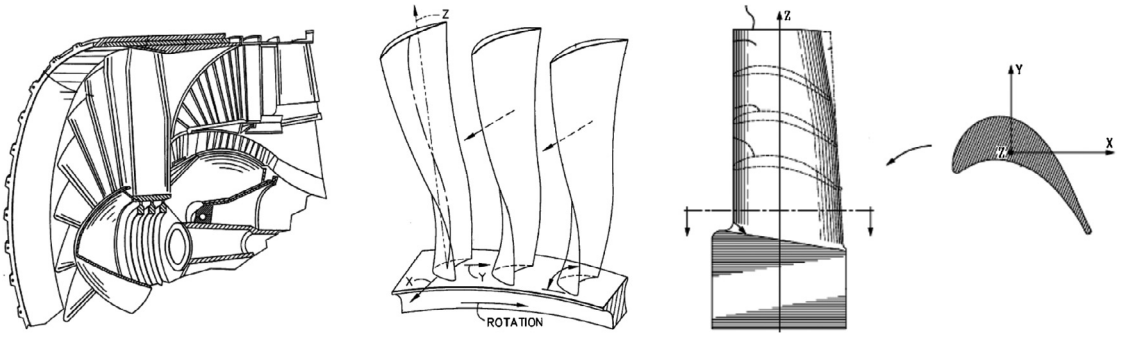

Figure 1.7 Close-up views of rotating modules' airfoils. (A) Fan. (B) Low pressure compressor stage. (C) High pressure turbine stage. Source: From patents: (A) patent EP-0763164B1, (B) US patent 6,331,100, and (C) US patent 8,038,411.

of a rotating (rotor) and a static (stator) element. These elements support a set of airfoils. Characteristic airfoils of each module are given in Fig. 1.7 for (A) the fan, (B) the low pressure compressor (LPC) rotor, and (C) the high pressure turbine (HPT) rotor. The dimensions of the airfoils will directly impact the smallest turbulent scale in each module. Characteristic orders of magnitude will be given in the last section of this chapter. The next subsections present key quantities used to characterize each module by considering a turbomachine consisting of two shafts. The first shaft connects the LPC and the LPT and the second shaft connects the HPC and the HPT. They have respective rotational speeds N_1 and N_2. Detailed descriptions are given in El-Sayed [14] and PLC [15].

1.2.1 Intake and fan

The intake of the turbofan engine refers to the diffuser located upstream of the fan. The intake's role, during subsonic cruise, is to decelerate the flow stream prior to its passage through the fan to minimize the transonic regime of the flow throughout the fan, and particularly at the blade tips of the fan. The intake is defined by its stagnation pressure ratio and its efficiency η_i:

$$\frac{P_{0,2}}{P_a} = \left(1 + \frac{\gamma - 1}{2}\eta_i \mathrm{Ma}^2\right)^{\frac{\gamma}{\gamma-1}}. \tag{1.9}$$

The stagnation temperature ratio is defined by

$$\frac{T_{0,2}}{T_a} = \left(1 + \frac{\gamma - 1}{2}\mathrm{Ma}^2\right). \tag{1.10}$$

The fan is located downstream of the subsonic diffuser inlet inside the engine casing. The fan provides an essential part of the engine thrust. The fan is defined by its total pressure ratio:

$$\pi_f = \frac{P_{2A,0}}{P_{2,0}}, \tag{1.11}$$

where P_{2A} is the stagnation pressure on its downstream side and P_2 is the stagnation pressure on the upstream side. The ratio of total temperatures writes

$$\frac{T_{2A,0}}{T_{2,0}} = \left(1 + \left[\frac{\pi_f^{(\gamma-1)/\gamma} - 1}{\eta_f}\right]\right). \tag{1.12}$$

The exhaust velocity of the fan nozzle (outer guide vane) can be determined using the following expression:

$$V_{eB} = \left(2\eta_{f,ogv}\frac{\gamma}{\gamma-1}RT_{2A,0}\left(1 - (P_a/P_{2A,0})^{(\gamma-1)/\gamma}\right)\right)^{1/2}. \tag{1.13}$$

1.2.2 Compressor

The LPC and HPC components (as well as each of the compressor stages) are characterized with the following pressure and temperature ratios. For the LPC, one has

$$\pi_{LPC} = \frac{P_{2B,0}}{P_{2A,0}}, \tag{1.14}$$

where $P_{2B,0}$ is the stagnation pressure on its downstream side and $P_{2A,0}$ is the stagnation pressure on the upstream side. The ratio of total temperatures writes

$$\frac{T_{2B,0}}{T_{2A,0}} = \left(1 + \left[\frac{\pi_{LPC}^{(\gamma-1)/\gamma} - 1}{\eta_{LPC}}\right]\right). \tag{1.15}$$

For the HPC, these expressions are written, for the pressure ratio, as

$$\pi_{HPC} = \frac{P_{3,0}}{P_{2B,0}}, \tag{1.16}$$

where $P_{3,0}$ is the stagnation pressure on its downstream side and $P_{2B,0}$ is the stagnation pressure on the upstream side. The ratio of total temperatures writes

$$\frac{T_{3,0}}{T_{2B,0}} = \left(1 + \left[\frac{\pi_{LPC}^{(\gamma-1)/\gamma} - 1}{\eta_{LPC}}\right]\right). \tag{1.17}$$

1.2.3 Combustor

As pointed out earlier in this book, the combustor has a central role in the operation of the engine. This section describes key elements of that module. The variation of total (stagnation) pressure through the combustor is defined as $\Delta P_c = P_{3,0} - P_{4,0}$. The upstream pressure and temperature T_3 and P_3 are key for the combustion processes as they drive the conditions that will be seen by the flame region. These variables are controlled by the altitude, the phase of the flight, and the design of the turbomachinery through the quantities defined previously. The equivalence ratio inside the combustor is defined by

$$\Phi = \frac{\dot{m}_f/\dot{m}_a}{[\dot{m}_f/\dot{m}_a]_{st}} = \mathrm{FAR}/s_a, \tag{1.18}$$

where FAR is the fuel to air ratio and s_a is the stoichiometric ratio for a chemical reaction between fuel and air. For a fully premixed mixture of fuel and oxidizer, the equivalence ratio writes

$$\Phi = (Y_f/Y_{O_2})/s_{O_2}, \tag{1.19}$$

where s_{O_2} is the stoichiometric ratio for a chemical reaction between fuel and oxygen.

The equivalence ratio Φ_g can be expressed as the global equivalence ratio based on the total air mass flow rate through the core turbomachinery. It includes the air flowing through the flame front, through the dilution jets and the cooling holes. Alternatively, it can be defined as the equivalence ratio Φ_i based on the air flowing through the injector only (not the dilution holes nor the cooling holes).

While in previous subsections, the thermodynamic analyses allowed to determine components' pressure and temperature ratios and efficiencies, such analyses also enable to determine the equivalence ratio Φ_g at a given operating condition. The thermal energy balance between the energy exiting the compressor plus the energy added by combustion is equal to the thermal energy entering the turbine. This balance is written as

$$\dot{m}_{a,C}(1 + \Phi_g s_a)C_{p,h}T_{4,0} = \dot{m}_{a,C}C_{p,c}T_{3,0} + \dot{m}_f \Delta h_f, \tag{1.20}$$

where $\dot{m}_{a,C}$ is the total air mass flow rate through the core of the turbomachine and consequently includes the primary air (flowing through the injector) and the secondary air (flowing through the dilution holes) within the combustor. The derivation for the expression of the global equivalence ratio and thus the FAR leads

to

$$\Phi_g = \frac{(C_{p,h}/C_{p,c})(T_{4,0}/T_{3,0} - 1)}{s_a \Delta h_f/(C_{p,c}T_{3,0})) - (C_{p,h}/C_{p,c})(T_{4,0}/T_{3,0})}. \tag{1.21}$$

This expression can be used to provide estimates of the global equivalence ratio Φ_g required to reach a given outlet burned gas temperature in the combustor, expressed in term of stagnation temperature. The effect of the dilution holes air stream inside the combustor and the effect of the mode of combustion inside the combustor are not explicitly included in this expression. In other words, it assumes that the whole mass flow of air is used for the combustion process. The specifics of premixed combustion are discussed in the last section of Chapter 2. In that perspective, it is important to be cautious and to distinguish between the adiabatic flame temperature of combustion with the turbine inlet temperature (TIT), particularly when discussing premixed combustion and in the presence of the dilution hole. The optimization of the equivalence ratio, mode of combustion, power output, TIT, and adiabatic flame temperature is key to fuel burn reduction. It will require global integrated theoretical and experimental work, and local computer-based simulations to optimize the fuel burn.

1.2.4 Turbine

The turbine is the second module of the so-called hot section of the engine after the combustor. This component ensures the extraction and conversion of kinetic energy from the flow to the shaft in order to intrinsically entrain the upstream fan. Contrarily to the compressor module, the turbine includes the additional challenge of high temperature environments. A key quantity defined for the turbine is the so-called TIT. The TIT $T_{4,0}$ is equal to the stagnation temperature at the inlet of the HPT. The energy balance between the HPT and the HPC leads to the following expression:

$$T_{4A,0} = T_{4,0} - \frac{\dot{m}_{aC} C_{p,c}}{\dot{m}_{aC}(1 + \Phi_g s_a) C_{p,h}}. \tag{1.22}$$

The pressure ratio through the HPT is given by the following expression:

$$\frac{P_{4A,0}}{P_{4,0}} = \left[1 - \frac{1}{\eta_{HPT}}\left(1 - \frac{T_{4A,0}}{T_{4,0}}\right)^{\gamma/(\gamma-1)}\right]. \tag{1.23}$$

Similar expressions are obtained through the LPT energy balance with the LPC. For the temperature, one has

$$T_{5,0} = T_{4A,0} - \left[\frac{\beta \dot{m}_a C_{p,c}(T_{2A,0} - T_{2,0})}{\dot{m}_a(1 + \Phi_g s_a)C_{p,h}} + \frac{\dot{m}_a C_{p,c}(T_{2B,0} - T_{2,0})}{\dot{m}_a(1 + \Phi_g s_a)C_{p,h}} \right]. \tag{1.24}$$

The stagnation pressure at the outlet is given by

$$\frac{P_{5,0}}{P_{4A,0}} = \left[1 - \frac{T_{4A,0} - T_{5,0}}{\eta_n T_{4A,0}} \right]^{\gamma/(\gamma-1)}. \tag{1.25}$$

1.2.5 Exhaust nozzle

The exhaust velocity of the exhaust nozzle with no augmenter and considering outlet atmospheric pressure can be determined using the following expression:

$$V_{eC} = \left(2\eta_n \frac{\gamma}{\gamma - 1} R T_{5,0} \left(1 - (P_a/P_{5,0})^{(\gamma-1)/\gamma} \right) \right)^{1/2}. \tag{1.26}$$

1.3 Thermodynamics and nonreacting fluid dynamics

This section focuses on the thermodynamic description and the nonreacting fluid dynamic governing equations that are widely used in turbomachinery systems. The underlying assumptions are introduced along with the applications of these equations to each module. Particular emphasis of this section is on the link between the thermodynamics and the fluid dynamics and their global and local perspectives.

1.3.1 Thermodynamic formalism

The objective of thermodynamic analysis is to evaluate the pressure, temperature, and density of a fluid (gas or liquid) in a system at a given state. This description can take various forms, expressed over a control volume of different size whose size determines global or local quantities with respect to the geometry considered. In other words, thermodynamics can be firstly expressed with integrated quantities such as inside each stage of the engine's modules previously described and whose states were expressed in terms of stagnation variables. For example, the stagnation pressure and temperature at the injector inlets are given by (P_{03}, T_{03}). In addition, thermodynamic quantities can be evaluated locally at the typical scale of the fluid control volume, for example, represented by a numerical simulation mesh grid cell.

Thermodynamics of systems have several important assumptions and principles. First of all, the system considered is defined by boundaries where mass, heat, and work can be exchanged. Also, the changes between two states must be slow so that the fluid is in thermodynamic equilibrium, i.e., the perfect gas law is valid. This assumption is for example supported by the static state of a system with no time-dependent evolution that can be obtained for example by extracting the boundary value problem solution of an unsteady problem. In practical applications such as discussed in the present book, thermodynamic equilibrium is assumed to hold for all operating conditions considered.

The three foundational principles and laws of thermodynamics are now introduced. The first principle regards the temperature equilibrium of a system: A set of connected system evolves towards the same temperature as time increases. The second principle regards the conservation of total energy: The total energy is conserved (but not constant) and its variation through the passage from an initial state (1) to a final state (2) is balanced by the energy transfers from the heat q and from the work done w. The total energy per kilogram of mass e in turbomachinery systems essentially includes the internal thermal energy e_i, the kinetic energy $e_k = \mathbf{v}^2/2$, and the potential energy $e_p = gz$. The second principle can be written as

$$de_t|_1^2 = dw|_1^2 + dq|_1^2, \tag{1.27}$$

where de_t is the total energy variation per unit mass during the thermodynamic transformation which corresponds to the variations of work done dw (such as from the rotor of a compressor stage) on the system and the heat dq added to the system (such as due to the combustion of fuel). The thermodynamic transformation or process can be qualified as (i) adiabatic, when no heat is added or subtracted ($\delta q = 0$), (ii) reversible, when diffusion phenomena (thermal, mass, and momentum) are neglected, and (iii) isentropic, i.e., both adiabatic and reversible. The third principle of thermodynamics states that there is an additional thermodynamic variable, called entropy s, which is used to quantify the isentropic assumption. In other words, entropy is used to evaluate how much a thermodynamic transformation is close to the isentropic conditions. This third principle is known as the second law of thermodynamics, and is written

$$ds|_1^2 = \frac{dq_{rev}}{T} + ds_{irrev}. \tag{1.28}$$

By definition, the change of entropy between the initial and final states is always positive or null. It is by definition zero for an

isentropic thermodynamic transformation $ds|_1^2$. The first term relates to the exterior environment of the system, while the second term corresponds to the internal fluid dynamics of the system. The term ds_{irrev} characterizes the degree of nonisentropicity and is due to the diffusion phenomena. As pointed out in Vincent [16], "entropy-increasing operations taking place in any system reduce its capacity to deliver mechanical work." It is also worthwhile to note that by Eq. (1.28), the area under a T-S diagram is equal to the heat added to or lost by the system during operation. The first and second laws of thermodynamics can also be written in their local forms.

For a control volume of fluid, the material derivative of the total energy e_t is given by

$$\rho \frac{d}{dt}\left[e_i + \frac{\boldsymbol{v}^2}{2} + e_p\right] = -\nabla \cdot (p\boldsymbol{v}) + \nabla \cdot (\boldsymbol{\tau} \cdot \boldsymbol{v}) - \nabla \cdot \boldsymbol{q}, \tag{1.29}$$

where the right-hand terms represent from left to right the power of the pressure forces, the power of the viscous forces, and the heat flux. A similar expression can be obtained for the entropy combining the first and second thermodynamic principles assuming a reversible transformation where $dw|_1^2 = pdV|_1^2$:

$$Tds = de_i + pd(1/\rho). \tag{1.30}$$

This equation also holds for a nonreversible process. Associating the latter equation with the conservation equation of the internal energy e_i, one obtains

$$\rho T \frac{ds}{dt} = -\nabla \cdot \boldsymbol{q} + \boldsymbol{\tau} : \nabla \boldsymbol{v}, \tag{1.31}$$

which demonstrates that the sources of entropy are the thermal, mass (included into the complete expression of the heat flux vector for reacting flows), and the momentum diffusion. A process would then be isentropic when these sources are zero. Detailed thermodynamic presentations relevant to turbomachinery can be found in Candel [17], Hill and Peterson [18], Vincent [16], Oates [19], Anderson [20]. In general, the relationships and the transport coefficients presented in this section can be retrieved with statistical physics approaches considering an ensemble of interacting molecules of distributed positions and velocities. Such description is beyond the scope of the present book.

It is now important to discuss and introduce the equations of state in addition to the thermodynamic principles. These equations link the state variables (pressure, temperature, and den-

sity or volume). For systems where the intermolecular force between molecules is neglected (such as in the pressure range 0.1 to 10 atm) compared with their collisions, the equation of state is the equation of state of perfect gases and can write $p = \rho r T$, where $\rho = m/V$ is the density, r is the perfect gas constant defined by $r = \mathcal{R}/M$, where $\mathcal{R} = 8.314\ \mathrm{J\,mol^{-1}\,K^{-1}}$, and M is the molar weight of the considered gas. For systems at higher pressure, when the intermolecular forces are important because of the reduced mean free path and stronger particle interactions occur, the equations of state of real gases are used. There are many forms of the latter, such as the van der Waals equation of state. In the applications that are discussed in the present book, the perfect gas law is a valid assumption for a wide range of conditions. The internal energy introduced earlier can be obtained from $de_i|_1^2 = c_v dT|_1^2$ when the specific heat at constant volume c_v is temperature-dependent for a thermally perfect gas, or from $e_i = c_v T$ for a calorically perfect gas. Other notation includes using the enthalpy $h = e_i + p/\rho$ instead of the internal energy, and the specific heat at constant pressure c_p. The specific heats are linked by $c_p - c_v = r$ and $\gamma = c_p/c_v$.

1.3.2 Nonreacting fluid dynamics formalism

In a turbofan engine, there are countless physical mechanisms and processes that are driven by fluid dynamics, either nonreacting or reacting. Most of the flow regimes that occur in a turbofan gas turbine engine are unsteady, nonisothermal, turbulent, noisy and subsonic, and reacting in the combustion chamber. This section is devoted to the nonreacting fluid dynamics governing equations, the Navier–Stokes equations, whose goal is to determine the flow velocity components for example at each location in the engine. The reacting governing equations will be detailed in Chapter 2. Two-phase flows and phase change fluid dynamics will be discussed in Chapter 6.

The equations of fluid motion express the conservation of mass, momentum, and energy over a control volume for a fluid particle of position $\mathbf{r}(x, y, z, t)$ and of velocity $\boldsymbol{v}(v_x, v_y, v_z, t)$ at instant t. Their complete derivation can be found for example in Candel [17] and Kuo and Acharya [21]. They can be written in the following forms in Cartesian coordinates.

The mass budget writes

$$\frac{\partial \rho}{\partial t} + \nabla \cdot (\rho \boldsymbol{v}) = 0. \tag{1.32}$$

The momentum budget writes

$$\rho\left[\frac{\partial \boldsymbol{v}}{\partial t} + \boldsymbol{v}\cdot\nabla\boldsymbol{v}\right] = -\nabla p + \rho\boldsymbol{g} + \nabla\cdot\boldsymbol{\tau}, \tag{1.33}$$

where p is the static pressure, $\boldsymbol{g}$ is the gravity, and the viscous stress tensor $\boldsymbol{\tau}$ of a Newtonian fluid is

$$\tau_{ij} = 2\mu d_{ij} + \left[\kappa - \frac{2}{3}\mu\right] d_{kk}\delta_{ij}, \tag{1.34}$$

where μ is the dynamic viscosity, κ is the second viscosity coefficient (neglected in most applications), and the velocity gradient (or strain-rate) tensor d_{ij} is

$$d_{ij} = \frac{1}{2}\left[\frac{\partial v_i}{\partial x_j} + \frac{\partial v_j}{\partial x_i}\right]. \tag{1.35}$$

The energy budget in its temperature form is written as

$$\rho c_v\left[\frac{\partial T}{\partial t} + \boldsymbol{v}\cdot\nabla T\right] = -\nabla\cdot\boldsymbol{q} - p\nabla\cdot\boldsymbol{v} + \boldsymbol{\tau} : \nabla\boldsymbol{v}. \tag{1.36}$$

The previous set of equations coupled to the equation of state allows to determine the density, the velocity components, the temperature, and the pressure of a fluid in its Eulerian description, i.e., when describing these quantities at fixed spatial points as a function of time. The other description of fluid motion is the so-called Lagrange description, which tracks the position of the fluid particle as a function of time. It is not used in general in turbomachinery or combustion simulations.

1.3.3 Overall cycle and component efficiencies

The overall thermodynamic cycle of a geared turbofan two-shaft engine is now discussed. The Brayton cycle is a thermodynamic cycle describing the operation of a constant-pressure heat engine. Originally used for piston engines, it is also the basis for gas turbine engines. Although the cycle was initially designed for closed systems such as internal combustion engines, it is also used for the thermodynamic analysis of open system such as gas turbine engines. The most representative schematics associated with the Brayton cycle are the temperature–entropy and pressure–specific volume diagrams. Representative diagrams are sketched in Fig. 1.8 and Fig. 1.9 for a geared turbofan engine. In these figures, stations 3, 4, and 5 correspond to the station numbers depicted in Fig. 1.3.

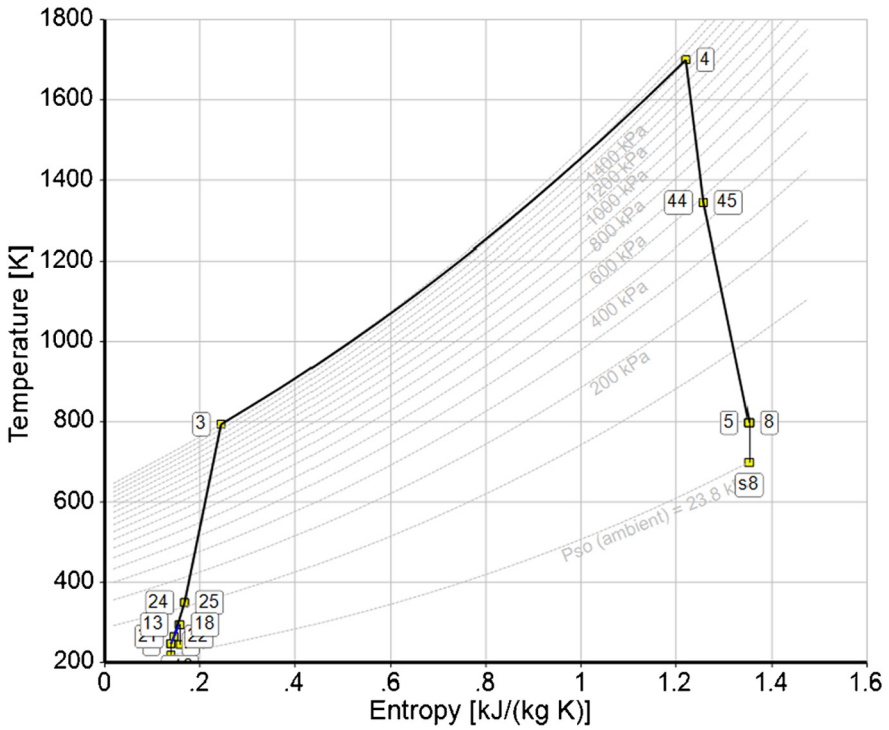

Figure 1.8 Overall thermodynamic Brayton cycle. Typical temperature (T)–entropy (S) diagram for a geared turbofan gas turbine engine.

The ideal Brayton cycle consists of several steps: an isentropic process, where the ambient air flows into the compressor to increase its pressure, an isobaric process, where heat is added to the compressed air inside the combustion chamber, an isentropic process, where the hot, pressurized air expands through the turbine modules where the work done entrains the turbine/compressor shaft, and finally an isobaric process, where the heat exits the exhaust nozzle. The actual Brayton cycle is as follows: a compression adiabatic process (2 to 3), a heat addition isobaric process (3 to 4), an expansion adiabatic process (4 to 5), and a heat rejection isobaric process (5 to 8).

In Section 1.2, the components' efficiencies have been introduced. In the present section, the focus is on the overall thermodynamic description of the engine. Firstly, the static and total variables' definitions are recalled because of their use in turbomachinery systems. The total or stagnation temperature (subscript 0) is defined as $T_0 = T + u^2/2c_p$ and is obtained from the conservation of energy for an isentropic process. This ratio can also be

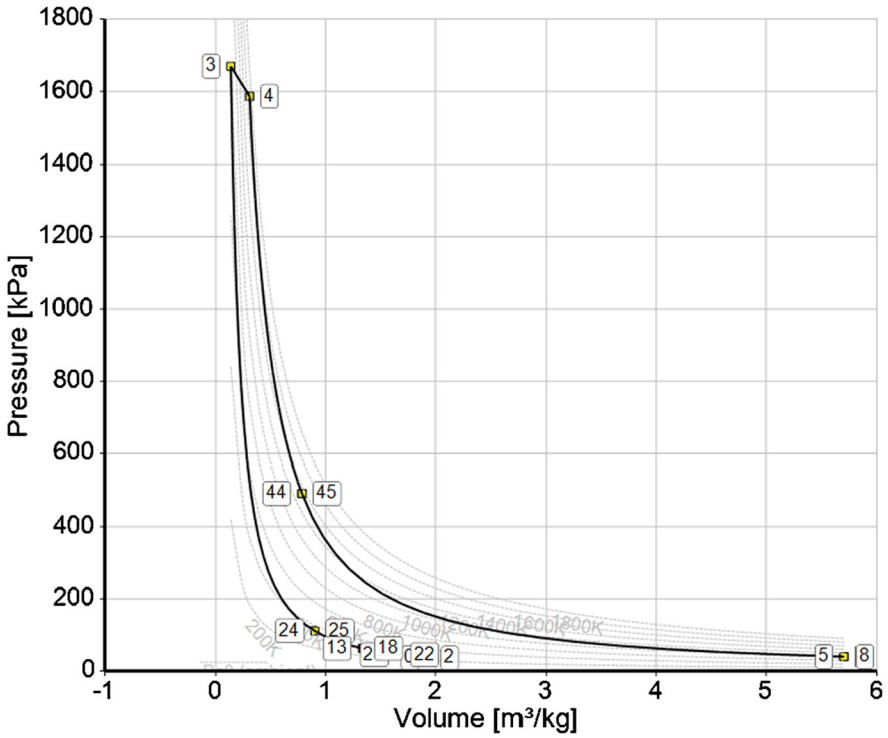

Figure 1.9 Overall thermodynamic Brayton cycle. Typical pressure (P)–specific volume (V) diagram for a geared turbofan gas turbine engine.

formulated as a function of the Mach number Ma, i.e.,

$$\frac{T_0}{T} = 1 + \frac{(\gamma - 1)}{2}\mathrm{Ma}^2. \tag{1.37}$$

Similarly, the pressure ratio of stagnation to static pressure at a given engine station can be written as

$$\frac{P_0}{P} = \left[1 + \frac{(\gamma - 1)}{2}\mathrm{Ma}^2\right]^{\gamma/(\gamma-1)}. \tag{1.38}$$

And the density ratio is expressed by making use of the perfect gas equation of state as

$$\frac{\rho_0}{\rho} = \left[1 + \frac{(\gamma - 1)}{2}\mathrm{Ma}^2\right]^{1/(\gamma-1)}. \tag{1.39}$$

These expressions are used to determine the isentropic evolutions inside multiple components of the jet engine, such as the com-

pressor and turbine stages, and correspond to component efficiencies of unity. The corresponding expressions with the actual efficiencies are presented in Section 1.2. In order to evaluate the differences between isentropic and actual thermodynamic transformations, one uses the efficiencies of the components defined by the following expressions. For the inlet diffuser, the efficiency writes, in term of stagnation enthalpies,

$$\eta_d = \frac{h_{0,2,is} - h_a}{h_{0,2} - h_a}. \tag{1.40}$$

For the compressor, one has

$$\eta_c = \frac{h_{0,3,is} - h_{0,2}}{h_{0,3} - h_{0,2}}. \tag{1.41}$$

For the turbine, one has

$$\eta_t = \frac{h_{0,4} - h_{0,5}}{h_{0,4} - h_{0,5,is}}. \tag{1.42}$$

And for the outlet nozzle,

$$\eta_n = \frac{h_{0,5} - h_{0,6}}{h_{0,5} - h_{0,6,is}}. \tag{1.43}$$

The previous expressions can also be used to determine the bulk velocity at various locations inside a turbomachine considering 1D variable section areas and isentropic transformations. The mass flux conservation is expressed as $\dot{m} = \rho v_x S$ for a section area S. By combining the perfect gas law, the expression of the axial bulk velocity $v_x = \mathrm{Ma} \times c = \mathrm{Ma}(\gamma r T)^{1/2}$, and the stagnation to static temperature and pressure ratios (Eq. (1.37) and Eq. (1.38)), one obtains

$$\dot{m} = S\mathrm{Ma}P_0\left[\frac{\gamma}{rT_0}\right]^{1/2}\left[1 + \frac{\gamma - 1}{2}\mathrm{Ma}^2\right]^{\frac{-(\gamma+1)}{2(\gamma-1)}}. \tag{1.44}$$

From this equation, one can retrieve the axial velocity knowing the section area, and it is also possible to show that the peak of mass flow $\dot{m}$ per unit area S reaches a maximum for a Mach number of unity, a condition that is not met in a turbofan engine in any section due to the gas temperature dependency of the sound speed (see the flow quantities evaluated at the end of this chapter).

When combustion occurs (nonisentropic case), the stagnation temperature changes due to the heat addition of combustion and the previous expressions take the following form, where (1) refers

to the initial state and (2) to the final state. For the stagnation temperature ratio, one has

$$\frac{T_{0,2}}{T_{0,1}} = \left[\frac{1+\gamma \mathrm{Ma}_1^2}{1+\gamma \mathrm{Ma}_2^2}\left(\frac{\mathrm{Ma}_2}{\mathrm{Ma}_1}\right)\right]^2 \left(\frac{1+\frac{\gamma-1}{2}\mathrm{Ma}_2}{1+\frac{\gamma-1}{2}\mathrm{Ma}_1}\right). \tag{1.45}$$

For the pressure ratio, one has

$$\frac{P_{0,2}}{P_{0,1}} = \left[\frac{1+\gamma \mathrm{Ma}_1^2}{1+\gamma \mathrm{Ma}_2^2}\left(\frac{\mathrm{Ma}_2}{\mathrm{Ma}_1}\right)\right]^2 \left(\frac{1+\frac{\gamma-1}{2}\mathrm{Ma}_2}{1+\frac{\gamma-1}{2}\mathrm{Ma}_1}\right)^{\gamma/(\gamma-1)}. \tag{1.46}$$

Similar expressions can be obtained for the static temperature and pressure ratios. For the temperature ratio, one has

$$\frac{T_2}{T_1} = \left[\frac{1+\gamma \mathrm{Ma}_1^2}{1+\gamma \mathrm{Ma}_2^2}\left(\frac{\mathrm{Ma}_2}{\mathrm{Ma}_1}\right)\right]^2. \tag{1.47}$$

And for the pressure ratio, one obtains

$$\frac{P_2}{P_1} = \left[\frac{1+\gamma \mathrm{Ma}_1^2}{1+\gamma \mathrm{Ma}_2^2}\right]. \tag{1.48}$$

1.3.4 Components design, challenges, and future trends

In this section, some elements of component design are presented along with the challenges associated with those. Finally, future trends of turbofan engines are introduced. Each engine module (fan, compressor, combustor, and turbine) has its own design challenges, and the objective of this section is to briefly provide an overview of those.

The speed and the section area of the fan drive the thrust of the bypass stream. The design requirements are thus to enhance the fan surface area and to impart a high speed to this component. The challenges associated with those requirements are known. The increase of the fan thrust is limited by two factors: (i) the distance between the engine casing lower side and the tarmac of the airport (engine fan diameter) and (ii) the flow speed reached at the tips, at the highest radius of the fan blades, which should remain subsonic to avoid extra aerodynamic loading and unsteadiness on the blades. The compressor design requirement is to ensure the highest compression ratio possible in the minimum number of stages possible to minimize the weight of the engine. In practice, a fluid flows from the highest to the lowest pressure, when not subjected to external forces. In a compressor, the reverse is expected; one applies an external force to enable the flow through the compressor stage. Under certain circumstances, the unsteady flow on

the airfoils (boundary layer flow separation) can lead to stall when the force applied on the fluid reduces. If this effect is amplified and the forces applied to the fluid are further reduced, if the unsteadiness is too large, this local stall can lead to compressor surge where the imposed flow direction is reversed and engine power is lost. The combustor also has to face multiple challenges; the most important one is to create a localized flame without melting the walls of its ultraconfined environment. Other challenges related to the combustion chamber are described in the next sections. The turbine design requirement is to ensure efficient conversion of the translational kinetic energy to rotating kinetic energy to transmit the forces to the shaft in order to entrain the compressor. As the fluid in the turbine stages exits the combustion chamber, the hot gases induce challenges for the thermal resistance of the blades in terms of material and coating layers. The loading due to the aerodynamic forces is also a challenge for the design of the stages. Each blade/airfoil of the engine fan, compressor, or turbine stage (rotor or stator) has a specific profile, angle, and geometry to address these challenges and improve the efficiency of each module. It is also worthwhile to indicate that the way cooling is conducted (cooling flow, material coating, thermal protection systems, etc.) will affect the efficiency of the force transmitted between the flow and the rotating components.

In this section, some design criteria, elements of geometry, and guidelines are described for each module. There are various degrees of turbomachinery analyses distinguishable by their level of complexity. These analyses can be conducted theoretically, experimentally, or numerically. The first one consists of analyzing the different stages of the turbomachinery core with 0D approaches where each quantity/flow variable is approximated by one single number at each station number. This description is fundamental and has been carried out in the previous sections. A second approach relies on the description of the 2D mean flow quantities throughout the engines' stages. In that description, the flow velocity component in the radial direction (along the blade height) is neglected compared with the axial and tangential velocity components, and the flow is modeled or measured on a 2D cascade. This description relies on the velocity triangle upstream and downstream of each compressor or turbine stator and rotor. Additional theoretical analyses rely on the radial equilibrium assumption for turbomachines where the variation of the blade angle (twist) is taken into account. Finally, another approach is to take into account the full 3D module or component such as a compressor or turbine stator or rotor or a blade. It is straightforward to understand the advantages and the disadvantages of each method. The

0D approaches allow to describe a full engine system at various operating conditions in a rapid manner but provides only some bulk variables without detailed flowfield. The 3D approach contrarily allows to resolve the full 3D flowfield for a limited duration and spatial domain of the engine. The 2D approach is a trade-off between these two methods.

The turbofan engine represents a trade-off between the turbojet and the turboprop in terms of global efficiency. Indeed, the turbojet engine has a high jet velocity, superior to the flight velocity, to maximize the thermal efficiency but also has consequently a low propulsive efficiency. The turboprop reversely has a high propulsive efficiency because its jet speed (throughout the propeller) is of the order of the flight velocity. To maximize both the thermal and the propulsive efficiency and consequently reduce the thrust-specific consumption for long-distance transport, the turbofan jet and fan exhaust flow velocities are of similar magnitudes. The idea beyond the turbofan is to create the thrust by accelerating a large amount of air a little bit. Future trends will then include higher bypass ratios and reduced core size of the turbomachinery, in order to reach better overall efficiencies, with less engine weight and reduced global size, along with less fan and jet noise. To do so, the geared turbofan engines are designed to allow the fan and the low pressure compressor/turbine shaft to rotate at different speeds. The lower fan speed indeed enables higher bypass ratios, leading to reduced specific fuel consumption and also reduced fan noise.

2 Combustor role, requirements, and environment

2.1 Overall view

In this section, some elements of thermodynamics are again given in order to briefly recall the essential role of the combustor within the thermodynamic cycle and the principle of the gas turbine engine. The starting point is the first principle of thermodynamics, which states that the total energy per unit mass (including internal, kinetic, and potential energies) variation $e_2 - e_1$ of a given system from one state to a second state is equal to the sum of the work done w and heat q received by the working fluid per unit mass. The second thermodynamic principle states that the entropy variation per unit mass $s_2 - s_1$ between two states is equal to the sum of the entropy variation resulting from external source additions $\delta_e S$ and from internal source additions $\delta_i S$. When the latter is zero, the transformation is reversible. The thermodynamic

principles presented here and in the previous section are key for the derivation of the equations of state for perfect gases. In addition, those relations are the basic elements to describe the gas turbine engine components' efficiencies when assuming an isentropic state.

Gas turbines and jet engines have similarities to some internal combustion engines. In an internal engine, the working fluid is subject to a series of transformations, i.e., an isentropic compression step, where the working fluid pressure increases, a constant-pressure combustion, where heat is added to the working fluid, an isentropic expansion, where the pressure decreases and the heat gained by the working fluid is converted to mechanical energy, and an exhaust step, where the burned gases are rejected. In a gas turbine, the process is similar except that those steps are distributed spatially and not temporally. Indeed, in an internal combustion engine, the steps occur at one location, while in a gas turbine, these steps occur at different locations on the working fluid flow path.

In a gas turbine engine, the description of the working fluid state is performed along the flow path at selected stations numbered, such as presented in figure 1.3. At those locations, the properties such as stagnation pressure, temperature, and Mach numbers are evaluated to determine characteristics such as efficiencies or variable ratios across components such as the LPC/HPC stages, the combustor, and the HPT/LPT stages. In figures 1.8 and 1.9, the Brayton cycle is represented, where the numbers correspond to the station numbers relevant to a gas turbine, including the postcombustion chamber, while these are not included in figure 1.3 because there is no postcombustion on turbofan.

The role of the combustor is to convert energy. Chemical energy is first converted into thermal energy to increase the temperature from the outlet compressor, and the thermal energy is then converted into kinetic energy to increase the velocity at the inlet of the turbine. This overall process occurs at constant pressure when not considering the details of the combustor's swirling flowfield. In general, the flowfield (in the combustion chamber or elsewhere) can indeed be affected by the effects of transients due to changes of altitude or variations from perturbation of the upstream gas turbine fluid state. The temperatures at the stations numbered 3, 4, and 5 in figure 1.3 have an important role in the turbine components' efficiencies and in the thermal efficiency of the gas turbine engine.

The conversion of chemical energy into thermal energy can be achieved through multiple different combustion modes. These modes are the premixed, stratified premixed, partially premixed,

and nonpremixed combustion regimes, and occur in the gas phase. The premixed mode involves the perfect mixing of fuel and air, so that each given fluid control volume upstream of the flame has the same equivalence ratio, see the reviews on premixed combustion by Huang and Yang [22] and Candel et al. [23] on swirling flames and Taamallah et al. [24], Rashwan et al. [25] focusing on hydrogen combustion and the monograph of Dunn-Rankin and Therkelsen [26]. In practice, the equivalence ratio can slightly vary due to effects of convection and diffusion of the multi-component mixture. The stratified premixed regime consists of a flow where the equivalence ratio is not constant as in the premixed case and where multiple homogeneous zones of equivalence ratio are seen by the flame front. The partially premixed case characterizes regimes where both nonpremixed and premixed burning occur or where the premixture equivalence ratio is time- and space-dependent. The nonpremixed combustion or diffusion flame regime is observed when the flame is generated by two distinct streams of fuel and air so that a given fluid control volume upstream of the flame is located either in the fuel or the air stream. Those regimes are at work in different injector/combustor configurations. The major types of combustors will be described next.

2.2 Design and requirements

The design space for an injector is at the intersection of combustion physics, combustor constraints, and jet engine operating conditions. Each of these aspects has to be described in detail to determine a given design space. A summary of the design space for the lean fully premixed (LFP) injector presented in Chapter 7 is given in Fig. 1.10. Each main element of this schematic is expanded in Fig. 1.11. The combustor has to fulfill multiple requirements. Combustor architectures have different behavior with respect to those requirements. The combustor has to satisfy a set of constraints to ensure safe functioning while minimizing the environmental impact and optimizing efficiencies of the jet engine.

The jet engine operating conditions are intrinsically linked to the performance requirements for a given aircraft at the considered operating point. In general the design point corresponds to cruise conditions. The jet engine design procedure is a complex procedure and its details are beyond the scope of the present book. The design of an injector/combustor can be enabled by assuming a defined aircraft and engine characteristics from literature allowing to develop the main steps of a methodology for design. As seen in a previous section, the ISA is the reference

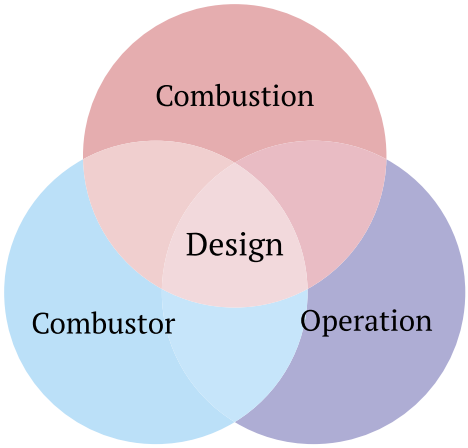

Figure 1.10 Design space of next-generation combustors. The design is at the intersection of combustion physics, combustor requirements, and the operating envelope.

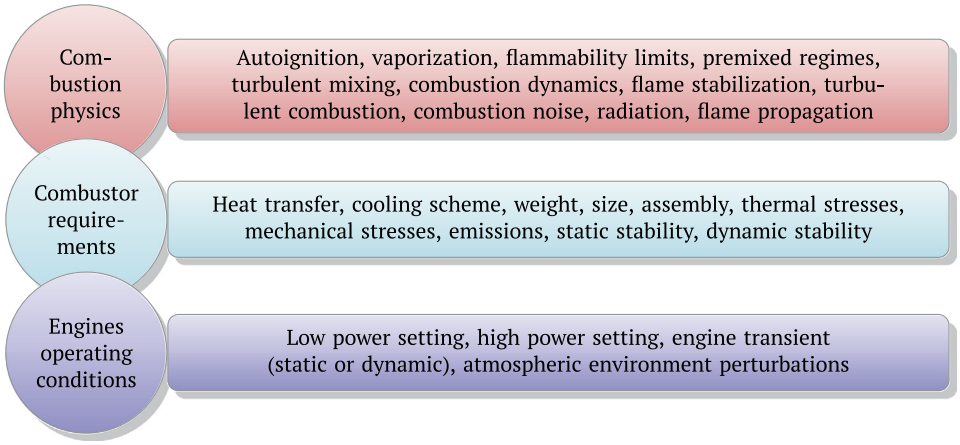

Figure 1.11 Main elements of the design components. Each component contains various elements. The present list is not exhaustive.

model for the evolution of pressure, temperature, and density of the Earth's atmosphere and it is used in aeronautics to determine the jet engine upstream conditions along the flight path.

At certain operating conditions, such as take-off, the gaseous fresh mixture can be in the critical thermodynamic regime where the pressure and the temperature are above the critical point. At this critical point, the thermodynamic properties and the transport coefficients correspond to a supercritical fluid. This regime has been studied in applications such as liquid rocket engines,

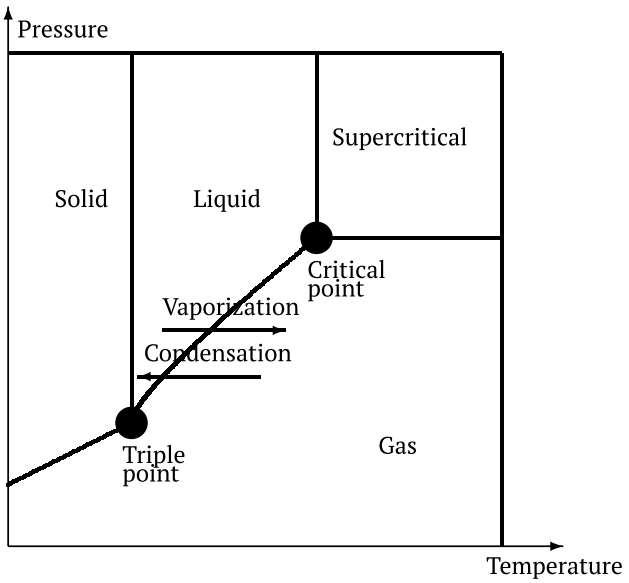

Figure 1.12 Pressure–temperature phase diagram. As the pressure and temperature change, the material changes state.

see Oefelein and Yang [27], where the pressure and temperature reached require the modeling to be appropriate to this supercritical regime. This is also the case for internal combustion engine operation at high pressures, see Ma et al. [28]. For gas turbine engines, the treatment of the fluid as supercritical is justified due to the high OPR jet engines trend targeted by multiple international agencies and jet engine manufacturers. Near the critical point, fluid mixture properties exhibit liquid-like densities and gas-like diffusivities. Surface tension and enthalpy of vaporization approach zero, and the isothermal compressibility and the specific heat increase significantly.

In Fig. 1.12, an illustrative phase diagram is sketched. This diagram indicates the phase changes between solid, gas, and liquid states along with the critical point where the gas and fluid states become not distinct and thus in the supercritical state. It is important to point out that depending on the operating conditions and thus on the ISA, the local fluid state (fuel and air) inside the injector will vary accordingly. It is expected that for a high OPR combustor, at take-off conditions, the fresh gases will be in the supercritical fluid regime while at cruise conditions (at high altitude, low local ambient pressure P_3 near 15 atm) they will not be in that particular regime.

Table 1.3 Supercritical pressure and temperature for various substances.

	Pressure [atm]	Temperature [K]
Air	37.4	133
O_2	49.4	155
N_2	34	126
H_2	12.8	33
CH_4	45.8	191
Kerosene	21.4	662
H_2O	217.7	647
CO_2	72.8	304

Tab. 1.3 lists the critical pressure and temperature of multiple species, fuels, and substances. Beyond those values, the fluid is expected to be in the supercritical regime.

Combustion physics is one component of the design space represented in Fig. 1.10. It broadly encompasses many aspects, such as autoignition, chemical kinetics, vaporization, flammability limits, flame propagation, turbulent mixing, combustion instability, flashback, blowout, turbulent combustion, and radiation. One of the most important aspects of premixed combustion is the balance between the flame surface speed, the flow speed, and the burning velocity. Indeed, this balance drives the flame surface position within the combustor and subsequently impacts static stability. In addition, this balance includes implicitly most physical processes at work. The flow processes determine the flow velocity vector, while the chemical ones determine the flame speed. The flame speed contains two terms: the thermal diffusion term and the reaction term. It is worthwhile to recall that the flame speed reduces with increasing operating pressure and increases with increasing upstream unburned gas temperature. Recently, the link between the flame speed and the flow speed has been studied, and the results indicate that the instantaneous flame surface speed is controlled predominantly by flow effects, see Palies [29]. It was further shown that the flame stabilizes in regions of balance between flow and flame speeds or regions of approximate balance between flow fluctuations and flame speeds. For these reasons, particular attention needs to be paid to the resolution of the quantities of the flame surface speed, flow speed, and burning velocity budget in the numerical simulations. Another important aspect of combustion physics relevant to the design of fully premixed injec-

tors is the autoignition phenomenon. This phenomenon occurs when the following three required elements are at work together: presence of heat, oxidizer, and fuel, with the appropriate levels to trigger autoignition. Autoignition requires a mixture of oxidizer and fuel within the flammability limits and with a local temperature above a threshold. The lower and upper flammability limits are function of the pressure, temperature and the fuel. In addition, the flow strains can induce local extinction of the premixed flame or inhibit local autoignition. These are important elements with respect to injector design.

The second component of the design space represented in Fig. 1.10 consists of the combustor requirements. Pollutant generation is strongly related to the combustion mode (premixed, nonpremixed, partially premixed, etc.), how the flame is stabilized, and which fuel is used in the combustor. Static and dynamic stability are also closely linked to the combustor through the boundary conditions, the flowfield, and the flame region, which are highly dependent on the design of the injector and the swirler. The role of the combustor is to provide energy, i.e., chemical energy converted first into thermal energy to increase the temperature from the compressor outlet and then into kinetic energy to raise the velocity at the inlet of the turbine. The conversion of chemical energy to thermal energy can be achieved through multiple different combustion modes (premixed, stratified premixed, partially premixed, and nonpremixed combustion modes), occurring in the gas phase. The premixed mode involves the perfect mixing of the fuel and the air so that each given fluid control volume upstream of the flame has nearly the same equivalence ratio, see the reviews on premixed combustion by Huang and Yang [22] and Candel et al. [23] on swirling flames. In practice, the equivalence ratio can slightly vary due to effects of convection and diffusion of the species. The stratified premixed regime involves a flow where the equivalence ratio is not constant as in the premixed case and where multiple homogeneous zones of equivalence ratio are seen by the flame front. The partially premixed case characterizes regimes where both nonpremixed and premixed burning occurs. The nonpremixed combustion or diffusion flame regime is observed when the flame is generated by two distinct streams of fuel and air so that a given fluid control volume upstream of the flame is located either in the fuel or in the air stream until these streams mix up to the stoichiometric line. Laboratory-scale and jet engine combustors operate in these regimes, depending on the injector/combustor configurations.

The combustor must satisfy multiple requirements. The relevant requirements to the fully premixed design are (i) sustain

static stability (the flame must be sustained over the flight envelope); (ii) avoid blowout (the combustor must be able to function in the lean combustion regimes); (iii) allow reignition (ignition must be enabled in case of flameout); (iv) limit pollutant emissions; (v) mitigate dynamic stability (combustion instabilities have to be suppressed); and (vi) prevent fuel deposit.

The third component of the design space represented in Fig. 1.10 consists of the jet engine operating conditions. They are intrinsically linked to the performance requirements for a given aircraft at the considered operating point. In general, the design operating point corresponds to cruise conditions. The take-off conditions can be selected to evaluate static stability challenges (flashback, flame stabilization) at these critical conditions on the flight envelope of commercial aircraft. It is also assumed that any LFP operating at cruise conditions will have reduced pollutant emissions compared with nonpremixed flames. Aircraft and engine characteristics from literature can be used to develop the main steps of a methodology for injector design. As seen earlier in this chapter, the ISA is the reference model for the evolution of pressure, temperature, and density of the Earth's atmosphere and it is used in aeronautics to determine the jet engine upstream conditions along the flight path. The index 0 marks the station upstream of the fan, while station 3 refers to the upstream condition of the combustor (or compressor outlet without taking into account the diffuser effect). The conditions are usually given for the total variables and not the static ones. As the stagnation values are higher than the static ones, they can be selected for design purposes providing design margins. In addition, by assuming the thrust and the thrust-specific fuel consumption of existing engines from public domain literature data, one can estimate the mass flow of fuel.

2.3 Combustor, injector, and swirler designs

2.3.1 Gas turbine combustor requirements and combustion modes

It is important to recall that swirling flames are located and stabilized in real combustors at various operating conditions, including high pressures and temperatures. Inside the combustor, the conversion of chemical energy to thermal energy can be achieved through different combustion modes. Those modes are at work in different injector/combustor configurations. Among them, three architectures are mostly studied and developed, see Tacina [30]: the lean direct injection (LDI), lean premixed/prevaporized (LPP), and RQL combustion systems. The LDI concept directly injects the fuel (liquid or gaseous) into the reaction zones. The LPP combus-

Table 1.4 Comparison of combustor types: LDI, LPP, and RQL.

Combustor	LDI	LPP	RQL
Principle	Direct fuel injection	Premixing prevaporizing injection	Sequenced combustion zones
Manufacturer	Rolls-Royce	CFM	Pratt and Whitney
Model	TrentXWB	LEAP	PW1000 GTF
References	Buelow et al. [31]	Dhanuka et al. [32]	Sen et al. [33]

tor involves a mode where liquid fuel is mixed and vaporized prior to combustion. The RQL has three distinct combustor regions, i.e., the front one, where the rich combustion zone limits the formation of NO_x, the centered one, where additional air quenches the flame and reduces the equivalence ratio, allowing a lean combustion zone minimizing the thermal NO_x in the downstream location of the combustor (third region of the combustor). The three types of combustors are listed in Table 1.4 along with the engines that use those.

The combustor has to satisfy the following requirements while ensuring its function during operation:

- limit weight: The combustor must remain compact to limit the weight and subsequently the size of the overall core.
- ensure proper pattern factor: The temperature profiles at the inlet of the turbine must be uniform.
- maintain static stability: The flame must be maintained over the flight envelope.
- avoid blowout: The combustor must be able to function in lean combustion regimes.
- allow reignition: Ignition must be enabled in case of flameout.
- keep cool walls: Combustor walls must be cooled.
- limit pollutant emissions.
- limit noise emission.
- mitigate dynamic stability: Combustion instabilities have to be suppressed or controlled.

The previously presented types of combustor have different behavior with respect to these requirements. To summarize this section, the combustor has to satisfy a set of constraints to ensure a safe operation while minimizing the environmental impact and optimizing efficiencies of the jet engine.

2.3.2 Combustor physics

The role of the combustor has been introduced in the previous section. In this section, the focus is on the physical mechanisms underlying combustor technologies, which have been examined by Lefebvre [34]. One key aspect of combustor physics, discussed in Lieuwen [35], is stability, which is split into static and dynamic stability. Static stability includes flame stabilization, flashback, and blowout phenomena. In addition, blowout and ignition are linked because when blowout occurs, reignition is required. Static stability refers to the capability of maintaining the flame in the combustion chamber without blowout. Flame stabilization or static stability in combustors is a key element of a successful combustor design. Figure 1.13 shows flame stabilization at various conditions. When the combustion region is not stabilized and blowout occurs (for example due to the rapid decrease of the fuel mass flow following a sudden deceleration), the flame has to be reignited to avoid loss of power. This affects the operating envelope of the system and therefore the operability and performances of the engine. It is therefore important to understand the mechanisms by which the flame blows out and the fundamental mechanisms driving the ignition process to respectively avoid and mitigate blowout and ensure reignition. Also, flame flashback inside the injector can lead to detrimental effects on the metal components due to unexpected sudden heat fluxes.

Flashback usually occurs when the flame propagates towards the upstream fresh gases at a speed higher than the incoming flow speed. The articles of Caffo and Padovani [37] and Plee and Mellor [38] have reviewed flashback mechanisms. In Sommerer et al. [39], fundamentals mechanisms leading to flashback were also studied and briefly reviewed. The recent monograph of Benim and Syed [40] provides an overall description of the mechanisms of flashback in premixed combustion systems. Flashback of swirling flames has received significant attention in the literature. The phenomenon has been studied with simultaneous high speed laser diagnostics (PLIF and PIV) by Konle et al. [41] and Konle and Sattelmayer [42] for confined swirling flows. The authors identified the interaction of heat release by chemical reactions and flow turbulence as the main contributors to flame transition to flashback. Flashback has also been investigated by Heeger et al. [43] using time-correlated, simultaneously acquired PIV, OH-PLIF, and chemiluminescence data at several kHz acquisition rates. It was observed that flashback in this configuration was often associated with negative axial velocities beneath the flame base tip. The role of the wall's boundary layer low velocity region has been recognized as a significant contributor to the upstream flame propa-

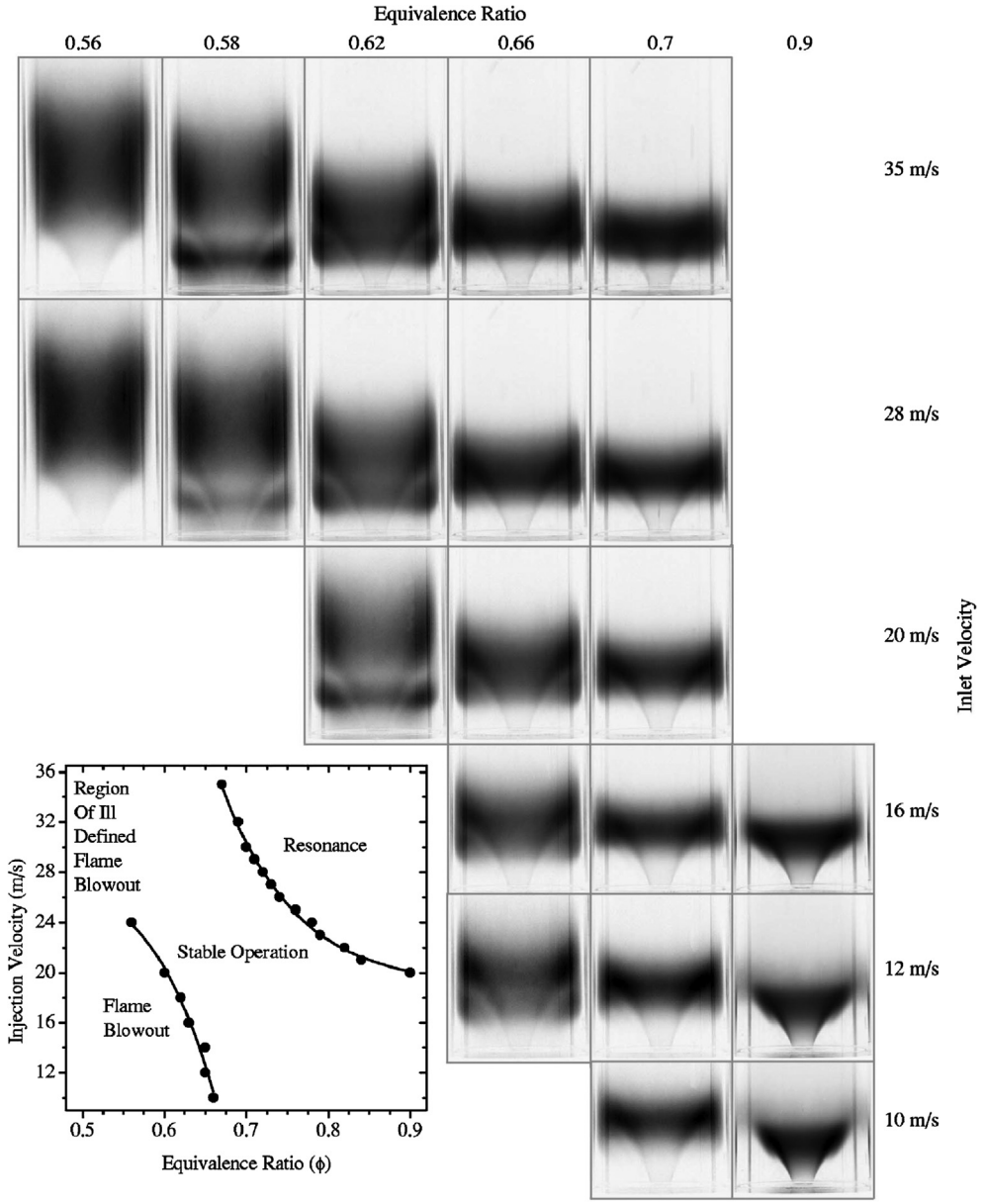

Figure 1.13 Operating envelope for a lab-scale combustor. Operating envelope for a combustor when fueled on methane–air mixtures, with an inset plot showing the conditions leading to flame blowout or audible resonance. The matrix of images shows a sample of flames observed over a range of equivalence ratios varying horizontally and inlet velocities varying vertically. Each image has been converted to grayscale, inverted, and individually scaled to highlight flame structure. Source: Figure taken from Williams et al. [36].

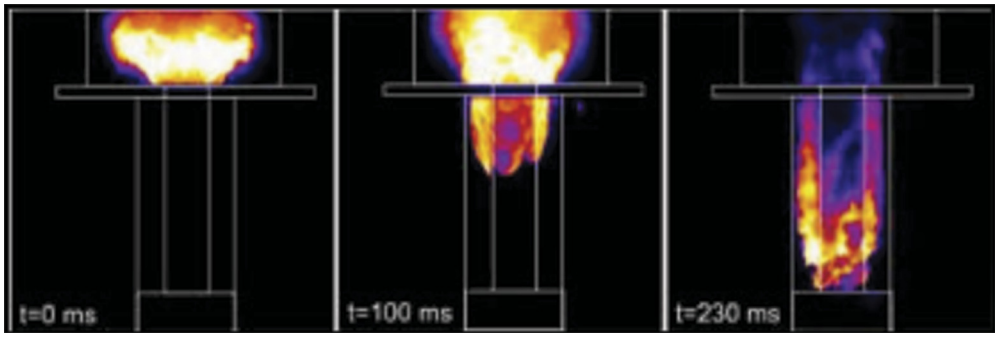

Figure 1.14 Flashback transient sequence. Time sequence of flame luminosity during flashback of a methane–hydrogen swirl flame. Source: Figure reproduced with permission from authors Ebi and Clemens [47].

gation of premixed flames and was initially studied by Kurdyumov et al. [44]. This aspect was also studied by Kurdyumov et al. [45] analytically and experimentally considering the propagation in a duct. The role of the wall boundary layer was investigated in Eichler and Sattelmayer [46] for methane–hydrogen–air premixtures. It was observed that the turbulent transport inside the boundary layer considerably increased the flashback propensity. Recently, Ebi and Clemens [47] experimentally investigated the upstream flame propagation during boundary layer flashback of swirl flames. The study focused on lean premixed methane–hydrogen–air flames in a model combustor featuring a swirler and a center bluff-body and reported detailed velocity measurements during the flashback process. Figure 1.14 depicts a flashback transient sequence.

The reviews of Plee and Mellor [48] and Shanbhogue et al. [49] focused on blowout and blowoff but not specifically for swirling flames. Blowout of swirling flames has been investigated experimentally with high speed video and OH filtering by Muruganandam et al. [50], Muruganandam and Seitzman [51], where the blowout events preceding the total extinction of the flame in the gas turbine model combustor were linked to the presence of cold reactant in the inner recirculation zone. Stöhr et al. [52] investigated partially premixed swirling flames close to the lean blowout limit using chemiluminescence imaging, stereo-PIV, and OH-PLIF high speed measurements. Flame stabilization occurred in two regions, i.e., the helical region along the PVC on the inner shear layer and at the flame base. The levels of strain rate influenced the zone where the reaction took place. For example, in the maximum strain regions like the flame base, the flame was not robustly stabilized. It was concluded that the flowfield modification

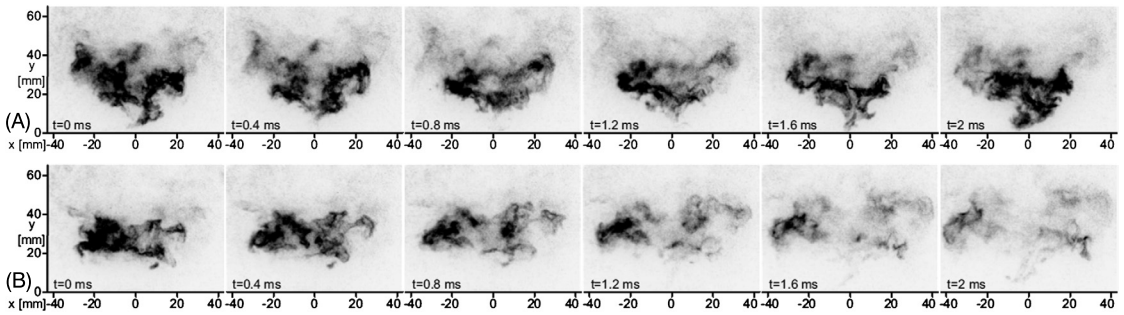

Figure 1.15 Lean blowout sequence. Time sequence of flame chemiluminescence during blowout of a swirling flame. (A) Statistically stable combustion. (B) Transient to blowoff. Source: Figure taken from Stöhr et al. [52].

at the flame base could shift the lean blowout limit lower. This article demonstrated the role of the local high strain rates as a local stage to blowout. An illustration of lean blowout on a swirling premixed flame is given in Fig. 1.15, taken from Stöhr et al. [52]. In the article of Cavaliere et al. [53], premixed, diffusion, and spray flames were experimentally studied at conditions near blowout. It was shown that the premixed flame changed shape prior to blowout, and the diffusion flame exhibited holes in the flame front, occurring at higher frequencies on approaching blowout. The diffusion and spray flames showed randomly occurring lift-off events due to localized extinction. The lift-off height and their occurrence were characterized and a Damköhler number collapsed the blow-off velocity data for all flames with reasonable accuracy. The work of De Giorgi et al. [54] made use of a high speed camera to characterize the blowout limits by varying the fuel/air ratio of a liquid-fueled gas turbine combustor operating in diffusion flame mode. Wavelet-based analysis of flame images was used to investigate local unsteadiness in the flame area. In Ganji and Ebrahimi [55], the authors investigated with numerical simulations blowout, flashback, and flame position. Different equivalence ratios were studied and thermal coupling of the reacting flow with the walls of the combustor was taken into account. In Sigfrid et al. [56], the temperature of the gas was shown to affect the stability limits at blowout in a dry low emission gas turbine. In Santhosh and Basu [57], the partially premixed swirling flame was shown to blow out due to excessive straining and due to entrainment of large amounts of oxidizer due to partial premixing. The blowout phenomenon was studied by increasing the swirling flow rotation from zero to high values. It was shown to have a strong effect on the flame shape. In Muruganandam and Seitzman [58], the authors investigated extinction–reignition events occurring in

swirl-stabilized combustors and analyzed the interaction of these precursor events interacting with the double helical mode of the vortex breakdown leading to blowout. Numerical simulation has also been used to capture blowout phenomena and describe its physical processes. In Esclapez et al. [59,60], the authors investigated with two-phase flow large eddy simulation the blowout phenomenon sensitivity to different fuels. Tyliszczak et al. [61], Zhang and Mastorakos [62], Giusti et al. [63], Giusti and Mastorakos [64] studied the blowout phenomena initially observed by Cavaliere et al. [53] with numerical simulations of the diffusion and spray flames. Significant differences between experimental measurements and the predictions with numerical simulations were seen.

A description of ignition of reacting flows is now given. The fundamental principle is that an energy source initiates the combustion reactions of the mixed reacting species through heat transfer and species/radical formation. Significant challenges exist in achieving that objective in combustion devices for a wide range of operating conditions because of the complexity of the physics associated with the transfer of energy and species or radicals between the igniter and the flowfield. As a consequence, there is a need for analysis and modeling of ignition processes with respect to real combustors. In the present section, a brief presentation of the key known ignition processes and mechanisms that initiate chemical reactions within a flow with fuel and air is given. Specifically, the role of spark, laser, and plasma ignition is described. Continuous combustion systems such as swirl-stabilized and bluff-body-stabilized systems induce a recirculation zone of hot gases producing the heat source of the upstream fresh reactants, see Lefebvre [34], Shanbhogue et al. [65], Huang and Yang [22] and favorable fluid velocity regions for flame anchoring, see the recent description by Palies [29]. While these methods for stabilization are robust, they need an initial start and can suffer from blowout phenomena along the flight envelope. Continuous systems for flame stabilization need an external igniter after blowout, or to start the engine. The three main ones are now detailed. Spark ignition involves an igniter located within the combustor that will create a local energy source. This is achieved by imposing an electrical current between two electrodes. This induces a local energy discharge and a local ionized gas with high local thermodynamic temperature, see Lacaze et al. [66], Maly and Vogel [67] that will be convected by the gas flow, see Swett Jr [68]. As this spark kernel is created, it propagates and ignites the combustor fresh gases, see Kravchik and Sher [69]. One important aspect is that the spark kernel has to cross a region of appropriate FAR in order to initiate

and sustain combustion. This is a difficult task for RQL combustors but an easier task for premixed combustion. Spark igniters are not expensive but suffer from a fixed location in a combustor and therefore can result in nonignition in some situations. Depending on the combustion mode (premixed versus nonpremixed), the ignition has different challenges. For example, for a diffusion flame, there is a limited zone where the flame can be ignited, contrarily to a fully premixed flow. Laser ignition involves using laser beams to induce a local increase of temperature that will initiate combustion. Laser ignition is more complex to implement but has the potential to be oriented in the combustion chamber to focus on different spatial locations so that energy addition occurs in favorable locations. Plasma discharge induces ignition in a similar manner to the spark ignition in that the plasma ionized gas created (by a current between two electrodes) impacts the local flowfield adding heat and chemical radicals and allowing potential ignition, see Grisch et al. [70]. The application of plasma in combustion has recently been reviewed, see Ju and Sun [71], Starikovskiy and Aleksandrov [72], including its application in ignition in combustors.

The mechanisms of ignition have been divided into the following scenarios by Poinsot [74]: an energy deposition model, see Von Elbe and Lewis [75]; the effects of ionized gas on electron temperature and radical species created initiating combustion, see Starikovskiy and Aleksandrov [72], Stancu et al. [76]; the induced temperature by the pressure wave formed by the local spark, see Liu and Zhang [77], Freeman and Craggs [78]; and the presence of local hot surfaces, see Shepherd et al. [79]. The first type of ignition mechanisms is called the energy deposition model and is the result of a spark igniter or a laser, see Lacaze [80]. The process is described by Lacaze [80] in four steps. The first is the prebreakdown phase (0 to 1 ns), where a weak current is established between the electrodes and the gas is qualified as nonequilibrium cold plasma. Breakdown (1 to 30 ns) follows, where current intensity increases and the number of electron collisions increases. At the end of this phase, the gas is a hot plasma and the associated temperature rise generates a strong wave. The arc phase takes place between 30 ns and 1 μs and the now conducting gas from previous phases is subject to a current flow, see Lacaze [80], Ternel [81]. The high temperature and radical species created start initiating the combustion reactions. The glow phase (1 to 2 μs) is when the temperature decreases and most of the energy is deposited to sustain the developing flame kernel. The following influential parameters have been determined to influence spark ignition (as reviewed in Lacaze [80]): minimum ignition energy deposited, min-

imum radius of ignition, duration of deposition, and flow conditions (pressure, temperature, mixing, velocity, and local heat dissipation). A sequence of ignition (taken from Bourgouin et al. [73]) for a premixture is given in Fig. 1.16 which focuses on the "light-around" mechanisms that occur at engine start, ensuring flame spreading from one injector to the next, eventually leading to stabilized swirling flames on each injector of the laboratory-scale MICCA2-EM2C-Bourgouin combustor.

On the other hand, while the flame can be stabilized in the combustion chamber for certain operating conditions or during the design stage, dynamic stability can still be a challenge during final testing or at certain operating conditions. Dynamic stability occurs when the unsteady heat release of the combustion region couples to the acoustics of the combustor through different possible physical mechanisms. The study and the understanding of these fundamental mechanisms (reviewed in Chapter 5) are important in order to address this challenge. Dynamics stability corresponds to combustion instabilities and is the focus of Chapter 5.

2.3.3 Combustor design

The role of the combustor and the subsequent requirements have been presented in previous sections along with some elements of the state of the art in combustors physics. In the present section, the emphasis is on combustor design for gas turbine engine geometry.

Jet engine combustor geometries taken from patents will be depicted in Section 3 on combustor architectures. Several monographs have focused on the design of jet engines and aircraft propulsion. Among those books, Oates [19] describes in detail the aerothermodynamics of aircraft gas turbine engines, covering all aspects in a comprehensive manner. In [15], the overall principle of the jet engine is examined along with detailed component descriptions (including compressor, combustion chamber, turbine, and fuel system) with important descriptive and informative illustrations. Functioning (starting/ignition, performance) and maintenance of engines are also discussed. In Hünecke [82], the fundamentals of theory, design, and operation are treated in a compact manner, providing an overall view of the jet engine. The aerodynamic and thermodynamic design and performance of jet engines are treated by Cumpsty [83] in a comprehensive manner and include the analysis of a high bypass ratio turbofan engine for large aircraft such as the A380. Aircraft propulsion and gas turbine engine components are also presented comprehensively by El-Sayed [14]. Fundamentals of propulsion systems including jet engines

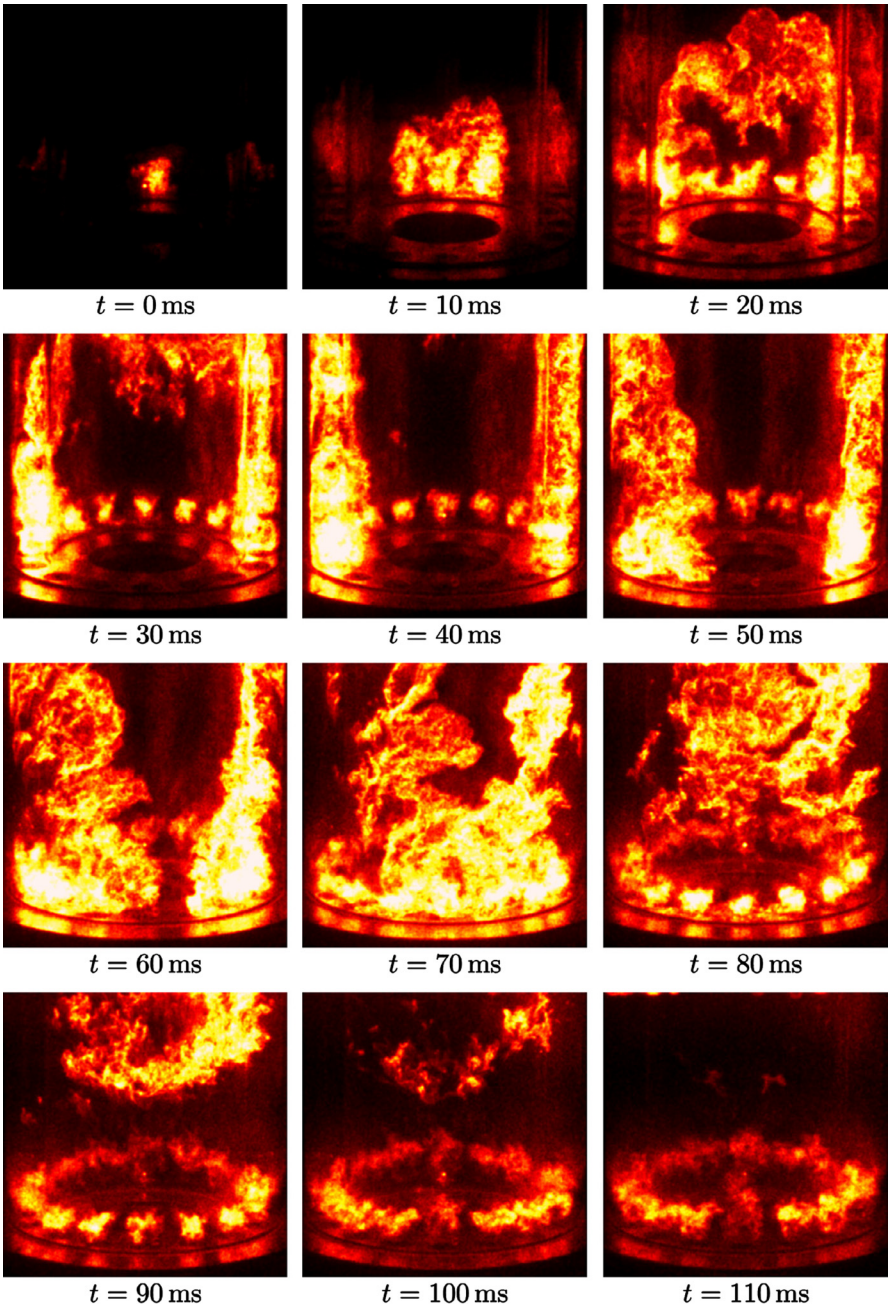

Figure 1.16 Sequence of transient ignition in the MICCA2-EM2C-Bourgouin combustor. Light-round sequence of annular chamber ignition. Source: Figure taken from Bourgouin et al. [73].

are investigated in the book of Hill and Peterson [18] along with the corresponding relevant equations. A dedicated monograph focusing on combustor design was written by Lefebvre and Ballal [84].

Combustion instability for propulsion and power generation has been considered in a series of edited books by the American Institute of Aeronautics and Astronautics (AIAA), see Anderson and Yang [85], Dranovsky [86], Lieuwen and Yang [87], Natanzon and Culick [88]. The edited book from the North Atlantic Treaty Organization (NATO) by Culick et al. [89] focused on combustion instabilities and their active control. More recently, researches on unsteady combustor physics have been presented in Lieuwen [35].

Combustor design relies heavily on numerical simulations, experimental measurements, and testing. Jet engine manufacturers deploy integrated approaches to accelerate the design cycle time and minimize costs. In these approaches, large data sets are generated and data analysis reduction methods, processing algorithms, and physical understanding are required to reach data-driven decisions. Such integrated approaches have been documented in the literature, see Anand et al. [90], James et al. [91] for Rolls-Royce, Mongia et al. [92], Mongia [93] for GE, McKinney et al. [94], Sen et al. [33], Ma et al. [95] for Pratt and Whitney, and Boudier et al. [96], Musaefendic et al. [97], Lacombe and Méry [98] for SAE. Current and future combustor design challenges and requirements have been discussed in Mongia [99], Liu et al. [100], with the emphasis on emission reductions.

2.3.4 Design of injector's swirler

Within the combustor, two key parts are the injector and the swirler(s) because of their role in static stability and overall flow features. Their design has received considerable attention in the literature. The injector role is to carry the fuel up to the combustion zone while satisfying the combustor design requirements previously presented. The swirlers have to ensure common roles among the different types of combustors: (i) induce mixing zone(s) of the continuously upcoming fresh gases (air and fuel) and (ii) create a hot and low speed flow region allowing flame stabilization.

In Figure 1.17, multiple geometries of swirlers are surveyed. Fig. 1.17B presents a type of axial swirler that consists of axial vanes located on a centerbody plus additional holes arranged along the ring for the passage of the liquid fuel and secondary air injections, see Han et al. [102]. The axial swirler of the lean direct injector from Tacina et al. [103] is displayed in Fig. 1.17C.

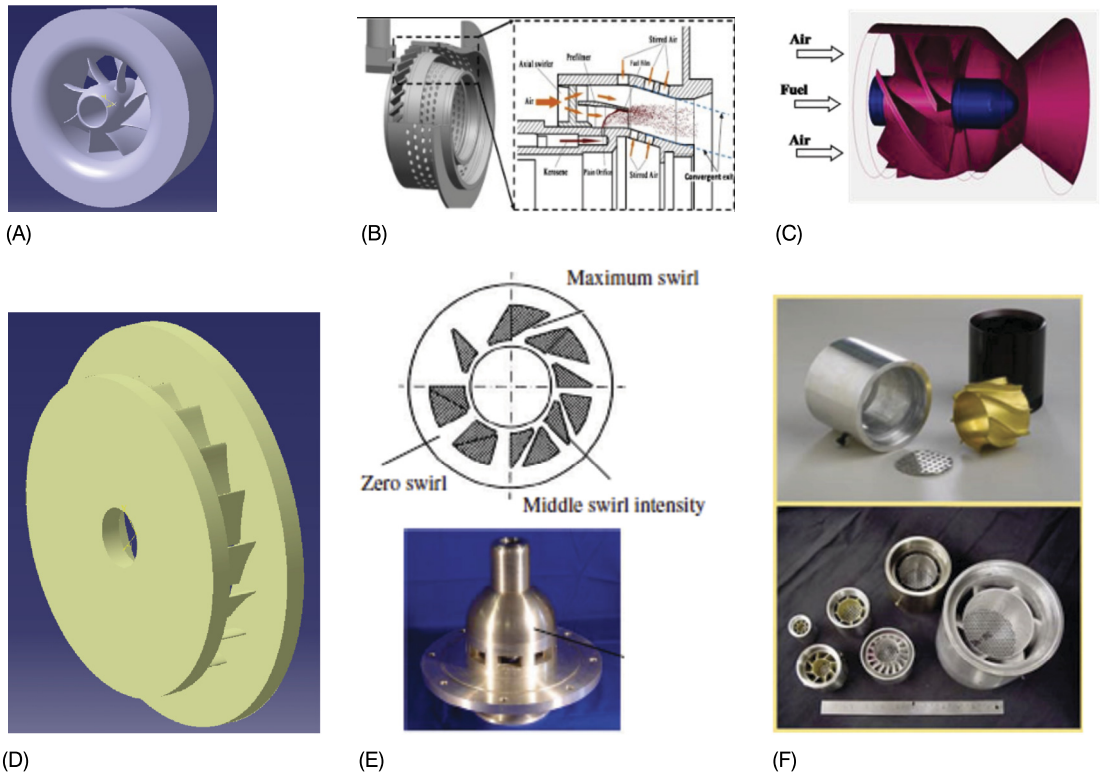

Figure 1.17 Review of swirler configurations. (A) MICCA1-EM2C-Palies axial swirler from Palies et al. [101]. (B) Teless axial swirler from Han et al. [102]. (C) LDI from Tacina et al. [103]. (D) MICCA1-EM2C-Palies radial swirler from Palies et al. [101]. (E) Movable-block swirler from Palm et al. [104]. (F) LSI axial swirler from Cheng et al. [105].

The movable-block swirler of Palm et al. [104] allowing variation of the swirl number is given in Fig. 1.17E. In Fig. 1.17F, multiple designs of the low swirl injector (LSI) of Cheng et al. [105] are given. The axial and radial swirlers of Palies et al. [101] are presented in Fig. 1.17A and D, respectively. The geometries of those swirlers were optimized to obtain a given value of the swirl number corresponding to a flow featuring a strong inner recirculation zone, as characterized by its reversal flow velocity. Another objective was to reduce the perturbation level produced downstream of the swirler due to the presence of the vanes. This was obtained by using NACA 8411 airfoil profiles to design the swirler's vanes. The result of the design process for the axial swirler was a swirler comprising eight periodically spaced vanes. The vanes were twisted, so that the angle at the trailing edge evolves linearly from 30 degrees at the hub to a value of 58 degrees at the vane tip. Twisting

was employed to impose the same rotation to the flow streamlines along the vane. In the absence of twist there would be regions near the vane tip in which the flow might not be deflected enough. The swirler was manufactured by fast prototyping of plastic material. The swirl number was determined experimentally by integrating the profiles of mean axial and azimuthal velocities measured at the injector outlet. The evolution angle at the trailing edge as a function of the radius is given by

$$\delta(r) = \delta_1 \left[1 + \alpha \left(\frac{r - r_1}{r_2 - r_1} \right)^m \right], \tag{1.49}$$

where $\alpha = 1$ and $m = 1$ are the coefficients of the profile and $\delta_1 = 30$ degrees is the vane angle at the trailing edge at the hub ($r = r_1$). The swirl number computed from the experimental measurement was 0.55.

The radial swirlers were made of 18 vanes periodically spaced at 20 degrees. These vanes were also made of NACA 8411 airfoil profiles. Two parameters characterized the radial geometry: the thickness of the circular inlet section of the swirler and the trailing edge angle of the vanes. Two swirlers were designed. The trailing edge angle was equal to 58 degrees for the first one and 72 degrees for the second one. The thickness of the circular inlet section was 6 mm for the first swirler and 4 mm for the second one. They provide two distinct swirl numbers, measured respectively at $S = 0.55$ and $S = 0.65$.

In many combustion systems, the flow is set in rotation with axial swirlers equipped with straight or twisted vanes. The design of the first type of swirler was carried out for example by Gupta et al. [106]. It is also worthwhile examining the latter case. The vane angle effect on the steady swirl number is now investigated, starting with the following expression:

$$S = \frac{\int_{r_1}^{r_2} \rho v_\theta v_z r^2 \, \mathrm{d}r}{r_2 \int_{r_1}^{r_2} (\rho v_z^2 + p) r \, \mathrm{d}r}. \tag{1.50}$$

One can assume that the axial velocity v_z is constant over the radius r and that the density of the fluid is also constant. Neglecting the pressure term p, one obtains

$$S = \frac{2}{r_2(r_2^2 - r_1^2)} \int_{r_1}^{r_2} \frac{v_\theta(r)}{v_z} r^2 \, \mathrm{d}r. \tag{1.51}$$

The ratio $v_\theta(r)/v_z$ can be directly linked to the angle $\delta(r)$ of the flow at the trailing edge of the vane of the swirler by $\tan \delta(r) = v_\theta(r)/v_z$.

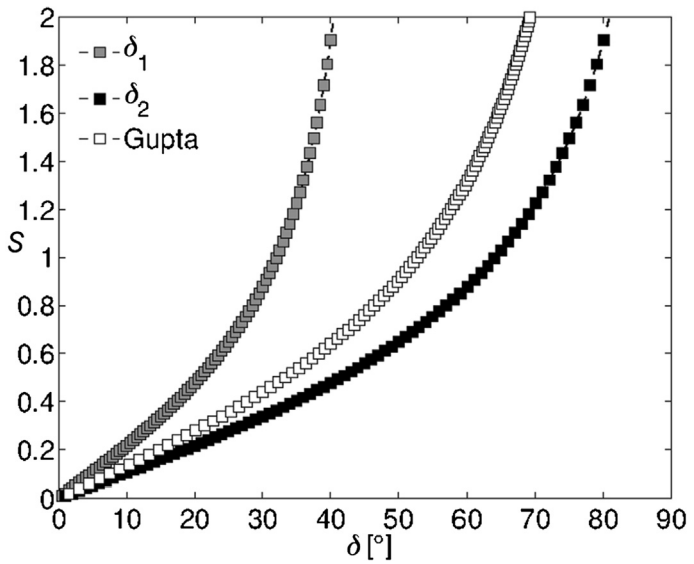

Figure 1.18 Swirl number evolution. The swirl number S obtained with Eq. (1.52) taking into account the radius dependency of the axial swirler as a function of the angle of vane $\delta(r)$. Data obtained theoretically are compared with expressions based on straight vanes assumptions.

This leads to the following expression:

$$S = \frac{2}{r_2(r_2^2 - r_1^2)} \int_{r_1}^{r_2} \tan\delta(r) r^2 \, \mathrm{d}r. \tag{1.52}$$

This expression reflects the effect of the dependency of the swirl number on the angle of the trailing edge of the vane.

When the velocity distribution is not known, it is possible to determine the level of swirl by specifying the angle distribution of the swirler vanes. This can be used in the swirler design process. The swirl number S defined by Eq. (1.52) can be numerically determined for a given $\delta(r)$ distribution. The choice was made for this distribution to use Eq. (1.49) for the design of the axial swirler. Substituting this expression in Eq. (1.52), one obtains results plotted in Fig. 1.18. The center curve corresponds to straight vane expressions, see Gupta et al. [106], in which $\delta(r)$ is a constant. The two other curves correspond to a preset value of the swirl number S and provide the inner and outer angles δ_1 and δ_2 which need to be specified to reach this number. These curves have been obtained by using $\alpha = 1$ and $m = 1$. For example, to obtain a swirl number of 0.6 at the swirler outlet, it is necessary to have $\delta_1 = 23.5$ degrees and $\delta_2 = 47.5$ degrees. To obtain a swirl number near 0.6 at the in-

jector outlet, additional constraints have to be taken into account, such as the effect of section area reductions or increases.

The sensitivity of the flowfield to swirler design is the topic of the article by Bourgouin et al. [107]. The study of two radial geometry swirlers showed that the induced different swirl numbers (0.84 for swirler 1 and 0.70 for swirler 2) strongly impact the subsequent flowfield while the swirler designs were slightly different: the section passage area (impacting the azimuthal velocity, higher for swirler 1) and swirler vane shape were different. It was shown with numerical simulations that with an increase of the swirl number, the internal recirculation zone expands in the radial direction. The frequency of the PVC was also increased, which was linked to the increase of the mean azimuthal velocity in this higher swirl number case. The amplitude of the PVC was larger but its modal shape was more concentrated than in the lower swirl number case.

The swirler and the injector geometries directly affect the turbulent combustion processes through the range of scales induced (from the largest turbulent/integral length scale to the smallest ones) and the subsequent turbulent cascade and unsteadiness impacting the combustion region. Some elements of turbulent combustion relevant to swirling flows will be reviewed next.

3 Combustor architectures

A standard combustor architecture is presented in Fig. 1.19. There are multiple geometrical elements sketched on this combustor.

Low emission combustors can be categorized into two categories: rich-burn and lean-burn combustor architectures. In addition, lean-burn combustors can be further distinguished into LDI and LPP combustor architectures. In both LPP and LDI, the entire combustor air mass flow, except for liner cooling flow, enters through the combustor upstream inlet so that combustion occurs at the lowest possible flame temperature without any additional dilution holes in the combustor walls. The LPP combustor architecture has been shown to have the lowest NO_x emissions compared with other existing architectures, but for future high OPR engines, the possibility of autoignition or flashback is a significant drawback. The LDI is different from the LPP because the fuel is injected directly into the flame zone, avoiding autoignition or flashback. As it is not premixed and prevaporized, high efficient atomization and uniform fast mixing are necessary so that the flame temperature is low and NO_x formation stays at low levels. Nevertheless, even lean-burn combustor architectures such as

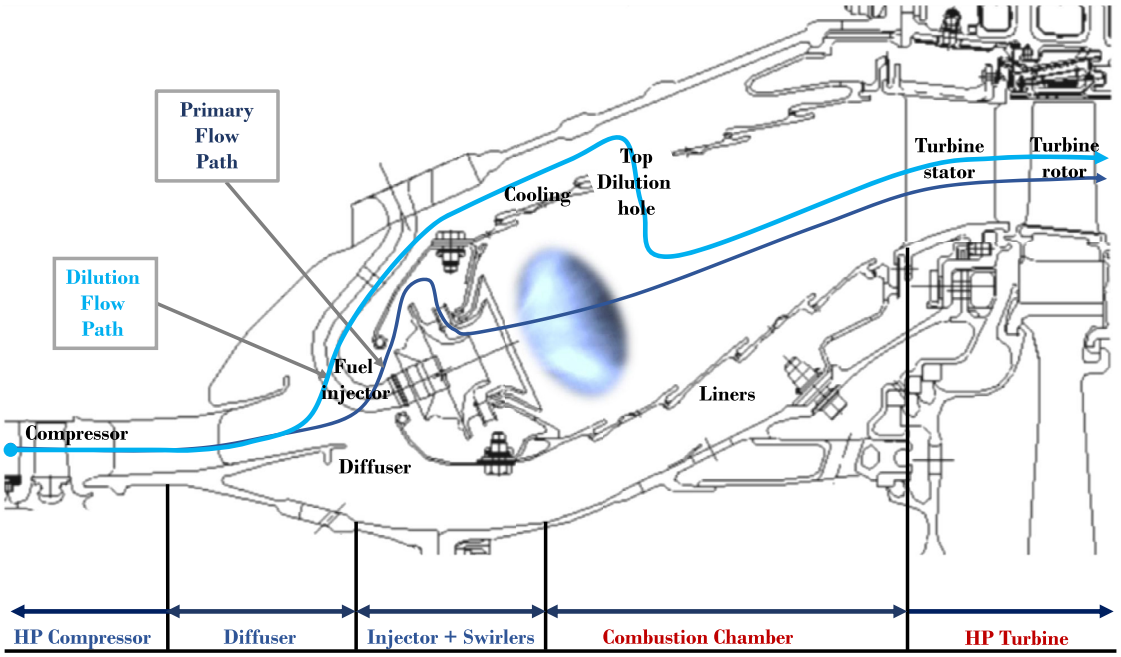

Figure 1.19 Combustor geometry. The main geometrical elements of the combustors are highlighted. Source: Adapted from CFM56 image. CFM56 engines are a product of CFM International, a 50/50 joint company between GE and SAE.

the LPP, operating at low equivalence ratio near the lean blowout limit with kerosene fuel, have temperatures that are too high with respect to the maximum possible temperature allowed by the turbine material, thus requiring some dilution air to reduce that temperature.

3.1 Rich-burn quick-quench lean-burn

The abbreviation RQL stands for rich-burn, quick-quench, lean-burn. In this section, some generalities are provided and elements of literature on this type of combustor. In the RQL combustor, as described in Chang and Holdeman [108], the air is mixed with the fuel into two stages. In the most upstream location of the combustor (the primary zone), an overall rich combustion zone is provided with excessive fuel that is burning in the downstream location of the combustor (the secondary zone) with the addition of oxidizer from the dilution jet air streams. The design intent of this combustor architecture is to reduce the temperature in the

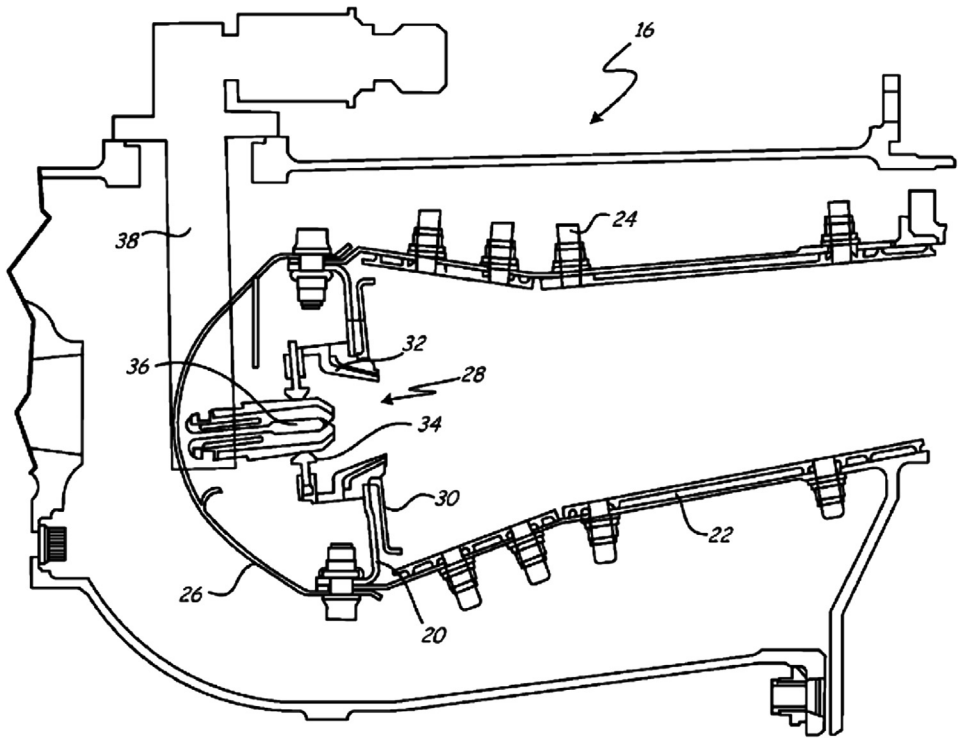

Figure 1.20 Jet engine RQL combustor geometry. Fuel nozzle guide plate design. The dilution holes are not sketched. Source: From US patent 8,689,563 and Low [110], Pratt and Whitney.

primary zone by operating at rich conditions, and thus limit the formation of NO_x, which is formed at high temperatures. One issue is that the primary zone operates in a diffusion flame regime where the reactions are occurring at the stoichiometry, where the associated temperature of this combustion regime is peaking and where maximum NO_x levels are reached, see Tacina [109]. While this is a severe issue, the main advantage of the RQL combustor is its relative dynamic stability with respect to combustion instability compared with other combustor architectures. As of today, a typical turbofan engine equipped with RQL combustor is the Geared Turbofan (PW 1000G GTF) of Pratt and Whitney, see McKinney et al. [94]. A jet engine RQL combustor geometry is provided in Fig. 1.20.

3.2 Lean direct injection

The abbreviation LDI stands for lean direct injection, a combustor architecture where the fuel is directly injected into the

combustion zone. LDI is also a technology aiming at reducing the emissions of NO_x in aircraft engine gas turbine combustors, see the LDI summary by Tacina [111]. Like all fuel-lean combustor concepts, the LDI architecture targets NO_x emission reductions by minimizing local flame temperatures because the thermal formation rate of NO_x is a direct function of flame temperature. Consequently, minimizing the local flame temperature induces the avoidance of local near-stoichiometric zones requiring efficient fuel atomization, fuel vaporization, and uniform fuel–air mixing. In order to achieve this objective, the injection system is made of multiple small fuel–air LDI injectors. Multi-point LDI is a combustor concept where multiple fuel injectors and fuel–air swirlers are used to rapidly and uniformly mix the fuel and the air so that ultralow levels of NO_x are produced. Each fuel injector has an air swirler associated with it for fuel–air mixing in order to create a small recirculation and burning zone. Various arrangements of these injectors have been studied to understand the impact on the NO_x levels for various realistic operating conditions: single-injector design and testing, seven-injector assembly by Hicks et al. [112], nine-injector assembly by Tacina et al. [113] and Hicks et al. [114], 12-injector assembly by Tacina et al. [115], and 25- and 36-injector assemblies by Tacina et al. [116]. The main disadvantages of the LDI systems are the limited compactness of the combustor, which may limit its implementation into future high pressure small core engines, and the high number of swirler units, increasing the engine cost. An example of LDI system is sketched in Fig. 1.21.

3.3 Lean premixed/prevaporized

The abbreviation LPP stands for lean premixed/prevaporized. It is accepted that NO_x is produced mainly by oxidation of nitrogen in the regions of high temperature that exist within the reaction zone and around large burning droplets. The LPP injector/combustor architecture attempts to reduce this issue by limiting the gas temperature. The LPP injector/combustor has been defined by the Lean Premixed/Prevaporized Combustion 1977 Cleveland Workshop, see the proceedings report edited by Lefebvre [117]. A key feature of the LPP concept is targeting complete vaporization of the fuel and complete mixing between the fuel and the air prior to combustion. By attempting to avoid droplet combustion and by operating the combustion zone at a lean equivalence ratio, NO_x emissions are reduced due to the low reaction temperature and “hot spots” are minimized in the combustion zone. In the report by Lefebvre [117], the authors identified several

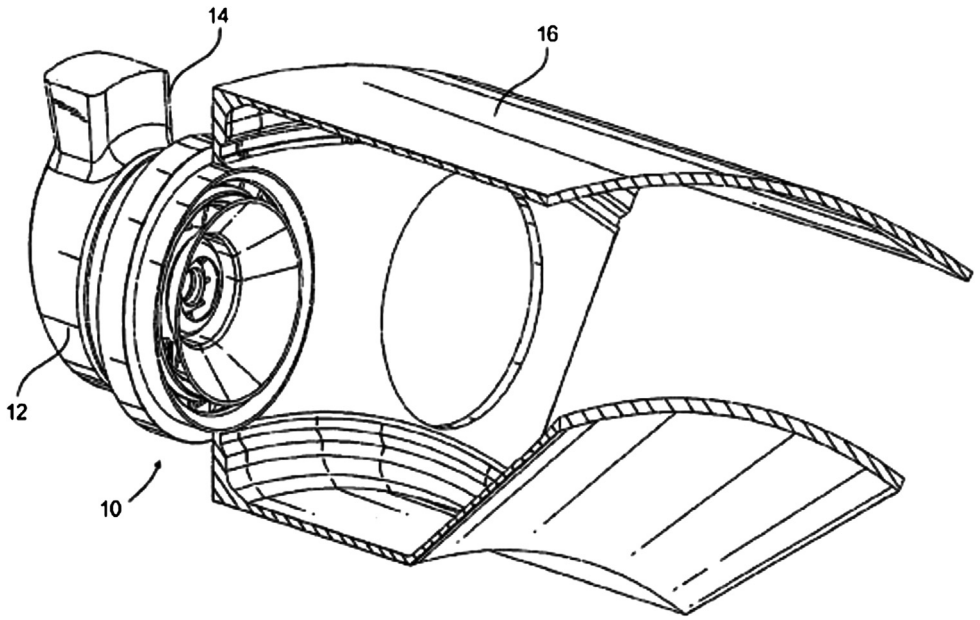

Figure 1.21 Jet engine LDI combustor geometry. LDI atomizer for gas turbine engines. Source: From US Patent 7,779,636 and Buelow et al. [31], Rolls-Royce.

challenges for LPP combustion: flameout, autoignition and flashback, altitude reignition, application of variable geometry, achieving satisfactory premixing and prevaporization, advanced control systems, and the impact of LPP burners on overall engine operation. An example of LPP system is given in Fig. 1.22.

3.4 Low swirl injector

The abbreviation LSI stands for low swirl injector. LSI is an ultralow emissions technology for gas turbines and industrial heaters, see the reference article of Cheng et al. [105] and Cheng et al. [119]. It uses an aerodynamic flame stabilization method developed for fundamental research on turbulent premixed combustion, see Cheng [120] and Chan et al. [121]. The specific flowfield and self-similarity features as well as the flame characteristics have been investigated by laser diagnostics. The LSI is another land-based gas turbine engine injector but not an aircraft engine injector. It has been developed for industrial and domestic heaters and electricity generation systems, such as for gas turbine engines. Lean premixed combustion involves burning gaseous fuels mixed with air at low equivalence ratio. This method allows to lower

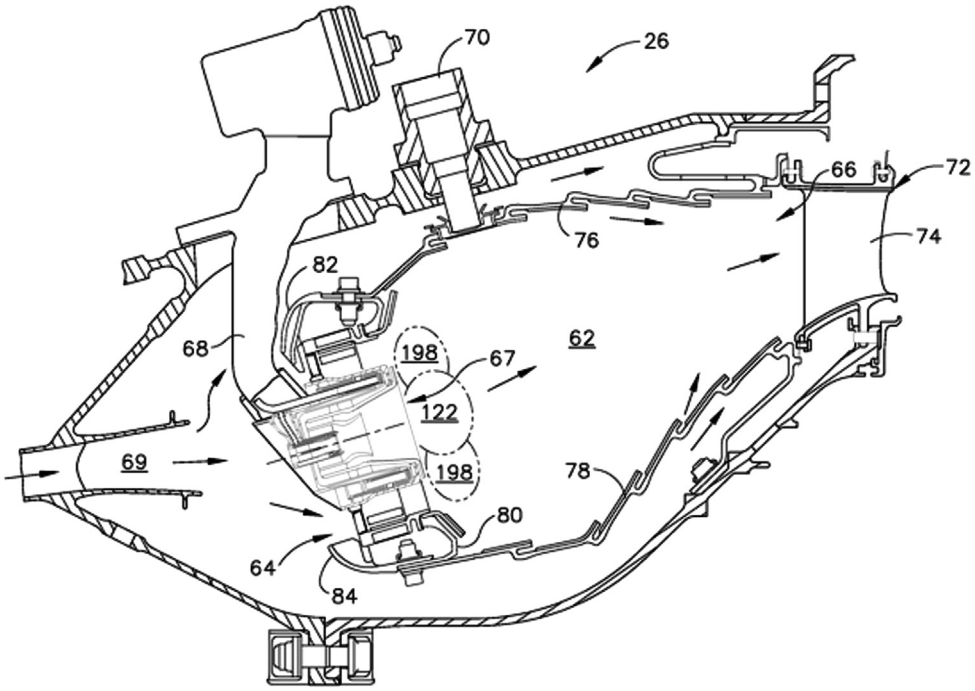

Figure 1.22 Jet engine LPP combustor geometry. Mixer assembly for gas turbine engine combustor. Source: From US Patent 8,171,735 and Mancini and Mongia [118], GE.

NO_x formation by lowering the flame temperature. The LSI differs from other swirl-stabilized premixed combustion systems by the absence of an inner recirculation zone. Indeed, the flame stabilization of the LSI is such that the flame speed balances the flow speed at a near-zero flow velocity without reversal flow. The LSI injector has been developed for electricity generation gas turbine engines ensuring 7.7 MW of electrical production from natural gas. This engine was rated for NO_x emissions between 15 to 25 ppm. The LSI allows gas turbines to operate on hydrogen and natural gas. The LSI for the Flexible Fuel Near Zero Emissions Gas Turbine, see Littlejohn et al. [122], is designed for use in gas turbines from 70 kW for on-site power generation to over 250 MW in power plants burning gaseous fuels such as hydrocarbons (including natural gas, liquified natural gas, waste gases, petroleum production and refinery gases, and biogases), syngases (a blend of H_2 and CO produced by gasification of coal), and pure hydrogen.

3.5 Lean fully premixed

The abbreviation LFP stands for lean fully premixed. This combustor architecture is different from the LPP because it is a sprayless system where all fuel is expected to be fully vaporized before its mixing with air. It has dilution holes as in the RQL combustion system to decrease the TIT, whereas LDI and LPP do not, in principle, which could be a limitation of these technologies operating in lean regimes where the flame temperature is still too high for the downstream turbine material requirements. While the LPP design target is to reduce the temperature of the gas in the combustor for the entire flight envelope, the LFP design goal is to achieve fully premixed regimes along the flight envelope, achieving NO_x reduction compared with existing technologies. The LFP combustion technology consists of three separated linked units: a vaporization unit, a premixing unit, and a premixing-stabilizing unit. The LFP design is described in detail in Chapter 7 of the present book.

4 Operating conditions and flight envelope

The combustor is a central piece of the gas turbine engine for several reasons, i.e., firstly because of its geometrical location at the center, secondly because of the complexity of the physical processes involving reacting gas dynamics coupled to heat transfer, and thirdly because this technology enables to sustain these processes in a confined manner. The combustor is indeed the place on the turbomachinery core flow path where the heat is added to the working fluid through combustion of the upstream air exiting the compressor with the injected fuel. The combustor implies various coupled disciplines, presented in the schematic of Fig. 1.23. In an industrial combustor, all these physical aspects are at work together in a coupled fashion.

It is now relevant to first describe qualitatively (and later more quantitatively) the impact of the upstream combustor flowfield and the relevant geometry (swirler, casing, compressor, diffuser, etc.) affecting the flowfield and thus the combustion process itself. It is important to study the combustor flowfield and its impact on the downstream turbine module. In this section, we begin by focusing on the upstream flame's flowfield. The flowfield that will see the flame front is strongly dependent on the fluid particle path. For example, the turbulence levels are a direct consequence of geometrical elements such as the swirler or the rotor of the compressor. These turbulence sources are then convected and dissipated as well by the flow up to the flame front. Similar observations hold for the acoustics levels. In other words, these geometrical elements will influence the combustion processes at various

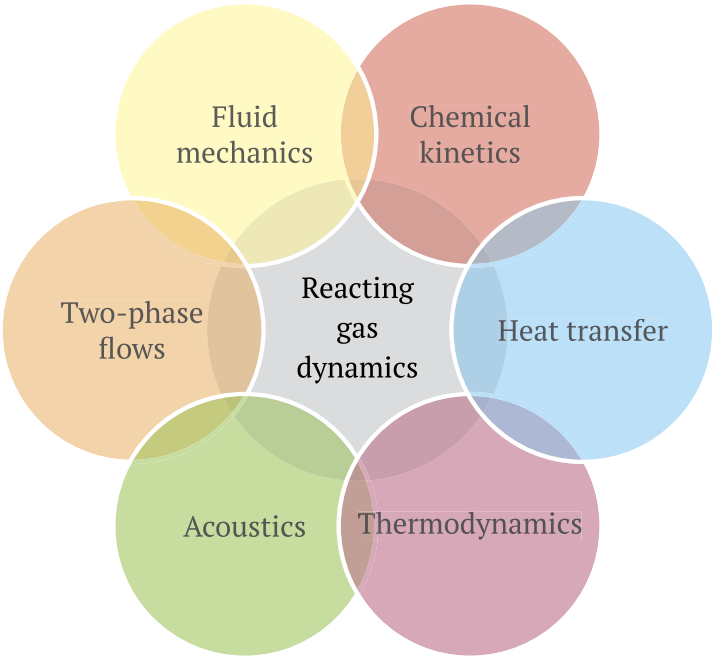

Figure 1.23 Reacting gas dynamics. Combustionencompasses multiple physical aspects.

Table 1.5 Orders of magnitude at various engine power settings.

	$\dot{m}_{bypass}$ [kg s^{-1}]	$\dot{m}_{core}$ [kg s^{-1}]	$\dot{m}_f$ [kg s^{-1}]	Power [MW]	Φ_{global} [1]	Thrust [kN]	TSFC [g kN^{-1} s^{-1}]
Ground idle	71.9	2.33	0.009		0.05		
Take-off	628.4	47.74	1.16	50	0.4	124	9.4
Cruise	146.9	12.4	0.335	14.4	0.4	24	14.1

TSFC stands for thrust-specific fuel consumption.

scales. It is therefore important to understand that the geometrical elements, and their design and operation, influence the combustion processes. This points toward the critical role of geometry in understanding turbulence and its generation. This should be emphasized for numerical modeling. Another important aspect, already highlighted in the previous section, is the static pressure and temperature, which depend on the flight envelope point and

Table 1.6 Orders of magnitude at various engine stations.

	Intake	Fan	LPC	HPC	Comb.	HPT	LPT	Exhaust
Geometry								
Section edge size [m]	2.15	0.77	0.07	0.018	0.037	0.034	0.119	0.128
Idle								
Pressure P [kPa]	101	101	101	105	100	93	93	85
Temperature T [K]	288	288	288	294	NA[a]	380	376	365
Density ρ [kg m^{-3}]	1.225	1.225	1.225	1.24	0.87	0.87	0.87	0.8
Rotor speed [RPM]		733	1832	4748		4748	1832	
Velocity U [m s^{-1}]	13	5	10	60	80	37	2	150
Kolmogorov scale [μm]	141	223	73	13	20	35	420	18
Mach Ma [1]	0.04	0.02	0.03	0.17	0.2	0.1	0.01	0.37
Reynolds Re ($\times 10^3$)	1894	262	48	74	112	49	9.3	707
Take-Off								
Pressure P [kPa]	101	105	210	3400	3000	650	105	101
Temperature T [K]	288	300	380	850	1750	1250	800	725
Density ρ [kg m^{-3}]	1.225	1.35	2.0	13.5	6.0	2.0	0.55	0.5
Rotor speed [RPM]		3030	7575	15008		15008	7575	
Velocity U [m s^{-1}]	155	135	175	115	245	330	145	270
Kolmogorov scale [μm]	22	18	7	3	4	7	35	23
Mach Ma [1]	0.45	0.39	0.44	0.2	0.3	0.49	0.26	0.49
Reynolds Re ($\times 10^3$)	22581	7567	1107	731	934	464	255	495
Cruise								
Pressure P [kPa]	24	25	60	1625	1500	400	25	24
Temperature T [K]	245	250	300	770	1700	1275	800	725
Density ρ [kg m^{-3}]	0.4	0.45	1.0	7.25	3.25	1.1	0.2	0.15
Rotor speed [RPM]		4000	10000	18000		18000	10000	
Velocity U [m s^{-1}]	155	160	175	115	235	345	200	475
Kolmogorov scale [μm]	46	32	10	4	7	10	60	37
Mach Ma [1]	0.5	0.5	0.5	0.2	0.3	0.5	0.37	0.9
Reynolds Re ($\times 10^3$)	8407	3462	663	418	493	263	128	261

[a] Convergence issue.

thus directly impact the combustion process, for example through the flame speed and the adiabatic flame temperature for a future fully premixed combustor.

Table 1.5 lists key orders of magnitude at various engine power settings (ground idle, taxi, take-off) for a geared turbofan engine, including bypass and core mass flow rate, fuel mass flow rate, corresponding equivalence ratio, thrust, and specific consumption.

In Table 1.6, orders of magnitude at various engine stations of a two-shaft turbofan engine are given. These orders of magnitude are given at the exit of each of the following modules: fan, LPC, HPC, diffuser, combustor, HPT, LPC, and exhaust nozzle. Elements that can be used to perform the variable calculations are now given. The static pressure, temperature, and density can be obtained from the previously introduced isentropic ratio throughout the engine. The rotation speed of the first or second shaft is deduced from the power balance in the compressor or turbine rotor modules (low or high pressure). The characteristic sections of each module are given by a minimum scale (the airfoil trailing edge thickness) and a maximum scale (the section area edge size calculated as $(\dot{m}/\rho U)^{1/2}/N$, where N is the number of blades of the stage considered). In addition to this list, the Kolmogorov scale η_k is computed at each module exit with the following expression: $\eta_k = l_t \times \mathrm{Re}_t^{-3/4}$, where l_t is the turbulent integral length scale taken as the maximum scale and Re_t is the turbulence Reynolds number defined by $\mathrm{Re}_t = \rho u' l_t/\mu$. The turbulence level u' is taken as 20% of the axial flow velocity and the dynamic viscosity function of the temperature is obtained from separate calculations. The thermal flame thickness δ^{th} is computed from the Blint thickness formula $\delta^{th} = (2\lambda/\rho c_p S_L) \times (T_b/T_u)^{0.7}$ and corresponds to the thermal flame front thickness. The Mach number is defined by the local ratio of axial fluid velocity to the sound speed. The local Reynolds number is defined by $\mathrm{Re} = \rho U L/\mu$, where L is the characteristic size of the module interblade section area. The Karlovitz number is defined by the ratio of chemical time to the smallest eddies characteristic time such that $\mathrm{Ka} = (\delta^{th}/\eta_k)^2$. The Damköhler number is defined as the ratio of largest turbulent eddies to the chemical time and writes $\mathrm{Da} = l_t/\delta^{th}$. These relations allow to provide some useful estimates that were computed and documented in Table 1.6.

2

Premixed combustion for combustors

1 Mathematical descriptions

1.1 Governing equations of reacting flows

Some of the variables that can be solved with the governing equations are the density of the gas $\rho = m/V$, the mass fraction $Y_k = m_k/m$ of the species that compose the N-species gas considered, the fluid velocity vector $\mathbf{v}(v_x, v_y, v_z)$, and the temperature T. The equation of state of a reacting gas writes

$$p = \rho \frac{R}{\overline{W}} T, \tag{2.1}$$

where the average molar mass $\overline{W}$ is given by

$$\frac{1}{\overline{W}} = \sum_{k=1}^{N} \frac{Y_k}{W_k}. \tag{2.2}$$

For a multi-component mixture of N species, one can also describe the static pressure p as the sum of the partial pressure p_k of each species k, i.e.,

$$p = \sum_{k=1}^{N} p_k. \tag{2.3}$$

The density ρ can be described as the sum of the partial densities ρ_k,

$$\rho = \sum_{k=1}^{N} \rho_k. \tag{2.4}$$

The perfect gas law can consequently be written for each species of such mixture as

$$p_k = \rho_k \frac{R}{W_k} T. \tag{2.5}$$

In the metric system of units, the pressure is in Pascal, the temperature is in Kelvin, the molar mass is in kg kmol^{-1}, and the per-

Stabilization and Dynamic of Premixed Swirling Flames
https://doi.org/10.1016/B978-0-12-819996-1.00010-X

fect gas constant R is 8314 J kmol^{-1} K^{-1}. The governing equations (mass, momentum, and energy) of compressible reacting gas are written below for a 3D Cartesian fixed frame of reference.

The mass conservation writes

$$\frac{\partial \rho}{\partial t} + \frac{\partial}{\partial x_i}(\rho u_i) = 0, \tag{2.6}$$

where ρ refers to the fluid density and u_i to the ith component of the velocity vector.

The momentum conservation equation writes

$$\frac{\partial \rho u_j}{\partial t} + \frac{\partial}{\partial x_i}(\rho u_i u_j) = -\frac{\partial p}{\partial x_j} + \frac{\partial \tau_{ij}}{\partial x_i} + \rho \sum_{k=1}^{N} Y_k f_{k,j}, \tag{2.7}$$

where p is the pressure, Y_k is the mass fraction of species k, $f_{k,j}$ is an external force acting on species k in the j direction (such as gravity), and τ_{ij} is the viscous stress tensor.

The viscous stress tensor is expressed as

$$\tau_{ij} = -\frac{2}{3}\mu \frac{\partial u_k}{\partial x_k}\delta_{ij} + \mu\left(\frac{\partial u_i}{\partial x_j} + \frac{\partial u_j}{\partial x_i}\right). \tag{2.8}$$

The species equations are written

$$\frac{\partial \rho Y_k}{\partial t} + \frac{\partial}{\partial x_i}(\rho(u_i + V_{k,i})Y_k) = \dot{\omega}_k, \tag{2.9}$$

where Y_k is the mass fraction of species k, $\dot{\omega}_k$ refers to the reaction rate of each k species ($k = 1, N$), and $V_{k,i}$ are the species diffusion velocities in the i direction. The unit of $\dot{\omega}_k$ is kg m^{-3} s^{-1}. The expression of the diffusion velocities $V_{k,i}$ can be obtained with different levels of assumptions. For a multi-component/multi-species system, see the treatment by Kuo and Acharya [123], the diffusion velocities V_k are obtained by resolving the following system:

$$\nabla X_p = \sum_{k=1}^{N} \frac{X_p X_k}{D_{pk}}(V_k - V_p) + (Y_p - X_p)\frac{\nabla p}{p} + \frac{\rho}{p}\sum_{k=1}^{N} Y_p Y_k (f_p - f_k). \tag{2.10}$$

The coefficient D_{pk} expresses the binary mass diffusion of species p into k. X_k represents the mole fraction of species k. The Soret effect expressed as a function of $\nabla T/T$ representing the diffusion of mass due to the temperature gradients is neglected in this expression. The Hirschfelder–Curtiss approximation is a simplified form

of this equation where the system reduces to

$$V_k X_k = -D_k \nabla X_k, \tag{2.11}$$

where the coefficient is defined for each species k with respect to the mixture and writes

$$D_k = \frac{1 - X_k}{\sum_{j \neq k} X_j / D_{jk}}. \tag{2.12}$$

Other expressions include the diffusion velocities with Fick's law for the mass fractions or use constant Lewis number(s) methodology. In that approach, the diffusion of species mass is treated as a function of the Lewis number for each species, i.e., as a function of thermal diffusion. It can be unity Lewis number, in which case the species and thermal diffusion are modeled with the same diffusion coefficient.

The energy conservation equation writes in terms of temperature as

$$\begin{aligned}\rho c_p \left[\frac{\partial T}{\partial t} + v_i \frac{\partial T}{\partial x_i} \right] = \dot{\omega}_T + \frac{dp}{dt} + \frac{\partial}{\partial x_i}\left(\lambda \frac{\partial T}{\partial x_i} \right) \\ - \left(\rho \sum_{k=1}^{N} c_{p,k} Y_k V_{k,i} \right) \frac{\partial T}{\partial x_i} + \tau_{ij} \frac{\partial u_i}{\partial x_j} + \mathcal{Q}_{st} \\ + \rho \sum_{k=1}^{N} Y_k f_{k,i} V_{k,i}.\end{aligned} \tag{2.13}$$

The Dufour effect which is neglected here is the energy flux associated to diffusion velocities variations. In this equation, $\mathcal{Q}_{st}$ is a heat source term and $\dot{\omega}_T$ refers to the heat release rate, expressed as

$$\dot{\omega}_T = -\sum_{k=1}^{N} h_{sk} \dot{\omega}_k - \sum_{k=1}^{N} \Delta h^0_{fk} \dot{\omega}_k, \tag{2.14}$$

where the sensible enthalpy h_{sk} is defined by

$$h_{sk} = \int_{T_{ref}}^{T} c_{pk} dT. \tag{2.15}$$

The chemical enthalpy Δh^0_{fk} is a quantity defined by the enthalpy required to form (subscript f) one kilogram of species k at the reference temperature T_0 (superscript 0). The sensible and chemical enthalpies have the same unit, which is $\mathrm{J\,kg^{-1}}$. The reaction rate

$\dot{\omega}_k$ of species k is expressed in $\mathrm{kg\,m^{-3}\,s^{-1}}$. Accordingly, the heat release rate term is expressed in $\mathrm{W\,m^{-3}}$. The integration of that quantity over the combustion volume leads to the heat release of the flame, expressed in Watt.

The chemical kinetics of reacting gas dynamics is modeled by considering a system of N species reacting through M reactions:

$$\sum_{k=1}^{N} \nu'_{kj} \mathcal{M}_k \rightleftharpoons \sum_{k=1}^{N} \nu''_{kj} \mathcal{M}_k, \tag{2.16}$$

where the molar coefficients ν of species $\mathcal{M}_k$ in reaction j are denoted with single prime for the reacting species and double prime for the product species. The mass conservation[1] for the reaction leads to

$$\sum_{k=1}^{N} \nu_{kj} W_k = 0, \tag{2.17}$$

where $\nu_{kj} = \nu''_{kj} - \nu'_{kj}$. In addition, the mass reaction rate of species k due to the M reactions writes

$$\dot{\omega}_k = \sum_{j=1}^{M} \dot{\omega}_{kj} = W_k \sum_{j=1}^{M} \nu_{kj} \mathcal{Q}_j, \tag{2.18}$$

where the rate of progress of reaction j, written as $\mathcal{Q}_j$, is equal to $\dot{\omega}_{kj}/(W_k \nu_{kj})$. The unit of the rate of progress of a reaction is $\mathrm{m^{-3}\,s^{-1}}$. This rate takes the following form:

$$\mathcal{Q}_j = K_{fj} \prod_{k=1}^{N} \left(\frac{\rho Y_k}{W_k} \right)^{\nu'_{kj}} - K_{bj} \prod_{k=1}^{N} \left(\frac{\rho Y_k}{W_k} \right)^{\nu''_{kj}}. \tag{2.19}$$

The rate constants K_{fj} and K_{bj} are modeled with the Arrhenius law,

$$K_{fj} = A_{fj} T^{\beta_j} \exp\left(\frac{-E_{a,j}}{RT} \right), \tag{2.20}$$

where A_{fj} are the preexponential factors with unit $\mathrm{s^{-1}}$, β_j are the temperature exponents, and $E_{a,j}$ is the activation energy of reaction j. The preexponential factor quantifies the number of collisions per second occurring between species that can induce reaction, while the activation energy reflects the probability that any given collision will result in a reaction given an activation temperature threshold $T_a = E_a/R$. The activation energy unit is $\mathrm{J\,mol^{-1}}$.

[1] Lavoisier: Rien ne se perd, rien ne se crée, tout se transforme.

When the local temperature increases or if a reaction has a lower activation energy, the rate of that reaction increases.

There are three important quantities to define because of their wide usage: the equivalence ratio Φ, the adiabatic flame temperature T_{ad}, and the determination of the gas composition expressed in terms of mass fraction at equilibrium Y_{eq}. These quantities are now detailed.

1.1.1 Equivalence ratio

The equivalence ratio Φ is defined as the ratio of the fuel mass flow rate to the air mass flow rate divided by the same ratio at the stoichiometry of the reaction considered. The equivalence ratio can take a global form such as used for diffusion flames and combustor design. It can also take a local form to characterize various combustion regimes locally. It writes between fuel and air as

$$\Phi = \frac{[\dot{m}_f/\dot{m}_a]}{[\dot{m}_f/\dot{m}_a]_{st}} = \frac{[\dot{m}_f/\dot{m}_a]}{s_a}, \tag{2.21}$$

or, expressed as a function of the oxidizer O_2,

$$\Phi = \frac{[\dot{m}_f/\dot{m}_{O_2}]}{[\dot{m}_f/\dot{m}_{O_2}]_{st}} = \frac{[\dot{m}_f/\dot{m}_{O_2}]}{s_{O_2}}. \tag{2.22}$$

The stoichiometric ratios s can be defined with respect to air (s_a) or oxygen only (s_{O_2}). For a premixture, the equivalence ratio can also take the following form:

$$\Phi = \frac{Y_f/Y_a}{s_a} = \frac{Y_f/Y_{O_2}}{s_{O_2}}. \tag{2.23}$$

Now we consider three different fuels reacting with air: methane, hydrogen, and decane. The overall chemical reaction mechanisms have the following stoichiometries:

- $CH_4 + 2(O_2 + 3.76\,N_2) \Longrightarrow CO_2 + 2H_2O + 7.52N_2$,
- $2H_2 + (O_2 + 3.76\,N_2) \Longrightarrow 2H_2O + 3.76\,N_2$,
- $2C_{10}H_{22} + 31(O_2 + 3.76\,N_2) \Longrightarrow 20CO_2 + 22H_2O + 116.56\,N_2$.

The ratio of oxygen in air (3.76 moles of N_2 for 1 mole of O_2 in air) is obtained with the following expression:

$$\text{Ratio} = \frac{W_{O_2}}{W_{O_2} + 3.76 W_{N_2}} = 0.233. \tag{2.24}$$

By definition of the equivalence ratio, one has $\dot{m}_f = \Phi s_a \dot{m}_a$. The total mass flow rate can be expressed as $\dot{m} = \dot{m}_f + \dot{m}_a = (1 + \Phi s_a)\dot{m}_a$. By writing the mass fractions of oxidizer (o) and fuel (f) as $Y_f = \dot{m}_f/\dot{m}$ and $Y_o = \dot{m}_o/\dot{m}$, one obtains the following expressions:

$$Y_f = \frac{\Phi s_a}{1 + \Phi s_a}, \tag{2.25}$$

$$Y_o = \frac{0.233}{1 + \Phi s_a}. \tag{2.26}$$

In addition to these expressions, it is good to know the following fuel to air ratios (FARs), defined by $\dot{m}_f/\dot{m}_a$. For kerosene, the FAR at stoichiometry is 0.067. For methane, the FAR at stoichiometry is 0.058. For hydrogen, the FAR at stoichiometry is 0.029. The lower heating values of these fuels are respectively 43, 50.1, and 120.5 MJ/kg. The lower heating value considers the product H_2O as vapor. The higher heating value considers the product H_2O as liquid.

These expressions are used to determine the fresh gas composition in Tab. 2.1.

1.1.2 Equilibrium composition

The equilibrium composition can be determined from the global reaction mechanism. For a given equivalence ratio Φ, the previous reaction mechanisms can be written as follows in the lean regime ($\Phi \leq 1$):

- $\Phi CH_4 + 2(O_2 + 3.76\ N_2) \Longrightarrow \Phi(CO_2 + 2H_2O) + 2[(1\text{-}\Phi)O_2 + 3.76N_2]$,
- $\Phi 2H_2 + (O_2 + 3.76\ N_2) \Longrightarrow 2\Phi\ H_2O + [(1\text{-}\Phi)O_2 + 3.76\ N_2]$,
- $2\Phi C_{10}H_{22} + 31(O_2 + 3.76\ N_2) \Longrightarrow 20\Phi\ CO_2 + 22\Phi H_2O + 31[(1\text{-}\Phi)O_2 + 3.76\ N_2]$.

The mass fractions of H_2O and CO_2 can be computed as follows. For the CH_4–air reaction, for Y_{H_2O} one has

$$Y_{H_2O} = \frac{2\Phi(2W_H + W_O)}{2\Phi(2W_H + W_O) + \Phi(W_C + 2W_O) + 2[(1-\Phi)2W_O + 2 \times 3.76W_N]}, \tag{2.27}$$

and for Y_{CO_2} one has

$$Y_{CO_2} = \frac{\Phi(W_C + 2W_O)}{2\Phi(2W_H + W_O) + \Phi(W_C + 2W_O) + 2[(1-\Phi)2W_O + 2 \times 3.76W_N]}. \tag{2.28}$$

Similarly, for the H_2–air reaction mechanism, for Y_{H_2O} one has

$$Y_{H_2O} = \frac{2\Phi(2W_H + W_O)}{2\Phi(2W_H + W_O) + [(1-\Phi)2W_O + 2 \times 3.76W_N]}. \tag{2.29}$$

No CO_2 is formed in this reaction. Finally, for the $C_{10}H_{22}$–air reaction, for Y_{H_2O} one has

Table 2.1 Mass fractions at various equivalence ratios Φ for combustion of methane (CH_4), hydrogen (H_2), and decane ($C_{10}H_{22}$) with air. Adiabatic flame temperatures are also listed. Operating conditions are atmospheric pressure and temperature.

Φ	0.5	0.6	0.7	0.8	0.9	1.0	1.1	1.2
CH_4–air								
Y_{CH_4}	0.0283	0.0337	0.0392	0.0445	0.0498	0.0550	0.0602	0.0653
Y_{O_2}	0.2264	0.2251	0.2238	0.222	0.2213	0.2201	0.2189	0.2177
Y_{H_2O}	0.0637	0.07601	0.0881	0.1002	0.1121	0.1238	0.1355	0.1470
Y_{CO_2}	0.0778	0.0929	0.1077	0.1224	0.1370	0.1514	0.1656	0.1797
Y_{N_2}	0.7452	0.7411	0.7369	0.7328	0.7288	0.7247	0.7208	0.7168
T_{Ad}	1480	1665	1838	1996	2133	2224	2209	2136
H_2–air								
Y_{H_2}	0.0143	0.0171	0.0199	0.0227	0.02555	0.0283	0.0310	0.0337
Y_{O_2}	0.2296	0.2289	0.2283	0.2276	0.22704	0.2264	0.2257	0.2251
Y_{H_2O}	0.1292	0.1546	0.1798	0.2050	0.22998	0.25481	0.2795	0.3040
Y_{CO_2}	0	0	0	0	0	0	0	0
Y_{N_2}	0.7559	0.7538	0.7516	0.7495	0.7474	0.7452	0.7432	0.7411
T_{Ad}	1500	1850	1950	2075	2250	2375	2400	2350
$C_{10}H_{22}$–air								
$Y_{C_{10}H_{22}}$	0.0323	0.0385	0.0446	0.0507	0.0567	0.0625	0.0684	0.0741
Y_{O_2}	0.2408	0.2423	0.2440	0.2454	0.2469	0.2485	0.2501	0.2516
Y_{H_2O}	0.0450	0.0536	0.0622	0.0706	0.0790	0.0872	0.0953	0.1034
Y_{CO_2}	0.1001	0.1192	0.1383	0.1570	0.1756	0.1938	0.2119	0.2297
Y_{N_2}	0.7269	0.7191	0.7114	0.7038	0.6963	0.6888	0.6815	0.6742
T_{Ad}	1520	1700	1900	2060	2200	2280	2300	2220

$$Y_{H_2O} = \frac{22\Phi(2W_H + W_O)}{22\Phi(2W_H + W_O) + 20\Phi(W_C + 2W_O) + 31[(1-\Phi)2W_O + 2 \times 3.76W_N]}, \tag{2.30}$$

and for Y_{CO_2} one has

$$Y_{CO_2} = \frac{20\Phi(W_C + 2W_O)}{22\Phi(2W_H + W_O) + 20\Phi(W_C + 2W_O) + 31[(1-\Phi)2W_O + 2 \times 3.76W_N]}. \tag{2.31}$$

All equilibrium mass fractions are displayed in Tab. 2.1.

1.1.3 Adiabatic flame temperature

In this section, the focus is on the calculation of the adiabatic flame temperature T_{ad}. The adiabatic flame temperature of a premixed flame corresponds to the maximum temperature that the flame can reach for a given equivalence ratio if the flame is the only source of heat; any heat transfer will lower that temperature. The calculation of T_{ad} here is based on the balance between the specific enthalpy of the mixture and the corresponding specific energy released during combustion. The premixed combustion adiabatic flame temperature in the lean regime can be estimated with

$$T_{ad} = T_u + QY_f/c_p, \tag{2.32}$$

where T_u is the unburned fresh gas temperature of the mixture with a mass fraction of fuel Y_f and Q is the specific heat of reaction of the fuel considered with unit kJ kg^{-1}. The adiabatic premixed flame temperatures for various fuels are reported in Tab. 2.1 for multiple equivalence ratios for an upstream mixture at $T_u = 300$ K. The reported values were calculated with detailed chemical mechanisms.

1.2 G-equation formalism

Mathematically, a surface obeys the equation $G(x, y, z, t) = 0$ and the normal to that surface writes $\mathbf{n} = -\nabla G/|\nabla G|$. The unit normal vector $\mathbf{n}$ of the surface points towards the fresh gases. The curvature of the surface is given by $\nabla \cdot \mathbf{n}$. The material derivative of the surface, i.e., its motion within the flow as a function of time, takes the following expression:

$$\frac{d}{dt}G(x, y, z, t) = \frac{\partial}{\partial t}G(x, y, z, t) + \mathbf{w} \cdot \nabla G(x, y, z, t) = 0, \tag{2.33}$$

where $\mathbf{w}$ is the flame surface speed within the flow. This equation is the time derivative (rate of change) of the points following the surface. In addition, the flame surface speed, the flow speed, and the flame displacement speed are linked by the kinematic relationship $\mathbf{w} = \mathbf{v} + S_D\mathbf{n}$. The G-equation models the evolution of a flame front without solving the explicit contributions of the chemical reactions but considering them implicitly through a burning flame speed at which the flame front propagates. The finally obtained kinematic equation is the G-equation, derived by Markstein [124], Williams [125], Kerstein et al. [126], written as

$$\frac{\partial G}{\partial t} + \mathbf{v} \cdot \nabla G = S_D|\nabla G|, \tag{2.34}$$

where one of the isocontours G defines the flame front location, $\mathbf{v}$ is the local flow velocity, and S_D designates the local displacement velocity of the flame. This equation is valid along multiple successive isocontours G as long as the velocity field and the flame speed are consistently taken on those particular isocontours. In most cases, the flame speed S_D denotes the unburned displacement speed.

The G-equation has been investigated in many researches, both theoretical and numerical, including applications to laminar and turbulent premixed flames and particularly flame dynamics, see the pioneering articles of Baillot et al. [127], Ducruix et al. [128], Schuller et al. [129] for laminar flames and the reviews by Ducruix et al. [130], Lieuwen [131]. In laminar flame configurations, the application of the G-equation is straightforward while in turbulent flow the G-equation is valid to model the evolution of the turbulent flame under specific assumptions. In the turbulent regime, when the flame can be considered as a sheet and when the burning velocity is well defined, such as when the flame front exhibits a locally laminar flame front structure, the G-equation can be used. While the reacting flow governing equations allow to model any regime of laminar or turbulent combustion, the G-equation is limited to certain regimes constrained by specific assumptions. But for those regimes, the G-equation allows to describe much of the physical behavior at work with only one equation instead of multiple $(5 + N)$ equations. These assumptions and regimes are detailed now.

In the next section, it will be shown that turbulent premixed combustion of swirling flames evolves mainly in the so-called corrugated flame regimes. This regime corresponds to physical length scales where the chemical reactions are faster than the turbulence time scales and the flame thickness is smaller than the Kolmogorov scale, so that turbulent fluctuations have a relatively weak effect on the flame structure with respect to laminar combustion. In addition, in that regime, the amplitude of the largest turbulent scale velocity fluctuation is higher than the unstretched laminar flame speed. In other words, in that flamelet regime, the premixed flame front keeps a laminar-like flame front inner structure locally. In practice, it is more accurate to indicate that the flame front in that regime can be defined by a local flame displacement speed while its inner structure remains 3D due to the three-dimensionality of the swirling flow for swirl-stabilized combustors. The main physical phenomena that can be observed in the corrugated flamelet premixed combustion regime are a combination of wrinkling and formation of pockets of fresh and burned gases.

Because laboratory-scale and gas turbine swirl-stabilized combustion under take-off conditions will be in the corrugated flamelet regime, it is important to investigate the analytical, experimental, and numerical literature related to that regime. This is achieved in the next sections.

The laminar flame front characterization is first provided here. Firstly, the inner flame structure of a methane–air 1D laminar premixed flame is introduced in Fig. 2.1, which corresponds to atmospheric pressure (1 atm) and temperature ($T = 300$ K) at equivalence ratio $\Phi = 0.7$. The results were obtained with a detailed chemical mechanism. Fig. 2.1A depicts the profile of temperature and heat release throughout the flame front. Fig. 2.1B depicts the profiles of mass fractions of the unburned and burned species. In that 1D case, we have the following relationship throughout the flame front: $\rho(x)S_D(x) = \rho_u S_L^0$.

2 Physical-chemical description

2.1 Premixed combustion overview

Premixed combustion consists of the chemical reactions within a flow of a premixture of reacting species. These reactions occur in a fluid in motion such as would occur in a gas turbine combustor. The chemical kinetics induce various temporal and spatial scales because of the multiple preexponential factors and activation energies between all species of each reaction at stake. Furthermore, the flow, due to its motion (through various geometrical elements) adds a wide range of both temporal and spatial scales, particularly if turbulent. Selected geometrical scales quantified in turbulent combustion are listed in Tab. 2.2 and estimated in Tab. 2.3. The first spatial scales of this list are the geometrical dimensions of the combustor and the swirler. For the primer, the size corresponds to that of the combustion chamber length (maximum) and transversal direction (minimum). For the latter, it corresponds to the swirler diameter. Next, the turbulent integral scale, which is directly linked to the geometrical size, is listed and calculated as 90% of the minimum geometrical dimension. The Kolmogorov scale η_k is computed with $\eta_k = l_t \times \mathrm{Re}_t^{-3/4}$, where Re_t is the turbulent Reynolds number. This scale is computed as a function of the turbulent Reynolds number and integral length scale in Fig. 2.2. The Gibson scale is defined as $l_G = l_t(S_L^0/u')^3$ and characterizes the scale at which eddies interact with the flame front. The Taylor scale is defined as $\lambda_T = l_t\sqrt{10} \times \mathrm{Re}_t^{-1/2}$. The length scales that are larger than the Taylor scale are not significantly impacted by viscosity and are in the inertial range of the turbulent spectrum.

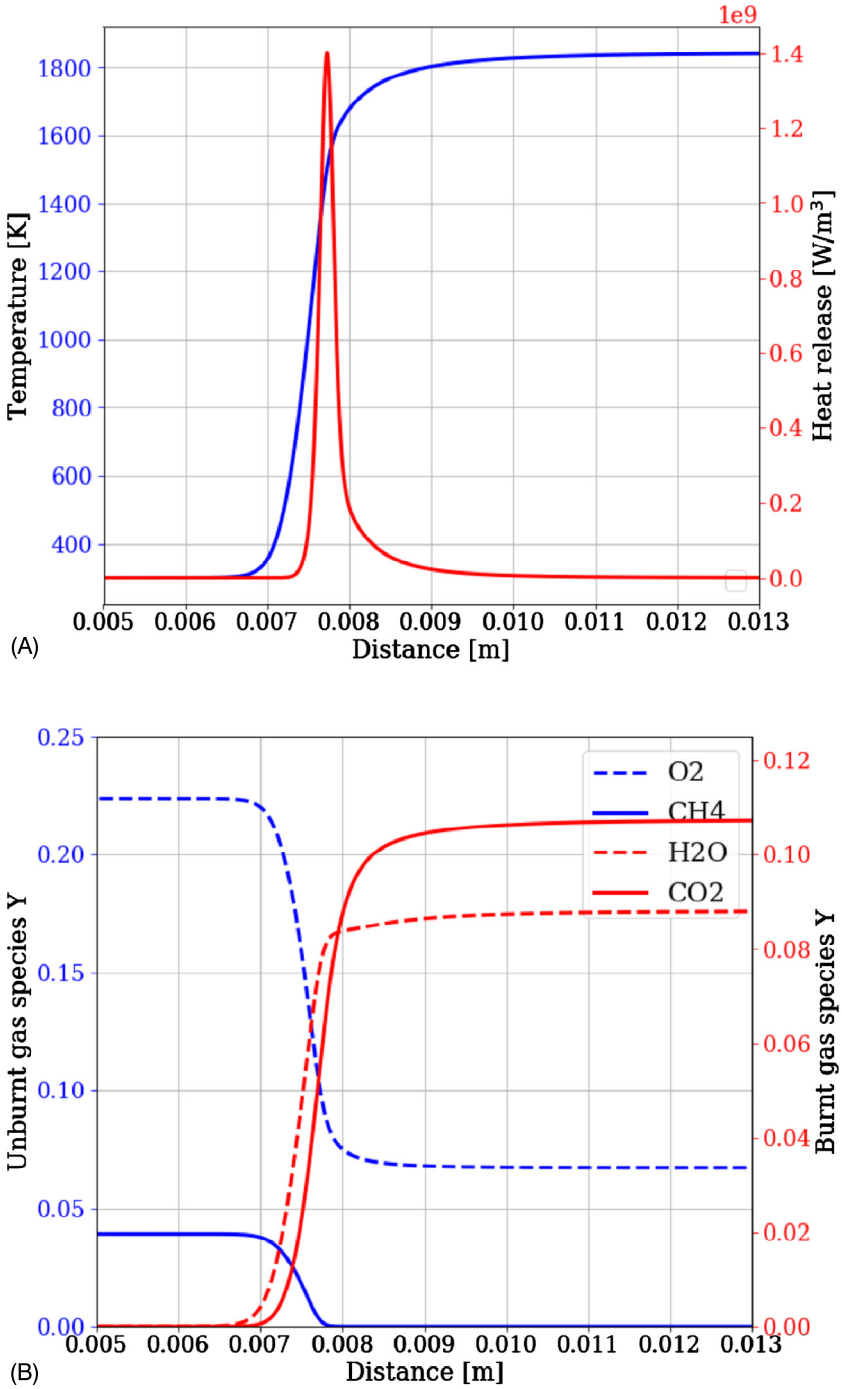

Figure 2.1 Methane–air 1D premixed flame inner structure. (A) Temperature and heat release profiles. (B) Mass fraction profiles.

Table 2.2 List of scales and nondimensional numbers. Some are particularly used for turbulent combustion characterization.

Scale/number	Definition	Comment
Scale		
Geometrical size 1	L	Transverse combustor size
Geometrical size 2	D	Swirler diameter
Integral scale l_t	$90\%\ L$	Largest scale
Kolmogorov scale η_k	$l_t \times \mathrm{Re}_t^{-3/4}$	Turbulence dissipation scale cutoff
Gibson scale l_G	$l_t (S_L^0/u')^3$	Eddies/flame front cutoff scale
Taylor scale l_T	$l_t \sqrt{10} \times \mathrm{Re}_t^{-1/2}$	Inertial range cutoff scale
Diffusive thickness δ	D_{th}/S_L^0	Diffusive flame thickness
Thermal thickness δ^{th}	$2\delta(T_{ad}/T_u)^{0.7}$	Blint flame thickness
Mean free path[c] l	$k_B T/\sqrt{(2)}\pi d^2 p$	
Nondimensional number		
Turb. Damköhler	$\mathrm{Da}_t = \tau_{l_t}/\tau_c = S_L^0 l_t/u'\delta$	Turbulent integral to chemical
Turb. Karlovitz	$\mathrm{Ka}_t = \tau_c/\tau_{\eta_k} = (\delta/\eta_k)^2$	Chemical to Kolmogorov time
Knudsen	$\mathrm{Kn} = l/L$	Mean free path to geometrical size
Lewis	$\mathrm{Le} = \lambda/(\rho c_p D_k)$	Heat to species k diffusion time
Mach	$\mathrm{Ma} = u/c$	Flow velocity to sound speed
Markstein	$\mathcal{M} = \mathcal{L}/\delta^{th}$	Markstein to flame length
Peclet (m)	$\mathrm{Pe}_m = Lu/D_m$	Convection to mass diffusion
Peclet (th)	$\mathrm{Pe}_{th} = Lu/\alpha$[a]	Convection to thermal diffusion
Prandtl	$\mathrm{Pr} = \nu/\alpha$	Momentum to heat diffusion
Reynolds	$\mathrm{Re} = \rho u L/\mu$	Convection to momentum diffusion
Schmidt	$\mathrm{Sc} = \nu/D_m = \mathrm{Le}\,\mathrm{Pr}$	Momentum to mass diffusion
Strouhal	$\mathrm{St} = fL/u$	Convective to oscillating
Turb. Reynolds	$\mathrm{Re}_t = u' l_t/\nu = \mathrm{Ka}_t^2\ \mathrm{Da}_t^{2,b}$	
Zeldovich β	$E_a/RT_{ad} \times (T_{ad} - T_u)/T_{ad}$	

[a] $\alpha = D_{th} = \lambda/\rho c_p$.

Scales that are lower than the Taylor scale are subject to significant viscous forces and their kinetic energy is dissipated into heat. The turbulent scales are such that $l_t > \lambda_T > l_G > \eta_k$. These temporal and spatial scales are also largely described by making use of many important nondimensional numbers. Selected nondimensional numbers are specifically listed in Tab. 2.2.

Table 2.3 List of spatial scales and nondimensionalized numbers for turbulent combustion characterization. Orders of magnitude.

	Atmospheric lab-scale combustor	Take-off GT combustor
Scale		
Combustor size	$0.03 < L < 0.20$	$0.03 < L < 0.20$
Swirler size	$0.020 < L = D < 0.15$	$0.020 < L = D < 0.15$
Integral scale l_t	$0.018 < l_t < 0.18$	$0.018 < l_t < 0.18$
Kolmogorov scale η_k	35[a] μm	8[b] μm
Gibson scale l_G	45[a] μm	10[b] μm
Taylor scale λ_T	940[a] μm	430[b] μm
Diffusive thickness[c] δ	60 μm	2 μm
Thermal thickness[c] δ^{th}	500 μm	9 μm
Mean free path[d] l	100 nm	5 nm
Number		
Turb. Damköhler	$40 > 1$	$550 > 1$
Turb. Karlovitz	$2.5 > 1$	$0.06 < 1$
Knudsen	$5\ 10^{-6} << 1$	$0.25\ 10^{-6} << 1$
Lewis	1.0[e]	2.7[e]
Mach	0.04	0.2
Markstein		
Peclet (m)	12 733	463 977
Peclet (th)	12 031	635 896
Prandtl	0.7	0.80
Reynolds	18 874	417 791
Schmidt	0.72	2.2
Turb. Reynolds[f]	8232	1120
Turb. Reynolds[g]	3362	136 939
Zeldovich	16.5	11.3

[a] With $l_t = 0.018$ and $u' = 3\ \mathrm{m\,s^{-1}}$.

[b] With $l_t = 0.018$ and $u' = 20\ \mathrm{m\,s^{-1}}$.

[c] At $\Phi = 1$ (CH_4 for lab-scale data and kerosene for TO data).

[d] Based on nitrogen.

[e] Based on fuel species.

[f] Based on the definition $\mathrm{Re}_t = \mathrm{Ka}^2\ \mathrm{Da}^2$, where $\mathrm{D}_{th} = \nu$ is assumed and $\Phi = 1$.

[g] Based on the definition $\mathrm{Re}_t = u' l_t / \nu$, where $\nu \neq D_{th}$.

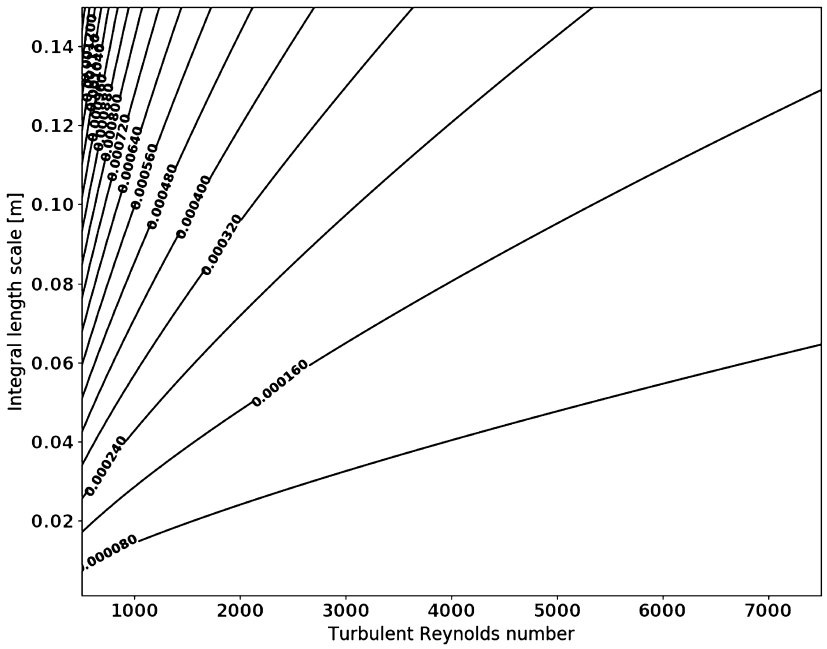

Figure 2.2 Kolmogorov scale η_k values. Evolution of the Kolmogorov scale η_k as a function of the integral length scale l_t and the turbulence Reynolds number Re_t.

Laminar flame front thickness definitions and estimates are provided in Tab. 2.3 and Fig. 2.3. Fig. 2.3 presents the evolution of the flame thickness for three definitions (thermal, diffusive, and reactive thickness) as a function of the equivalence ratio. One observes the order of magnitude of those and the trend as the equivalence ratio is decreased.

The scales and nondimensional numbers aim at describing different regimes of premixed combustion and their subsequent modeling. It is important to remember that those scales and nondimensional numbers vary in space and time, such as in a combustion chamber. This is important for an accurate description. For example, the Reynolds number in a cylindrical duct is expected to be of the order of 3500 when it transits from laminar to turbulence. But the same duct with a swirler inside will be turbulent at any Reynolds number. To conclude, care must be taken when evaluating the nondimensional numbers.

Turbulent combustion aims at describing physically the interaction of chemical kinetics and flow turbulence. These descriptions are required for multiple reasons: (i) advance the state of the art, (ii) enhance modeling capabilities of such phenomena,

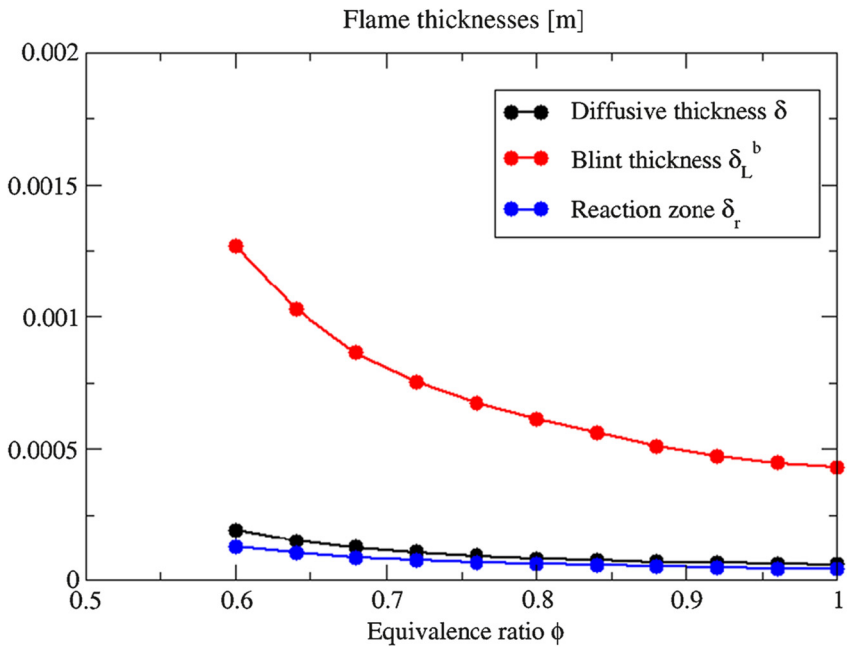

Figure 2.3 Premixed 1D laminar flame thicknesses. Evolution of the laminar premixed flame thickness as a function of the equivalence ratio ($T_u = 300$ K and $p = 1$ atm).

and (iii) improve technologies that rely on these processes. Turbulent premixed combustion is usually described by the use of the Borghi diagram, which allows to categorize various turbulent combustion regimes as a function of two main groups of parameters: (i) the ratio of the velocity fluctuation u' to the unstretched laminar flame speed S_L^0 and (ii) the ratio of the integral length scale l_t to the diffusive flame thickness δ. The derivation of the diagram makes use of the relationship between nondimensional numbers and their representation in a log-log scale. The classical turbulent premixed combustion diagram is sketched in Fig. 2.4. Various regimes of premixed turbulent combustion are now briefly described with respect to the scales and nondimensional numbers introduced in the previous paragraphs. When the Damköhler number Da is beyond unity, the chemical reactions are faster than the integral turbulence time scale, so that the flow, at the first order, does not impact the reaction. In that perspective, the flame has a so-called flamelet structure so that its local structure is nearly that of a 1D flame, while its global structure is wrinkled by turbulent fluctuations. In practice, for a turbulent swirling flow, the flow is highly 3D. While the flame temperature profile would appear 1D, the local velocity field is not. For high

Damköhler numbers, there are two regimes, which depend on the Karlovitz number (Ka). For low Ka, turbulent eddies do not enter the flame front (flamelet regimes), while for higher Ka, these eddies can enter the flame front (thickened flame regime). Indeed, when the Karlovitz number is lower than unity, the chemical time is shorter than turbulence time scales, and the flame front thickness is smaller than the turbulence scales, inducing the evolution of a turbulent wrinkled 1D-like flame front. Depending on the values of the turbulence fluctuations and the unstretched laminar flame speed, the flamelet regime is split into two regimes: (i) the wrinkled flamelet regime ($u' < S_L^0$) and (ii) the corrugated flamelet regime ($u' > S_L^0$) inducing pockets of fresh and burned gases. When both the Damköhler and the Karlovitz number are well beyond unity, the regime is known as the thickened flame regime or distributed reaction zone regime. When the Damköhler is lower than unity, the chemical reactions are slower than the flow motion. This regime corresponds to the well-stirred reactor where turbulent mixing is shorter than chemical reaction times. All these regimes are reported in Fig. 2.4.

In addition to these scales, there are many quantities that are key to the understanding of the generation, propagation, and extinction of premixed flames. The generation of a premixed flame is the consequence of natural ignition, which is called autoignition, or of forced ignition, simply called ignition. In both cases, the required elements are the fuel, the oxidizer, and heat. These elements are necessary but they are not sufficient. Indeed, in order to ignite, the sufficient conditions include that there may be no extinction processes at work (flame stretch, vorticity, flammability limits, etc.) or they have not reached a threshold level. The generation of a premixed flame begins with an initial kernel that will propagate until flame stabilization is reached. This propagation will be dependent on the geometry of the system considered and subsequently of the velocity field. Extinction of the flame can be caused by a multitude of physical processes, such as the effects of the flame stretch, vorticity, and local flammability limits.

The most important quantities at work during premixed combustion are now introduced and discussed. They are listed in Fig. 2.5. The operating condition corresponds essentially to the static pressure P and temperature T of the fresh upstream gases. The equivalence ratio Φ is determined by the engine configuration, the fuel, and the operating conditions. The operating conditions and the equivalence ratio drive the flame speed value S_D. The flame thickness δ^{th} estimate is deduced from the flame speed, the fresh gas thermophysical properties (conductivity, constant pressure specific heat, density), and the adiabatic flame

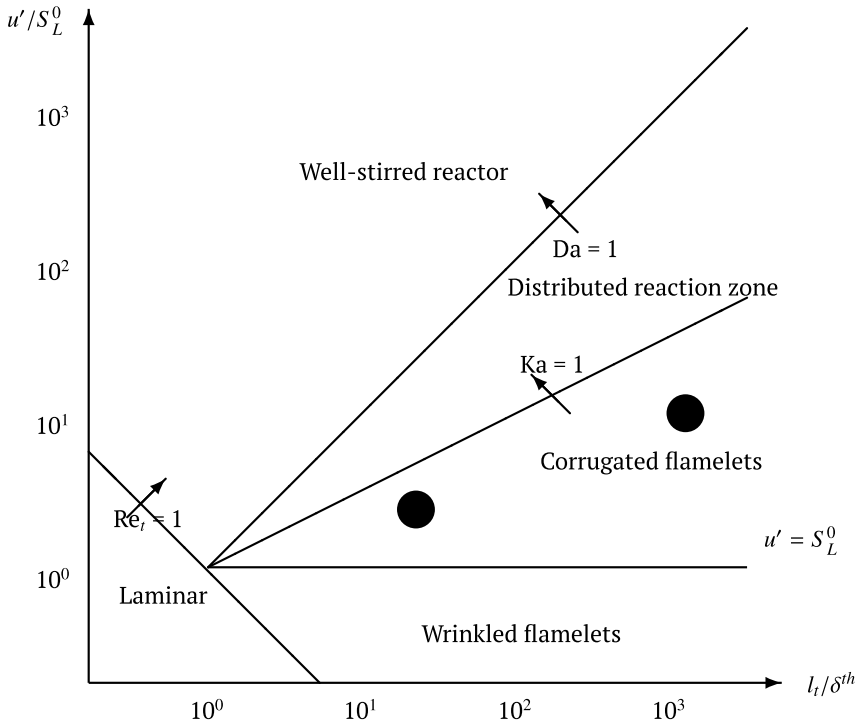

Figure 2.4 Turbulent combustion regime diagram. The diagram depicts the various premixed combustion regimes. The left dot indicates the premixed combustion regime typical of laboratory-scale studies, while the right dot indicates the regime at take-off of current gas turbine engines.

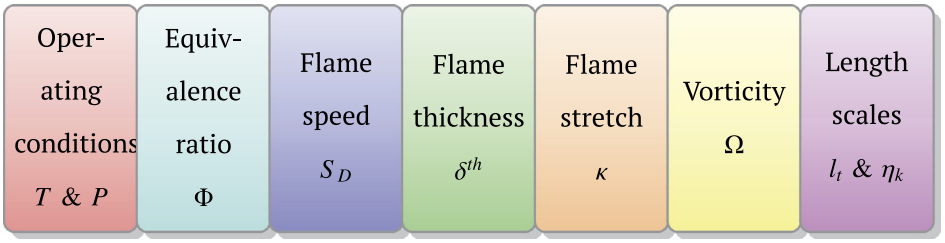

Figure 2.5 Important premixed combustion aspects. Each aspect plays a key role in the description of premixed combustion.

temperature. The flame stretch κ, which consists of three terms (flow strain, volume expansion, and flame curvature), is a relevant quantity in premixed combustion because of its impact on extinction and flame speed. Similarly, the vorticity Ω levels can impact the local flame structure, inducing local extinction. Flame stretch and vorticity levels are direct consequences of the velocity

field at stake. Finally, these scales are important because they will control the interaction of the flowfield with the flame front and associate with the operating conditions to determine the combustion regime.

There are several types of flame anchoring methods for premixed combustion. Among them, there are two essential ones for turbulent premixed flames: the bluff-body-stabilized and the swirl-stabilized type. Both rely on forming a recirculation zone of burned gases continuously igniting the upstream fresh gases. The former is mainly used in gas turbine engine augmenters, while the latter is the focus of the present book and is used in the main combustors of commercial aircraft and fighters. The next section focuses on documenting briefly the main features of premixed swirling flames.

2.2 Swirling flames overview

This section focuses on the description of swirling flames, which are swirling flows with chemical reactions. The MICCA-EM2C-Palies laboratory-scale combustor is used to introduce key features of premixed swirling flames. The experimental setup comprises three main parts: a plenum ended by a contraction with a constant diameter (not shown here), the injector where the swirler made of NACA 8411 vanes is located, and a cylindrical quartz tube allowing optical access. An air–methane premixture of equivalence ratio 0.7 is generated and the rotation of the flow is induced by the swirler equipped with twisted vanes arranged periodically around the central rod. Velocity measurements with hot wire anemometry and LDV have been carried out on this setup. Photomultiplier signal acquisition and ICCD camera flame imaging were also conducted. The time-average velocity field in the $(r\text{-}z)$ plane colored by axial velocity is displayed in the left panel of Fig. 2.6, while in the right panel the instantaneous photograph of the chemiluminescence light signal showing the flame wrinkling by various turbulence scales is given. Swirling jet boundaries and iso-0 axial velocity contours identified from the left panel are superimposed on the right panel for illustration.

The key features of swirling flames are presented in Fig. 2.6. It includes the inner recirculation zone (IRZ) and outer recirculation zones (ORZs) identified on the time-average velocity field, along with the shear layers positioned on the sides of the swirling jet (inner and outer shear layers). The flame chemiluminescence image allows to distinguish the flame surface and the relative location of this surface with respect to the time-average velocity field for this statistically steady operating condition. No precessing vortex

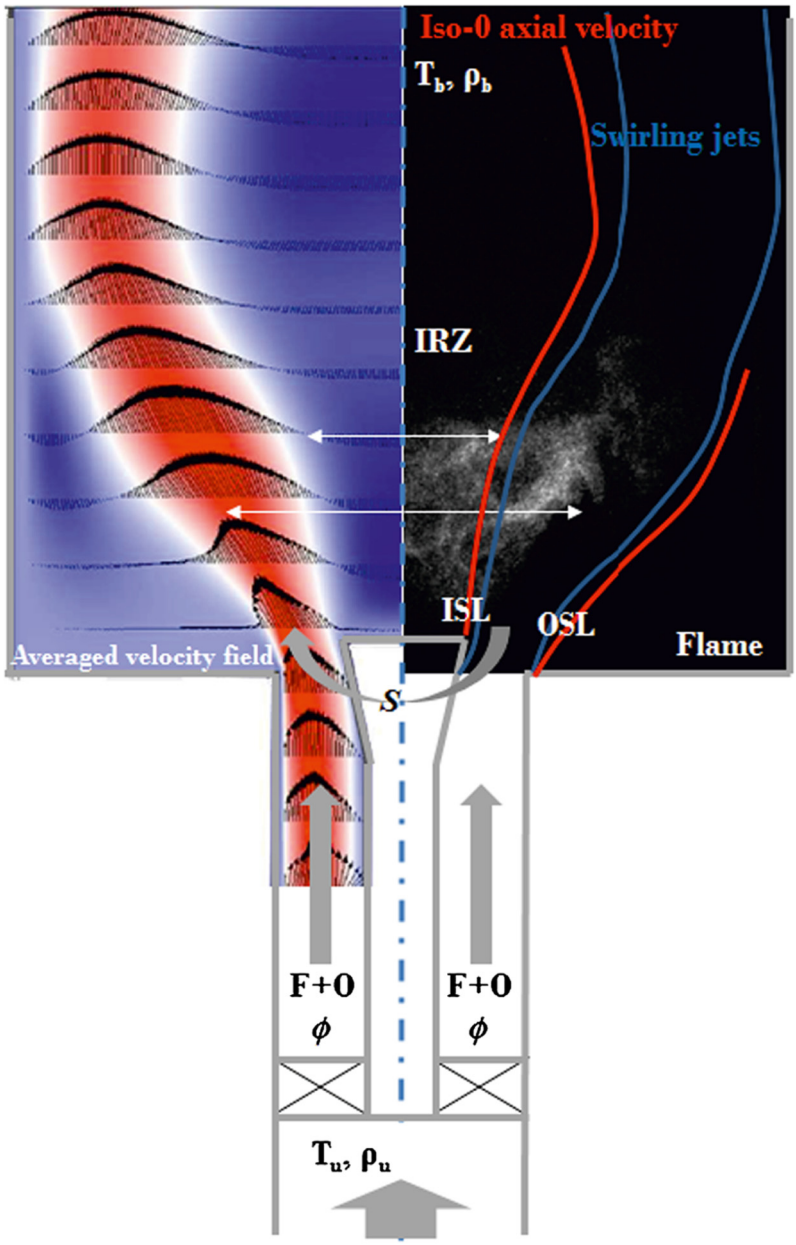

Figure 2.6 Swirling flame chemiluminescence and time-average velocity fields. MICCA-EM2C-Palies premixed confined swirling flame configuration. Left panel: Time-average velocity field in the (r-z) plane colored by axial velocity. Right panel: Instantaneous photograph of the chemiluminescence light signal from the flame showing the flame wrinkling by turbulence. Swirling jet boundaries and iso-0 axial velocity contour identified from the left panel are superimposed. The quartz tube diameter is 70 mm.

Table 2.4 List of possible swirling flame flow features under stable configuration.

Flow feature	Comments
Swirl flow rotation	Oscillation frequency associated with $v_\theta = \Omega r$
Inner/central recirculation zone (IRZ)	Central reversal flow
Outer/corner recirculation zone (ORZ)	Corner reversal flows
Azimuthal shear layer (ASL)	Shear layers due to azimuthal velocity gradients
Swirling jet (SJ)	Main momentum stream
Inner shear layer (ISL)	Due to velocity gradients interface IRZ/SJ
Outer shear layer (OSL)	Due to velocity gradients interface ORZ/SJ
Vortex shedding	Swirler vortex shedding function of swirl number
Swirler's vane wakes	Wakes associated with the vanes inducing velocity deficit
Vortex breakdown	Bubble type or spiral type
Precessing vortex core (PVC)	Precessing of the central vortex core

core has been identified in this configuration at those operating conditions, which may be due to the presence of the central rod inhibiting the central vortex core generation.

Tab. 2.4 lists the possible swirling flame flow features under stable configuration. The present section discusses some of those. Each of these phenomena has a specific oscillating frequency that depends on the particular configuration considered. Future work should include systematic investigation and identification of each of those flow patterns on a single configuration. A key aspect of swirling flames is the existence of flow features which interact with the flame front. The axisymmetric vortex breakdown mode consists of a reverse flow downstream of the swirler in the combustion chamber. This reverse flow, also known as inner or central recirculation zone (IRZ), is used to stabilize the flame by recirculating the hot combustion products acting as a heat source. For swirling flows above a certain threshold, a strong recirculation zone will exist, while for lower swirl number, there is no recirculation zone or vortex breakdown appearing. In reality, this swirl number threshold is not universal and can vary from configuration to configuration due to geometry and the specific velocity profiles created. The IRZ has effects on the flow strain at the flame surface, the associated pressure gradients will have an effect on the flame speed, and the flow balance between flame speed and local velocity will be impacted. The precessing vortex core is an oscillating pattern occurring near the shear layers and the IRZ. It consists of a helical vortex tube precessing around the axis of the combustor such

that the center of rotation of the helical vortex is not the center of the combustor. This structure is present in nonreacting and reacting flowfields and impacts the upstream flow/flamefield, like the mixing. The precessing vortex core (PVC) impacts other local contributors, like the vorticity, the flow strain, the local equivalence ratio, and the local flow versus flame speed balance. Between the IRZ and the ORZ, the shear layers are zones of intense gradient of velocity on both sides of the swirling jets. The inner shear layers at the interface of the swirling jets and the IRZ will significantly impact the level of flow strain at the flame surface and the vorticity field. The outer shear layer is at the interface of the IRZ and ORZ. The ORZs present a reverse flow on the sides/corners of the combustion chamber confinement and participate in the organization of the overall swirling flowfield for a specific design. It is worthwhile to mention that these flow features are important to the understanding of the local flowfield in the swirl-stabilized combustion chamber. In other words, these large-scale phenomena are directly responsible for some local contributors identified, which will directly affect the flow physics. In addition to these large flow scales, it is important to highlight the swirler as a central source of turbulence generation upstream of the flame front. This function usually ensures mixing of fresh gases. The generation of turbulence by the swirler will also play a key role in the determination of the flame speed. This point will require detailed analysis of the turbulent flowfield, turbulence levels, and turbulence spectra generated by various swirlers. Finally, generation and existence of some of these structures/features (for example, PVC and vortex shedding) depend on the geometry. This is the case for swirling flows with or without the presence of a swirler and with or without the presence of a central rod (bluff-body).

2.3 Acoustic wave–flame interactions

There are four main acoustic wave–flame interactions: (i) the interaction of acoustic waves propagating from the unburned mixture with the flame front, (ii) the interaction of acoustic waves propagating from the burned gases with the flame front, (iii) the acoustic waves propagating in the unburned gases and leading to convective vortical/velocity waves through mode conversion processes, and (iv) the generation of acoustic waves by the flame front, covered in combustion noise studies. These interactions have been the topic of many studies and reviews, see Lieuwen [132] for (i), see Lieuwen [133] for (ii), see Palies et al. [134] for (iii), and see Candel et al. [135] for (iv).

The interaction of acoustic waves propagating from the unburned mixture with the flame front has been investigated in a

multitude of geometrical configurations in the laminar regime. These studies rely largely on the determination of the so-called flame transfer function, which is the flame response to inlet loudspeaker modulations. Transfer functions are characterized in terms of nondimensionalized heat release fluctuations with respect to the upstream nondimensionalized acoustically induced velocity fluctuations for a range of frequencies. When the input velocity signal is also a function of the amplitude level, the function is called the flame describing function. In Ducruix et al. [128], the authors focused on laminar conical flames submitted to acoustic waves, and the comparison between theory and experiments led to the verification of model assumptions for the phase of the transfer function, i.e., for the propagation speed of disturbances. In Schuller et al. [129], the authors used an acoustics and a convective model for the flame transfer function of conical and "V" flames, the latter allowing more precise predictions and confirming the convective propagating mechanism of disturbances. Laminar "V" flames were considered by Durox et al. [136], clearly demonstrating experimentally the vorticity mode convected along the flame front. These studies have shown the role of the mode conversion processes in these configurations. A systematic experimental approach for various laminar flame configurations was reported by Durox et al. [137]. Various scalings of the flame transfer function have been proposed based on these studies, see Schuller et al. [138], Cuquel et al. [139]. An important aspect in the scaling is that of the mean flow speed along the flame front, an influential parameter for combustion dynamics and self-sustained oscillations. These types of studies have been extended to turbulent conical flames by Preetham and Lieuwen [140], who used G-equation modeling. The authors noted that the turbulence affects the time-average flame shape. The case of turbulent "V" flames submitted to upstream acoustic waves was investigated experimentally by Balachandran et al. [141,142] and numerically by Armitage et al. [143]. Similarly, the turbulent "V" flame configuration was studied by Chapparro et al. [144]. While these studies have led to tremendous improvements in our understanding of the interaction of upstream acoustic waves with premixed laminar and turbulent flame fronts, future work should be undertaken to analyze the mechanisms at work in a transient time sequence to measure, simulate, and observe the finest interactions between the flow modulation and the flame front dynamics, including the flowfield–reacting flame front interaction. The interaction of acoustic waves propagating from the burned gases with the flame front is significantly less documented in the literature. It has been studied analytically by Lieuwen [133], but there is a lack of nu-

merical and experimental studies allowing to precisely isolate and study those effects for harmonic and broadband noise. It is straightforward to understand the challenges associated with numerical simulations and experiments enabling those researches in a reacting medium. While the acoustic waves propagating in the unburned gases and leading to convective vortical/velocity waves through mode conversion processes have been discussed for canonical configurations in the previous paragraph, the case of swirling flames will be considered further in a dedicated section of Chapter 5. Finally, the generation of acoustic waves by the flame front, known as combustion noise, has been the topic of recent investigations, see Rajaram and Lieuwen [145], Blanchard et al. [146], Haghiri et al. [147]. These interactions will be further detailed in a dedicated next section.

2.4 Autoignition

The phenomenon of autoignition, also called spontaneous ignition, is of importance to the design of novel advanced combustion systems, such as the LFP, detailed in Chapter 7. Autoignition can be defined as the ignition of a mixture without any external sources (of heat or additional radical/species). In other words, the local temperature and mixture composition of the mixture are sufficient to activate the ignition. Autoignition is often characterized with an ignition time that corresponds to the time taken to evolve from the unburned gas temperature to the burned gas temperature. The ignition time varies considerably with the temperature and pressure considered for a given fuel mixture. There are a few methods to determine this ignition time. Computations where the flow is not taken into account are practical to obtain rapid and comprehensive trends of the ignition times for various conditions. Unlike these computations, measurements imply the need to take the flow time until ignition into account, requiring additional calculations. It is important to understand that in such experiments this ignition time is reflected as a distance which depends on the geometrical configuration and intrinsically on the turbulent mixing. Consequently, the ignition time corresponds to the ignition distance too, and consequently depends on the detailed fluid dynamical processes within the flowfield. This is important for the design of injectors for combustors. The ignition time is inversely proportional to the pressure and the reaction rate. At high pressure, the ignition time is short. For example, for kerosene at 50 atm, it is of the order of one millisecond. A short ignition time also corresponds to a high reaction rate, expressed as an Arrhenius law. Measurements of ignition time delays are experimentally

carried out with three main tests: rapid-compression machines, shock-tube, and flow reactor/continuous preheated flows experiments. The shock-tube experiment makes use of the downstream shock side high temperature level as thermal energy source. The flow reactor allows to measure the distance from the fuel injector to the reaction front to determine the ignition time. In those experiments, the flow can be swirling or not.

In Lefebvre et al. [148], the authors studied the autoignition of lean hydrocarbon mixtures with temperature range between 670 K and 1020 K at various pressures. For gaseous mixtures, the autoignition time is the sum of the time for the fuel vapor to mix with the air and the time of the chemical kinetics. The mixture then autoignites at some distance downstream, depending on the air velocity. Similar studies have been undertaken on jet flames by Cabra et al. [149,150], where the coflowing hot vitiated flow provides the heat to the central fuel jet stream, leading to a distance where the flame stabilizes. This has been further studied by Schulz et al. [151], where limited reactions were observed immediately downstream of the injection prior to the autoignition and flame stabilization of the methane–air jet in the 1350 K vitiated coflow occurring far downstream. It is clear that the role of the turbulent flow and associated heat losses, see Mastorakos et al. [152] is significant in terms of impact on the ignition time delay, and the method to determine its value has to be the closest to the target application.

2.5 Blowout

Lean blowout (LBO) is important because this phenomenon can occur at regimes that are relevant to the performance and operation of gas turbine engines. In addition, they are of interest for the reduction of NO_x emissions. While a review of lean blowout has been carried out for bluff-body flames, see Shanbhogue et al. [49], no such review exists for swirl-stabilized flames. As a first step in reviewing the literature, it is important to recall the definition of the blowout or blowoff given by Zinn [153]: "A significant issue for both Lean Premixed Pre-vaporized (LPP) type combustors and conventional (partially premixed) combustors is flame stability during lean operation, i.e., lean blowout, which can result in a severe operability loss. Flame stabilization involves competition between the rates of the chemical reactions and the rates of turbulent advection and diffusion of species and energy to and from the flame, and includes local ignition and extinction behavior. As the equivalence (or fuel-air) ratio of a reaction zone is reduced, extinction events become more likely, and the lean limit for stable operation may be reached." Blowout is defined as the observation that

the flame is blown away from the combustor. Blowoff is the total extinction of the flame. Extinction usually refers to blowoff or local extinction events. Blowout and blowoff processes are a unique process: blowoff and blowout are coupled. A dedicated section in Chapter 4 will review the mechanisms by which blowout occurs (the term blowout will encompass blowoff too) for lean regimes in swirl-stabilized combustors. We refer here to lean regimes for the following types of applications: lean premixed/prevaporized (LPP) and lean fully premixed (LFP). The main objective of that review is to identify in the literature the existing mechanisms responsible for blowout.

2.6 Chemical kinetics

Chemical kinetics of reacting flows are crucial for the understanding and the design of injection/combustor systems. While the next chapters will show the key role of the flowfield in flame stabilization and the dynamics of swirling flames, there are specific aspects of future combustion systems that will require detailed chemical mechanisms. This is for example the case to model autoignition in LFP systems such as presented in Chapter 7. It is also the case for the evaluation of the sensitivities of chemical mechanisms with respect to vorticity vector components and flame stretch terms. It will enable to compare the local flame displacement speed in turbulent 3D swirling reacting flows for single-step and complex chemical combustion mechanisms. Chemical kinetics is defined by the chemical reactions that occur between a given oxidizer and a fuel. These chemical reactions involve various chemical species, substances, and radicals that collide together which determine their rates of variations. These collisions are modeled with two main elements: a reaction mechanism and the parameters of those reactions. The reaction mechanism can be simplified or detailed. It is a model of the collisions taking place between substances. It informs on the chemical reaction occurring between substances, species, and radicals. The parameters of those reactions are the parameters of the Arrhenius law that controls each reaction. The Arrhenius law is generally written as the product of the collision factor A with the exponential term $\exp(-E_a/RT)$. The collision factor A for each reaction of a given chemical combustion mechanism provides the number of collisions per second between the substances/species considered. The activation energy E_a of those reactions reflects an energy threshold that is required to trigger the reactions implied by those collisions, i.e., the passage from one species/substance to another one. The modeling of combustion in combustors requires an approach that takes into account the chemical kinetics. This step

needs the determination of a design intent or a goal. For example, the prediction of emission of pollutants such as NO and NO_2 requires a set of mechanisms able to model the formation of those species (prompt NO, thermal NO, etc.), that is, a mechanism of relevant complexity. Single-step or global mechanisms have shown tremendous impact in turbulent reacting flows, for example in the modeling of combustion instabilities. The advantage of these simplified mechanisms is that they enable numerical simulations of highly refined large-scale combustion systems. The main disadvantage of these simplified mechanisms is that they cannot predict pollutant emissions, unless using a posteriori processing, and their validity is usually limited to the lean regime only for premixed combustion. In addition, the single-step mechanisms are very stiff compared to complex chemical mechanisms, i.e., the temperature gradients and the reactions throughout the flame front are taking place on very small spatial scales, which has limited their usage due to grid requirements. There are various methods to investigate complete detailed combustion mechanisms and single-step combustion mechanisms: analytically reduced chemical mechanisms, virtual chemical mechanisms, or mechanisms based on data mining studies. It is also important to outline for future applications that some substances generated as intermediates during combustion are ionized, i.e., these substances have lost or gained electrons. Accordingly, these aspects may be modeled considering the set of electromagnetism equations in a coupled fashion to the full reacting (magneto-hydrodynamic) flow equations and potentially lead to the discovery of control methods for combustion. To finalize this section, it is also important to point out that some of the substances emit radiation (along a wide spectrum or at discrete spectral bands, depending on the species) during the chemical reactions and obviously some of them release heat.

2.7 Combustion noise

In addition to elements of turbulent combustion, combustion noise aspects relevant to swirl-stabilized combustors are reviewed in this section. The theoretical framework of combustion noise has been established by Chiu and Summerfield [154], who focused on the identification and quantitative description of the mechanisms of noise emission from different combustion processes. This pioneering article also emphasized the need of detailed understanding of the interaction between waves such as acoustic, entropy, and vortical waves in the combustion zone as an essential step towards the identification and the description of

the noise sources. The reviews of Strahle [155,156] have been focused on presenting the state of the art in physical understanding, prediction, and scaling for combustion noise in different combustion systems, including gas turbine engines. The main message in these articles was that combustion noise is a turbulence–combustion interaction. The article of Putnam and Faulkner [157] reviewed broadband noise emission of diffusion flames. More recently, attention has been paid to the fundamental noise generation mechanisms from premixed flames, see the progress and perspectives review of Candel et al. [135]. The article of Duran et al. [158] documented the standard method to predict the direct and indirect combustion noise from aeroengine combustors by using a combination of large eddy simulation (LES) and analytical methods, respectively, for the noise sources and their propagation through the engine components. The article of Dowling and Mahmoudi [10] reviewed in detail theoretical, numerical, and experimental studies on combustion noise. In the review of Ihme [11], the focus was on turbulent reactions and exhaust jet noise and the effect of flow disturbances. The focus of the book of Schwarz and Janicka [159] was on predicting methods for combustion noise and the investigation of emission sources.

This section examines specifically the noise emitted from swirl-stabilized combustion regions. In a jet engine, the contribution of the noise emitted from the combustor to the environment increases as the other sources of noise (fan, exhaust, airframe) are reduced. In a geared turbofan jet engine, the fan has a reduced rotational speed, contributing to the fan noise reduction along with a high bypass ratio, allowing reduced exhaust jet velocities. These two complementary design choices have significantly reduced the overall noise signature of geared turbofan engines but in the meantime increased the combustor noise contribution.

Combustion noise has been traditionally split into two categories: direct and indirect combustion noise. Direct combustion noise refers to the noise emitted directly by the flame, while indirect combustion noise is the noise induced by the former (the reacting flowfield) interacting with the combustor flowfield and the combustor boundary conditions. Indirect noise can be referred to as combustor noise, as it is strongly dependent on the combustor geometry and the operating conditions. Direct noise can be referred to as flame noise, as it relates strongly to the unsteady heat release of the flame (the latter also having some dependency on the geometry of the combustor through the flowfield and the operating conditions).

The identification of mechanisms and sources of direct noise or flame noise has been the subject of a few investigations for

swirling flames. One important aspect for combustion noise relies on the experimental measurements of both the turbulence–chemistry interaction and the associated density fluctuations, as those fluctuations are directly associated with the unsteady heat release. Such measurements have been undertaken by Greiffenhagen et al. [160] with laser interferometric vibrometry in order to calculate the overall sound power emitted by the flame. In Merk et al. [161], the authors compared the sound pressure amplitudes and spatial distributions from experiments and predictions from LES for a confined turbulent premixed swirl burner, reaching a good agreement. Another approach for the modeling of combustion noise applied to the Preccinsta swirling flame implied the use of time-average and fluctuating flowfields coupled to linear equations to model the sound propagation, see Grimm et al. [162]. The indirect noise or combustor noise is related to the interaction of entropy, vortical, or acoustic waves with the boundary conditions of the combustor. An evaluation of both contributions on an aero-engine combustor was attempted by Liu et al. [163] by splitting the modeling approach for the source generation and the propagation within the combustor, and similarly by O'Brien et al. [164] making use of theoretical and numerical simulation results to predict the far field radiated noise. The article of Grimm et al. [162] presented a developed framework to identify acoustic sources which was applied to the DLR-Preccinsta-Lartigue configuration. The methodology relied on the averaged flowfield and the turbulence statistics from numerical simulations and attempted to determine the direct versus indirect noise in the combustor. Entropy noise has been the subject of multiple fundamental studies on canonical configurations experimentally, numerically, or theoretically, see the review by Morgans and Duran [165]. The article of Livebardon et al. [166] focused on the theoretical coupling between LES results obtained on a full annular chamber (where the waves are generated) and an actuator (where the waves are transmitted), confirming the importance of the contribution of entropy noise to overall radiated noise. The article of Silva et al. [167] focused on assessing the effects of full LES versus hybrid LES/acoustic analogy combination on combustion noise modeling of a swirl-stabilized combustor. In Silva et al. [168] the authors focused on the BRS-TUM-Komarek configuration and assumed that sound is generated firstly by the unsteady heat release induced by turbulent fluctuations and secondly from the response of the flame to incoming acoustic perturbations. The first effect is described by a source term for combustion noise, i.e., a spectral distribution of the unsteady heat release rate. The second is described by a flame transfer function. Both quantities were identified from time se-

ries data for fluctuating velocity and heat release rate, generated with LES of a premix swirl burner. The subsequent impact of those sources in terms of thermoacoustics modeling was also investigated.

Combustion noise has been documented and reviewed by several authors, see Chiu and Summerfield [154], Strahle [155,156], Putnam and Faulkner [157], Candel et al. [135], Leyko et al. [169], Tam et al. [170], Duran et al. [158], Dowling and Mahmoudi [10], Ihme [11], and in a book, see Schwarz and Janicka [159].

2.8 Combustion instability

Combustion instability refers to a coupling between the combustion and the flowfield through the acoustics of the combustor. The field of combustion dynamics focuses on the interaction of waves, aerodynamic structures, and combustion processes inside the combustion chamber. Due to this challenge as well as fundamental interest, swirling flame dynamics have been extensively investigated, see the reviews by Huang and Yang [22], Candel et al. [23]. Future advanced propulsion and power systems may operate in lean premixed mode, i.e., when fuel and air are homogeneously mixed to form a premixture to achieve lower pollutant emissions. The lean premixed mode is sensitive to combustion dynamics, see Candel [171], Poinsot and Veynante [172], Lieuwen [35]. Combustion instability stems from the resonant closed loop involving the flowfield, the flame region, and the combustor acoustics. When an unsteady heat release source is generated due to flow structures or waves, it induces an unsteady pressure field that feeds back to the initial flow disturbances through the combustor cavity acoustics and the mode conversion processes. The mechanisms by which flames respond to flow oscillations are of primary importance for unsteady heat release modeling.

Research on swirling flames dynamics and combustion instabilities in swirl-stabilized combustion systems has been the subject of several monographs, studies, and review articles. Prediction of combustion instabilities at the design and developmental stages of jet engines and gas turbine combustors is a challenge. There has been a significant amount of research on combustion instabilities, and this topic has been reviewed in many articles, including, but not limited to, Crocco [173], Putnam [174], Culick [175], Candel [171] for canonical configurations, Huang and Yang [22], Candel et al. [23], O'Connor et al. [176] for swirling flames, and Lawn and Penelet [177], Juniper and Sujith [178] for other configurations. The prediction and control of combustion instabilities in realistic geometries has been recently reviewed by Poinsot

[179]. It is known that high performance combustors feature instabilities which are mainly driven by the unsteady heat release rate. In these systems, the heat release rate fluctuations can be delayed with respect to incident perturbations and give rise to growing oscillations, see Crocco [173], Putnam [174], Culick [175]. These perturbations can be generated in many different ways, as seen in the previous section, but in most cases they are associated with convection of aerodynamic perturbations, see Candel [171], Palies [180], or fluctuations in reactant composition, see Lieuwen and Zinn [181].

2.9 Flame speed

The flame speed is a key quantity in laminar and turbulent premixed combustion. The former is very well characterized in 1D and validated experimentally, while the latter will benefit from new perspectives in experiments and modeling in the future. This section begins with reviewing the existing flame speed definitions and expressions. The flame surface speed vector is given by $\mathbf{w}$. The burning velocity, also referred as the displacement speed, is denoted as S_D. In laminar regimes, the flame speed writes $S_D = S_L$ for any laminar stretched flame and $S_D = S_L^0$ for the unstretched flames configuration, such as obtained from 1D laminar premixed flame calculations or from theoretical solutions. The 1D laminar flame speed, also known as the unburned laminar flame speed, is defined as the upstream axial velocity of the velocity profile in such calculations, where the flame has constant position. Theoretical solutions of unstretched laminar premixed flames aim at characterizing the flame speed for different assumptions. They enable to study trends of laminar flame speed for various pressures and temperatures for example. Derivations and expressions of unstretched laminar flame speeds are documented in Poinsot and Veynante [172]. For stretched flames, there are analytical expressions enabling to define S_L. As will be discussed in the next section, the flame stretch κ includes various terms (flow strain, flame curvature, flow dilatation) and consequently requires expressions that depend on those terms. These effects are classically defined by the following expression: $S_D = S_L = S_L^0 - \mathcal{M}\kappa\delta$, where the Markstein number is defined by $\mathcal{M} = \mathcal{L}/\delta$, where the Markstein length $\mathcal{L}$ is the variation of flame speed with respect to the flame stretch. These previous results are very important for the understanding of premixed turbulent combustion flame speed in the flamelet regimes (corrugated or wrinkled), as these expressions may hold for these turbulent regimes too. There is also an additional flame speed, known as the turbulent flame speed S_T,

that is important to discuss in the present context. We will see that these notions are points of discussion in the literature and that their definitions may be modified with respect to recent results discussed in Chapter 4. The first notion is that of the equivalence of the ratio of turbulent flame speed to the unstretched laminar speed S_T/S_L^0 and the ratio of turbulent flame area to the flame surface area A_T/A. The second notion is that the turbulent flame speed correlation S_T has many forms, see the reviews by Lipatnikov and Chomiak [182] and Kuo and Acharya [21], and is mostly defined as $S_T/S_L^0 = 1 + a(u'/S_L^0)^b$, where a and b are experimentally obtained. Another important definition of the displacement speed is now given:

$$S_d = \frac{\nabla \cdot \lambda/c_p \nabla T + \dot{\omega}_T/c_p}{\rho|\nabla T|}. \tag{2.35}$$

This flame speed includes two elements: the thermal diffusion and the reacting terms. This definition will be used throughout the book. In Chapter 3, the flame speed will be particularly studied in the context of flame stabilization and combustion instability with a recently developed approach.

2.10 Flame stretch

The flame stretch κ is a variable that quantifies three effects on the flame front: (i) the flow strain effect, (ii) the flow dilatation effect, and (iii) the flame curvature effect. These effects impact the flame surface area evolution as a function of time. The flow strain effect consists of the velocity gradients of the flow expressed at the flame surface as $\mathbf{nn} : \nabla\mathbf{v}$, where $\mathbf{n}$ is the normal to the flame front and $\mathbf{v}$ the velocity vector. It is important to recall that the flow strain is the summation of nine terms. The term associated with flow dilatation writes $\nabla \cdot \mathbf{v}$, and the term associated with the flame curvature is expressed as $S_D \nabla \cdot \mathbf{n}$. The flame stretch is consequently made up of a sum of 15 terms, and each of these terms has specific effects on the flame speed and the inner flame structure in 3D turbulent flow. Flame stretch is an important quantity because it influences the local flame speed S_D, it impacts flame extinction, and it affects flame surface area variation. While flame stretch effects are very well documented for canonical configurations, allowing to isolate some specific terms, the effects of the individual 15 terms on the flame stretch in 3D turbulent premixed flame are largely unknown, and would require detailed 3D investigations with large data analysis capabilities. Flame stretch is important for flames in laminar, unsteady laminar, and turbulent flowfields. Because of the 1D-like flame structure in the turbulent flamelet

regime, flame stretch is a quantity to take into account for flame understanding and modeling. Flame stretch and detailed expression of this quantity will be further discussed in Chapter 4, which focuses on flame stabilization.

2.11 Flammability limits

The flammability limits of a premixed flame are defined as the lower and upper equivalence ratio for which combustion can occur. These limits depend on the fuel considered and vary as a function of the pressure and the temperature. For fully premixed flames, upper rich and lower lean extinction limits are known for specific values of the global equivalence ratio, which depends on the fuel. The flammability limits are functions of local temperature and pressure Williams [125], Lovach Ev [183] as well. Flammability limits directly impact extinction and lean blowout phenomena. Unlike perfectly premixed combustion, where the composition of the mixture is homogeneous, significant variation of the local composition of the mixture is observed in other types of premixed flames, as the mixture is still premixed but at various levels. Thus, in those flames, local pockets of fuel-lean or fuel-rich composition, which may be outside the flammability limits, can be reached.

2.12 Flashback

Flashback usually occurs when the flame propagates towards the upstream fresh gases at a speed higher than the incoming flow speed. The articles of Caffo and Padovani [37] and Plee and Mellor [38] have reviewed flashback mechanisms. In Sommerer et al. [39], fundamental mechanisms leading to flashback were studied and briefly reviewed. The recent monograph of Benim and Syed [40] provides an overall description of the mechanisms of flashback in premixed combustion systems. Flashback of swirling flames has received significant attention in the literature. The phenomenon has been studied with simultaneous high speed laser diagnostics (PLIF and PIV) by Konle et al. [41], Konle and Sattelmayer [42] for confined swirling flows. The authors identified the interaction of heat release by chemical reactions and the flow turbulence as the main contributors to flame transition to flashback. Flashback has also been investigated by Heeger et al. [43] using time-correlated, simultaneously acquired PIV, OH-PLIF, and chemiluminescence data at acquisition rates of several kHz. It was observed that flashback in this configuration was often associated with negative axial velocities beneath the flame base tip. The role of the wall boundary layer low velocity region was initially studied by Kurdyumov

et al. [44] and has been recognized as a significant contributor to upstream flame propagation of premixed flames. This aspect was also analytically and experimentally studied by Kurdyumov et al. [45], considering the propagation in a duct. The role of the wall boundary layer was investigated in Eichler and Sattelmayer [46] for a methane–hydrogen–air premixture. It was observed that the turbulent transport inside the boundary layer considerably increased the flashback propensity.

2.13 Ignition

The description of ignition of reacting flows is now carried out. The fundamental principle is that an energy source initiates the combustion reactions of the mixed reacting species through heat and species/radicals formation. Significant challenges exist in achieving that objective in combustion devices for a wide range of operating conditions because of the complexity of the physics associated with the transfer of energy and species or radicals between the igniter and the flowfield. As a consequence, there is a need for analysis, modeling, and study of ignition processes with respect to real combustors. In the present section, a brief presentation of the key known ignition processes and mechanisms that initiate chemical reactions within a flow with fuel and air is given. Specifically, the role of spark, laser, and plasma ignition is presented. Continuous combustion systems such as swirl-stabilized and bluff-body-stabilized systems induce a recirculation zone of hot gases, producing the heat source of the upstream fresh reactants, see Lefebvre [34], Shanbhogue et al. [65], Huang and Yang [22], and favorable fluid velocity regions for flame anchoring, see the recent description by Palies [29]. While these methods for stabilization are robust, they need an initial start and can suffer from blowout phenomena along the flight envelope. Continuous systems for flame stabilization need an external igniter after blowout, or to start the engine. The three main ones are now detailed. Spark ignition involves making use of an igniter located within the combustor that will create a local energy source. This is achieved by imposing an electrical current between two electrodes. This induces a local energy discharge and a local ionized gas with high local thermodynamics temperature, see Lacaze et al. [66], Maly and Vogel [67], that will be convected by the gas flow, see Swett Jr [68]. As this spark kernel is created, it propagates and ignites the combustor fresh gases, see Kravchik and Sher [69]. One important aspect is that the spark kernel has to cross a region of appropriate FAR in order to initiate and sustain combustion. Spark igniters are not expensive but suffer from fixed location in the combustor and

therefore can result in nonignition in some situations. Depending on the combustion mode (premixed versus nonpremixed), ignition has different challenges. For example, for a diffusion flame, there is a limited zone where the flame can be ignited, contrarily to a fully premixed flow. Laser ignition involves using laser beams to induce a local increase of temperature that will initiate combustion. Laser ignition is more complex to implement but has the potential to be oriented in the combustion chamber to focus on different spatial locations so that energy addition occurs in favorable locations. Plasma discharge induces ignition in a manner similar to spark ignition in that the plasma ionized gas created (by a current between two electrodes) impacts the local flowfield, adding heat and chemical radicals and allowing potential ignition, see Grisch et al. [70]. Plasma in combustion application has been recently reviewed, see Ju and Sun [71], Starikovskiy and Aleksandrov [72], including its application for ignition in combustors.

2.14 Pollutant emissions

The reduction of combustion systems' CO_2 emissions is today one of the top priorities, not only in combustion sciences and technologies but in public policies as well. Two specific approaches will enable such drastic reductions: premixed and hydrogen combustion. The first involves utilizing fully premixed gases prior to combustion as a way to reduce pollutant emissions with respect to existing combustion architectures. The second method is the use of hydrogen to stop CO_2 emission. The technological motivations of current research and development projects are to enable technologies to reduce or stop the formation of CO_2. To do so, these projects are dedicated to develop fundamental scientific understanding of processes with premixed hydrocarbons and hydrogen combustion. One method for nitric oxide (NO_x) emission reduction involves burning in a lean premixed mode, where fuel and air are premixed before they react. This method also reduces the formation of CO_2 in lean regimes compared with stoichiometric conditions. While this method allows reduction in pollutant emissions, it does not allow complete suppression. One possible method for complete suppression of pollutant emissions, including NO_x and CO_2, is hydrogen combustion, for which the reaction between the three species at work writes $2H_2 + O_2 \Rightarrow 2H_2O$. This single-step combustion reaction indicates that the reaction of dihydrogen and dioxygen will generate water vapor and release heat. This is a major argument in favor of hydrogen/oxygen combustion to suppress the formation of pollutants. While it gives rise to many technical challenges, it is now a technical path that could be considered.

2.15 Turbulent combustion

In the present section, the focus is on turbulent combustion with specific emphasis on premixed combustion. A comparison between laboratory-scale and representative jet engine operating conditions is firstly given to set orders of magnitude. The focus is on laboratory-scale experimental and numerical simulation results. It is important to recall the differences between operating regimes of laboratory-scale and jet engine configurations. For example, the operating pressure and inlet temperature are different. Typical lab-scale combustors operate at atmospheric conditions (1 atm, 300 K) while jet engines operate at higher values (30 atm, 750 K). This affects turbulence and combustion processes, particularly the characteristic Kolmogorov and flame thickness scales.

Premixed turbulent combustion has been examined in many monographs, such as Poinsot and Veynante [172] and Kuo and Acharya [21]. Turbulent combustion regimes are generally studied with the turbulent premixed combustion diagram in order to build a bridge between the operating conditions of a configuration and the subsequent turbulent combustion modeling approach required. The classical turbulent combustion diagram of Peters [184] consists of characterizing the regime with the level of turbulence (RMS velocity nondimensionalized by laminar flame speed) versus the integral length scale of the largest eddies nondimensionalized by the flame thickness. The diagram allows for example to distinguish regimes where the combustion can be described as thin reaction zones or distributed reaction zones. It is also worthwhile to point out that for a given configuration, multiple regimes can coexist, depending on the location inside the flame region and the operating conditions. Multiple characterizations of the turbulent combustion regions have been carried out with DNS to describe and understand the interaction of a turbulent flowfield with a premixed flame front on canonical configurations represented by 3D boxes. These configurations have allowed tremendous progress in turbulent combustion but have been limited to a small computational domain due to the high CPU requirements. In addition, 3D boxes cannot replicate some key spatial scales of realistic configurations due to size limitations. For example, the influences of the turbulent integral length scale (such as for the swirler or injector diameter) or the wavelengths of propagating acoustic waves (through reflections at the walls) on the local velocity field cannot be captured. 3D box simulations will continue to be a fundamental tool for turbulent premixed combustion research and will benefit from the inclusion of relevant parameters of additional applications. This will require novel modeling strategies: embedded DNS, hybrid DNS/LES approaches, and lo-

cal mesh refinements (static or dynamic). Because numerical simulations have made and will make tremendous impacts on technology design, such possible future strategies have to be complemented with improvements of the present existing tools, for example for turbulent combustion with LES modeling. Some of the challenges discussed in this section are in direct connection with the Model Validation for Propulsion Workshop held by the AIAA, an open forum bringing together researchers and modelers to help improve the understanding and capabilities of modeling turbulent reacting flows in relevant aerospace propulsion systems.

Few direct numerical simulations have been carried out to fill this need, see the two swirling flame configurations shown in Fig. 4.4. The challenge of these direct simulations is the development of dedicated, fast postprocessing tools to improve our physical insight and to refine the design of technologies. On the other hand, experimental visualization of turbulent flames at jet engine operating conditions is rare too. These data, from both experiments and numerical simulations, will be key in order to refine our understanding of the physical mechanisms at work and some aspects of the technologies that rely upon them.

2.16 Turbulent mixing

Turbulent mixing is an important process that is used to form a premixture between fuel and air. It is consequently an important aspect of the injection design. In any combustion application, at the laboratory scale or at the gas turbine engine scale, the fuel and air flow through two distinct streams. They are both required to mix to form a premixture to enable premixed combustion. There are various forms of mixing. Turbulent mixing is one of the most efficient ways to achieve full premixing in a given injection system. This is usually carried out with the use of so-called swirlers (also known as mixers), as these systems generate high turbulence levels. A mixing tube can also be employed to enhance mixing downstream of a swirler. Perforated plates also impact mixing.

3 Combustion modes

3.1 Overview

The combustion mode can be defined as the state of the mixture upstream of the flame zone in the injection system. As is known, there are two main types of flames: nonpremixed (also known as diffusion) flames and premixed flames. The former are mostly used in rich-burn quick-quench lean-burn (RQL) and lean

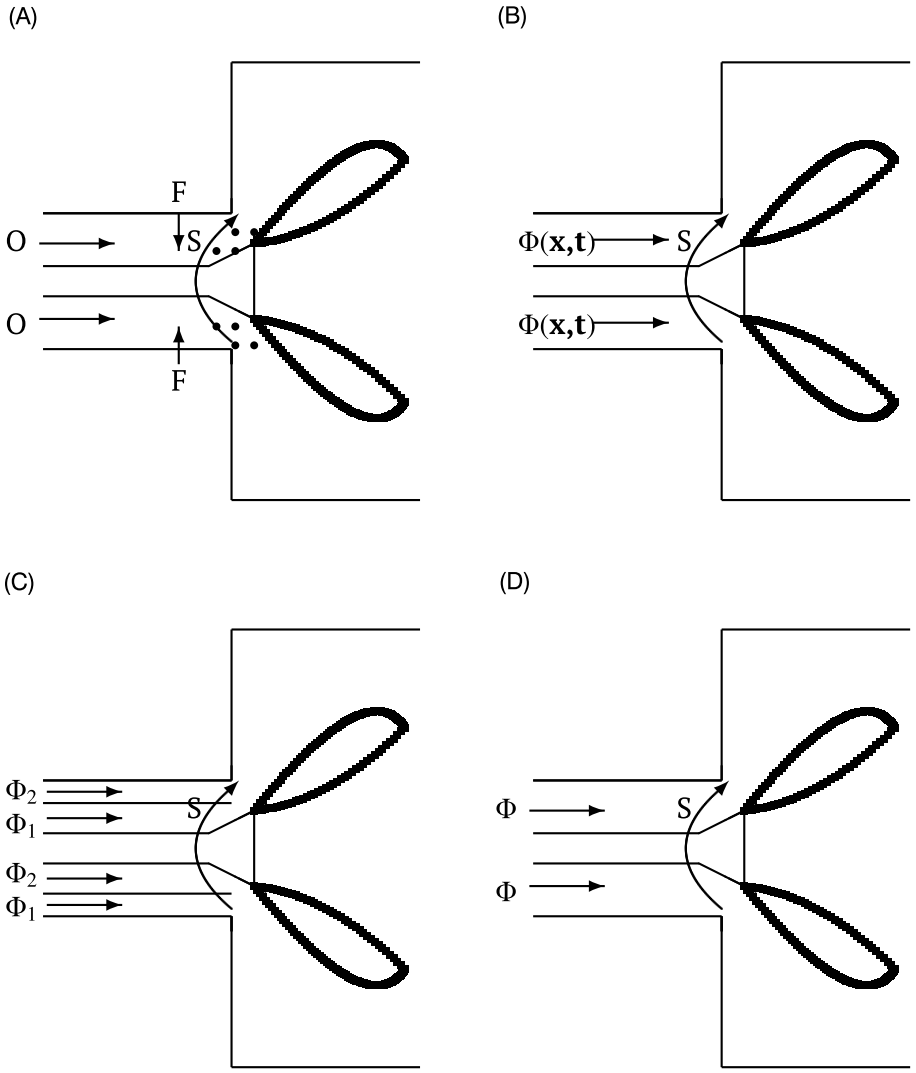

Figure 2.7 Premixed combustion modes. These figures depict the multiple premixed combustion modes for a turbulent swirling flame configuration. (A) Prevaporized mode. (B) Partially premixed mode. (C) Stratified premixed mode. (D) Fully premixed mode.

direct injection combustor architectures. In the present book, the focus is on the following four premixed combustion modes: (A) prevaporized/premixed, (B) partially premixed, (C) stratified premixed, and (D) fully premixed. These four combustion modes are depicted in Fig. 2.7. Prevaporized/premixed combustion and fully premixed combustion are the most studied nowadays. The for-

mer can be found in the LPP combustor architecture. The latter has been significantly studied at the laboratory scale. Partially and stratified premixed combustion modes are less investigated but surely will be combustion modes in future combustion devices. The prevaporized mode consists of a separate injection of air and fuel, where first the fuel vaporizes due to the radiation of the flame and second the vaporized fuel and the air mix downstream of one or more swirler(s) prior to combustion. There are many challenges associated with this mode. Among them is the achievement of full vaporization and the full mixing of the gaseous fuel and air. Indeed, in practice, full vaporization requires strong heat transfer, i.e., to be close to the flame. Particularly, fuel injection has to be between the swirler outlet and the flame, as the swirler acts as a radiation heat transfer frontier. But in the meantime, the injection has to be sufficiently far to enable full mixing. In other words, full vaporization and full mixing in LPP have opposite requirements. The fully premixed mode is largely used at the laboratory scale for fundamental studies. In those configurations, the injection is such that the premixing occurs in a dedicated separate unit without any space or weight constraints, allowing various possibilities. The stratified combustion mode is achieved when different streams of a given equivalence ratio are injected into a combustion system. The partially premixed combustion mode is defined as an injection system where the local equivalence ratio is unsteady and spatially varying but locally fully premixed.

3.2 Prevaporized mode

This combustion mode is depicted in Fig. 2.7A. The prevaporized combustion mode is the mode of combustion of LPP combustor architectures. This combustor architecture has been shown to have the potential of using LPP combustion in aircraft gas turbine engine combustor systems to reduce NO_x formation in many previous investigations, see Lefebvre [117], Mularz [185], Dickman et al. [186]. These initial studies have identified most of the current challenges of premixed combustion systems. They are now reviewed. The challenges associated with the practical application of the LPP concept were found to be: blowout, flashback, autoignition, altitude reignition, application of variable geometries for performance optimization, achieving satisfactory premixing and prevaporization, advanced control systems, and the impact of the LPP burner on overall engine operation (system level study). Among these challenges, some have been particularly studied in that context at the laboratory scale in order to enable LPP technology.

Lean blowout in LPP combustors has been investigated in many researches. Most early studies focused on the establishment of correlations between the occurrence of LBO and temperature, pressure, and equivalence ratio, along with other geometrical parameters, see Leonard and Mellor [187], Blust et al. [188], Xie et al. [189]. While these studies enable to capture trends and first-order effects, they lack in the precise description of the phenomena at work. Those descriptions have been and will be enabled by recent and future numerical simulations and highly temporally and spatially resolved laser diagnostics experiments. Numerical simulations of lean blowout have for example been undertaken by Esclapez et al. [59] to study the fuel effects and by Ma et al. [190] to study the transient evolution to LBO. Early laser diagnostics experimental measurements applied to LBO were undertaken by Galley et al. [191], Sommerer et al. [39], Galley et al. [192]. Flashback was also investigated in those studies. Various mechanisms were reviewed regarding lean blowout and flashback. These processes will be detailed in Chapter 4. The phenomenon of autoignition has been identified as a challenge too by early studies on LPP combustion systems. The autoignition in LPP systems occurs because of one key cause. The overlap of the high local temperature in the presence of both oxidizer and fuel species is the root cause. This overlap can occur for regimes in nonpremixed and premixed cases. The temperature increase can be caused by the isentropic increase of temperature from a propagating acoustic wave, triggering autoignition. It can also be due to flame radiation, impacting the surfaces of the liquid spray or the wall surfaces. Autoignition can be suppressed by many local effects, including processes such as vorticity, flow strain and/or flame stretch, the local flammability limits, and the control of wall temperatures. Altitude reignition is another challenge once the flame is extinguished. Indeed, at high altitude, the radiation of the flame does not allow the spray temperature increase and may not guarantee its vaporization either, because the only source of heat is the upstream flow exiting the high pressure compressor, without specific flow path to enable full vaporization. The application of variable geometries for performance optimization would be a great progress, allowing several optimization and performance increases. Achieving satisfactory premixing and prevaporization in LPP systems is one of the mostly studied and documented aspects in the literature. This section now reviews some of these studies. Prevaporization involves the passage of the liquid phase to the gas phase, while premixing involves the mixing between the vaporized fuel and air. Prevaporization of liquid fuel involves many coupled complex processes. There is one main route for the pas-

sage from liquid to gas, which is that of boiling, i.e., the change of phase from liquid to gas by heating effects (radiation, conduction, convection). In addition, the liquid fuel follows a succession of transformations during the phases of prevaporization and premixing that are due to the local fluid dynamic effects. These transformations are also directly linked to the fuel injection device used, see Lefebvre [34]. They are usually split into two sequences consisting of three elements (liquid column, ligaments, and spray droplets). The primary breakup consists of the passage from the liquid column exiting the injection system to a series of so-called ligaments of liquid fuel. This breakup occurs due to the flowfield and possible instability on the surface of the liquid column. The second transformation is that of the passage from these ligaments to spray droplets. Some injection devices ensure the direct passage to spray droplets. The boiling phase acts on the liquid fuel column and spray droplet surfaces and induces evaporation/vaporization of the fuel. At those surfaces, heat conduction and convection are actively at work as well. Vaporization of fuel droplets and spray combustion have been reviewed by Sirignano [193]. Once prevaporization is achieved, the obtained fuel gas can be premixed with the local air. This is carried out through (i) the mass (species), thermal, and momentum diffusion processes, (ii) the convection processes, and (iii) turbulence. The specific effects of each of these processes are not very well documented in multicomponent swirling flows, and further studies are required. It is recognized that turbulence induced by the swirler is the main source of mixing, leading to satisfactory premixing. One aspect that was not originally identified by Lefebvre [117] is the combustion dynamics challenges associated with LPP combustion systems. They have been summarized and reviewed by Lieuwen and McManus [194], and will be discussed in Chapter 5.

3.3 Partially premixed mode

This combustion mode is depicted in Fig. 2.7B. In the literature it is also described as hybrid flames possessing characteristics of both premixed and nonpremixed flames. In the present book, the partially premixed mode involves an unsteady spatially variable field of equivalence ratio (within or outside the flammability limits) upstream of the flame front, without any nonpremixed regions. This is coherent with the definition of Masri [195]. In the article, the author reviewed recent advances in our understanding of the structure of turbulent partially premixed and stratified flames with the emphasis on the local flowfield effects on the flame front. The partially premixed mode has been studied in various config-

urations, both experimentally and numerically. The present section reviews some of these studies. Canonical experiments and numerical simulations of well-controlled canonical experiments in partially premixed regimes such as defined here are not well documented. Contrarily, simulations and experiments closer to industrial setups have been achieved by Galley et al. [192] with detailed investigations of the fuel mixing with laser diagnostics or with LES by Galley [196]. Stöhr et al. [197] performed an experimental study of unsteady flame structures of an oscillating swirl flame in a gas turbine model combustor focusing on the combustion dynamics of swirling partially premixed flames. The investigation of the temporally resolved planar measurements of transient phenomena in a partially premixed swirl flame in a gas turbine model combustor was undertaken by Boxx et al. [198]. Franzelli et al. [199] focused on LES of combustion instabilities in a lean partially premixed swirling flame to study the effects of incomplete mixing between fuel and air at the combustion chamber inlet, giving rise to a partially premixed regime. The study of Stöhr et al. [52] focused experimentally on the transient to LBO for partially premixed regimes. Stöhr et al. [200] focused on the same regime and configuration when the interaction between velocity fluctuations and equivalence ratio fluctuations synchronized and sustained thermoacoustic oscillations. While these studies were focused on the combustion dynamics, the mixing challenge (once the decoupling from the acoustics is executed) was addressed in other studies. In Dem et al. [201], the authors focused on the experimental study of turbulence–chemistry interactions in perfectly and partially premixed confined swirl flames. The study investigated the influence of the mode of premixing on the combustion behavior with laser diagnostics. By decoupling the acoustic oscillations of the system, the authors measured the mode of premixing, which has been shown to have no major influence on the general flame behavior characteristics. Differences were observed with respect to flame anchoring, the flowfield in the IRZ, and the CO concentration level. They were attributed to the unsteadiness of the equivalence ratio and variation from very lean to rich mixtures. Stöhr et al. [202] focused on a lean partially premixed turbulent swirl flame using coupled particle image velocimetry and OH-PLIF at high frequency, enabling local flame dynamics analysis between the identified precessing vortex core and the partially premixed fresh gases. The study of the partially premixed mode for combustion as defined in this section has been carried out mostly by experiments equipped with swirlers because of the difficulty to achieve similar conditions on canonical setups. It is worthwhile to point out that nowadays, there are limited capabilities enabling

such studies. Further work should be undertaken to investigate the level of unsteadiness (both temporally and spatially) of the equivalence ratio field and the impact on the inner flame structure and thus on the flame speed. The detailed modeling and numerical simulations of the flowfield at the flame surface will also be worthwhile to study. This will be important for the description of flame dynamics and the development of future combustor systems, such as described in Chapter 7.

3.4 Stratified premixed mode

This combustion mode is depicted in Fig. 2.7C. It consists of two or more streams at a given equivalence ratio. This mode is used for the laboratory-scale combustor and can be investigated in configurations without swirlers. Like the partially premixed mode discussed in the previous section, the experiments with the stratified mode have to be considered as fundamental and relevant for model validation. Indeed, it offers a well-controlled partially premixed regime. The review article of Masri [195] also considered stratified injection systems. There are several setups that have been developed and subsequently investigated with experiments and numerical simulations to study stratified flames. Among them, the Cambridge/Sandia swirl burner was designed to investigate the effect of stratification under no-swirl, see Sweeney et al. [203], and swirl, see Sweeney et al. [204], operating conditions. It has two main annular streams, where each stream has its own equivalence ratio. This experiment, initially developed and studied by Barlow et al. [205], allowed the detailed structure of turbulent stratified flames to be investigated. The laser diagnostics enabled resolving the internal structure of stratified flames at atmospheric pressure, and the local equivalence ratio and the temperature gradient were measured. These experiments have been used for validation of numerical simulation models and strategies, see the works by Proch and Kempf [206], Turkeri et al. [207]. Another experiment dedicated to stratified lean premixed flames was designed and studied by Seffrin et al. [208] and enabled the determination of radial profiles of mean axial velocity, mean radial velocity, and turbulent kinetic energy, as well as integral time scales. The case of low swirling stratified premixed flames was studied by Nogenmyr et al. [209–211] with both experiments and LES. Results by Fooladgar and Chan [212] show that spatial and temporal nonuniformity of mixture stratification not only affect the structure of turbulent premixed flames but also alternate the stability and pollutant emissions of the swirl burner at the same global operating conditions. In addition, NO_x emission for axial

stratified flames was found to be more pronounced from medium to high swirl numbers.

3.5 Fully premixed mode

This combustion mode is depicted in Fig. 2.7D. It consists of a single stream of a given equivalence ratio. The fully premixed mode relies on the perfect mixing of fuel and air so that each given fluid control volume upstream of the flame has the same equivalence ratio. In practice, the equivalence ratio can slightly vary due to effects of convection and diffusion of the species. To comply with future engine emission certifications, the fully premixed combustion mode could be a preferred candidate. Future advanced propulsion and power systems may operate in premixed mode, which occurs when fuel and air are homogeneously mixed to form a premixture to achieve low pollutant emissions. Premixed combustion has received significant attention over the last few decades, with tremendous advances both in physical understanding and modeling, see for examples the articles of Huang and Yang [22], Candel et al. [23], Palies et al. [213], but there is still understanding of physical mechanisms to gain from detailed analysis, thus enabling the derivation of improved models. Premixed combustion is a promising candidate for satisfying the future FAA requirements on NO_x and soot emissions. It has indeed been shown in various settings at the laboratory scale to reduce NO_x and soot emissions Tacina [30], Yegian and Cheng [214] compared with other combustion systems. Fully premixed combustion, which has been widely studied at the laboratory scale, may consequently become the future mode of operation of gas turbine engines at the industrial level. Stabilization of swirling flames inside combustion chambers, also known as static stability, is important over the entire envelope of operation and is a challenge of any future fully or partially premixed combustion system. There have been multiple series of work considering flame stabilization, but currently few theoretical foundations, such as discussed in Chapter 3 of the present book, have been suggested to avoid systematic numerical modeling and experimental testing. Combustion dynamics and flame stabilization are important for the design of current and future combustion systems. Considerable experimental testing and design iterations are usually required at the laboratory scale or at industrial scales to achieve flame stabilization and to ensure that the flame, once stabilized, is not dynamically unstable. This has been shown through the development of many novel engines and combustor architectures/injectors, and it could be the case for many future combustion systems, such as gas turbine engines

for aircraft propulsion. In that perspective, it is very important to continue studies in these fields to enhance and propose new directions and refine the state-of-the-art approaches to understand the fundamental mechanisms responsible for flame stabilization and combustion dynamics. In addition, to reduce the cost associated with the development of a novel injection system, it is necessary to minimize the systematic use of CFD or experiments.

4 Effects of operating conditions on premixed combustion and the flame

4.1 Current operating conditions

One important challenge in the design of future combustors that operate in one of the previously presented premixed modes is the consideration of the power settings, i.e., the operating conditions of the gas turbine engine. Indeed, many combustor and combustion parameters change with respect to the power settings. As a consequence, both the design and the modeling have to take into account those aspects. In this section, we discuss some of these aspects and present key variables that are modified with respect to the power settings. For future design, the most significant impact of the aircraft operating envelope on combustion and combustor operation will be: (i) the air mass flow, (ii) the fuel mass flow, (iii) the operating temperature, and (iv) the operating pressure. The air and fuel mass flows (along with the fuel type and the fraction of flow used for dilution) combine to determine the equivalence ratio of the swirl-stabilized flame inside the combustion chamber. The operating pressure and temperature determine the corresponding 1D laminar flame speed, adiabatic flame temperature, and laminar thermal flame front thickness. These variables will be important for the investigation of the swirling flame stabilization inside the combustion chamber. Tabs. 2.5 and 2.6 list these quantities for take-off and cruise operating conditions of an existing kerosene-fueled turbofan aircraft engine. It is important to recall that these are orders of magnitude, as the combustion regime of current aircraft is not premixed combustion. These tables also include the values of these quantities for two other fuels (CH_4 and H_2) at the same operating conditions for possible future retrofitting. The operating conditions will be different with those fuels but are expected to have similar values. The tables list a wide range of equivalence ratios for design purpose. Tab. 2.7 lists also the unstretched laminar flame speed, the adiabatic flame temperature, and the laminar flame thickness as a function of the power settings for all premixtures.

Table 2.5 Flame speed, adiabatic flame temperature, and flame thickness as functions of the fuel and the equivalence ratio Φ. The inlet pressure is 30 atm and the inlet temperature is T = 850 K.

Φ	0.5	0.6	0.7	0.8	0.9	1.0	1.1	1.2
CH_4–air								
S_L^0 [m/s]	0.228	0.363	0.514	0.657	0.773	0.847	0.863	0.801
T_{Ad} [K]	1934	2109	2270	2414	2536	2616	2612	2546
δ_{th} [μm]	68	46	34	28	25	23	23	24
H_2–air								
S_L^0 [m/s]	1.152	2.218	3.62	5.28	7.01	8.61	9.94	11
T_{Ad} [K]	2099	2283	2446	2592	2716	2803	2824	2801
δ_{th} [μm]	21	12	8	6	5	4	4	4
$NC_{10}H_{22}$–air								
S_L^0 [m/s]	0.333	0.532	0.733	0.912	1.054	1.14	1.175	1.126
T_{Ad} [K]	1978	2162	2332	2481	2601	2679	2688	2636
δ_{th} [μm]	44	29	22	18	16	15	14	14

Table 2.6 Flame speed, adiabatic flame temperature, and flame thickness as functions of the fuel and the equivalence ratio Φ. The inlet pressure is 15 atm and the inlet temperature is T = 770 K.

Φ	0.5	0.6	0.7	0.8	0.9	1.0	1.1	1.2
CH_4–air								
S_L^0 [m/s]	0.207	0.348	0.506	0.652	0.768	0.838	0.843	0.760
T_{Ad} [K]	1865	2041	2204	2349	2469	2549	2546	2480
δ_{th} [μm]	134	85	62	50	44	42	41	45
H_2–air								
S_L^0 [m/s]	1.628	3.002	4.617	6.287	7.852	9.202	10.313	11.187
T_{Ad} [K]	2031	2215	2382	2527	2648	2731	2752	2729
δ_{th} [μm]	27	16	12	9	8	7	7	7
$NC_{10}H_{22}$–air								
S_L^0 [m/s]	0.297	0.486	0.675	0.845	0.979	1.067	1.095	1.047
T_{Ad} [K]	1908	2094	2264	2414	2533	2610	2620	2568
δ_{th} [μm]	87	56	42	34	30	28	27	27

Table 2.7 Comparison of engine settings for three different fuels.

	Th. power [MW]	α[a]	Φ_g[d]	Φ_i[e]	T_{Ad} [K]	S_L^0 [m/s]	δ_{th} [μm]
Current engine							
Kerosene							
Take-off	50	20/80	0.4	1.81	2679[b]	1.14[c]	15
Cruise	14.4	20/80	0.4	2.01	2610[b]	1.067[c]	28
Take-off	50	40/60	0.4	0.90	2679[b]	1.14[c]	15
Cruise	14.4	40/60	0.4	1.00	2610[b]	1.067[c]	28
Premixed engine							
Kerosene							
Take-off	50	50/50	0.4	0.725	2350	0.75	23
Cruise	14.4	50/50	0.4	0.806	2414	0.84	34
Premixed engine							
Methane							
Take-off	50	50/50	0.359	0.718	2300	0.52	32
Cruise	14.4	50/50	0.399	0.799	2414	0.66	28
Premixed engine							
Hydrogen							
Take-off	50	50/50	0.30	0.600	2283	2.218	12
Cruise	14.4	50/50	0.333	0.607	2215	3.000	16

[a] α is the injectors/dilution holes air split; a value of 20/80 indicates that 20% of the total core air mass flow goes through the injector and 80% through the dilution holes.

[b] Assuming that combustion in the combustors occurs in the diffusion flame regime.

[c] Whereas a diffusion flame does not have flame speed, the quantity can still be defined to estimate flame thickness.

[d] Global equivalence ratio taking into account core air stream.

[e] Injector/main flame equivalence ratio, not taking into account dilution air.

4.2 Fuel, equivalence ratio, and power settings engine matching

The previous section provided orders of magnitude for premixed combustion in terms of the current turbofan operating conditions. In the present section, the fuel (hydrogen, methane, or kerosene) and the power settings are discussed to match the power requirements at three targeted operating conditions (idle, take-off, and cruise). Particular attention is paid to the ratio of pri-

mary air (flowing through the injector) and secondary air (flowing through the dilution holes). There is a trade-off between reducing NO_x emissions and keeping a sufficient mass flow rate on the secondary stream to ensure dilution/cooling of the burned gases prior to reaching the turbine blades. From this table and the equivalence ratios obtained, one can deduce the obvious advantage of being able to adapt the parameter α through an adaptive geometry in order to mitigate or avoid lean blowout and combustion instability. Results of matching the thermal power of the current engine at take-off and cruise for three different fuels are reported in Tab. 2.7. The table compares the operation of existing engines operating with kerosene with future premixed engines operating with methane or hydrogen fuels.

3

Premixed swirling flame stabilization

1 Mechanisms and processes of stabilization

In the next two sections, the mechanisms of stabilization for premixed swirling flames are investigated and large eddy simulations (LESs) are used to support the analyses. The reacting flowfield is studied with a set of local contributors that are referred to as implicit or explicit. These local contributors consist of all possible variables into the flowfield along with their time and spatial derivatives (gradient and divergence) that belong to the governing equations. The explicit local contributors include for example the equation of state variables, the velocity field, the mass fractions, the reaction rates, and the gradient or the time rate of those variables. The implicit variables are quantities that are derived from the explicit variables. The implicit variables are the local equivalence ratio, flame speed, flame stretch, and the vorticity vector components. Flame-resolved numerical simulations are carried out to evaluate some of the local contributors on the flame surface with a compressible finite volume reacting code named LociCHEM, see Luke et al. [215], Luke and George [216]. The swirl-stabilized MICCA-EM2C configuration is used and operated at an inlet bulk velocity of 30 m s^{-1}, a factor nearly 10 times higher than the original initial experiment. A quarter of the injector and the flame tube are modeled. The structured mesh, consisting of nearly nine million cells, is refined so that only the dissipation scales are modeled while the smallest eddies are expected to be captured in both the fresh and burned gases. The methane–air combustion chemistry is modeled with a single global step and the reaction rate is computed based on the resolved quantities. Multiple explicit and implicit local contributors are determined on the flame surfaces along with their distributions and median, mean, and peak values. By examining the flame surface, flame speed, and flow speed budget relationships and the local contributors, it is deduced that the flame is stabilized by flow effects, including both low and hot flow velocity regions and unsteady velocity fluctuations. In particular, thermal diffusion from the burned gas of the recirculation zone does not appear to be the only mechanism of stabilization.

Stabilization and Dynamic of Premixed Swirling Flames
https://doi.org/10.1016/B978-0-12-819996-1.00011-1

1.1 Definitions

This chapter focuses on the definition of flame stabilization and flame propagation. It is known that a deflagration is a combustion wave. As a wave, it has its own (burning or displacement) speed. Consequently, it is said to propagate in the flowfield at this speed. Nonetheless, while the flame front is propagating, it can also be said to be stabilized if the flame surface speed is nearly zero, i.e., the position of the flame surface in the laboratory frame of reference is nearly constant. Therefore, in this chapter, we will refer to a stabilized flame when its flame surface speed is nearly zero and its static flame surface speed is exactly zero.

1.2 Key stabilization mechanisms: local contributors

Flame stabilization mechanisms, and subsequently those determining the evolution towards lean blowout or flashback, are a combined effect of local quantities and local and global effects of flow features, which are referred to as local contributors throughout this chapter. The focus of this section is on the contributors that ensure flame stabilization and it is worthwhile to point out that they are not restricted to one type of flame, but can be applied to swirl-stabilized or bluff-body flames. Also, as will be shown in this section, it is important to indicate that these quantities are not independent, and some of their dependencies are discussed. It is possible to list the local quantities, processes, and flow features that will have a role in flame stabilization. Those are identified and discussed in the following subsections. The local contributors presented in this section, responsible for flame stabilization, will be analyzed with detailed flame-resolved numerical simulation data in this chapter to determine the most important contributors. A summary of the local contributors is given in Fig. 3.1.

1.3 Local equivalence ratio

The equivalence ratio is the ratio of fuel mass to oxidizer mass divided by the same ratio at stoichiometry for a given reaction, see Poinsot and Veynante [172], Kuo and Acharya [21]. This quantity is usually defined at the injector inlets through the mass flow rates of fuel and air to characterize the quantity of fuel versus the quantity of air available for reaction in a combustor. It can be defined locally also for premixtures as the fraction of the reacting fuel to oxidizer mass fractions ratio to the stoichiometric ratio by

$$\Phi(\mathbf{x}) = \frac{Y_{CH_4}/Y_{O_2}}{(Y_{CH_4}/Y_{O_2})_{st}}. \tag{3.1}$$

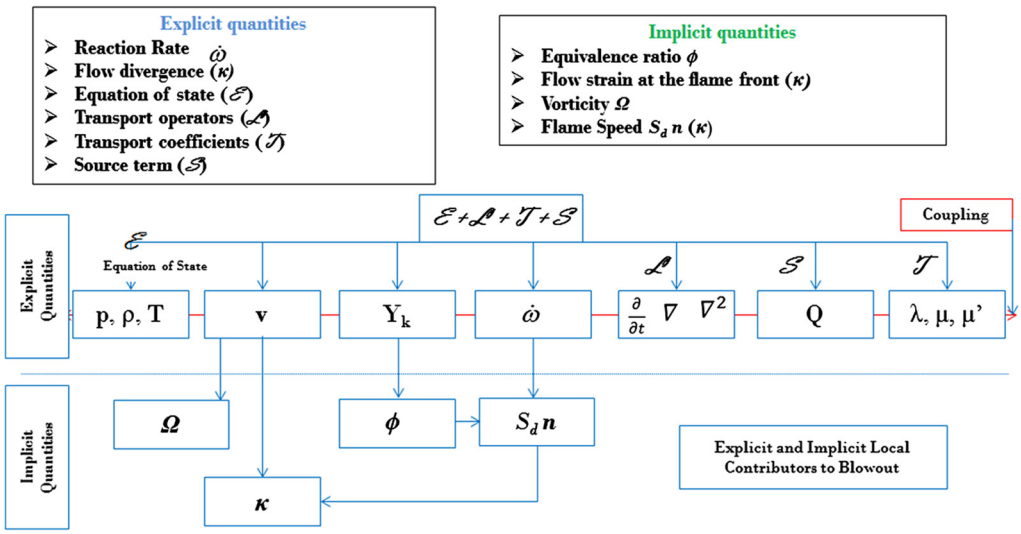

Figure 3.1 Local contributors for flame stabilization analysis. A list of explicit and implicit local contributors and schematic highlighting some of the possible couplings and interactions.

For fully premixed flames, upper rich and lower lean flammability limits are known and occur for specific values depending on the fuel. The flammability limits are functions of local temperature and pressure as well, see Williams [125]. These flammability limits will directly impact flame stabilization and the blowout/blowoff/extinction phenomena. Another important relation between flame stabilization and the equivalence ratio is the role of this latter on the displacement speed for premixed flames. The lower and upper flammability limits could be responsible for the generation of flame holes in the flame sheet in certain cases.

Another subtle aspect of the role of the local equivalence ratio is through the distributions of mass fractions due to transport processes. In Fig. 3.2, one can see three injection configurations that will affect the flame front because the spatial equivalence ratio distribution will be impacted. For an overall single equivalence ratio mixture injected, the flame speed is usually assumed to be single-valued for modeling purposes, but variations will occur due to these transport processes. For a configuration with two streams of different equivalence ratio, the flame will see gradients of the inlet mixtures and the flame speed will be impacted. The third configuration illustrates the impact of swirl on the previous jet flame configuration. The effect of the swirl through the axial and radial pressure gradients will impact the balances in the reacting flow governing equations so that the local equivalence ratio

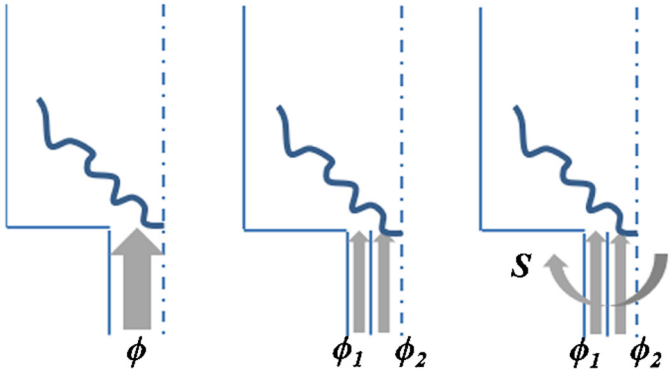

Figure 3.2 Configurations of injection. Injection configurations for fully and partially premixed combustion systems with or without swirl.

is not the same as upon injection. These transport processes include convection and diffusion. As these effects may be limited, they have received little attention.

1.4 Flame stretch

Flame stretch is an important quantity in combustion, and it is used to characterize the interaction of the flowfield with the flame front surface. Flame stretch is defined formally for all types of flames with a flame surface area A by Kuo and Acharya [21], Candel and Poinsot [217], Matalon [218], Law [219] as

$$\kappa = \frac{1}{A}\frac{dA}{dt}. \tag{3.2}$$

For turbulent and laminar premixed flames (because the flame is a propagating deflagration wave characterized by a displacement speed in contrast to a diffusion flame) the expression of flame stretch can be written as follows:

$$\kappa = -\mathbf{nn}{:}\nabla\mathbf{v} + \nabla\cdot\mathbf{v} + S_d\nabla\cdot\mathbf{n}. \tag{3.3}$$

The first right-hand side term of Eq. (3.3) is associated with the flow strain at the flame front, the second one with the dilatation of the flowfield, and the third one with the curvature of the flame front surface. For premixed flames, it has been shown by Law and Sung [220] that the flame front will extinguish at a local extinction stretch rate limit that can be expressed with a Karlovitz number which depends on the stretch, with $\mathrm{Ka} = \tau_c \times \kappa$, where τ_c is the chemical time (defined by the ratio of the flame thickness to its displacement speed) and κ is the flame stretch. It has been found

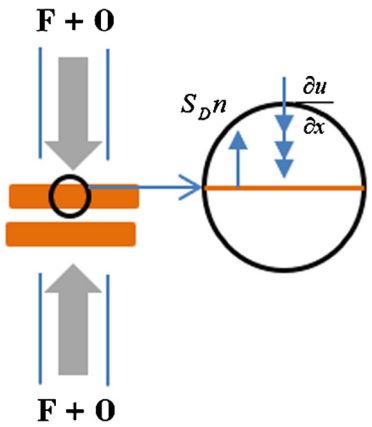

Figure 3.3 Strained flame front. Illustration of the counterflow premixed flame configuration where two streams of premixture are in opposite directions, forming a stagnation point separating two planar premixed flames.

that this extinction Karlovitz number is close to unity or slightly higher than unity by Law and Sung [220], Chung et al. [221]. The stretch value for premixed flames at which extinction occurs depends on the local thermodynamic conditions, the type of fuel, and the local equivalence ratio, see Cho et al. [222]. Many studies have been carried out to determine those limits for different types of fuel in counterflow flame configurations Chung et al. [221], Cho et al. [222], Law et al. [223] or in inwardly/outwardly expanding spherical configurations, see Law and Sung [220].

Fig. 3.3 presents the classical counterflow experiment configurations used to measure the flame speed of stretched premixed flames, such as by Wu and Law [224], Fayoux et al. [225], Renard et al. [226]. Flame stretch depends on flow and flame quantities. In other words, to capture the local extinction due to flame stretch with numerical simulations such as LES, the flow speed and the flame speed, which will determine the wrinkling of the surface through the surface normal vector (which appears in the expression of the flame stretch), have to be accurately modeled. In Candel and Poinsot [217], the evolution of the flame surface area per unit mass explicitly takes the flame stretch into account in the modeling approach of the flame front dynamics.

1.5 Flame speed versus flow speed

The local flame front surface velocity of a fully or partially premixed flame $\mathbf{w}$ is defined as $\mathbf{w} = \mathbf{v} + S_d\mathbf{n}$, where $\mathbf{v}$ is the flow velocity vector, S_d is the flame displacement speed, and $\mathbf{n}$ is the normal vector of the flame front. This flame surface velocity $\mathbf{w}$

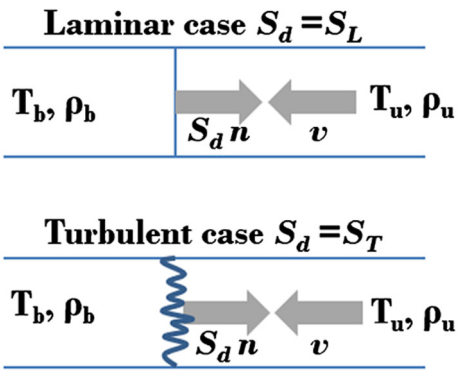

Figure 3.4 Flame speed versus flow speed balance. The top schematic represents the balance between the laminar flame speed and the local flow speed. The bottom schematic represents a similar balance between the turbulent flame speed and the flowfield.

is important as it will determine the surface position so it is directly linked to the blowout, flashback, and flame stabilization mechanisms. This velocity balance is key for both laminar and turbulent premixed flames. The determination and definition of the flame speed in laminar studies has led to many analytical and experimental research efforts for intrinsic characterization and for turbulent combustion modeling, see Egolfopoulos et al. [227], Vagelopoulos et al. [228], Wu and Law [224], Andrews and Bradley [229], Lee et al. [230], Botha and Spalding [231], Tien and Matalon [232]. The determination of the turbulent flame speed has also been the subject of many research articles, see Lipatnikov and Chomiak [182], Daniele et al. [233], Spalding [234]. While the flame speed is intrinsically linked to premixed combustion, it is natural to possibly apply that characteristic to a partially premixed flame.

The flame speed S_d and the reaction rate in turbulent combustion models are directly linked as the flame consumes the fresh reactants. It is also important to compare the flame speed and the local flow velocity as their balance determines the location of the flame. This balance participates locally in the flashback, blowout, and flame stabilization mechanisms.

The illustration of Fig. 3.4 depicts laminar and turbulent configurations for the flame speed and flow velocity balance. In a laminar case or in turbulent premixed combustion where the flame structure retains its laminar thermal structure, the local flame front surface position is constant in time in the laboratory frame of reference if the flow velocity balances the flame speed. If the flow velocity is higher than the flame speed locally, this can lead to global blowout (typical in bluff-body-attached flames); in-

versely, if the flow speed is lower, flashback can occur. For a swirl-stabilized system with an inner recirculation zone (IRZ), due to the reverse flows of the IRZ and outer recirculation zone (ORZ), the balance between flame speed and flow speed can lead to a more complex flame motion. For the turbulent illustration, the phenomenological observed effect of turbulence is to increase the flame surface by wrinkling it. The G-equation LES model for turbulent combustion makes use of a turbulent flame speed to define the propagation of the front in turbulent flow, defined as S_T. In LES turbulent combustion modeled with the G-equation, the modeling of this quantity is of primary importance to capture flame stabilization, lean blowout, and flashback. We will see that the next sections offer novel perspectives in modeling this quantity and thus would be useful for LES models.

1.6 Reaction rates

For all types of flames, the reaction rates are functions of fuel and oxidizer mass fractions, density, and temperature, see Williams [125], Poinsot and Veynante [172], Kuo and Acharya [21]. The reaction rate of the fuel can be written in the following form for a single-global step reaction:

$$\dot{\omega}_{CH_4} = -W_{CH_4} A \left[\frac{\rho Y_{CH_4}}{M_{CH_4}}\right]^{n_{CH_4}} \left[\frac{\rho Y_{O_2}}{M_{O_2}}\right]^{n_{O_2}} \exp(-E_a/RT). \qquad (3.4)$$

Each variable (ρ, Y_{CH_4}, Y_{O_2}, and T) of that equation can lead to local flame extinction when that variable reaches a threshold. Consequently, the reaction rates are important in the local extinction phenomena and they can drive consequently local flame holes in the flame sheet, specifically for the partially premixed regime. The local equivalence ratio ϕ is indirectly linked to the reaction rate through the mass fractions. Analytical expressions of the reaction rates as functions of the equivalence ratio are available, see for example Mitani [235]. The reaction rate has also a role in flame stabilization through the flame speed. In addition, it is worthwhile to recall that the flame speed is directly linked to the ability of the LES turbulent combustion model to capture the consumption rate of the fresh gases.

1.7 Vorticity

When vortices or vorticity interacts with a flame front, it can lead to local extinction. This has been determined experimentally by Renard et al. [236], Brockhinke et al. [237], Fayoux et al. [225], Renard et al. [226] and it was pointed out that the reduction in

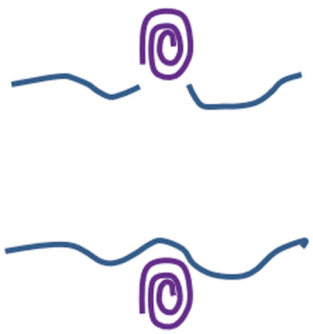

Figure 3.5 Interaction of vorticity with a flame front. The bottom schematic represents a flame front and an upstream vortex. The top schematic represents the flame front after the passage of the vortex.

flame surface leads to extinction. It was postulated that the flame stretch and/or the vorticity effects are responsible for flame extinction. It is important to point out that while each component of the vorticity vector components is included in the flow strain expression, their specific relationships are not.

Fig. 3.5 illustrates the local extinction of a flame front after the passage of a vortex such as observed experimentally in Renard et al. [238].

1.8 Temperature, pressure, and density (equation of state)

Temperature is one criterion for the reaction to occur and is strongly coupled to density and pressure through the equation of state. These three variables will thus have a role in the local extinction/ignition participating in flame stabilization. In a swirl-stabilized system, the role of the pressure gradient is also important to establish the flow and the resulting pressure field may impact the reaction rate and, therefore, the flame speed. For laminar premixed flames, an increased pressure decreases the flame speed for a given inlet fresh gas temperature and stoichiometric equivalence ratio, see Kuo and Acharya [21], Metghalchi and Keck [239]. But the reverse effect occurs if the inlet fresh gas temperature is increased, see Kuo and Acharya [21], Gu et al. [240]. The effect of wall temperatures on local extinction, see Poinsot and Veynante [172], can also play a role because the low wall temperatures (cooled in a jet engine combustor) inhibit the reaction (through the reaction rate). The local thermodynamic conditions will consequently affect local flame stabilization.

1.9 Governing equations

We refer here to the transport operators (unsteady terms, spatial derivatives), transport properties (viscosity, thermal conductivity, species diffusion coefficients), and source terms such as radiation in the governing equations (density, velocities, mass fractions, and temperature). Most phenomena experimentally observed should be captured by the governing equations of compressible reacting flows using a reacting compressible DNS code. The transport terms are responsible, for example, for determining the local values of mass fractions and temperature due to transport phenomena. The mixing of species in the premixture due to the swirling flow or the mixing of premixed gases with burned gases will also impact the temperature, velocity, and mass fractions locally. All previous quantities are the result of the transport operators, transport coefficients, and source terms, and all terms are coupled.

1.10 Role and impact of global flow/flame features

The previous sections have described the local quantities and mechanisms, referred to as local contributors, which have a role in flame stabilization. The main stabilization mechanisms of swirling flows and the large-scale features of these flows impact these local quantities directly. The objective of the present section is to briefly document them and to elaborate on their roles. Stabilization mechanisms and coherent flow structures for swirling flames have been investigated and reviewed in several articles, see the reviews by Syred and Beer [241], Peters and Williams [242], Coats [243], Paschereit et al. [244], Huang and Yang [22], Gicquel et al. [245], and in the book of Beer and Chigier [246]. A swirling flame is stabilized with an IRZ, where the recirculating hot combustion products participate to continuously sustain flame propagation toward the upcoming upstream reactants by being a heat source. The mechanisms of stabilization of swirl-stabilized flames is particularly studied in Sections 2 and 3 of this chapter.

The level of flow strain induced by the main flow features onto the local flowfield and how the flame will stabilize in these conditions is important for all combustion regimes. For the fully premixed flame, stabilization can be seen as a balance between the flame speed and the flow speed, thus making the determination of these speeds by LES models critical. It is also important to point out the role of the large flowfield structures for lean blowout of swirling flames, as those features will impact, for example, the local levels of strain and thus the ability of the flame to stabilize. The following flowfield features are now briefly detailed: vortex break-

down, precessing vortex core (PVC), shear layers, and IRZ/ORZ. While describing those features, it is important to note the importance of the environment, the swirler and the combustor geometry, that also acts on those.

- Vortex breakdown/IRZ
  The axisymmetric vortex breakdown mode consists of a reverse flow downstream of the swirler in the combustion chamber. This reverse flow, also known as IRZ, is used to stabilize the flame by recirculating the hot combustion products and generating a heat source. It also provides a low speed region for flame stabilization, as will be seen next. For swirling flows with swirl number above a certain threshold, a strong recirculation zone will exist, while for lower swirl numbers, no recirculation zone or vortex breakdown appears, see Beer and Chigier [246]. This swirl number threshold is not universal and can vary from configuration to configuration due to geometry and specific velocity profiles at stake upstream of the flame. The IRZ has an effect on the flow strain at the flame surface, and the associated pressure gradients will have a small effect on the flame speed but a significant effect on the flame surface speed, as the flow balance between flame speed and local velocity will be impacted.
- Precessing vortex core
  This flow feature is an oscillating pattern occurring near the shear layers and the IRZ and taking roots in the swirling flow vortex core. It consists of a vortex tube precessing around the axis of the combustor such that its center of rotation is not the center of the combustor. This feature has been reviewed by Syred [247] and recently discussed in the context of LES by Gicquel et al. [245]. This structure is present in nonreacting and reacting flowfields and impacts the upstream flow/flamefield, like the mixing. The PVC impacts other local contributors, like the vorticity, the flow strain, the local equivalence ratio, and the local flow versus flame speed balance. The PVC is suppressed when the central vortex core is suppressed, i.e., when a central rod hinders such vortex core to be formed.
- Shear layers in swirling flows
  Between the IRZ and the ORZ, the axial, radial, and azimuthal shear layers are zones of intense gradient of velocity on both sides of the swirling jets O'Connor [248], Foley et al. [249]. The inner shear layers at the interface of the swirling jets and the IRZ will significantly impact the level of flow strain at the flame surface and the vorticity field. The outer shear layer is at the interface of the IRZ and the ORZ. It is also worthwhile to point out the effects of the azimuthal shear layers and the role of density

in the case of reacting swirling jets versus nonreacting swirling jets.

- Outer recirculation zone
  The ORZs present a reverse flow on the sides/corners of the combustion chamber confinement and participate in the organization of the overall swirling flowfield for a specific design. In general, these outer reversal flows are filled with burned gases flowing at low flow speeds.

It is important to mention that these flow features are important to the understanding of the local flowfield in the swirl-stabilized device. In other words, these large-scale phenomena are directly responsible for local contributors' values identified in this section which will directly affect the flame stabilization. For the modeling of the stabilization mechanisms, the effects of these large-scale features on the local flowfield have to be pointed out. For example, the flow features can be responsible for the generation of flame holes in the flame sheet due to the entrainment of fresh or burned pockets of gases to or on the flame sheet.

2 Framework for flame stabilization study: application

2.1 Numerical procedure

The numerical procedure used to generate the data forming the basis to investigate the local contributor is now presented. It consists of multiple steps, including mesh size determination and generation, boundary conditions selection, and combustion and turbulence modeling. The mesh size has been determined according to two main criteria: the Kolmogorov scale and the thermal flame thickness. The Kolmogorov scale is determined both in the fresh and in the burned gases as it varies significantly, and respective values of 25 and 250 μm were determined. The Kolmogorov scale is resolved in most of the combustor domain filled with hot gases where the dynamics of the flame occur. In the fresh gases, the Kolmogorov scale (nearly 25 μm) is not resolved, as the mesh size is nearly 100 μm, with a minimum of 60 μm in the flame anchoring region.

The determination of the cell area S_{cell} of the mesh was carried out along a $(z-r)$ slice and used to compute the quantity $S_{cell}^{1/2}$ to obtain an estimate of the cell length throughout the domain. The maximum values are located on the downstream outer side of the modeled domain and maximum values are of the order of 400 μm and located in the burned gases exiting the domain. The turbulence Reynolds number is equal to $Re_t = \rho u' l_0/\mu$, where ρ

Table 3.1 Characteristic nondimensional numbers and summary of variables' orders of magnitude.

Inlet bulk velocity U_b [m/s]	30	30
Inlet Reynolds number Re	41 300	41 300
Turbulent velocity fluctuation u' [m/s]	6	6
Gas temperature T [K]	300	1850
Dynamic viscosity μ [Pa.s]	1.82E−5	6.3E−5
Density ρ [kg m^{-3}]	1.14	0.18
Integral length scale l_0 [m]	0.022	0.022
Turbulent Reynolds number Re_t	8300	380
Kolmogorov scale η [µm]	25	257
Fresh gas temperature T_u [m s^{-1}]	300	300
Inlet equivalence ratio Φ	0.6	0.7
Flame speed S_L [m s^{-1}]	0.11	0.20
Burned gas temperature T_b [K]	1670	1850
Thermal conductivity λ [W m^{-1} K^{-1}]	0.027	0.154
Heat capacity c_p [J K^{-1} kg^{-1}]	1058	1517
Diffusive flame thickness δ [µm]	203	112
Blint flame thickness δ_L^B [µm]	1353	800

is the density of the fluid, u' is the turbulent velocity fluctuation taken equal to 20% of the mean injection bulk velocity, l_0 is the integral length scale, assumed here to be equal to the outer injector diameter, and μ is the dynamic viscosity. In addition, the Kolmogorov scale η can be written as $\eta = l_0 Re_t^{-3/4}$. The mesh was designed to resolve the thermal thickness (Blint thickness). The Blint thickness (close to the thermal flame front thickness) is defined by $\delta_L^B = 2\delta(T_2/T_1)^{0.7}$, where δ is the diffusive flame thickness defined by $\delta = \lambda/(\rho c_p S_L)$, where λ is the thermal conductivity, c_p is the heat capacity at constant pressure, and S_L is the unstretched laminar flame speed. Values are documented in Tab. 3.1.

The refined structured mesh obtained consists of nearly nine million cells with resolution at the flame base such that Δx is equal to 60 µm, corresponding to more than 10 points in the thermal flame thickness in that region. In regions where the grid density is lower, approximately five points are at least resolving the thermal thickness. The swirler blades are meshed with 100 points along the chord direction. The chord is nearly 10 millimeter in length, ensur-

ing a spacing Δx of 100 µm. The present mesh models a quarter of the geometry. This mesh is equivalent to a nearly 200 million tetrahedron mesh of the 3D domain. The entire modeled domain and selected mesh close-up views are given in Fig. 3.6. Other coarser meshes of one, five, and seven million cells were used to advance the nonreacting and reacting solutions in time. The time step of the numerical time integration was set to 1E−8 s.

Because the present mesh allows to capture most possible vortices sizes in the flame dynamics region, in both fresh and burned gases, no turbulence–chemistry model was retained. LES is used here though with a subgrid turbulence–viscosity model expected to act only for the dissipation scales in the fresh gases. No model is employed for the chemical reaction rates. The thermal thickness of the flame front is modeled with 5 to 15 points throughout.

The chemical combustion mechanism is a one-step global mechanism including five species which is written as

$$CH_4 + 2(O_2 + 3.76N_2) \longrightarrow 2H_2O + CO_2 + 7.52N_2. \tag{3.5}$$

The parameters of this global reaction are a preexponential factor equal to 8.332E12 s^{-1}, a zero temperature exponent, and an activation temperature of 10 065 K. This mechanism leads to an unstretched laminar flame speed of 0.2 $m\,s^{-1}$ at an equivalence ratio of 0.7. The heat release rate of this mechanism is obtained a posteriori with

$$\dot{\omega}_T = \Delta h_0 W_{CH_4} A \left[\frac{\rho Y_{CH_4}}{M_{CH_4}}\right]\left[\frac{\rho Y_{O_2}}{M_{O_2}}\right]^2 \exp(-E_a/RT). \tag{3.6}$$

2.2 Statistically steady flame dynamics

2.2.1 Reacting flowfield description

This section presents the results obtained with the numerical simulations of reacting swirling flames. In Fig. 3.7, a cutaway through the numerical domain is displayed with the vorticity magnitude contour. In addition, two isosurfaces are displayed. The first one corresponds to the isosurface at a heat release rate of 200 $MW\,m^{-3}$, colored by temperature, while the second one is an isosurface of temperature at 1420 K, colored in gray. One can see that the isosurface of temperature is located in between the two surfaces contributing to the isosurface of heat release rate. Indeed, the isosurface of temperature was selected as the corresponding temperature of a 1D laminar flame heat release rate peak.

One can observe from the results displayed in Fig. 3.7 that the flowfield exhibits the following features. First of all, upstream of

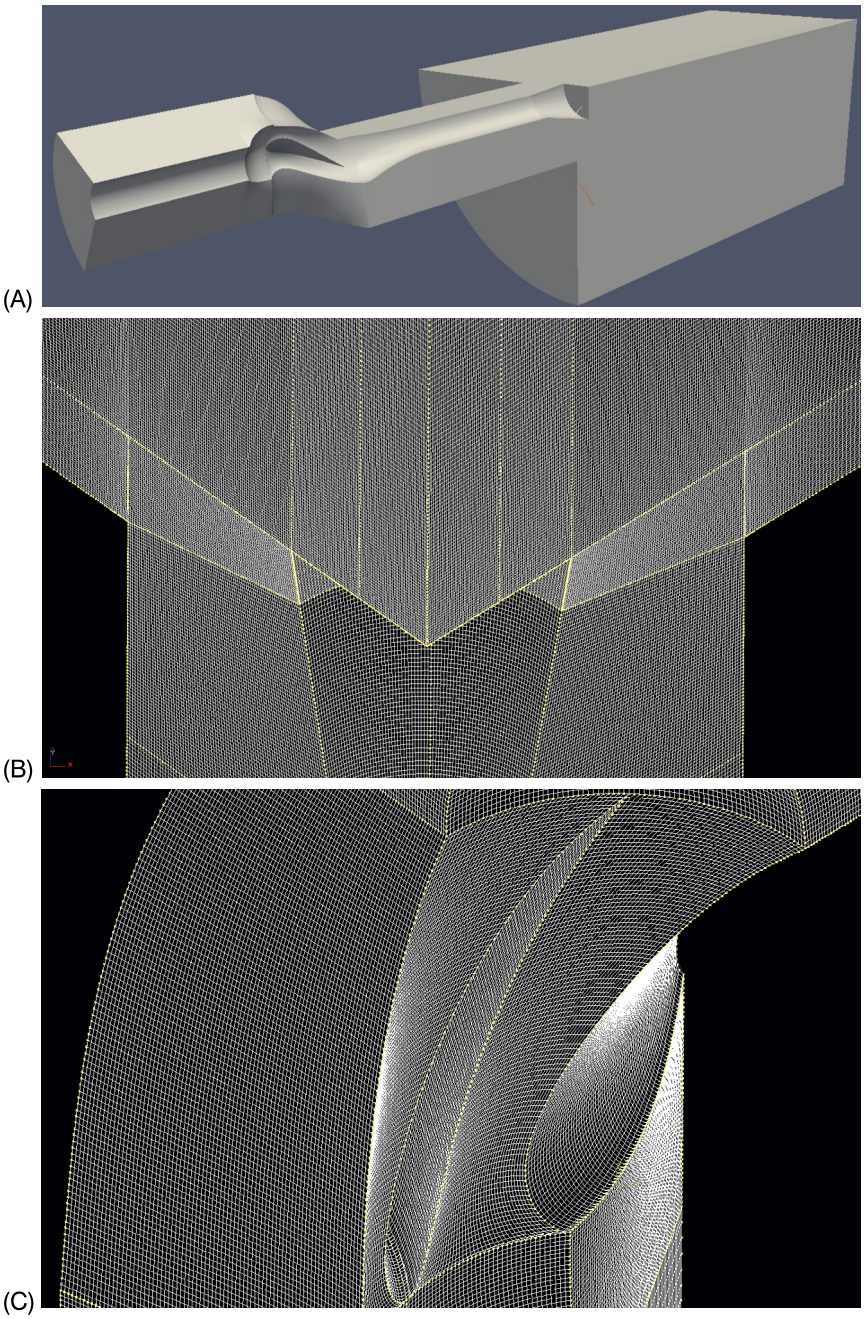

Figure 3.6 Mesh view of the setup. (A) CFD domain modeled. (B) Close-up view of the cone/rod. (C) Close-up view of the swirler vanes.

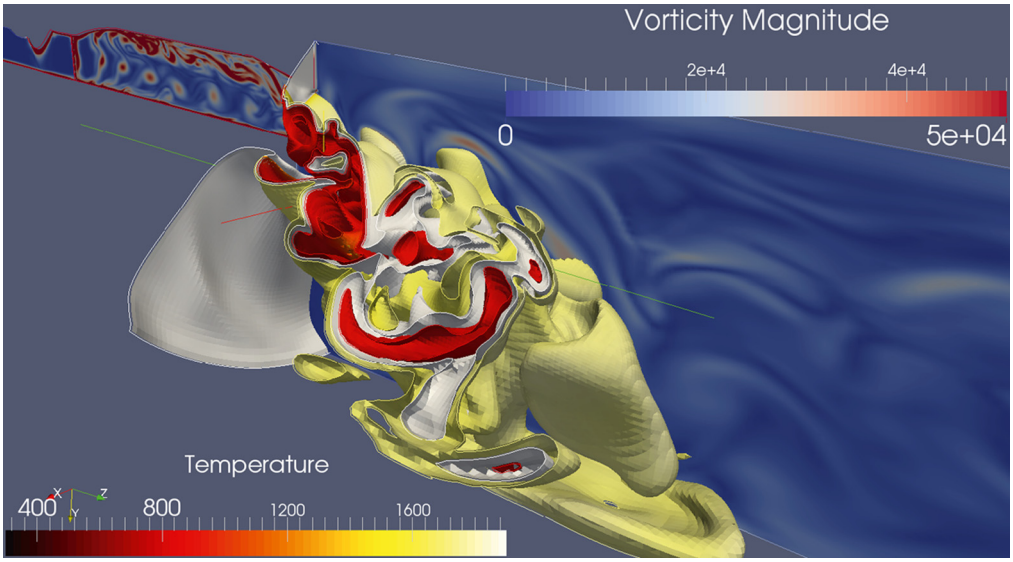

Figure 3.7 Visualization of the reacting flowfield. Flow and flame visualization. Cutaway through the CFD domain is displayed with the vorticity magnitude contour. Isocontour of heat release rate at 200 MW m^{-3} colored by temperature and isocontour of temperature at 1420 K colored in gray.

the flame front, in the injector, a clear periodic vorticity field can be seen along with a zone of high vorticity magnitude beginning downstream of the swirler and located near the central rod. These distinct features correspond respectively to a vortex shedding associated with the wakes of the swirler vanes trailing edges and to a flow separation occurring on the center rod immediately downstream of the diffuser region, such as the von Karman street occurring downstream of an airfoil for certain Reynolds numbers. This complex flowfield is located upstream of the flame front. The flame front of the statistically steady flame is also complex due to that upstream flowfield being convected. In addition, time sequence animation of the reacting flowfield not reported here indicates that this shedding impacts the shear layers. It is probable that the upstream flame front dynamics dominate the shear layers' dynamics. The impact of this shedding on the flow–flame interaction was not investigated further, but it is worthwhile to point out that the interaction of the flow and the flame includes this natural shedding plus the classical shear layers. The analysis of the coupling, generation, and merging of those multiple vorticity sources upstream of the injector and in the flame tube is out of the scope of the present section. The possible impact on flame stabilization is taken into account in the next section.

Table 3.2 List of local contributors evaluated and their mean values extracted.

Variable	Unit	Mean	Median	Peak
p	Pa	101252	101260	101250
$\|\|\nabla p\|\|$	Pa m^{-1}	5.38E4	3.04E4	13500
ρ	kg m^{-3}	0.244	0.243	0.241
Y_{CH_4}	1	0.111	0.112	0.1125
Φ	[1]	0.393	0.398	0.399
$\|\|V\|\|$	m s^{-1}	30.63	28.10	23
$\|\|\Omega\|\|$	s^{-1}	1.845E4	1.389E4	7500
T	K	1420	1420	
$\|\|\nabla T\|\|$	K m^{-1}	1.26E6	1.01E6	5.5E5
Ω_x	s^{-1}	2265	1575	500
Ω_y	s^{-1}	117	182	−500
Ω_z	s^{-1}	−896	−304	0
w_s^x	m s^{-1}	10.79	10.13	9
w_s^y	m s^{-1}	7.79	6.74	2.5
w_s^z	m s^{-1}	20.45	20.61	24
$\nabla \cdot [\lambda/c_p \nabla T]$	K kg/s m^{-3}	−1.39E5	−5.5E4	7500
$\dot{\omega}_T/c_p$	K kg/s m^{-3}	4.88E5	4.87E5	4.85E5
$\|\|S_d\mathbf{n}\|\|$	m s^{-1}	2.34	1.64	0.20
S_d	m s^{-1}	2.24	1.62	0.15
κ	s^{-1}	−3137	−2154	−750

2.2.2 Local contributor fields

In this section, the focus is on the local contributors described in Section 1. The local contributors are computed on the flame surface defined by an isosurface of a heat release rate of 200 MW m^{-3}. This isosurface is selected in order to capture the two folds on the sides of the reaction zone where the maximum heat release occurs. The isosurface is given in Fig. 3.7, where it is possible to see that the reaction zone surface (colored gray) is located in between the isoreaction rate surfaces of 200 MW m^{-3} colored by temperature (respectively red and yellow). The evaluated local contributors are listed in Tab. 3.2. Other local contributors are discussed next.

The local contributors computed are presented in Figs. 3.8 and 3.9 and are now discussed. Each subfigure corresponds to the

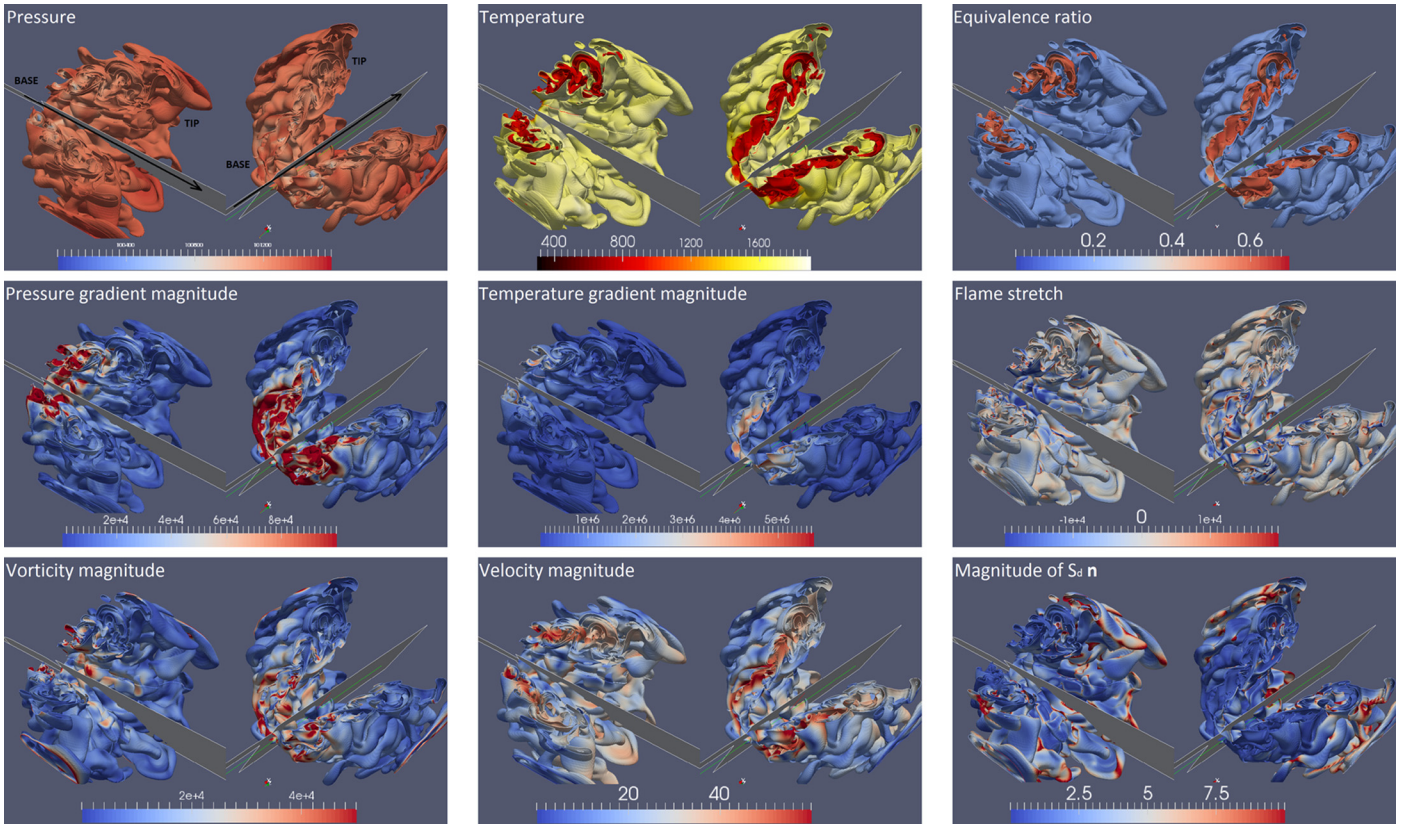

Figure 3.8 Visualization of the reacting flowfield. Selected implicit and explicit local contributors computed on the isosurface of reaction rate of 200 MW m^{-3}. In each figure a local contributor is plotted. The figure is made up of two views, front and rear, to enhance visualization of the flame surface. The local contributors are given in Tab. 3.2.

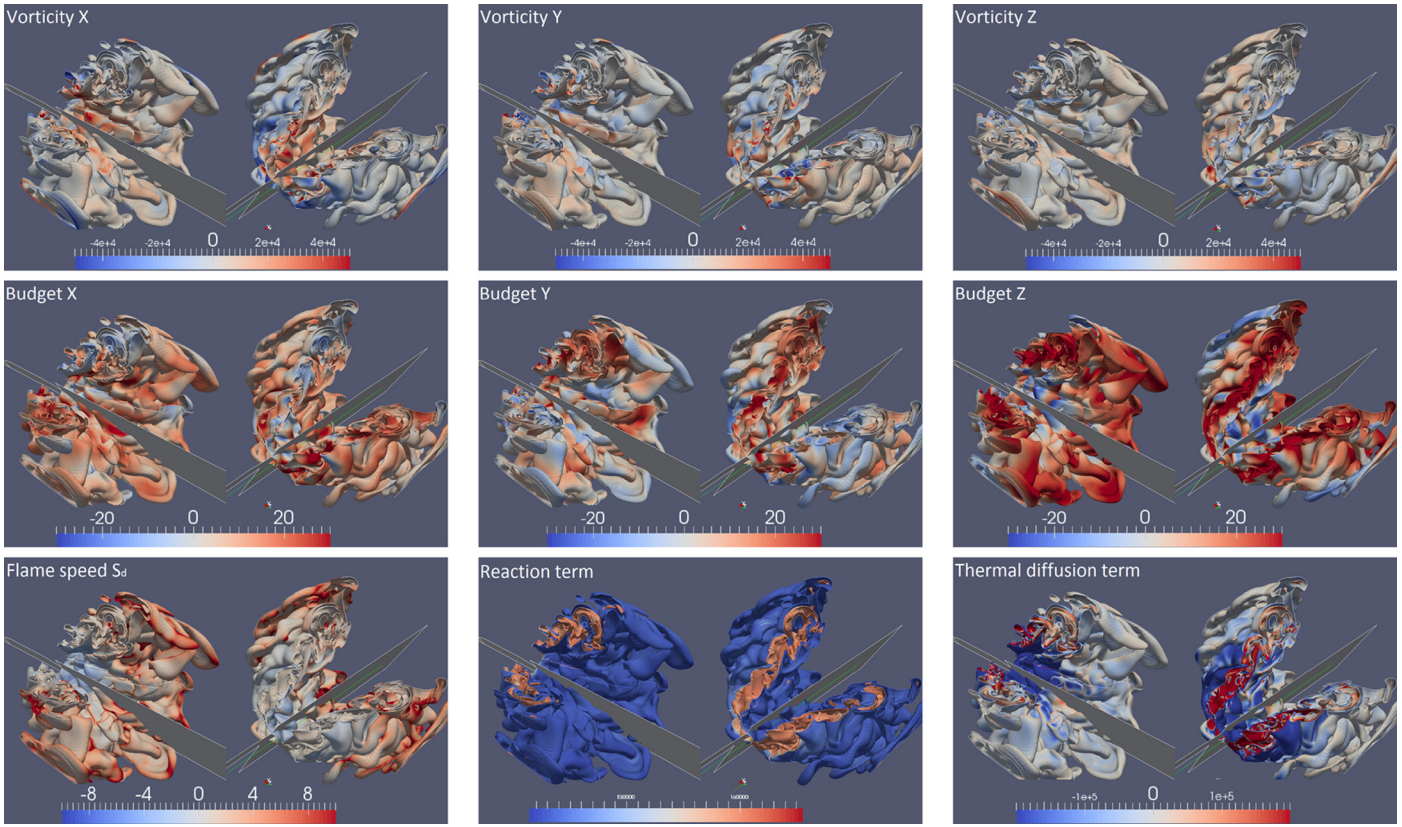

Figure 3.9 Visualization of the reacting flowfield. Selected implicit and explicit local contributors computed on the isosurface of reaction rate of 200 $\mathrm{MW\,m^{-3}}$. In each figure a local contributor is plotted. The figure is made up of two views, front and rear, to enhance visualization of the flame surface. The local contributors are given in Tab. 3.2.

front (left) and rear (right) view of the flame surface for a given local contributor. Each local contributor has been presented in the previous section. The visualization of the pressure field shows that the flame surface evolves essentially on an isobaric region, except in the near-flame base region, where a lower pressure field is observed. This is highlighted by the pressure gradient magnitude where high values are reached in the flame base region. This can be attributed to the swirling motion inducing radial and axial pressure gradients. Next, the temperature field is computed on the isosurface of constant 200 $\mathrm{MW\,m^{-3}}$ heat release rate. This allows to distinguish two different temperature surfaces, respectively associated with the burned gases (colored in yellow) and the unburned gases (colored in red) as the peak of heat release is located in between in the reaction zone. The figure also shows the existence of pockets of fresh and burned gases in the upper flame region. One also observes that the distance between the two surfaces increases (the flame thickness) as a function of the distance from the flame base. This is attributed to (i) the decrease of the equivalence ratio increasing the flame thickness as the axial distance increases, (ii) the effects of the swirling motion on the coherence of the vortices, (iii) the turbulent diffusion, and (iv) the possible (but unlikely) effect of the nonconstant mesh size. These effects were not quantified. The magnitude of the temperature gradient is the highest in the near-flame base location, where the flame thickness is the smallest. The flame stretch local contributor (including flow strain at the flame front, flow divergence, and flame curvature terms) is plotted as well in Figs. 3.8 and 3.9, and one can observe that the values taken by this local contributor are distributed on the entire flame surface. In addition, the flame stretch is shown to reach most of its peak values on the upstream side of the flame near the flame base. Contrarily on the downstream side at the flame tip, values appear to be centered on zero.

Next, the magnitudes of the vorticity vector, the velocity vector, and the quantity $S_d\mathbf{n}$ are computed. The vorticity magnitude shows the highest values in the near-flame base region and on the swirling jets (located in between the two folds of the flame surface) with annular distributions associated with vortices from the shear layers and from the swirler. This observation is confirmed by the vorticity components in the x and y directions, which are directly associated with the vorticity along the azimuthal direction. The axial vorticity (z) shows that it has a small contribution to the overall vorticity magnitude. The distribution of the velocity magnitude shows its highest values on the swirling jet due to the high axial velocity values on them. The magnitude of the product of the flame speed with the flame front normal (oriented towards

the unburned gases) demonstrates overall that this quantity takes low values.

The flame surface speed budgets along each direction are next discussed. These budgets correspond to the previously defined components w_s^x, w_s^y, and w_s^z. The three components have a wide range of values between -30 m s^{-1} and 30 m s^{-1}. The most notable aspect observed is with respect to the z direction budget, which presents the highest values, particularly along the swirling jets. The flame speed is next displayed, and one observes that the values range from near -10 m/s to near 10 m/s. Most of the flame surface displays flame speed values near zero. The next two graphics display the reaction term and the thermal diffusion term of the flame speed computed as detailed in Chapter 2. They will be further discussed in Section 3.

2.2.3 Local contributors' distributions

The local contributors' distributions are now evaluated and analyzed at the flame isosurface defined by temperature $T = 1420$ K and for which the heat release rate is superior to 100 MW m^{-3}, so that only the regions of high temperature with reaction are taken into account. This is done to analyze the reaction zones. This isosurface is used to track the flame reaction zone position. On this isosurface corresponding to the reaction zone location, a set of local contributors' distributions, presented in Section 2 and in Fig. 4.3, are computed. It includes all the implicit local contributors, quantities that are usually measured experimentally. The evaluated local contributors are listed in Tab. 4.1.

The distributions of the local contributors and the previously defined isosurface are presented in Figs. 3.10 and 3.11. Each distribution has an integral equal to unity by definition. These plots present the occurrence of each value for a given local contributors on the flame front defined in the previous paragraph. These graphics complement the local contributors' maps of the previous subsection and allow to extract important information. Tab. 4.1 lists the mean, median, and peak values for each distribution. It is interesting to note that multiple variables follow a Gaussian type of distribution. The pressure distribution on the flame isosurface is centered on a value slightly below the average atmospheric pressure at 101 250 Pa. The local equivalence ratio distribution is centered on 0.4 and distributed around that value within a range from 0.3 to 0.5, while the temperature is set constant at 1420 K. The mass fraction of methane is centered on 0.1125. A similar distribution for the oxygen mass fraction (not shown here) shows that the peaks of oxygen and methane mass fractions correspond to the local equivalence ratio peak.

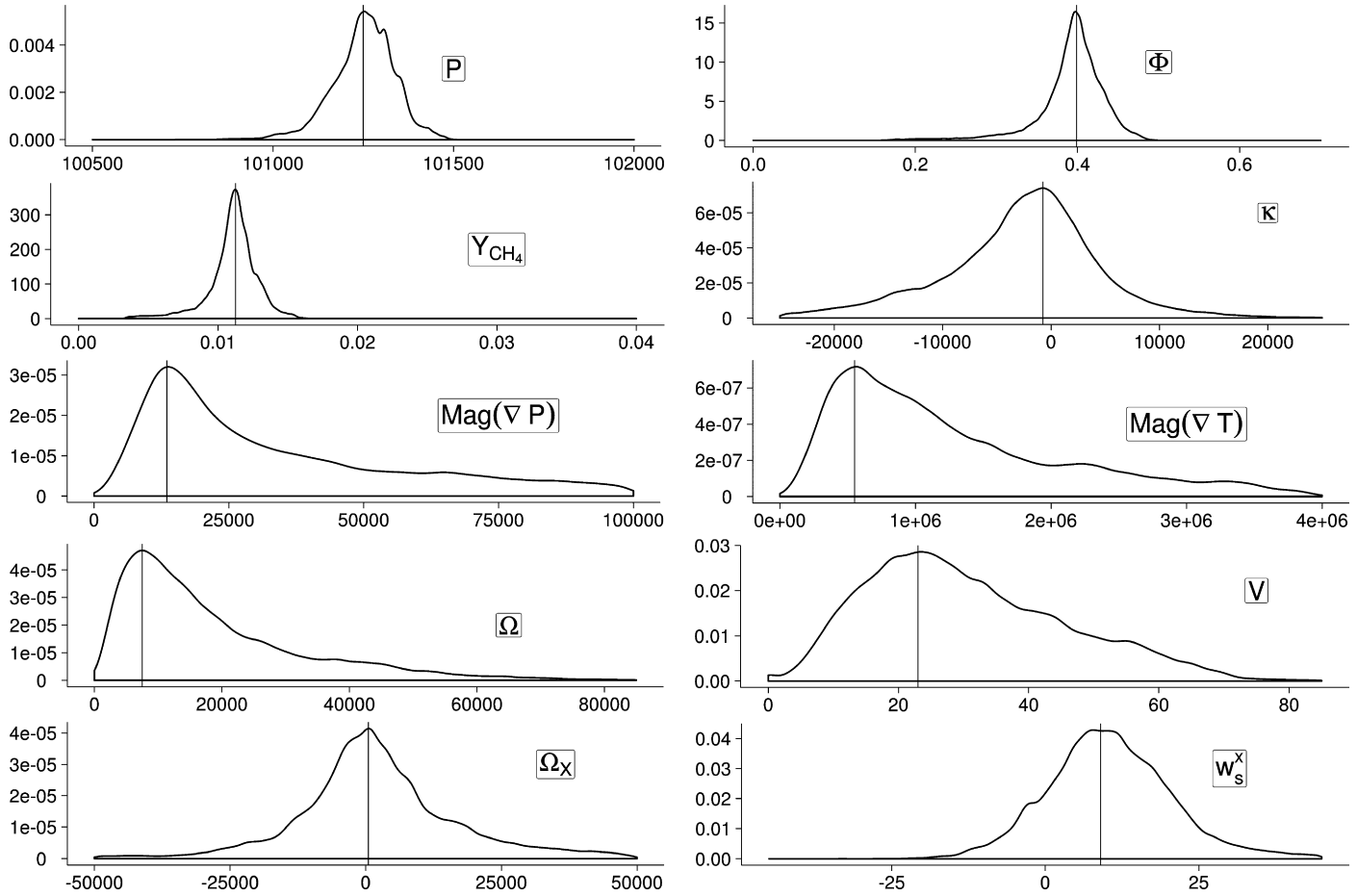

Figure 3.10 Distributions of the reacting flowfield variables. Local contributors' distributions determined on the flame reaction zone isosurface. The median, mean, and peak values are given in Tab. 3.2.

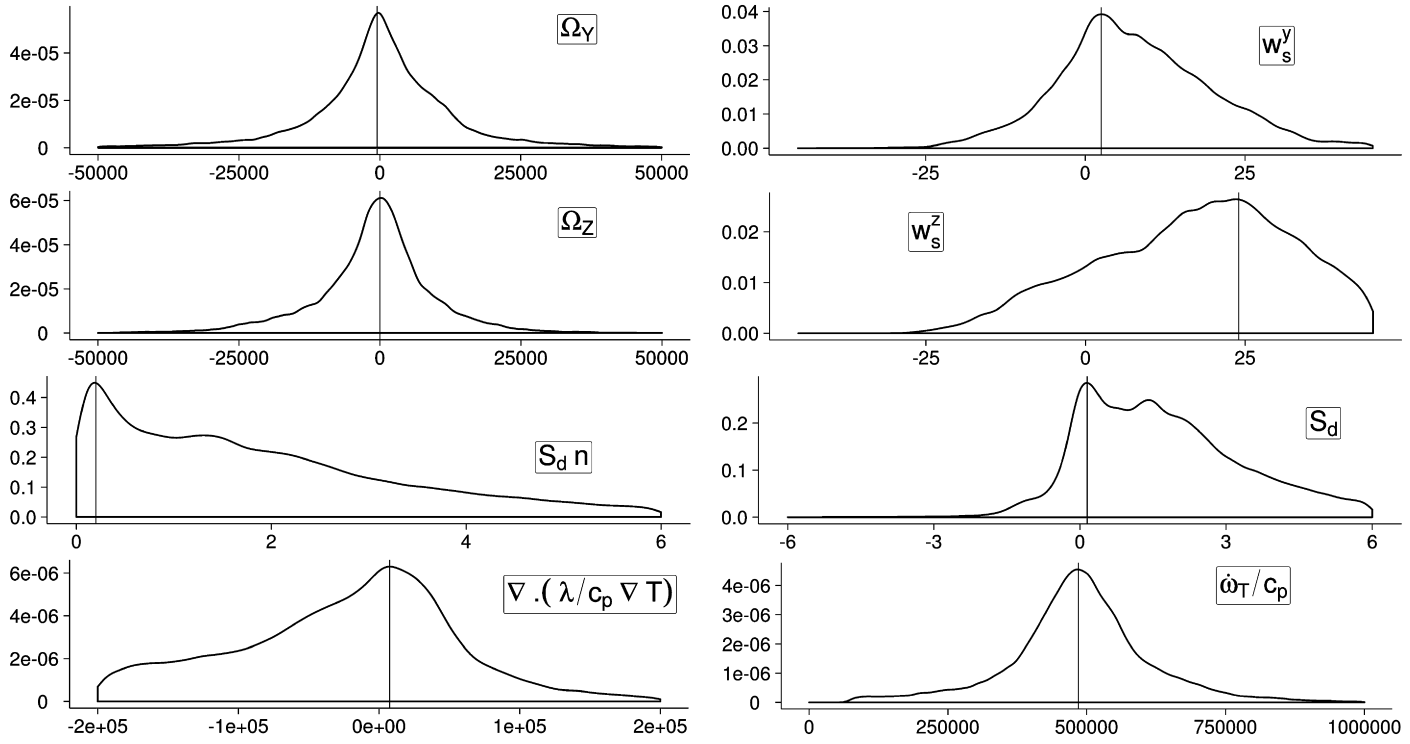

Figure 3.11 Distributions of the reacting flowfield variables. Local contributors' distributions determined on the flame reaction zone isosurface. The median, mean, and peak values are given in Tab. 3.2.

Another interesting quantity to present is the flame stretch. The distribution of the flame stretch shows that most values on the flame surface are near zero. The magnitudes of the pressure and temperature gradients are then plotted, indicating that their distributions are centered respectively on 13 500 Pa m^{-1} and on 5.5E5 K m^{-1}. The vorticity magnitude shows a similar pattern with a peak value centered on 7500 s^{-1}, while the three vorticity components are centered on near-zero values. The peak of occurrence of the velocity magnitude is nearly 23 m s^{-1}, while the mean and median values are near the injector bulk velocity of 30 m s^{-1}.

Next, the net budgets of the flame speed versus the flow speed along each Cartesian direction are given and correspond to the flame surface speeds, respectively w_s^x, w_s^y, and w_s^z. Those budgets indicate that most spatial occurrences peak on positive values, reflecting a motion of the flame surface in the positive directions. In addition, the maximum values are reached in the longitudinal direction with a peak at 24 m s^{-1}. This reflects strong axial flame surface motion.

The last four plots correspond to the magnitude of the product between the flame speed and the flame front normal $S_d\mathbf{n}$, to the flame speed S_d, to the thermal diffusion term, and to the reacting term of the flame speed defined in Chapter 2. Remarkably, the flame speed peaks at 0.15 m s^{-1} and the quantity $||S_d\mathbf{n}||$ peaks at a value of 0.2 m s^{-1}, which is the 1D laminar flame speed value of methane–air combustion at an equivalence ratio of 0.7.

2.2.4 Flame stabilization mechanism descriptions

The present section builds upon the previous observations to determine the flame stabilization mechanisms of swirling flames under numerical study. The starting point is the flame surface speed budget $\mathbf{w} = \mathbf{v} + S_d\mathbf{n}$. It has been shown with their spatial fields and distributions that the budget components are mostly positive with values above the quantity $||S_d\mathbf{n}||$ median and mean values. This indicates that the dominant term of the instantaneous budget originates from the flow speed. In other words, the instantaneous flame surface speed and motion (and subsequently location) is mostly driven by the flow speed and not by the flame speed. The flame speed can be expressed as containing the two following terms: the thermal diffusion term and the reacting term, see Chen and Im [250] and Kuo and Acharya [21]. Both terms are plotted as local contributors in Figs. 3.8 and 3.9 along with the flame speed. This latter quantity is mostly uniform and near the unstretched laminar flame speed value over the flame surface plotted. The thermal diffusion term contributing to the flame speed is dominant in the flame base region and can be associated

with the IRZ of the burned gases. It is also supported by the temperature gradient magnitude in that region associated with the heat flux. The reacting term contributing to the flame speed is contrarily nearly constant along the flame surface. These results indicate firstly that the instantaneous flame propagation is driven by both reaction and thermal diffusion in the near-flame base region, with a prominent role of the thermal diffusion from the recirculation zone, and most importantly that the instantaneously flame surface position is dominated by flow effects.

It is now important to understand and describe further how the flame surface evolves and stabilizes and thus which flow effects are at work. The positive budget reflects the fact that an element of the flame surface is displaced downstream. The flame surface downstream extends or the flame length ends when no more fuel is available for the reaction. Flame stabilization mechanisms are comprehensively documented analytically in Section 3 of this chapter, where it is shown that the propagation of turbulent premixed flames is due to either the static or the dynamic component of the flow. The present local contributors analysis has demonstrated the importance of the flow speed intrinsically linked to the convective effects on the instantaneous flame surface budgets' components.

One can also look at the flame stabilization not from the instantaneous perspective but from the static/dynamic components perspective. The flow speed can be further split into a static and a dynamic component, see Palies et al. [213], and the flame surface budget can also be split accordingly into a static and a dynamic component. The next subsection focuses on these two contributions.

The decomposition of the flowfield into a static and a dynamic component is now carried out. The decomposition can be written for a variable α as $\overline{\alpha} = \alpha_0 + \overline{\alpha'_0}$, where $\overline{\alpha}$ is the time average and $\overline{\alpha'_0}$ the average of the fluctuation component. In the present case, the focus is on the square of the velocity vector $\overline{\mathbf{v}^2}$ so that an estimate of the velocity static mode can be obtained: $\mathbf{v}_0^2 \simeq \overline{\mathbf{v}^2} - \overline{\mathbf{v}'^2}$, assuming that $\overline{\mathbf{v}'_0} = 0$ and $\overline{\mathbf{v}'_0} = \overline{\mathbf{v}'}$, implicitly assuming that the flow nonlinearities are weak, such as for this statistically steady data set. This estimation procedure was applied to the statistically steady swirling flame data, and the results are displayed in Fig. 3.12. In this figure, the top row presents the front view of the flame surface and the bottom row presents the rear view of the flame surface. The first column corresponds to the time-average velocity magnitude, the second column to the extracted static mode, and the third column to the dynamic mode time average. The results indicate that the time average and the static component are different,

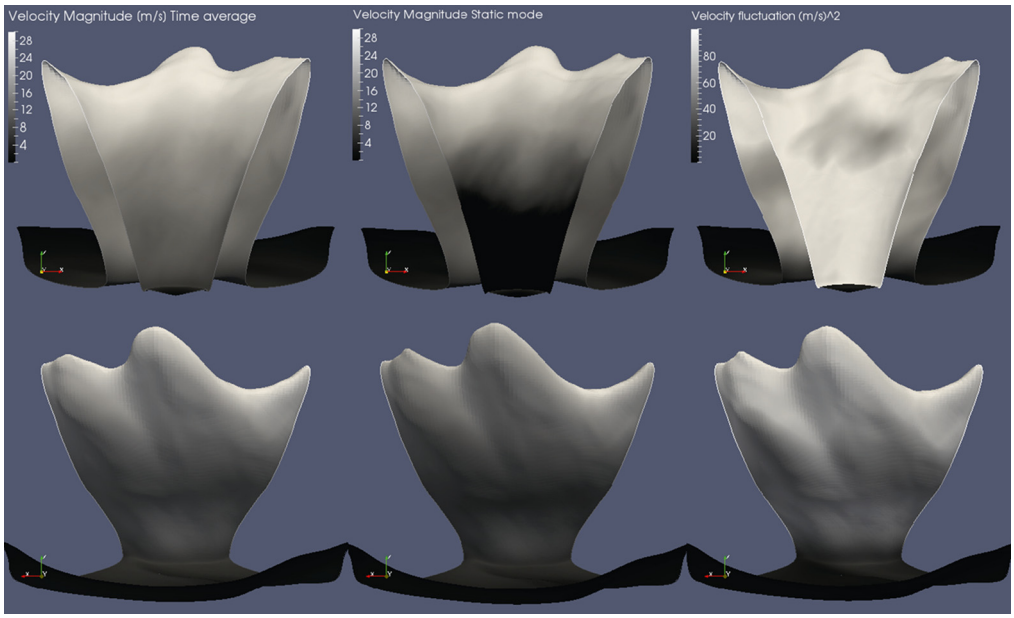

Figure 3.12 Distributions of the reacting flowfield variables. Front (top row) and rear (bottom row) views of the isosurface of the swirling flame with superimposed velocity vector magnitude (left/center) and its fluctuation (right). Left column: Time average. Center column: Static component. Right column: Dynamic component average.

particularly for the inner flame near the injector region, where low values of the flow speed are reached. The dynamic component average shows an overall significant level of fluctuations distributed on the entire flame surface, in the IRZ, and on the swirling jets.

Theoretical flame stabilization is documented in Section 3 of this chapter, where the flowfield decomposition into a static and a dynamic component leads to the following system of equations for the flame speed:

$$
\begin{aligned}
&S_{d,0}^2 = u_0^2 + v_0^2 + w_0^2, \\
&S'_d S_{d,0} = u_0(u' - w'^x_s) + v_0(v' - w'^y_s) + w_0(w' - w'^z_s), \\
&S'^2_d = (u' - w'^x_s)^2 + (v' - w'^y_s)^2 + (w' - w'^z_s)^2.
\end{aligned}
\tag{3.7}
$$

The system of equations (3.7) links the static flow, flame surface, and flame speeds with their dynamic components for a stabilized turbulent flame for which the static flame surface speed $w_{s,0} = 0$ without any other assumptions. The first equation of this system reflects the equality between the static flame speed and the static flow velocity vector magnitude. The second equation couples the

Table 3.3 Mean, median, and peak values for the time average, static component, and dynamic component average.

Value	Mean	Median	Peak
Time average $\overline{v}$	16.04	15.62	11.25
Static component v_0	11.08	11.35	11.25
Dynamic component average $\sqrt{\overline{v'^2}}$	10.61	11.30	11, 13.2

static and dynamic flow, flame, and flame surface speed components and could be responsible for transition phenomena from laminar to turbulent combustion or transition to blowout and flashback, as coupling between static and dynamic components occurs. The third equation of the system describes the dynamic component evolution.

The static component in Fig. 3.12 provides the evaluation of the velocity vector magnitude, and it is shown that this magnitude reaches low values of the order of the unstretched laminar flame speed in the inner flame branch near the injector region. These results are supported by the first equation of the system. The third equation of the system can be discussed with respect to the last column of Fig. 3.12. This equation shows that the flame will be perfectly stabilized around the static mode if the fluctuations of the dynamic component of the flow and flame speeds perfectly compensate each other so that $w'_s = 0$. In reality one can expect that value to be alternatingly positive and negative, so that the flame is still stabilized (the flame is fixed in the laboratory frame of reference) for bounded fluctuation levels.

In Fig. 3.13, the distributions taken on the flame isosurface are displayed in the left column and velocities as a function of the flame element distance to the center of the geometry are displayed on the right. These distribution graphics are now discussed. The time average and the static component differ mainly in the low speed region. They both present a strong peak near the mean value. The corresponding data are represented as a function of the distance from the center of the geometry (right figures). This reflects the two regions, respectively the near-injector region and the remaining location, where the first one is dominated by low speed values of the time average or the static velocity component, while the second region is dominated by higher speeds and high levels of fluctuations, as revealed by the dynamic component average values.

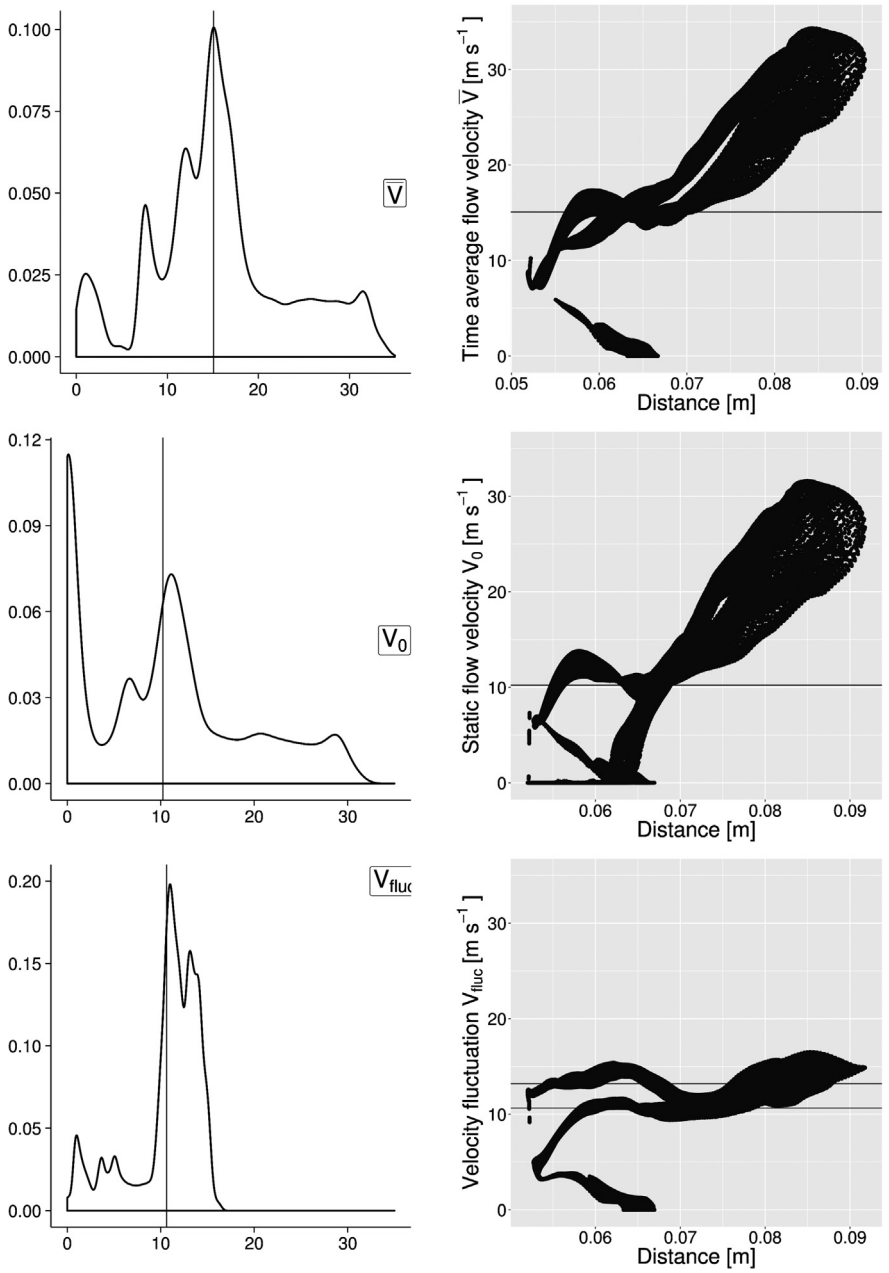

Figure 3.13 Comparison of time average versus static and dynamic components. Time average (top row) and static (center row) and average dynamic (bottom row) components of the velocity vector magnitude. Distributions taken on the flame isosurface are displayed in the left column. Velocities as a function of the flame element distance to the center of the geometry are displayed on the right. The mean values of the distribution taken from Tab. 3.3 are superimposed as horizontal lines.

2.2.5 Summary

The present section described the mechanisms of flame stabilization of turbulent premixed swirling flames. A framework was also introduced that reviewed the multiple possible local contributors of flame stabilization. Those local contributors were categorized as explicit and implicit. The explicit contributors are quantities directly found in the governing equations of reacting flows, while the implicit contributors are derived from them. Numerical simulations were carried out for the MICCA-EM2C swirl-stabilized configuration at operating conditions of a bulk velocity equal to 30 $\mathrm{m\,s^{-1}}$ and an equivalence ratio of 0.7. A detailed meshing strategy allowed to capture the flame front dynamics with quasi-DNS resolution. In addition, the data generated were extensively used to compute the local contributors. The analysis focused first on the instantaneous values of those local contributors. While each local contributor was discussed, a significant emphasis of the analysis was on the flame, flow, and flame surface speed budgets. It was demonstrated that the instantaneous budget was dominated by the flow effects over the combustion effects. Those latter were investigated with the evaluation of the thermal diffusion and reaction effects on the flame speed on the iso-heat release surface. It was shown that on those surfaces the thermal diffusion effects are of lower amplitude compared with the reaction effects, particularly in the upstream near-injector location. To advance our understanding of flame stabilization and the contribution from the nonreacting and the reacting flowfield, the analysis then split the flame, flow, and flame surface speed budgets into their static and average dynamic components. With this decomposition, the static flow effects were shown to be prominent at the near-injector inner flame branch location, while the dynamic flow effects are dominant at the other locations. This result highlights the importance of turbulence and acoustics fluctuations from the IRZ and the swirling jets, as well as those from the swirler and the bluff-body, and the low velocity speed at the near-injector location for flame stabilization. A summary of these results is provided in Fig. 3.14.

3 Theoretical results on flame stabilization and propagation

Expressions linking the flame, flow, and flame surface speeds are now derived and discussed. The theoretical decomposition of the flow variables previously introduced is used throughout this section. The decomposition leads to static and dynamic flow

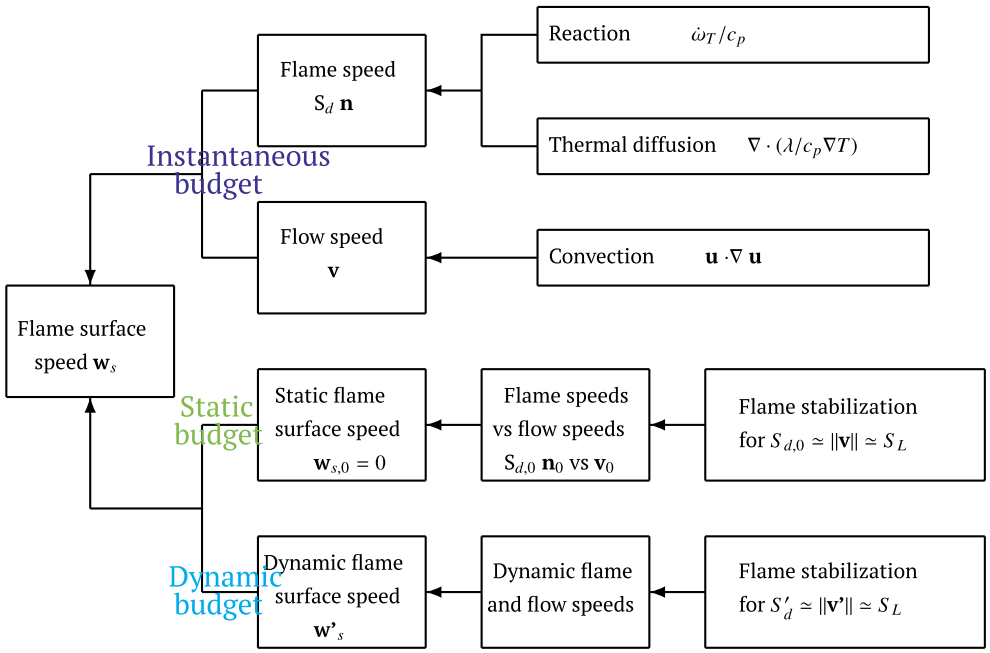

Figure 3.14 Illustration of flame stabilization mechanisms. Flame stabilization can be studied with two approaches. The first one is by considering the instantaneous budget of the flame surface, flow, and flame speeds, and it corresponds to the upper row of this schematic. The second approach is to split the budget into a static and a dynamic component (lower rows of the schematic). In the instantaneous form, the flow speed dominates the budget and the flame surface is successively transported along the swirling jet. In the second case, the flame is stabilized because of two mechanisms. Firstly, the local flow speed balances the local flame speed, and secondly, the fluctuations of the flame speed are of the order of the fluctuations of the flow speed, so that the flame surface speed that oscillates ensures stabilization.

components. The static component is a nonoscillating field (also called base flowfield), while the dynamic component includes fluctuations due to turbulence, noise, and harmonic modulations (acoustic or vortical). The G-equation, which models the propagation of a deflagration combustion wave into a flowfield, is then used along with the kinematic expressions linking the flame, flow, and flame surface velocity vectors. These expressions are the starting point to derive relationships between these quantities for multiple configurations of practical interest, such as turbulent and modulated flames. The terms of those relationships are discussed and lead to the determination of the propagation mode for turbulent flames. Phenomena such as blowout and flashback are discussed with the perspectives brought by those obtained expressions. In addition, the case of a modulated turbulent swirling

flame brings an exact expression for the fluctuating turbulent burning velocity ratio, which is compared with an expression from the literature. The numerical simulations conducted previously to support the theoretical development and to determine the stabilization mechanisms of swirling flames are reused here. It is concluded that for the near-injector region, the flame is stabilized by a competing mechanism where both the static flow and the dynamic component (due to turbulence and acoustics) are important, while the remaining location of the flame is stabilized by the dynamic component only.

The objective of the present section is to derive mathematical expressions linking the flame, flow, and flame surface speeds in order to analyze stabilization in laminar, turbulent, and modulated flame configurations. It is of interest to express the flame speed budgets for known canonical configurations and to express them with the flame surface speed as a function of other speeds in order to have an expression in the laboratory frame of reference. In addition, these expressions are shown to revisit the known turbulent flame speed definition found in the literature. It is presented next.

3.1 Flowfield decomposition and theoretical approach: framework

One starts by assuming that each flowfield variable can be decomposed into a static (nonoscillating) and a dynamic component, see Palies et al. [213], which both satisfy a set of governing equations. The static component is the base state at any time of the system for which the unsteady time derivatives of these equations are zero. An important aspect of this decomposition is that the time average and the static component are two different quantities/fields. It is worthwhile to highlight the fact that the static component excludes any effect from harmonic modulations or turbulent fluctuations. The present section provides an understanding of these two components in the context of turbulent flame propagation.

The theoretical approach adopted here is to derive relationships for flame, flame surface, and flow speeds in different practical situations, to discuss the effects of each term of these relationships, and to elaborate on their consequences. The decomposition framework can be implemented on the governing equations and is demonstrated here on the G-equation. The G-equation is written

$$\frac{\partial G}{\partial t} + \mathbf{v} \cdot \nabla G = S_d |\nabla G|, \tag{3.8}$$

where an isosurface of the G field models the flame isosurface, $\mathbf{v}$ is the velocity vector at the flame surface, and S_d is the flame speed. The flowfield decomposition leads to the following equation for the static component

$$\mathbf{v}_0 \cdot \nabla G_0 = S_{d,0} |\nabla G_0|. \tag{3.9}$$

The static flame front normal is obtained with

$$\mathbf{n}_0 = -\nabla G_0 / |\nabla G_0|. \tag{3.10}$$

In the present section, the fluctuation is selected as a fluctuation from turbulence, a fluctuation from a modulation, or both.

The general expression linking the premixed flame displacement speed $S_d\mathbf{n}$, the flame surface speed $\mathbf{w}_s$, and the flow speed $\mathbf{v}$ is

$$\mathbf{w}_s = \mathbf{v} + S_d \mathbf{n}, \tag{3.11}$$

where the vectors are written

$$\mathbf{w}_s = w_s^x \mathbf{e}_x + w_s^y \mathbf{e}_y + w_s^z \mathbf{e}_z, \tag{3.12}$$

$$\mathbf{v} = u\mathbf{e}_x + v\mathbf{e}_y + w\mathbf{e}_z, \tag{3.13}$$

$$\mathbf{n} = n_x \mathbf{e}_x + n_y \mathbf{e}_y + n_z \mathbf{e}_z. \tag{3.14}$$

These vectors can also be split into their static and dynamic components.

While this section has presented the general framework, the next sections focus on the derivation, the data set analyses, and subsequent observations supporting this framework. In addition, it is worthwhile to remember that propagation can either refer to flame surface propagation or to the flame burning propagation, depending on the frame of reference. Accordingly, flame stabilization refers to a flame surface that is fixed or that presents small variations around the static component, in the laboratory frame of reference.

It has been shown in Palies et al. [213] that the time average and the nonoscillating (static) mode are identical if the dynamic contribution's time average is zero. The associated analytical development is reported now. The dynamic mode decomposition, see Schmid [251], of a field variable $\alpha(x, y, z, t)$ can take the following form:

$$\alpha(x, y, z, t) = \sum_{k=1}^{N-1} \hat{\alpha}_k \exp(\lambda_k t) \phi_k(x, y, z), \tag{3.15}$$

where N is the total number of snapshots, $\hat{\alpha}_k$ is the amplitude of the kth mode, $\lambda_k = \sigma_k + i2\pi f_k$ is its complex pulsation, and $\phi_k(x, y, z)$ is its spatial distribution. One can now apply the time average operator to this equation:

$$\overline{\alpha(x, y, z, t)} = \sum_{k=1}^{N-1} \hat{\alpha}_k \exp(\lambda_k t)\phi_k(x, y, z), \tag{3.16}$$

which leads to

$$\overline{\alpha(x, y, z, t)} = \hat{\alpha}_1 \overline{\exp(\sigma_1 t)}\phi_1(x, y, z) + \overline{\sum_{k=2}^{N-1} \hat{\alpha}_k \exp(\lambda_k t)\phi_k(x, y, z)}, \tag{3.17}$$

which can also be written as

$$\bar{\alpha} = \frac{\hat{\alpha}_1\phi_1}{\sigma_1 T}\left(\exp(\sigma_1 T) - 1\right) + \frac{1}{T}\sum_{k=2}^{N-1} \frac{\hat{\alpha}_k\phi_k}{\lambda_k}\left(\exp(\lambda_k T) - 1\right). \tag{3.18}$$

The time average $\bar{\alpha}$ over a time range from 0 to $T = N\delta t$ is the summation of two contributions: the nonoscillating mode and the time average of the dynamic component. This can be summarized as

$$\bar{\alpha} = \alpha_0 + \overline{\alpha'_0}. \tag{3.19}$$

The first contribution is due to the nonoscillating 0 Hz mode ($k = 1$); the second contribution contains the nonlinear modes interactions affecting the time average.

3.2 Regimes and configurations

The present section focuses on deriving the mathematical expressions for laminar and turbulent flame configurations such as represented in Fig. 3.15. These configurations have characteristic flame surface, flow, and flame displacement speeds, which are summarized in Tab. 3.4.

3.3 Expressions for laminar and turbulent planar flames in open tubes

3.3.1 Laminar flame propagating in an open tube

For laminar flames propagating in an open tube configuration, the expression of the flame surface speed $\mathbf{w}$ is immediately obtained from Eq. (3.11) as the upstream flowfield in which the flame

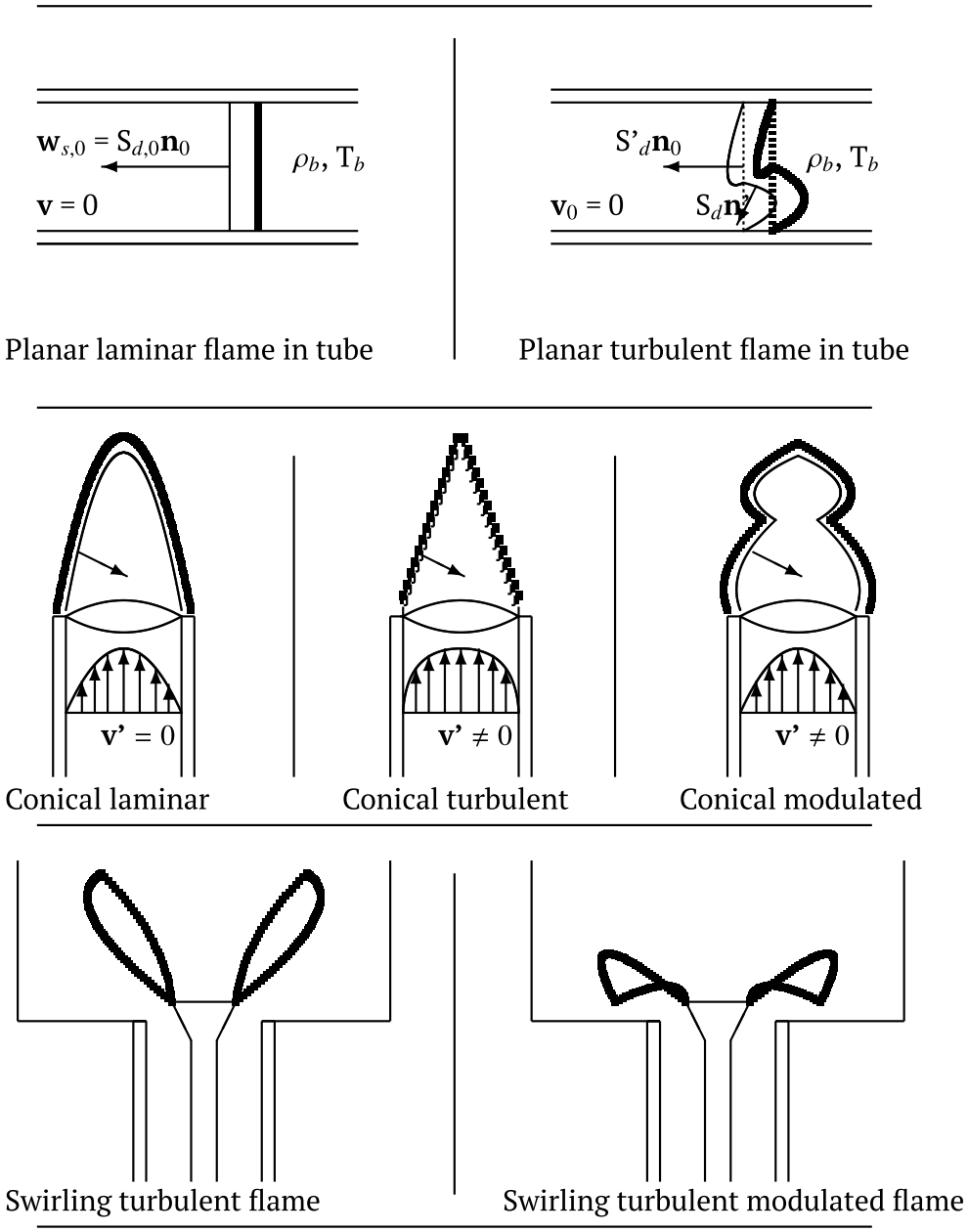

Figure 3.15 Global schematics of the considered configurations. Illustration of laminar and turbulent flame configurations. Planar flames in tubes and conical and swirling flames are represented. The flame structure is sketched with two solid lines corresponding to the extent of the flame. Characteristics of the flame, flow, and flame surface speeds of each of these configurations are given in Tab. 3.4.

Table 3.4 Characteristic flame surface, flow, and flame displacement speeds for typical configurations.

Configuration	$\mathbf{w}_s$	$\mathbf{w}_{s,0}$	$\mathbf{w'}_s$	$\mathbf{v}_0$	$\mathbf{v'}$	$S_{d,0}$	S'_d
Planar laminar	$\neq 0$	$\neq 0$	$= 0$	$= 0$	$= 0$	$\neq 0$	$= 0$
Planar turbulent	$\neq 0$	$\neq 0$	$\neq 0$	$= 0$	$\neq 0$	$\neq 0$	$\neq 0$
Conical laminar	$= 0$	$= 0$	$= 0$	$\neq 0$	$= 0$	$\neq 0$	$= 0$
Conical turbulent	$\neq 0$	$= 0$	$\neq 0$	$\neq 0$	$\neq 0$	$\neq 0$	$\neq 0$
Conical modulated	$\neq 0$	$= 0$	$\neq 0$	$\neq 0$	$\neq 0$	$\neq 0$	$\neq 0$
Swirled turbulent	$\neq 0$	$= 0$	$\neq 0$	$\neq 0$	$\neq 0$	$\neq 0$	$\neq 0$
Swirled modulated	$\neq 0$	$= 0$	$\neq 0$	$\neq 0$	$\neq 0$	$\neq 0$	$\neq 0$

front propagates at rest. The expression takes the following form:

$$\mathbf{w}_{s,0} = S_{d,0}\mathbf{n}_0. \tag{3.20}$$

In that case, the local flame displacement speed is the laminar flame speed S_L.

3.3.2 Turbulent flame propagating in an open tube

When turbulence exists in the region upstream of the flame front and the nonoscillating (static) component of the fluid velocity is zero, an expression linking the variations of flame surface speed and flame speed fluctuations can be determined. One starts by splitting the variables into the nonoscillating (static) component and the fluctuating dynamic component as defined in Section 3.1. Eq. (3.11) is then written

$$\mathbf{w}_{s,0} + \mathbf{w'}_s = \mathbf{v}_0 + \mathbf{v'} + (S_{d,0} + S'_d) \times (\mathbf{n}_0 + \mathbf{n}'). \tag{3.21}$$

This equation can be split into two equations, related to the static and dynamic components. For the static component, as the upstream velocity field $\mathbf{v}_0$ is zero, one obtains

$$\mathbf{w}_{s,0} = S_{d,0}\mathbf{n}_0. \tag{3.22}$$

This equation reflects the global motion of the flame towards the fresh unburned gases. This relationship is identical to the laminar case.

The dynamic component of Eq. (3.21) becomes

$$\mathbf{w'}_s = \mathbf{v'} + S_{d,0}\mathbf{n'} + S'_d\mathbf{n}_0 + S'_d\mathbf{n'}. \tag{3.23}$$

This equation expresses the fact that the dynamic fluctuating component of the flame surface velocity (left-hand term) depends on four terms: (i) the turbulent velocity fluctuation field, (ii) the motion of the fluctuating flame surface at the static flame speed, (iii) the motion of the static flame surface at the fluctuating flame speed, and (iv) the motion of the fluctuating flame surface at the fluctuating flame speed. One observes that term (iii) contributes to the flame surface speed in the direction of the static component. This expresses an anisotropy behavior of the flame surface motion in the static direction, while other terms have components in all directions. If we also assume that the product of the fluctuations is small or that the product of the fluctuations is strictly zero, assuming that the fluctuations are balanced by their order, the propagation of the flame in the plane orthogonal to the main static direction is strictly the consequence of a balance between the turbulent velocity fluctuation and the motion of the local wrinkled surface at the static flame speed. In the main static direction, the three terms determine the dynamic component $\mathbf{w'}_s$.

By assuming that the turbulent velocity field is incompressible (and implicitly that the fluctuation is here a turbulent fluctuation), one obtains

$$\nabla \cdot \mathbf{w'}_s = \nabla \cdot (S_{d,0}\mathbf{n'} + S'_d\mathbf{n}_0 + S'_d\mathbf{n'}). \tag{3.24}$$

By expanding the right expression, one can obtain the following:

$$\nabla \cdot \mathbf{w'}_s = S_{d,0}\nabla \cdot \mathbf{n'} + \mathbf{n'} \cdot \nabla S_{d,0} + S'_d\nabla \cdot \mathbf{n}_0 + \mathbf{n}_0 \cdot \nabla S'_d + S'_d\nabla \cdot \mathbf{n'} + \mathbf{n'} \cdot \nabla S'_d. \tag{3.25}$$

As the case of a planar flame is considered here, there is no curvature of the static component, so that the third term is zero. The last term is also zero, as the product of the gradient of the fluctuating flame speed and the fluctuating flame surface normal is zero, reflecting the orthogonality between the flame surface propagation and the flame surface contour. One can then derive the following expression linking the different terms (where the last one can also be considered equal to zero assuming a balanced budget between fluctuations):

$$\nabla \cdot \mathbf{w'}_s = S_{d,0}\nabla \cdot \mathbf{n'} + \mathbf{n'} \cdot \nabla S_{d,0} + \mathbf{n}_0 \cdot \nabla S'_d + S'_d\nabla \cdot \mathbf{n'}. \tag{3.26}$$

To conclude this section, there are two modes of propagation of the flame at work. The first one is a global propagation mechanism which is sustained by the static component, and the second one is intrinsically linked to the dynamic component of the flowfield.

3.4 Expressions for the static component of stabilized flames

Static components of stabilized flame configurations are analyzed and derived in the present section. The starting point is Eq. (3.11), where the flame surface speed is zero, as the static flame component is fixed in the laboratory frame of reference. This is reflected by

$$\mathbf{v}_0 = -S_{d,0}\mathbf{n}_0. \tag{3.27}$$

From Eq. (3.10), one obtains the static normal vector components

$$\left.\begin{aligned} n_{x,0} &= -\frac{\partial G_0}{\partial x}\left[\left(\frac{\partial G_0}{\partial x}\right)^2+\left(\frac{\partial G_0}{\partial y}\right)^2+\left(\frac{\partial G_0}{\partial z}\right)^2\right]^{-1/2} \\ n_{y,0} &= -\frac{\partial G_0}{\partial y}\left[\left(\frac{\partial G_0}{\partial x}\right)^2+\left(\frac{\partial G_0}{\partial y}\right)^2+\left(\frac{\partial G_0}{\partial z}\right)^2\right]^{-1/2} \\ n_{z,0} &= -\frac{\partial G_0}{\partial z}\left[\left(\frac{\partial G_0}{\partial x}\right)^2+\left(\frac{\partial G_0}{\partial y}\right)^2+\left(\frac{\partial G_0}{\partial z}\right)^2\right]^{-1/2} \end{aligned}\right\}. \tag{3.28}$$

Making use of those vector components in Eq. (3.27), one has

$$\left.\begin{aligned} u_0 &= -S_{d,0}n_{x,0} = S_{d,0}\frac{\partial G_0}{\partial x}\alpha_0 \\ v_0 &= -S_{d,0}n_{y,0} = S_{d,0}\frac{\partial G_0}{\partial y}\alpha_0 \\ w_0 &= -S_{d,0}n_{z,0} = S_{d,0}\frac{\partial G_0}{\partial z}\alpha_0 \end{aligned}\right\}, \tag{3.29}$$

where α_0 is defined as

$$\alpha_0 = \left[\left(\frac{\partial G_0}{\partial x}\right)^2+\left(\frac{\partial G_0}{\partial y}\right)^2+\left(\frac{\partial G_0}{\partial z}\right)^2\right]^{-1/2}. \tag{3.30}$$

Combining equations two by two in equation system (3.29) leads to

$$\left.\begin{aligned} u_0\frac{\partial G_0}{\partial y} &= v_0\frac{\partial G_0}{\partial x} \\ v_0\frac{\partial G_0}{\partial z} &= w_0\frac{\partial G_0}{\partial y} \\ w_0\frac{\partial G_0}{\partial x} &= u_0\frac{\partial G_0}{\partial z} \end{aligned}\right\}. \tag{3.31}$$

It is now possible to explicitly link the flame speed and the flow speed components. This is achieved by making use of sys-

tems (3.29) and (3.31). One obtains

$$u_0 = S_{d,0}\frac{\partial G_0}{\partial x}\alpha_0 = S_{d,0}\frac{\partial G_0}{\partial x}\left[\left(\frac{\partial G_0}{\partial x}\right)^2 + \left(\frac{\partial G_0}{\partial y}\right)^2 + \left(\frac{\partial G_0}{\partial z}\right)^2\right]^{-1/2}, \tag{3.32}$$

which can be written as

$$u_0 = S_{d,0}\frac{\partial G_0}{\partial x}\left[\left(\frac{\partial G_0}{\partial x}\right)^2 + \left(\frac{v_0}{u_0}\right)^2\left(\frac{\partial G_0}{\partial x}\right)^2 + \left(\frac{w_0}{u_0}\right)^2\left(\frac{\partial G_0}{\partial x}\right)^2\right]^{-1/2}. \tag{3.33}$$

By factorizing the axial component of the gradient of G_0, one obtains

$$u_0 = S_{d,0}\frac{\partial G_0}{\partial x}\left[\left(\frac{\partial G_0}{\partial x}\right)^2\left(1 + \left(\frac{v_0}{u_0}\right)^2 + \left(\frac{w_0}{u_0}\right)^2\right)\right]^{-1/2}, \tag{3.34}$$

$$u_0 = S_{d,0}\frac{\partial G_0}{\partial x}\left(\frac{\partial G_0}{\partial x}\right)^{-1}\left[1 + \left(\frac{v_0}{u_0}\right)^2 + \left(\frac{w_0}{u_0}\right)^2\right]^{-1/2}. \tag{3.35}$$

The last expression becomes

$$u_0 = S_{d,0}\left[1 + \left(\frac{v_0}{u_0}\right)^2 + \left(\frac{w_0}{u_0}\right)^2\right]^{-1/2}. \tag{3.36}$$

The same operations lead to the following expressions for the other velocity vector components:

$$v_0 = S_{d,0}\left[1 + \left(\frac{u_0}{v_0}\right)^2 + \left(\frac{w_0}{v_0}\right)^2\right]^{-1/2} \tag{3.37}$$

and:

$$w_0 = S_{d,0}\left[1 + \left(\frac{u_0}{w_0}\right)^2 + \left(\frac{v_0}{w_0}\right)^2\right]^{-1/2}. \tag{3.38}$$

Any of these expressions leads to the following result for a configuration where the static flame surface speed is zero:

$$S_{d,0}^2 = u_0^2 + v_0^2 + w_0^2. \tag{3.39}$$

This expression states the balance between the static flame speed and the components of the static velocity vector. For example, for a 1D laminar or turbulent flame, one has $S_{d,0} = u_0$. For a 3D turbulent flame, this expression indicates that the local static flame speed is directly related to the three velocity components at the flame front, which is a key result for turbulent combustion. Indeed, flame speed is a well-defined known quantity for

unstretched and to some extent for stretched laminar flames, and this quantity holds for certain regimes of premixed combustion corresponding to low Karlovitz numbers, where the flame front is wrinkled by the upstream turbulence and propagates at that speed. Knowing the estimates of the flow speeds in a combustor and the laminar flame speed of characteristic fuel premixtures, see Chapters 1 and 2, it is possible to indicate that the previous expression implies two consequences. The first one is that the static flame component is fully determined by the components of the static velocity vector. As it is expected that the static flame speed is equal to the stretched laminar flame speed, this implies that the flame stabilizes in low velocity regions, regions satisfying Eq. (3.39). The second consequence is that for the case of turbulent flames, the previous expression can be seen as a surrogate of the turbulent flame speed S_T. This consequently rises another question regarding the local propagation of the flame surface. The mechanism of propagation will be discussed in the next section, similarly to the turbulent flame surface propagating into a medium at rest.

3.5 Expressions for the dynamic component of stabilized flames

3.5.1 Canonical form

The approach to derive the link between flow, flame, and flame surface speeds is equivalent to that of the previous section. Starting with Eq. (3.11), one obtains

$$\left.\begin{aligned} u &= w_s^x + S_d \frac{\partial G}{\partial x}\alpha \\ v &= w_s^y + S_d \frac{\partial G}{\partial y}\alpha \\ w &= w_s^z + S_d \frac{\partial G}{\partial z}\alpha \end{aligned}\right\}, \tag{3.40}$$

where α is defined as

$$\alpha = \left[\left(\frac{\partial G}{\partial x}\right)^2 + \left(\frac{\partial G}{\partial y}\right)^2 + \left(\frac{\partial G}{\partial z}\right)^2\right]^{-1/2}. \tag{3.41}$$

Similarly to the previous section, the calculations lead to the system

$$\left.\begin{aligned}(u-w_s^x)\frac{\partial G}{\partial y}&=(v-w_s^y)\frac{\partial G}{\partial x}\\(v-w_s^y)\frac{\partial G}{\partial z}&=(w-w_s^z)\frac{\partial G}{\partial y}\\(w-w_s^z)\frac{\partial G}{\partial x}&=(u-w_s^x)\frac{\partial G}{\partial z}\end{aligned}\right\}. \tag{3.42}$$

Combining systems (3.40) and (3.42), the following system is determined:

$$\left.\begin{aligned}u&=w_s^x+S_d\left[1+\left(\frac{v-w_s^y}{u-w_s^x}\right)^2+\left(\frac{w-w_s^z}{u-w_s^x}\right)^2\right]^{-1/2}\\v&=w_s^y+S_d\left[1+\left(\frac{u-w_s^x}{v-w_s^y}\right)^2+\left(\frac{w-w_s^z}{v-w_s^y}\right)^2\right]^{-1/2}\\w&=w_s^z+S_d\left[1+\left(\frac{u-w_s^x}{w-w_s^z}\right)^2+\left(\frac{v-w_s^y}{w-w_s^z}\right)^2\right]^{-1/2}\end{aligned}\right\}. \tag{3.43}$$

These expressions can also be written as

$$\left.\begin{aligned}\frac{u-w_s^x}{S_d}&=\left[1+\left(\frac{v-w_s^y}{u-w_s^x}\right)^2+\left(\frac{w-w_s^z}{u-w_s^x}\right)^2\right]^{-1/2}\\\frac{v-w_s^y}{S_d}&=\left[1+\left(\frac{u-w_s^x}{v-w_s^y}\right)^2+\left(\frac{w-w_s^z}{v-w_s^y}\right)^2\right]^{-1/2}\\\frac{w-w_s^z}{S_d}&=\left[1+\left(\frac{u-w_s^x}{w-w_s^z}\right)^2+\left(\frac{v-w_s^y}{w-w_s^z}\right)^2\right]^{-1/2}\end{aligned}\right\}. \tag{3.44}$$

The first equation of (3.44) can be recast after introducing the decomposition in the static and dynamic components as

$$\begin{aligned}S_{d,0}+S_d'=\Big[&(u_0+u'-w_{s,0}^x-w_s'^x)^2+(v_0+v'-w_{s,0}^y-w_s'^y)^2\\&+(w_0+w'-w_{s,0}^z-w_s'^z)^2\Big]^{1/2}.\end{aligned} \tag{3.45}$$

This expression links the flame surface, flow, and flame displacement static and dynamic speeds. This is a general expression. When considering only static components, this expression is equal to Eq. (3.39). This expression states that both the static and dynamic components of the flame speed, flame displacement speed, and flow velocities are balanced.

3.5.2 Expression for turbulent stabilized flames

By taking the second power of Eq. (3.45) and identifying terms on the left- and right-hand sides by the order of fluctuations, one obtains

$$\left.\begin{aligned} S_{d,0}^2 &= u_0^2 + v_0^2 + w_0^2 && (a)\\ S'_d S_{d,0} &= u_0(u' - w'^x_s) + v_0(v' - w'^y_s) + w_0(w' - w'^z_s) && (b)\\ S'^2_d &= (u' - w'^x_s)^2 + (v' - w'^y_s)^2 + (w' - w'^z_s)^2 && (c) \end{aligned}\right\}. \tag{3.46}$$

The first equation of (3.46) has been discussed in the previous section. The second equation couples the static and dynamic flow, flame, and flame surface speed components and could be responsible for transition phenomena from laminar to turbulent combustion or transition to blowout and flashback, as coupling between static and dynamic component occurs. The last expression only regards the dynamic components and shows that for a stabilized flame, the propagation of the flame surface is solely due to turbulence and local dynamic flame speed. The impacts of those results are that (i) the flame stabilizes where the static components of flow and flame speeds satisfy the first condition, (ii) at that location the flame stabilizes (the dynamic flame surface component is zero) in the turbulent flow at the local dynamic flame speed close to the laminar flame speed, as the only physical values that can be taken by the fluctuating local dynamic flame speed are of the order of the laminar flame speed, and (iii) at that location the flame surface propagates through turbulence fluctuations. The turbulent flame propagates (the flame surface changes position and wrinkles) through the flowfield fluctuation mechanisms with the turbulent fluctuations below or above the laminar flame speed S_L. These fluctuations change the flame position around the static component. In other words, the propagation will proceed if the turbulent or harmonic fluctuations are above or below S_L. This can further lead to flashback or blowout triggering for very low or high values of the turbulent fluctuation. Amplitudes and frequencies of the fluctuations are then central to the flame stabilization process. Indeed, while the flame propagates for values of the turbulent fluctuations below or above the laminar flame speed order of magnitude, the stabilization is consequently ensured for alternating periodic positive and negative turbulent/acoustic fluctuations around the static field.

3.5.3 Expression for modulated stabilized flames

In this section, the dynamic component (the fluctuation field) is made up of a harmonic modulation and turbulent fluctuations. We consider the specific case of Eq. (3.45) when the static component of the flame surface speed is zero so that Eq. (3.39) is satisfied. This leads, after expanding the squared terms and neglecting the products of fluctuations, to

$$\frac{S'_d}{S_{d,0}} = \frac{u' - w'^x_s}{u_0}\left(\frac{u_0}{S_{d,0}}\right)^2 + \frac{v' - w'^y_s}{v_0}\left(\frac{v_0}{S_{d,0}}\right)^2 + \frac{w' - w'^x_s}{w_0}\left(\frac{w_0}{S_{d,0}}\right)^2. \tag{3.47}$$

This last equation can be reformulated in cylindrical coordinates. The starting points are the expressions of the components of velocities v and w in cylindrical coordinates. This is carried out with

$$\left.\begin{aligned} v\,\mathbf{e}_y &= u_r \sin\theta\,\mathbf{e}_r + u_\theta \cos\theta\,\mathbf{e}_\theta \\ w\,\mathbf{e}_z &= u_r \cos\theta\,\mathbf{e}_r - u_\theta \sin\theta\,\mathbf{e}_\theta \end{aligned}\right\}. \tag{3.48}$$

These last relationships can be expressed with their static and dynamic components. For the w term, one obtains by assuming small angle fluctuations

$$(w_0 + w')^2 = \left[(u_{r,0} + u'_r)\cos(\theta_0) - (u_{\theta,0} + u'_\theta)\sin(\theta_0)\right]^2, \tag{3.49}$$

which leads, by neglecting the second-order term, to

$$w_0^2 + 2w_0 w' = \left[(u_{r,0} + u'_r)\cos\theta_0\right]^2 + \left[(u_{\theta,0} + u'_\theta)\sin\theta_0\right]^2. \tag{3.50}$$

The identification of the components by order of fluctuations leads to

$$\left.\begin{aligned} w_0^2 &= u_{r,0}^2 \cos{\theta_0}^2 + u_{\theta,0}^2 \sin{\theta_0}^2 \\ 2w_0 w' &= 2u_{r,0}u'_r \cos{\theta_0}^2 + 2u_{\theta,0}u'_\theta \sin{\theta_0}^2 \end{aligned}\right\}. \tag{3.51}$$

The ratio of these two last quantities and a similar calculation for the term v give the following expressions, relating velocities in Cartesian and cylindrical coordinates:

$$\left.\begin{aligned} \frac{v'}{v_0} &= \frac{u'_r \sin^2\theta_0 u_{r,0} + u'_\theta \cos^2\theta_0 u_{\theta,0}}{u_{r,0}^2 \sin^2\theta_0 + u_{\theta,0}^2 \cos^2\theta_0} \\ \frac{w'}{w_0} &= \frac{u'_r \cos^2\theta_0 u_{r,0} + u'_\theta \sin^2\theta_0 u_{\theta,0}}{u_{r,0}^2 \cos^2\theta_0 + u_{\theta,0}^2 \sin^2\theta_0} \end{aligned}\right\}. \tag{3.52}$$

The expressions of the fluctuation ratios are now evaluated at $\theta = 0$ to simplify the calculations. This leads to the following ratios: $v'/v_0 = u'_\theta/u_{\theta,0}$ and $w'/w_0 = u'_r/u_{r,0}$. Similar expressions can be obtained under the same assumptions for the flame surface speed. Substituting those expression into Eq. (3.47) leads to

$$\frac{S'_d}{S_{d,0}} = \frac{u' - w'^x_s}{u_0}\left(\frac{u_0}{S_{d,0}}\right)^2 + \frac{u'_\theta - w'^\theta_s}{u_{\theta,0}}\left(\frac{u_{\theta,0}}{S_{d,0}}\right)^2 + \frac{u'_r - w'^r_s}{u_{r,0}}\left(\frac{u_{r,0}}{S_{d,0}}\right)^2. \tag{3.53}$$

Next, the equation is developed so that one obtains

$$\frac{S'_d}{S_{d,0}} = \left[\frac{u_0^2}{S_{d,0}^2} - \frac{w'^x_s}{u_0}\frac{u_0}{u'_x}\right]\frac{u'}{u_0} + \left[\frac{u_{\theta,0}^2}{S_{d,0}^2} - \frac{w'^\theta_s}{u_{\theta,0}}\frac{u_{\theta,0}}{u'_\theta}\right]\frac{u'_\theta}{u_{\theta,0}} + \left[\frac{u_{r,0}^2}{S_{d,0}^2} - \frac{w'^r_s}{u_{r,0}}\frac{u_{r,0}}{u'_r}\right]\frac{u'_r}{u_{r,0}}. \tag{3.54}$$

It is then possible to show that the ratios $u'_r/u_{r,0}$ and $u'_\theta/u_{\theta,0}$ are equivalent if dominated by the harmonic modulation. Indeed, expressions for the azimuthal and radial fluctuating amplitudes and their wavevectors can be obtained. The starting point is the linearized Euler momentum equations in cylindrical coordinates along the radial and azimuthal directions with the axisymmetric assumption for the flow. These equations are the governing equations that can describe the nonreacting flow downstream of a swirler in linear regimes. The fluctuating quantities are assumed to depend only on the longitudinal direction z. These equations are

$$\bar{\rho}\frac{\partial u'_r}{\partial t} - \frac{\bar{\rho}\bar{u}_\theta^2}{r} - \frac{\rho'\bar{u}_\theta^2}{r} - \frac{2\bar{\rho}\bar{u}_\theta u'_\theta}{r} + \bar{\rho}\bar{u}_z\frac{\partial u'_r}{\partial z} = 0, \tag{3.55}$$

$$\bar{\rho}\frac{\partial u'_\theta}{\partial t} + \frac{\bar{\rho}\bar{u}_r\bar{u}_\theta}{r} + \frac{\rho'\bar{u}_r\bar{u}_\theta}{r} + \frac{\bar{\rho}\bar{u}_r u'_\theta}{r} + \frac{\bar{\rho}u'_r\bar{u}_\theta}{r} + \bar{\rho}\bar{u}_z\frac{\partial u'_\theta}{\partial z} = 0. \tag{3.56}$$

The fluctuating density has an upstream and a downstream propagating component:

$$\rho' = \left(\hat{\rho}^+ \exp\left(ik_\rho^+ z\right) + \hat{\rho}^- \exp\left(-ik_\rho^- z\right)\right)\exp\left(-i2\pi f t\right). \tag{3.57}$$

To reflect the convective nature (downstream propagation) of the fluctuating velocities u'_r and u'_θ along the axial direction, the following canonical forms are used:

$$u'_r = \hat{u}'_r \exp\left(ik_{u_r} z\right)\exp(-i2\pi f t), \tag{3.58}$$

$$u'_\theta = \hat{u}'_\theta \exp(ik_{u_\theta} z) \exp(-i2\pi f t). \tag{3.59}$$

Injecting Eqs. (3.57)–(3.59) into Eqs. (3.55) and (3.56) leads to two equations which are functions of the fluctuating quantities $\hat{u}'_r$ and $\hat{u}'_\theta$ and their respective wavevectors k_{u_r} and k_{u_θ}. Coupling the two obtained equations leads to

$$\begin{aligned}\hat{u}'_r\left[-\bar{\rho}i2\pi f + \bar{\rho}\bar{u}_z ik_{u_r} + \frac{\bar{\rho}\bar{u}_\theta^2}{r\bar{u}_r}\right]\exp(ik_{u_r} z) \\ + \hat{u}'_\theta\left[\frac{-2\bar{\rho}\bar{u}_\theta}{r} - \frac{\bar{\rho}i2\pi f\bar{u}_\theta}{\bar{u}_r} + \frac{\bar{\rho}\bar{u}_\theta}{r} + ik_{u_\theta}\frac{\bar{\rho}\bar{u}_z\bar{u}_\theta}{\bar{u}_r}\right]\exp(ik_\theta z) = 0.\end{aligned} \tag{3.60}$$

The next step consists in expressing the real and imaginary parts of Eq. (3.60) and expressing them for $z = 0$, which corresponds to the swirler outlet. For the real part this leads to

$$\hat{u}'_r\left[\frac{\bar{\rho}\bar{u}_\theta^2}{r\bar{u}_r}\right] + \hat{u}'_\theta\left[\frac{-2\bar{\rho}\bar{u}_\theta}{r} + \frac{\bar{\rho}\bar{u}_\theta}{r}\right] = 0, \tag{3.61}$$

and for the imaginary part this leads to

$$\hat{u}'_r\left[-\bar{\rho}2\pi f + \bar{\rho}\bar{u}_z k_{u_r}\right] + \hat{u}'_\theta\left[\frac{-\bar{\rho}2\pi f\bar{u}_\theta}{\bar{u}_r} + \frac{k_{u_\theta}\bar{\rho}\bar{u}_z\bar{u}_\theta}{\bar{u}_r}\right] = 0. \tag{3.62}$$

As a consequence, the ratio of radial and azimuthal convective wave amplitudes is obtained:

$$\frac{\hat{u}'_r}{\hat{u}'_\theta} = \frac{\bar{u}_r}{\bar{u}_\theta}. \tag{3.63}$$

Making use of $k_{u_r} = 2\pi f/v_r$ and noting the convective velocity of the radial fluctuations v_r, the azimuthal component of the wavevector is

$$k_{u_\theta} = \frac{2\pi f}{\bar{u}_z} \times \left[1 + \left(\frac{\bar{u}_r}{\bar{u}_\theta}\right)^2 \times \left(1 - \frac{\bar{u}_z}{v_r}\right)\right]. \tag{3.64}$$

It has been shown in previous work, see Palies et al. [134], that the azimuthal fluctuations propagate at the convective axial velocity of the flow, implying that the term in brackets of Eq. (3.64) is unity. It implies that $v_r = \bar{u}_z$. This demonstrates that the radial fluctuations also propagate at the axial velocity of the flow. To conclude this analytical development, the wavevector and amplitude calculation leads to the equality $u'_r/u_{r,0} = u'_\theta/u_{\theta,0}$. Taking into account

that equality and rearranging the terms of Eq. (3.54), the following expression is determined:

$$\frac{S'_d}{S_{d,0}} = \zeta_e \frac{u'}{u_0} + \chi_e \frac{u'_\theta}{u_{\theta,0}}, \tag{3.65}$$

where

$$\zeta_e = \left[\frac{u_0^2}{S_{d,0}^2} \left(1 - \frac{w'^x_s}{u'} \right) \right] \tag{3.66}$$

and

$$\chi_e = \left[\frac{u_{\theta,0}^2}{S_{d,0}^2} \left(1 - \frac{w'^\theta_s}{u'_\theta} \right) + \frac{u_{r,0}^2}{S_{d,0}^2} \left(1 - \frac{w'^s_r}{u'_r} \right) \right]. \tag{3.67}$$

In Eq. (3.65), one can see that the expression is similar to that of Palies et al. [252], except that terms here are evaluated at the flame front, whereas in Palies et al. [252] the flow velocity ratios were expressed upstream of the flame front. To retrieve that expression, a phase shift should be included into Eq. (3.65). This result confirms that the burning flame speed is a function of the axial and azimuthal components and leads to an exact expression for the previously reported result. The ratios of flame surface speed to velocity fluctuation along each direction in the last equation are expected to be of the order of unity, because the flow speed will dominate the overall budget between the flow, the flame, and the flame surface speeds.

3.5.4 Mathematical-physical description

In this section, the previous results are described with a geometrical representation and further discussed. By recognizing that Eqs. (3.45) and (3.46) are equations of spheres, one can propose the graphic given in Fig. 3.16. The three axes of this graphic represent the velocity components u, v, and w. The first sphere is centered on $(w_{s,0}^x = 0, w_{s,0}^y = 0, w_{s,0}^z = 0)$ and its radius is equal to $S_{d,0}$, which is equivalent to $\mathbf{v}_0$ according to Eq. (3.46)(a). This sphere illustrates static stability. Indeed, on the surface of this sphere, each velocity satisfies Eq. (3.46)(a) so that the flame surface static speed component is zero, which corresponds to a stabilized flame in the laboratory frame of reference. The second sphere is centered on a velocity point (u_0, v_0, w_0) of the first sphere surface. It illustrates the propagation of the flame front. This velocity point is defined by its position (w'^x_s, w'^y_s, w'^z_s) in the second sphere frame of reference. The radius of the second sphere is equal to the fluctuation of flame speed S'_d. This indicates that propagation of the flame front

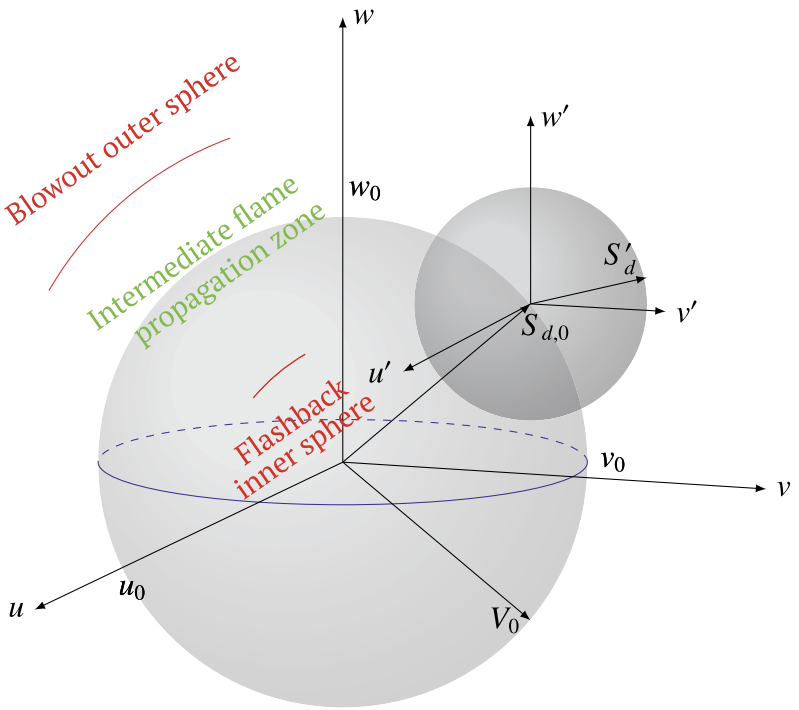

Figure 3.16 Illustration of flame propagation. Mathematical-physical geometrical representation of Eq. (3.46)(a) and (c).

occurs when the turbulent fluctuation is of the order of the laminar flame speed. In addition, when the turbulent fluctuation is above or below the laminar flame speed, the position of the flame surface will change because $(w'^{x}_{s}, w'^{y}_{s}, w'^{z}_{s})$ will not be zeros. The turbulent fluctuation scale on the schematic is for illustration purposes only (radius of the second sphere).

This graphic allows the determination of three distinct zones which are now described.

- Propagation zone
  This zone is the domain where turbulence is the driver of the propagation. It is centered on the static component (surface of the first sphere) and extends through the turbulent fluctuation radius of the second sphere. This zone is located between the flashback and blowout zones and it will be important for the transition to blowout or flashback.
- Flashback zone
  The flashback zone corresponds to an inner sphere where the flow velocity is lower than the static flame speed or to high am-

plitude low or high frequency turbulent or acoustic fluctuation events lower than the fluctuation of flame speed.

- Blowout zone
  The blowout zone corresponds to an outer sphere where the flow velocity is larger than the static flame speed or to high amplitude low or high frequency turbulent or acoustic fluctuation events higher than the fluctuation of flame speed.

3.6 Swirling flame numerical simulations: results and discussion

The modeling methodology has been presented in Section 2.1 of this chapter. In this section, the results of the numerical simulations are presented and discussed, in a similar fashion as previously, considering now 2D fields instead. The variables investigated are the magnitude of the velocity vector, its fluctuation, and the flame isosurface defined at 1420 K as being the premixed reaction zone peak location. The flame isosurface defined by this value includes regions without reaction, typically occurring in the ORZ/injector backplane zone and above the injector central cone. The choice is made to exclude those regions in the analysis by applying a criterion on the y and z coordinates above 0.0051 m and 0.051 m, respectively. Firstly, the time average, the estimate of the static component, and the fluctuating fields are plotted in Fig. 3.17 (left column). Secondly, the distributions of time average, static component, and fluctuation velocities on the flame surface are plotted in Fig. 3.17 (right column). Finally, these velocities are further documented with their levels as a function of a distance along the flame in Fig. 3.18.

One can see in Fig. 3.17 (top left and center left) that the time average and the static component are slightly different. The estimate of the static component was obtained by subtracting the fluctuating field from the square of the time average magnitude, $v_0^2 = \overline{v^2} - \overline{v'^2}$, as discussed earlier. The results indicate that the static flame component extends slightly further than the time average and is overall similar for this statistically steady flame. The associated velocity distributions computed on the flame isosurface are reported in the right figures along with vertical lines at the distribution mean values. One observes that the distributions are different mostly at near-zero speeds. While it is expected that a low velocity region dominates the static component, the estimation procedure of this static component amplifies this effect. The distributions show otherwise similar shapes with strong decreases in levels as the velocity is increased beyond the central peak, which is reflected in the median and mean values listed in

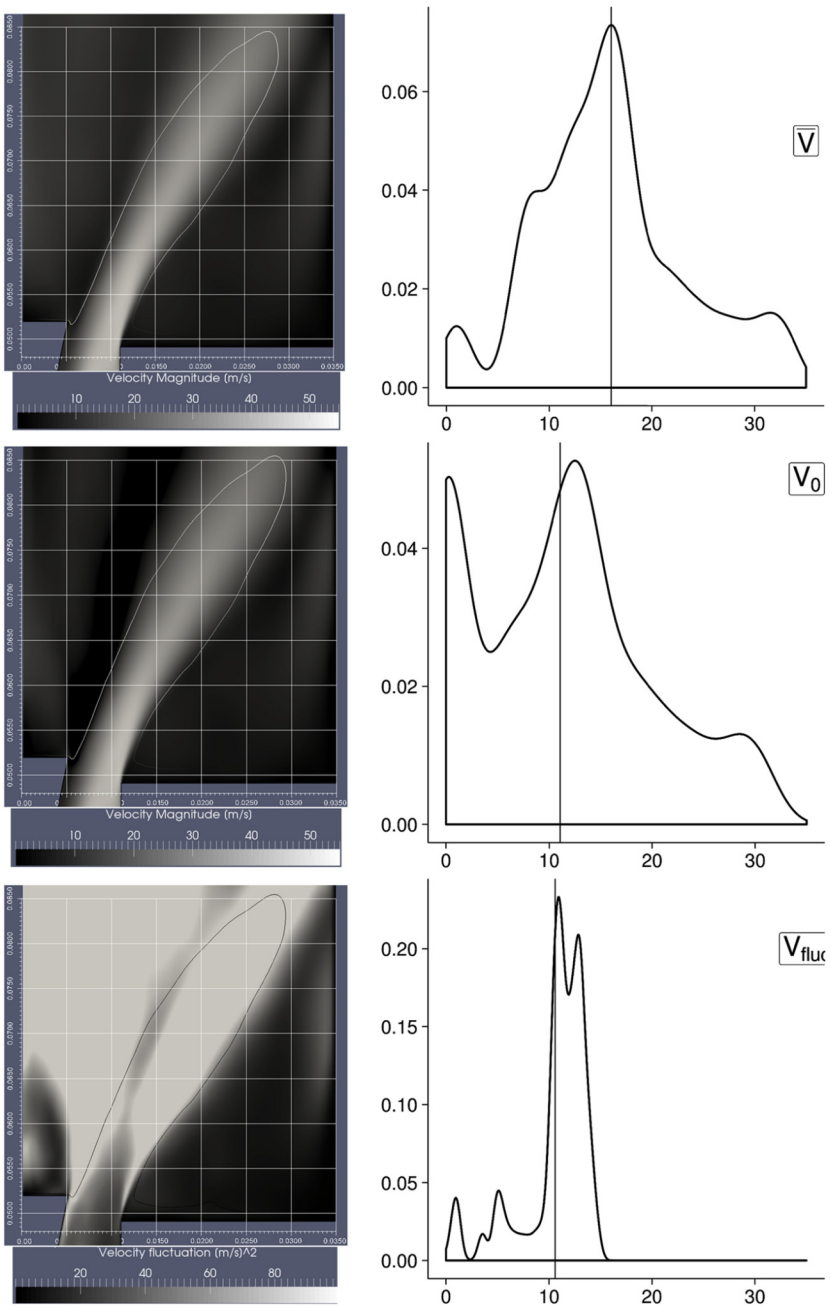

Figure 3.17 Comparison of the time average and the static component. Time average, estimate of static mode, and fluctuating fields, along with the time average distributions and static mode and fluctuation velocities on the flame surface, on top, center, and bottom rows, respectively. The flame surface is colored by velocity fluctuation level in top and center rows and by a solid curve in the bottom row.

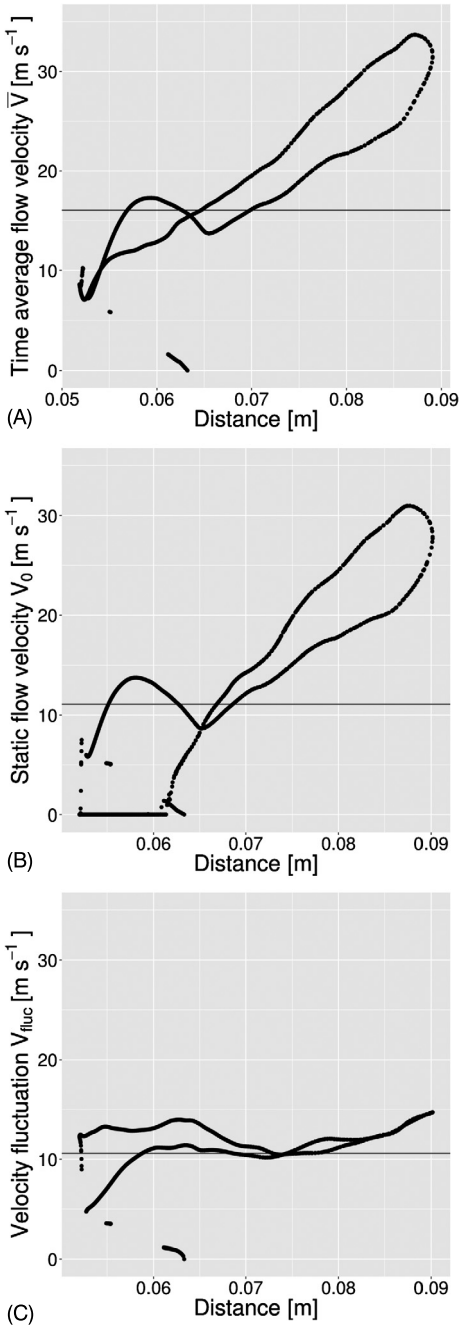

Figure 3.18 Evolution of variables on the flame front. Maps of flow velocities, (A) time average, (B) static mode, and (C) fluctuation, versus the distance from the geometry center to a flame element on the flame isosurface.

Table 3.5 Distribution averages over the flame isosurface.

Value	Mean	Median
Time average $\overline{v}$	16.73	14.61
Static mode v_0	11.08	11.35
Fluctuation $\sqrt{\overline{v'^2}}$	10.61	11.30

Tab. 3.5. Both have a strong peak near 15 m s^{-1}, which appears to be the preferred value where the static flame is located. The time average and the static component of flame isosurfaces are located on both sides of the swirling jet. The fluctuating field $\overline{v'^2}$ plotted in Fig. 3.17 shows that the highest fluctuation levels are situated on the swirling jet and inside the IRZ. Contrarily, the shear layer zones located at the interfaces of the IRZ/ORZ and swirling jet have weaker fluctuation levels. The corresponding distribution is plotted in the right of Fig. 3.17. One can see a central peak (made up of two distinct low amplitude peaks) in the distribution of velocity fluctuations $\sqrt{\overline{v'^2}}$. The vertical line corresponds to the mean value of the fluctuation distributions.

Fig. 3.18 present the levels of flow velocities, for (A) the time average, (B) the static component, and (C) fluctuation, versus the distance from the geometry center to a flame element on the flame isosurface. In addition, mean values of the velocity distributions are superimposed as gray horizontal lines. The ensemble of the present results allows to determine the preferred mechanism of propagation for the present swirling flame with respect to the previously introduced theoretical analysis. This is now carried out.

Theoretical elements presented in precedent sections led to the equation system (3.46) for turbulent flames, which has been discussed. While the flame speed was not determined for the static and time-average fields, and thus no validation of this previous system of equations can be achieved as of now, the theoretical results are used to investigate the flame stabilization mechanisms. The system of equations has been illustrated graphically in Fig. 3.16. On these graphics, the flame speed and the subsequent flame stabilization are shown to be due to two contributors: the static and dynamic components. The static component median value is 11.35 m s^{-1}. Lower values indicate a regime where the flame speed S_d would be in the range of stretched laminar flame speed and higher values correspond to turbulent flame speeds. The dynamic component can be analyzed with the graphic of dis-

tribution given in the left-hand side of Fig. 3.17. One observes that the distribution has a central peak, as mentioned earlier. This peak mostly occurs for fluctuating values near the static or time average mean value. In other words, this central peak bounds the flame stabilization dynamics and limits the flame surface evolution/displacement by the alternating positive and negative turbulent/acoustic fluctuations around the static mode as defined by Eq. (3.46)(c).

It is now interesting to determine where each flame stabilization mechanism (static or dynamic) is dominant. To do so, the graphics in Figs. 3.17 and 3.18 are analyzed. In Fig. 3.18A, the time-average flow velocity plotted as a function of the distance from the center of the system shows the evolution of the two flame branches (respectively the inner flame branch at the interface of the IRZ/inner axial/radial shear layers and the outer flame branch at the interface with the ORZ/ outer axial/radial shear layers). The horizontal line represents the time average mean value. In Fig. 3.17, the static mode is represented. In those two figures, one observes clearly that the lowest velocities are reached for the lowest radius values. This indicates that the near-injector flame stabilization dynamics are dominated by the low values of the flame speed, where Eq. (3.46)(a) is important. At higher radius, the flame is dominated by higher velocities. In Fig. 3.18C, the level of velocity fluctuation evolves closely around the mean fluctuation value. At the near-injector location, the inner flame branch is dominated by higher fluctuation levels than the outer flame branch. These two branches evolve on the two low amplitude peaks of the central peak identified in the distribution graphic. The combination of theoretical and numerical simulation results demonstrates that the flame is made up of two main regions where the stabilization is different. In the near-injector region, the flame is stabilized by a competing mechanism where both static mean flow and the dynamic component (due to turbulence and acoustics) are important, while the remaining locations of the flame are stabilized by the dynamic component only.

3.7 Summary

In this section, mathematical expressions linking the flame, flow, and flame surface speeds were derived based on a decomposition of the flowfield into a static and a dynamic component. By using this decomposition into a static and a dynamic component, a general expression for the flame, flow, and flame surface speeds was obtained and applied in specific configurations. A set of expressions was determined for those different configurations. Lam-

inar and turbulent cases including the configuration of a modulated turbulent premixed swirling flame were investigated. Some of the obtained expressions can be written as equations of spheres in a velocity space, leading to a mathematical-physical description of those expressions and their subsequent discussion. Those theoretical expressions provide perspectives for premixed turbulent combustion, as it is shown from the present analysis that the propagation of the turbulent flame is due to either the static flow speed or the turbulent velocity fluctuation. Numerical simulations of quasi-DNS resolutions are carried out to investigate the swirling flame stabilization mechanisms. It is concluded that in the near-injector region, the flame is stabilized by a competing mechanism where both static mean flow and the dynamic component (due to turbulence and acoustics) are important, while the remaining locations of the flame are stabilized by the dynamic component only. In addition, the present results provide a route towards the understanding of flashback and blowout phenomena where velocity fluctuation due to for example turbulence or acoustics low or high frequency high amplitude events could cause the propagation zone to shift towards either the flashback or the blowout zones.

4 Effects of operating conditions, swirl number, and fuel on flame stabilization

The effects of the operating conditions on swirling flame stabilization have been addressed by many research works, which are now reviewed. The operating conditions include the Reynolds number, the equivalence ratio, the operating pressure, and the inlet temperature of the fresh gases. Flame stabilization of perfectly premixed flames has been pioneered by a few experimental studies. For low swirling flames, a fully premixed flame was stabilized by Cheng [120] and patented. The stabilization was guided by the idea that the turbulent flame speed must balance the flow speed. For higher swirl number flow, devices enabling the region of low flow velocity were developed with axial swirler by Palies et al. [253] and radial swirlers by Palies et al. [101], ensuring a balance with the local flame displacement speed. Nonperfectly premixed flames were widely studied for other configurations prior to and after these studies. The article of Janus et al. [254] undertook a study on the stabilization of swirl flames in the Preccinsta combustor with fuel injected in the injector center, for different operating points with varying combustor pressure between 2 and 6 bar at constant inflow bulk velocities. The authors measured

velocity with LDV and characterized the flame shapes with OH-PLIF measurements. The study by Schefer et al. [255] focused on a premixed, swirl-stabilized flame operating with CH_4 with the addition of H_2 at fuel-lean conditions. The swirl vanes were at an angle of 45 degrees. It was experimentally measured that hydrogen addition resulted in a significant change of the flame structure. Flame stability was examined for the effects of amount of hydrogen addition, combustion air flow rates, and swirl strengths (with different swirlers) by Kim et al. [256]. The reported results showed that the lean stability limit was extended by hydrogen addition. The stability limit was reduced at higher swirl intensity for the fuel–air mixture operating at low adiabatic flame temperatures. Hydrogen addition was shown to increase NO_x emissions for that geometry and operating condition. This effect was damped by increasing either the excess air or the swirl intensity. NO_x and CO emissions were compared between premixed flames and diffusion flames under the same operating conditions, and were shown to be reduced in the case of premixed flames. The effects of the fuel composition (CH_4–H_2–air mixture), swirler blade angle and heat loss, and Reynolds number were documented by Taamallah et al. [257]. With the same experimental setup, Shanbhogue et al. [258] investigated the flame shape taken by the flame at various CH_4–H_2–air equivalence ratios at atmospheric pressure and temperature, constant Reynolds number of 20 000, and fixed swirler angle. The influence of the numerical boundary condition at the backplane wall of combustors on swirling flame stabilization has been studied by Chong et al. [259], where the authors observed two different flames, “M” or “V” shapes, depending on the boundary conditions, i.e., adiabatic or isothermal. A similar observation was made by Benard et al. [260]. Future works should include the determination of the thermal and momentum boundary layer thicknesses and their resolutions in the injection system because of the importance on capturing the local flow–flame–wall interactions such as for flame stabilization and flashback. In Kim and Hochgreb [261], time-averaged and phase-synchronized CH chemiluminescence signals were obtained experimentally, and it was demonstrated that the stabilization mechanism was a function of the equivalence ratio gradients for a constant inlet global equivalence ratio. For fully premixed regimes, an M-shaped flame was observed, and under stratified conditions, a V flame and a toroidal detached flame developed in the outer stream and inner stream fuel enrichment cases, respectively. The article of Nogenmyr et al. [262] focused on the use of LES to study the influence of the adiabatic wall boundary condition on the flame shape. In Guiberti et al. [263], the authors investigated the stabi-

lization mechanisms that modify the flame shape for hydrogen-enriched swirling flames. The effects of wall boundary conditions on swirling flame stabilization have been investigated by Guiberti et al. [264] along with the effects of adding hydrogen to the incoming premixture. It was shown that the flame changed shape according to the hydrogen concentration in the mixture. When that concentration increased, the probability of stabilizing an "M" flame shape over a "V" flame shape was increased. Additionally, during thermal transient and at steady state, it was shown that the combustor wall temperature played a role in the flame shape transition through the effect of the temperature of the burned gases in the ORZ. This study confirmed that the shape of swirling flames is sensitive to heat transfer to the combustion chamber walls because the subsequent local flowfield is modified and the flame stabilization budget impacted. The article of Kim et al. [265] focused on the effects of swirl level and hydrogen addition on the overall time-average flame shape, heat release intensity, temperature, and species concentrations. In Burguburu et al. [266], the authors also investigated the effects of hydrogen addition to kerosene on flame stability with the objective to investigate the effects of such addition at constant power for its application to aircraft engines. The article of Malanoski et al. [267] described an experimental investigation of flow forcing effects on the dynamics of the leading edge of a swirl-stabilized flame. Flame and flow dynamics were characterized using high speed PIV and CH^* chemiluminescence imaging. It was shown that the strong motion of the flame leading edge impacted little the spatially integrated, forced response of the flame, which was dominated by vortical motion. In Foley et al. [249], many challenges were raised regarding stabilization of swirling flames where burning occurs on the swirling jets and shear layers. To start solving those, a wide range of parameters were varied, including equivalence ratio, bulkhead temperature, flow velocity, and preheat temperature. The effects of flame stabilization on axial forcing were also investigated by Iudiciani and Duwig [268], where the authors showed with LES and proper orthogonal decomposition on the results that globally, forcing at frequencies lower than the PVC characteristic frequency displaced the recirculation zone upstream of the combustor in the premixing tube, while higher frequencies did not significantly impact the flow or the flame. The article of Williams et al. [36] documented the behavior of a swirling flame at multiple equivalence ratios and inlet bulk velocities and mapped the regimes including blowout, stable and thermoacoustically coupled regimes. The effects of local plasma discharges on flame stabilization (both for static and dynamic stability) have been studied by Lacoste et al. [269] in a

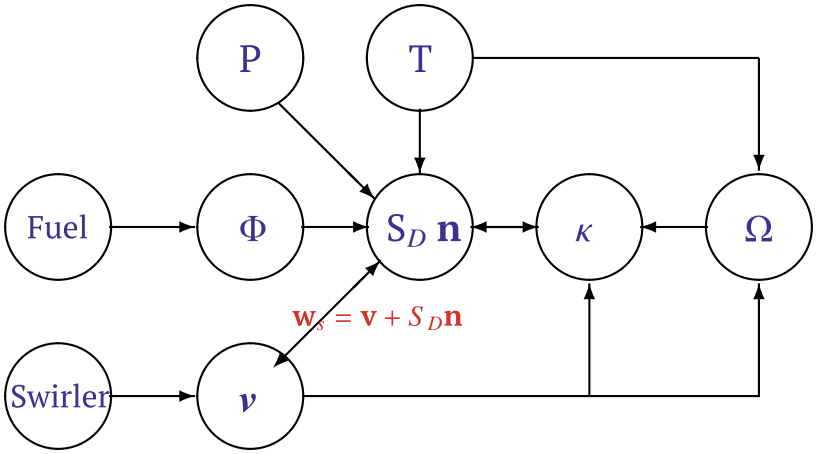

Figure 3.19 Schematic illustrating the influence of parameters on the flame displacement speed. This schematic also indicates the subsequent effects on the flame surface, flow, and flame speed budgets.

configuration similar to the MICCA-EM2C-Palies case and by Barbosa et al. [270] for a range of parameters.

Fig. 3.19 shows the influence of parameters on the flame displacement speed and the subsequent effects on the flame surface, flow, and flame speed budgets. The operating pressure P and inlet temperature T of premixed flames directly affect the flame speed S_D. For various fuels, the increase of pressure reduces the flame speed, while the increase of inlet temperature increases the flame speed. In addition to these effects, the selected fuel and its mixture equivalence ratio Φ have a key effect on the flame speed, where the flame speed reaches a peak slightly above the stoichiometry value and reduces as the equivalence ratio reduces or increases. The other quantities influencing the flame displacement speed are the flame stretch κ, which includes the flow strain, the flow divergence, and the flame curvature. The flame stretch of premixed flames includes 15 different terms. The vorticity vector Ω components also impact the local flame speed through the flame stretch. The velocity vector $\mathbf{v}$ drives the flow strain and the vorticity and subsequently impacts the flame speed. It is also a major component of the flame surface speed budget driving the flame location in the combustion chamber. The velocity field is driven to a large extent by the injector and the combustor geometries, including the swirler, and also by the low and high viscosity regions.

4

Transient combustion

1 Introduction

1.1 Definitions

Transient combustion includes a wide range of phenomena and processes and it is worthwhile to define what it refers to. There are three types of transient combustion, which have in common that they are all time-dependent. Fig. 4.1 presents typical signals for these three definitions. The first group includes generally unsteady combustion and consequently effects from acoustics, turbulence, and vorticity. It also includes transition processes such as transition from laminar to turbulent combustion regimes. The second group of transients includes the engine transients: acceleration during take-off (TO), deceleration during the landing phase, engine starting/ignition, and altitude reignition. The third group of transients is that of static and dynamic stability. It includes lean blowout (LBO), flashback, and combustion instabilities. While the previous description follows a technological and physical point of view, another characterization can be carried out taking into account the description of the time-dependent signals at stake. Transients can be indeed described in terms of transient growth/decay, or transients toward a steady state or between multiple steady states. The former is typical of the transition toward a combustion instability where the frequency of the signal has both a real and an imaginary part. This is for example the case when the thermal boundary conditions of walls are changed as a function of time. All these three groups of transients are directly linked to the engine power settings. Consequently, any transient has to take into account the given operating conditions considered.

In the context of transient combustion, it is worthwhile as well to review the various definitions of nonlinearities in reactive fluid dynamics. One may usually refer to the nonlinearity of the flow, of the flame, and of the signals. Nonlinearity of the flow is defined by the convective term of the Navier–Stokes equations, and is due to the term $\mathbf{v} \cdot \nabla \mathbf{v}$. Nonlinearity can also refer to the level of the perturbed field assumed to be small such as in acoustics and thus in the linear regime. The nonlinearity of the flame in the context of the flame response to flow modulation is defined by the fact that the flame transfer function (FTF) or the flame describing function

Stabilization and Dynamic of Premixed Swirling Flames
https://doi.org/10.1016/B978-0-12-819996-1.00012-3

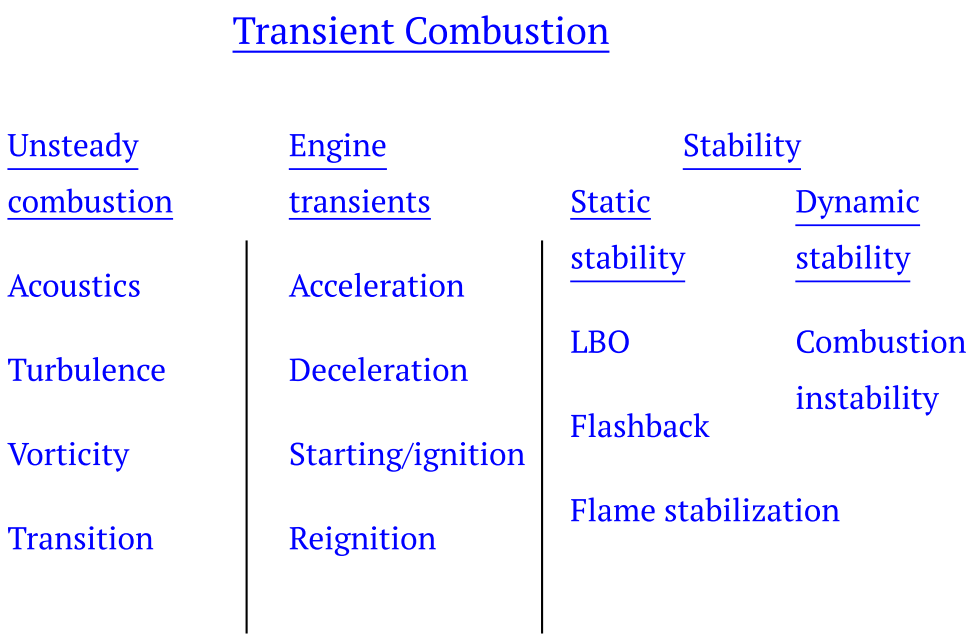

Figure 4.1 Schematic illustration of combustion transient definitions. Transients include unsteady combustion, engine transients, and static and dynamic stability.

(FDF) gain does not follow a linear behavior as the amplitude of modulation is increased, i.e., a linear relationship. In combustion, nonlinear also refers to the Arrhenius law exponential terms of the reaction rates and heat release terms. For signals, the mathematical definition of nonlinear is straightforward. If the signal is not linear, it is nonlinear. In other words, it is nonlinear if the signal does not satisfy the three relationships of linearity: additivity, homogeneity, and superposition. These expressions are respectively

$$f(x_1 + x_2) = f(x_1) + f(x_2), \tag{4.1}$$

$$f(\lambda x) = \lambda f(x), \tag{4.2}$$

$$f(\lambda x_1 + \mu x_2) = \lambda f(x_1) + \mu f(x_2). \tag{4.3}$$

The other definition used for linearity of signals in statistics is

$$f(x) = ax + b. \tag{4.4}$$

This expression is used in general to fit a so-called linear model to scatter plot data, and evaluate the subsequent degree of nonlinearity. The nonlinear regime in solid mechanics is defined by the level of force applied to a material beyond which the deformation

is not elastic anymore and it becomes permanent. It is then important to specify what type of nonlinearity occurs for a particular system considered.

Tab. 4.1 presents a few characteristic signals to illustrate typical transient signals. Tab. 4.1A and B represent respectively low frequency transient growth and low frequency transient decay. In these cases, the modulation oscillation time period is so long (the frequency is so low) that the transient sequence appears to be nonoscillating, or as a drift. Tab. 4.1C and D represent oscillating transient growth and decay where the envelope level of the signals are respectively increasing and decreasing. Tab. 4.1E and F depict low and high frequency transient growth and decay.

1.2 Data sciences and data analysis

The application of the governing equations in numerical code to model a combustion system, for the realization of numerical experiments, and for realtime jet engine or gas turbine monitoring of variables lead today or will lead to vast data generation, enabling to carry out detailed analysis, thanks to high spatial and time resolutions. In order to analyze those transient data, it is required to use and develop postprocessing tools and algorithms to extract flow quantities and features of interest. As an example of such approach, Fig. 4.2 presents the workflow from numerical simulation or experimental data generation to analyses of the results and conclusions.

Data management is a key aspect when the data are generated from numerical simulations or experiments, as it will determine the amount of space needed. Both the data's format and their metadata will be important for the subsequent steps given in Fig. 4.2. Indeed, the development of postprocessing tools that include advanced algorithms requires appropriate formats and metadata.

While the Big Data era has been reached, it is worthwhile to point out a few of the recent tools that have emerged for database processing. Those tools include for example Hadoop MapReduce or RStudio. Hadoop MapReduce is a framework to perform two main operations called "map" and "reduce" on data by distributing the tasks among a cluster of computing nodes. The map operation consists in selecting a subset of a large data set, and the reduce operation consists in the application of a given operation on this subset. MapReduce has been applied in the analysis of supersonic jet flowfields by Nichols [271], where the propagation of the jet sound was captured with the Ffowcs Williams–Hawkings acoustics analogy implemented with the MapReduce framework. RStudio is software that allows statistical analysis of data sets.

Table 4.1 Signal processing. (A and B) Low frequency transient growth and low frequency transient decay. (C and D) Oscillating transient growth and decay where the envelope level of the signals are respectively increasing and decreasing. (E and F) Low and high frequency transient growth and decay.

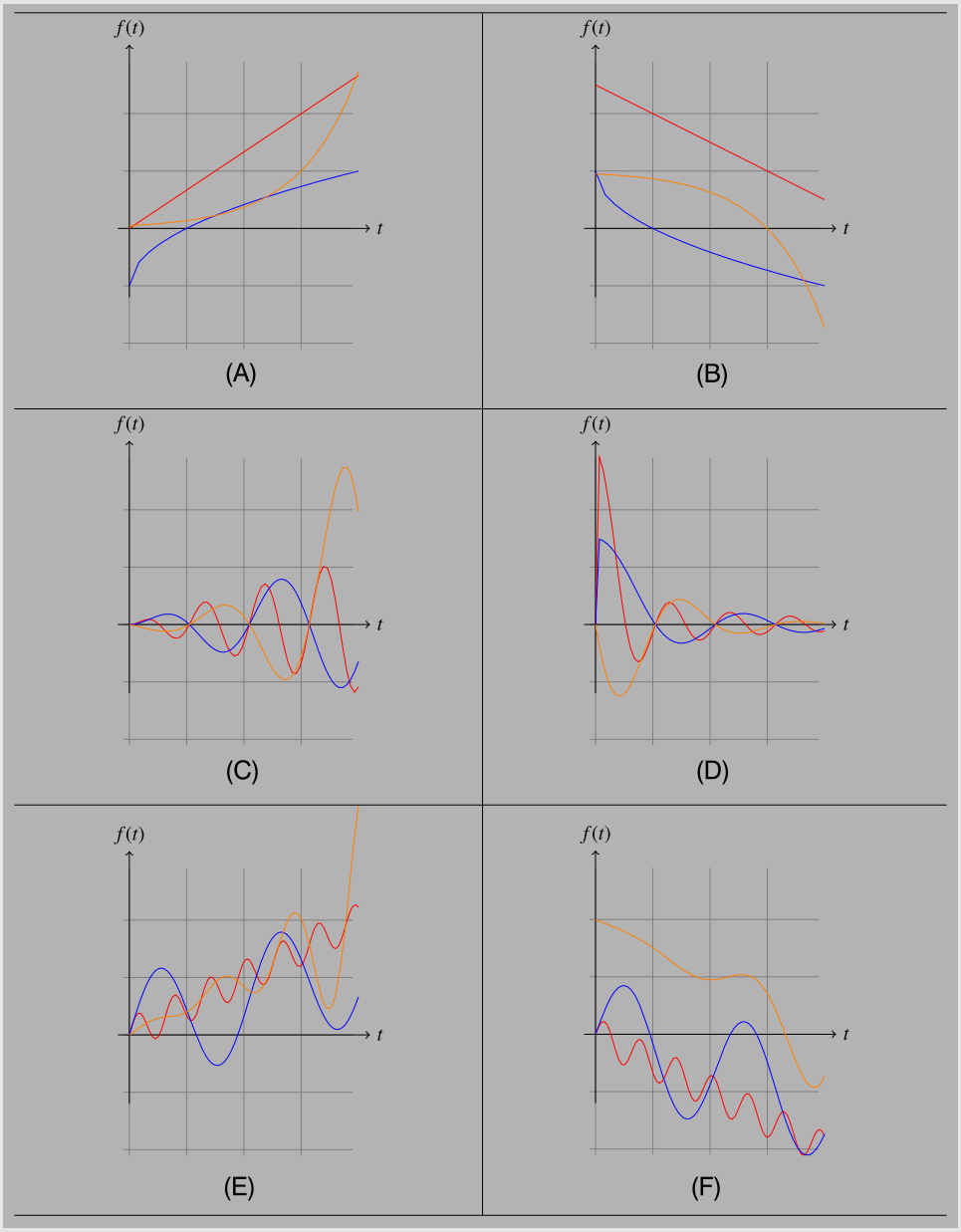

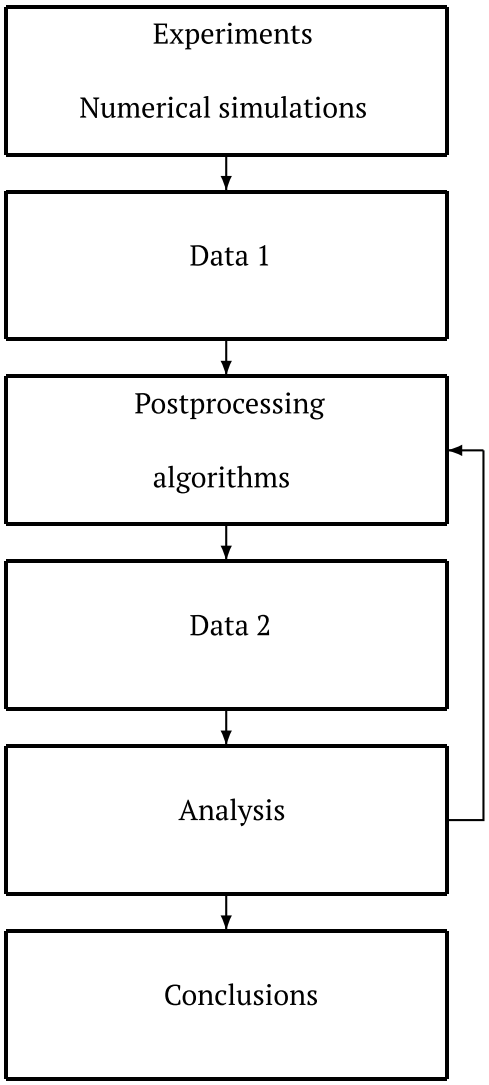

Figure 4.2 Workflow from numerical simulations or experiments to their conclusions.

In addition to these two tools, it is important to recall specific selected diagnostics for combustion dynamics. These diagnostics include the transfer function, Fourier transform, the Rayleigh index, proper orthogonal decomposition (POD), and dynamic mode decomposition (DMD). The transfer function provides the amplitude ratio of two signals at a given frequency and their phase. The FTF, see Crocco [272], or FDFs, see Dowling [273], Noiray et al.

[274], can be formed globally, such as in Palies et al. [253], by computing the global flame response with respect to a perturbation level or locally, see Pun et al. [275], Kang et al. [276], by evaluating the local flame response to an inlet perturbation. For the global flame response, the expression of the FTF can be written as

$$\mathcal{F}(\omega) = \frac{\dot{\omega}_T(t)/\overline{\dot{\omega}_T(t)}}{u'(\boldsymbol{x}_0,t)/\overline{u(\boldsymbol{x}_0,t)}} \approx \frac{I'(t)/\overline{I(t)}}{u'(\boldsymbol{x}_0,t)/\overline{u(\boldsymbol{x}_0,t)}}, \tag{4.5}$$

where $\dot{\omega}_T(t) = \int_V \dot{\omega}_T(\boldsymbol{x},t)dV$ is the unsteady heat release estimated by recording the global emission signals of excited radicals like CH* or OH* using a photomultiplier detecting the total light radiated by the flame I, and $\boldsymbol{x}_0$ is the location of the reference signal measurement upstream of the flame. The evaluation of heat release rate with flame chemiluminescence can be carried out with OH* or CH* signals that are obtained by filtering the full light signals respectively at 307 and 432 nm.

Fourier transform of time domain periodic signals can be performed with the fast Fourier transform (FFT) algorithm, leading to frequency spectra. The objective of the FFT algorithm is to determine the Fourier decomposition coefficients with a minimum number of operations, see Cooley and Tukey [277]. Spatial signals can be considered as well with Fourier transform to compute for example the turbulence energy spectrum in the space domain. The Rayleigh index consists in forming the product of fluctuating pressure and heat release signals to identify regions of driving and damping, see Samaniego et al. [278]. The 2D Rayleigh index maps are formed and integrated in time over a time series. The Rayleigh index time integral $RI(\boldsymbol{x})$ is defined as

$$RI(\boldsymbol{x}) = \frac{1}{\overline{\dot{\omega}_T}(\boldsymbol{x})\bar{p}(\boldsymbol{x})} \int_0^T \dot{\omega}'_T(\boldsymbol{x},t) \times p'(\boldsymbol{x},t)dt. \tag{4.6}$$

POD has been applied in combustion systems analysis to describe and identify structures for swirling flows by Wang et al. [279] and for swirling flames by Davis et al. [280]. DMD has been applied on swirling flames by Motheau et al. [281], Palies et al. [213]. The algorithm to compute those two decompositions is now recalled, following the presentation by Schmid [251]. A set of flame image or particle image velocimetry (PIV) flowfield snapshots are selected and organized into two matrices $\mathbf{V}_1$ and $\mathbf{V}_2$ such that $\mathbf{V}_1$ contains the data from instants t_0 to t_{N-1} while $\mathbf{V}_2$ is made up of data from instants t_1 to t_N. The derivation of the algorithm is as follows. First, the singular value decomposition of the first matrix $\mathbf{V}_1$ is computed ($\mathbf{U}$ and $\mathbf{W}^H$ being unitary matrices). We have

$$\mathbf{V}_1 = \mathbf{U}\Sigma\mathbf{W}^H. \tag{4.7}$$

The POD is obtained by forming the matrix $\mathbf{Q} = \mathbf{U}\Sigma$ so that $\mathbf{V}_1 = \mathbf{Q}\mathbf{W}^H$, where the POD modes are in $\mathbf{W}^H$ and their time coefficients in $\mathbf{Q}$. Making use of the previous singular value decomposition Eq. (4.7) and assuming that the operator $\mathbf{A}$ can be defined such that $\mathbf{A}\mathbf{V}_1 = \mathbf{V}_2$, the following expression is obtained:

$$\mathbf{A}\mathbf{V}_1 = \mathbf{A}\mathbf{U}\Sigma\mathbf{W}^H = \mathbf{V}_2. \tag{4.8}$$

This can be rewritten as

$$\mathbf{U}^H\mathbf{A}\mathbf{U}\Sigma\mathbf{W}^H = \mathbf{U}^H\mathbf{V}_2. \tag{4.9}$$

The following matrix $\tilde{\mathbf{S}}$ is then obtained:

$$\tilde{\mathbf{S}} = \mathbf{U}^H\mathbf{A}\mathbf{U} = \mathbf{U}^H\mathbf{V}_2\mathbf{W}\Sigma^{-1}. \tag{4.10}$$

The eigenvectors y_i of the matrix $\tilde{\mathbf{S}}$ are calculated and the DMD modes ϕ_i are formed. We have

$$\phi_i = \mathbf{U}\mathbf{y}_i, \tag{4.11}$$

$$\tilde{\mathbf{S}}\mathbf{y}_i = \mu_i\mathbf{y}_i, \tag{4.12}$$

$$\lambda_i = log(\mu_i)/\delta t. \tag{4.13}$$

Finally, the eigenvalues μ_i are used to compute the frequencies f and growth rates σ of the DMD modes: $f = \Im(\lambda_i/2\pi)$ and $\sigma = \Re(\lambda_i)$, with δt being the inverse of the data sampling frequency F_s. The snapshots used for the analysis of the LSI-LBNL-Cheng configuration presented in the present chapter are OH-filtered flame images obtained as a function of time so that the captured growth rates correspond to the temporal growth rates.

1.3 Measurements and diagnostics

Diagnostics are implemented in a given experiment to determine flowfield quantities and boundary conditions for subsequent comparison to simulations. Among many aspects that have to be taken into account, the time and the spatial resolution of the measurements of the diagnostics are very important. Experimental measurements are used for multiple reasons. Measurements are utilized to compare results from numerical simulations and evaluate the predictive capabilities of models. Measurements are used to extract patterns and flow features through postprocessing algorithms. Measurements are also used to set the numerical simulation boundary conditions. Moreover, measurements are performed to confirm hypotheses and to discover physical mechanisms. Most variables can be measured in a turbulent reacting

Table 4.2 List of experimental measurement methods and diagnostics.

Method	Acronym	Variable	Principle	Ref.
Shadowgraph imaging	SI	$\nabla\rho$, $\nabla\mathbf{n}$	Refractive index variation	Settles [282], Van Dyke [283]
Schlieren imaging	SI	$\nabla\rho$, $\nabla\mathbf{n}$	Refractive index variation	Settles [282], Van Dyke [283]
Mach–Zehnder interferometry	MZI	$\nabla\rho$, $\nabla\mathbf{n}$	Refractive index variation	Toker [284], Van Dyke [283]
Hot wire anemometry	HWA	$\boldsymbol{v}$	Joule's effect, King's law	Lomas [285]
Subsonic pitot tube	PT	$\boldsymbol{v}$	Bernoulli Ma $<<1$	Goldstein [286]
Supersonic pitot tube	PT	$\boldsymbol{v}$	Rayleigh pitot formulae	
Laser Doppler velocimetry	LDV	$\boldsymbol{v}$	Interferometry laser	Boutier and Most [287]
Particle image velocimetry	PIV	$\boldsymbol{v}$	Cross-correlation	Riethmuller et al. [288]
Particle tracking velocimetry	PTV	$\boldsymbol{v}$	Cross-correlation	Maas et al. [289]
Pressure-sensitive paint	PSP	p	Fluorescence	Gregory et al. [290]
Differential pressure measurement	DPM	p	Bernoulli	Goldstein [286]
Photomultiplier tube	PMT	$\dot{\omega}_T$	Photoelec./second emiss.	Iams and Salzberg [291]
Intensified CCD camera	ICCD	$\dot{\omega}_T$	Photoelectricity	
Laser-induced fluorescence	LIF	$[X_k]$, T	Light absorption/emission	Daily [292]
Planar laser-induced fluorescence	PLIF	$[X_k]$, T	Light absorption/emission	Lozano et al. [293]
Mie scattering	MS	d	$d/\lambda >> 1$	Chigier [294]
Raman scattering	RS	$[X_k]$, T		Chigier [294]
Rayleigh scattering	RS	ρ, T	$d/\lambda << 1$	Chigier [294]
Phase Doppler particle anemometry	PDPA	d, $\boldsymbol{v}$, $[X]$	LDV	Albrecht et al. [295]

flow with different degrees of resolution. A summary of diagnostics is given in Tab. 4.2. When directly comparing experimental and numerical simulation results, particular attention has to be paid to the time and spatial resolutions and to which quantities to compare with.

2 Unsteady premixed combustion

Laminar combustion refers to a regime where the reacting flowfield is not turbulent. Turbulence is defined by the presence of fluctuations of various frequencies and intensities. Laminar

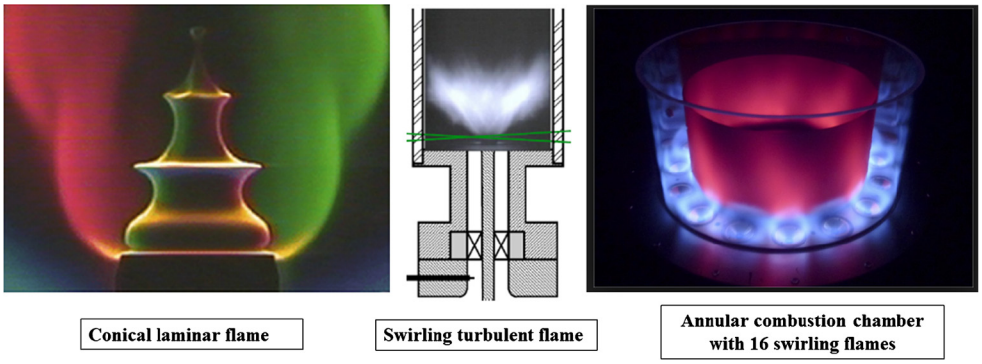

Figure 4.3 Example of unsteady combustion configurations. Left: Modulated conical flame by Ducruix et al. [128]. Center: Swirling flame by Palies [180]. Right: Annular combustion chamber with 16 swirling flames by Bourgouin et al. [73]. Source: EM2C.

combustion can be transient though, for example having a time-dependent reacting flowfield due to harmonic fluctuations/oscillations. In this section, the focus is on both sources of unsteadiness for laminar and turbulent regimes: harmonic and nonharmonic fluctuations. A set of unsteady combustion configurations is sketched in Fig. 4.3. The left figure represents a modulated conical laminar flame by Ducruix et al. [128], the center figure represents the turbulent swirling flame of Palies [180], and the right figure illustrates the annular combustion chamber with 16 swirling flames by Bourgouin et al. [73].

2.1 Laminar unsteady premixed combustion

The study of steady laminar premixed combustion is well documented theoretically, numerically, and experimentally. The flame structure is essentially known and characterized under strained flow with or without curvature. The studies focusing on unsteady laminar flames are less numerous. There are two main categories of unsteady laminar flames. The first one consists of aerodynamically unsteady strained laminar flames on radially expanding or counterflow flame configurations. These studies aim at characterizing the effects of flame stretch (flow strain, flame dilatation, and flame curvature) in unsteady situations. It is important for physical understanding and subsequent numerical modeling. Studies of the second category essentially focus on the effects of flow modulation for combustion instability. Several of those studies are now reviewed. Most of the configurations used for the latter studies are either canonical conical or bluff-body "V" flames.

2.1.1 Strained and curved flames

There are a few key configurations that have been used to investigate strained and curved premixed flames in an unsteady fashion. The first one is that of the counterflow flame configuration, where two streams of premixed reactants impact each other, inducing a stagnation point and the stabilization of two planar steady premixed flames. The unsteadiness in that configuration is generated by imposing upstream flow modulation. The role of the flow modulation is to generate a perturbation of the axial centerline flow strain. A second set of configurations consists of radially expanding spherical premixed flames. In that setting, the flame curvature is time-dependent. These two configurations enable to study the axial component of the flow strain and the flame curvature term of flame stretch separately. Comprehensive descriptions of these configurations can be found in Law [296,297]. The flow strain and flame curvature grouped under the flame stretch quantity have a key effect on flame speed and local flame extinction. These effects are reviewed now for laminar unsteady premixed flames. Egolfopoulos [298] have shown that the effect of the radiation on the flame response and extinction becomes important only for near-limit premixed flames characterized by large thicknesses. Rutland and Ferziger [299] investigated the transient response of laminar flames to strain numerically. The authors found that two time scales enabled to characterize the flame response during straining: at low strain, a slow time scale associated with the preheat zone is dominant, while for higher strain, a faster time scale related to the reaction zone was important. The authors concluded that the flame response time and history (i.e., convective and diffusive) effects should be included for flamelet models based on the local strain rate. Petrov and Ghoniem [300] studied the time-dependent response of a premixed laminar flame subjected to a sudden change in strain and a periodic strain to investigate the validity of the assumption that the flame response to strain is instantaneous. It was shown that for most cases, the flame response can be assumed to be instantaneous.

2.1.2 Flames submitted to flow modulation

The study of oscillating flames, i.e., flames submitted to external flow modulations in laminar configurations, is an important contribution to the understanding of static and dynamic stability of more complex configurations. There are three main types of flames investigated in this context: the conical flame, the planar flame, and the bluff-body flame, also known as the inverted conical flame. In addition, usually, these flames are submitted to either flow velocity modulation or equivalence ratio modulation.

Experimental, theoretical, and numerical studies are documented in the literature. Pioneering research on theoretical analysis of conical flames was tackled by Baillot et al. [301], where kinematic effects of a space-time forced velocity field upon a thin premixed flame have been studied in order to examine the nonlinearities due to a sufficiently high velocity perturbation level. Bourehla and Baillot [302] performed experimental measurements of the same flame and identified various regimes as a function of the frequency and amplitude of the upstream modulation. Extensive studies of laminar flames submitted to external flow modulations were carried out by Durox et al. [303] for high amplitudes of modulation where coupling between the oscillating and the mean flow were investigated, by Ducruix et al. [128] for moderate amplitudes with both experimental and numerical studies, by Schuller et al. [129] for both conical and bluff-body "V" flames theoretically, and by Durox et al. [136] for bluff-body flames experimentally. Birbaud et al. [304] investigated the "V" flame configuration with confinement walls. Nonlinear features of flame dynamics have been characterized by measuring the FTFs for different input levels by Durox et al. [305]. Birbaud et al. [306] investigated the dynamics of an inverted laminar "V" flame submitted to equivalence ratio modulations numerically. These series of works have documented and informed on the fundamental mechanisms responsible for combustion dynamics of laminar unsteady flames, and also determined the flame responses of these flames to various perturbation types at different frequencies and amplitudes. The dynamic response of strained premixed flames to equivalence ratio gradients has been investigated by Marzouk et al. [307]. It was concluded that in comparison with fully premixed flames, stratified lean flames burn faster and into mixtures whose equivalence ratios are lower than those corresponding to flammability limits. The mechanism responsible for these changes was identified as the establishment of spatial gradients in temperature and the accompanying radical concentrations in the wake of the flame gradients acting as a temporary "heat (and chemical) reservoir" for new incoming reactants. As a result, for the same heat release rate, the reaction zone of a flame burning in a stoichiometric-to-lean equivalence ratio gradient is broader than that of the nominal steady flame, with a lower temperature at the peak and a higher radical concentration throughout.

2.1.3 Laminar combustion studies and DNS modeling relevant for turbulent combustion

In this section, the focus is on the laminar combustion studies directly relevant to turbulent combustion along with DNS con-

ducted in this regime. In Clavin [308], the author detailed the structure and dynamics of wrinkled fronts of premixed flames in turbulent and laminar flowfields, and highlighted theoretical analyses and experimental results to form a complete description of the coupling between diffusive transport processes, the hydrodynamical phenomena associated with gas expansion, and the complex chemical kinetics. Peters [184] reviewed the laminar flamelet concept that covers the regime of turbulent combustion where chemistry (as compared to transport processes) is fast such that it occurs in asymptotically thin layers called flamelets embedded within the turbulent flowfield. Echekki and Chen [309] investigated the unsteady strain rate and curvature effects in turbulent premixed methane–air flames. DNS of turbulent premixed stoichiometric methane–air flames was carried out with a four-step combustion mechanism. It was found that radical species correlated strongly with strain rate and curvature depending upon their individual mass diffusion rates. The authors concluded that a single Lewis number representation of all species would be inadequate in predicting the heat release rate and evolution of the flame surface. It was also found that the highly diffusive and fast reactive species H and H_2 were correlated with curvature, while the less diffusive species CO, with a slow oxidation rate, was more susceptible to unsteady strain rate effects. Chen and Im [250] focused on DNS of 2D unsteady premixed methane–air flames to extract the correlation of flame speed with flame stretch for various curvatures and strain rates generated by intense 2D turbulence. The results showed that exceedingly large negative values of stretch can be obtained solely through curvature effects, which give rise to an overall nonlinear correlation of the flame speed with stretch. Over a narrower stretch range, $-1 \leq Ka \leq 1$, which includes 90% of the sample, the correlation was approximately linear, and consequently the asymptotic theory for stretch was found to be applicable. Hawkes and Chen [310] conducted DNS with complex chemistry to compute statistics of displacement and consumption speeds in turbulent lean premixed methane–air flames. The authors focused on evaluating to what extent a turbulent flame in the thin reaction zones regime can be modeled by an ensemble of strained laminar flames. Displacement speeds in the inner reaction layer were found to agree very well with the laminar flame calculations for a wide range of strains at high Damköhler number. For lower Damköhler numbers, a reduced response to strain was observed, consistent with previous studies and theoretical expectations. Indeed, in these regimes, the flame sheet model is not necessarily satisfied and the definition of the flame surface and

the flame speed can become challenging. This issue is discussed in Chapter 3 of the present book.

The transition from laminar flame to turbulent flame is not a topic that has been studied and documented as comprehensively as each topic separately. The principal challenges lie in designing dedicated experiments for these studies.

2.2 Turbulent premixed combustion

In the present section, the focus is on turbulent combustion with specific emphasis on premixed (fully, partially, and stratified) combustion. The focus is on laboratory-scale experimental and numerical simulation results. A comparison between laboratory-scale and representative jet engine operating conditions is firstly conducted to set orders of magnitude. It is important to recall the differences between operating regimes of laboratory-scale and jet engine configurations. For example, the operating pressure and inlet temperature are different. Typical laboratory-scale combustors operate at atmospheric conditions (1 atm, 300 K) while jet engines operate at higher values (30 atm, 850 K) at TO. This affects the turbulence and combustion processes, particularly the characteristic Kolmogorov and flame thickness scales. For example, the thermal flame front thickness at stoichiometry of a 1D laminar flame at atmospheric conditions is of the order of 500 μm, while it is of the order of 10 μm at TO operating conditions.

Premixed turbulent combustion has been examined comprehensively in the monographs of Poinsot and Veynante [172] and Kuo and Acharya [21]. Turbulent combustion regimes are generally studied with the turbulent premixed combustion diagram in order to build a bridge between the operating conditions of a configuration and the subsequent turbulent combustion regime modeling approach required. The classical turbulent combustion diagram of Peters [184] consists of characterizing the regime with the level of turbulence (RMS velocity nondimensionalized by laminar flame speed) on the y axis versus the integral length scale of the largest eddies nondimensionalized by the flame thickness on the x axis. This diagram allows for example to distinguish regimes where combustion can be described as flamelets or distributed reaction zones. It is also worthwhile to point out that for a given configuration, multiple regimes can coexist, depending on the location of the estimates inside the flame region and the operating conditions. Multiple characterizations of the turbulent combustion regions have been carried out with DNS to describe and understand the interaction of a turbulent flowfield with a premixed flame front in canonical configurations represented by a 3D CFD

periodic domain. These configurations have allowed tremendous progress in turbulent combustion but have been limited to small computational domains due to the high CPU requirements. In addition, 3D boxes cannot replicate some key spatial scales of realistic configuration due to the size limitations. For example, influences of the turbulent integral length scale (such as taken as the swirler or the flame tube diameter) or the interactions of the various wavelengths of propagating acoustic waves (through reflections at the walls) on the local velocity field cannot be captured. These simulations will continue to be a fundamental tool for turbulent premixed combustion research and will benefit from the inclusion of additional applications' relevant parameters, such as high pressure. Simulation of real systems will require novel modeling strategies: embedded DNS, hybrid DNS/large eddy simulation (LES) approaches, or local mesh refinements (static or dynamic) to capture the flow dynamics and add value to the design procedure. Numerical simulations have had and will have significant impacts on technology design. Consequently, future strategies have to be complemented with improvements of the existing tools; for example, the LES modeling of turbulent combustion should be revisited in terms of subgrid scale models. It is indeed important to improve our understanding and capabilities of LES modeling turbulent reacting flows for power and propulsion systems, because high pressure systems will require LES due to the scales at work.

Few simulations at DNS resolutions have been carried out to fill the need of exploring realistic combustors at full modeling scale, see the two swirling flame configurations shown in Fig. 4.4. One of the challenges of these direct simulations is the development of dedicated, accurate, and fast postprocessing tools for physical insight extraction in order to refine the design of technologies. On the other hand, experimental visualizations of turbulent flames at jet engine operating conditions are rare too. These data, both from experiments and numerical simulations, will be key in order to refine the understanding of the physical mechanisms at work and some aspects of the technologies that rely upon them. In addition, it is worthwhile to add that the combustion chamber has to be modeled within its context, and the multi-physics aspects, including for example heat transfer, have to be taken into account.

For combustion dynamics and combustion instability studies, turbulent combustion modeling in numerical simulations is important for two main reasons. Firstly, turbulent combustion modeling impacts the flame position, which has been shown to be a driver of combustion instability. Secondly, the flow velocity fluctuations (acoustic, vortical, and turbulent) are directly responsible

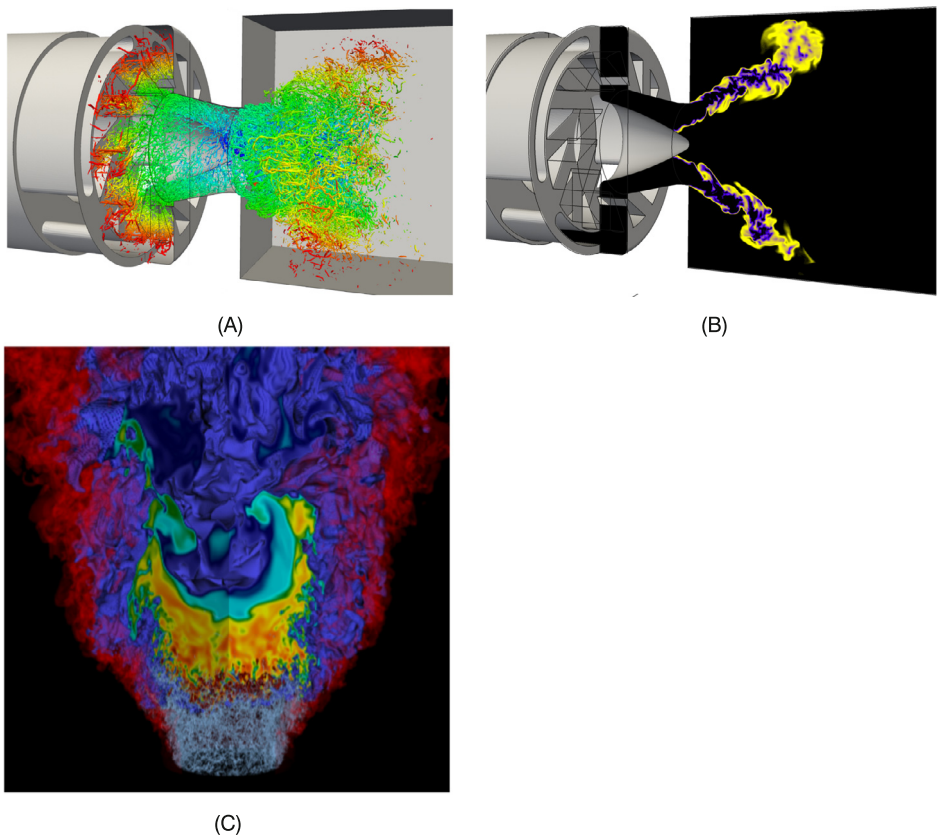

Figure 4.4 Examples of unsteady combustion configurations. Left: Modulated conical flame by Ducruix et al. [128]. Illustration of turbulent combustion numerical studies for swirling flames. (A) Preccinsta-DLR-Lartigue combustor vorticity field colored by axial velocity from simulations with 2.6 billion cell mesh from Moureau et al. [322]. (B) Corresponding cutaway of temperature. (C) Direct LSI-LBNL-Cheng low swirl flame numerical simulation from Bell et al. [334].

for the spatial and temporal unsteady heat release rate, and are also directly responsible for flame stabilization. In the next section, the recent literature in turbulent combustion modeling for LESs is documented.

LESs of gaseous flows in gas turbine combustion chambers have been reviewed by Gicquel et al. [245]. Turbulent combustion modeling for LES has been reviewed by Pitsch [311], Mercier [312], Fiorina et al. [313], Bray [314] and has always been challenging, see Lilley [315–317]. The emphasis of this section is on four main methods used to model turbulent combustion. The first one is the no-model approach, where the turbulence–chemistry interaction is not specifically modeled and where the reaction rates

are expressed with Arrhenius law functions of the filtered quantities. This approach of the turbulent combustion closure tends to DNS when the grid size allows to resolve the flame thickness and the Kolmogorov scale at work. The second approach is based on the flamelets theory, assuming that the flame retains its laminar structure within the turbulent flowfield, see Pitsch [311]. In that method, the combustion chemistry calculations are partially decoupled from the flowfield computation by involving tabulation of the chemistry parameters, for example using a flamelet progress variable. These methods are used for regimes where the assumption of flamelets holds, i.e., when the 3D flowfield does not impact the 1D laminar profile, a severe assumption for the intrinsic velocity field in swirling flows. The third method is based on the probability density function (PDF) for the reaction rate terms, see the review by Haworth [318]. In flamelet methods and PDF methods, the deterministic character of the flowfield through its fluctuations may be lost. Finally, the fourth method consists of thickening the flame front to be able to resolve its structure on meshes that are coarser than DNS meshes, see Colin et al. [319]. In this approach, the turbulence–chemistry interaction is modeled with an efficiency function, see Charlette et al. [320,321].

There are several different comparisons between numerical simulations and experimental results that can be carried out, depending on the level of flow analysis performed. Usually, the first step relies on comparing the mean and statistics between the reacting numerical simulations and the experimental measurements. Secondly, the turbulent spectra are sometimes computed from the data available. In addition, the reacting flowfield and its features (flame shape, wrinkling, coherent structure frequencies, flame surface area, etc.) can also be used for comparison between simulations and experiments. Finally, nowadays, the comparison of instantaneous reacting flowfield snapshots has become important to compare experimental and numerical simulation data.

The Preccinsta-DLR-Lartigue configuration has been widely used to compare numerical simulations executed with different turbulent combustion models with experimental data. In Moureau et al. [322], numerical simulations of that combustor were carried out. Multiple LESs and a DNS resolving the thermal flame front thickness were conducted. The DNS contained approximately 2.6 billion cells in the computational domain, with an average cell length of 100 μm. The DNS results were used to perform a priori filtering and data analysis in order to investigate the flow–flame interactions for PDF modeling with detailed tabulated chemistry. Filtered tabulated chemistry for LES was introduced by Fiorina et al. [323], Auzillon et al. [324] and

applied to the Preccinsta-DLR-Lartigue configuration too by ensuring that the thickened flame speed was properly captured, assuming that the flame retains its laminar structure locally. In Veynante et al. [325], the authors focused on dynamic turbulent combustion models for LES. Dynamic formulations for the flame wrinkling factor of the thickened flame model were investigated with a priori filtering on the Preccinsta-DLR-Lartigue data set obtained by Moureau et al. [322] and a posteriori tests. The article of Franzelli et al. [326] investigated the effects of multiple chemical mechanisms of different degrees of complexity (5 species/2 reactions to 13 species/73 reactions) and showed the significant effect of the chemical mechanism on the flame shape. The reduced chemical mechanisms were shown to compare favorably with the experimental temperature field. In Wang et al. [327], a reduction chemistry approach was proposed and applied to the Preccinsta-DLR-Lartigue setup with overall agreement with the experimental data. The article of Ansari et al. [328] investigated the same setup with a filtered density function model. Multiple RANS models were assessed and compared in Anker et al. [329] for the Preccinsta-DLR-Lartigue configuration. In Mercier et al. [330], the authors studied the effects of the two LES filter operators of different sizes for the flowfield and the flame front, respectively. The consistency issues between flame and flow filter sizes in LES of turbulent premixed flames and the model applied to the Preccinsta-DLR-Lartigue burner were specifically discussed. A comparison of the dynamically thickened flame model and a flame surface density model was carried out through LES by Wang et al. [331]. Very good agreement between the LES and experimental data was obtained for the statistics of velocity, temperature, and major species. In Volpiani et al. [332], the authors focused on an adaptive dynamics model, where the parameters depend on the resolved variables of the simulations. It was shown that the dynamics wrinkling factor significantly affects the flame dynamics, as this latter was only captured with the dynamic model. Scale-adaptive simulation was carried out by Lourier et al. [333] to study the influence of turbulence–chemistry interaction on the structure and stability of the Preccinsta configuration. It was shown that the associated subgrid scale terms had minor importance for the resulting time-average quantities because of highly resolved velocity, temperature, and species fluctuations in the computations.

The LSI-LBNL-Cheng configuration, depicted in Fig. 4.4C, has been used for many experimental and a few numerical turbulent combustion studies. The initial design of the experimental setup for low swirl flames along with experimental measurements was

documented in Cheng [120]. The article of Plessing et al. [335] presented measurements of the turbulent burning velocity and the structure of premixed flames in that configuration. It was demonstrated that the turbulent flame brush thickness was not dependent on u'/S_L and that the turbulent burning velocity was well predicted from a model equation for the flame surface area ratio using the level set approach. In Bell et al. [336], the LSI-LBNL-Cheng flame was studied numerically with 3D DNS simulations and a two-step reaction mechanism with six species. Petersson et al. [337] carried out a detailed multi-diagnostics analysis of the low swirl flame to characterize the reacting flowfield. The effects of hydrogen addition on key quantities such as flame speed, NO_x emissions, and flowfield velocities were investigated by Cheng et al. [338] at high pressure and inlet temperature conditions. Comprehensive combined experimental and numerical studies were carried out by Day et al. [339] on methane flames and by Day et al. [340] on hydrogen flames with detailed characterization of the turbulent flame front. In Bell et al. [334], the authors conducted direct numerical simulations of the low swirl injector premixed air–hydrogen flames. The simulations were used to describe the levels and mechanisms of NO_x formation. Turbulence was also characterized at the flame front with visualization of the anchoring zone of the low swirl flame. Other low swirl flames have been studied, such as in Nogenmyr et al. [210], where the level-set G-equation, flamelet chemistry, and finite rate chemistry with reduced kinetics were compared with experimental results (stereoscopic PIV and PLIF).

The work of Minamoto et al. [341] focused on the DNS of a hydrogen-enriched swirling premixed flame. Two swirl numbers were simulated and showed the impact on the formation of the inner recirculation zone (IRZ) in the combustor. The large velocity gradients in the higher swirl number case produced high turbulence intensity in the upstream region compared with the lower swirl number case.

The turbulent premixed combustion regime of the gas turbine engine at real scale and operating conditions is an active point of discussion in the literature, along with the turbulent integral-scale determination. It has been presented in Chapters 2 and 3. DNS numerical simulations are very valuable because they enable capture of the finest continuum scales of the chemical and fluid dynamic processes. Such simulations are rare though due to the resources they require. The leading examples for swirling flames are those of Moureau et al. [322] and Bell et al. [334]. These types of simulations should become a tool for advanced learning of the several chemical and physical facets (convection–diffusion–reaction

problems) of swirling flames. In addition, turbulent combustion modeling of swirling flames at real gas turbine engine conditions should be continued for the same reasons and used to determine the regime of combustion at these conditions. Several insights will be gained from these simulations and could be for example employed to extract the local flame speed for subsequent modeling. Open underlying questions include (i) the assumption beyond the modeling of the flame as a flame sheet at gas turbine conditions, (ii) the effects of the individual flame stretch components (15 terms for a premixed flame) on local propagation/extinction, (iii) the verification of orders of magnitude of characteristic scales a posteriori and the verification of assumptions, (iv) the validation of chemical mechanisms for modeling chemical kinetics at relevant high pressure, high temperature conditions, and (v) the treatment of supercritical conditions at these operating conditions (such as TO). Such simulations will enable us to begin answering some of these questions, and will provide visualization at real scales, a major challenge.

3 Combustor engine transient

There are two main categories of gas turbine engine transients. Acceleration and deceleration consist of the first category. They logically occur during TO and landing for commercial aircraft. Ignition and reignition belong to the second category and are closely linked to the engine start phase and engine altitude reignition. Both of those categories are discussed now by reviewing the limited available literature in the public domain. For electricity generation gas turbine systems, the acceleration and deceleration phases correspond to the starting and stopping phases of the engine. It is worthwhile to indicate that engine transient studies are limited for various reasons, including proprietary issues and costs of realistic-scale tests. In addition, numerical simulations of realistic gas turbine engine combustors in transient conditions is also out of reach in terms of CPU cost for most current simulation strategies. Consequently, the literature is relatively weak or focused on quasisteady state approaches, where the transient is seen as a succession of quasisteady states. Most available studies have focused on the description of the engine dynamics in a 0D fashion, where the combustor is seen as a box and the input/outputs of that box are the modeled quantities for various combinations of parameters. This methodology enables to describe the first-order effects of certain parameters on the outputs of the combustor, but they do not allow the modeling of the 3D time-dependent dynamics of the reacting flowfield.

Peitsch [342] presents a variety of approaches for modeling transients of the entire engine behavior and discusses the limitations of these. Wang et al. [343] focused on the development of a method for the simulation of gas turbine fuel systems. The performance of each of the hydraulic components of the fuel system was simulated using physics-based models. Rosfjord and Cohen [344] designed and used a test rig to evaluate the transient response of advanced gas turbine combustors. The time-dependent mass flows of air and fuel and preheat temperatures were input parameters of the setup, allowing to determine or speculate some subsequent effects on the combustion process.

4 Configuration case study

In the next sections, a case study is investigated with numerical simulations. It includes the numerical procedure, the description of the setup, the study of flashback, the study of LBO, and the transient to transverse combustion instability in the same configuration.

4.1 Methodology and numerical procedure

The modeled geometry consists of a cylindrical injection unit connected to a 95 mm $\times$ 150 mm combustion chamber. The outlet was open to the atmosphere as in the experiment by imposing an outlet atmospheric pressure boundary condition. The injection unit includes a central bluff-body and a swirler equipped with six vanes at a 60 degree angle with respect to the flow axis. The experimental description of the setup can be found in Cavaliere et al. [53]. The modeled geometry is sketched in Fig. 4.5. Simulations were conducted with adiabatic or isothermal walls, and perfectly reflecting or partially reflecting outlet boundary conditions. All walls were modeled with no-slip boundaries. The presently reported results were obtained with fully reflecting boundary inlet and outlet, and adiabatic walls. The bulk velocity imposed at the computational domain inlet was calculated to match the bulk velocity at the annulus of the bluff-body tip, as this latter is known from the experimental measurement. There is no imposed turbulence field initialization or boundary condition, as the swirler drives the turbulence. The operating point considered is that of the premixed flame where lean blowoff (LBO) is observed at an equivalence ratio of 0.57. The present simulation was conducted as a sequence at an equivalence ratio between 0.7 and 0.55, as the CPU time requirement for a parametric study to capture the exact near-blowout (0.61) and blowout (0.57) cases was out of reach.

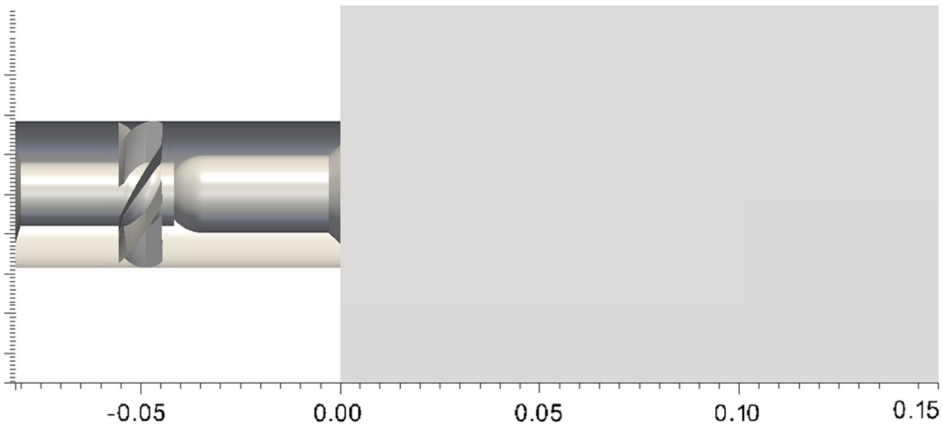

Figure 4.5 Setup geometry. View of the numerical model which includes the central cylindrical bluff-body, the swirler unit, and the 95 mm × 150 mm combustion chamber.

The simulation was performed with a 236 million cell structured grid with cell size enabling to resolve the thermal flame front thickness and nearly Kolmogorov scales. The turbulent Reynolds number is defined by $Re_t = \rho u' l_0/\mu$, where ρ is the density of the fluid, u' is the turbulent velocity fluctuation taken equal to 20% of the bulk velocity so that $u' = 4$ m s^{-1}, l_0 is the integral length scale assumed here to be equal to the inner injector diameter of 25 mm, and μ is the dynamic viscosity. The Kolmogorov scale η can be written as $\eta = l_0 Re_t^{-3/4}$. The calculations give 35 µm in the reactant and 360 µm in the products. The Blint thickness (close to the thermal flame front thickness) is defined by $\delta_L^B = 2\delta(T_2/T_1)^{0.7}$, where δ is the diffusive laminar flame thickness defined by $\delta = \lambda/(\rho c_p S_L^0)$, where λ is the thermal conductivity, c_p is the heat capacity at constant pressure, and S_L^0 is the unstretched laminar flame speed, leading to a value of 800 µm at $\Phi = 0.7$. The mesh was designed at that equivalence ratio as the laminar thermal flame thickness increases as the equivalence ratio decreases during the LBO sequence, up to values of 1.5 mm at $\Phi = 0.5$. This mesh is equivalent to a more than one billion tetrahedron cell mesh of the 3D domain in terms of resolution of those two scales. Selected mesh close-up views are given in Fig. 4.6. The time step of the numerical time integration was set to 1.0E−6 s. Because the present mesh allows to capture most possible vortex sizes in the flame dynamics region, both in fresh and burned gases, no turbulence–chemistry model was retained so that no model is employed for the turbulent combustion closure. An LES formulation is used here though with momentum subgrid model expected to act only for the small-

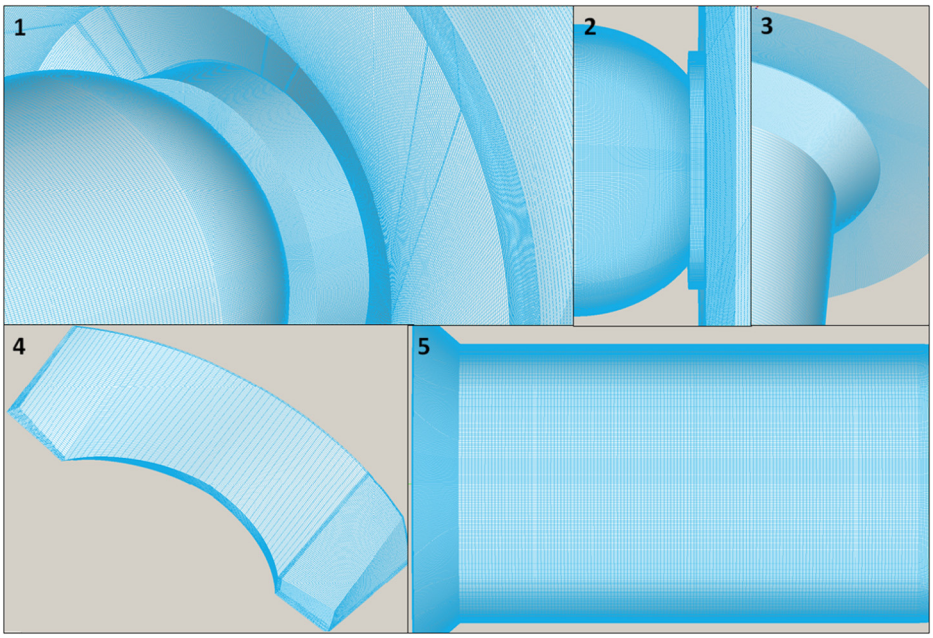

Figure 4.6 Setup geometry. Close-up views of the surface mesh. (1) Isometric view of the intersection bottom extremity of the bluff-body and swirler. (2) Side view of the swirler–bluff-body intersection. (3) Top bluff-body and backplane circular inlet. (4) Swirler vane view. (5) Side view of the top extremity of the bluff-body prior to the combustor backplane.

est dissipation scales in the fresh gases. The thermal thickness of the flame front is modeled with 5 to 15 points throughout. The combustion chemistry mechanism was a one-step global mechanism including five species fitted to retrieve flame speed and adiabatic flame temperature. The reacting simulations were performed with the Loci-CHEM code, a finite volume code for 3D chemically reacting turbulent flows Luke et al. [215]. The OH fields were reconstructed a posteriori. The procedure to reconstruct the OH field was as follows. A set of laminar premixed flames were computed for equivalence ratios between 0.5 and 1.0. From those, the mass fractions of OH and H_2O and the temperature variables were extracted and used to build an a posteriori look-up table implemented as a direct function f so that $Y_{OH} = f(T, Y_{H_2O})$.

4.2 Time-average versus instantaneous velocity field

This section presents a few numerical simulation results extracted from the configuration case study. Specifically, the instan-

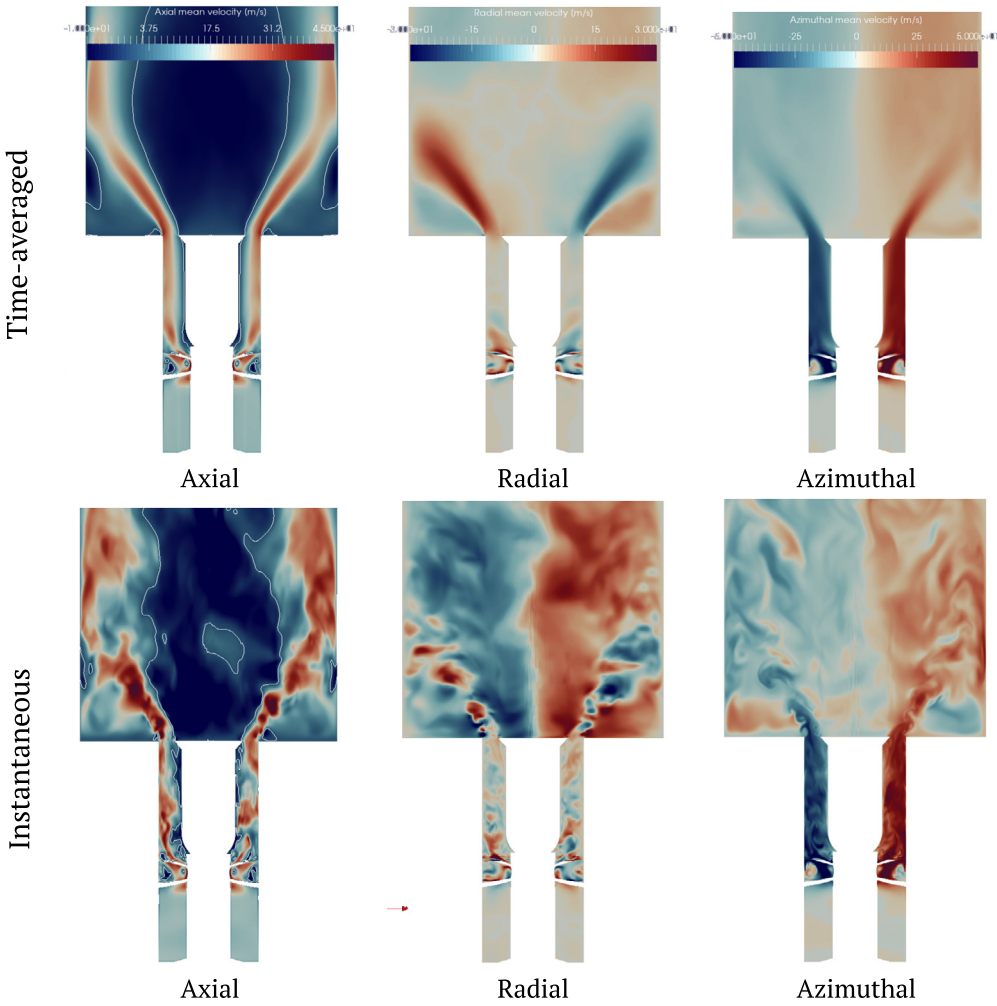

Figure 4.7 Comparison of time-averaged and instantaneous flowfields. Numerical simulations of the time-averaged (top row) and instantaneous (bottom row) axial, radial, and azimuthal flowfield velocities.

taneous and time-averaged velocity fields are discussed. These results are depicted in Fig. 4.7. The top row represents the time average, while the bottom row represents the instantaneous flowfield. The axial, radial, and azimuthal velocities respectively correspond to columns one, two, and three. The isoline of zero axial velocity is superimposed on the axial velocity fields.

Some observations from these flowfields can be made. First of all, the instantaneous and the time-averaged flowfield are very different. The time-averaged axial velocity shows that the IRZ ex-

tends relatively far downstream the combustion chamber, a feature that has been observed and visualized with PIV in several studies of reacting swirling flows. The radial time-averaged velocity component is shown to peak on the swirling jets and where the flame is located. It is also nearly zero inside the upstream injector annulus prior to the bluff-body. The azimuthal time-averaged flow component reaches distinct distributions in two regions of the flow. From the outlet swirler up to the flame tips, there is a first region of homogeneous azimuthal velocity associated with the swirling jets generated by the swirler. The intensity of the azimuthal velocity decreases as the distance from the swirler increases, particularly on the combustor swirling jets. The second region of homogeneous azimuthal velocity of opposite sign is the left and right parts of the combustor region. There are two most significant observations to be made on the instantaneous flowfields. Firstly, the spatial variation of these velocity components is significant and it leads to nonintuitive remarks. For example, on the instantaneous axial velocity field, there is a pocket of nonreversed flow inside the IRZ. The second observation is that the axial and radial velocity fields look qualitatively different from the azimuthal velocity component. This latter appears to be more turbulent-like and suggests an anisotropy of the scale and so a preferred direction. Both of these observations could impact the analytical and numerical modeling of turbulence and flow–flame interactions of swirling flames.

4.3 Flashback

One key issue and challenge of static stability and flame stabilization is flashback. This phenomenon can be described as the passage from a stabilized flame under normal operation to a flame anchored inside the injection unit, i.e., not in its normal operation location. The main issue associated with this phenomenon is that the flame is not located in its optimum performance location and can generate highly unsteady heat flux that can potentially melt certain injector components. A review of the state of the art of flashback studies is presented in Chapter 2. In this section, the flashback mechanism is discussed with respect to the configuration case study of this chapter. A sequence of flashback is depicted in Fig. 4.8 and now described.

Fig. 4.8 presents a transient sequence from a stabilized flame to a flashbacked flame. The sequence consists of nine snapshots taken every 0.15 ms. At t_1 the flame is stabilized robustly. At t_2, it is observed that a temperature peak is reached in the near-bluff-body left tip region. The origin of this local peak can be due to

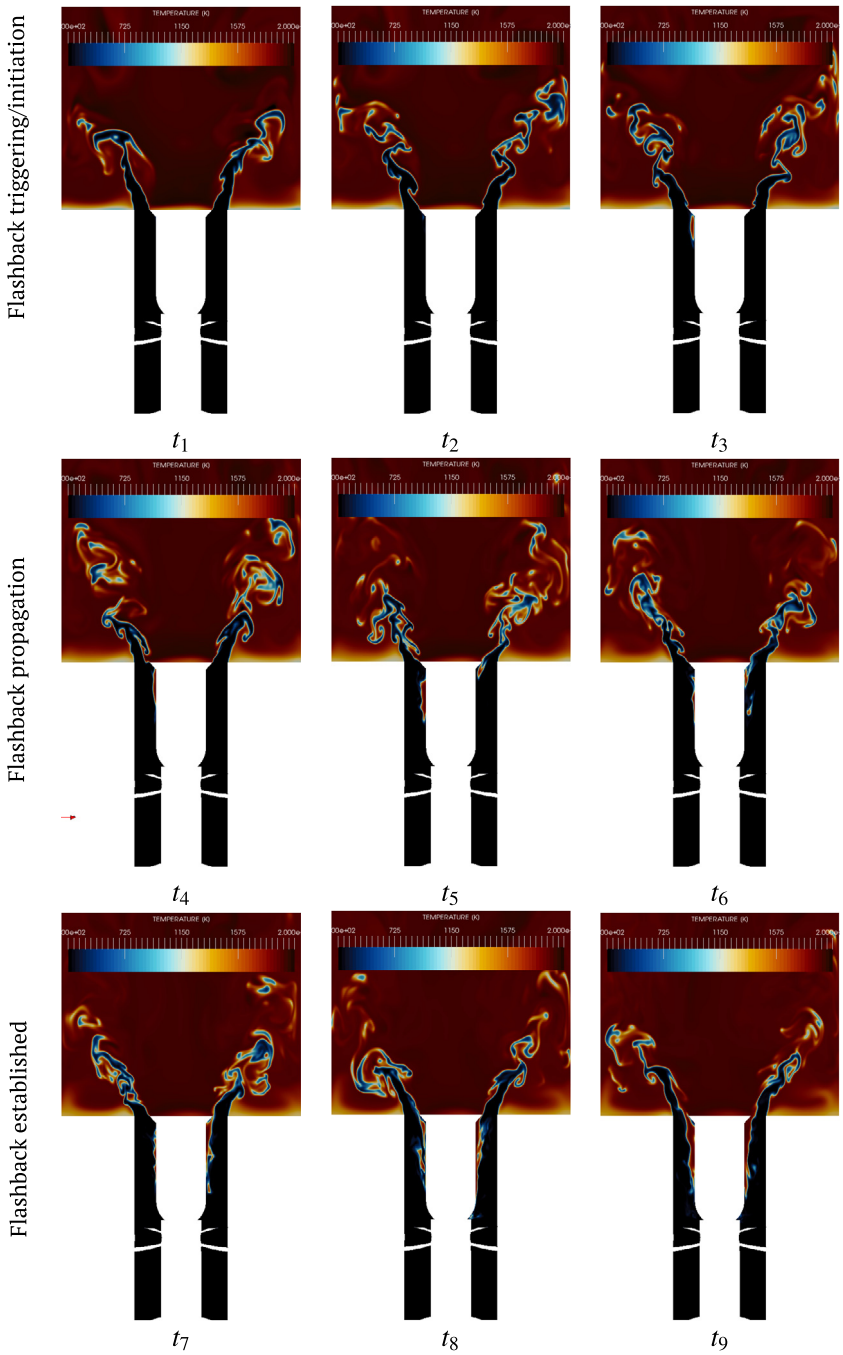

Figure 4.8 Flashback transient sequence. Numerical simulations of a sequence leading to flashback of the flame inside the injector.

multiple sources: (i) a velocity fluctuation superimposed on the low flow velocity region enables the transport of pockets of burned gases upstream, (ii) thermal diffusion is enabled in the boundary layer region of the bluff-body, and (iii) the heating/boundary condition of the bluff-body induces local heating. At t_3, this region is shown to expand mostly in the axial direction and to reach higher temperatures. At t_4, the flame is propagating upstream inside the injector through the low velocity region created by both the boundary layer at the bluff-body wall and the lower central swirling flow velocity. At t_5, the flashback zone spatially spreads and flashback is also initiated in the near-bluff-body right tip region. In addition to the mechanisms described for instant t_1, the generation of this initiation step could be the result of the propagation/transport of the left flashbacked region through the swirling motion. At t_6, reaction occurs on both sides of the bluff-body. From t_7 to t_9, one observes that flashback is established and the stabilized flame cannot be retrieved without external control. The analysis of the velocity field (not shown here) and the temperature field demonstrates that the low velocity region of the bluff-body wall is important. The role of the conical bluff-body extremity is also critical in flashback by (i) the generation of a high velocity region separating the burned gases from the inner injection unit low velocity region and (ii) its temperature. Consequently, this region can and needs to be optimized by design.

4.4 Lean blowout

This section investigates the evolution towards LBO with turbulence and flame-resolved simulations for the experiment of Cavaliere et al. [53]. These simulations include the swirler to capture the unsteady 3D velocity field and the chemistry is modeled with a single-step overall reaction. As presented in the first section, the grid requirement is such that the Kolmogorov scales in the fresh or the burned gases along with the flame front thickness are resolved throughout the computational domain. The corresponding structured grid consists of 236 million cells. A transient sequence corresponding to a step change of equivalence ratio Φ from 0.7 to 0.55 is modeled. Experimental and numerical data are compared and an overall good agreement is reached, except for the latest times of the sequence, for which possible causes are discussed. These data are used to support the analysis of the underlying mechanism. The analysis then focuses on the known LBO mechanisms from the literature in the present configuration. Multiple scenarios corresponding to several assumptions responsible for the evolution towards LBO are evaluated. These assumptions

include the roles of the precessing vortex core (PVC), acoustics, flame sheet holes, flame stretch, IRZ dynamics, and heat losses. In this section, each of these assumptions is briefly discussed based on key observations made from the experimental and numerical data. It is deduced that the process leading to LBO is associated with the convective motion of cooler combustion products towards the IRZ as the equivalence ratio is decreased. The mechanism leading to blowout in the present configuration is linked to the time required to fill the IRZ with those cooler burned gases.

4.4.1 Introduction

The modeling and the physical understanding of transient combustion phenomena for gas turbine engine combustors are two important coupled challenges. LES is needed to study these systems operating at high pressure where the chemical and flow scales at work hinder direct simulations. The use and development of LES subgrid-scale models is then a requirement. Turbulence and flame-resolved simulations at atmospheric conditions of 3D swirl-stabilized flames can enable that goal. In addition to the modeling challenge, the physical understanding of transient processes will enable future design optimization. In that context, the present section proposes to tackle selected aspects of these challenges: the LBO modeling with transient flame-resolved simulations. Blowout is defined as the observation by which the flame is blown away from the combustor. Blowoff is the total extinction of the flame by itself. In general, blowout and blowoff processes can be seen as separate phenomena because part of the flame is actually blown out while the other part is blown off. While the blowout of bluff-body flames has received significant attention Plee and Mellor [48], Shanbhogue et al. [49], research on LBO of swirling flames is less documented. The blowout of conical bluff-body flames has been investigated and detailed analysis of the flowfield in the flame stabilization zone obtained by PIV was carried out by Chaparro and Cetegen [345]. It was found that the blowoff equivalence ratio exhibits a dependence on the inlet flow acoustic modulation frequency. Blowoff characteristics of bluff-body-stabilized conical premixed flames with upstream spatial mixture gradients and velocity oscillations have been investigated by Chaudhuri and Cetegen [346]. With POD, the vortex shedding modes of a bluff-body-stabilized flame, including conditions near blowoff, were analyzed in Kostka et al. [347]. The dynamics of bluff-body flames were imaged by high speed flame imaging and the effects of local extinction prior to blowoff were observed by Tuttle et al. [348]. The effects of fuel stratification induced by fuel

injection on the transition of flames to blowout were studied in Kopp-Vaughan et al. [349].

Blowout of swirling flames has been investigated by high speed OH imaging, where the blowout events preceding the total extinction of the flame in the gas turbine model combustor were linked to the presence of cold reactant in the IRZ Muruganandam et al. [50], Muruganandam and Seitzman [51]. Cavaliere et al. [53] studied premixed, diffusion, and spray flames experimentally at conditions near blowoff. It was shown that the premixed flame changes shape prior to blowout; the diffusion flame exhibited holes in the flame front, occurring at higher frequencies upon approaching blowout. The diffusion and spray flames showed randomly occurring lift-off due to localized extinction. The lift-off height and events were also characterized and a Damköhler number collapsed the blowoff velocity data for all flames with reasonable accuracy. Using a high speed camera, the blowout limits have been characterized by varying the fuel/air ratio of a liquid-fuel gas turbine-derived burner in the diffusion flame mode in De Giorgi et al. [54]. Wavelet-based analysis of flame images was used to investigate local unsteadiness in the flame area. Numerical simulations of blowout, flashback, and flame position have been undertaken by Ganji and Ebrahimi [350]. Different equivalence ratios were studied and thermal coupling of the reacting flow with the solid structure of the combustor was taken into account. The temperature of the gas was shown to affect the blowout limit in an industrial dry low emission gas turbine in Sigfrid et al. [351]. Partially premixed swirling flames have been shown to be blown out due to excessive straining and due to entrainment of large amounts of oxidizer due to partial premixing in Santhosh and Basu [57]. The blowout phenomenon was studied by increasing the swirling flow rotation from zero to high values. It was shown to have a strong effect on the flame shape. A study has investigated extinction/reignition events occurring in a swirl-stabilized combustor and analyzed the interaction of these precursor events with the double helical mode of the vortex breakdown leading to blowout in Muruganandam and Seitzman [58]. The lift-off mechanism of swirl-stabilized premixed flames was investigated using PLIF, PIV, and OH* chemiluminescence in An et al. [352]. The authors observed that the lift-off process involved multiple coupled phenomena: local flame extinction near the flame base, the development of a helical PVC, and the total extinction of the flame base. In addition, the authors observed that the PVC increased the strain rate on the flame base, which eventually led to total detachment. The local extinction of the flame and this PVC flow feature impacted the strain rate on the flame base, leading to flame blowout. Numerical

simulations have also been used to capture blowout phenomena and describe the physics. Blowout sensitivity to different fuels using two-phase flow LES was recently conducted by Esclapez et al. [59,60]. The blowout phenomenon initially observed by Cavaliere et al. [53] was modeled with numerical simulations for the diffusion and spray flame cases in Tyliszczak et al. [61], Zhang and Mastorakos [62], Giusti et al. [63], Giusti and Mastorakos [64], but the premixed case has only been documented by one study as of today, see Nassini et al. [353].

An important aspect of the present section is firstly to investigate the known literature mechanisms and secondly to perform an analysis of the modeled transient sequence in order to describe the evolution towards LBO for the experiment by Cavaliere *et al.* Challenges associated with the latest time of the LBO sequence, i.e., the onset of LBO, are also discussed.

4.4.2 Results and comparison with experiment

Velocity field and flame shape

The validation and verification of the numerical procedure was carried out by comparing several quantities between experiment and simulation. The first aspect that is ensured is that the bulk velocity at the bluff-body extracted from the numerical simulation data matched the experimental bulk velocity at blowoff. In Fig. 4.9, the radial profiles of the three velocity components extracted at one millimeter above the bluff-body are plotted. The horizontal line corresponds to the experimental bulk velocities. The calculation of the bulk velocity from the left and right profiles of peak axial velocities confirmed that the simulation captured the experimental flow condition within 1%. Secondly, the instantaneous flame shapes were compared at two different representative time steps.

In Fig. 4.10, the experimental OH-PLIF data are compared with two instantaneous OH mass fraction fields. Two snapshots extracted from the transient simulation are compared with the statistically steady experiments respectively at equivalence ratio 0.7 and 0.61, which require to be cautious in the direct comparison of the data. A few key observations from the experiments can be made which are affirmed by the simulation. First of all, at the equivalence ratio $\Phi \simeq 0.7$, significant reactions occur in the outer recirculation zones (ORZs), as demonstrated by the levels of OH emission captured with OH-PLIF. In the center of the IRZ, the levels of OH in the simulations are slightly underpredicted. Secondly, at the equivalence ratio of $\Phi \simeq 0.61$, the reduction of OH levels in the ORZ is captured but the level does not reach the lowest level

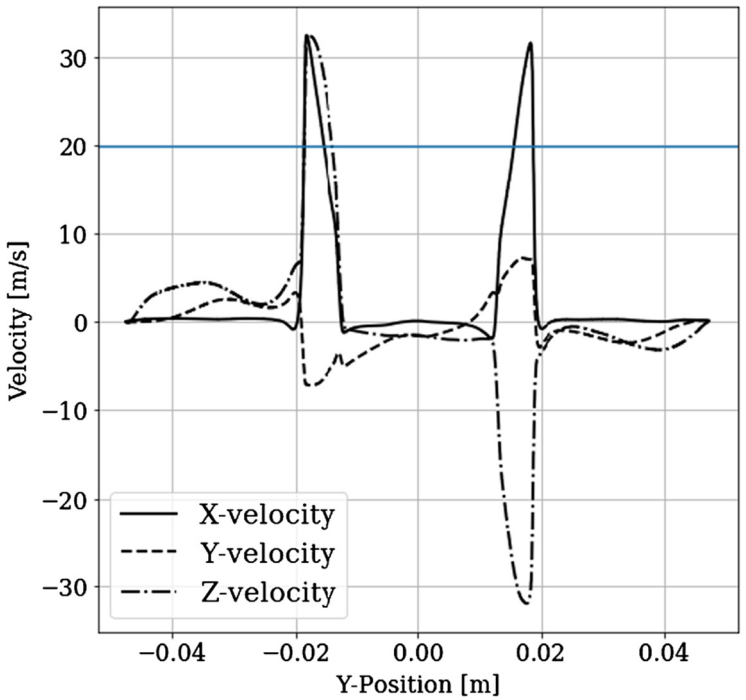

Figure 4.9 Setup geometry. Time-average velocity profiles extracted at 1 mm above the backplane in the reacting simulations. The horizontal line corresponds to the experimental bulk velocity calculated on the bluff-body annular passage.

seen in the experiments. For both equivalence ratios, the evolution of the flame front shape is qualitatively captured, as demonstrated by the wrinkling of the front by the largest scales, and pockets of fresh and burned gases are observed in both cases as well. Additional observations (not shown here) of the experimental flame images show that a characteristic wavelength is superimposed on the inner branch of the flame front, this latter possibly corresponding to a high frequency oscillation of the flame near the blowout limit. Moreover, the OH-PLIF experimental results show a global pulsation throughout the flame region where the levels of OH emission slightly changed. These two observations support a possible intermittent pressure oscillation at work in the combustor near blowout, which could not be confirmed due to the absence of pressure time trace experimental measurements and the low sampling rate of the OH-PLIF high speed imaging system with respect to this high frequency oscillation.

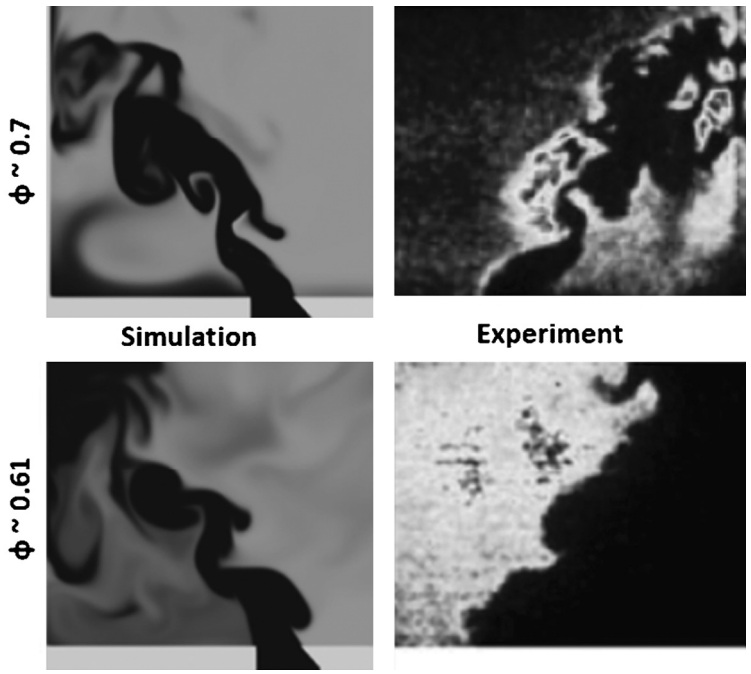

Figure 4.10 Flame shape comparison. Comparison of the instantaneous OH flame shape from simulations (left) versus experiments (right) at equivalence ratios of 0.7 (top) and 0.61 (bottom).

Transient sequence toward LBO

Next are compared in Fig. 4.11 the sequence of the a posteriori reconstructed OH mass fraction from the simulations (top two rows) and the OH emission from the OH-PLIF experiments (bottom two rows). The experimental and numerical data are taken at equivalent instants, with the time prior to LBO indicated in milliseconds. We first begin describing the experimental sequence. One observes that during the first four documented instants, there are significant variations of the OH field on the upper part of the flame between the sides and the centerline, and we see an alternating presence of flame ($t-40$ ms) or no flame ($t-25$ ms) in those regions. In addition, during these instants, the regions where OH emission is the highest are evolving upstream towards the bluff-body region, a feature also observed in the experimental OH* field line of sight integrated results of Cavaliere *et al.* At $t-20$ ms and beyond, the flame shape is strongly modified and the OH field is getting sparse and occurs on the centerline of the combustion chamber. A splitting of the upstream and downstream flame also takes place. The numerical simulations conducted enable to re-

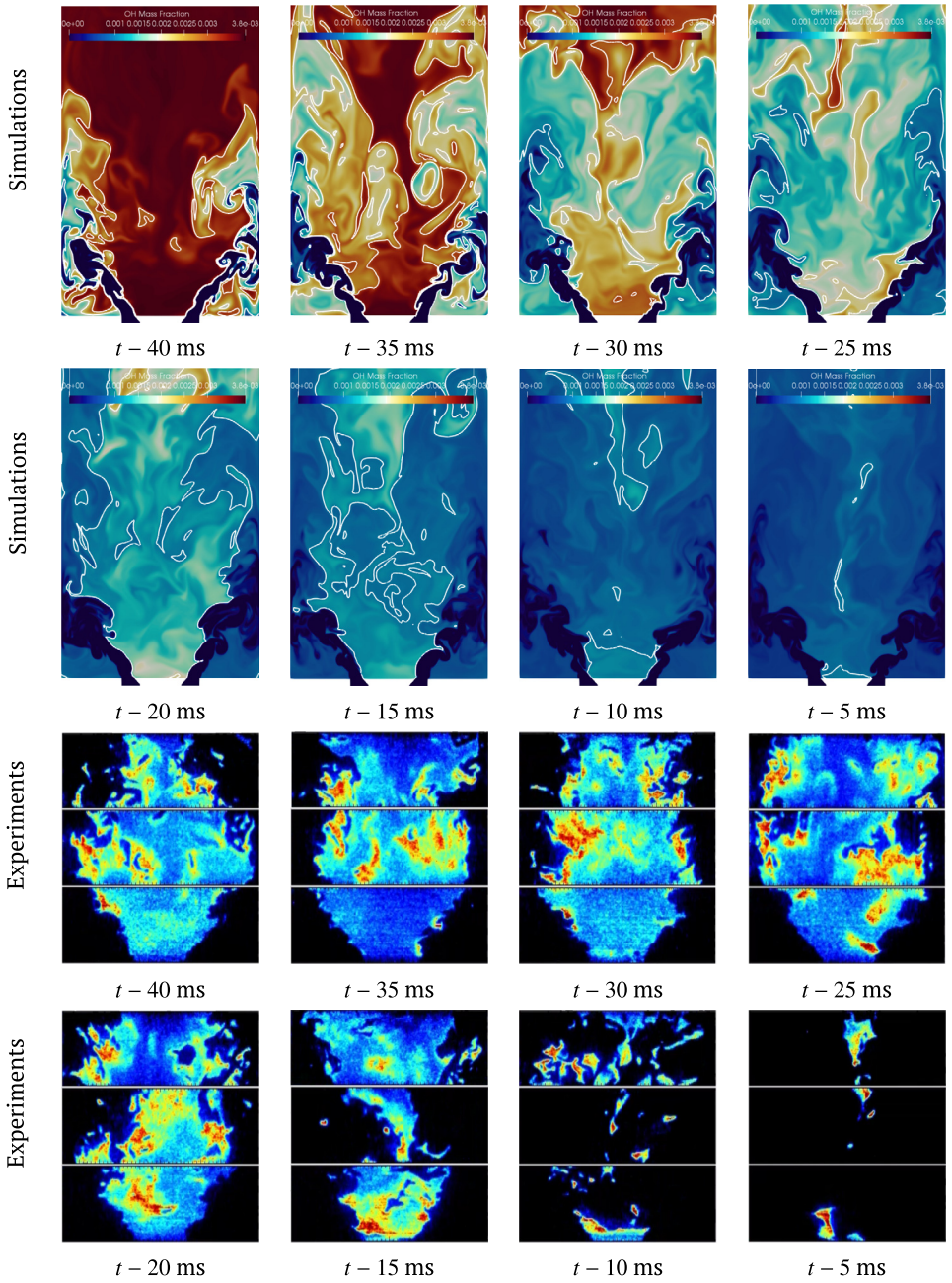

Figure 4.11 Comparison of experiment and simulations. Simulation (top rows) versus OH-PLIF experiment (bottom rows) results of the transient sequence evolving towards LBO showing the a posteriori reconstructed OH mass fraction. The global dynamics are also tracked with isocontours of the OH signal taken at three levels: 0.001, 0.002, and 0.003.

trieve most features of the experimental LBO process. First of all, the duration of the time sequence towards LBO is closely matched. It is 48 ms in the experiment. In the simulation, the LBO time is quantified by the time from the equivalence ratio step change to the time when the isocontour of OH mass fraction equal to 0.001 is not seen in the flowfield. This time is shown to be 50 ms. While the first four instants displayed in Fig. 4.11 have discrepancies with the experiments, this is attributed to the fact that the initial equivalence ratio between the experiment and simulation are different, i.e., 0.7 versus 0.61, respectively. The last four instants plotted in Fig. 4.11 show excellent qualitative agreement with the data. Indeed, the isocontours of the OH mass fraction show the splitting of the upstream and downstream flame pieces and the higher centerline levels of OH, as well as the evolution towards total extinction/blowoff, as shown by the evolution of the lowest isocontour of the OH mass fraction. These isocontours allow to capture the global dynamics of the documented experimental results.

Fig. 4.12 presents the pressure and OH signals inside the recirculation zone on the centerline at 60 mm above the bluff-body. These signals show the evolution toward LBO through the OH signal decrease. The pressure signal shows the transverse instability triggered during that transient sequence. The first time instant of the time sequence of Fig. 4.11 corresponds to 10 ms in Fig. 4.12. The OH time trace slope is reduced as reaching LBO as the equivalence reaches a value of 0.55. Other simulation results (not shown here) showed the link of this slope with the thermal wall BC temperature.

4.4.3 LBO physical mechanisms understanding

Observations

Several mechanisms that can lead to LBO have been identified in the literature. The present section summarizes the observations of those on the present configuration. The first mechanism is that of the PVC. In Stöhr et al. [52], the authors studied partially premixed swirling flames close to the LBO limit using chemiluminescence imaging, stereo-PIV, and OH-PLIF high speed measurements. Flame stabilization occurred in two regions: the helical region along the PVC on the inner shear layer and the flame base. The levels of strain rate influenced the zone where reaction took place such as in the highest strain region like the flame base where the flame was not robustly stabilized. It was concluded that the flowfield modification at the flame root could shift the LBO limit lower. This section demonstrated the importance of the local high strain rates due to the PVC as a local stage to blowout. In the present configuration, the DMD modes and frequencies of

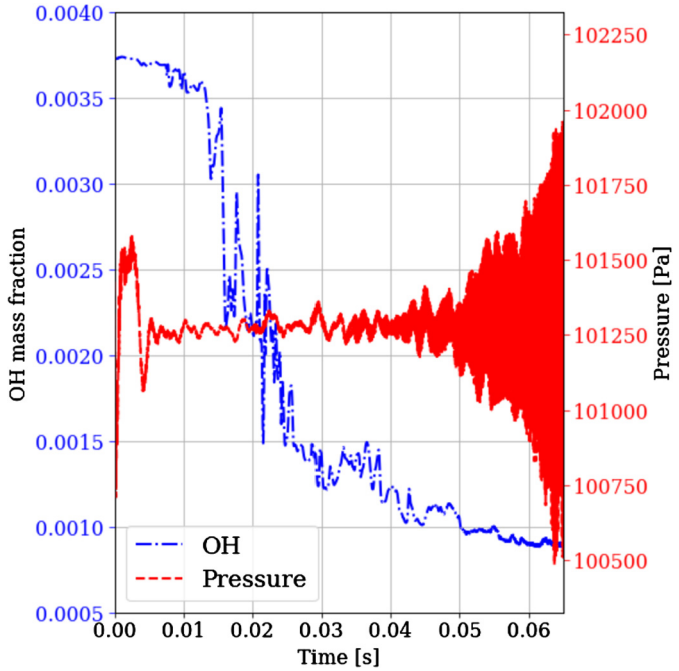

Figure 4.12 Time trace signals. Typical time traces of the OH mass fraction and pressure signals for a probe located 60 mm from the bluff-body inside the IRZ on the centerline.

velocities and temperature data did not show a mode that would correspond to a PVC, which is likely due to the central bluff-body hindering vortex core formation. Sequences of transition to blowout have been captured with high speed flame imaging, see Shanbhogue et al. [49], Chaudhuri et al. [354]. It was observed that a partial or total extinction of the flame sheet occurring along the shear layers plays a key role, leading to blowoff for bluff-body flames. These holes can be due to flame stretch (flow strain, curvature, and dilatation) or combustion product pockets crossing the flame front. Such holes as prestage to LBO along the flame front were not observed in the present swirling flame case, see Fig. 4.11.

Another mechanism possibly triggering blowoff is that of strong acoustic waves which could cause the reaction to be cut or create LBO triggering velocity fluctuation, as seen in Prieur et al. [355]. This phenomenon was not observed in the present configuration. The transverse mode identified with DMD during the evolution toward LBO is plotted in Fig. 4.13. The associated oscillating frequency of this mode is 7850 Hz. The observed transient growth was not shown to impact the LBO, whereas acoustics have been shown to be a precursor of LBO, see Nair and Lieuwen [356]. Sim-

Figure 4.13 DMD pressure mode distribution. DMD pressure transverse mode distribution and associated oscillation frequency.

ilar pressure transient growth was here observed for all boundary conditions tested near the LBO limit. Whereas the global trend of the evolution to LBO was captured here, the ultimate extinction events were not captured, possibly due to the following reasons: (i) the transients' thermal boundary conditions were not taken into account as the temperature inside the combustion chamber decreased, and (ii) the effects of complex chemistry on the heat release and hence on the temperature distribution were not taken into account.

Mechanistic description

The mechanistic description of the evolution towards LBO is now carried out. A key observation made from the transient sequences of temperature and OH mass fraction is that as the equivalence ratio is decreased from 0.7 to 0.55, the temperature of the chemical reaction occurring on the swirling jets is consequently reduced, and the combustion products, now at lower temperature, are convected downstream and transported toward the centerline due to the IRZ dynamics. These combustion products are then convected back upstream toward the bluff-body by the reversed flow of the IRZ. In other words, the convection of decreasing temperature combustion products from the swirling jet to the IRZ generate a cooler IRZ, sustaining a moderate reaction of the upstream inlet fresh reactants. One can expect that this dynamic imposes a loop where the temperature and the heat loss to the walls are the key driver. It is expected that this loop leads to a complete blowoff which is not captured in the present simulation, possibly due to the CPU time required to capture the entire dynamics and due to current model limitations. Similar challenges in capturing the latest events of LBO have been reported recently in the same premixed configuration by Nassini et al. [353].

To support this mechanistic description, time-dependent integrated OH mass fractions were obtained by spatially averaging over the longitudinal x and transversal y directions of the square combustor. The results are plotted in Fig. 4.14. The top figure corresponds to the quantity $\overline{OH}(x,t)$ and the bottom figure to $\overline{OH}(t,y)$. The top figure shows a pattern of succession of oblique stripes inclined toward the right side, corresponding to the convective motion of the OH field toward the outlet of the computational domain. The bottom figure of Fig. 4.14 shows a pattern where a series of oblique stripes point toward the center. From left to right in the top figure of Fig. 4.14, the reduction of OH mass fraction reflecting the evolution towards LBO is clear. The bottom figure of Fig. 4.14 shows the same trend as time increases. Finally, it is interesting to evaluate the total duration of this dynamic. The most direct approach is to form a convective time as the ratio of the reversal centerline velocity to the IRZ distance where the cooler combustion products are propagating towards the bluff-body. This estimated time is equal to $\tau_{cv} = d_{IRZ}/u_{IRZ}$, which leads to a value of $\tau_{cv} = 0.055/5.0 = 11$ ms. In other words, there are multiple convective times of the cooler combustion products required prior to blowoff, which is supported by the number of stripes observed in Fig. 4.14.

4.4.4 Conclusions

This section investigated the evolution towards LBO with unique swirler-induced turbulence and thermal flame front-resolved numerical simulations. Though the ultimate LBO event was not captured, the sequence toward LBO enabled a mechanistic description. This latter indicated that as the equivalence ratio is decreased, the lower temperature combustion products from the swirling jets are convected towards the IRZ. In that zone, the reversal flow imposes those cooler gases to flow toward the flame and reduces further the chemical reaction. The present description points out the key roles of the swirling flow velocity field and its consequence on the heat transfer inside the IRZ in driving the LBO physics. The consequences of the present findings in terms of design are straightforward and methods keeping the IRZ at the highest temperature possible in the lean limit should be developed.

4.5 Transient to limit cycle

In this section, the focus is on the transition to instability, which has received little attention in the literature. These transients have to be studied further in future works. Most combustion

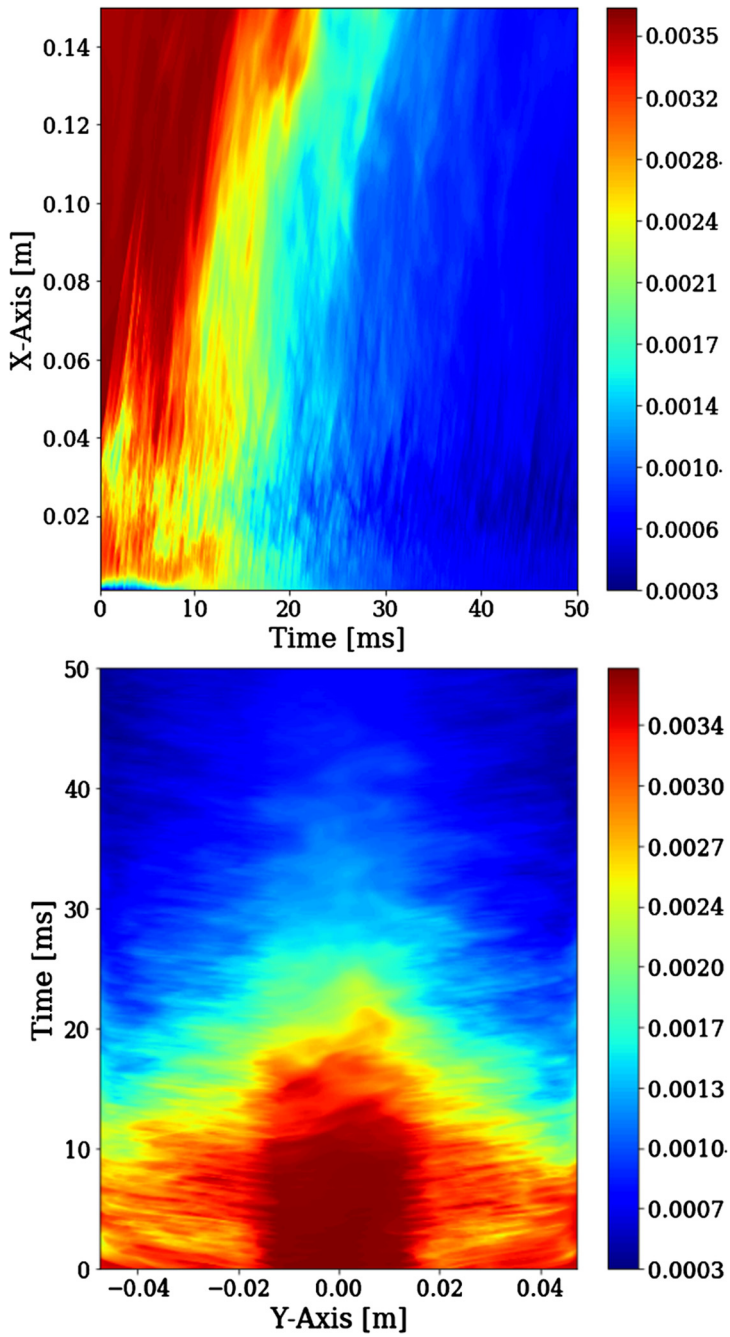

Figure 4.14 Averaged OH fields. Spatially averaged OH fields with superimposed lines used to extract convective times associated with the IRZ dynamics. Top: $\overline{OH}(x,t)$ field. Bottom: $\overline{OH}(t,y)$ field. The evolution over 1000 snapshots is plotted.

instability studies have been undertaken for unsteady combustion, i.e., for the limit cycle, and only a few studies have focused on transient regimes. The present section is devoted to transient (oscillating) growth that reflects a growing instability. This section takes into account two examples: (i) a longitudinal instability studied experimentally and (ii) a transversal instability studied numerically in the configuration of the study case presented at the beginning of this section.

4.5.1 Longitudinal mode

It is first required to review the state of the art. In the experiments of Broda et al. [357] and Seo [358], the inlet temperature of the premixture was shown to impact the transition from stability to instability. Numerical simulations of the experiment performed by Huang and Yang [359] confirmed that the flame structure changed at an inlet temperature threshold with a transition to instability. The effects of an increase of the equivalence ratio on transition to instability have been investigated by Gotoda et al. [360], Therkelsen et al. [361], Taamallah et al. [362]. The transition to instability has been investigated by Nagaraja et al. [363], where numerical methods to capture transient growth rates were discussed. The present section presents elements of analysis of the transition by making use of DMD directly on experimental flame data where different regimes of oscillation were observed, see Palies et al. [364]. DMD is a data-driven postprocessing algorithm for numerical simulation or experimental data. It provides a robust identification of key features when associated with other diagnostics to gain physical insight, as it decomposes the data into a set of spatial modes and corresponding frequencies and growth rates. DMD has been used by Bourgouin et al. [365] to study azimuthal acoustics modes in a system of 16 swirling injectors, where DMD was applied directly to the light emission of the flames to identify the nature of the azimuthal mode: rotating or standing. Sayadi et al. [366] investigated the transient regime of a flame exhibiting oscillation to capture the growth rate. Motheau et al. [281] has applied DMD to filter data and capture oscillation frequencies in an aeroengine combustor presenting self-sustained entropy instability. DMD was also applied to the swirling flowfield in the work of Labry et al. [367], where transition from stability to instability was experimentally investigated. Three regimes of oscillations were characterized by Palies et al. [364,213] in the LSI-LBNL-Cheng configuration: stable, local transient to instability, and limit cycle, each corresponding to a unique equivalence ratio. Recently, the transient thermal heat transfer at the combustor's wall has been investigated by Bonciolini et al. [368]

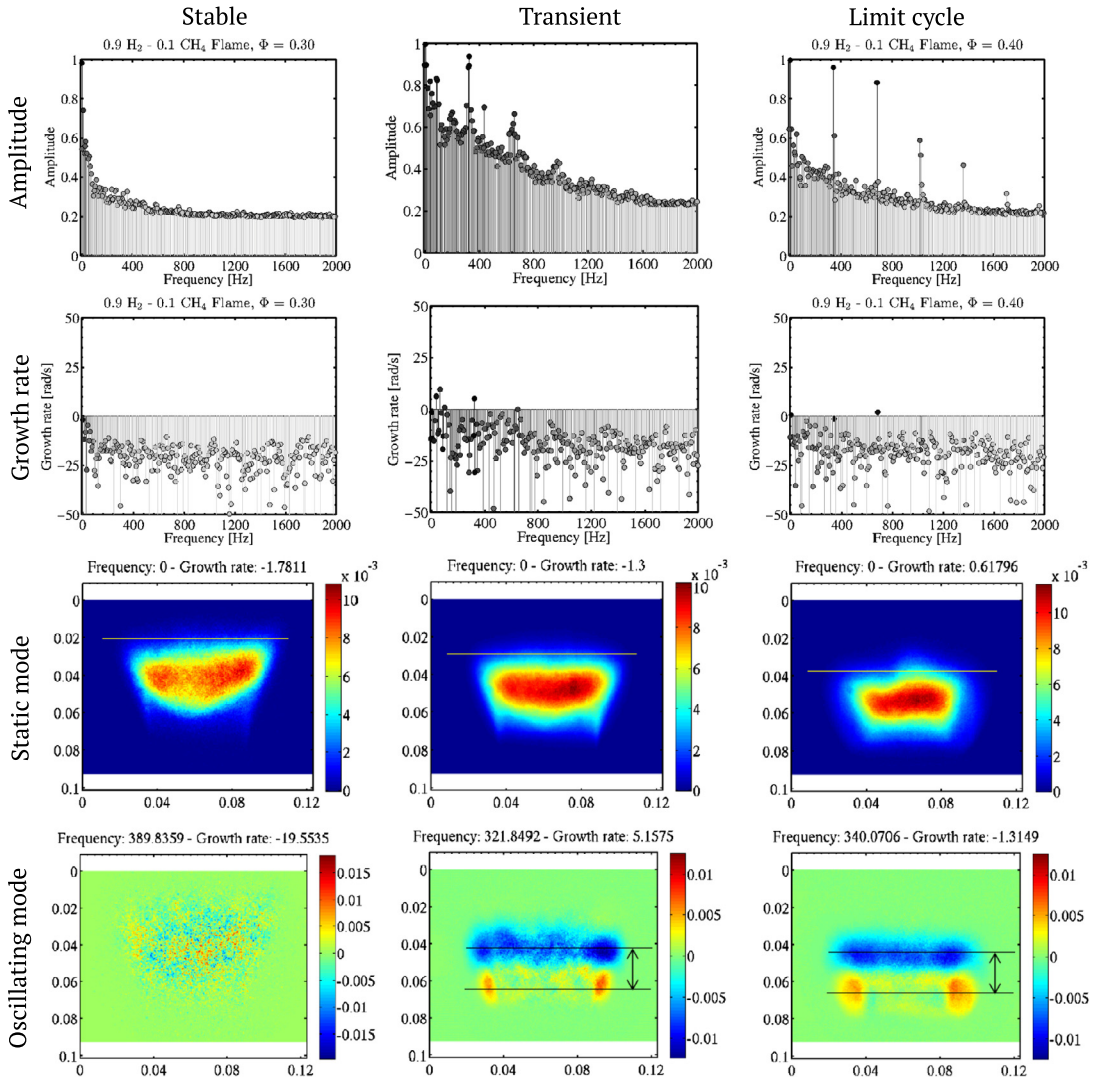

Figure 4.15 Comparison of DMD flame data results. Stable, transient, and limit cycle regimes DMD spectra and DMD modes. Figures were taken from Palies et al. [213].

for swirl-stabilized combustors. This article documented an experimental study where a change of the flame shape was induced by a wall temperature increase.

The use of DMD on the flame images obtained in the LSI-LBNL-Cheng configuration led to the spectra plotted in Fig. 4.15, see Palies et al. [213]. The amplitudes (a) and the growth rates (b) are plotted as functions of the frequency f. It is observed that the

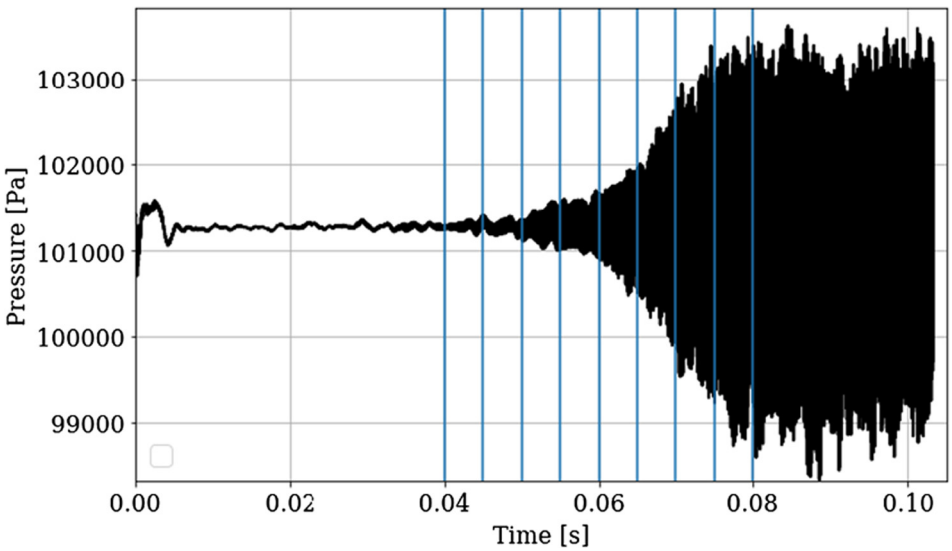

Figure 4.16 Pressure time trace of the transient toward the combustion limit cycle. Pressure probes on the centerline inside the IRZ taken at 60 mm above the bluff-body.

spectrum exhibits a peak frequency at $f = 321.8$ Hz with a growth rate of $\sigma = 5.15\ \text{rad}\,\text{s}^{-1}$. This mode is associated with the transient oscillation inside the system. Indeed, this is the only mode close to the FFT pressure signal frequency with a positive growth rate. Other modes in the spectrum near the frequency of oscillations are damped and feature a negative growth rate.

4.5.2 Transversal mode

The case of transverse instability is now documented based on the numerical configuration case study. A transient sequence toward a transverse combustion instability is described. Each time instant is separated by 5 ms. The objective of this sequence is thus not to describe the dynamics over one cycle. The objective is more to describe the features over the entire transient to the limit cycle. The temperature and the pressure fields are discussed. They are depicted in Fig. 4.18. This sequence of obtained snapshots is typical of the time series plotted in Fig. 4.16 showing the transient growth of the pressure signal towards the limit cycle. The sequence of snapshots and the corresponding pressure signal can be split into three stages: stable (0 to 40 ms), transient growth (40 to 75 ms), and the limit cycle (beyond 75 ms). In Fig. 4.16, several vertical lines are sketched to indicate the time instants where the nine snapshots of Fig. 4.18 are taken.

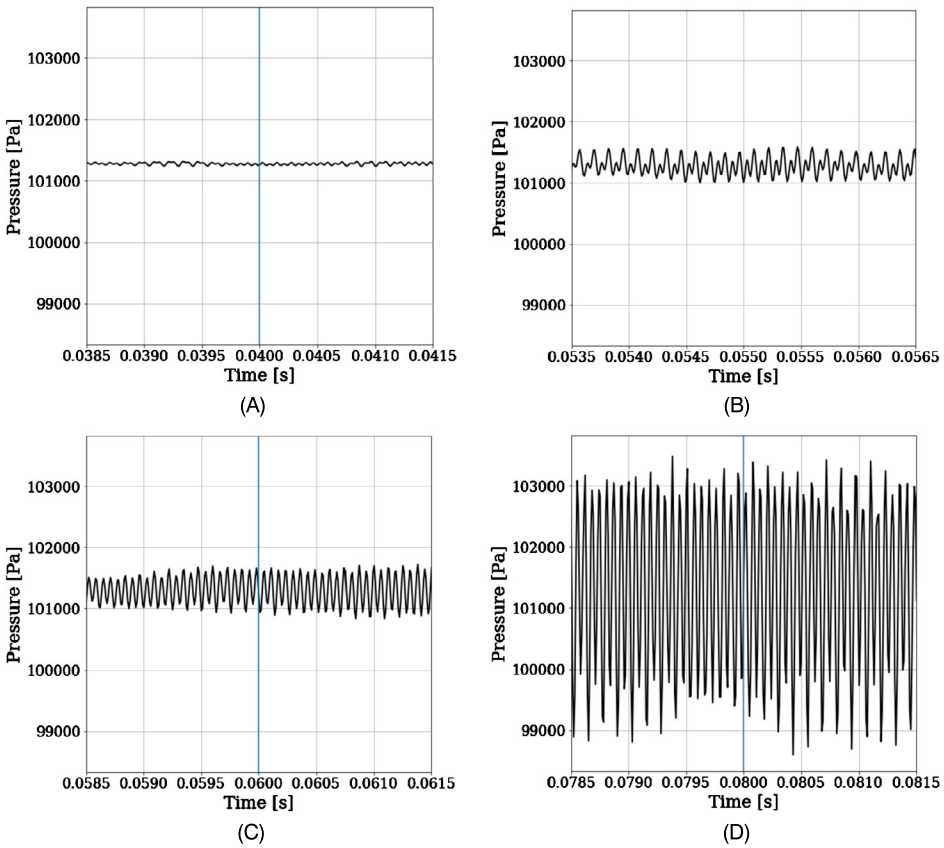

Figure 4.17 Close-up views of the pressure signals. Pressure probes on the centerline inside the IRZ taken at 60 mm above the bluff-body.

Several time window taken from the pressure signal of Fig. 4.18 are given in Fig. 4.17 to zoom in on the signal content. Fig. 4.17A clearly corresponds to a stable pressure time trace without any specific frequency of oscillation and a constant amplitude. Fig. 4.17B corresponds to the transient growth. There is twice the same frequency at work for this signal with a phase lag, and a different amplitude. This signal suggests that there are two distinct pressure modes at work, with the same frequency. Fig. 4.17C shows a signal with a single well-defined oscillation. Fig. 4.17D presents similarities with a higher amplitude envelope characteristic of the limit cycle.

We now describe the time sequence of temperature and pressure fields at nine successive instants separated by 5 ms. The stable state corresponds to the instant t_1 of the sequence, where the

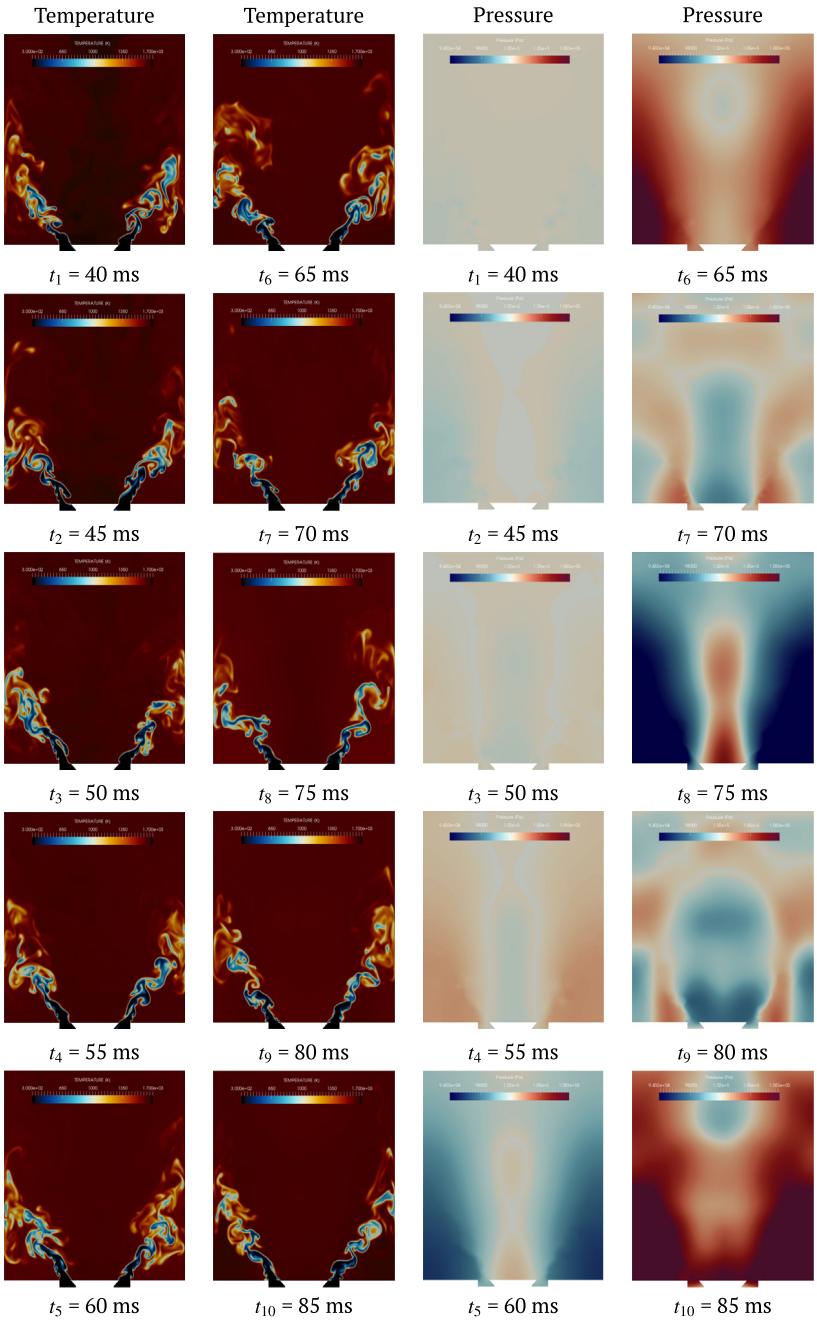

Figure 4.18 Transient growth toward a transverse combustion instability. Numerical simulations of a sequence leading to the limit cycle of a transverse combustion instability. Time instants are separated by 5 ms.

pressure field is spatially uniform and nearly at atmospheric conditions. The observed time trace undulation corresponds to the transverse mode noise, the residual nonthermoacoustically coupled acoustics mode. This first snapshot corresponds to the time instant 40 ms of the time trace in Fig. 4.16 and is materialized by the first superimposed vertical line. At this instant, there is no direct impact of this undulation on the flame front. The transient growth corresponds to time instants t_2 up to t_8. Several observations have to be highlighted. The pressure snapshots present two regimes: a regime of transverse mode only in the first part of the transient growth and a regime of transverse-longitudinal mode in the second part of the transient growth. The transition between these two modes occurs approximately between 55 and 60 ms, when the oscillation is being coupled. It is supported by the time trace signal of pressure at those time windows, see Fig. 4.17B, where the oscillations are being coupled. The full coupling is observed in Fig. 4.17C. During the first regime, clear high frequency shedding is observed from the dump plan along the outer branches of the swirling flame. This feature is associated with the transient regime toward the instability. The pressure fields during the transient also allow to distinguish the pressure mode at work. In Fig. 4.18, one observes that the pressure is mostly varying in the transverse direction, see instants 45 and 50 ms. At 55 ms, one can see a transversal-longitudinal coupling. Between 55 ms and 75 ms, the mode is fully coupled. The flame front vortex shedding is less clear as the pressure of the oscillation is increased and as these pressure oscillations induce local transverse velocity fluctuations that will affect the coherence of the vortex shedding. The limit cycle is a fully coupled transverse-longitudinal (1T-1L) mode where the pressure snapshots clearly show the pressure variation in both transversal and axial directions. The limit cycle also presents a strong global transversal motion of the flame front induced by the 1T-1L acoustic mode.

5 Fundamental mechanisms and link between steady and unsteady combustion

5.1 Static and dynamic stability link

Static stability corresponds to a regime where the flame is stabilized, i.e., a regime avoiding blowout and flashback. Dynamic stability corresponds to combustion instabilities. In general these two issues are investigated separately. It is proposed here to link those through the flame surface speed budget, the kinematic relationship uniting flame, flame surface, and flow speeds. It has been

discussed in Chapter 3 that static and dynamic stability are intrinsically linked through the flame surface speed budget. The static component of the flame surface speed budget drives the flame position in a combustor because this budget balances the flow and flame speeds. The dynamic stability is described by the fluctuation components in the governing equations or in the flame surface speed budget splitting. Static and dynamic stability are linked through the equation(s) that link(s) static and dynamic components. For the flame surface speed budget, there are indeed three equations: (i) a steady/static flow relationship, (ii) a coupling equation, and (iii) an equation for the dynamics, i.e., for the fluctuations.

There are several ways and methods to uncouple static and dynamic stability, i.e., to suppress dynamic stability. It is worthwhile to summarize the key approaches. The flame location is the first one, as it drives the phasing between unsteady fluctuations and subsequent transient growth toward the limit cycle, see Palies et al. [213]. The length of the combustor has also been shown to be a key driver of combustion instability for the longitudinal velocity coupled mode, see Palies et al. [369], Taamallah et al. [370]. The swirler location has been shown to affect the dynamics of swirling flames for longitudinal modes, see Richards and Yip [371], Straub and Richards [372], Komarek and Polifke [373], Palies [180].

5.2 Static stability

The steady power or combustion heat released in Watt, for a fully premixed flame, is a direct function of the flame speed, flame surface, and fuel mass flow. It is convenient to link these quantities as follows. The thermal power or heat released assuming complete combustion inside a combustion chamber can be expressed as

$$\mathcal{P} = \dot{\mathcal{Q}} = \dot{m}_f \times \Delta h_f^0, \tag{4.14}$$

where the fuel mass flow $\dot{m}_f$ is equal to the product of density ρ_f of the fuel, the axial velocity u of the stream, and the section area S. For the case of a planar flame propagating at S_L^0, the mass conservation writes $\rho_f u S = \rho_f S_L^0 A$, where A is the flame surface area. In addition, one has $\rho_f/\rho = Y_f$, so that for a planar flame one has

$$\mathcal{P} = \rho Y_f S_L^0 A \Delta h_f^0. \tag{4.15}$$

For a 3D flame, this expression holds assuming a constant displacement speed S_d over the flame surface A, and it writes

$$\mathcal{P} = \rho Y_f S_d A \Delta h_f^0. \tag{4.16}$$

This expression can be recast with the equivalence ratio Φ of the premixed flame making use of $\Phi = (Y_f/Y_{air})/s_a$ and assuming that the mass fraction of fuel is negligible. One obtains

$$\mathcal{P} = \rho \Phi s_a S_d A \Delta h_f^0. \tag{4.17}$$

Without assuming that the displacement speed is constant over the flame surface, this latter expression becomes the instantaneous thermal power:

$$\mathcal{P}(t) = \Phi s_a \Delta h_f^0 \int_A S_d(dA(x, y, z, t))dA. \tag{4.18}$$

These expressions indicate that the thermal power is a direct function of (i) the equivalence ratio Φ, (ii) the fuel, and (iii) how the mixture burns. It enables to conclude that optimization of the flame surface, understanding of the flame speed, and its measurements are key elements of future design. The consequences in term of fuel burn will be discussed in the conclusion and future perspective of this book.

5.3 Dynamic stability

Dynamic stability or combustion instabilities are largely documented by investigating the associated unsteady heat release generated. It is specifically reviewed in Chapter 5. Unsteady heat release is made up of two contributions: the fluctuating flame surface area and the fluctuating flame speed. They are discussed here. We first start with the decomposition of the global unsteady heat release or thermal power q'/q_0, written as

$$\frac{q'}{q_0} = \frac{A'}{A_0} + \frac{S'_{d,0}}{S_{d,0}}. \tag{4.19}$$

In this expression, the variation of flame surface area of the flame is given by A'/A and the variation of flame speed by $S'_{d,0}/S_{d,0}$. This global expression is obtained assuming an overall flame speed of the entire flame surface. In practice with numerical simulations, Eq. (4.18) should be used to determine the instantaneous power by knowing the flame speed at every flame surface element. One first derives an expression for the unsteady flame surface area assuming that the considered swirling flame follows such dynamics at low modulation amplitudes. The flame surface area fluctuating term can indeed be expressed as a truncated cone whose length equal to the flame length and outer radius is modulated. The inner radius is here assumed to be constant as the flame is nearly

attached to a center bluff-body. The instantaneous lateral area of a truncated cone is

$$A(t) = \pi \times [R(t) + r(t)]\sqrt{L_f(t)^2 + [R(t) - r(t)]^2}. \tag{4.20}$$

The static component of the flame surface is given by the lateral area of a truncated cone and writes

$$A_0 = \pi \times (R_0 + r_0)\sqrt{L_{f,0}^2 + [R_0 - r_0]^2}. \tag{4.21}$$

One next makes use of the following relationships to determine A': $L_f = L_\Sigma \cos\alpha$ and $R^2 + L_f^2 = L_\Sigma^2$, where the angle α is defined as the angle between the flame front and the vertical axis. Subtracting the instantaneous $A(t)$ to the static component A_0, one obtains the fluctuation

$$\begin{aligned} A'(t) = \pi &\left[L_f(t)\tan\alpha(t) + d/2\right]\left[L_f(t)\left(1 + \tan\alpha(t)\right)^{1/2}\right] \\ &- \pi\left[L_{f,0}\tan\alpha_0 + d/2\right]\left[L_{f,0}\left(1 + \tan\alpha_0\right)^{1/2}\right]. \end{aligned} \tag{4.22}$$

One can then write the ratio of unsteady fluctuation of $A'(t)/A_0$ as

$$\begin{aligned} \frac{A'(t)}{A_0} = &\left[\left[L_f(t)\tan\alpha(t) + d/2\right]\left[L_f(t)\left(1 + \tan\alpha(t)\right)^{1/2}\right]\right]/ \\ &\left[\left[L_{f,0}\tan\alpha_0 + d/2\right]\left[L_{f,0}\left(1 + \tan\alpha_0\right)^{1/2}\right]\right] - 1. \end{aligned} \tag{4.23}$$

For the fluctuating displacement speed, the derivation is now carried out by considering global quantities averaged over the flame surface. One begins with coupling the expression of the static flame speed and the fluctuating displacement flame speed ratio obtained in Chapter 3 and expressed as

$$\frac{S'_d}{S_{d,0}} = \frac{u_0(u' - w_s'^x)}{u_0^2 + v_0^2 + w_0^2} + \frac{v_0(v' - w_s'^y)}{u_0^2 + v_0^2 + w_0^2} + \frac{w_0(w' - w_s'^x)}{u_0^2 + v_0^2 + w_0^2}. \tag{4.24}$$

After some manipulations, this equation can be written as

$$\frac{S'_d}{S_{d,0}}\Big/\frac{u'}{u_0} = \frac{1 - w_s'^x}{1 + \frac{v_0^2}{u_0^2}} + \frac{\frac{v'}{u'} - w_s'^y}{\frac{v_0}{u_0} + \frac{u_0}{v_0} + \frac{w_0^2}{u_0 v_0}} + \frac{\frac{w'}{u'} - w_s'^z}{\frac{w_0}{u_0} + \frac{u_0}{w_0} + \frac{v_0^2}{u_0 w_0}}. \tag{4.25}$$

Gathering the previous expressions for the unsteady flame surface and the unsteady displacement speed leads to an expression for the unsteady heat release.

6 Technologies and control for flame stabilization and combustion instability

There are many technologies and methodologies of control both for flame stabilization (static stability) and combustion instability (dynamic stability). In this section, a literature review of these technologies and methodologies is conducted. In addition, the effects of swirler position, swirler geometry dimensions, operating conditions, the equivalence ratio, and fuel are discussed.

6.1 State of the art

This section discusses the flame stabilization and the dynamic stability of canonical flames, including laminar and turbulent flames. The case of laminar flames includes conical and bluff-body flames. The case of turbulent flames includes jet, bluff-body, and swirling flames. We review here the mechanisms, observations, and results from the literature. It is worthwhile to note that in practice, the approach to obtain static and dynamic stability for a premixed system over a given envelope of operation should combine existing active and/or passive control methods, resulting in a significant but reachable optimization procedure.

6.1.1 Laminar flames

The case of canonical laminar flames is now documented. This configuration has been widely studied for various reasons. First, it is a canonical configuration for the measurement of flame speed, such as by Vagelopoulos and Egolfopoulos [374], and for the validation of diagnostics measurements, as the flame structure is well characterized in that case, see Bouvet et al. [375]. The laminar conical flame is stabilized aerodynamically and the flame speed balances the flow speed in a manner so that the flame surface speed is zero. The tip of the conical flame presents a certain flame curvature modifying the flame speed which is associated with the centerline flow velocity only as on the centerline the radial component of the flow is zero. In addition, a characteristic feature of conical flame is the superimposed buoyancy effect, see Bédat and Cheng [376]. The laminar conical configuration has been investigated for various different conditions, including pressure, preheat temperature, fuel, fuel blend, and inlet mixture, for oxycombustion. For combustion dynamics, there are considerably fewer studies. Pioneering studies have focused on flame dynamics, see Bourhela and Baillot [302], Ducruix et al. [128] for the unconfined case and Karimi et al. [377] for the confined case. The configuration with combustion instability was investigated by Noiray et al.

[378]. Bluff-body laminar flames are less documented. Pioneering studies have been documented by Durox et al. [136].

6.1.2 Turbulent flames

Turbulent flames, including jet flames (turbulent conical), bluff-body flames, and swirling premixed flames, are now reviewed with respect to static and dynamic stability. Turbulent conical jet flames in premixed cases have been significantly documented. Lyons [379] reviewed the understanding of turbulent, lifted hydrocarbon jet flames and the conditions under which they stabilize. The authors reviewed the experiments which focused on the importance of several effects: partial premixing, edge flames, local extinction, streamline divergence, and large-scale structures. Mansour [380] investigated the stability characteristics of partially premixed turbulent lifted methane flames. Lifted, attached, blowout, and blowoff regimes were studied. The authors concluded from the experimental measurements that the mixture fraction field of the stabilization region was characterized by a certain level of mean and RMS fluctuations, suggesting that the stabilization mechanism was likely to be controlled by premixed flame propagation. An experimental investigation of the application of fractal geometry concepts in determining the turbulent burning speed in the wrinkled flame regime and responsible of flame stabilization was carried out by Smallwood et al. [381]. The article of Gülder et al. [382] focused on the flame front surface characteristics (wrinkling, fractal parameter) of turbulent premixed propane–air combustion for multiple conditions, i.e., nondimensional turbulence intensity and Reynolds number. The influence of the Damköhler number on the average thickness of conical turbulent premixed methane–air flames was examined experimentally by Boukhalfa and Gökalp [383]. The measurements included flame height and average flame thickness deduced from centerline and transverse evolutions of the mean density. The variations of the average flame thickness with respect to large and small eddy Damköhler numbers and the global density ratio were measured and discussed. Cheng and Shepherd [384] investigated the effects of burner geometry on premixed turbulent flame propagation experimentally by studying the turbulent transport, turbulence production, and burning rate in three flame configurations: bluff-body, conical, and swirl flame. The authors concluded that turbulence transport processes were sensitive to the flame geometry but the burning rates and turbulence production were not.

For bluff-body flames, many studies have focused on static and dynamic stability. Pioneering visualizations of bluff-body turbu-

lent flames with Schlieren diagnostics have been documented by Zukoski [385] for various bluff-body geometries and various turbulence intensities. These visualizations enabled the observations of flame wrinkling due to turbulence and the fact that the effect of turbulence has a limited effect on the static flame front. This second observation supports the theoretical analysis undertaken in Chapter 3. The stabilization of bluff-body premixed flames has been investigated theoretically by Kundu et al. [386], while the correlation was determined by Plee and Mellor [48]. In the latter article, time scales associated with turbulent mixing, homogeneous chemical kinetics, liquid droplet evaporation, and fuel injection were quantified for LBO. The obtained correlation linked the combustor pressure, inlet temperature, air velocity, flameholder geometry, fuel type, and injector size using data obtained from three different bluff-body stabilizers that simulate the same fundamental combustion processes of both conventional and advanced prevaporizing-premixing gas turbine combustors. The article of Michaels and Ghoniem [387] investigated the interaction between the flame structure, the flowfield, and the coupled heat transfer with the flameholder of a laminar lean premixed CH_4–air flame stabilized on a heat conducting bluff-body in a channel. This paper demonstrated the impact of heat losses to the flameholder on the flame–flow feedback mechanism in lean premixed flames. Turbulent bluff-body flames have also been investigated at near-blowoff conditions experimentally by Chaudhuri et al. [388], Kariuki et al. [389]. Balachandran et al. [141] investigated the nonlinear response of turbulent premixed bluff-body flames to imposed inlet velocity oscillations. Chaparro et al. [390] determined transfer function characteristics of such propane–air-fueled flames.

6.1.3 Control methods for flame stabilization

There are two main methods/technologies for premixed flame stabilization: mechanical and nonmechanical methods. The former include all types of aerodynamic devices, i.e., bluff-bodies, swirlers, and dump combustors. They have been used for a long time in many combustion system applications. They are reliable and dependable. Their main disadvantages are that they are neither adaptive nor time-dependent nowadays, i.e., they cannot change their shapes or position as a function of time. The second category of flame stabilization tools has to be seen as complementing the previous ones as they are not a flame stabilization technology by themselves. This category includes plasma and laser sources. They are additions to existing technologies.

Table 4.3 Technologies for the control of flame stabilization.

Technology	Principle	Pros	Cons
Aerodynamics	Swirler-stabilized IRZ	Robust Mechanical	Not time-dependent
Laser	Laser beam focus	Time-dependent Localized	Location
Plasma	Rapid pulse plasma ignition	Time-dependent Localized	Location

They can enhance flammability limits, enable reignition, mitigate combustion instability, or modify pollutant emissions. Ju and Sun [71] has reviewed plasma-assisted combustion to improve engine performance, increase lean-burn flame stability, and reduce emissions. Flammability limit extension of lean premixed swirling flames has been undertaken by Barbosa et al. [270], where the effects of several parameters were studied: pulse repetition frequency, global flow rate, and electrode location. A major effect of plasma discharges is the induction of a local increase of the thermodynamic temperature and a modification of the local state of chemical reactions, thus initiating chemical combustion reactions. This is achieved through both the temperature level reached and the creation of local radicals during the discharge. Kim et al. [391] focused on the chemistry effects induced by the plasma on the combustion reactions. Laser ignition is another method that has been studied as well, see the experimental works of El-Rabii et al. [392], Cordier et al. [393] and the numerical simulations from Lacaze et al. [66]. Technologies for the control of flame stabilization are summarized in Tab. 4.3.

6.1.4 Control methods for combustion instability

The control of combustion instabilities can be achieved with two major methods: passive and active control technologies. The passive control methods consist in modifying, adding, or removing a geometrical element that drives combustion oscillations. The active control methods involve an external device that monitors the combustion and acts when oscillations are detected to damp those. The control of combustion instabilities depends to a large extent on the system considered, the propulsion or power generation device. Indeed, the geometry and space available for control devices and systems are highly dependent on each of these configurations. Technologies for the control of combustion instabilities are summarized in Tab. 4.4.

Table 4.4 Technologies for the control of combustion instabilities.

Technology	Principle	Pros	Cons
Geometry modification High swirl level	Disturbance phasing Acoustic-convective mode conversion Vortex shedding suppression	Robust Reliable	Not adaptive Single frequency
Swirler location Distance swirler to dump plane	Disturbance phasing Acoustic-convective mode conversion	Robust Reliable	Not adaptive Single frequency
Injector quarl	Vortex shedding intensity reduction	Robust	Not adaptive
Helmholtz resonator	Acoustic cavity damping	Robust	Single frequency Power application only
Combustor length	Uncoupling acoustics/combustion	Robust	Practical limitations
Microjet injection of air or hydrogen	Local flowfield modification	Practical	Not adaptive Low TRL
Laser/plasma	Local flowfield modification	Adaptive	Low TRL

6.2 Effects of swirler position

The swirler position impacts the occurrence of combustion instabilities due to the effects of the mode conversion mechanism on flame dynamics. It has been demonstrated analytically that the flame response is driven by two major mechanisms inducing unsteady heat release: (i) the swirl number oscillation mechanism, which has been initially studied in Richards and Yip [371], Straub and Richards [372] and Komarek and Polifke [394], due to the unsteady velocity field affecting the flame front by changing the flame base angle, and (ii) the vortex shedding at the dump plane impacting the upper flame region. The mode conversion process inducing swirl number oscillations was further analyzed with numerical simulations, experimental measurements, and analytical work in Palies et al. [134]. It was shown that an acoustic wave impinging on an airfoil cascade induces a transverse in 2D (or az-

imuthal in 3D with a swirler) convective velocity oscillation on its downstream side. Numerical simulations were also performed to investigate the flowfield of the experiment and included an upstream manifold, an injector, and a flame tube, see Palies et al. [395]. Consequently, modifying the position of the swirler directly passively controls combustion instabilities.

6.3 Effects of geometry

The geometry of the combustion chamber is also an important aspect to consider in order to control combustion instabilities. Indeed, the dispersion relation that describes the occurrence of combustion instabilities, as derived in the next chapter for a swirling flame configuration within a setup made up of three cylindrical cavities, directly implies parametric dimensions, such as the length of the ducts and their section areas, play a role. Consequently, variation of these parameters may be used to control stability too. The effect of the combustor length has been shown to be important in many configurations, see Palies et al. [369], Taamallah et al. [362], as it drives the acoustic frequency of the combustor. In practice, for a gas turbine engine, the length of the combustor has a very narrow range of possible values for all dimensions.

6.4 Effects of operating conditions, equivalence ratio, and fuel

The effects of operating conditions will be very important for the design and operation of future commercial aircraft engines. It will be critical to ensure that static and dynamic stabilities are satisfactory under all operating conditions along the flight envelope. This requirement will drive future experimental and modeling capabilities. For a given design (geometry + fuel), the operating conditions (pressure, air, fuel mass flows, equivalence ratio, and inlet temperature) are set for a given mission envelope. It is then important that the design ensures stabilities satisfying all these elements. The methodology should be as follows:

- determine an engine class for a given aircraft,
- determine the mission envelope,
- select a fuel,
- determine the operating equivalence ratio(s),
- select/design/test the geometry for static stability,
- select/design/test the geometry for dynamic stability.

5

Swirling flame dynamics and combustion instability

1 Combustor acoustics

1.1 Combustion instability loops

Combustion dynamics focuses on the interactions of waves, aerodynamic structures, and the combustion processes inside the combustion chamber. Combustion instability stems from the resonant closed loop involving the flowfield, the flame region, and the combustor acoustics. This loop is represented in Fig. 5.1 for swirling flames and will be detailed along the next three sections of this chapter. When an unsteady heat release source is generated due to flow structures and/or waves disturbances, it induces an unsteady pressure field that feeds back to the initial flow disturbances through the combustor acoustics and the mode conversion processes. The mechanisms by which swirling flames respond to flow oscillations are of primary importance for unsteady heat release modeling. The determination of the acoustic mode shapes and frequencies prior to the investigation of flame dynamics or self-sustained oscillations is key in the description of the mechanisms and for prediction. Multiple tools can be employed to achieve such studies. They are reviewed next.

1.2 Network acoustics model

A first approach to acoustics modeling consists of determining analytically the mode shapes and frequencies of a given combustion system by making use of a network acoustics model where the wave propagation is modeled inside a set of connected elements with prescribed boundary conditions at their extremities and jump conditions at their interfaces, see Poinsot and Veynante [172] for a general detailed treatment. The analysis of combustion instabilities with acoustics network coupled to the swirling flame response is discussed in Section 3 of this chapter. This network method for swirl-stabilized combustor systems was derived and applied by Palies [180] to a set of three cylindrical connected elements, respectively the upstream plenum, the injector, and the

Stabilization and Dynamic of Premixed Swirling Flames
https://doi.org/10.1016/B978-0-12-819996-1.00013-5

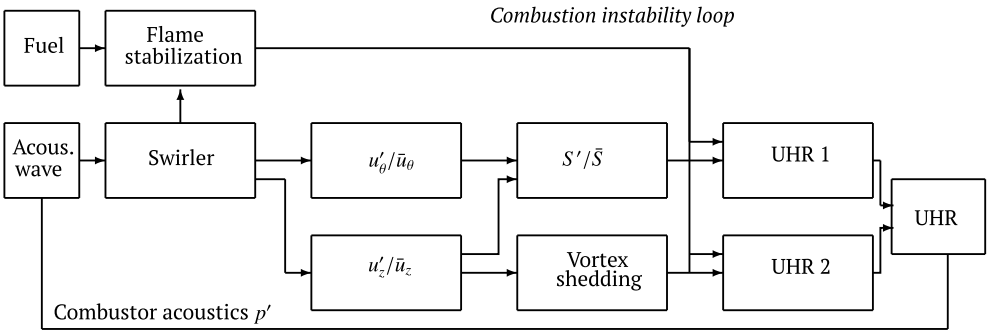

Figure 5.1 Schematic of the combustion instability loop for swirling flames. The acoustic modulation induces a mode conversion process at the swirler that generates fluctuations of axial and azimuthal velocities. The swirl number is then modulated by this unsteady velocity field, giving rise to unsteady heat release (local time intensity variation) through Eq. (5.12). The axial velocity oscillation leads to an unsteady heat release rate through the vortex shedding. These two contributions determine the total unsteady heat release (local spatial variation). Source: Schematic modified from Palies et al. [213].

flame tube. The configuration and corresponding network model are given in Fig. 5.2. For longitudinal waves propagating in the three-duct system and neglecting the mean flow terms, the derivation of the dispersion relation is now summarized with its major steps.

Considering plane wave propagation in the different components of the system with amplitudes A_j and B_j, it is possible to write that the pressure and acoustic volume flow rate perturbations are equal at the successive area changes and to use the equation of the jump condition to link the acoustic volumetric flow rate perturbations through the flame. These various equations combine with the boundary conditions at the system inlet (a rigid wall where $u' = 0$) and exhaust (an open outlet where $p' = 0$) to yield a system of linear equations $\mathbf{M} \times \mathbf{X} = 0$, where $\mathbf{M}$ is given by the following matrix:

$$\begin{vmatrix} e^{ik_1l_1} & e^{-ik_1l_1} & -1 & -1 & 0 & 0 \\ 1 & -1 & 0 & 0 & 0 & 0 \\ \alpha_1 e^{ik_1l_1} & -\alpha_1 e^{-ik_1l_1} & -\alpha_2 & \alpha_2 & 0 & 0 \\ 0 & 0 & K\alpha_2 e^{ik_2l_2} & K\alpha_2 e^{-ik_2l_2} & -\alpha_3 & \alpha_3 \\ 0 & 0 & 0 & 0 & e^{ik_3l_3} & e^{-ik_3l_3} \\ 0 & 0 & e^{ik_2l_2} & e^{-ik_2l_2} & -1 & -1 \end{vmatrix},$$

where $\alpha_i = S_i/\rho_i c_i$, lengths l_1, l_2, l_3 are defined in Fig. 5.2, k_j is the wavevector in the jth section, and $\mathbf{X}$ is a vector of wave

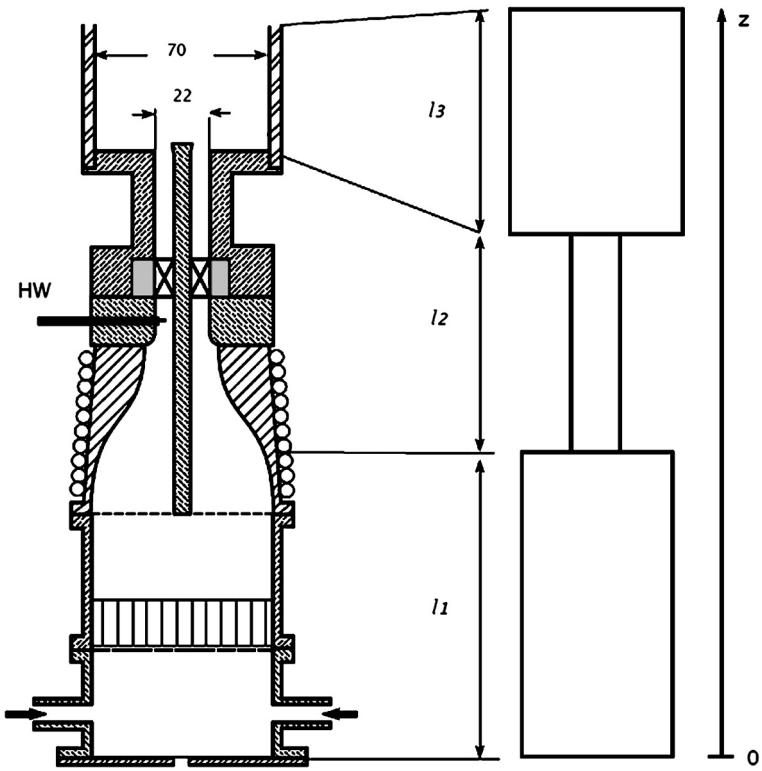

Figure 5.2 Setup geometry. Schematic of the MICCA-EM2C-Palies experimental laboratory-scale combustor on the left and an acoustic network model representation on the right. Source: Figure taken from Palies et al. [396].

amplitudes in the various cylinders of the system so that $\mathbf{X}^T = [A_1 \quad B_1 \quad A_2 \quad B_2 \quad A_3 \quad B_3]$.

This set of equations includes the flame describing function (FDF) (presented in Section 2.1) in the factor K. Nontrivial solutions of this system correspond to a vanishing determinant. This defines the dispersion relation which now depends on the level of perturbations impinging on the flame. The determinant of this matrix was derived analytically and leads to $\mathrm{Det}[\mathbf{M}] = 0$, which can also be written as

$$\begin{aligned} 0 = {} & \cos(k_3 l_3)\left[\cos(k_1 l_1)\cos(k_2 l_2) - \frac{S_1}{S_2}\sin(k_1 l_1)\sin(k_2 l_2)\right] \\ & - K\,\Xi \sin(k_3 l_3)\left[\cos(k_1 l_1)\sin(k_2 l_2) + \frac{S_1}{S_2}\sin(k_1 l_1)\cos(k_2 l_2)\right], \end{aligned} \tag{5.1}$$

where the factor K depends on the oscillating frequency and the velocity fluctuation amplitude of the modulation and takes the

following form:

$$K = \left[1 + Ge^{i\varphi}\left(\frac{T_3}{T_2} - 1\right)\right]. \tag{5.2}$$

The coupling factor Ξ writes

$$\Xi = \frac{\rho_3 c_3}{\rho_2 c_2}\frac{S_2}{S_3}. \tag{5.3}$$

For isothermal connected cylinders, without taking into account the flame, the factor K becomes unity. The obtained dispersion relation Eq. (5.1) is key in the understanding and prediction of combustion instabilities. Indeed, this dispersion relation contains the most important elements for combustion instability: (i) the geometry, through the characteristic sizes (section areas S_i and lengths l_i) of the various ducts, and (ii) the operating conditions, through the flame response (and implicitly the effects of the geometry and the mode conversion processes), the speeds in the wavevectors k_i, and the temperature ratio of the burned and fresh gases T_3/T_2. Other types of boundary conditions can be taken into account prior to deriving this dispersion relation, see Schuller et al. [397]. Accordingly, the dispersion relation can be used to derive stability criteria for passive control and combustion instability prediction. These aspects are discussed in Section 3.2. The present network approach developed has been continued, improved, and automated within the Open Source Combustion Instability Low Order Simulator (OSCILOS) code, see Han et al. [398].

1.3 Acoustics codes

Other acoustic analyses of combustion systems are based on solutions solved numerically. In those codes, the governing equations for the fluctuating variables are solved in the frequency domain in order to predict the possible acoustics modes and frequencies at work, including the effect of the flame response. This latter case is discussed in the last section of this chapter. Finite element codes have been used to perform these objectives. The AVSP code has been developed to compute modes and frequencies in multiple different combustor geometries, see Wolf et al. [399] for annular geometries and see Roux et al. [400], Ghani et al. [401], Motheau et al. [402] for longitudinal configurations. This tool has also been used by Silva et al. [403] to model the acoustics of the MICCA-EM2C-Palies experimental setup. The software Comsol has also been used to compute acoustics modes and frequencies in multiple configurations. For example, it has been employed for the computation of nonreacting longitudinal modes of

swirl-stabilized configuration by Kraus et al. [404], annular modes by Blimbaum et al. [405], Bourgouin et al. [365], and transverse modes by Saurabh and Paschereit [406].

1.4 Upstream flow modulation versus self-sustained oscillations

Combustor acoustics knowledge, obtained through an acoustic network or an acoustics code, is important for the prediction of combustion instability, for the derivation of passive control approach, and for the understanding of the feedback mechanism between the unsteady heat release mechanisms and the combustor acoustics. It is also important to distinguish the study of modulated flame dynamics (Section 2) and self-sustained oscillations (Section 3). Indeed, the former requires that the acoustics of the combustor are uncoupled from the combustion to obtain a flame response experimentally or numerically (uncoupled from the acoustics feedback). This is difficult in practice both for experiments and numerical simulations. The latter requires that the acoustics, the flow, and the flame dynamics are fully coupled. The next two sections focus respectively on those two cases: firstly the reacting swirling flame dynamics (Section 2) where the flame is submitted to upstream flow modulations of different types, and secondly combustion instabilities of swirl-stabilized combustion systems (Section 3) where the resonant loop is fully captured.

1.5 Flow modulation and Navier–Stokes characteristic boundary condition models

Numerical simulations of flame dynamics and the extraction of the flame response for its coupling to an acoustic network rely on many aspects that overlap with the classical modeling of turbulent combustion systems under statistical conditions, with the additional complexity of the considered acoustics modeled within the domain and at its boundary conditions. Specifically, flame dynamics requires methods to modulate the flow and the flame on its upstream side, at the inlet of the numerically modeled domain, and appropriate approaches to control and prescribe acoustics at these boundaries. These aspects have been the focus of a few key articles.

Most flow modulation methods are used and derived within the Navier–Stokes characteristic boundary condition framework. In that framework, the boundary conditions are obtained by solving the Navier–Stokes equations expressed in a characteristic form at the boundaries, see the articles of Thomson [407], Poinsot and

Lele [408], where the wave amplitudes L_i entering the domain have to be specified to satisfy the physical boundary conditions. The article of Kaufmann et al. [409] focused on inlet velocity modulations (IVMs) and inlet wave modulations (IWMs) in that context and showed the differences between the two techniques. It was demonstrated that the IWM method was more appropriate for flame response determination, as IVM, and not IWN, could lead to resonance of the combustion system during the modulation, see Chapter 6. In Ducruix and Candel [410], the authors studied similar methods. IWM, which is of nonreflecting nature, was applied to an acoustics–combustion interaction. Indeed, in the IVM formulation, the incoming and outgoing wave amplitudes are coupled (leading to resonance) at the inlet, while in the IWM formulation, they are not (avoiding resonance). In the article of Selle et al. [411], the focus was on the nonreflecting nature of the outlet characteristic boundary condition and the influence of its relaxation factor. A criterion was obtained to decouple the domain acoustics from the inlet modulation, allowing to impose both an inlet modulation and an outlet nonreflecting boundary and to avoid the outlet pressure drift. This is of particular interest for the determination of flame transfer functions (FTFs). Experimentally, the flame response is usually obtained by submitting the flame to upstream flow modulations generated with a loudspeaker. In Section 2, experimentally, numerically, and theoretically obtained swirling flame responses are reviewed.

2 Modulated swirling flame dynamics

In this section, the dynamics of swirling flames submitted to upstream flow modulations is described. Firstly, the flame responses, including the FTF and the FDF, are comprehensively reviewed. The method to determine the flame responses is established and widely used as a component of combustion instability prediction and flame dynamics analysis. Both experiments and models (numerical or theoretical) of flame responses can be used as prediction tools for design trend evaluation. Most advances will come from the extension to relevant operating conditions and combustor geometries, a difficult and costly challenge, which is necessary to reflect all effects of different processes on the flame response. A step towards this goal will be the development of an analytical model to capture the swirling flame response such as derived in Palies et al. [252]. Secondly, the flow dynamic mode conversion processes occurring upstream of the flame are described prior to the description of the unsteady flame front dynamics and the combustion dynamics mechanisms at work. This

latter analysis includes the vortex roll-up and the swirl number oscillation effects on the unsteady heat release. These mechanisms are described in detail and have been obtained and recognized in many research studies.

2.1 Flame responses

In the next three subsections, the review of research works on the flame responses gained from experiments, numerical simulations, and theoretical work is carried out. Flame responses of canonical flames have been widely documented, but the swirling flame dynamics transfer functions were not documented until the work of Palies et al. [253], who described a coupled experimental, numerical, and theoretical approach. Since then, such flame responses have been largely investigated and many results have been obtained.

2.1.1 Experiments

Flame dynamics studies are generally guided by the flame response obtained by submitting the flame to well-controlled, externally imposed disturbances. The FTF $\mathcal{F}(\omega)$ is defined as the ratio of relative heat release rate and axial velocity fluctuations. It is expressed in the frequency domain as

$$\mathcal{F}(\omega) = Ge^{i\varphi} = \frac{\dot{Q}'/\overline{\dot{Q}}}{u'/U_b}, \tag{5.4}$$

where u' is measured upstream of the flame and U_b corresponds to the bulk velocity inside the injector. The flame response of swirling flames has been experimentally investigated initially by Bellows et al. [412,413], Külsheimer and Büchner [414], Kim et al. [415]. Some of these studies have shown that it is essential to take into account the frequency dependency and the nonlinearities associated with the flame. Experimental work indicated that the inner recirculation zone (IRZ) intensity and location can be influenced by incoming perturbations, see Thumuluru et al. [416], Bellows et al. [412,413]. In an unconfined flame study by Külsheimer and Büchner [414], it was concluded that at a swirl number of 0.79 the flame was more susceptible to instabilities, and that its response can amplify the perturbation, contrarily to confined flames. When the flame is unconfined, only the IRZ stabilizes the combustion because ambient air is entrained and flame stabilization has differences with confined cases where the outer recirculation zone (ORZ) is also present. In a confined swirled burner submitted to velocity modulations with mixtures kept at a fixed equivalence ra-

tio, Kim et al. [415] have shown that the flame length was reduced as the modulation frequency increases. In the linear regime and for a fixed perturbation level, the authors collapsed the obtained data for FTFs at different lean operating conditions into a single curve using a Strouhal number based on the relative length scale ratio of the flame length to the convective length scale of the inlet velocity fluctuations. As the magnitude of the inlet velocity fluctuations increased, a saturation appeared due to nonlinear effects, and the gain of the FTFs decreased. The amplitude of the perturbation where this saturation occurred depended on the frequency. In this case, saturation appeared faster when the frequency was lower, but the phase remained almost unaffected for relative perturbation levels lower than 0.2. Other authors Thumuluru et al. [416], Bellows et al. [412] also indicated the nonlinear behavior of swirling flames submitted to increasing levels of mass flow fluctuations. It was shown that the unsteady shape of the flame was a strong function of the mass flow rate fluctuation level, as also observed for nonswirling flames by Balachandran et al. [141], Durox et al. [137]. The main conclusions were that the flame response saturated when the mass flow rate fluctuation was augmented, and that it became difficult to determine the time delay between flow rate fluctuations and the resulting perturbations of the heat release rate. Furthermore, FTFs have often not been complete or limited to linear perturbations, see Borghesi et al. [417], with the exception of the studies by Thumuluru et al. [416], Kim et al. [415], Bellows et al. [418].

Multiple articles by Thumuluru et al. [416], Bellows et al. [413], Külsheimer and Büchner [414], Kim et al. [415,419], Palies et al. [253] have focused on the effects of flow modulations on the dynamics of confined swirling flames and provided some of the data needed to predict combustion instability limit cycles, as described more comprehensively in Section 3. In Kim et al. [419], the laboratory-scale gas turbine combustor used to measure FTFs and predict instability frequencies was mainly in the linear regime. FTFs measured for this combustor indicated that the Strouhal number constituted a relevant dimensionless parameter, see Kim et al. [420]. In Kim and Santavicca [421], the authors additionally proposed to take into account the interference mechanisms of vortical and acoustic disturbances in the FTF scaling. This was done with the use of two different Strouhal numbers, reflecting the mode conversion process from the swirler and the convection of perturbation along the flame length. Other investigations have focused on the influence of the swirler design on FTFs, see for example Gentemann et al. [422], Hirsch et al. [423]. It was found that the transfer functions of radial and axial swirlers featured the same

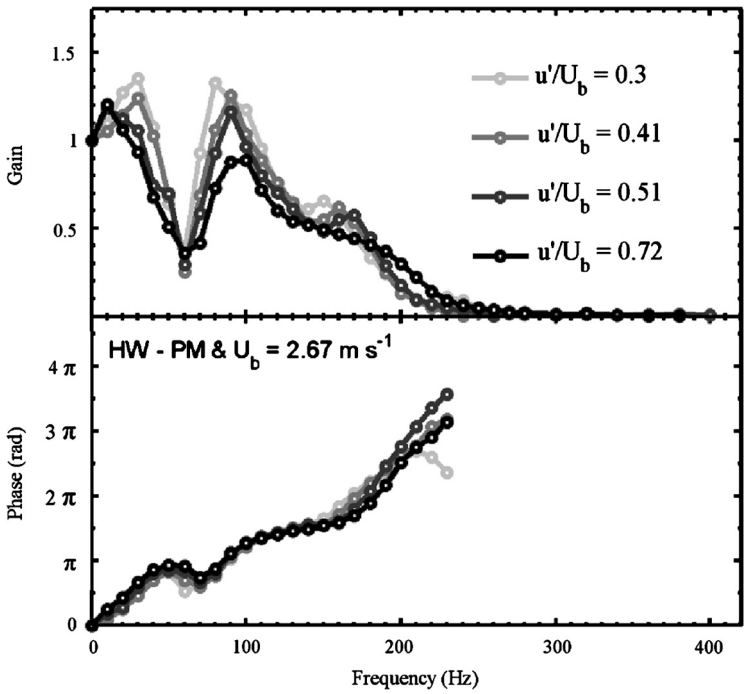

Figure 5.3 Flame describing function. Flame case A with an inlet bulk velocity of 2.67 m s^{-1} at an equivalence ratio of 0.7. The functions are obtained by varying the inlet modulation frequency and amplitude. The velocity signal was measured with a hot wire anemometer inside the injector upstream of the swirler and the heat release rate was measured with a photomultiplier. Source: Figure taken from Palies et al. [396].

behavior at moderate and high frequency, but slight differences were observed in the low frequency range.

The articles of Palies et al. [253,396,424] completed the nonlinear description of swirling flame dynamics by making use of transfer functions of increasing perturbation levels. The FTF results were used for two main purposes: (i) to guide the unsteady flame dynamics analysis (Section 2.3) and (ii) to determine the regimes of instability by coupling the flame response to an acoustic description of the combustion system (Section 3.1). These articles focused on both axial and radial swirler flame responses, showing similar results. The FDF of the MICCA-EM2C-Palies configuration is plotted in Fig. 5.3, consisting of flame responses obtained for several frequencies and amplitudes of upstream modulation. The gain G and the phase φ of Eq. (5.4) are plotted. The given results are for flame case A, corresponding to an inlet bulk velocity of 2.67 m s^{-1} at an equivalence ratio of 0.7. The velocity signal was measured with a hot wire anemometer inside the injector upstream of

the swirler, see Fig. 5.2, and the heat release rate was measured with a photomultiplier. Flame response data indicated that extremum responses are reached at specific frequencies and that the gain depended on the input level most notably in frequency ranges where this gain reaches an extremum. The phase was less dependent on the input level and featured a quasilinear behavior with respect to frequency, indicating that the flame responds with a delay to the incoming perturbations. Measurements of transfer functions with velocity signal taken upstream or downstream of the swirler indicated that this latter did not add an additional time delay between the axial velocity signal and the flame heat release signal, as the axial fluctuation propagates acoustically between the swirler and the flame base inside the upstream injector. The frequency beyond 250 Hz did show a very low amplitude global flame response.

Experimental FTFs have been obtained in the BRS-TUM-Komarek configuration by Komarek and Polifke [394] for three different spatial locations of the swirler, other parameters being constant. The results demonstrated the effect of the swirler position on the flame response, an effect that was linked to swirl number fluctuations with companion analyses. The scaling of the FTFs was based on the diameter of the injector. Characteristic minimum and maximum responses were measured in the FTF. These characteristic features of minimal and maximal gains of the flame response were also observed by Bellows et al. [426] in the GTCS-Gatech-Bellows configuration. The study of FTFs for low swirl combustors reveals similar behavior for the FTF, see Kang et al. [276] for the LSI-LBNL-Cheng configuration. This configuration was also investigated with hydrogen addition by Yilmaz et al. [427]. In the MGTC-UnivCambr-Kim configuration, the minimum response gain and associated undulated phase were specifically captured with transfer function measurements, confirming previous observations, see Kim and Hochgreb [428]. In the Longi-TUB-Terhaar configuration, the effect of the swirl number on the flame response was studied, and it was numerically confirmed that the lowest swirl number showed the highest gain and the highest swirl number showed the lowest gain at low forcing amplitudes by Stone and Menon [429]. This trend was reversed at higher amplitudes of inlet modulation. It was shown that the flame response at perfectly premixed conditions was strongly influenced by the growth rate of vortical structures in the shear layers, see Terhaar et al. [425]. Figure 5.4 depicts a series of time average for various swirl numbers and levels of flow modulation. This is in agreement with observations by Palies et al. [395], where the phasing between swirl number fluctuation inducing flame angle

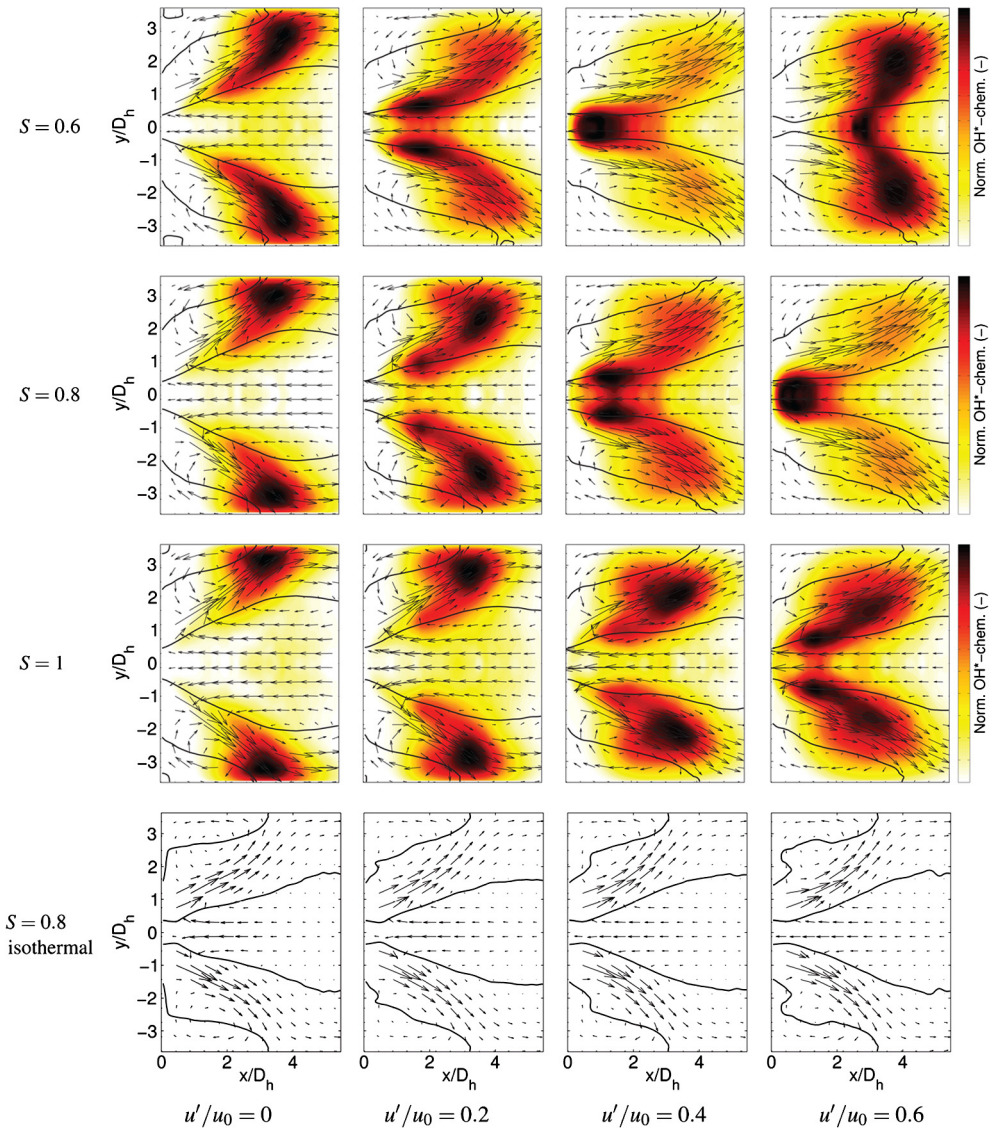

Figure 5.4 Time-averaged flowfield superimposed on the normalized OH* chemiluminescence distribution at increasing forcing amplitudes. Solid lines indicate zero axial velocity. First row: $S = 0.6$. Second row: $S = 0.8$. Third row: $S = 1$. Fourth row: $S = 0.8$ nonreacting. Source: Figure taken from Terhaar et al. [425].

variation and vortex roll-up defined the growth rate of the vortical structure. The general shapes of the FDFs were also confirmed by experimental measurements by Schimek et al. [430]. The thesis of Bunce [431] investigated systematically the flame response of the

swirl-stabilized Longi-PennState-Kim configuration. The findings also confirmed the global shape of the flame response exhibits a minimum and maximum response, see Bunce et al. [432]. In addition, the authors showed highly repeatable data and nearly identical results obtained for the transfer function obtained by evaluating the heat release rate with the flame chemiluminescence of OH^*, CH^*, or CO_2^* signals. These data allowed also to determine the uncertainty level of the measurements of FTFs. The investigation of the stratified swirling flame response for two different fuel split was carried out by Han and Hochgreb [433] on a laboratory-scale combustor where the swirling flow was generated by two swirlers located at different axial locations. The article of Gatti et al. [434] confirmed also the global FTF characteristics of premixed confined swirling flames for multiple-injector designs. The swirling flow was generated with a swirler unit made up of tangential injection holes with varying diameters, and where the mode conversion process occurs at these flow passages. The inner diameter of the injector and the injector central rod cone's top side diameter were also changed, giving rise to multiple different swirling flames, to study multiple configurations. The mean flame shapes were characterized at these multiple levels of swirl, showing that the flame location and flame angle were impacted by the swirl number. The effects of pressure on methane–air and propane–air swirling flames have been studied by Di Sabatino et al. [435]. The experimental measurements showed that at high pressure, the previously identified mechanisms at work determine the FTF characteristic shape. The measured data demonstrated the effects of pressure and fuel on the amplitude of the gain, and the phase was slightly modified. The effects of fuel (methane versus propane) were investigated by Di Sabatino et al. [436], who showed that the fuel does not affect the FTF shape but impacts the high gain peak amplitude.

The case of equivalence ratio oscillation characterized by the FTF was documented in Ranalli et al. [437], where the authors investigated the flame response with respect to both velocity oscillation and equivalence ratio oscillations in the Virg-PolyTechInst-Ranalli configuration. This effect was studied in the high amplitude case by Ćosić et al. [438] as well. The authors measured in the Longi-TUB-Terhaar configuration the dynamics of the flowfield and the flame with high speed PIV and OH chemiluminescence for multiple frequencies and amplitudes. The FDF results and analysis confirmed the hypothesis of a superposition of equivalence ratio perturbations and velocity fluctuation effects both for low and high forcing amplitudes for most of the frequency range. The flame response due to the coupling between equivalence ratio

and velocity oscillation was studied by Kim et al. [439]. The authors concluded that the phase difference between velocity and equivalence ratio oscillations were controlled by varying the fuel injection location and the mean injector velocity. In the MGTC-UnivCambr-Kim configuration, the article of Kim and Hochgreb [261] provided measurements of the impact of the nonuniform reactant field on combustion dynamics, its effect on flame location, and the interaction with unsteady flow structures. In Schuermans et al. [440], FTFs at industrial-scale high pressure were obtained experimentally with multiple measurement methods.

The case of transverse fluctuations on unsteady flame heat release has also been investigated with the determination of the FTF by O'Connor and Acharya [441]. The authors highlighted that the coupling between transverse acoustics in the main combustor section and longitudinal acoustics in the injector cavity induced the acoustic field. In Malanoski et al. [442], the analysis of the forced flame response in the Transverse-GaTech-OConnor configuration showed that the dominant fluid mechanic structures during transverse modulation varied from injector to injector, depending upon the phase characteristics of the acoustic modulation field. The article of Blimbaum et al. [405] built upon the fact that simulation and experimental studies have shown that most of the flame response during transverse instabilities was due to the longitudinal fluid oscillation induced by the fluctuating pressure field above the injector outlet. In that article, the acoustic field induced by transverse acoustic disturbances was investigated to understand the impact on the flame response. In Hauser et al. [443], it was shown that the transverse velocity fluctuation was converted into a rotational flow oscillation through a convective process function of the modulation frequency and the mass flow rate. The effects of these transverse velocity fluctuations on the global flame dynamics were subsequently determined through FTF measurements. In Aguilar et al. [444], Smith et al. [445], the authors measured and compared the velocity field of single- and multi-nozzle experiments submitted to transverse forcing, and concluded that the jet interactions did not have a significant influence on the unsteady flow structures in that setup. The article of Saurabh et al. [446] focused on the effects of transverse forcing on the flame response, showing that both the magnitude of transverse velocity and its phase with respect to axial forcing are important factors.

The study of Mirat et al. [447] focused on the swirl-stabilized spray FTF. The experimentally measured transfer functions of spray flames featured many similarities with the transfer function of perfectly premixed swirling flames, indicating that the dy-

namics are also controlled by interference mechanisms. The study of Szedlmayer et al. [448] compared single-injector and multi-injector (MNCC-PennState-Santavicca configuration) FTFs, and showed similar results except in the high frequency range.

2.1.2 Numerical simulations

Transfer functions have also been determined from numerical simulations. This requires an unsteady flow solver and broadband or harmonic modulations of the incoming flow. The transfer function is then derived in the frequency domain by postprocessing results of the obtained time-dependent calculations. Flame responses from numerical simulations have been obtained through URANS or through the large eddy simulation (LES) approach. The numerical approach can also help to discover or confirm the mechanisms at work.

In the MICCA-EM2C-Palies configuration, the time traces of relative heat release rate signals were determined numerically to reveal the differences between the flame response at two characteristic frequencies ($f = 60$ Hz and $f = 90$ Hz) and to get some insight in the nonlinearity of this response. At $f = 60$ Hz, experimental and numerical results agree in terms of signal amplitude. The minimum responses in experiments and numerical simulations were found at the same phase in the cycle. The shape of the signal was however not reproduced by the numerical simulations. At $f = 90$ Hz, the amplitude of experimental and numerical signals agreed well with a shift in phase. The shape of the signal was accurately reproduced by numerical simulations, see Fig. 5.5.

Broadband forcing was applied by Chong et al. [259] at the inlet of the BRS-TUM-Komarek configuration simulated with LES in order to identify the flame response. A good agreement with the experimental measurements was obtained. The case of equivalence ratio modulation for swirl-stabilized combustion systems has been initially taken into account by Smith [449] with URANS and LES comparisons. Industrial configurations have also been investigated with LES and modulation of the velocity by Hermeth [450] and modulation of the equivalence ratio by Hermeth et al. [451] for one frequency of inlet modulation. The analysis showed that the mixture fluctuations are convected to the combustion chamber inlet, are phased with velocity fluctuations, and combine with those to lead to different levels of flame response. In the Longi-TUB-Terhaar configuration, FDFs have been computed by Krediet et al. [452] imposing upstream IVM at the inlet of the CFD domain. Multiple amplitudes and frequencies were computed to form the FDF and compared with experiments, leading to a global agreement in terms of general trend, while exact lev-

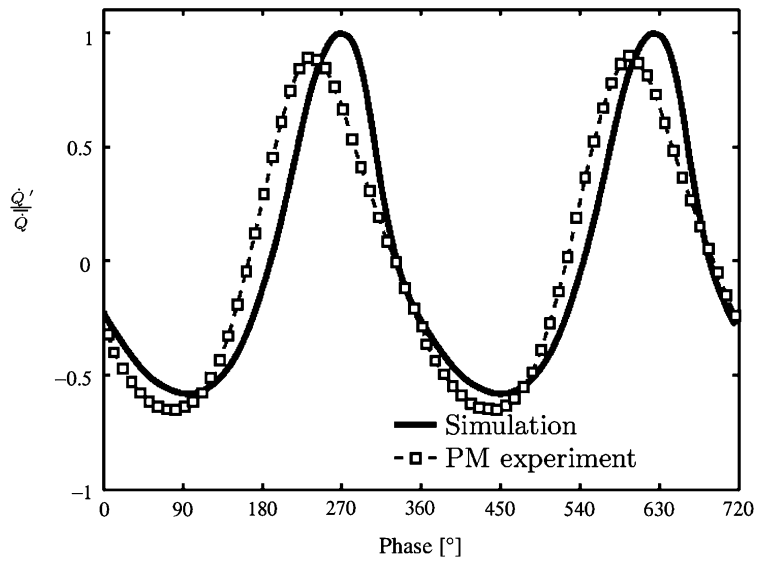

Figure 5.5 Heat release rate signals $\dot{Q}'/\overline{\dot{Q}}$ at $f = 90$ Hz. Solid lines correspond to simulation results and were obtained by phase-averaging over nine periods of modulation. The black square curve was obtained by integrating the heat release rate in a window which captures the signal that would be recorded by a photomultiplier like in the experiment. This window excludes points located inside the injector and does not account for heat release associated with the part of the flame which flashes back. The open square curve was obtained experimentally with a photomultiplier capturing the light radiated by the flame, but not that originating from the flame inside the injector. Source: Figure taken from Palies et al. [396].

els were slightly off for the gain and the phase curves, particularly for the response peak. In Krediet et al. [453], the authors studied the cause of the saturation, which was linked to a nonlinear evolution of the area of the flame surface when increasing the inlet modulation amplitude. The authors also showed that the heat release and flame surface fluctuations were linearly dependent on the tangential component of velocity fluctuations upstream of the flame, while they increased nonlinearly with the axial component of velocity fluctuations. In Acharya and Lieuwen [454], the authors determined the FTF numerically with URANS. The configuration modeled the swirler with a prescribed velocity field. IVM was then applied with three methods, i.e., axial, azimuthal, or combined inlet velocities forcing, to model the swirler response to upstream acoustic modulations (the mode conversion process) and observe the subsequent impact on the FTF. The amplitude of modulation was set to 10% of the mean flow velocity and the frequency ranged from 150 to 1000 Hz. The results indicated that the combination of azimuthal and axial forcing was required, as expected, to obtain the swirling flame response characteristic shape such

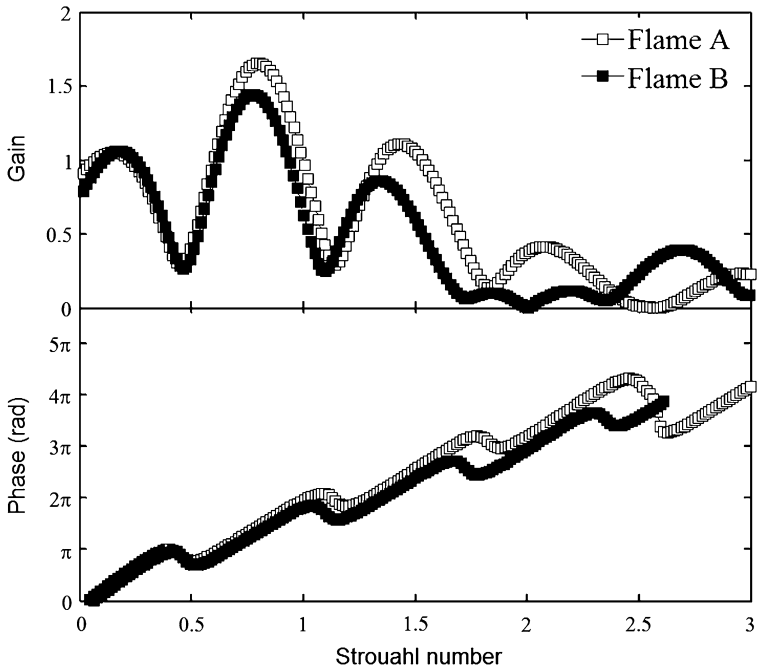

Figure 5.6 Flame transfer function of the MICCA-EM2C-Palies configuration. Flame cases A and B with inlet bulk velocities of 2.67 m s^{-1} and 4.13 m s^{-1} at an equivalence ratio of 0.7. The functions depend on a reduced frequency expressed with a Strouhal number. The functions are obtained with Eq. (5.10). Source: Figure taken from Palies et al. [252].

as presented in Fig. 5.6. Furthermore, the comparison for different phasing between the axial and tangential modulated components at the inlet showed the subsequent impact on the flame response. In Rofi et al. [455], the focus was on comparing LES and URANS approaches for the modeling of the FTF. In Andreini et al. [456], the authors captured the FTF with a combination of FTF and system identification (SI). In Ghani et al. [457], the authors investigated the combustion dynamics of a swirl-stabilized kerosene-fueled combustor (LOTAR-ONERA-Apeloig) configuration. The role of the precessing vortex core (PVC), the frequency of which scaled with the bulk axial velocity, was linked to the transverse-longitudinal first acoustic mode resonance. In Biagioli et al. [458], the authors proposed a methodology based on the linearization of the progress variable transport equation to determine the separate contribution of the irrotational and rotational velocity components to the FTF.

The study of Innocenti et al. [459] concentrated on coupling URANS and SI to obtain the FTF of a reacting spray flame. The ar-

ticle of Tay-Wo-Chong et al. [460] compared the flowfield, flame characteristics, and dynamics between experiments and simulations obtained with the addition of stretch and heat loss effects into an LES combustion model, and extracted the FTF with SI. In Laera and Morgans [461], FDFs of a single-injector swirl-stabilized flame of the annular experiment of Worth and Dawson [462] were reported for two levels of IVM and a range of frequencies from 300 Hz to 1900 Hz using LES. The work of Bauerheim et al. [463] showed that the azimuthal confinement ratio, thermal conditions, and the fuel type affected the flame response of swirling flames and controlled the stability of the tangential acoustics instability. The Siemens-DLR-Stopper configuration was used to model the flame response with low Mach number numerical simulation by Xia et al. [464]. Iudiciani and Duwig [268] also used the URANS solver, focusing on high amplitude flame responses. The article of Pampaloni et al. [465] focused on the numerical determination of the FTF with LES at four frequencies and three amplitudes. The data were also used as input of a stability analysis, leading to prediction of the instability.

2.1.3 Theoretical transfer function

There are very few theoretical transfer function models for swirling flames, see You et al. [466], Borghesi et al. [417], Komarek and Polifke [394], Palies et al. [252]. The main mechanisms contributing to the flame response are those generating large vortex structures or flame angle oscillations, as described in the next subsections. The first one can be produced by the swirler, the backplane, and the centerbody. They are all synchronized to the modulation frequency. Detailed characterizations of the flow dynamics however showed that for the MICCA-EM2C-Palies setup the main contributing mechanisms were due to the swirler and the backplane of the combustor. Previous studies by You et al. [466], Borghesi et al. [417] provided a swirling FTF model but did not account for the presence of the azimuthal velocity disturbance convected by the flow and superimposed onto the initial upstream axial component propagating at the speed of sound. The effect of this convective mode was not included until the article of Komarek and Polifke [394], which provided a phenomenological representation for the FTF. The presence on the downstream side of the swirler of a perturbation featuring acoustic and convective components was documented in Palies et al. [396], and this complex perturbed flowfield was taken into account to determine the flame response of swirling flames.

The study of Palies et al. [252] improved the modeling of swirling FTFs by accounting for the swirler-induced flowfield os-

cillations. The approach was based on a G-equation derived by first taking its ensemble average with respect to the turbulent fluctuations. This equation was then separated into a steady and a phase-average component, corresponding to imposed flow modulations leading to the perturbed G-equation. It was then shown that the response of swirling flames resulted from the direct effect of axial velocity perturbations and from the combined effects of axial and azimuthal velocity components. The latter were taken into account by considering that the turbulent flame velocity was perturbed by these disturbances. It was shown that the transfer function of swirling flames can be deduced from the transfer function of "V" flames submitted to convective flow disturbances. This was carried out by taking into account the relative level of axial and azimuthal disturbances and the phase shift between these two components. These last quantities were estimated theoretically and deduced from measurements of the axial and azimuthal velocity signals. The main steps of the analysis are summarized now. To start this analysis, it is assumed that the flame is instantaneously described as a surface defined by a kinematic G-equation, see Markstein [467]:

$$\frac{\partial G}{\partial t} + \boldsymbol{v}\cdot\nabla G = S_D|\nabla G|. \tag{5.5}$$

One can obtain the following form for the perturbed flame front:

$$\frac{\partial G_1}{\partial t} + (\boldsymbol{v}_0 + S_{T_0}\boldsymbol{n})\cdot\nabla G_1 = \left[\boldsymbol{v}_1\cdot\boldsymbol{n} - \frac{S_{T_1}}{S_{T_0}}\boldsymbol{v}_0\cdot\boldsymbol{n}\right]|\nabla G_0|. \tag{5.6}$$

This expression indicates that the unsteady flame motion is controlled by flow velocity perturbations $\boldsymbol{v}_1$ and turbulent flame velocity perturbations S_{T1}. To use this expression, one relates the relative fluctuations in turbulent burning velocity S_{T_1}/S_{T_0} to the incoming velocity modulations. This relation can be written as

$$\frac{S_{T_1}}{S_{T_0}} = \chi\frac{v'_\theta}{\overline{v}_\theta} + \zeta\frac{v'_x}{\overline{v}_x}, \tag{5.7}$$

where $\overline{v}_\theta$ is the azimuthal component and $\overline{v}_x$ the axial component of the swirling flow. An expression similar to Eq. (5.7) has recently been derived in Palies [29], confirming this initial choice. In addition, the phasing ϕ between axial and azimuthal fluctuations, measured experimentally, writes

$$\frac{v'_\theta}{\overline{v}_\theta} = \frac{v'_x}{\overline{v}_x}\exp(i\phi). \tag{5.8}$$

By making use of Eqs. (5.7) and (5.8), one obtains the following expression for the swirling FTF:

$$\mathcal{F}^{s}_{\text{th}}(\omega) = \mathcal{F}^{v}_{\text{th}}(\omega)\Big[1 - (\zeta + \chi \exp(i\phi))\Big]. \tag{5.9}$$

To use this result one has to provide an expression for $\mathcal{F}^{v}_{\text{th}}$. The following expression is obtained from Schuller et al. [129]:

$$\begin{aligned}\mathcal{F}^{v}_{th}(\omega)(\omega_*, \alpha) = &\frac{2}{\omega_*^2}\frac{1}{1-\cos^2\alpha} \\ &\times\left[\exp(i\omega_*) - 1 - \frac{\exp(i\omega_*\cos^2\alpha) - 1}{\cos^2\alpha}\right] \\ &+ \frac{2i}{\omega_*}\frac{1}{1-\cos^2\alpha} \times \Big[\exp(i\omega_*\cos^2\alpha) - \exp(i\omega_*)\Big],\end{aligned} \tag{5.10}$$

where $\omega_* = \omega R/S_{T_0}\cos\alpha$, S_{T_0} is the turbulent burning velocity defined by $S_{T_0} = \overline{v}_x \sin\alpha$, R is the injector tube radius, and α is the flame angle defined between the flame front and the vertical axis. The relative fluctuation of the swirl number $S'/\bar{S}$ defined in Palies et al. [396] writes

$$\frac{S'}{\bar{S}} = \frac{u'_\theta}{\bar{u}_\theta} - \frac{u'_z}{\bar{u}_z}, \tag{5.11}$$

where $u'_z/\bar{u}_z$ and $u'_\theta/\bar{u}_\theta$ are the relative fluctuations of axial and azimuthal velocities. This definition of the swirl number is a linearized form of the classical swirl number definition based on momentum conservation equations. Introducing Eq. (5.11) into Eq. (5.7), one can show that the turbulent burning velocity is linked to the swirl number fluctuation:

$$\frac{S_{T_1}}{S_{T_0}} = \chi\frac{S'}{\bar{S}}. \tag{5.12}$$

The turbulent flame speed is therefore directly dependent on the oscillation of the swirl number, which is important for unsteady heat release modeling in swirling flames, and was used in the study of the limit cycle in the LSI-LBNL-Cheng configuration in Palies et al. [213].

A comparison of the flame response model Eq. (5.9) with experiments conducted in Han and Hochgreb [433] provided a good agreement for stratified premixed flames in the low turbulence level regime. Partially premixed flames require adapting the model to account for the local variation of the flame speed due to the equivalence ratio stratification, a modeling aspect that needs to

be considered. Theoretical FTFs have been the topic of other research efforts. For longitudinal modulation, the article of Acharya et al. [468] focused on the flame response of swirling premixed flames modulated by helical disturbances and studied the impact of these perturbations on the flame surface area modulation and the heat release fluctuations. It was shown that these two quantities exhibited different sensitivities to the frequency and the dimensionless swirl number. In Acharya and Lieuwen [469], the authors focused on the theoretical response of nonaxisymmetric premixed swirling flames to helical disturbances. The authors showed that helical modes impact the flame response of axisymmetric and nonaxisymmetric mean flames differently. For axisymmetric mean flames, the axisymmetric contribution of the flame area modulation contributes to the global fluctuating area, but for nonaxisymmetric mean flames, helical modes make nonzero contributions to the flame response. It was also shown that the strength of the asymmetry, the flame length, and the Strouhal and swirl numbers impact the helical mode contribution to the flame response, possibly leading to a dominant contribution when compared with the symmetric mode contribution. The case of transverse forcing on the flame response of swirling flames was considered analytically by Acharya et al. [470], where the modeling approach was developed to determine the flame response by making use of the experimentally determined unsteady filtered disturbances field and the time-average flowfield, leading to good comparison between experiments and theoretical predictions. The response of swirling premixed flames with constant burning velocity to nonaxisymmetric harmonic excitation was further studied in Acharya et al. [471].

The current section reviewed in detail the contribution of many authors to the understanding and description of swirling flame responses. As indicated in the subsection's introduction, the next advances will be from the extension to relevant operating conditions and combustor geometries and from the enhancement of analytical models of flame responses, such as for partially premixed flames, considering velocity and equivalence ratio coupling.

2.2 Flow dynamic mode conversion processes occurring upstream of the flame

In this section, the mode conversion process is introduced and a theoretical modeling strategy is presented. In the next subsections, the relevant observations from experiments and numerical simulations are discussed and summarized, along with theoret-

ical results. These observations are critical to the determination and understanding of the subsequent effects on flame dynamics. There have been a limited number of studies of such observations, which may be attributed to the optical access requirement. Such observations should be undertaken in future efforts prior to their understanding and modeling.

2.2.1 Observations from experiments and numerical simulations

The previous section described the analytical derivation of the swirling flame response. This derivation was enabled by the understanding of the perturbed velocity field induced by the mode conversion process and its subsequent impact on the unsteady heat release. Mode conversion is a mechanism where one type of propagating disturbance generates another type of wave. It involves convective waves (entropy and vorticity) and acoustic waves and takes place in many situations in fluid dynamics. The next sections focus on the configuration where an acoustic wave is incident on an airfoil cascade or a swirler, producing a vorticity wave in the downstream flow. This phenomenon has been observed in experiments by Richards and Yip [371], Straub and Richards [372] and in simulations by Huang and Yang [22], Wang and Yang [472], Komarek and Polifke [394]. It was concluded from LES calculations by Huang and Yang [22], Wang and Yang [472] and indirectly from transfer function measurements by Komarek and Polifke [394] that on the downstream side of the swirler, the perturbation comprises an acoustic and a convective component. While the presence of the convective component was observed, there were no direct measurements of the axial and azimuthal velocity components such as depicted in Fig. 5.7.

2.2.2 Theoretical results

It is possible to investigate the mode conversion in 2D considering the swirler as a cascade of airfoils. The set of jump conditions written by Cumpsty and Marble [473] can be used to relate perturbations on the upstream and downstream sides of this cascade:

$$s_1' = s_2', \tag{5.13}$$

$$\frac{\rho_1'}{\overline{\rho}_1} + \frac{w_1'}{\overline{w}_1} - \theta_1' \tan\overline{\theta}_1 = \frac{\rho_2'}{\overline{\rho}_2} + \frac{w_2'}{\overline{w}_2} - \theta_2' \tan\overline{\theta}_2, \tag{5.14}$$

$$\frac{p_1'}{\gamma\overline{p}_1} + \frac{s_1'}{(\gamma-1)c_p} = \frac{p_2'}{\gamma\overline{p}_2} + \frac{s_2'}{(\gamma-1)c_p}, \tag{5.15}$$

where s' is the entropy fluctuation and $\rho'/\overline{\rho}$ is the relative density fluctuation. Subscripts 1 and 2 refer to the inlet and outlet of the

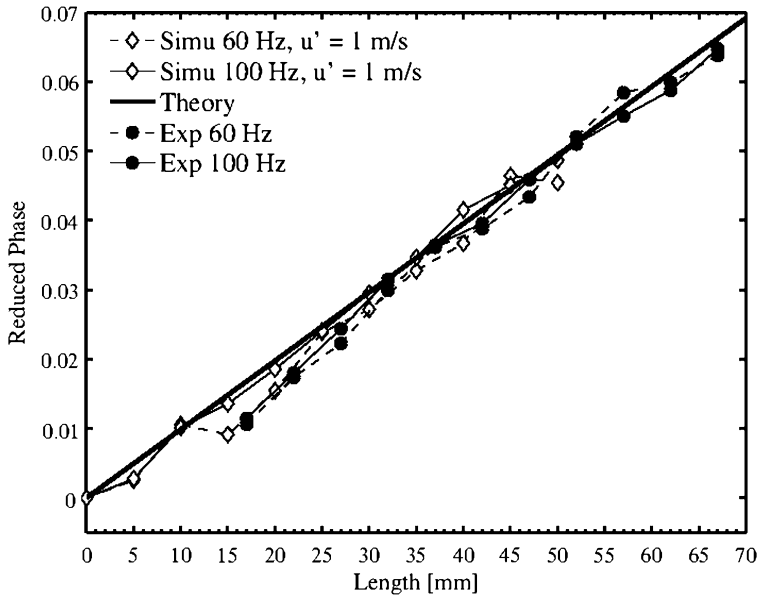

Figure 5.7 Comparison of simulations, theory, and experiments with the reduced phase as a function of the length. Results of simulations indicate that the phase shift at the cascade trailing edge plane $\varphi_0 = \pi$ because of the negative value of the blade trailing edge angle. Results of experiments indicate that $\varphi_0 \simeq 0$ at the swirler backplane. Source: Figure taken from Palies et al. [134].

cascade vanes. The ratios $w_1'/\overline{w}_1$ and $w_2'/\overline{w}_2$ are the relative velocity fluctuations on each side of the cascade, θ_1' is the fluctuation of the angle of incidence θ_1, θ_2' is the fluctuation of angle θ_2 at the trailing edge, p' refers to the fluctuation in pressure, γ is the specific heat ratio, and c_p is the specific heat of the working fluid. At the trailing edge, the Kutta condition implies that the flow should leave the blade in a direction tangent to the mean camber line so that the perturbation angle vanishes, $\theta_2' = 0$, at that location. Upstream of the cascade, in region 1, the pressure field is formed by incident and reflected acoustic waves which are taken as plane waves propagating in the axial direction:

$$p_1' = A \exp i(kx - \omega t) + AR \exp i(-kx - \omega t), \tag{5.16}$$

where A is the amplitude of the incident acoustic wave, R is the reflection coefficient of this wave, and $k = \omega/c$ designates the acoustic wavevector. The velocity fluctuation corresponding to this field is expressed as

$$u_1' = \frac{A}{\overline{\rho}_1 \overline{c}_1} \exp i(kx - \omega t) - \frac{AR}{\overline{\rho}_1 \overline{c}_1} \exp i(-kx - \omega t), \tag{5.17}$$

where $\overline{\rho}_1$ and $\overline{c}_1$ are the density and the speed of sound in region 1. It is assumed in the present analysis that the mean density and speed of sound are the same on both sides of the swirler, so $\overline{\rho}_1 = \overline{\rho}_2 = \overline{\rho}$ and $\overline{c}_1 = \overline{c}_2 = \overline{c}$. In region 2, downstream of the cascade, the transmitted acoustic pressure fluctuation also propagating in the axial direction writes

$$p_2' = AT \exp i(kx - \omega t), \tag{5.18}$$

where T is the transmission coefficient and the corresponding acoustic velocity component (with subscript a) is

$$(u_2')_a = \frac{AT}{\overline{\rho}\,\overline{c}} \exp i(kx - \omega t). \tag{5.19}$$

A vorticity wave (subscript v) is also generated at the swirler. This wave comprises a single velocity component of amplitude B in the transverse direction:

$$(v_2')_v = B \exp i\left[\frac{\omega x}{\overline{w}_2 \cos\overline{\theta}_2} - \omega t\right]. \tag{5.20}$$

We now seek the expressions of the amplitudes T, R, and B. After coupling the jump conditions and the expressions of the upstream and downstream fields, the calculations lead to the following expressions:

$$T = 1, \tag{5.21}$$

$$R = 0, \tag{5.22}$$

$$B = \frac{A}{\overline{\rho}\,\overline{c}} \tan\overline{\theta}_2. \tag{5.23}$$

It is thus possible to write the velocity components on the downstream side of the swirler in the following form:

$$u_2' = \frac{A}{\overline{\rho}\,\overline{c}} \exp i\left[\frac{\omega}{\overline{c}} x - \omega t\right], \tag{5.24}$$

$$v_2' = \frac{A}{\overline{\rho}\,\overline{c}} \tan\overline{\theta}_2 \exp i\left[\frac{\omega}{\overline{u}_2} x - \omega t\right]. \tag{5.25}$$

The axial velocity perturbation propagates at the speed of sound, while the transverse velocity component is convected at the local flow velocity $\overline{u}_2 = \overline{w}_2 \cos\overline{\theta}_2$ in the axial direction. The previous calculations indicate that the swirler acts as a mode converter. When it is submitted to axial acoustic waves it generates a vorticity wave which is convected by the flow in the axial direction. This

convective wave is characterized by a velocity component in the transverse direction (2D) or in the azimuthal direction (3D). The relative amplitude of this component is equal to the relative amplitude of the axial velocity perturbation $v_2'/\overline{v}_2 \simeq u_2'/\overline{u}_2$. The results from this 2D theory are consistent with the 3D theory presented in Section 2.

2.2.3 Summary

This subsection summarizes the characterization of the mode conversion process conducted experimentally, theoretically, and numerically. The major results are compared in Fig. 5.7. Circles correspond to experiments and diamonds to numerical predictions. The horizontal axis indicates the distance from the swirler outlet where velocity signals are extracted to determine the phase shift. Measurements were carried out at points separated by an interval of five millimeters. The evolution of the phase shift between u' and v' was specifically examined. A reduced phase that collapsed the experimental data and numerical results was introduced and compared with the theory. This was carried out by multiplying the phase by the convection velocity u_{cv} and dividing by the frequency f:

$$\varphi^* = (\varphi - \varphi_0)\frac{u_{cv}}{2\pi f}, \tag{5.26}$$

where φ_0 is the phase between axial and azimuthal velocity signals at the cascade backplane in 2D or at the swirler in 3D and is respectively equal to $\varphi_0 = \pi$ and $\varphi_0 = 0$. This reduced quantity is plotted in Fig. 5.7 as a function of distance from the airfoil cascade (simulations) and from the swirler outlet (experiments). One finds that numerical simulations and experimental data closely match theory, confirming that the transverse perturbations are well described by the model.

The impact of the acoustic and convective perturbations on the flame dynamics will be discussed next. Indeed, the combination of acoustics and vortical disturbances downstream of the swirler directly modulates the swirl number in a nonlinear fashion, while the axial acoustic disturbances additionally induce vortex roll-up at the flame through the interaction with the backplane of the combustor.

2.3 Unsteady flame front dynamics

As indicated in previous sections, the FTF guides the unsteady flame dynamics analysis. The minimum and maximum flame responses were indeed expected to present strong flame dynamics

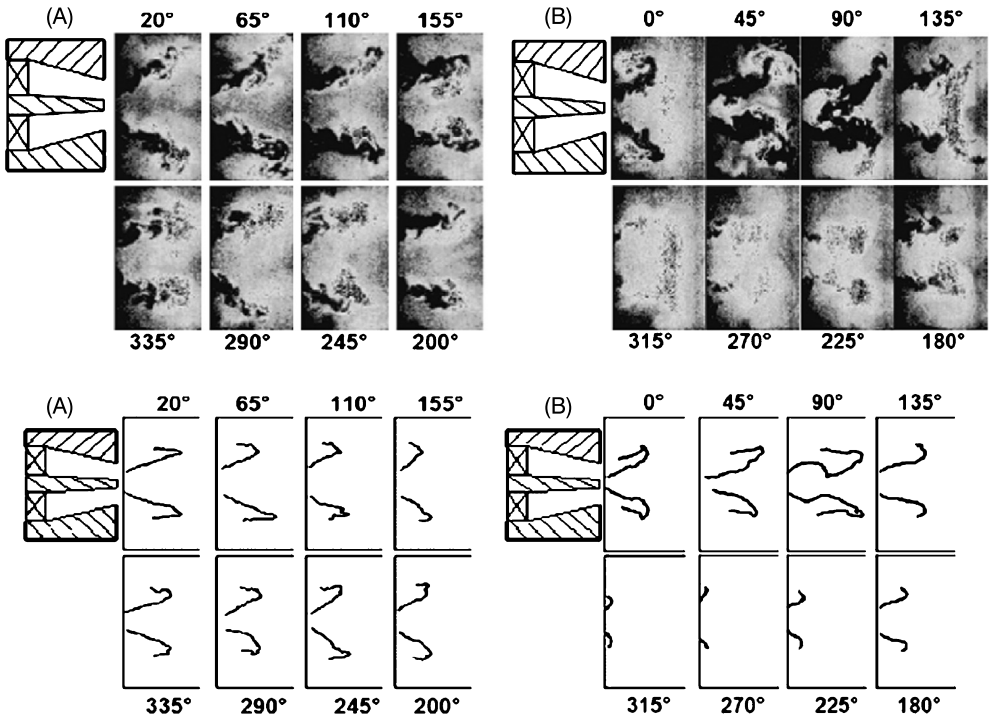

Figure 5.8 Experimental swirling flame dynamics sequence. Top figures: Instantaneous OH PLIF images showing the evolution of the flame response over one cycle of acoustic forcing for (A) low (linear, $u'/u_0 = 0.2$) and (B) high (nonlinear, $u'/u_0 = 0.6$) velocity oscillation amplitudes ($f = 410$ Hz). Bottom figures: Phase-averaged flame edges showing the evolution of the flame response over one cycle of acoustic forcing for (A) low (linear, $u'/u_0 = 0.2$) and (B) high (nonlinear, $u'/u_0 = 0.6$) velocity oscillation amplitudes ($f = 410$ Hz). Source: Images taken from Bellows et al. [412].

differences, a feature identified in many other studies. It subsequently oriented the identification of the underlying mechanisms responsible for the unsteady heat release. Phase-locked analysis is nowadays a standard for combustion dynamics studies and enables to describe the flame front at a set of phase instants of a harmonic oscillation. In addition, direct flame chemiluminescence signal extraction from these images allows to reconstruct integrated signals for comparison with photomultiplier signals.

The unsteady flame dynamics of the MICCA-EM2C-Palies setup were examined by considering the evolution of the volumetric heat release rate distribution during a modulation cycle both numerically and experimentally. Light emission by the flame was recorded with an ICCD camera. Six phase-locked images were recorded during an oscillation cycle to define the motion of the flame at the modulation frequency. Each image, separated by a

phase angle of 60 degrees, was formed by accumulating one hundred instantaneous images. An Abel transform was then applied to each image to get the 2D flame slice. The final images are scaled in terms of volumetric heat release rate and the levels are given in $\mathrm{W\,m^{-3}}$. Results are plotted in Fig. 5.9 for an IWM of $f = 90$ Hz. Numerical simulations were also phase-averaged by calculating the dynamics over nine periods and by spatially averaging the results over 32 axial slices around the axis. As can be seen, the overall dynamics are well captured by the LESs. These results characterized the flame dynamics and were used to interpret the corresponding heat release rate signals plotted in Fig. 5.5.

The flame dynamics at $f = 90$ Hz are given in Fig. 5.9. From 90 degrees to 270 degrees, the ratio $\dot{Q}'/\overline{\dot{Q}}$ increases continuously in Fig. 5.5 (squares, PM experiment). During this time period, the flame tip is progressively rolled up at the extremity, while the angle at the flame root reduces regularly, but with a limited variation compared with its maximal value reached for a phase comprised between 60 degrees and 120 degrees, see Fig. 5.9. The remaining part of the cycle, the flame surface area reduces regularly, while the distribution of the heat release rate takes a compact shape. No flashback occurs during the cycle and the flame remains attached to the central rod. In this case, the flame angle features a reduced oscillation over a modulation cycle and the flame dynamics are essentially controlled by the roll-up mechanism at the flame tip with large heat release fluctuations. At $f = 60$ Hz (results not shown), the flame features strong fluctuations in the flame angle and roll-up at the flame tip while at $f = 90$ Hz, variations of the flame angle remain limited and the tip roll-up determines the dynamics of the flame front inducing large variations in the heat release rate, see Fig. 5.5 for $f = 90$ Hz.

The unsteady flame dynamics observations are key to orient and guide the subsequent analysis. The distinct flame response observed at the two frequencies was attributed to the interference between two processes which are detailed in the next sections.

2.4 Combustion dynamics mechanisms

While the unsteady heat release characterization has been carried out in several studies, the description, identification, modeling, and understanding of the mechanisms at work that induce the unsteadiness of swirling flames were not fully documented and unknown prior to Palies [180]. The unsteady heat release signals and distributions are investigated in this section to identify and characterize the following two mechanisms: (i) the swirl number oscillation, inducing flame angle oscillations, and (ii) the vortex

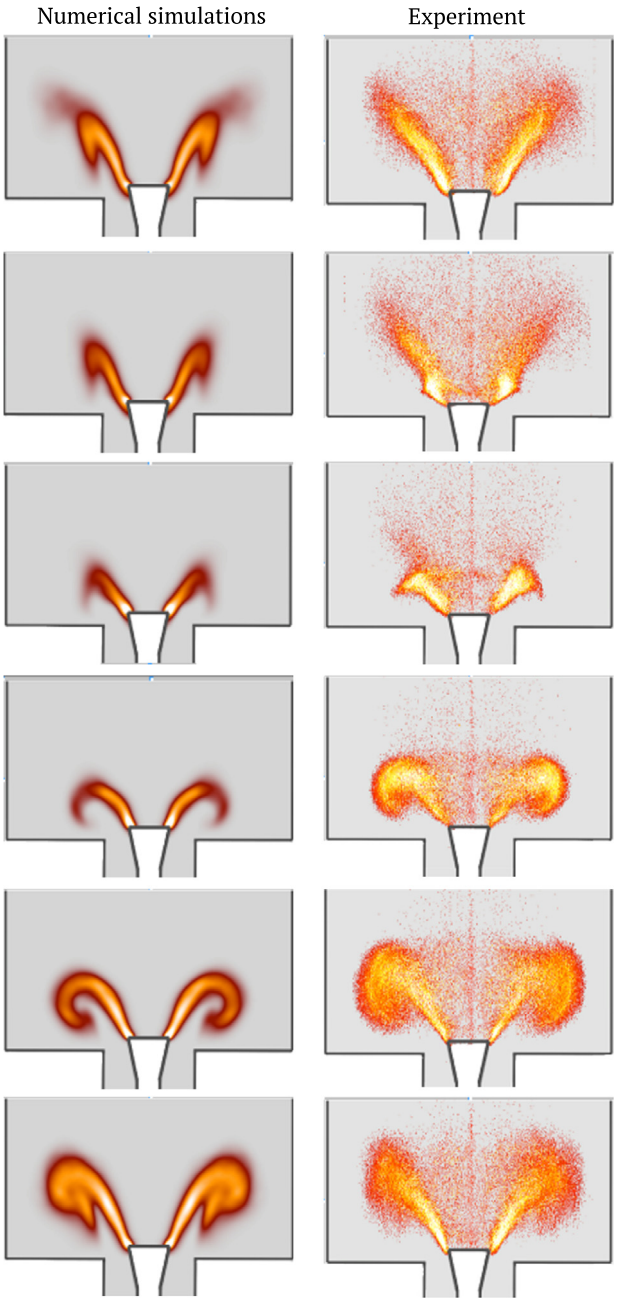

Figure 5.9 Simulated and measured swirling flame dynamics. Phase-conditioned average heat release rate distribution in W m^{-3} obtained numerically (left) and experimentally (right) with an inlet wave modulation at $f = 90$ Hz. A set of phase instants are represented from top to bottom, from 0 to 300 degrees of phase, spaced by 60 degrees. The color bar ranges from 5 (red) to 200 (white) MW m^{-3}. Source: Images taken from Palies et al. [395].

roll-up, inducing flame surface oscillations. Prior to their detailed description, the context and some observations are discussed.

Mechanisms like vortex roll-up have been studied previously, for example by Bellows et al. [412], Huang and Yang [22], Kang et al. [276], Bellows et al. [413], Külsheimer and Büchner [414]. This phenomenon is similar to the roll-up motion observed at the tip of laminar and turbulent "V" flames by Durox et al. [136], Balachandran et al. [141]. Vortices are shed from the injector backplane in response to the flow pulsations (through a mode conversion process at the backplane) and roll-up of the flame edge, resulting in large heat release rate fluctuations due to the flame surface area variations. Results of swirling flame dynamics from Bellows et al. [412] are depicted in Fig. 5.8. Perturbations of different types can impact the flame dynamics. One class is formed by velocity fluctuations which accompany pressure oscillations, see Poinsot et al. [474], Yu et al. [475], Paschereit et al. [476]. Another type of perturbation consists in equivalence ratio disturbances, which can be created by the differential response of fuel and air injectors to pressure waves generated by unstable combustion, see Keller [477], Lieuwen and Zinn [181], Sengissen et al. [478]. The dynamics of swirling flames have been investigated experimentally by Külsheimer and Büchner [414], Weigand et al. [479], Bellows et al. [412], Kim et al. [415]. The articles of Armitage et al. [143], Thumuluru et al. [416], Bellows et al. [413] dealt with nonlinear effects of flow modulations on the dynamics of confined turbulent swirling flames. The flame motion induced by incoming perturbations has been analyzed using optical imaging techniques to interpret FDF data by making use of OH PLIF methods, see Thumuluru et al. [416], Lee et al. [480], Bellows et al. [412], or by directly recording the flame emission with an ICCD camera, such as by Bellows et al. [413], Külsheimer and Büchner [414].

The investigation of the unsteady heat release distribution data by plotting phase-space diagrams for the MICCA-EM2C-Palies setup is now discussed. A reference frame where the vertical axis is the phase and the horizontal axis corresponds to the axial coordinate in the flame is used. The space–phase diagram corresponding to a modulation at $f = 90$ Hz is plotted in Fig. 5.10 for flame A. This diagram is formed by summing emission over the pixels in each line of the phase-average images. For a given phase ψ one starts from the phase-average image acquired with the ICCD camera. Let $I(j, l, \psi)$, $j = 1, ..., 512$, $l = 1, ..., 512$, be the local pixel intensity on the CCD screen. One forms a transversally averaged emission signal $< I > (j, \psi)$ and then subtracts the time-average intensity from this signal. The result is then divided by this average to obtain a relative intensity fluctuation ($< I >$

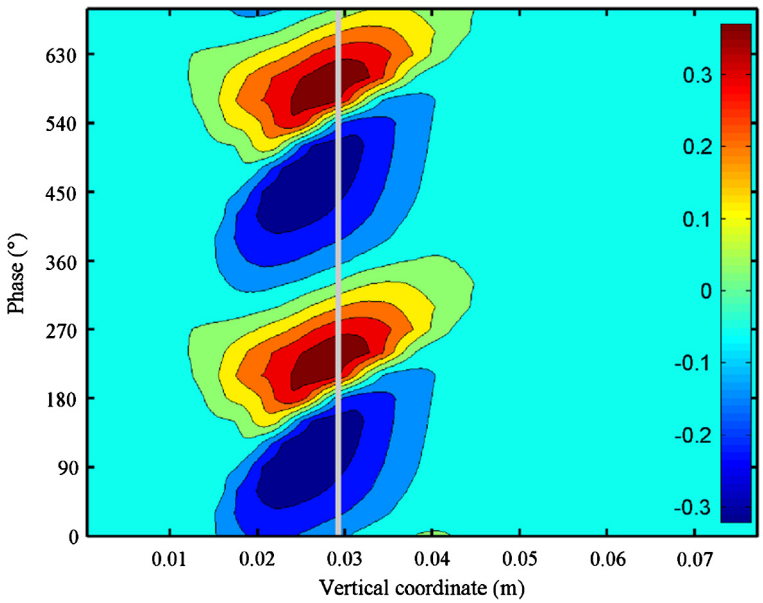

Figure 5.10 Space–phase distributions of light emission for flame A modulated at $f = 90$ Hz. The diagrams are formed by summing emission over the pixels in each line of the phase-average images. For a given phase this quantity defines the spatial distribution of relative emission, which can be interpreted as the spatial distribution of transversally integrated heat release. The gray line indicates the limit used to split both windows. Source: Figure taken from Palies et al. [396].

$(j, \psi) - \overline{< I >})/\overline{< I >}$. For a given phase ψ, this quantity defines the spatial distribution of relative emission, which may be interpreted as the spatial distribution of the transversally integrated heat release rate. This operation was repeated for a set of phases and results are gathered in the form of contours. In Fig. 5.10, the vertical gray line indicates the limit of the lower window (LW) and upper window (UW) defined as where the heat release is integrated.

An examination of the diagram (not shown here) corresponding to flame A for a modulation $f = 60$ Hz indicated also the presence of alternate positive and negative fluctuations. For a given phase, a region in the flame was determined where the fluctuation was positive while in another region the fluctuation was negative. These regions were convected downstream and the process was repeated periodically. This explained observations made previously where the two regions located in the LW and UW operated in phase opposition when the flame was modulated at $f = 60$ Hz. When this took place, the total heat release fluctuation in the flame was low. For $f = 90$ Hz, shown in Fig. 5.10, both sides of the

gray line were nearly in phase and both contributed positively or negatively to the heat release fluctuations. Under these circumstances the global level of heat release fluctuations was high. From this analysis it became clear that the flame response can be weak when two regions in the flame operate sequentially and give rise to a destructive interference of their heat release rates, an important observation to link global and local flame responses. Furthermore, the pattern orientation in these maps were different, suggesting that the response was determined by a combination of perturbations.

It has been shown in the previous sections that the perturbed velocity field comprises an axial and an azimuthal component. It is also known from previous studies that when the axial velocity perturbation reaches a maximum, a vortex is shed from the injector backplane. This vortex is convected by the flow and eventually rolls up the flame tip. This is the first mechanism of unsteady heat release which induces large flame surface area fluctuations which mainly operates near the tip of the flame and produces most of the heat release fluctuation detected in the UW defined in the previous section. The second mechanism is associated with the combined axial and azimuthal velocity perturbations. It induces fluctuations in swirl number, which in return generate variation of the IRZ reversal flow velocity, resulting in an angular modulation of the flame. Convective propagation is clearly visible in Fig. 5.10 with the slope of the patterns in the time-space diagram. These key experimental observations are furthermore described and modeled next.

2.4.1 Swirl number, flame angle, and turbulent flame speed oscillations

When the flow is swirling, one direct effect of the upstream oscillation is to modulate the swirl number and subsequently change the flame angle and the IRZ reversal flow strength, thus modifying the distance between the injector backplane and the flame front. Typical swirl number oscillations are depicted in Fig. 5.11. One clearly observes the wave pattern of the swirl oscillation.

Because of the prior section analysis, it is possible next to interpret the unsteady heat release distributions of the MICCA-EM2C-Palies setup and specifically consider the minimum and maximum gain of the flame response. This analysis was carried out for flame A, featuring a minimum and a maximum gain at $f = 60$ Hz and $f = 90$ Hz, respectively, and similar results were obtained for flame B. The flame angle changes in response to the incoming perturbations of axial and azimuthal velocity components. It is in-

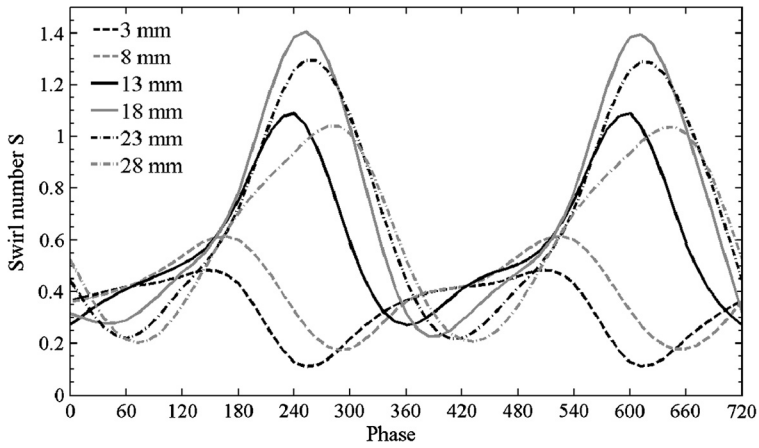

Figure 5.11 Swirl number oscillation as a function of the phase in two cycles of modulation for six positions z downstream of the swirler. Data are extracted from large eddy numerical simulations. These results clearly show the swirl number oscillation along the cycles. Modulation at $f = 60$ Hz. Source: Unpublished results from Palies [180].

teresting to estimate the relative angular fluctuation induced by this mechanism. This can be done by describing the normal propagation of the flame in terms of a turbulent burning velocity S_T. The flame angle α is then defined by

$$\sin\alpha = \frac{S_T}{u}. \tag{5.27}$$

This expression can be linearized around the mean state assuming small variations of the fluctuating quantities:

$$\sin(\overline{\alpha} + \alpha') = \frac{S_{T_0} + S_{T_1}}{\overline{u} + u'}. \tag{5.28}$$

After some calculations in which one only retains first-order terms, one finds the following relation:

$$\frac{\alpha'}{\overline{\alpha}} \simeq \frac{\tan\overline{\alpha}}{\overline{\alpha}}\left[\frac{S_{T_1}}{S_{T_0}} - \frac{u'}{\overline{u}}\right]. \tag{5.29}$$

It is assumed that the fluctuations in turbulent burning velocity ($S_T \sim v_{max}$ from Ishizuka et al. [481]) are linked to the axial and azimuthal velocity perturbations. A first-order expansion consists in assimilating S_{T_1}/S_{T_0} to the weighted sum of relative fluctuations in azimuthal and axial velocities, leading to Eq. (5.7). The relative fluctuation of the flame angle then becomes

$$\frac{\alpha'}{\overline{\alpha}} \simeq \frac{\tan\overline{\alpha}}{\overline{\alpha}}\left[\chi\frac{v'}{\overline{v}} + (\zeta - 1)\frac{u'}{\overline{u}}\right]. \tag{5.30}$$

To use the previous model one has to determine the coefficients defining the relative perturbations in the turbulent burning velocity in Eq. (5.7). The following values were used: $\chi = -0.4$ and $\zeta = 0.4$, deduced from a trial and error process. These values were also used by separate analysis of the theoretical transfer function of swirling flames presented in the previous section. The present choice corresponded to a trade-off. These coefficients could be determined more precisely by investigating the formulation derived in Palies [29] and documented in Chapter 4.

One expects from the previous analysis that swirl number fluctuations will be reflected in flame angle fluctuations. Also, the fluctuations in burning velocity and flame angle will directly translate into fluctuations in heat release rate. It is then possible to consider the mechanism which defines the heat release perturbation of the flame in the LW and link these perturbations to fluctuations of the flame angle α and the burning velocity S_T. The heat released by the flame in the LW is proportional to the burning velocity and flame surface area:

$$\dot{Q}_{lw} = \rho Y_f S_T A_f \Delta h, \tag{5.31}$$

where ρ is the density of the fresh stream, A_f is the flame surface, Δh is the heat release per unit mass of fuel, and Y_F is the mass fraction of fuel in the premixed stream. In the LW, the flame surface area may be estimated as a truncated cone:

$$A_f = \frac{\pi(r_2^2 - r_1^2)}{\sin\alpha}, \tag{5.32}$$

where r_2 is the radius of the flame at the top of the LW at a distance d_{lw} from the central rod and r_1 is the radius of the rod. Now, $r_2 = d_{lw}\tan\alpha$ and $r_1 << r_2$ so that A_f is proportional to $\sin\alpha/\cos^2\alpha$. The heat release fluctuation in the lower region $\dot{Q}'_{lw}$ may be obtained by expanding Eq. (5.7):

$$\dot{Q}'_{lw} = \rho \Delta h Y_{FO}(S_{T_1} A_f + S_{T_0} A'_f). \tag{5.33}$$

The relative fluctuation in heat release is then determined by

$$\frac{\dot{Q}'_{lw}}{\overline{\dot{Q}}_{lw}} = \frac{S_{T_1}}{S_{T_0}} + \alpha' \frac{1 + \sin^2\overline{\alpha}}{\cos\overline{\alpha}\sin\overline{\alpha}}. \tag{5.34}$$

To allow a comparison with experimental data, it is convenient to obtain the ratio of the heat release rate perturbation in the LW to the total heat release in the flame. This is obtained from the previ-

ous expression:

$$\frac{\dot{Q}'_{lw}}{\overline{\dot{Q}}} = \eta\left[\frac{S_{T_1}}{S_{T_0}} + \alpha'\frac{1+\sin^2\overline{\alpha}}{\cos\overline{\alpha}\sin\overline{\alpha}}\right]. \tag{5.35}$$

Here $\eta = \overline{\dot{Q}}_{lw}/\overline{\dot{Q}}$ represents the ratio of mean heat release in the LW to the total mean heat release of the flame, and its value is approximately equal to $\eta = 0.3$ for flame A.

Eq. (5.35), together with Eqs. (5.7) and (5.30), fully determines the heat release fluctuations detected in the LW. The combination of these fluctuations with those induced at the flame tip determines the flame response to incident perturbations.

This scenario was verified by examining signals detected in the experiments and comparing these data with theoretical estimates based on the previous expression. For this analysis one considers the following signals: $v'/\overline{v}$, $u'/\overline{u}$, $\alpha'/\overline{\alpha}$, $\dot{Q}'_{lw}/\overline{\dot{Q}}$, $\dot{Q}'_{uw}/\overline{\dot{Q}}$, and $\dot{Q}'/\overline{\dot{Q}}$. All these signals are obtained from measurements. In addition, it is important to plot the swirl number fluctuations $S'/\overline{S}$ deduced by subtracting the axial velocity fluctuation from the azimuthal velocity fluctuation and theoretical estimates of $\alpha'/\overline{\alpha}$ deduced from Eq. (5.30) and $\dot{Q}'_{lw}/\overline{\dot{Q}}$ obtained from Eq. (5.35).

The signals corresponding to $f = 90$ Hz for flame A are displayed in Fig. 5.12. The relative axial and azimuthal velocity fluctuations are still of the same order of magnitude, as expected from the actuator disk theory, but the signals are now nearly in phase. The swirl number fluctuations deduced from experimental velocity signals are much weaker than at 60 Hz (not shown here). The flame angle is also weakly perturbed by these fluctuations, see Fig. 5.12C, as seen in the flame dynamics data as well. Concerning the heat release rate in the UW, the mechanism involving flame surface fluctuations is present in this case. The experimental signals $\dot{Q}'_{lw}/\overline{\dot{Q}}$ and $\dot{Q}'_{uw}/\overline{\dot{Q}}$ are nearly in phase, yielding a maximum response in terms of total heat release rate fluctuation.

2.4.2 Vortex roll-up and flame surface modulation

To examine the additional mode conversion process of the vortex shedding initiated at the injector backplane inducing the roll-up of the flame, one may first locate the vortex structures in the flow at various instants during a modulation cycle. The identification of vortex structures was conveniently achieved by postprocessing the LES and calculating phase-average Q-criterion fields, see Haller [482]. Axial velocity fields and Q-criterion fields are plotted in Fig. 5.13 together with phase-average flame contours superimposed for each phase of the cycle separated by 60 degrees.

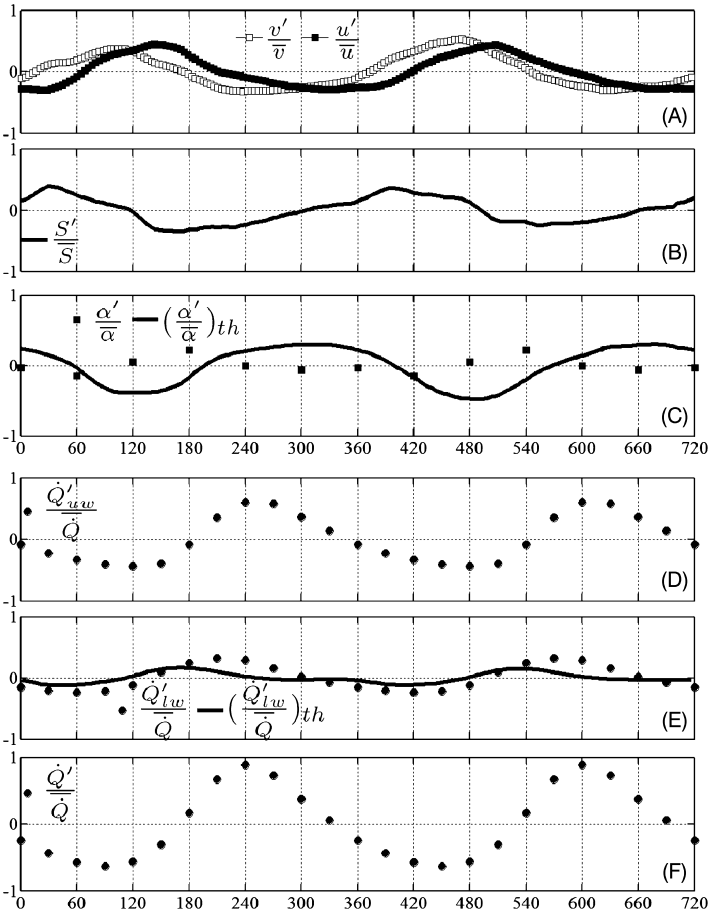

Figure 5.12 Signal time traces. Characteristic signals describing the response of flame A at $f = 90$ Hz versus phase (in degrees) during two cycles. Reconstructed signals are plotted as solid lines and experimental points are represented by symbols. (A) Relative velocity fluctuations. Open squares: $v'/\overline{v}$, dark squares: $u'/\overline{u}$. (B) Relative swirl number fluctuations $S'/\overline{S}$ deduced from the velocity signals. (C) Angular fluctuations $\alpha'/\overline{\alpha}$. Squares: experiment. Solid line: prediction. (D) Relative heat release rate in the upper window $\dot{Q}'_{uw}/\overline{\dot{Q}}$. (E) Relative heat release rate in the lower window $\dot{Q}'_{lw}/\overline{\dot{Q}}$. Symbols: experiment, solid line: prediction. (F) Relative total heat release rate fluctuation in the flame $\dot{Q}'/\overline{\dot{Q}}$. Source: Figures taken from Palies et al. [396].

These results were obtained by taking the phase average over nine cycles and spatially averaging along the azimuth. The color bar for the Q-criterion is set from $-2 \cdot 10^6$ s^{-2} in blue to $2 \cdot 10^6$ s^{-2} in red. The description of the dynamics was analyzed by examining vortex patterns in the flow and their interactions with the flame front. Heat release rate contours were also used to track the flame front dynamics during one modulation cycle.

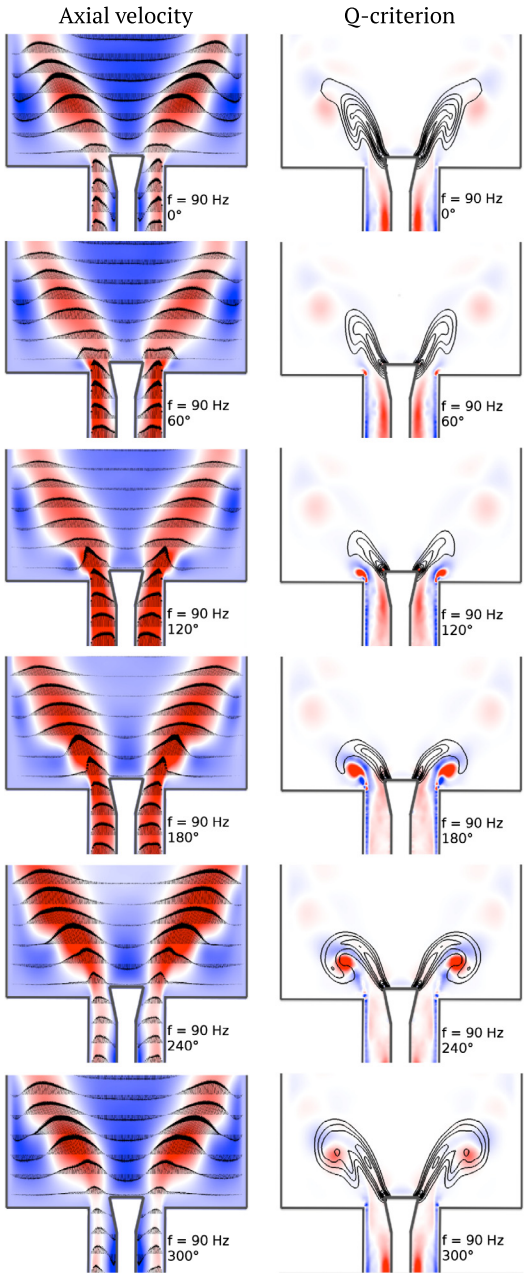

Figure 5.13 Velocities and Q-criterion. Axial velocity and velocity vectors are shown on the left column. The maximum velocity is $4\ \mathrm{m\,s^{-1}}$ and colored in red, while the minimum velocity is $-2\ \mathrm{m\,s^{-1}}$ and colored in blue. The Q-criterion contour is shown in color on the right column. The color bar is set from $-2 \cdot 10^6\ \mathrm{s^{-2}}$ in blue to $2 \cdot 10^6\ \mathrm{s^{-2}}$ in red. Heat release rate contours in black are used to track the flame front during one cycle of modulation. Frequency of modulation: $f = 90$ Hz. Source: Results taken from Palies et al. [395].

Only the dynamics at $f = 90$ Hz are discussed here. At a phase corresponding to 60 degrees, an annular vortex is shed from the injector backplane. The corresponding flame angle α at that instant in the modulation cycle is significantly smaller than at $f = 60$ Hz because swirl number fluctuations are substantially reduced in this case. This vortex is thus convected by the flow and increases in size and strength before interacting with the flame for a phase of about 180 degrees. At this instant in the cycle, it is strong enough to roll up the flame tip from 180 to 300 degrees, thereby increasing the flame surface area. Finally, during the next part of the cycle, the vortex is dissipated, the flame front extremities collapse, and the flame spreads over a broad area, and one observes the formation of a new vortex pattern in the duct due to the mode conversion process taking place at the swirler.

The previous results indicate that a strong vortex rolls up the flame at $f = 90$ Hz, which is confirmed by experiments, see Fig. 5.9. It was also found that the vortex shedding was significantly less important at $f = 60$ Hz. The formation of the vortex was canceled by the level of swirl number at $f = 60$ Hz, while at $f = 90$ Hz, its formation took place in a quasinonswirling jet (see the occurrence of the vortex shedding with respect to the IRZ reverse flow intensity at each phase instant). This clearly shows that the rate of rotation of the flow which oscillates (swirl number oscillation) and its phasing have an impact on the annular vortex shedding. The present LES calculations also indicate that the flame motion is determined by the relative phasing between the IRZ strength fluctuations, controlling the flame angle and the incident axial velocity fluctuations. At 60 Hz, the phasing is such that the flame angle changes significantly and the vortex created by the axial velocity fluctuation rapidly interacts with the flame without the possibility to gain in size and strength. At 90 Hz, the IRZ dynamics combined with the axial velocity fluctuations keep the flame angle at an essentially constant value, and this provides time for the vortex generated by the axial velocity fluctuation to fully develop and gain in strength before interacting with the flame. These interfering mechanisms can only be explained by taking into account the mode conversion mechanism at the swirler outlet, which is at the origin of the swirl number and flame surface angle fluctuations.

2.4.3 Other elements of the literature

It was determined in previous sections that the flame response inducing the unsteady heat release is driven by two major mechanisms: (i) the swirl number oscillation mechanism, which has been initially studied in Richards and Yip [371], Straub and

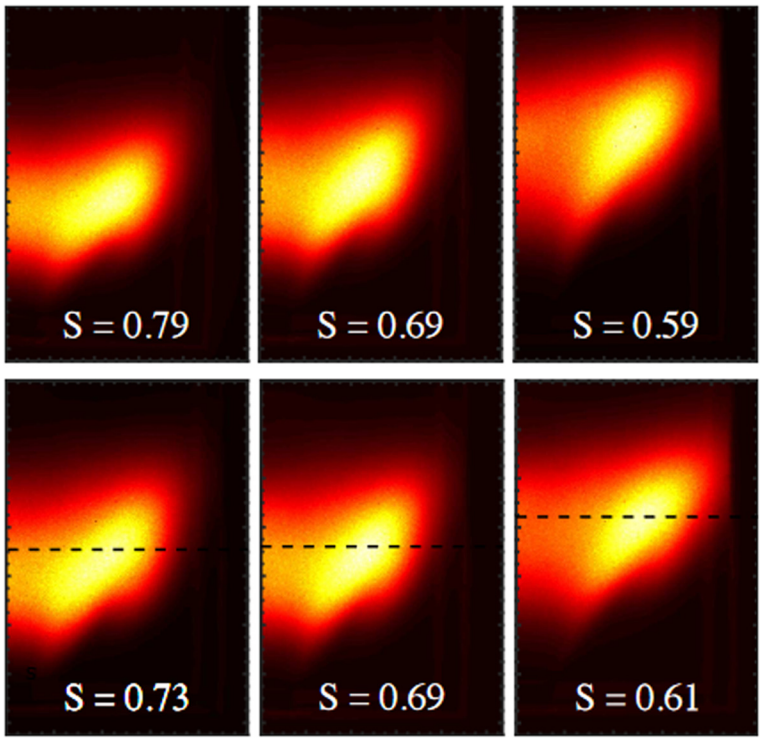

Figure 5.14 Effect of the injector modification. It induces swirl number modification on the flame shape, flame angle, and flame location. Source: Image taken from Gatti et al. [434].

Richards [372] and Komarek and Polifke [394], due to the mode conversion processes and subsequent unsteady velocity field affecting the flame front by changing the flame angle, and (ii) the vortex shedding impacting the flame.

These results have been explored and confirmed by researchers and published in several articles. Among them, the article of Kim and Santavicca [483] characterized in detail self-sustained oscillations of the Longi-PennState-Kim swirl-stabilized combustor as a function of axial swirler location, oscillation frequency, and mean injector velocity, confirming previous findings. In Fig. 5.15, stability maps with Rayleigh index on the y axis and phasing between the axial and azimuthal velocity fluctuations on the x axis were shown to group the limit cycle and stable operating points well. The article of Caux-Brisebois et al. [484] measured swirl number oscillations in a gas turbine model combustor, confirming previous findings, and demonstrated its impact on the helical vortex core and subsequent unsteady heat release oscillations.

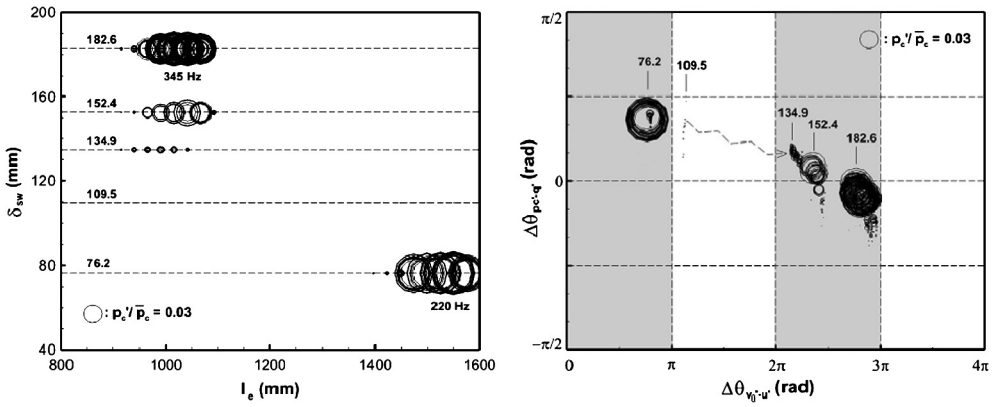

Figure 5.15 Effects of axial swirler location on self-excited instability. Left: Combustion instability intensity as a function of combustor length for $d_{sw} = 76.2$, 109.5, 134.9, 152.4, and 182.6 mm. Right: Corresponding stability map in terms of Rayleigh and velocity phasing. The diameter of symbols indicates the normalized amplitude of combustor pressure oscillations for a given combustor length. Source: Figure taken from Kim and Santavicca [485].

The thesis of Bunce [431] and the article of Bunce et al. [432] analyzed the contribution of the flame response by splitting the flame into two zones, as described in a previous section. The results showed the sensitivity of the window division location to the contribution of the UW and LW unsteady heat release. In addition, the results confirmed that swirl number fluctuations are an important velocity fluctuation mechanism for swirl-stabilized combustion systems. The article of Hermeth et al. [451] investigated the flame dynamics of the swirling flame of the DSTPB-Sie/Ansaldo-Hermeth configuration submitted to equivalence ratio oscillations with phase-averaged numerical simulation results. It was shown with the LES fields and a reduced-order model that mixing in the swirler did not minimize the heterogeneities from the unsteady fuel flow stream. These mixing fluctuations were phased with the velocity modulations and impacted the flame response to inlet forcing. Acharya and Lieuwen [454] investigated premixed swirling flames with numerical simulations and confirmed previous findings that the phasing between the azimuthal and axial velocity fluctuation is dependent on the frequency and controls the flame response. Furthermore, the fluctuating vorticity field generated by the unsteady flowfield and its impact on the flame response were analyzed. The article of De Rosa et al. [486] investigated the effects of the confinement ratio, defined as the ratio of the diameter of the nozzle relative to the combustor diameter, for values of 0.5, 0.37, and 0.29 for identical inlet flow velocities. The confinement ratio modifies the swirl number through

the velocity field and thus changes the mean flame angle. The measurements of the FTF for those three ratios showed a similar trend with characteristic extremum values of the FTF. Scaling of those flame responses was proposed based on the flame length Strouhal number firstly, and with that Strouhal number multiplied by the confinement ratio secondly. Results from scaling did not show agreement across the entire data set measured. In Gatti et al. [434], the authors investigated the flame response by splitting the unsteady heat release into two spatial contributions as well. The results indicated that for the peak response, the LW and UW heat release contributions of the flame were nearly in phase and the level of heat release increased in each window as the swirl number was reduced without modifications of their phase shift. For the weakest response at the largest swirl number operated, the LW and UW of the flame heat release were out of phase, in agreement with previous findings. Multiple-injector configurations were investigated, giving rise to various swirl numbers, as illustrated in Fig. 5.14.

In O'Connor and Lieuwen [488], the authors showed that the amplitude of the transverse acoustic forcing impacted the time average and the dynamic characteristics of the base flow of the swirling jet. It was also determined that the dynamic behavior of the flame was dependent on both the time-average flame angle and the unsteady velocity field. In Moeck et al. [487], the authors investigated the dynamics of the helical flow structure in a premixed swirling flame. It was measured that the acoustic modulation imposed by forcing and the helical mode at work induced a rotating heat release rate disturbance at a frequency corresponding to the frequency difference of the two mechanisms taken separately. An example of flame dynamics submitted to the helical pattern and inducing the rotating unsteady heat release is shown in Fig. 5.16. The helical mode was shown to scale with a constant Strouhal number. The article of Alekseenko et al. [489] studied the impact of inlet forcing, generating large axisymmetric roll-up, on turbulent combustion intensity and PVC on a swirling flame. It was shown that for inlet modulation amplitudes above that of the reverse flow inside the bubble-type recirculation zone, the PVC in the reacting case was suppressed. In Wang et al. [490], the authors performed ultrahigh speed (20 kHz) simultaneous PIV and PLIF measurements of an unconfined acoustically excited swirling flame to investigate the heat release rate oscillation and flame front motion due to vortical structures, enabling the recording of a detailed time sequence of the reacting flowfield.

Swirling flame dynamics have received considerable attention in the 2010s and were reviewed in this section. There are still open

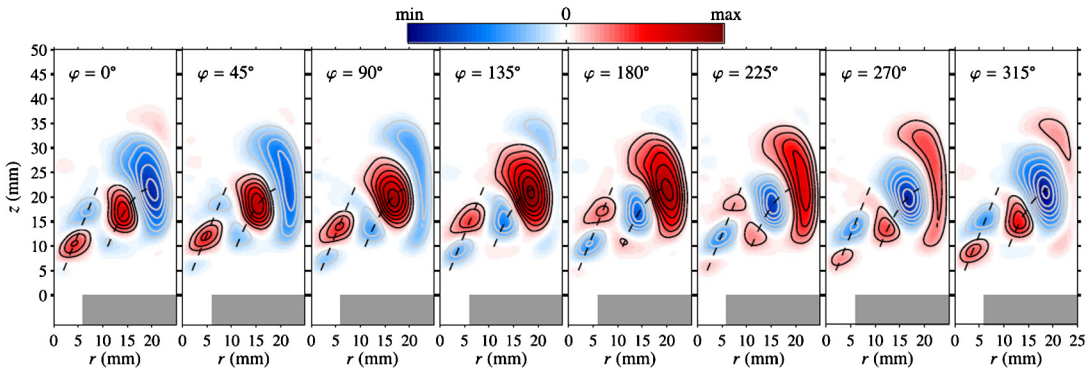

Figure 5.16 Tomographic reconstruction of the light intensity perturbation associated with the helical mode. Only the contribution of the first circumferential Fourier component is shown. The dashed lines represent conjectural trajectories along inner and outer shear layers. Source: Image taken from Moeck et al. [487].

questions regarding the role of velocity fluctuations (from vortical waves, acoustic waves, and turbulence), the nonlinearity of the flame response, and the effects of the static flame position that need to be examined. There is a relationship pointing out the direct role of fluctuation of the swirl number as a driver of the relative burning flame speed ratio, and subsequently of the unsteady heat release. This work should be continued to quantify these effects. Injecting harmonic velocity fluctuation components into the definition of the swirl number leads to strong nonlinear interactions, as characterized by coupling of the oscillations of individual velocity components that will thus affect the unsteady heat release through the relation between the relative flame speed and relative swirl number oscillations. This opens a possible route towards the understanding of flame nonlinearities. Open questions also include the effects of turbulence on the mean (time-average) flame position and the measurement, extraction, and computation of the static mode and its comparison with the time average.

3 Combustion instability

The previous section has comprehensively described the physical and chemical mechanisms at work for swirling flames submitted to inlet flow modulation. The present section focuses on combustion instability prediction and limit cycle physics, i.e., when no external forcing is applied and the dynamics are self-sustained. Prediction of combustion instabilities at the design and developmental stages of jet engines and gas turbine combustors is a challenge. There has been a significant amount of research on

combustion instabilities and this topic has been reviewed in many articles, including those of, but not limited to, Crocco [173], Putnam [174], Culick [175], Candel [171] for canonical configurations, Huang and Yang [22], Candel et al. [23] for swirling flames, and Lawn and Penelet [177], Juniper and Sujith [178] for other configurations. The prediction and control of combustion instabilities in realistic geometries has been recently reviewed by Poinsot [179]. While the limit cycle has been significantly studied, the transient to the limit cycle has received more attention only recently, and will be a research path to explore further, as discussed next in a specific subsection.

3.1 Combustion instability prediction

This section describes the context of combustion instability predictions and the two major methods for such predictions. The first method is based on the coupling of a network acoustics model with the flame response (obtained numerically, analytically, or experimentally) and the derivation of a dispersion relation leading to frequency-growth rate trajectories, enabling prediction trends. The second method is based on numerical simulations.

3.1.1 Predictive methods

The two main methodologies for combustion instability analysis and prediction have pros and cons, and are discussed now.

- Methods based on an acoustics analysis of the system relying on networks of compact acoustic elements and employing a linear (FTF) or nonlinear description (FDF) for the flame response, along with a set of boundary conditions. These methods have been documented by Poinsot and Veynante [172], Munjal [491] and by Stow and Dowling [492], Nicoud et al. [493], Schuermans et al. [494]. In these methods, the prediction of the combustion instability trend is conducted by combining the flame response (obtained experimentally, theoretically, or numerically) with the system acoustics in order to obtain the frequency-growth rate trajectory. The stability of the system is determined by evaluating the growth rate level in the obtained frequency-growth rate trajectory. These methods enable screening various parameters and obtaining trends but they lack in terms of accuracy with respect to the second approach. One of their strengths is to inform on the most important first-order effects on the flame dynamics, allowing to guide the subsequent analysis. They reach their limit of use though in evaluating marginally unstable systems. This is a known aspect of such approaches.

- Direct methods where LESs of the complete 3D, compressible reacting Navier–Stokes equations are used as illustrated by Selle et al. [495]. This direct approach relies on the full numerical resolution of the governing equations to capture the possible limit cycle behavior and assess the stability of a configuration. The evolution of perturbation amplitudes in the LESs is monitored to detect the stability. While this approach is accurate and valuable for capturing both forced and self-sustained flame dynamics, they require large capabilities in terms of CPU power, and streamlined data processing and CFD software for analysis. Their biggest advantage is to offer the full spatiotemporal field to investigate physics of the phenomena and guide design. They need careful boundary conditions and LES model treatments.

In the following subsections, prediction results obtained in the MICCA-EM2C-Palies configuration are presented. Experimental studies of combustion instabilities are reviewed, along with various existing types of instabilities occurring in combustion systems, such as in lean premixed/prevaporized and also rich-burn quick-quench lean-burn combustors.

3.1.2 Stability map

Stability analysis of swirling flames is of importance in the design of advanced combustor concepts for aircraft propulsion and power generation. Experimental stability maps indicate the occurrence and the level of oscillations in a combustor under various conditions, including geometrical and operating parameters. These maps are employed to validate theoretical predictions. As a demonstration, the experimental stability map of the EM2C-MICCA-Palies setup is presented in this section. The geometrical parameters of the upstream plenum and of the flame tube were varied. In Fig. 5.17, the stable cases are indicated with gray circles, and black stars indicate a high level of velocity and pressure fluctuations corresponding to self-sustained oscillation within the system. Gray stars indicate slightly unstable cases also known as marginally stable. Fig. 5.15 (left) presents another stability map for the Longi-PennState-Kim combustor, where the influence of the swirler location on the occurrence of instability was determined.

3.1.3 Frequency-growth rate trajectories

The network acoustic modeling approach was presented in Section 1.2. As the obtained dispersion relation is coupled to the flame response, it allows the determination of the frequency-growth rate trajectories. Those are now introduced and discussed.

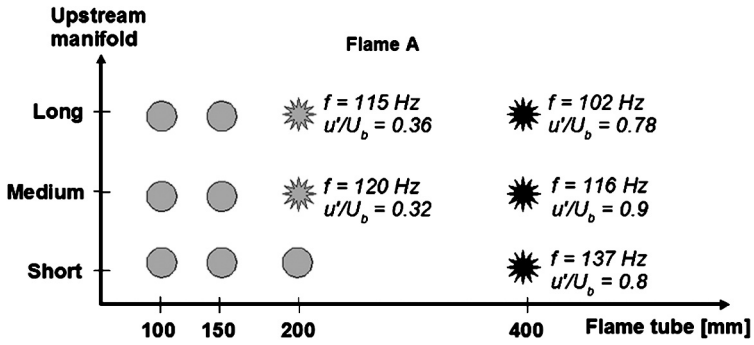

Figure 5.17 Experimental combustor stability map for flame A. Source: Figure taken from Palies et al. [369].

When the FTF is replaced by an FDF concept that depends on both the frequency and the amplitude of perturbations impinging on the flame, a frequency domain stability analysis then yields growth rates and frequencies which depend on the amplitude, see Noiray et al. [274]. The results presented in this section obtained in the MICCA-EM2C-Palies configuration followed a similar approach with a specific method to solve for the root locus in the frequency-growth rate trajectory to determine frequencies and amplitudes at the limit cycle of the self-sustained instability. The predictions for the swirling flame A configuration with the FDF framework are shown in Fig. 5.19 for the medium-size upstream plenum. This plot can be used to predict the stable or unstable behavior of a configuration. With the medium-size upstream manifold, one finds that for a flame tube size smaller than 170 mm, the combustor is stable. For greater lengths, the combustor is unstable. Increasing the flame tube length, the amplitude of the velocity disturbance at the limit cycle increases to reach very high levels. A longer upstream plenum slightly improves the stability of the combustor. Self-sustained oscillations occur for flame tubes longer than $l_3 = 220$ mm and the fluctuation level at the limit cycle rapidly reaches high values.

This methodology has been extended by multiple authors in the MICCA-EM2C-Palies configuration and in other configurations such as annular combustion systems, see the results plotted in Fig. 5.18. Results of the application of the FDF coupled to an acoustic network to the EM2C-MICCA-Palies configuration are plotted in Fig. 5.20. They were obtained by solving the dispersion relation of the system. The particular approach to solve the dispersion relation, contrarily to that of previous studies and used in multiple subsequent studies, is as follows. The dispersion relation has a real and an imaginary part, and the solution searched

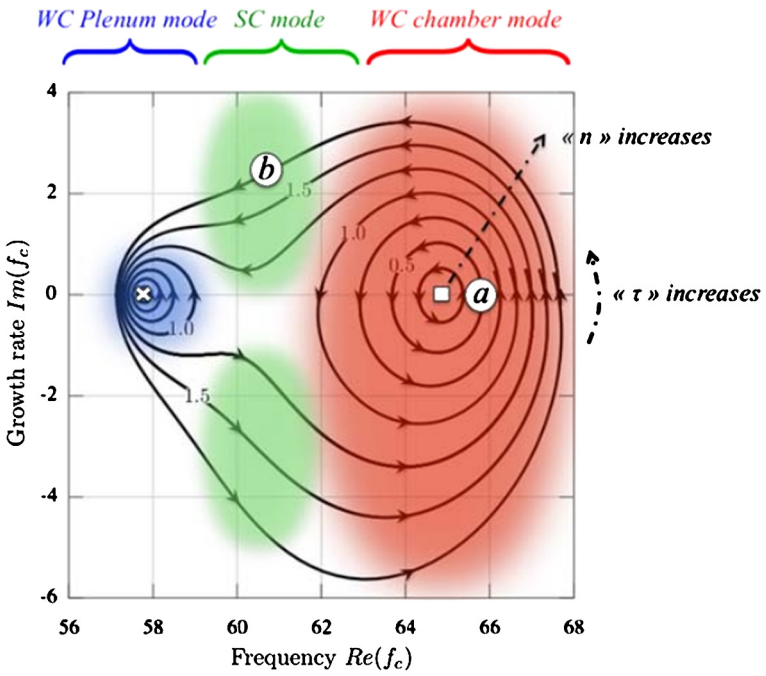

Figure 5.18 Frequency-growth rate map. Frequency-growth rate map for the annular combustors showing plenum and combustion chamber mode bifurcation as a function of the flame transfer function gain and phase. Source: Figure taken from Bauerheim et al. [496].

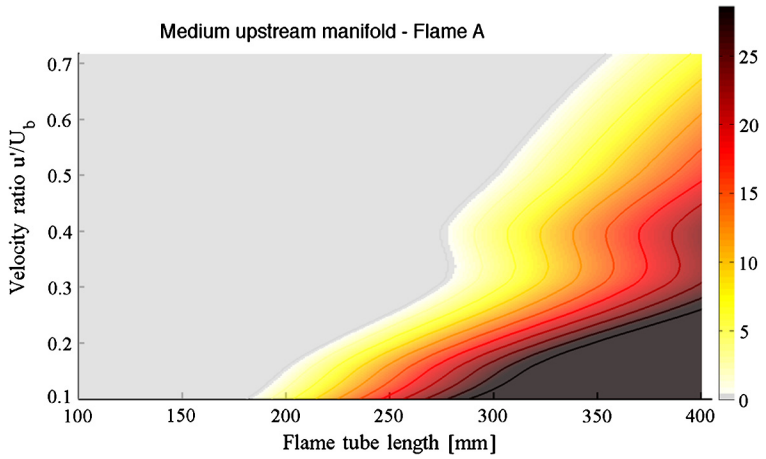

Figure 5.19 Stability maps of the burner for flame A as a function of the flame tube length varying between $l_3 = 100$ and $l_3 = 400$ mm. The color bar indicates values of $\omega_i - \alpha$ in s^{-1} (negative values correspond to the gray region). The line separating gray and white regions corresponds to points where $\omega_i - \alpha = 0$, meaning that the limit cycle is reached. For medium upstream plenum/manifold. Source: Figure from Palies et al. [369].

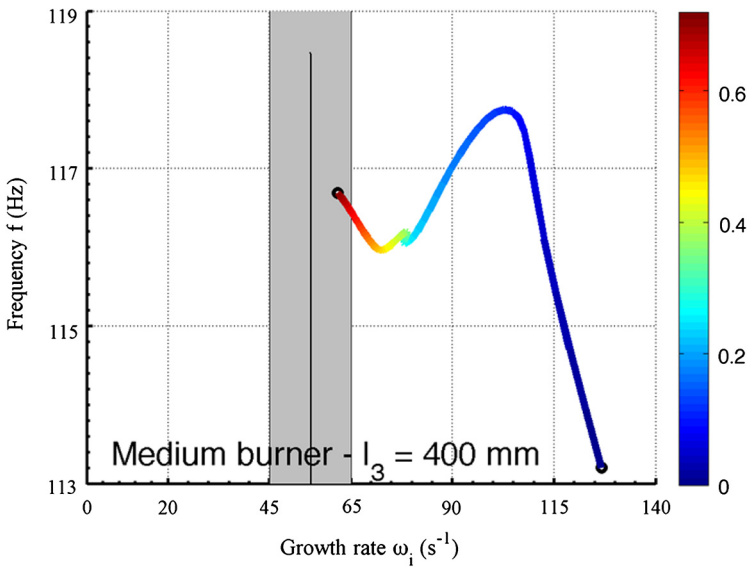

Figure 5.20 Example of frequency-growth rate trajectories plotted as a function of the velocity disturbance level u'/U_b. The value of the damping rate α is shown in the form of a gray region representing the error bar on this quantity. The stable and unstable regions are located respectively on the left and on the right of the gray region. The root locus is plotted on a color scale as a function of the relative fluctuation level u'/U_b. Flow conditions are those of flame A. Source: Figure from Palies et al. [369].

for too. Indeed, we are focusing on complex frequencies here, so while the flame response is only dependent on the real frequency, the wavevectors are dependent on the damping/growth rates of the complex pulsation. Consequently, solving the dispersion relation leads to two equations, for the real and imaginary parts, which are solved geometrically iteratively when these parts are zeros to determine the frequency and the growth rate satisfying these equations.

Fig. 5.20 shows the root locus $(\omega_i(u'_2), f(u'_2) = \omega_r(u'_2)/(2\pi))$ when the relative velocity fluctuation level upstream of the flame is progressively increased. The error bar on the damping rate is also shown in the form of a vertical gray region. When the trajectory is on the left of the estimated damping, the system is stable. When the trajectory begins on the right of the region corresponding to the estimated damping, the system is unstable and reaches a limit cycle at the cross-point between the root locus and the vertical region corresponding to the damping rate and its error bar shown in gray. The root locus is plotted in a growth rate–frequency $(\omega_i\text{-}f)$ diagram respectively expressed in s^{-1} and Hz. A color scale is used to represent the velocity disturbance amplitude. Twenty-

four cases are considered, twelve corresponding to flame A and twelve to flame B. The demonstration of the FDF framework in this generic configuration indicated that it can be used in more general situations of technological interest.

The experimental measurements and the determination of the regime of instability presented in Fig. 5.17 and the obtained prediction such as presented in Figs. 5.19 and 5.20 have been obtained and confirmed with a similar method based on coupling the experimentally measured swirling FDF and an acoustic solver by Kulkarni and Nicoud [498] and Silva et al. [403]. The work of Laera and Camporeale [499] followed also a close method considering the FTF as distributed spatially coupled to an acoustic solver to determine the limit cycle condition in two configurations including the LRIA-CCA/Ansoldo-Rofi case. In Han et al. [398], the authors applied the network model approach to the prediction of combustion instabilities after validating the tools on the MICCA-EM2C-Palies configuration and associated results. In Fig. 5.21, stability analyses were conducted in a similar fashion to study the influence of the swirl number, see Durox et al. [497].

In this section, combustion instability prediction for swirl-stabilized combustors has been presented. There are several aspects that should be investigated for future work and which are active points of discussion. First of all, the estimation of the damping of the system enabling the determination of the limit cycle frequency and amplitude is a challenge and theoretical studies enabling the calculation of this quantity are needed. In addition, the effects of various flow nonlinearities (such as the PVC) on the FDF and the subsequent limit cycle prediction should be investigated. The effects of the static mode versus the time average on combustion instability prediction with reduced-order models will also be of technological and fundamental interest.

3.2 Coupling and stability criteria

There are many combustion instability criteria, which are reviewed in this section. The Rayleigh criterion is the most well known and it reflects the fact that combustion instability occurs when the heat release rate and the pressure fluctuation signals are such that their phase is between 0 and 90 degrees, see the articles by Nicoud and Poinsot [500], Culick [501]. This criterion can be evaluated globally or locally.

To evaluate the regions where vortex roll-up are driving regions of the oscillation, the 2D Rayleigh index maps were formed and integrated in time over the whole time series in Palies et al. [213] in the LSI-LBNL-Cheng experiment. The Rayleigh index time inte-

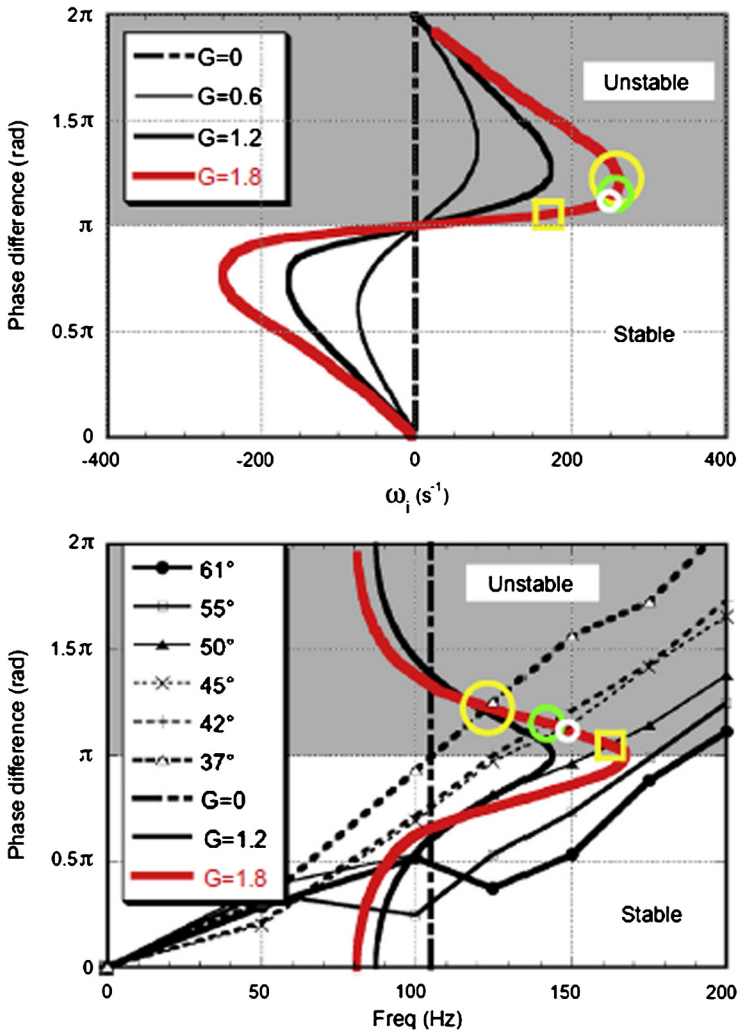

Figure 5.21 Stability analysis results for the first acoustic mode. Top figure: Phase difference plotted as a function of the amplification rate for different fixed values of the gain. The unstable band is found to be between $[\pi, 2\pi]$. Bottom figure: Phase difference plotted as a function of frequency. The experimental FTF phase curves and the theoretical root locus calculated for $G = 1.8$ are plotted in this graph. The circles and the square indicate the intersections between the experimental phase curves and the theoretical root locus in the unstable band. Source: Figure taken from Durox et al. [497].

gral was defined as the time integral of the nondimensional product of the fluctuation of pressure and chemiluminescence signals. The quantity RI(x, y) for the CH_4 flame (see Fig. 5.22) shows that the driving region corresponds to the upper part of the flame, while the damping region is located on the sides of the flame front.

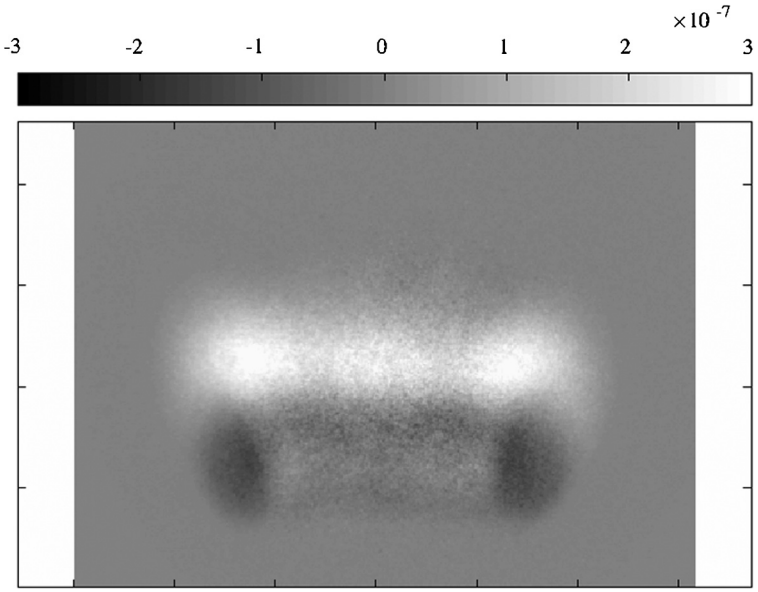

Figure 5.22 Rayleigh index map. Rayleigh index map obtained in the LSI-LBNL-Cheng configuration. Source: Figure taken from Palies et al. [213].

The Rayleigh index criterion has been applied in many studies of swirling flames, see Kang et al. [276] for longitudinal inlet modulation and Zellhuber et al. [502] for transverse combustion instabilities. Rayleigh index maps of combustors operating with kerosene fuel have been published in Apeloig et al. [503].

Another stability criterion is the parameter Ξ from Eq. (5.3) allowing to determine coupled or uncoupled acoustic modes within a given geometry. This criterion has been derived and applied in multiple configurations, see Palies [180], Schuller et al. [397] for longitudinal cases and Bauerheim et al. [504] for annular combustors. Another criterion for swirling flames is to directly use the phasing between the axial and azimuthal velocity perturbations, see Palies et al. [396]. This criterion has been demonstrated by Kim and Santavicca [485] in combination with the Rayleigh criterion to allow to categorize the regime on stability maps, see Fig. 5.15 (right). These criteria can also be used to perform passive control through the parameters included in them. In general, studies on swirling flame instabilities should attempt to quantify these criteria comprehensively. The Rayleigh index map and integral values are widely used in combustion system studies. The phasing between the axial and azimuthal velocity oscillation criterion should

be used in swirl-stabilized combustion dynamics and instability studies.

Swirling flames under self-sustained oscillations are not commonly investigated with DNS-like simulations even though such a configuration allows nowadays resolving of all the physics at work at a reachable CPU cost when considering a limited domain size and atmospheric conditions. Extensive analysis and postprocessing of such data sets will allow to further (i) investigate the effects of turbulence on the transition to instability through the conversion of turbulence fluctuation into acoustic harmonic fluctuation and (ii) study and compare the impact of the static and time-average flame front positions on the instability triggering and on stability analysis. It is an important topic of discussion to clarify the role of the static mode versus the time average.

3.3 Longitudinal instabilities

This section summarizes the state of understanding of velocity coupling, equivalence ratio coupling, and entropy mode combustion instabilities that occur in the longitudinal direction of swirl-stabilized combustors. These are the three main mechanisms that can be at work in such systems. Instabilities in that direction have been widely studied. The mechanisms are generally studied with laser diagnostics and numerical simulations. There is a need though for further analytical works to study and guide analysis of such instabilities.

3.3.1 Velocity coupling

Longitudinal combustion instabilities of swirling flames induced through velocity coupling have been the subject of many researches. It has been previously reviewed by Huang and Yang [22] and it is the topic of many chapters of the edited book by Lieuwen and Yang [87]. In the present section, the state of the art is presented.

In the Longi-MIT-Taamallah configuration, the effects of equivalence ratio and combustor length have been investigated, see Taamallah et al. [362,370]. It was shown that the short combustor operated under stable conditions over a range of equivalence ratios from nearly the lean flammability limit to 0.75. Contrarily, for the long combustor, depending on the equivalence ratio, strong unstable operating conditions were observed. The analysis of the mean flowfield and of the flame shape showed small differences in their global structures over the range of equivalence ratios. The global shapes were shown to be similar between the long and short combustors over that range of equivalence ratios, while the

stability behavior was strongly different due to the modification of the acoustics of the system and the subsequent interaction with the flame. Spatial local characterization of the differences for the flowfield and flame shapes between short and long combustors were reported, see the examples given in Figs. 5.23 and 5.25. The transition to low frequency instability was further studied and was associated with an unsteady heat release located in the ORZ.

The article of Lartigue et al. [505] focused on the Preccinsta-DLR-Lartigue configuration and presented measurements techniques and results along with the operating condition for self-sustained oscillations occurring near 300 Hz and 500 Hz. In that article, initial simulations of the nonreacting flow were also reported. In the same configuration, the article of Roux et al. [400] investigated combustion instabilities with LES experiments and acoustic analyses. It was shown that the PVC is damped during self-sustained oscillation while a strong pattern existed in the nonreacting case. In addition, the main mode frequency dominating all unsteadiness was confirmed near 500 Hz by the analyses. The DSB-DLR-Weigand configuration was experimentally analyzed and investigated by Allison et al. [506]. High speed PLIF diagnostics was employed to determine and characterize the thermoacoustic flame occurrence. The time average of chemiluminescence of the thermoacoustically coupled versus stable case showed strong differences, which points toward the effects on the dynamic component.

The article of Stone and Menon [429] focused on the effect of the swirl number and overall equivalence ratio on the stability of a model swirl-stabilized, lean premixed gas turbine combustor numerically simulated using LESs. It was shown that for large values of the swirl number where vortex breakdown occurred, the fluctuating pressure amplitudes were attenuated significantly (over 6.6 dB reduction). These reduced pressure amplitudes were accompanied by reduced longitudinal flame front oscillations and reduced coherence in the shed vortices, a result consistent with findings presented in literature. Similar pressure fluctuation level reductions were achieved through changes in equivalence ratio. Compared with the leanest equivalence ratio simulated, the pressure oscillation at stoichiometry was reduced by 6.0 dB. The response of the combustion process to explicit swirl modulation was also investigated. Open loop control through swirl variation was demonstrated for a lean mixture with significant reductions in mass flow rate fluctuations and pressure fluctuations after a convective time delay.

Measurements of triggering and transient growth toward instability in the MGTC-UnivCambr-Kim configuration were carried

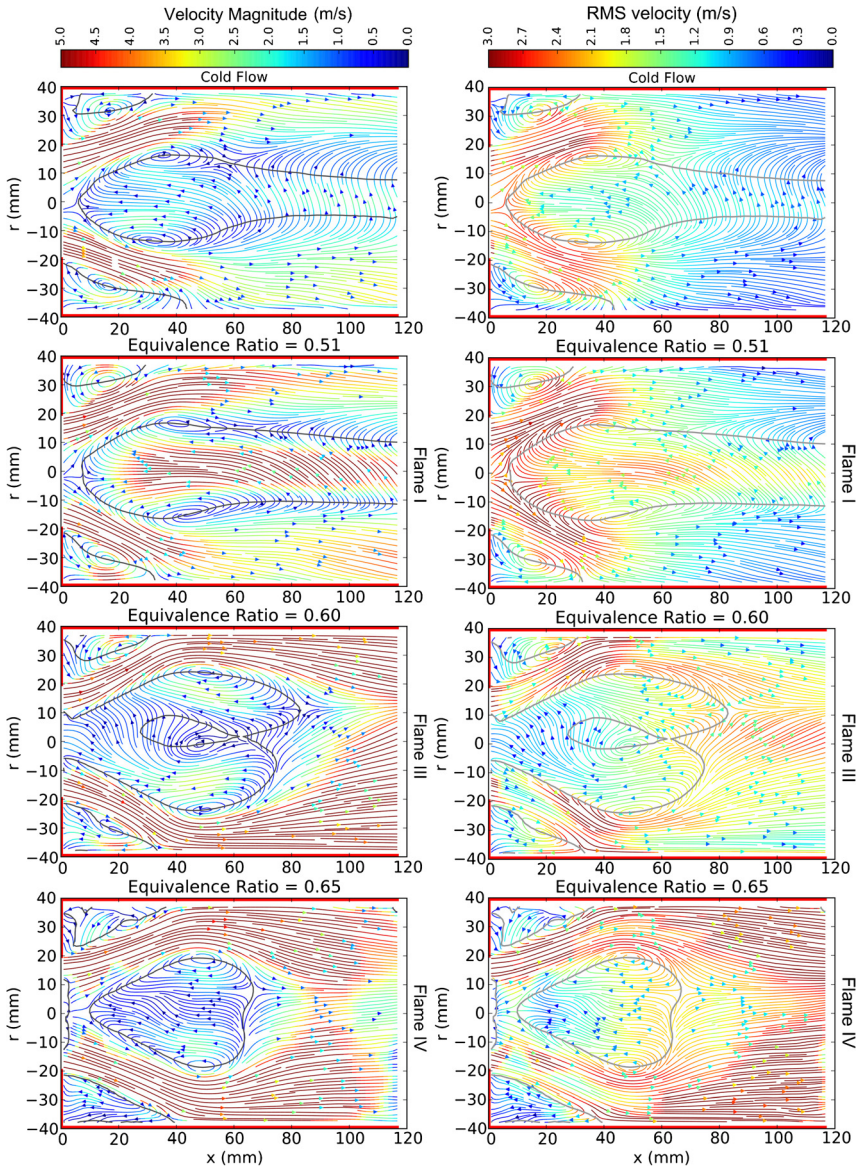

Figure 5.23 Visualization of the reacting flowfield. Left column: Mean velocity streamlines colored by velocity magnitude for nonreacting flow and flame shape. Right column: Mean velocity streamlines colored by total RMS velocity for nonreacting flow and flame shape. Source: Figures taken from Taamallah et al. [370].

out by Kim and Hochgreb [428]. Unsteady chemiluminescence, velocity, and pressure fluctuations were documented at the onset of the transition and at the subsequent limit cycle, see Fig. 5.24.

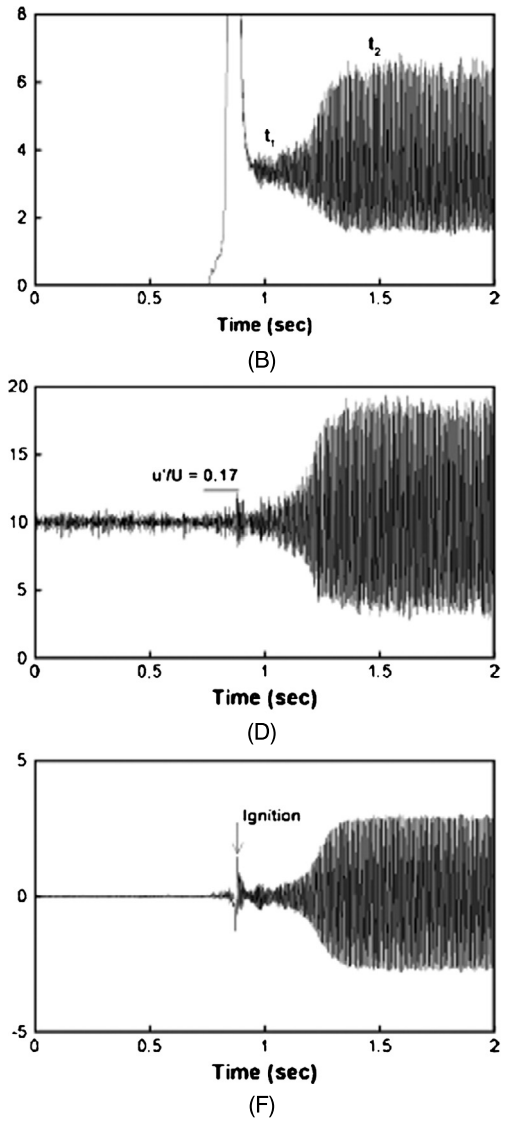

Figure 5.24 Time trace of unsteady heat release, velocity, and pressure. Temporal evolution of OH* emission chemiluminescence (top), inlet velocity (center), and combustor pressure (bottom) from stable to the limit cycle through successful combustion instability triggering. Inlet conditions: $T_i = 20°\text{C}$, $p_i = 1$ atm, $U = 10.0$ m/s, $\phi_g = 0.60$, $L_c = 800$ mm. Source: Signals taken from Kim and Hochgreb [428].

While the unsteady pressure signal showed a symmetrical behavior, the velocity and heat release signals showed a dissymmetry with respect to the centerline. These observations confirm the

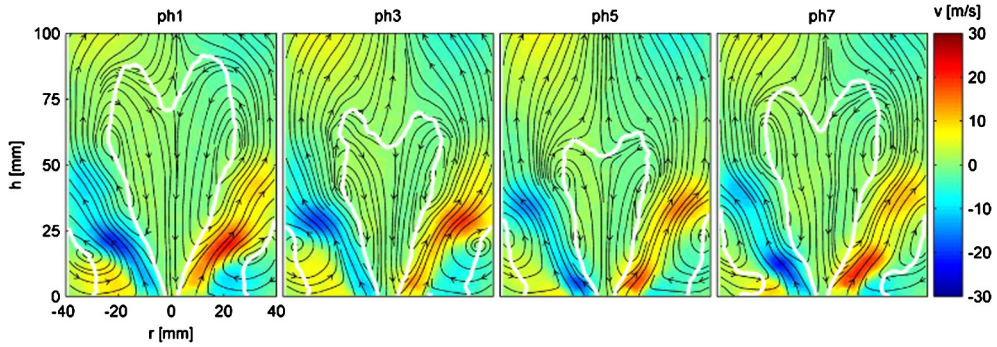

Figure 5.25 Phase-correlated mean values of the flowfield at multiple phases. The radial velocity is color-coded. The white lines represent the shape of the recirculation zones (zero axial velocity) along a cycle. Source: Figure taken from Arndt et al. [520].

stronger nonlinear content of the velocity and heat release signals compared with the pressure signal. This also supports theoretical results presented in chapter 3. Combustion instabilities were also characterized by Weigand et al. [479], with the emphasis on the comparison between stable and thermoacoustically coupled operating points. The inlet bulk velocity and equivalence ratio were adjusted to obtain these two conditions. Detailed characterization of the mean flame shape, instantaneous flame structure, and mean velocity field were carried out with PLIF (OH and CH) and LDV, respectively. Mixture fraction and temperature were also measured and documented in terms of mean and RMS quantities. The article of Schildmacher et al. [507] focused on the thermoacoustic behavior of the DSTPB-Siemens/Ansaldo-Hermeth configuration. The dynamics of the flowfield and of the flame were studied experimentally by phase-locked LDA and OH-LIF diagnostics. It was shown that increasing the equivalence ratio led to the transition from low to high oscillation pressure levels. In addition, swirl number level oscillations during instability were measured along a cycle.

Combustion instabilities have been observed in the EPICTETE-ONERA-Cochet configuration, see Cochet et al. [508]. The authors observed the following differences compared with stable operation: a change of the kerosene spray and flame shapes, a strong pressure fluctuation, and a sudden shift of the PVC frequency from 830 Hz to 1125 Hz. In the same configuration the stable operating points were characterized with laser diagnostics by Fdida et al. [509]. The article of Richecoeur et al. [510] focused on the determination of the acoustics content in the CESAM-EM2C-Richecoeur configuration and on the influence of the upstream

acoustic impedance and the downstream combustor length effect. In Huang et al. [511], the authors focused on the analysis of combustion instabilities of the LDI-PurdueUniv-Huang configuration where inlet air temperature and equivalence ratio were varied. The analysis was carried out with flow–flame dynamics results obtained from numerical simulations and a dynamic mode decomposition (DMD) algorithm highlighting a coupling between the low frequency acoustic mode and the IRZ. The article of Kraus et al. [512] compared self-sustained instabilities in the single SBS-KIT-Kraus setup and multiple sector setups. Different amplitudes of oscillations were observed depending on the operating conditions. The following hypothesis was concluded. The reduction of the swirl intensity, due to the multiple-injector arrangement with respect to the single injector, led to a shift of the high flame response frequency range to lower frequencies. In Kraus et al. [513], the authors focused on the SBS-KIT-Kraus configuration to study the effects of heat transfer from the combustion region to the combustor. The article compared two numerical simulations. The first one was computed with adiabatic walls, and an unstable mode was found near 635 Hz, while the second one took into account heat transfer to the combustor walls. In that case, the frequency of the unstable mode was near 725 Hz, which is closer to the experimentally measured frequency of 750 Hz.

Multiple-injector configurations have also been investigated. In Samarasinghe et al. [514], at operating conditions where all injectors are fueled equally in the MNCC-PennState-Santavicca configuration, it was shown that fuel staging suppressed the self-sustained instability both when the overall equivalence ratio was increased by staging and when the overall equivalence ratio was kept constant while staging. The authors observed that increasing fuel staging changed the distribution of the time-averaged heat release rate in the regions where adjacent flames interacted and reduced the amplitudes of heat release rate fluctuations in those regions. Increased fuel staging also induced a breakup in the monotonic phase behavior of disturbances convected along the flame.

The study of Roy et al. [515] focused on combustion instabilities of reacting swirling flows with the identification of large-scale flow structures between a stable and an unstable case. It was shown that an axisymmetric mode due to the self-sustained oscillation dominated the flowfield (as demonstrated with the DMD results), whereas under stable reacting conditions, a large-scale helical mode dominated the flowfield. The authors observed also consequently strong differences of the mean flow between the two cases. The studies of Karlis et al. [516,517] focused on the effects of

operating pressure on the dynamics of the Siemens-SGT-100 combustor at constant inlet bulk velocity. The authors visualized and measured with phase-locked synchronized diagnostics the limit cycle periodic flowfield with PIV, OH* chemiluminescence imaging, and dynamic pressure signals. It is worthwhile to point out that this experiment is pioneering in enabling the synchronized flow and flame dynamics measurements and visualizations at the limit cycle and elevated pressure conditions.

To summarize this section, the velocity coupling mechanism for swirl-stabilized flames during combustion instabilities is well documented and the underlying mechanisms are known and identified, thus enabling predictions with reduced-order models or LES simulations.

3.3.2 Equivalence ratio coupling

Kim and Santavicca [483] demonstrated that in the presence of equivalence ratio oscillation, the oscillating flowfield (azimuthal and axial velocity) controls the global flame dynamics in association with the flame–vortex structure interactions, depending on the phase difference between the two inlet perturbations. For liquid spray injection, the modulated velocity field necessarily induced an oscillation of the equivalence ratio. In Tachibana et al. [518], LES was used to capture the combustion instability of a single sector operating at high pressure and temperature with liquid fuel. The experimental flame dynamics obtained under thermoacoustic conditions at those operating conditions were compared with LES results, demonstrating a good agreement between global pressure and flame structure dynamics, while local flashback and pressure amplitudes presented discrepancies between LES and experiments. In the LPP-EM2C-Providakis configuration, the focus of Providakis et al. [519] was on the effects of the combustor fuel staging on flame stability. It was shown that the staging factor influences the flame shape and its position due to the modification of the fuel distribution. In addition, the acoustic coupling with the flame was further characterized, showing the global unsteady motion of the velocity field and the spray distribution at the frequency of the instability. The configuration of LOTAR-ONERA-Apeloig was studied by Apeloig et al. [503] to investigate the thermoacoustics coupling with temporal evolution of the spatial fuel distribution and flame structure during the limit cycle. Phase-locked liquid spray distributions, fuel vapor, and OH fields were characterized spatially along the limit cycle. In that study, the spray injection columns interacted with the walls within the injector to form liquid films which were shown to be convected toward the injector outlet and subsequently reatomized. It was

observed that when the air mass flow rate fluctuated, the liquid behavior was impacted through modifications of the jet trajectories, leading to large oscillations of the spray pattern in the combustion chamber. Selected results from that article are given in Fig. 5.26. The SBS-KIT-Kraus configuration was investigated by Arndt et al. [520]. The experimental measurements showed that the feedback mechanism of the thermoacoustics instability was due to an equivalence ratio oscillation with a convective delay for the transport of fuel from the fuel injector to the flame zone.

Unlike the velocity coupling phenomena, swirling flame combustion instabilities induced by equivalence ratio coupling are less documented. One particular aspect that is lacking is the formation of harmonic oscillation of the equivalence ratio when this latter is not associated with the velocity coupling mechanism. Furthermore, there is no fully documented theory for those mechanisms while they will be important for the design of future injectors that will make use of partially premixed combustion regimes prior to reaching a fully premixed regime.

3.3.3 Entropy modes

Combustion instabilities induced by entropy modes for swirl-stabilized combustors have been investigated and described comprehensively by Motheau et al. [281], allowing an overall theoretical description, understanding, and modeling of these types of combustion instabilities. An aeroengine combustor was analyzed with the use of DMD, phase-locked LES data (pressure, temperature, and velocity unsteady fluctuating field), and theoretical modeling. DMD and phase-locked data were use to identify and characterize the instability dynamics, see the results given in Fig. 5.27. Specific attention was paid to the characterization of the entropy wave convective motion. Theoretical derivation was also carried out to incorporate the effects of mean flow, which led to an expression of a delayed entropy coupled boundary condition, which once integrated into an acoustics model can be used to predict frequencies and growth rates of combustion instabilities induced by entropy modes. This approach was implemented, presented, and compared with LES and experiments by Motheau et al. [402]. The modeling of entropy modes responsible for combustion instabilities has also been studied in other works. LES of a model aeroengine combustor was carried out and an entropy mode was captured by Lacombe and Méry [98]. The analysis of the results led to a decomposition of the combustor into two zones responsible of the combustion instabilities: an overall rich premixed flame in the front of the combustor and an overall lean diffusion flame stabilized next to the dilution holes. In Giusti [521], the focus

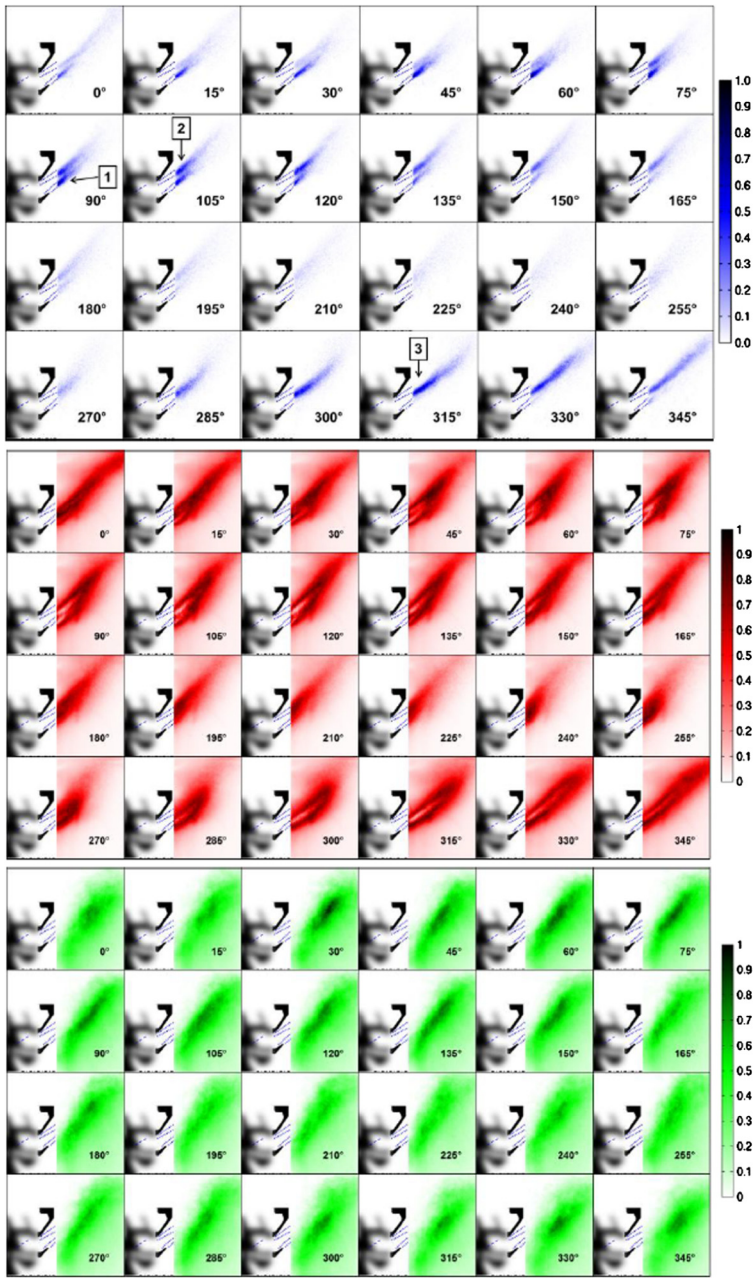

Figure 5.26 Temporal sequence during an instability cycle using phase-averaged analysis of PLIF images. Top set of images: Liquid kerosene spatial distribution. Center set of images: Kerosene vapor spatial distribution. Bottom set of images: OH radical spatial distribution. Source: Figures taken from Apeloig et al. [503].

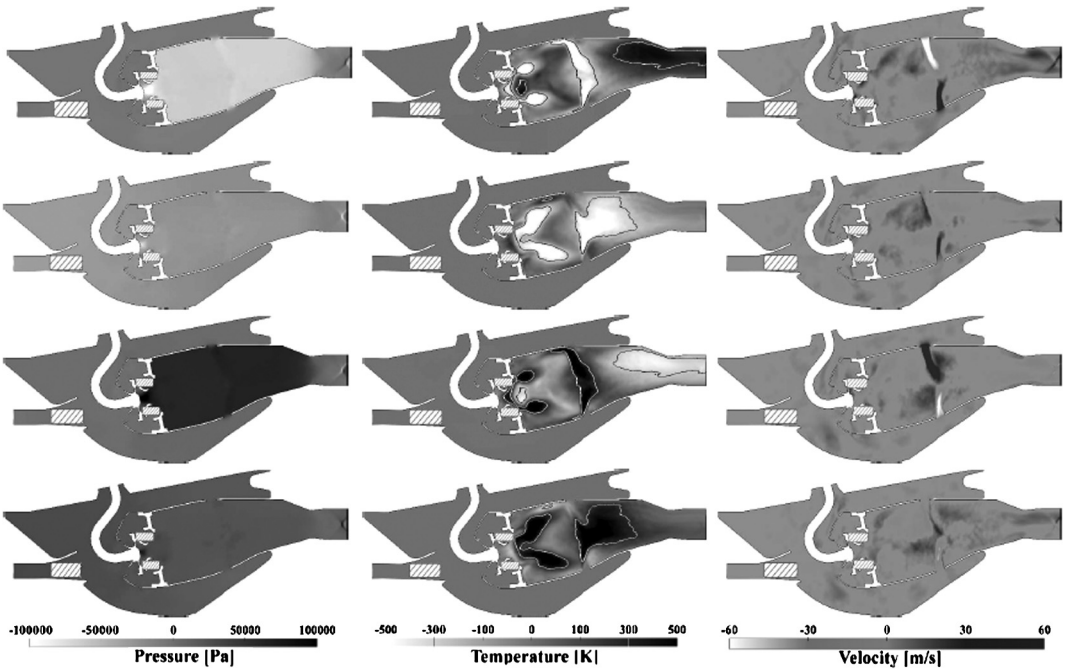

Figure 5.27 Phase-locked dynamics of a realistic combustion chamber under entropy combustion instability. Fluctuating pressure (left), temperature (middle), and velocity (right) obtained from dynamic mode decomposition mode analysis at 323 Hz for an operating point corresponding to an inlet temperature of 557 K. From top to bottom, the four rows correspond to phases 0, $\pi/2$, π, and $3\pi/2$. Source: Figure taken from Motheau et al. [281].

was on the dispersion and diffusion of inlet modulated entropy waves generated upstream of a swirl-stabilized flow. The objective of that work was also to characterize those phenomena for integration in lower-order reduced models.

Entropy instabilities have been documented for several decades, and the links between entropy noise or local equivalence ratio inhomogeneities in triggering entropy instabilities are still to be made.

3.4 Tangential instabilities

Tangential instabilities have become important in the analysis of swirl-stabilized flames in full annular combustion chambers because the acoustics mode can develop in the tangential direction. This technology aims at reducing weight, cooling complexities, and flame–wall interactions with respect to can combustors. The tangential instability research effort has been significant. In

the next section, the experimental, numerical, and theoretical literature is introduced and summarized.

3.4.1 Experimental results

Laboratory-scale annular combustion chambers equipped with swirler injectors and experiencing combustion instabilities have been the topic of recent researches as well. The annular combustor MICCA2-EM2C-Bourgouin was developed and designed for this purpose, see the article of Bourgouin et al. [365]. While acoustic analysis of the system allowed to describe mode shapes and frequencies, premixed flame imaging results led to the description of the unsteady heat release whose spatial distributions matched the predicted acoustics frequencies. Specifically, two different modes were observed: an azimuthal and a longitudinal instability mode. The same experimental setup was adapted to extend the study to spray swirl injectors by Prieur et al. [355]. Standing azimuthal modes were recorded at 750 Hz. In addition, it was observed that blowoff of some swirling flames located on the combustor azimuth may occur during the strong instability burst. Observations indicated that the unsteady combustion process changes with the position of the flame with respect to the azimuthal acoustic mode structure. The Annular-CambridgeUniv-Worth configuration was investigated by Worth and Dawson [462]. The authors observed that the instability annular acoustic mode shifted between standing and traveling modes, depending on the flame spacing, equivalence ratio, and swirl configuration. The analysis of the phase-averaged chemiluminescence signals showed that the traveling direction of the spinning waves coincided with changes in the spatial distribution of the peak heat release rate relative to the direction of the bulk swirl induced along the annular walls. For standing waves, it was shown that the globally integrated fluctuations in heat release rate vary in magnitude along the acoustic mode shape, with negligible contributions at the pressure nodes and maximum contributions at the pressure antinodes. In Worth and Dawson [522], the emphasis on that configuration was on the spacing between adjacent swirling flames and the subsequent effects on the self-sustained oscillations.

3.4.2 Numerical simulations

The articles of Wolf et al. [523,524] highlighted the potential of LES for studying combustion instabilities in annular gas turbine combustors. LES has demonstrated that one important effect of the traveling/spinning modes is the induction of longitudinal pulsations of the flow rates through individual burners, as shown by Staffelbach et al. [525]. In addition, the transfer functions of

all burners were shown to be the same, and no mechanism of flame interactions between burners within the chamber was identified. Numerical simulations of annular combustion chambers under self-sustained oscillations have been performed by Wolf et al. [399]. Simulations over 100 cycles were carried out, and it was determined that the azimuthal mode was a standing pattern with transitions from time to time to a traveling spinning mode, those changes being attributed to turbulent fluctuations.

3.4.3 Theory

Analytical studies of annular combustion instabilities have been summarized in the review article by Bauerheim et al. [496]. In that article, the general framework to predict annular instabilities was presented, including acoustic analyses of coupled annular plenum/injector/combustion chamber systems featuring coupling or not quantified by the coupling index, and acoustics/unsteady heat release model analysis taking into account the flame response. Longitudinal analytical results have been initially extended to annular chambers by Parmentier et al. [526] in order to predict such instabilities in configurations made up of multiple injectors annularly spaced in the combustion chamber. It consisted of a 1D zero Mach number formulation where multiple injectors were connected to an annular chamber, leading to a dispersion relation solved analytically when the interaction indices of the FTF were small, and numerically when they were not. The article of Noiray et al. [527] focused on the effects of azimuthal fuel staging on annular combustion instability development for gas turbine combustors. In addition, a criterion based on the thermoacoustic coupling strength and on the asymmetry degree provided the modal behavior in the annular combustor, i.e., standing or traveling waves. In Ghirardo and Juniper [528], the focus was also on the prediction of the modal behavior, standing or traveling acoustic mode, where the model of Noiray et al. [527] was extended to take into account the fluctuating unsteady heat release asymmetry induced by the annular azimuthal acoustic fluctuation. The article of Bauerheim et al. [529] extended the analysis of Parmentier et al. [526] to take into account the effects of the plenum on the prediction of combustion instabilities and the subsequent frequency, growth rate, and structure of all modes by solving the obtained dispersion relation. The article of Li and Sun [530] investigated the role of the vorticity wave on the azimuthal instability in an annular chamber with a compact flame sheet. It was shown to affect the prediction of annular instabilities, significantly reflecting the importance of the vortical waves in the flame responses. In Ghirardo et al. [531], the authors coupled the FDF of a single injector to a

Helmholtz solver or an acoustic network model in order to study the nonlinear dynamical system of a rotationally symmetric annular chamber containing multiple flames. The predictions led to the azimuthal oscillations stability map, including the amplitude and the type of oscillation: spinning/traveling or standing.

Combustion instabilities taking place in the tangential direction are important and have been significantly studied recently with numerical simulations providing fully detailed flowfields, and a few dedicated specialized experimental annular chambers, enabling direct visualizations. In addition, theoretical foundations have emerged by transferring and adapting existing results from the longitudinal direction to the azimuthal one. These types of studies are particularly valuable to describe phenomena at work for geometries closer to the relevant applications.

This last section described the two main prediction strategies for combustion instabilities. For longitudinal, azimuthal, and transversal instabilities, open questions remain. For example, what is the location of instability triggering? How does the synchronization of the unsteadiness processes take place? Can the criterion of axial and azimuthal velocities solely be used for categorizing instability regimes? Questions such as on the roles of the static versus time-average reacting flowfield in predictions still subsist too.

6

Design and numerical simulation modeling

1 Context and challenges

Design of combustors and injectors at the laboratory or industrial scale requires a methodological procedure. This procedure will rely more and more on advanced numerical simulations. Indeed, the simulations bring information on the flowfields at stake that is out of reach for most experimental facilities, and can also be used for their design. In that context, the simulations undertaken and their results will be valuable only if accurate. Accuracy will be quantified with two aspects: (i) the capacity of the code and the results to match experimental data on the same setup, or, when experimental data are not available, (ii) that the methodology has been shown to predict with a high level of confidence other experimental results on similar configurations or modeling results. It is obvious that to be able to assess the accuracy and validity of simulation results for a particular design parameter or aspect, engineers, modelers, and researchers will be required who have strong knowledge of the topic considered.

Combustor design relies heavily on numerical simulations and experimental measurements and testing. Jet engine manufacturers deploy integrated approaches to accelerate the design process and minimize costs. In these approaches, large data sets are generated, requiring data analysis reduction, processing algorithms, and physical understanding to reach data-driven decisions. Such integrated approaches have been documented in the literature, see Anand et al. [90], James et al. [91] for Rolls-Royce, Mongia et al. [92], Mongia [93] for General Electric, McKinney et al. [94], Sen et al. [33], Ma et al. [95] for Pratt and Whitney, and Boudier et al. [96], Musaefendic et al. [97], Lacombe and Méry [98] for Safran Aircraft Engines. Current and future combustor designs challenges and requirements have been discussed in Mongia [99], Liu et al. [100], with the emphasis on emission reductions.

Numerical simulations of industrial-scale combustors at relevant operating conditions will require URANS and large eddy simulation (LES) models, or other methods than DNS, as DNS will still

Stabilization and Dynamic of Premixed Swirling Flames
https://doi.org/10.1016/B978-0-12-819996-1.00014-7

be out of reach because of the dimensions of the full combustor (annular chamber with nearly 20 injectors) and the scales at stake (less than 10 micrometers for the flame front thickness at cruise conditions), thus requiring too many CPU resources for parametric studies. In that context, it will be important to assess and to understand the limits of these models in order to be able to evaluate the subsequent results, particularly for design purposes.

2 Modeling of flow modulations in numerical simulations

This section presents an application of two existing flow modulation models (forcing models) used to generate perturbations of velocity and pressure upstream of a flame front. The first model, called inlet velocity modulation (IVM), involves modulating the flow velocity at the inlet of the CFD domain, while the second model, called inlet wave modulation (IWM), modulates the acoustic wave amplitude. Implementations of both models in the LES code LESLIE3D, see Menon et al. [532], Menon [533], are here verified against analytical solutions. The verification is carried out on an isothermal duct where modulation is applied at the inlet, while the outlet boundary condition is selected as nonreflecting to set a traveling wave in the domain or reflecting to set a standing wave. For the traveling wave, it is shown that both models provide the same results. When the inlet forcing modulation frequency is selected close to a resonant mode of the duct in the standing wave case, results indicate that IVM leads to resonance of the duct mode while IWM does not. When the frequency of forcing is far from a resonant mode of the duct, it is shown that IVM excites duct modes while IWM does not. Finally, an application of both models is carried out on a turbulent bluff-body-stabilized flame. It is shown that IVM leads to unwanted modes inside the CFD domain while IWM does not.

2.1 Introduction

Combustion science is of importance for fundamental knowledge and for the development of new combustion systems. Combustion dynamics covers the field associated with unsteady combustion physics in combustion chambers like those used in gas turbines or jet engines. One design objective for these devices is to reduce the fuel injected for the same power output. By working in leaner premixed regimes, these combustors are sensitive to combustion instabilities which consist of a resonant loop between

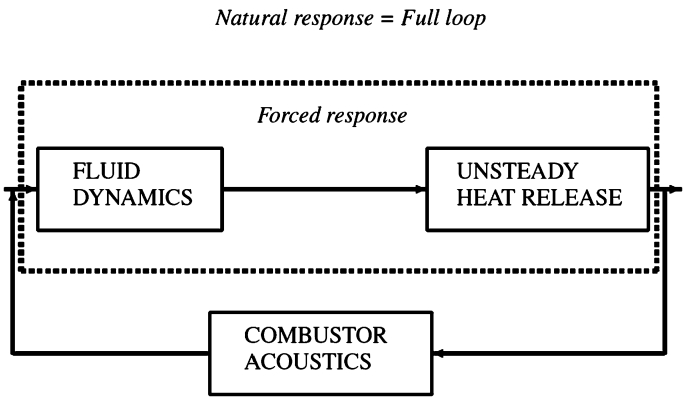

Figure 6.1 Self-sustained instability versus modulated flame response. Combustion instability is a resonant loop between the acoustics, the unsteady heat release, and the combustor acoustics.

three main elements: the fluid dynamics, the unsteady heat release, and the combustor acoustics, which are schematically presented in Fig. 6.1. In that context, the following mechanisms have to be understood: unsteady combustion, which is the flame response to flow perturbations, the associated pressure waves emitted by the flame, and the combustor acoustics, which is the interaction of those emitted pressure waves with the combustor cavity. This closed loop can be self-sustained and lead to large pressure oscillations in a combustion chamber. Its understanding is of importance in the development of new advanced aeroengine or gas turbine combustors. Indeed, it is still challenging to predict the stability of a combustor prior to operation. As a consequence, there are needs to model such complex combustors during the design stage. To fulfill this objective, there are two main approaches available to model the stability of a combustor. The first method is to model the full thermoacoustics loop through CFD, usually called the natural response or self-sustained oscillation. With CFD, the challenge is to model sufficiently large computational domains where boundary conditions are known along with significant simulation times to be able to observe a transition towards the limit cycle. This strategy requires large CPU resources. The second method involves studying the closed loop by dividing it into two blocks, where each block is studied separately. The fluid and flame dynamics blocks are obtained through CFD or experiment to get the flame transfer function, and the combustor acoustics are obtained with acoustic modeling tools. Both are then coupled to perform a stability analysis of the system in order to predict the stability of the combustor. This is the so-called forced

response approach. This approach has been used in many previous works.

In order to extract the flame transfer function for the forced approach, it is needed to impose flow modulation at the inlet of the CFD domain. This can be done with two different methods: one can use a modulation of the inlet velocity (IVM) or a modulation of the inlet wave amplitude (IWM), see Kauffmann et al. [534], Ducruix and Candel [410]. For CFD code with Navier–Stokes characteristics boundary conditions (NSCBCs), see Thomson [407], Thompson [535], Poinsot and Lele [408], Nicoud [536], both models can be used, while if this specific framework is not available, only the first one is possible. Kauffmann et al. [534] presented an approach to impose an IWM. In that study, a comparison between the two methods was carried out, but the explicit formulation in terms of characteristic wave variables was not provided. Both methods were also applied to a CFD case for a laminar premixed flame. It is then of interest to explore the use of those models in a turbulent configuration. The authors concluded their study pointing out the importance of their findings: "Results show that IVM leads to resonance phenomena perturbing measurements of transfer functions. Pulsation with a wave (IWM) is an alternative technique that assures [sic] finite amplitudes and monochromatic signals for transfer function determination. The application of IWM to the laminar burner of Le Helley showed that transfer functions can be predicted accurately using IWM, while IVM leads to the excitation of eigenmodes of the burner which prevent prediction of transfer functions. More generally, theses [sic] results suggest that extreme care must be taken in CFD codes to compute unsteady reacting flows since boundary conditions largely control the solution."

The present section focuses on the implementation of IVM and IWM models in the LESLIE3D LES reacting compressible code and their applications to a turbulent bluff-body-stabilized flame. The NSCBC framework is briefly described and the two combustor dynamics forcing models are detailed. The models' implementations are verified on an isothermal duct configuration. Both models are then compared on a turbulent configuration.

2.2 Combustor dynamics modulation models

2.2.1 Navier–Stokes characteristic boundary conditions

The NSCBC procedure relies on prescribing the wave amplitudes that enter into a CFD domain as defined by Poinsot and Lele [408]. Many different boundaries can be defined through this procedure. The idea behind the NSCBC approach is to solve

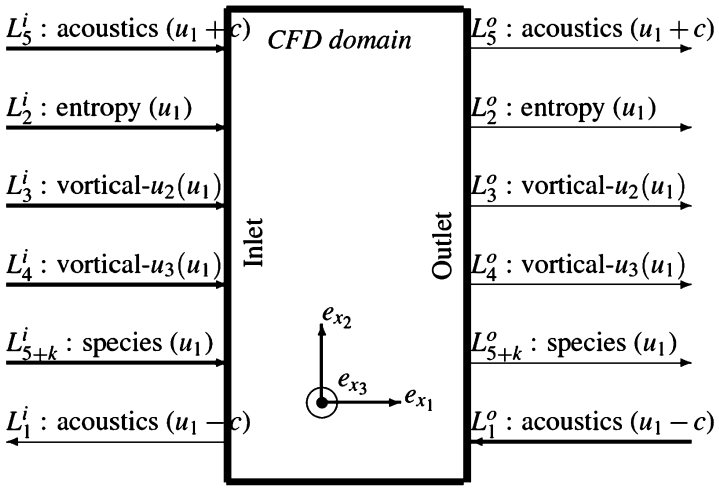

Figure 6.2 NSCBC nomenclature. Characteristic wave amplitude definitions at inlet/outlet of a CFD domain.

for the reacting Navier–Stokes (RNS) system of equations, recast in terms of wave amplitudes L_i, on the boundaries. The physical type of a boundary imposes some variables, excluding then some equations of the system (RNS). Then, the wave amplitudes L_i are computed through their definition if exiting the domain of Eqs. (6.1)–(6.6) or estimated through the local one-dimensional inviscid (LODI) equations if entering the domain of Eqs. (6.7)–(6.12). The characteristic wave velocities associated with the L_i waves are defined in Eq. (6.13). Once these wave amplitudes are known, the remaining equations of the reacting system (RNS) can be updated in time. Fig. 6.2 illustrates the characteristic wave amplitudes leaving and entering a CFD domain. At the inlet, $4 + k$ waves, with k being the number of species considered, have to be defined while only one is computed. At the outlet, only the one entering the domain has to be defined, with those leaving the domain being computed by the code with Eqs. (6.1)–(6.6).

Within this framework and in order to impose flow modulations at the inlet of a CFD domain, one has to prescribe incoming wave amplitudes L_i at the inlet of the domain. The definitions of these quantities are provided by Eqs. (6.1)–(6.6). The flow modulation will specifically concern L_5, associated with the acoustic wave entering the inlet domain. We have the following systems of equations:

$$\begin{cases} L_1 = \dfrac{\lambda_1}{2}\left(\dfrac{\partial p}{\partial x_1} - \rho c \dfrac{\partial u_1}{\partial x_1}\right), & (6.1) \\ L_2 = \lambda_2\left(\dfrac{\partial \rho}{\partial x_1} - \dfrac{1}{c^2}\dfrac{\partial p}{\partial x_1}\right), & (6.2) \\ L_3 = \lambda_3 \dfrac{\partial u_2}{\partial x_1}, & (6.3) \\ L_4 = \lambda_4 \dfrac{\partial u_3}{\partial x_1}, & (6.4) \\ L_5 = \dfrac{\lambda_5}{2}\dfrac{\partial p}{\partial x_1} + \rho c \dfrac{\partial u_1}{\partial x_1}, & (6.5) \\ L_{5+k} = \lambda_{5+k}\left(\dfrac{\partial Y_k}{\partial x_1}\right), & (6.6) \end{cases}$$

$$\begin{cases} \dfrac{\partial \rho}{\partial t} + \dfrac{1}{c^2}(L_5 + L_1) + L_2 = 0, & (6.7) \\ \dfrac{\partial p}{\partial t} + L_5 + L_1 = 0, & (6.8) \\ \dfrac{\partial u_1}{\partial t} + \dfrac{L_5 - L_1}{\rho c} = 0, & (6.9) \\ \dfrac{\partial u_2}{\partial t} + L_3 = 0, & (6.10) \\ \dfrac{\partial u_3}{\partial t} + L_4 = 0, & (6.11) \\ \dfrac{\partial Y_k}{\partial t} + L_{5+k} = 0, & (6.12) \end{cases}$$

$$\lambda_1 = u_1 - c, \lambda_2 = u_1, \lambda_3 = u_1, \lambda_4 = u_1, \lambda_5 = u_1 + c, \lambda_{5+k} = u_1. \quad (6.13)$$

2.2.2 Inlet velocity modulation

The IVM approach is defined by Kaufmann et al. [409] with a time harmonic fluctuation of velocity. This forcing function is written as

$$u_1'(x_0, t) = \frac{A^+}{\rho c}\exp(i(kx_0 - \omega t)), \quad (6.14)$$

$$u_1(x_0, t) = u_{1,0} + u_1'(x_0, t). \quad (6.15)$$

The natural method to derive the corresponding L_5 to be implemented in a CFD code is to insert this forcing function into the characteristic wave definitions Eq. (6.5). It is observed that one cannot obtain a solution for L_5 proceeding in this way. As a consequence, the LODI equations have to be used through Eq. (6.9).

The quantity L_5 is then written as

$$L_5^i = L_1^i + \Im\left[i\omega A^+ \exp(i(kx_0 - \omega t))\right]. \tag{6.16}$$

It is interesting to note that the ingoing characteristic wave amplitude L_5^i depends on the outgoing one L_1^i.

2.2.3 Inlet wave modulation

The IWM approach presented by Kaufmann et al. [409] is defined by a forcing function that takes into account both acoustic velocity and pressure fields. These fields are written as

$$u'(x_0, t) = \frac{1}{\rho_0 c_0}\left[A^+ \exp(ikx_0) - A^- \exp(-ikx_0)\right]\exp(-i\omega t), \tag{6.17}$$

$$p'(x_0, t) = \left[A^+ \exp(ikx_0) + A^- \exp(-ikx_0)\right]\exp(-i\omega t). \tag{6.18}$$

It is now possible to insert these fields in Eq. (6.5)(e), and we obtain the following expression for L_5:

$$L_5^i = \Im\left[i\omega A^+ \frac{\lambda_5}{c}\exp(ikx_0 - \omega t)\right]. \tag{6.19}$$

In the IWM case, the ingoing characteristic wave amplitude L_5^i does not depend on the one leaving the domain L_1^i, contrarily to the IVM case.

2.3 Inlet modulation in an isothermal duct

2.3.1 Verification with analytical solution

In order to verify the implementation into the LES code, two test cases were used, presented in Fig. 6.3. The geometry consists of a straight duct where the forcing is applied at the inlet of the duct while the outlet boundary condition is adapted to make the boundary perfectly nonreflecting (the relaxation factor K is set to zero such that $L_1^o = 0$, see Rudy and Strikwerda [537]) or perfectly reflecting (a pressure node is imposed at the boundary with $L_1^o = L_5^o$). In the first case, the acoustic motion corresponds to a traveling wave, while in the second case, a mode shape is set up into the domain. The matrix test cases are presented in Tab. 6.1. Cases 1 and 2 were first verified against analytical solution. The agreement obtained between the solutions and the simulation results is very good. Typical solutions taken at three different time

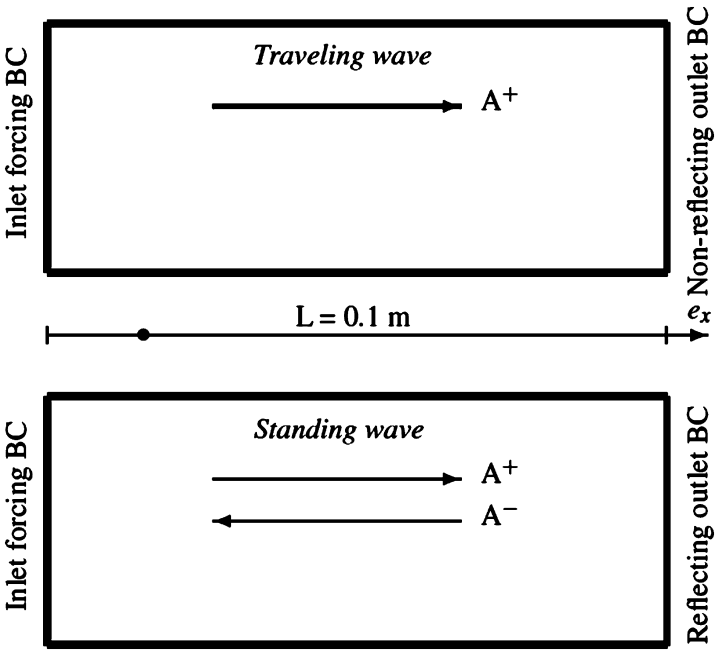

Figure 6.3 Verification case features. The first verification case is a traveling wave in an isothermal duct, while the second one corresponds to a standing wave. The two cases differ by the expression of L_1^o used at the outlet boundary. The bold dot indicates the location of the probe ($x = 0.0155$ m) where signals are extracted.

Table 6.1 Matrix test cases: boundary conditions.

	Inlet BC	Outlet BC	Wave	Frequency f
Case 1	IVM	Nonreflective	Traveling	2500 Hz
Case 2	IWM	Nonreflective	Traveling	2500 Hz
Case 3	IVM	Reflective	Standing	2500 Hz
Case 4	IWM	Reflective	Standing	2500 Hz
Case 5	IVM	Reflective	Standing	250 Hz
Case 6	IWM	Reflective	Standing	250 Hz

steps are plotted in Fig. 6.4 (top) for the IWM model. Results obtained with IVM are identical. Multiple time steps obtained in case 4 are plotted in Fig. 6.4 (bottom) and show the mode shape that is set up inside the duct.

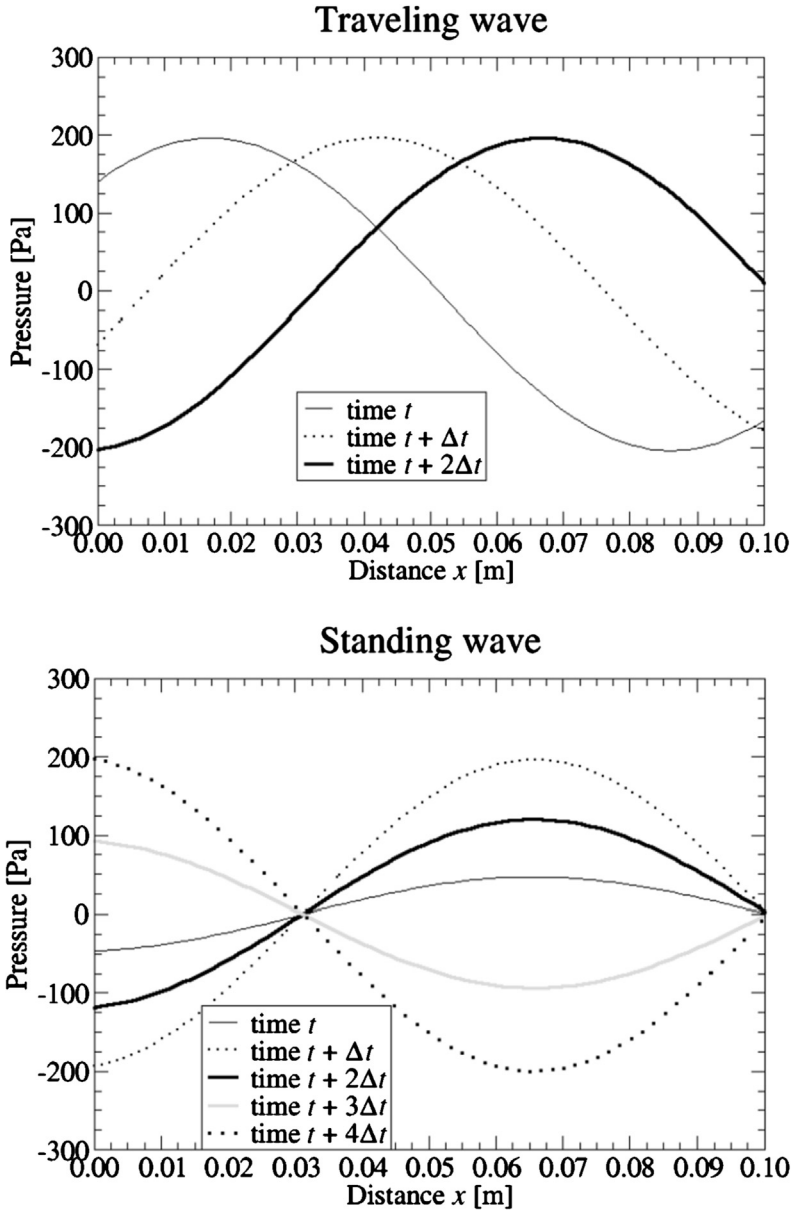

Figure 6.4 Unsteady pressure fluctuation envelope. Comparison of the fluctuating pressure field versus the axial location x in the duct for an inlet forcing frequency set to $f = 2500$ Hz with the IWM model. Top: Traveling wave obtained by imposing a nonreflecting outlet boundary condition. Three time instants are plotted respectively separated by $\Delta t = 65$ degrees. Bottom: Standing wave set up by imposing a pressure node at the outlet of the duct. Five time instants are plotted respectively separated by $\Delta t = 65$ degrees.

2.3.2 Analytical solutions for verification

Traveling wave

The traveling wave corresponds to a solution of the linearized Euler equations (6.17) and (6.18) for the acoustic velocity and pressure, where the leftward traveling wave A^- is zero. By then taking their imaginary parts, one can show that the solution is reduced to

$$u'(x,t) = \frac{A^+}{\rho c}\sin(kx - \omega t), \tag{6.20}$$

$$p'(x,t) = A^+ \sin(kx - \omega t). \tag{6.21}$$

These solutions were used to verify the implementation. It is interesting that the analytical solutions are identical for both forcing models, IVM and IWM, as the leftward traveling wave A^- is zero. Indeed, the coupling effect due to the formulation of IVM cancels out in that specific case.

Standing wave IVM

The derivation begins with the solution of the linearized Euler equations (6.17) and (6.18). The outlet boundary condition imposes that $p_0(x = L, t) = 0$, so that one obtains the expression of the acoustic pressure field (taking the imaginary part). By making use of the linearized momentum equation, the acoustic velocity is determined. From Ducruix and Candel [410], it is possible to add an expansion in terms of the duct normal modes in order to obtain the analytical solution that takes into account the initial condition:

$$u'(x,t) = \frac{-A^+}{\rho c}\frac{\cos k(L-x)}{\cos kL}\sin\omega t - \sum_{i=0}^{i=4}\frac{2A^+ k \sin k_i L \sin\omega_i t \cos k_i(L-x)}{\rho c L(k^2 - k_i^2)}, \tag{6.22}$$

$$p'(x,t) = -A^+\frac{\sin k(L-x)}{\cos kL}\cos\omega t - \sum_{i=0}^{i=4}\frac{2A^+ k \sin k_i L \cos\omega_i t \sin k_i(L-x)}{L(k^2 - k_i^2)}, \tag{6.23}$$

$$k = \omega/c, \tag{6.24}$$

$$k_i = \pi(2i+1)/2L. \tag{6.25}$$

These acoustic velocity and pressure fields do take into account the initial conditions $p(0) = 0$ and $u(0) = 0$.

Standing wave IWM

The derivation begins with the solution of the linearized Euler equations (6.17) and (6.18). The outlet boundary condition imposes that $p_0(x = L, t) = 0$, so that one obtains the expression of the acoustic pressure field (taking the imaginary part). By making use of the linearized momentum equation, the acoustic velocity is determined. The finally obtained analytical solution, modified from Kaufmann et al. [409], is

$$u'(x,t) = \frac{2A^+}{\rho c}\sin(kL - \omega t)\cos(k(x - L)), \tag{6.26}$$

$$p'(x,t) = 2A^+\cos(kL - \omega t)\sin(k(x - L)). \tag{6.27}$$

This solution does not take into account the initial conditions $p(0) = 0$ and $u(0) = 0$. As a consequence, a discrepancy will occur up to a time equal to $(2L - x)/c$ at a location x, see Ducruix and Candel [410].

2.3.3 Comparison between IVM and IWM

Cases 3 and 4 are now compared with the pressure time traces and their fast Fourier transform taken by a probe at location $x = 0.0155$ m in the duct. The forcing frequency was set to $f = 2500$ Hz for those cases and the outlet BC was reflective. Results are presented in Fig. 6.5. The signal obtained with IWM keeps a constant amplitude over time, while the one obtained with IVM skyrockets, indicating that the resonance of the duct is excited. Indeed, the frequency of forcing was selected close to the 3/4 wave mode of the cavity to highlight the differences between the models. The fast Fourier transform plot leads to the same conclusion, where the IWM model has a finite monochromatic peak while a strong peak appears for IVM and a small peak corresponding to the 1/4 wave mode is also present. Similar observations were made on the acoustic velocity signals but are not presented here.

Cases 5 and 6 were obtained with a similar procedure but the frequency was reduced to $f = 250$ Hz to separate the excitation frequency from a natural resonant mode of the duct. Results are plotted in Fig. 6.6. It is shown again that IWM leads to signals that contain only the forcing frequency, while IVM leads to multiple-frequency content in the domain. Specifically, the 1/4 wave mode is excited in the duct and the peak amplitude is of the same order as the inlet forcing frequency peak. On the other hand, a single peak is obtained with the IWM method. Again, similar observations have been made for the acoustic velocity signals but are not reported here.

It is interesting to point out a few features of those models.

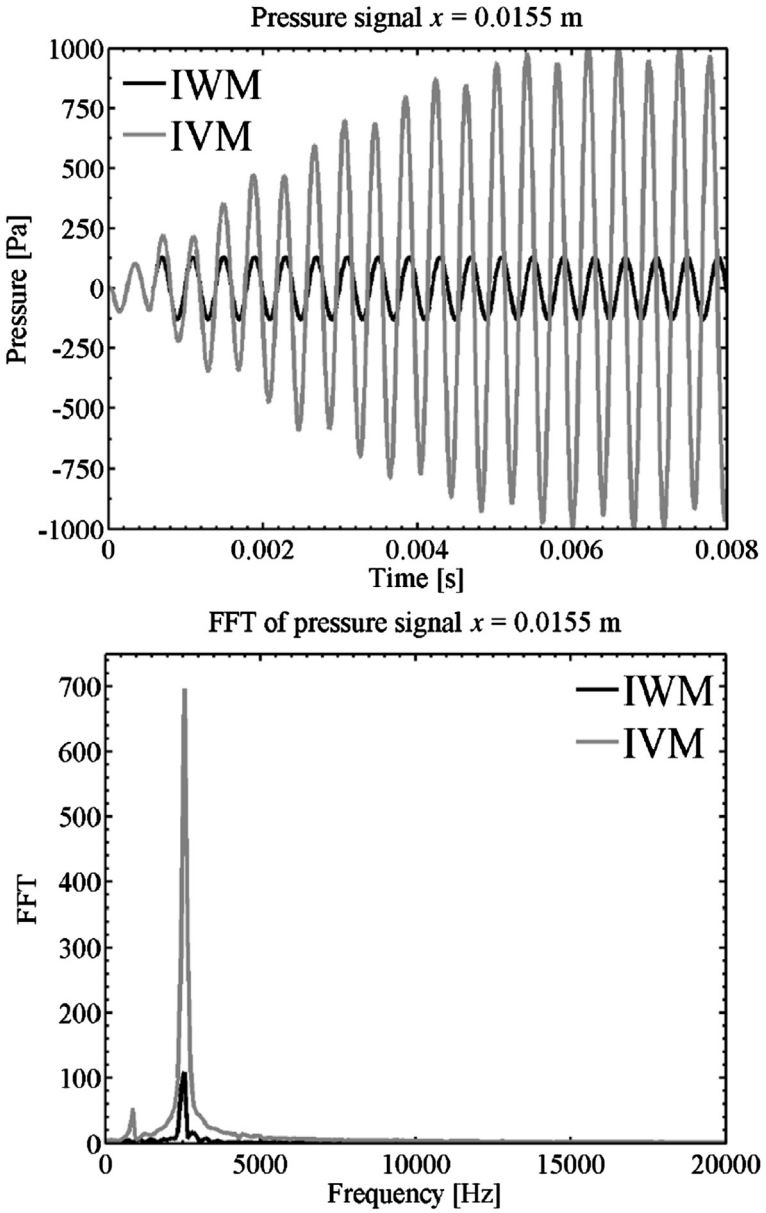

Figure 6.5 Unsteady pressure fluctuation time traces and fast Fourier transform. Cases 3 and 4. Signals of fluctuating pressure for IVM and IWM models and their fast Fourier transforms. The inlet frequency is $f = 2500$ Hz, which lies close to the 3/4 wave mode of the duct. The axial coordinate is $x = 0.0155$ m. Top: Pressure signal. Bottom: Corresponding fast Fourier transform. For the IVM model, the signals are skyrocketing as a function of time and the fast Fourier transform content shows distinct frequencies, while for the IWM model, the envelope of the signal remains constant and a single peak appears in the fast Fourier transforms.

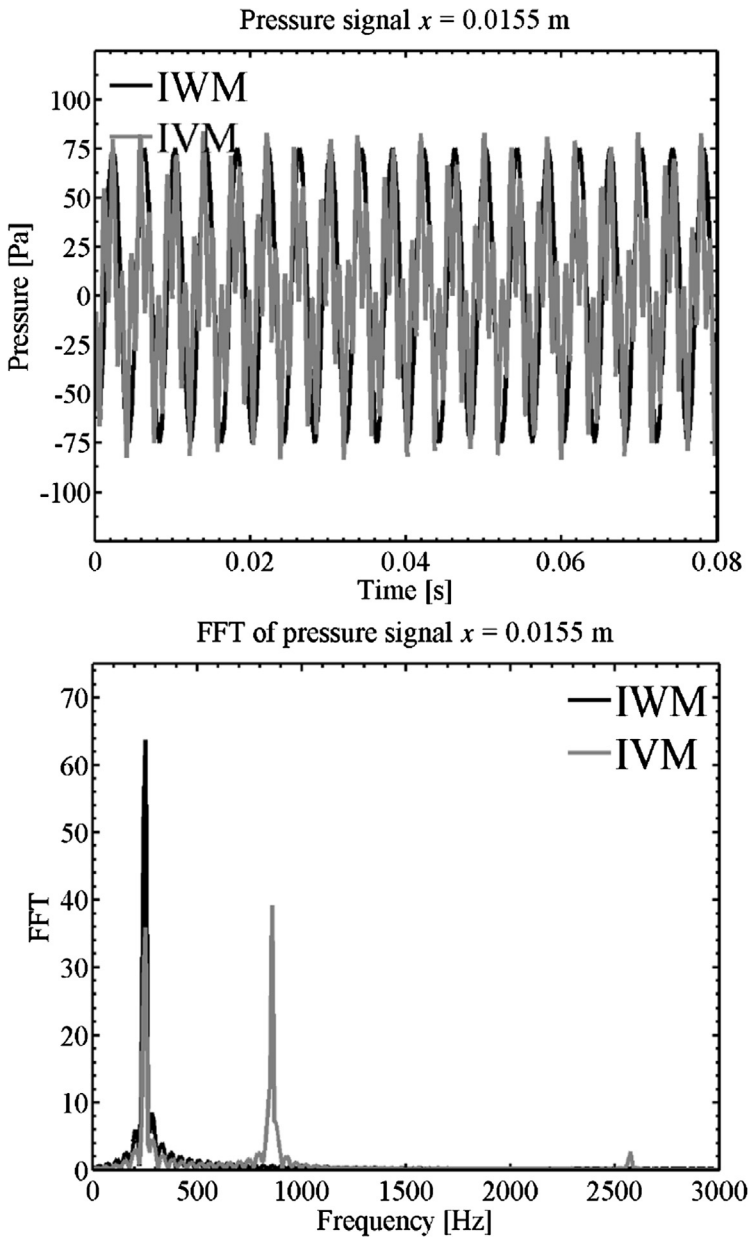

Figure 6.6 Unsteady pressure fluctuation time traces and fast Fourier transform. Cases 5 and 6. Signals of fluctuating axial velocity and pressure for IVM and IWM models and their fast Fourier transforms. The inlet frequency is $f = 250$ Hz, which does not correspond to any duct acoustics mode. The axial coordinate is $x = 0.0155$ m. Top: Pressure signal. Bottom: Corresponding fast Fourier transform. For the IVM model, the signals are strongly nonlinear as a function of time and the fast Fourier transform content shows distinct frequencies, while for the IWM model, the envelope of the signal remains constant and a single peak appears in the fast Fourier transforms.

- *Rightward and leftward waves coupling.* It is worthwhile to note that due to the formulation of the forcing models, the rightward L_5 and leftward L_1 waves are coupled in the IVM approach, while they are not in the IWM approach. As a consequence, models will give the same results for the traveling wave as the leftward wave has a zero amplitude. They will differ when a leftward wave propagates in the domain.
- *Inlet reflection coefficient R.* From this previous observation, one can determine the inlet reflection coefficient defined by the ratio of the wave amplitudes of both forcing models using the inlet impedance Z:

$$Z = \frac{1}{\rho c} \frac{p'(x_0)}{u'(x_0)}. \tag{6.28}$$

  For IVM, it is appropriate to use the analytical solutions Eqs. (6.22) and (6.23) to calculate this quantity at x_0, and by making use of $t = 0$ one can show that $Z_{IVM} = \infty$, which can be written as $R_{IVM} = 1$. Following the same approach for IWM, it is possible to demonstrate that $R_{IWM} = 0$ inserting Eqs. (6.26) and (6.27) into Eq. (6.28).

It is now natural to apply the two previous models in a more realistic configuration comprising a turbulent premixed flame and a more complex geometry.

2.4 Application to a bluff-body-stabilized flame

The selected geometry is the so-called "Volvo" configuration. A 3D bluff-body-stabilized premixed flame is anchored to a diedral flameholder, see the schematic of Fig. 6.7. A premixed propane–air mixture with an equivalence ratio equal to 0.65 is injected at the inlet. The inlet forcing is applied upstream of the flameholder with a modulation amplitude equal to $A^+ = 1250$ Pa at a frequency of $f = 250$ Hz. The axial velocity and pressure signals are recorded at two different locations in the CFD domain. The first probe P_1 is close to the inlet boundary with the coordinates $(x = -0.1,\ y = 0.06,\ z = 0.04)$ while P_2 is upstream of the flame at a location closer to the flame. The coordinates of P_2 are $(x = 0,\ y = 0.03,\ z = 0.04)$.

Results recorded at the first probe P_1 are first analyzed, see Fig. 6.8. In Fig. 6.8, the velocity signal obtained with the two forcing models is compared over multiple cycles of modulation. The signals are very similar for both models and a slight drift of the mean value is observed in both cases. The associated fast Fourier transform presents a peak at the forcing frequency and a very low frequency component that reflects the drift of the mean value. In

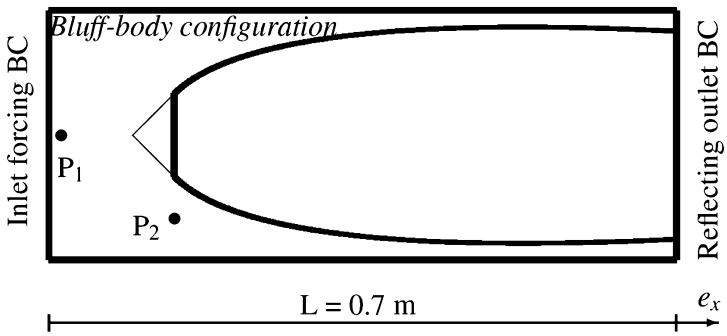

Figure 6.7 Schematic of the bluff-body-stabilized flame case and the location of two measurement probes. The first probe P_1 is close to the inlet boundary at the coordinates ($x = -0.1$, $y = 0.06$, $z = 0.04$), while P_2 is upstream of the flame at a location where the velocity signal needed for a flame transfer function could be extracted. The coordinates of P_2 are ($x = 0$, $y = 0.03$, $z = 0.04$).

Fig. 6.9, the pressure signals are very noisy for the IVM approach, indicating that the pressure is uncontrolled, while for IWM, the signal stays consistent over time. It is interesting to note that IWM produces one peak in the fast Fourier transform of this pressure signal, while multiple peaks are present in the spectrum for the IVM method. Furthermore, the amplitude of the forcing frequency is close to the amplitude of an excited mode, which is not appropriate to extract a flame transfer function from a numerical simulation. Indeed, the flame dynamics will be affected by that frequency. Results at probe P_2 lead to similar observations for the pressure signal. For the velocity signal, unlike at P_1, the signal contains multiple frequencies, which will affect the flame transfer function calculation.

2.5 Conclusions

The present section discussed using forcing models from the literature in order to study their differences. The main outcomes of this section are as follows. First, we have replicated results from the literature for a straight isothermal duct. It was demonstrated that the IVM approach leads to resonance in the duct when the forcing frequency is selected close to a resonant mode of the cavity, while IWM does not. It was also shown that the IVM approach leads to multiple-frequency signals when the forcing modulation is far from a resonant mode of the duct, while IWM does not. Secondly, the approach was applied to a turbulent bluff-body-stabilized premixed flame. It was shown that the IVM approach leads to spurious modes that will affect the flame transfer function. The IWM does not add spurious modes inside the combus-

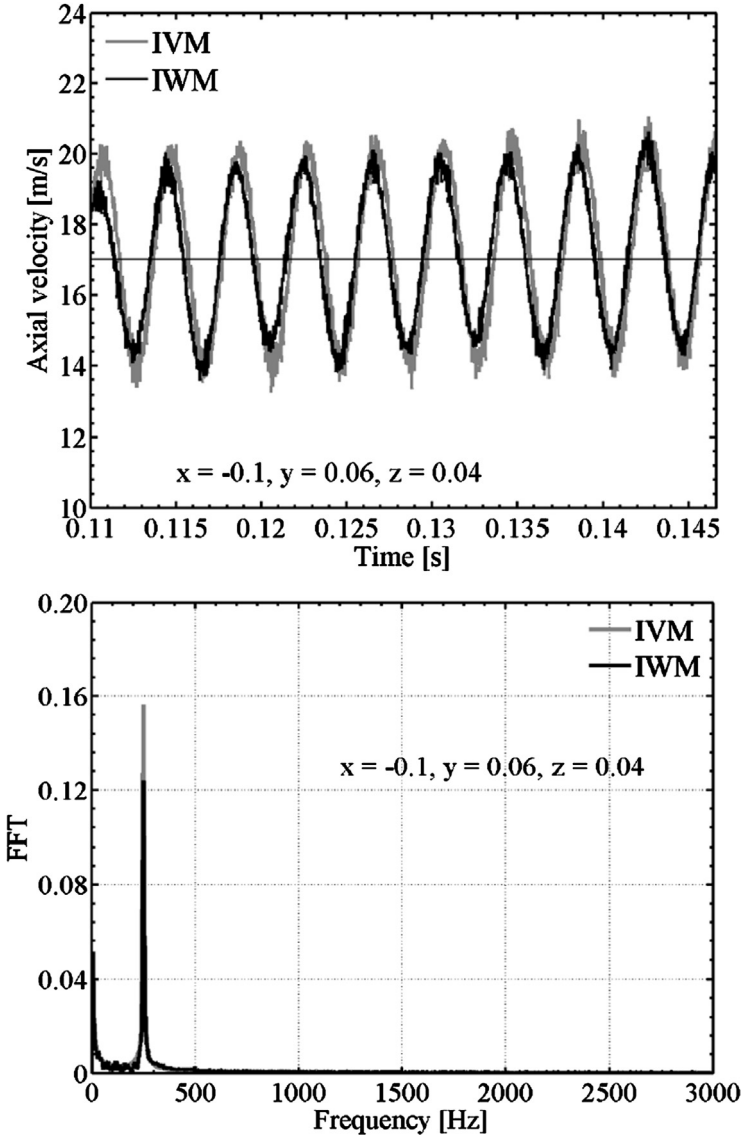

Figure 6.8 Signals of axial velocity for IVM and IWM models and their fast Fourier transforms. The inlet frequency is $f = 250$ Hz. Signal recorded at probe P_1, see Fig. 6.7, on the centerline of the combustor. Top: Velocity signal. Bottom: Corresponding fast Fourier transform. The fast Fourier transform content presents a single peak.

tor, but a slight velocity drift is observed. Thirdly, the leftward and rightward waves coupling effect was highlighted. The present section shows that IVM and IWM have different inlet acoustic reflec-

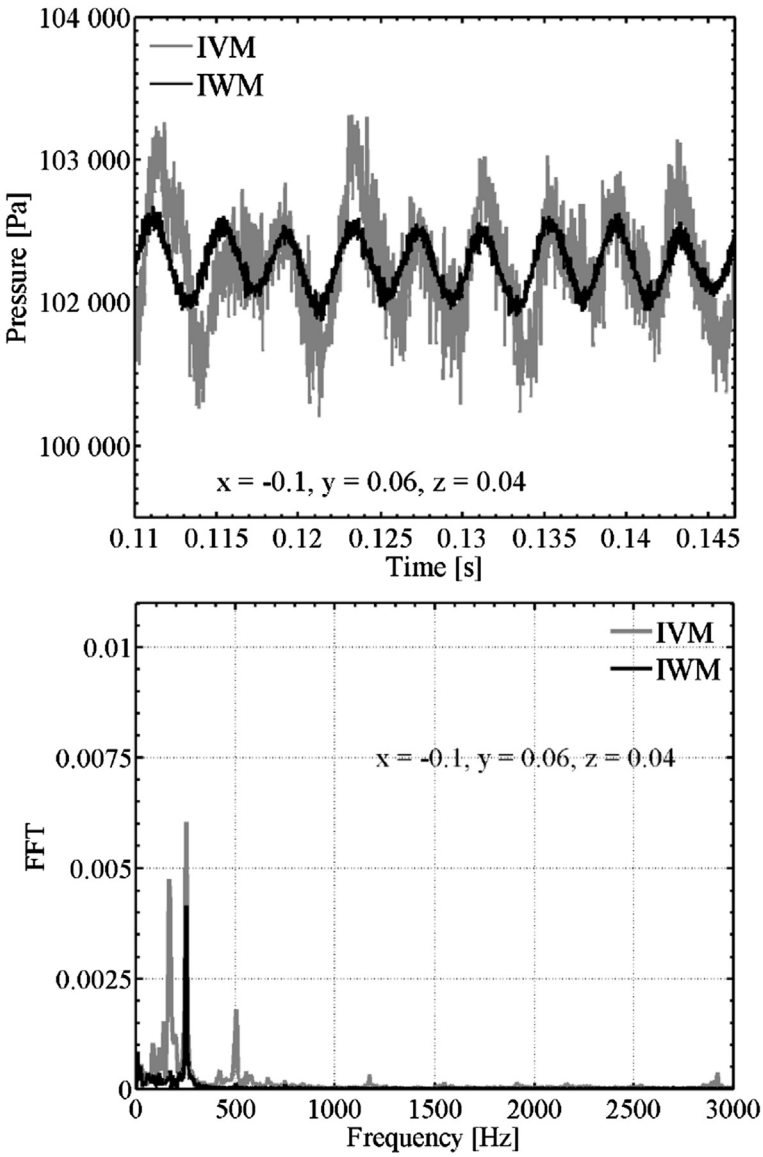

Figure 6.9 Signals of pressure for IVM and IWM models and their fast Fourier transforms. The inlet frequency is $f = 250$ Hz. Signal recorded at probe P_1, see Fig. 6.7, on the centerline of the combustor. Top: Pressure signal. Bottom: Corresponding fast Fourier transform. The fast Fourier transform content presents multiple peaks for the IVM case while it does not for IWM.

tion coefficients and that minimization of the interaction of the waves at the inlet of the domain is necessary to avoid resonance.

3 Modeling approaches and assumptions

3.1 Unsteady Reynolds-averaged Navier–Stokes

The URANS equations are obtained from the governing equations (used for DNS) presented in Chapter 2 by firstly considering any quantity of the variable density flow as the sum of a time-averaged Favre mean $\tilde{f}$ such that $\bar{\rho}\tilde{f} = \overline{\rho f}$ and a fluctuating component f'', such that $f = \tilde{f} + f''$, where $\widetilde{f''} = 0$. Secondly, the application of the time-averaged operator to the governing equations leads to the following set of rewritten equations, see Poinsot and Veynante [172].

The mass conservation equation writes

$$\frac{\partial \bar{\rho}}{\partial t} + \frac{\partial}{\partial x_i}(\bar{\rho}\tilde{u}_i) = 0. \tag{6.29}$$

The momentum conservation equation writes

$$\frac{\partial \bar{\rho}\tilde{u}_j}{\partial t} + \frac{\partial}{\partial x_i}(\bar{\rho}\tilde{u}_i\tilde{u}_j) = -\frac{\partial \bar{p}}{\partial x_j} + \frac{\partial}{\partial x_i}\left(\bar{\tau}_{ij} - \bar{\rho}\widetilde{u_i''u_j''}\right). \tag{6.30}$$

The species equations are written

$$\frac{\partial \bar{\rho}\widetilde{Y}_k}{\partial t} + \frac{\partial}{\partial x_i}(\bar{\rho}\tilde{u}_i\widetilde{Y}_k) = \bar{\dot{\omega}}_k - \frac{\partial}{\partial x_i}\left(\overline{V_{k,i}Y_k} + \bar{\rho}\widetilde{u_i''Y_k}\right). \tag{6.31}$$

The enthalpy equation becomes

$$\begin{aligned}\frac{\partial \bar{\rho}\tilde{h}_s}{\partial t} + \frac{\partial}{\partial x_i}(\bar{\rho}\tilde{u}_i\tilde{h}_s) = \bar{\dot{\omega}}_T + \frac{\partial \bar{p}}{\partial t} + \tilde{u}_i\frac{\partial \bar{p}}{\partial x_i} + \overline{u_i''\frac{\partial p}{\partial x_i}} \\ + \frac{\partial}{\partial x_i}\left(\overline{\lambda\frac{\partial T}{\partial x_i}} - \bar{\rho}\widetilde{u_i''h_s''}\right) - \frac{\partial}{\partial x_i}\left(\overline{\rho\sum_{k=1}^{N}h_{s,k}Y_kV_{k,i}}\right) \\ + \overline{\tau_{ij}\frac{\partial u_i}{\partial x_j}} + \mathcal{Q}_{st} + \overline{\rho\sum_{k=1}^{N}Y_kf_{k,i}V_{k,i}}.\end{aligned} \tag{6.32}$$

These equations exhibit unclosed terms that are not resolved in a numerical simulation, and consequently models for those unknowns are required. The terms requiring models are the Reynolds stresses model $\widetilde{u_i''u_j''}$, species $\widetilde{u_i''Y_k}$ and enthalpy turbulent fluxes $\widetilde{u_i''h_s}$, laminar diffusive fluxes for species $\overline{V_{k,i}Y_k}$ or enthalpy, species chemical reaction rates $\bar{\dot{\omega}}_k$, and pressure–velocity correlation. The literature review of these models is out of the scope of the present book.

3.2 Large eddy simulations

Contrarily to the URANS procedure that uses time averaging, LES uses spatial averaging for a given quantity. In the spatial domain, LES relies on the convolution product between a given spatial filter F and the quantity f itself. In the wavevector domain, it reduces to a direct multiplication between the quantity and the filter. The procedure to derive the LES equations is to apply this spatial filtering operator directly to the governing equations. The filter operation writes

$$\bar{f}(\boldsymbol{x}) = \int f(\boldsymbol{x}')F(\boldsymbol{x}-\boldsymbol{x}')d\boldsymbol{x}'. \tag{6.33}$$

The Favre average $\bar{\rho}\tilde{f} = \overline{\rho f}$ writes for the filter operation as

$$\bar{\rho}\tilde{f}(\boldsymbol{x}) = \int \rho f(\boldsymbol{x}')F(\boldsymbol{x}-\boldsymbol{x}')d\boldsymbol{x}'. \tag{6.34}$$

In the spatial/time domain the procedure leads to the following equations, see Poinsot and Veynante [172].

The mass conservation equation writes

$$\frac{\partial\bar{\rho}}{\partial t} + \frac{\partial}{\partial x_i}(\bar{\rho}\tilde{u}_i) = 0. \tag{6.35}$$

The momentum conservation equation writes

$$\frac{\partial\bar{\rho}\tilde{u}_j}{\partial t} + \frac{\partial}{\partial x_i}(\bar{\rho}\tilde{u}_i\tilde{u}_j) = -\frac{\partial\bar{p}}{\partial x_j} + \frac{\partial}{\partial x_i}\left(\bar{\tau}_{ij} - \bar{\rho}(\widetilde{u_i u_j} - \tilde{u}_i\tilde{u}_j)\right). \tag{6.36}$$

The species equations are written

$$\frac{\partial\bar{\rho}\tilde{Y}_k}{\partial t} + \frac{\partial}{\partial x_i}(\bar{\rho}\tilde{u}_i\tilde{Y}_k) = \bar{\dot{\omega}}_k + \frac{\partial}{\partial x_i}\left[\overline{V_{k,i}Y_k} + \bar{\rho}\left(\widetilde{u_i Y_k} - \tilde{u}_i\tilde{Y}_k\right)\right]. \tag{6.37}$$

The enthalpy equation for LES becomes

$$\begin{aligned}\frac{\partial\bar{\rho}\tilde{h}_s}{\partial t} + \frac{\partial}{\partial x_i}(\bar{\rho}\tilde{u}_i\tilde{h}_s) = \bar{\dot{\omega}}_T + \frac{\partial\bar{p}}{\partial t} + \overline{u_i\frac{\partial p}{\partial x_i}} \\ + \frac{\partial}{\partial x_i}\left(\overline{\lambda\frac{\partial T}{\partial x_i}} - \bar{\rho}\left[\widetilde{u_i h_s} - \tilde{u}_i\tilde{h}_s\right]\right) - \frac{\partial}{\partial x_i}\left(\overline{\rho\sum_{k=1}^{N} h_{s,k}Y_k V_{k,i}}\right) \\ + \overline{\tau_{ij}\frac{\partial u_i}{\partial x_j}} + \mathcal{Q}_{st} + \overline{\rho\sum_{k=1}^{N} Y_k f_{k,i}V_{k,i}}.\end{aligned} \tag{6.38}$$

For LES, multiple models are also required. The unresolved Reynolds stresses $\widetilde{u_i u_j} - \tilde{u}_i \tilde{u}_j$, the unresolved species fluxes $\widetilde{u_i Y_k} - \tilde{u_i} \tilde{Y}_k$ and enthalpy fluxes $\widetilde{u_i h_s} - \tilde{u}_i \tilde{h}_s$, the filtered laminar diffusion fluxes for species $\overline{V_{k,i} Y_k}$ and enthalpy, the filtered chemical reaction rate $\bar{\dot{\omega}}_T$, and the pressure velocity term are modeled.

4 Chemical kinetics

The chemical kinetics of reacting flows have a central role as the kinetics determine the reactions between various species, radicals, and compounds at stake. The kinetics have a first-order effect on two major quantities: the temperature and the species levels. Chemical kinetics aims at studying and modeling the interactions of the species, radicals, and compounds. The description of these interactions is usually conducted within the statistical physics framework. In that framework, the occurrence (i.e., the probability) of reactions between two species is for example determined by considering the mean free path and the atom diameters, among other parameters.

There are many methods to model chemical combustion kinetics with various degrees of fidelity and assumptions. The first one is to assume equilibrium of reactions so that no finite rate chemistry is required. This assumption is exact for the steady (static) case but lacks fidelity in the cases of transient and turbulent flows. The second approach is to make use of single-step mechanisms or global-step mechanisms, where the complexity of the chemistry is summarized into a small set of reactions with few species. This approach has many advantages, including the capacity to be used for large-scale gas turbine relevant combustor simulations with current modern computational capabilities. It enables to capture flame dynamics and finite rate effects. It can also be coupled to complex chemistry a posteriori with a look-up table. Skeletal and reduced chemical mechanisms are more accurate descriptions of the chemical reactions and can be envisioned for pollutant emission predictions. The complex chemical mechanisms involve hundreds of species and thousands of reactions that make their use beyond 1D or 2D axisymmetric flames a challenge. The literature review of chemical kinetics is out of the scope of the present monograph.

A key concept upon which combustion reaction models rely is that of the Arrhenius law. The Arrhenius law expresses the rate constant of a given reaction j. As pointed out in Poinsot and Veynante [172], these rate constants constitute a central problem of

combustion modeling. The general expression $K_{f,j}$ is given as

$$K_{f,j} = A_{f,j} T^{\beta_j} \exp\left(\frac{-T_{aj}}{T}\right). \tag{6.39}$$

There are three fundamental parameters in this rate constant: (i) the preexponential factor reflecting the occurrence that a given collision will trigger a reaction, (ii) the temperature exponent, which is an empirical parameter, and (iii) the activation temperature, which reflects the threshold temperature at which the reaction will proceed. The collisions between molecules need this threshold temperature to react, i.e., to ensure the passage from unburned species to burned species; otherwise they will collide without reacting.

Prior to introducing the turbulent combustion modeling aspects, it is worthwhile to discuss the case of laminar versus turbulent combustion regimes and the role of chemical kinetics and its modeling. As pointed out earlier, the RANS and LES modeling methodologies respectively perform time averaging and spatial averaging of the governing equations. In that respect, all quantities and processes are averaged respectively. In other words, performing a RANS or LES calculation with a refined complex chemical mechanism will induce to average either temporally or spatially the flowfield, and the accuracy of the complex chemical mechanism will be lost. It is then required to consider both chemical kinetics modeling and turbulent combustion closure together.

5 Turbulent combustion modeling

Turbulent combustion modeling is required for URANS and LES formulations, when the finest scales of the turbulence–chemistry interactions are not resolved but modeled. In that context, it would be important to consider both the chemical mechanism and the turbulent combustion closure together. For example, when considering LES premixed combustion modeling, it is important to ensure that the chemical combustion mechanism settings take into account the mesh resolution. This is generally achieved by ensuring that the laminar unstretched flame speed is obtained on a 1D flame with grid resolution identical to the targeted 3D configuration modeled.

5.1 Thickened flame models

The thickened flame model of Colin et al. [319] involves increasing the flame thickness artificially to solve it on an LES mesh

to capture the relevant gradients. To do so, the flame thickening factor F is introduced in the filtered species transport and energy equation. The diffusion term is multiplied by F, while the reaction rate is divided by the same factor. The obtained solution is a flame front propagating at the same speed towards the fresh gases but thickened. The fact that the turbulence–chemistry interaction is modified is taken into account by the use of an efficiency function which depends on the velocity fluctuation and the length scale of the flame and the grid spacing, see Charlette et al. [320], or which is dynamically adaptive, see Charlette et al. [321]. The thickened flame model can be applied to diffusion flames as well, see Legier et al. [538]. This indicates that this model could be useful for partially premixed combustion regimes as well.

The thickened flame model relies on the following principle. The LES mesh not being sufficiently refined to resolve the flame front structure, it is required to thicken it while maintaining its propagation speed. Consequently, the modeling of premixed combustion must ensure keeping the unburned unstretched flame front speed the closest possible to its experimental values, whatever the level of flame thickening. The formulation of the species equation for the thickened flame model is as follows:

$$\frac{\partial \rho Y_k}{\partial t} + \frac{\partial}{\partial x_i}(\rho(u_i + V_i^c)Y_k) = \frac{\partial}{\partial x_i}\rho E F D_k \frac{W_k}{W}\frac{\partial X_k}{\partial x_i} + \frac{E}{F}\dot{\omega}_k, \quad (6.40)$$

where F is the thickening factor and E is the efficiency function associated with the subgrid-scale modeling. An adaptive form of this model ensures that the species equations are actually modified accordingly only within the flame region, avoiding affecting diffusion processes in other regions. This is carried out with a sensor detecting reaction. In that version of the thickened flame model, the thickening factor F is not constant; it is unity outside the reaction zones.

5.2 Flamelet models

Premixed combustion flamelet models are based on the principle that the flame front structure of a turbulent flame is equivalent locally to that of a laminar flame subject to flame stretch and flame curvature. The usual modeling methodology to implement the flamelet model is to split chemistry and transport, where chemistry is included in look-up tables and transport is simplified to a progress variable transport equation. In those cases, the progress variable is a function of temperature of one or several species. In this method, the chemical species, most of which are not transported, are computed on the fly with the look-up table. The main

limitations of the flamelet method are that the impact of the three-dimensionality of the flowfield (convection and diffusion) on the flame structure is affected, the chemistry and transport are decoupled, and thus the finest chemistry–turbulence interactions are not captured. Flamelet models have been developed and studied by Pierce and Moin [539], Pitsch [540]. The major advantage of the flamelet model is its computational efficiency. For strongly 3D flows such as swirling flows, the assumption of flamelets may be valid for the thermal flame structure, but does not hold for the velocity field. In addition, the effect of the flame stretch usually only considers one of its components, and not all.

5.3 Flame surface models

There are two main methods for flame surface models of premixed combustion. These models have the advantage that they do not solve explicitly for the combustion kinetics as all these effects are folded into the flame speed or flame surface model. The first method makes use of the G-equation. In this framework, the flame front propagates at a prescribed flame speed S_D. This quantity can be modeled with various different models, such as a constant flame speed or a curvature- and/or flame stretch-dependent flame model. The G-equation has been shown to enable the analytical derivation of premixed flame dynamics. This method requires an accurate model for the flame speed. The flame surface area model is a method to model turbulent combustion based on a balance equation for the flame surface area. This equation describes the transport of the flame surface by the turbulent flowfield and the physical mechanisms which increase or decrease the reactive surface, see Candel et al. [541]. The original derivation was focused on diffusion flames and can be found in Marble and Broadwell [542]. Theoretical works by Candel and Poinsot [543] were carried out to provide a basis for such turbulent combustion models.

5.4 Probability density function models

In a transported probability density function (PDF) method, no implicit assumptions are made regarding the underlying local flame structure (e.g., flamelet versus nonflamelet combustion) or the degree of mixedness of the reactants (e.g., premixed versus nonpremixed). While PDF methods often have been associated with nonpremixed combustion systems, they are being applied with increasing frequency to partially premixed and premixed systems, see Haworth [318]. In a composition PDF method, one computes (by solving a modeled PDF transport equation) the joint

PDF of the thermochemical state of the mixture as a function of position and time in a turbulent flame. The composition variables are usually taken to be the mass fractions of all chemical species of interest, plus the mixture-specific enthalpy. From these composition variables, the chemical reaction rates and thermodynamic properties (mixture density and temperature) can be computed. In LES/PDF, there is no direct closure problem associated with the filtered chemical source terms; they can be written directly as integrals over the subfilter-scale PDF. The modeling or closure problem shifts to two other physical processes: (1) turbulent transport in physical space by unresolved (subfilter-scale) turbulent velocity fluctuations and (2) molecular transport in composition space, corresponding to unresolved scalar gradients. As in many other turbulent combustion models, gradient transport is usually invoked for (1), such that the subfilter-scale turbulent scalar flux is taken to be down the local resolved scalar gradient. Various mixing models are used for (2), and the mixing model is the most critical element of the modeling in a PDF method.

6 A priori filtering for turbulent combustion models

6.1 Introduction

Turbulent combustion involves the interaction of multiple spatial and temporal scales between the flowfield and the reacting flame front. LES in turbulent combustion has been developed and used to model the evolution of turbulent reacting flame fronts by Poinsot and Veynante [544], Pitsch [311], Acharya and Kuo [123]. The turbulence–chemistry interaction is represented by models in LES; the validity and applicability of these models depend upon the smallest resolved scale. The fidelity and quality of an LES calculation and the associated turbulence–chemistry model depends upon the filter size, which is usually the grid size, for implicit filtering LES. There have been multiple studies to assess the applicability and accuracy of different turbulence–chemistry models in comparison with experimental data or comparing between LES codes. The present section is motivated by future LES model development and by the evaluation of grid size effects on turbulent combustion modeling.

The LES filtering operation can be performed in the spatial or in the wavevector domain. In the wavevector domain LES consists in filtering the highest wavevectors (the smallest wavelengths) in order to capture the largest scale within the flow. In the wavevector domain, the filtering is performed with a product operation, while

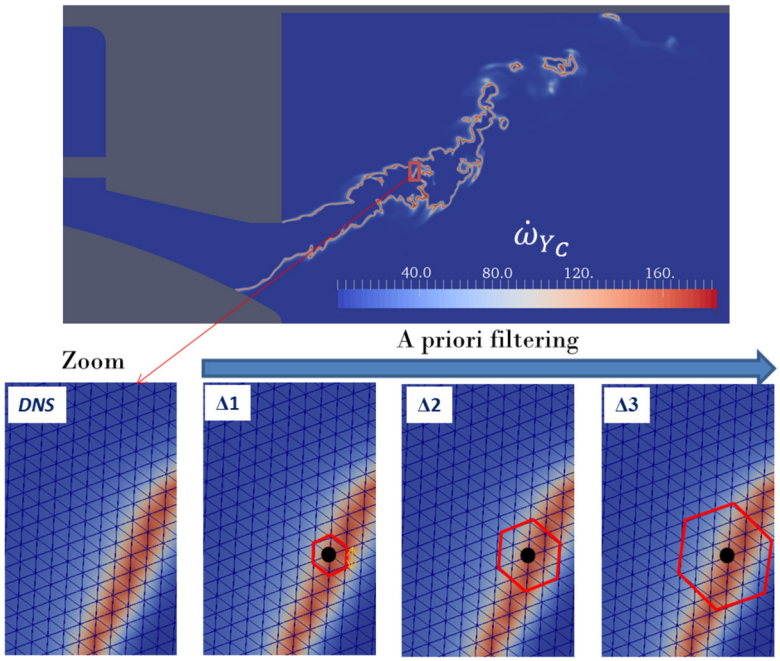

Figure 6.10 A priori filtering procedure. Top figure: Longitudinal slice of the Preccinsta premixed swirl-stabilized combustor with the reaction rate of the progress variable $\dot{\omega}_{Y_C}$. Bottom figure: Series of close-up views of the flame front with superimposed polyhedra filters of increasing size. Each filter size has respectively $M = 7$, 19, and 37 points for the spatial filtering operation. The polyhedra filter edge size varies from 100 to 300 micrometer.

in the spatial domain, the convolution product needs to be computed. The present section aims at presenting an a priori filtering method and at studying the effects of the spatial filtering operation on the flame front with this method. The application of this approach enables to evaluate the impact of spatial filtering on a set of reacting flowfield variables, to propose an index to quantify this impact, and to extract insights from the subsequent data analysis. In addition, this section evaluates the thickened flame model with respect to the conclusions of the a priori filtering analysis.

It is straightforward to conceptualize the role of the spatial filtering for turbulent combustion applications. This can be achieved with Fig. 6.10. One first assumes that a DNS field represents the real experimental flame front. Then, one expects the flame front captured with LES to have the same location as in the DNS, this location being determined by the boundary conditions and the reacting flowfield dynamics. In Fig. 6.10, the reaction rate of the progress variable $\dot{\omega}_{Y_C}$ within the Preccinsta combustor is plotted and a set of the same close-up views is given with the

superimposed filter shape for three different sizes. One can conceptualize immediately the effect of spatial filtering as averaging the variable at a given point with the neighborhood values belonging to the filter. The two immediate consequences of the spatial averaging will be the flame front location and the variable range modifications. One essential aspect of this section is to document and study these modifications and to elaborate on their impact for combustion dynamics modeling.

It is worthwhile to recall the importance of capturing the flame location correctly for combustion dynamic unsteady processes, such as for flame stabilization and combustion instability by Palies et al. [213], and to briefly list a few different methods to do so. Indeed, it has been shown recently that a key effect on combustion dynamics is due to the location of the nonoscillating component of the flame, this component being part of the flame time average. As a consequence, it is important to evaluate in numerical modeling approaches the factors affecting the flame location. Among the different approaches to solve for the reacting flows are five significantly used approaches: (i) the flame surface density models, where the flame speed and the surface density are the key elements that model the reacting source term; (ii) the flamelet progress variable methods, where the reactions are coupled through the tabulated chemistry, see Pierce and Moin [539]; (iii) the G-equation, where the nonreacting flame front propagates in the flowfield, see Kerstein et al. [126], Matalon and Matkowsky [545]; (iv) the statistical methods by Haworth [318], where the temporal and spatial deterministic characteristic of the fluctuating heat release field could be lost; and (v) the thickened flame model by Colin et al. [319], where the turbulence–chemistry interaction is modeled with the efficiency function.

DNS provides a possible path to the resolution of all spatial and temporal physical scales that can be resolved with a prescribed numerical scheme discretization and numerical procedure, a given computational mesh, a set of governing equations, and a set of boundary conditions. It has been shown that DNS can be used for model assumption assessment by Poinsot and Veynante [544], Veynante and Moureau [546] and model development purposes, see Poinsot and Veynante [544], Pitsch and Trisjono [547,548], Borghesi and Bellan [549], Trisjono and Pitsch [550]. There are two main approaches, respectively a priori filtering and a posteriori filtering, to fulfill these objectives. A priori filtering consists in performing the convolution product between a filter and the flowfield variable onto DNS data to assess hypotheses and extract information for model development. A posteriori filtering consists in making use of LES at different filter sizes/test

filters for comparison with the DNS results for an identical geometry and operating conditions. For implicit LES filtering, the grid size/shape represents the filter.

It is important to review current methods to perform the a priori filtering operation, see Sagaut [551]. A first method is to utilize the property of the convolution product, which has become a standard mathematical product in the wavevector domain. A second method is based on Taylor series expansion, see Sagaut [551], Moureau et al. [552]. An alternative method, not applied in combustion simulations for unstructured grids, is to compute the convolution product based on image processing methods, see Ludwig [553]. This is the method implemented for combustion simulations in the present section. While many a priori studies have been conducted on structured grids, the case of unstructured grid studies with the present method is novel.

A priori methods have been used in turbulent combustion to assess flame wrinkling models for LES, see Veynante and Moureau [546], Hawkes et al. [554], Moureau et al. [552], Veynante et al. [555]. In Veynante and Moureau [546], flame wrinkling models' factors of the thickened flame model of Colin et al. [319], Charlette et al. [556] from known resolved fields in LES of turbulent premixed combustion were investigated from a priori tests on the Preccinsta turbulent swirling flame data set. In Hawkes et al. [554], an LES model for flame wrinkling was favorably compared against a priori DNS tests. In Moureau et al. [552], a priori evaluation and model derivation was carried out on the Preccinsta data set. In Knikker et al. [557], a similarity model was developed which correctly reproduced the locations of the unresolved reaction rate with a comparison with a priori filtering, the reaction rate occurring below the cutoff scale. A priori and a posteriori filtering methods have also been developed to model the unclosed terms that appear in LES equations by Borghesi and Bellan [549]. In Volpiani et al. [558], dynamic models where model parameters are automatically adjusted from known resolved fields were investigated with a posteriori filtering. In Proch et al. [559], dynamic subfilter models for the artificially thickened flame LES combustion model were investigated with consistent a priori and a posteriori analyses. While these previous studies have focused on the subgrid scale, the present paragraph focuses mainly on the filtered/resolved variables, which has been the subject of fewer studies. Flame surface density models have also been investigated extensively with a priori filtering of DNS data, see Boger et al. [560], Chakraborty and Cant [561], Chakraborty and Klein [562], Gao et al. [563], Allauddin et al. [564].

This section is structured in four main subsections. The first one focuses on the filtering operation, with the emphasis on how the convolution product is formed. The second subsection discusses the data set obtained from Moureau et al. [552]. The results are detailed and discussed in the third subsection. The fourth subsection focuses on the application to the thickened flame model.

6.2 The a priori filtering method

The a priori filtering method consists in computing the convolution product between a given variable Φ and the filter F. The filter F is usually the numerical simulation mesh for LES implicit filtering, see Poinsot and Veynante [544]. It is a box or a Gaussian function centered on the mesh cell for explicit filtering. The present work is focused on implicit filtering and three filter sizes are considered, see Fig. 6.10. The filtering operation writes

$$\bar{\Phi}(\boldsymbol{x}) = \int_{-\infty}^{\infty} \Phi(\boldsymbol{x}') \times F(\boldsymbol{x} - \boldsymbol{x}') d\boldsymbol{x}'. \tag{6.41}$$

The filtered variable $\bar{\Phi}(x)$ can be expressed after discretization as

$$\bar{\Phi}(\boldsymbol{x}_i) = \frac{1}{M} \sum_{j=1}^{M} \Phi(\boldsymbol{x}_{i,j\in\Delta}) \times F(\boldsymbol{x}_{i,j\in\Delta}), \tag{6.42}$$

where the number of points i ranges from 0 to N_s. Each filter size has a given number of points j, respectively $M = 6$, 18, and 36 nearest points plus the center point. This equation is used to compute the filter quantities at each point of the selected window of data. The filter F is normalized with

$$\sum_{j=1}^{M} F(\boldsymbol{x}_{i,j\in\Delta}) = 1, \tag{6.43}$$

which is equivalent to the following normalization for LES filters by Poinsot and Veynante [544]:

$$\int_A F dA = 1 \tag{6.44}$$

for assumed constant elementary surfaces, such as triangles in the present case.

6.3 DNS Preccinsta data set

6.3.1 Governing equations

The Preccinsta DNS data subset from Moureau et al. [552] is used in the present study. It has been computed by Moureau et al. [552] with a premixed flamelet progress variable model coupled to a chemistry table model, see Galpin et al. [565], Moureau et al. [552]. The mass, momentum, and progress variable equations are solved by the code YALES2. Elements of the numerical procedure can be found in Moureau et al. [552]. The progress variable equation writes

$$\frac{\partial \rho Y_C}{\partial t} + \frac{\partial}{\partial x_i}(\rho u_i Y_C) = \frac{\partial}{\partial x_i}\left(\rho \mathcal{D} \frac{\partial Y_C}{\partial x_i}\right) + \dot{\omega}_{Y_C}, \tag{6.45}$$

where the normalized progress variable c is equal to $Y_C / Y_C^{eq}(\phi)$, where ϕ is the inlet equivalence ratio and the progress variable is $Y_C = Y_{CO} + Y_{CO_2}$. The progress variable reaction rate is $\dot{\omega}_{Y_C}$ and $\mathcal{D}$ is the diffusion coefficient. The equation of state is also used in the numerical procedure.

6.3.2 Variables, geometry, and operating conditions

The Preccinsta data set encompasses DNS and LES performed with the code YALES2 Moureau et al. [552] and corresponds to the experimental configuration of Meier et al. [566]. The experiment consists of a swirl-stabilized premixed methane–air flame at equivalence ratio 0.83 confined in a square section combustion chamber. In the present simulation, where the walls are adiabatic, the modeled swirling flame develops on the sides of the swirling jets. At this equivalence ratio, the combustor does not present combustion instability. The present section investigates variables from a longitudinal cutplane of the Preccinsta DNS data set at one time step because the emphasis is on spatial filter quantities. The slice is made up of a total number of N_t points, equal to 1 905 865.

6.3.3 Reconstructed variables

This section describes the data preparation carried out before the filtering operation. The first step is to minimize the number of points of the original slice by removing the points too close to each other. These points are due to the slicing operation through the tetrahedrons of the mesh. In addition, among the entire slice, a window is used to select data between $x = -7.5$ mm and $x = 57.5$ mm, which encompasses the whole flame region. The total number of points is reduced to a subset of $N_s = 334\,768$ points. The reconstructed variables are the flame speed and the equivalence ratio fields. The flame speed is determined as follows. Firstly,

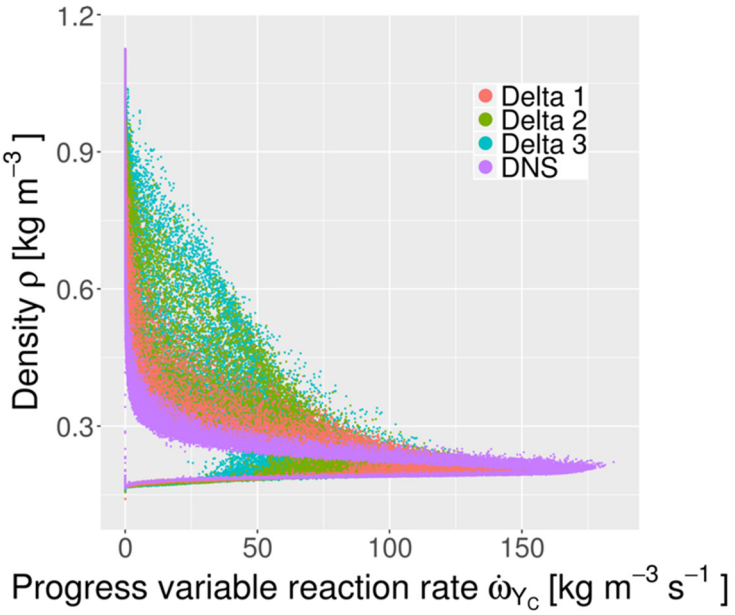

Figure 6.11 Filtered density variable. Scatter plot of DNS and a priori filtered density. The DNS data are shown in purple. The orange, green, and blue colors respectively correspond to filter sizes 1 to 3.

the isocontour of the progress variable taken at $c = 0.7$ is used to track the reaction zone at the flame front. Based on Eq. (6.47), the flame displacement speed is computed on this isocontour. In addition, the chemistry table is used to retrieve the CH_4 and O_2 mass fractions in order to form a local equivalence ratio by multiplying by the stoichiometric ratio $s = 4$.

6.4 Results and discussion

6.4.1 Density, temperature, and mass fraction ratio

The density, temperature, and mass fraction ratio scatter plots are provided in Figs. 6.11–6.13. Each variable is plotted versus the progress variable reaction rate $\dot{\omega}_{Y_C}$. DNS and a priori filtered variables for three different filter sizes are plotted. In these figures, the purple dots correspond to the DNS data. The density ranges from slightly above 0.15 kg m^{-3} in the burned gases to 1.12 kg m^{-3} in the fresh gases, and the temperature ranges from 300 K to 2030 K, the adiabatic flame temperature at this equivalence ratio. The mass fraction ratio varies between 0 and near 0.83 between the burned and the fresh gases. It is of interest to describe the results with respect to the peak reaction rate of the progress variable

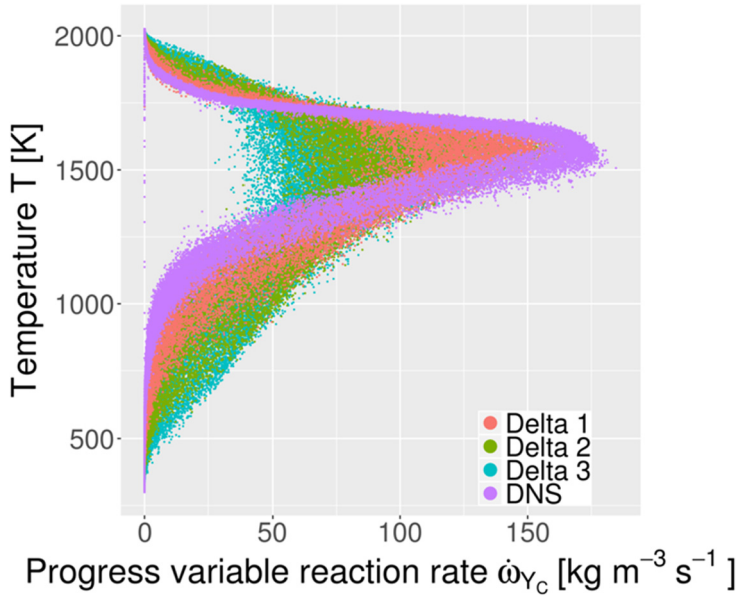

Figure 6.12 Filtered temperature variable. Scatter plot of DNS and a priori filtered temperature. The DNS data are shown in purple. The orange, green, and blue colors respectively correspond to filter sizes 1 to 3.

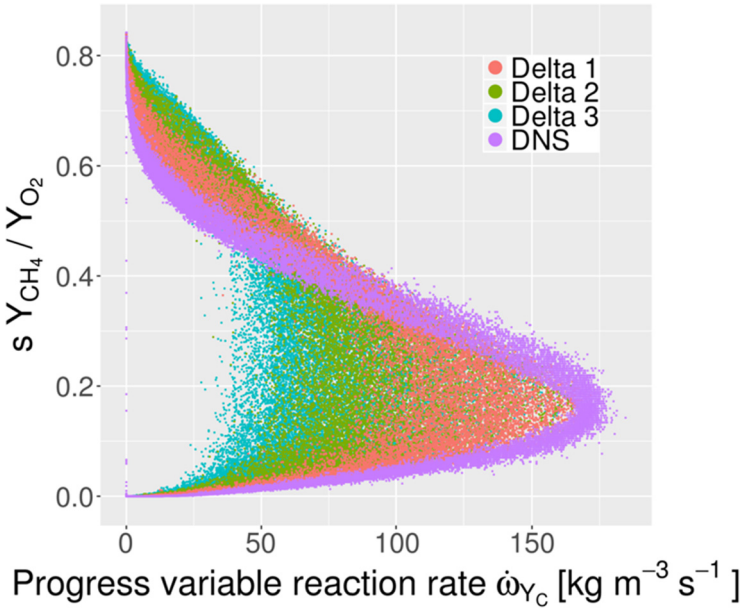

Figure 6.13 Filtered equivalence ratio variable. Scatter plot of DNS and a priori filtered local equivalence ratio. The DNS data are shown in purple. The orange, green, and blue colors respectively correspond to filter sizes 1 to 3.

($\dot{\omega}_{Y_C} > 150$). The maximum reaction rate occurs for a density value near 0.22 kg m^{-3}, a temperature close to 1625 K, and a local equivalence ratio near 0.15. In addition, the progress variable value is centered on 0.7 for the region where the progress variable reaction rate peaks.

The corresponding filtered values for the three filter sizes are presented in each graphic. One can conclude that for each filtered variable the distribution of values is strongly affected by the spatial filtering operation, and this impact is more pronounced as the filter size increases. While other variables that are not presented here were investigated as well, it is worthwhile to point out that the pressure field does not follow a specific distribution such as exhibited by the density, temperature, and mass fraction ratio distributions. This is attributed to the Poisson equation used to solve the pressure field, which is solely a function of the velocity field, this latter not having any specific shape. It is of interest to also remark that while the shapes of the density (Fig. 6.11), temperature (Fig. 6.12), mass fraction ratio (Fig. 6.13), and progress variable (Fig. 6.14) scatter plots are similar, their stiffness characters differ significantly. This is observed mainly between the density and the other variables and it is attributed to the diffusive character of the equations solved. Indeed, except for the density variable, the progress variable, temperature, and mass fraction ratio have a diffusion operator, directly or not through Eq. (6.45).

6.4.2 Flame structure

The results in Fig. 6.14 indicate that for the DNS, the peak progress variable reaction rate $\dot{\omega}_{Y_C}$ is obtained when the progress variable c is close to 0.7. In addition, it is observed that for the three filtered sizes, this relationship is lost and the peak reaction rate does not correspond anymore to a value of the progress variable of 0.7. This is an important aspect that will require further study with LES and direct evaluation of this aspect of the flame structure for that turbulent combustion regime with different combustion models.

The two direct and natural key effects of spatial filtering are illustrated by the results in Fig. 6.15. This set of figures presents the DNS and a priori filtered flame tip close-up views. The first observation is that the value range is reduced as the filter size is increased, which is a direct consequence of the spatial averaging operation. At a given point of the mesh, a given value is averaged with its neighbors, so high values decrease and low values increase. These conclusions also apply to the other variables. Another key aspect is that the flame location is modified due to the level of refinement of the filter; the higher the filter size in the

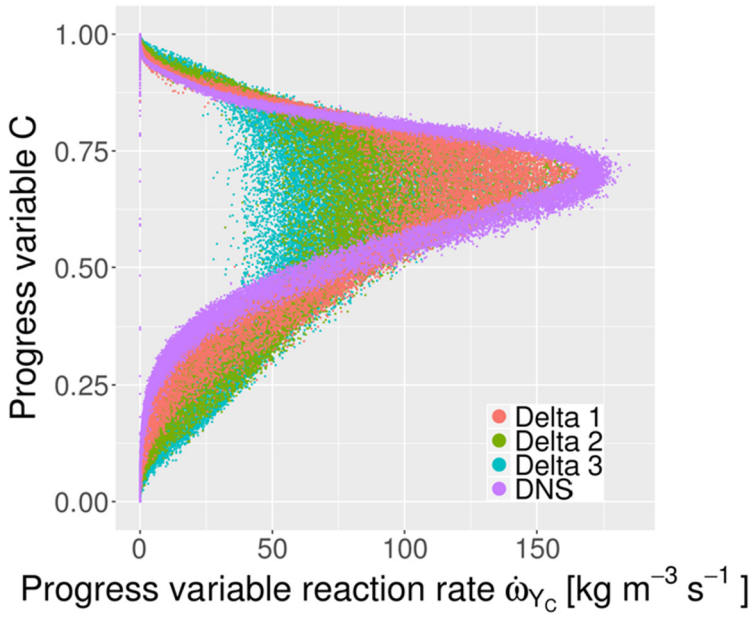

Figure 6.14 Filtered progress variable. Scatter plot of DNS and a priori filtered progress variable. The DNS data are shown in purple. The orange, green, and blue colors respectively correspond to filter sizes 1 to 3.

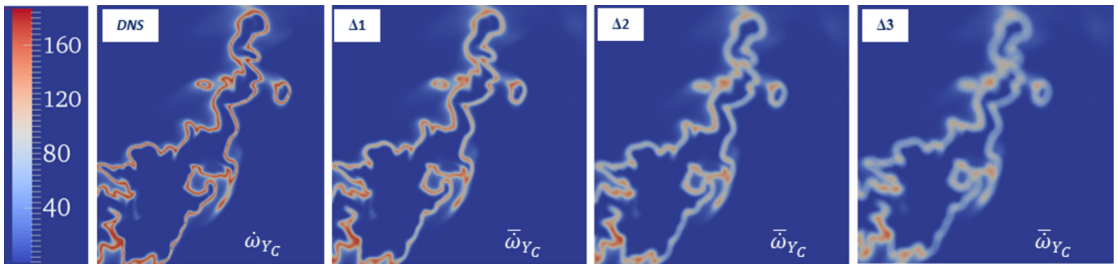

Figure 6.15 Filtered reaction rate variable. Flame tip close-up views of the reaction rate of the progress variable $\dot{\omega}_{Y_C}$ (right) for the DNS and the three filter sizes $\Delta 1$, $\Delta 2$, and $\Delta 3$.

spatial domain, the more pronounced is the effect. This is important for unsteady combustion dynamics where the evolution of the flame front, including its tip and its base, is critical.

The impact of the results on modeling are now discussed. Firstly, a simple expression linking the two previous effects (location and peak value of the reaction rate) is introduced. As observed, when the filter size increases, the peak reaction rate $\dot{\omega}_{max}$ decreases and the flame thickness δ increases. These two quantities can be linked locally by the following expression: $\rho Y_f S_d \simeq$

$\delta \times \dot{\omega}_{max}$, where ρ is the density of the fresh gas, Y_f is the mass fraction of fuel, and S_d is the flame speed. This expression can be obtained by approximating the area under the reaction rate curve function of the normal direction to the flame front by a single rectangle whose side lengths are respectively the peak reaction rate and the flame thickness. This expression indicates that for LES where the experimental flame thickness is below the grid size, the modeled flame thickness will be of the order of the grid size, so that the peak reaction rate will decrease. This relationship expresses the challenge of the development of any turbulent combustion model and points towards a condition that cannot be met with current approaches. For example, for the thickened flame model, this expression leads to a decrease in the reaction rate peak and an increase in the flame thickness, while keeping the flame speed constant. In other words, for the modeling of turbulent combustion, there is an intrinsic physics constraint between the flame speed, the reaction rate, and the flame thickness that has to be satisfied. Consequently, for LES models, a choice will have to be made between a model that conserves the flame speed or the reaction rate peak and other approaches.

6.4.3 Flame speed

It is convenient as a postprocessing step to make use of the G-equation in order to obtain an expression for the flame displacement speed S_D and to determine its values along the flame front. The G-equation writes

$$\frac{\partial G}{\partial t} + \mathbf{u} \cdot \nabla G = S_D |\nabla G|. \tag{6.46}$$

The flame front is determined with an isocontour of the normalized progress variable, and the flame speed S_D along this contour is calculated with Eq. (6.47). Indeed, the flame speed S_D can be defined with an analogy between the temperature equation and the G-equation, see Acharya and Kuo [123], or between the progress variable equation (6.45) and the G-equation (6.46), giving

$$S_D = \left[\frac{\nabla \cdot (\rho \mathcal{D} \nabla Y_C) + \dot{\omega}_{Y_C}}{\rho |\nabla Y_C|} \right]_{c=0.7}, \tag{6.47}$$

where the normalized progress variable of $c = 0.7$ corresponds to the inner layer (reaction zone). This expression is computed to determine the flame speed.

In Fig. 6.16, the isocontour of the progress variable $c = 0.7$ and the temperature field with the superimposed normal flame front vector $\mathbf{n}$ are given. The vector $\mathbf{n}$ is oriented towards the fresh

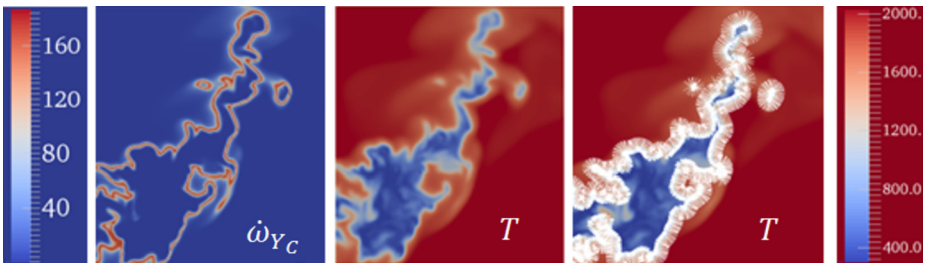

Figure 6.16 Flame tip close-up views. Reaction rate and temperature field with superimposed reaction zone contour and normal vector **n** on this contour. The normal vectors point towards the fresh gases.

gas and is formed with the normalized temperature gradient. The flame speed S_D computed with Eq. (6.47) is plotted in Fig. 6.17. Flame speed values between -20 and 20 m s^{-1} are plotted. Negative values are recorded as the normal vector **n** is not taken into account. Indeed, negative values of the flame speed are not physical. It is observed that the values are clustered mostly between -5 and 5 m s^{-1}. In addition, the maximum reaction rate of the progress variable for the DNS data is shown to not be linked to a specific flame speed, and this latter takes a wide range of values.

6.4.4 Index

In this section, a global index G is introduced to quantify the effects of a priori filtering on the DNS data. The utility of this index is twofold: (i) it can be used to compare a priori filtering methods for each variable, and (ii) it indicates directly the closeness of a variable to its filter value. This index is used to compare the DNS flowfield variables with respect to the a priori filtered ones, and it writes as follows:

$$G = \frac{1}{N}\sum_{i=1}^{N}\frac{\Phi(x_i, y_i) + |\Phi(x_i, y_i) - \bar{\Phi}(x_i, y_i)|}{\Phi(x_i, y_i)}. \tag{6.48}$$

Its value is unity for the DNS data. In Tab. 6.2, a summary of the index values computed for the three filtered sizes is given for density, temperature, local equivalence ratio, and reaction rate of the progress variable. Other variables, such as pressure, flame stretch, and vorticity, have been computed but are not reported here.

The results listed in Tab. 6.2 indicate that increasing the filter size increases the value of the index, as expected, and that the progress variable reaction rate is more affected by the filtering operation than the other variables. This is attributed to the fact that for a given subpiece of the flame, the reaction rate presents two

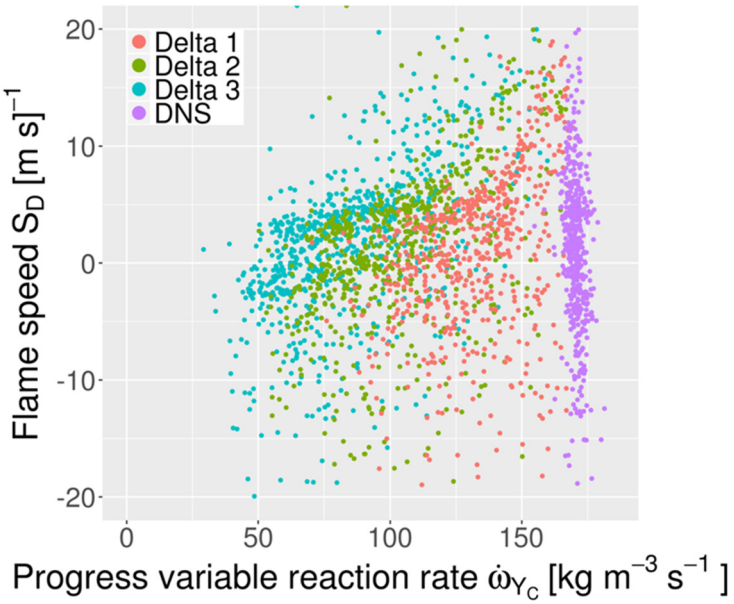

Figure 6.17 Filtered flame speed variable. Scatter plot of DNS and a priori filtered flame speed. The flame speed computed with Eq. (6.47) is plotted. The DNS data are shown in purple. The orange, green, and blue colors respectively correspond to filter sizes 1 to 3.

Table 6.2 A priori filtering index evaluated for three filter sizes.

Variable	$\Delta 1$	$\Delta 2$	$\Delta 3$
Density ρ	1.008	1.012	1.021
Temperature T	1.005	1.006	1.006
sY_{CH_4}/Y_{O_2}	1.021	1.019	1.026
$\dot{\omega}_{Y_C}$	1.159	1.266	1.379

distinct slopes/gradients, while temperature, mass fraction ratios, and density present only one. As a consequence, the reaction rate is more sensitive to the filtering operation than the other variables, which is reflected by the index value.

6.5 Comparisons for the thickened flame model

In this section, the thickened flame model is evaluated by isolating the effect of flame thickening from turbulence (and subsequently from the associated efficiency function) with 1D premixed

laminar flames computed in Cantera. The evaluation is carried out on the flame structure and includes temperature, heat release, and flow and flame speeds throughout the flame front. The effects of reaction and thermal diffusion on the flame speed are taken into account and compared with the flow speed. Comparisons are conducted for (i) detailed/complex versus single-step chemical combustion mechanisms, (ii) four different grid spacings Δx, and (iii) three thickening factors. The so-called no-model, also known as laminar chemistry, is used for comparison of every case.

Previous results have shown that the LES implicit filtering induces known but demonstrated and quantified effects. These effects include the loss of the flame structure as the mesh size is increased. The thickened flame model is now evaluated to observe its ability to capture the flame structure correctly for its application to turbulent combustion LES simulations. The particular emphasis, which has not been reported in previous studies, is on the respective location of the reaction zone and the thermal flame front, the calculated flame speed throughout the flame structure (not only the unburned unstretched flame speed), and the effects of various relevant parameters (mesh size, chemical combustion mechanism, thickening factor level) on these. In addition, many observations from these 1D premixed flame simulations are made. The flame speed presented in the next figures has been computed with the following expression:

$$S_D = \left[\frac{\nabla \cdot (\lambda / c_p \nabla T) + \dot{\omega}_T / c_p}{\rho |\nabla T|} \right]. \tag{6.49}$$

In Fig. 6.18, the effects of increasing mesh size Δx on temperature, heat release, and flow and flame speed profiles are compared when no model is used. The comparison is made for complex chemistry and single-step chemistry. By comparing the flame structure between Fig. 6.18A and Fig. 6.18B, one observes immediately that the single-step mechanism is stiffer than the complex chemistry one. This has one important consequence, i.e., the thermal thickness of the single-step mechanism is smaller than that of the complex chemistry one, and thus may require finer meshes. One also observes that for both chemical mechanisms, the flame front structure is well predicted up to a mesh size of 80 μm without the use of any model. That mesh size corresponds to approximately 10 to 15 points throughout the thermal flame front. The flame speed shows some discrepancies with the flow speed for larger mesh sizes, indicating that the flame structure is not anymore captured, as shown by the heat release peak amplitudes and locations for a mesh size of 400 μm.

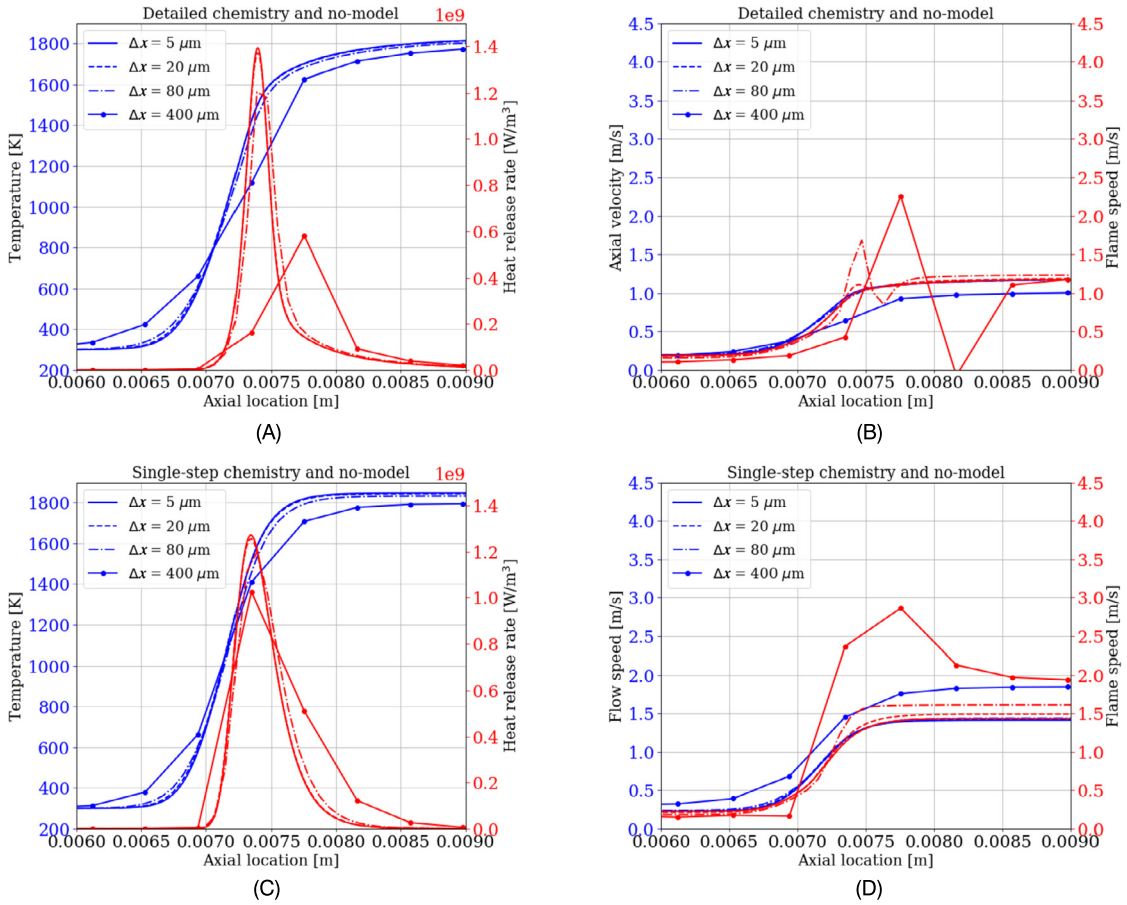

Figure 6.18 Effects of mesh size Δx. Temperature and heat release distributions for (A) complex chemistry and (C) single-step chemistry. Flow and flame speeds for (B) complex chemistry and (D) single-step chemistry.

In Figs. 6.19 and 6.20, the emphasis is on the effect of the thickening factor F on the flame front structure with respect to the no-model approach for constant mesh sizes Δx of 20 μm and 80 μm respectively. At $\Delta x = 20$ μm, the effect of increasing the factor F is an increase in the thermal thickness, as expected by the thickened flame model, and a decrease in the peak amplitude of the heat release. The peak heat release is observed to occur at similar temperatures for all cases. These observations are identical for the single-step and complex chemical mechanisms. The most significant difference is observed in the flame speed profiles throughout the flame front. These differences are consequences of the shapes of the temperature and heat release profiles (amplitude reduc-

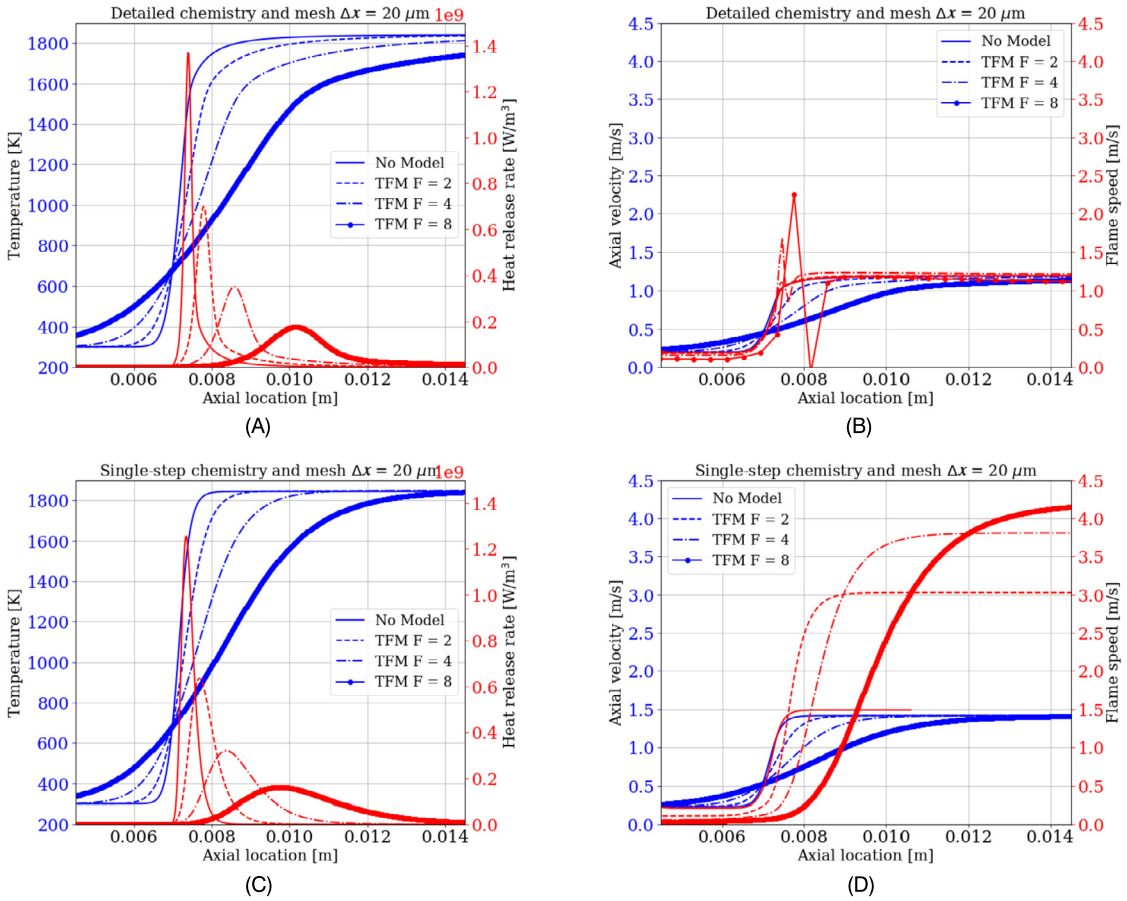

Figure 6.19 Effects of the chemical mechanism and thickening factor F for size $\Delta x = 20$ μm. Temperature and heat release distributions for (A) complex chemistry and (B) single-step chemistry. Flow and flame speeds for (C) complex chemistry and (D) single-step chemistry.

tion) and their relative positions. This is noticed particularly for the simplified mechanism as the thickening factor increases and for both chemical mechanisms as the grid spacing increases.

6.6 Conclusions and perspectives

In this chapter, a method to compute the convolution product for a priori filtering on unstructured grids is implemented and applied to swirl-stabilized data. A priori spatial filtering is performed and the effects of this spatial averaging on the data are shown to affect both the amplitude and the spatial location of a given variable. It is shown that the filter size amplifies this effect.

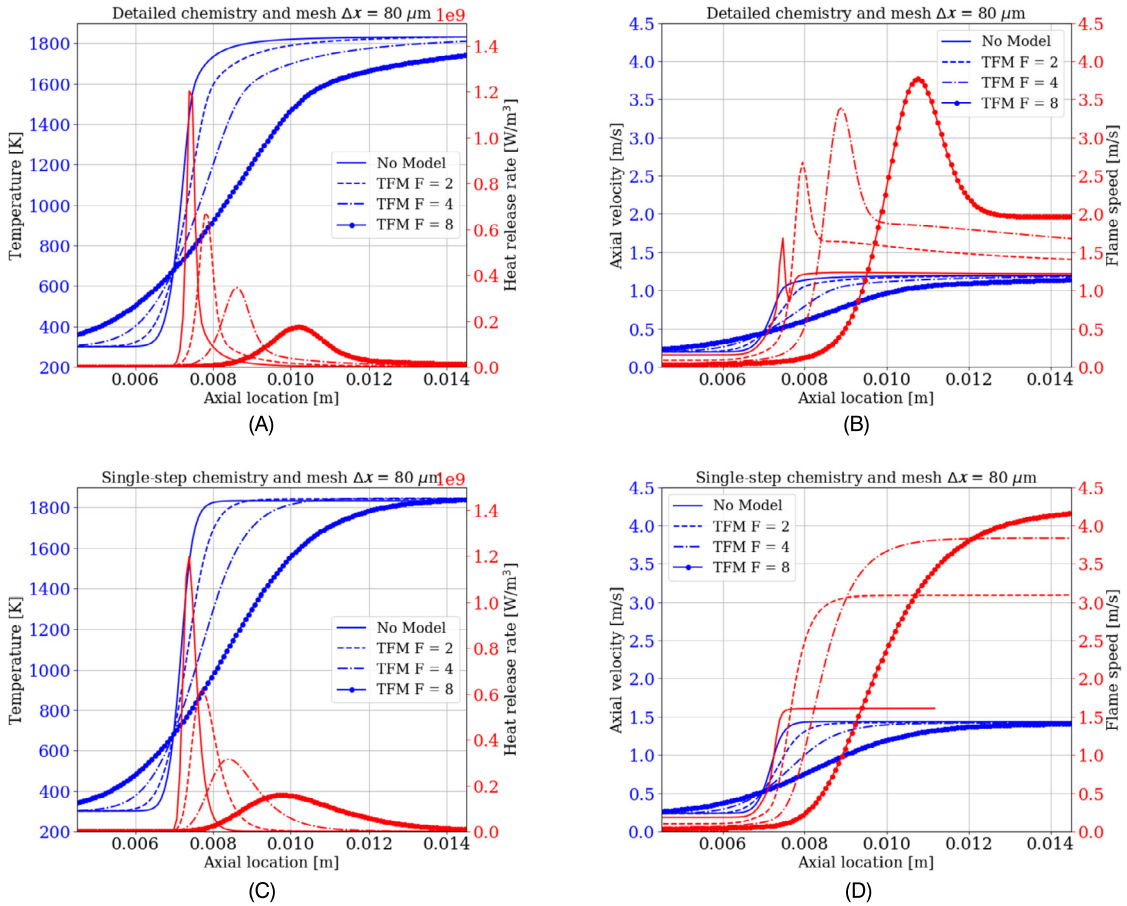

Figure 6.20 Effects of the chemical mechanism and thickening factor F for size $\Delta x = 20$ μm. Temperature and heat release distributions for (A) complex chemistry and (B) single-step chemistry. Flow and flame speeds for (C) complex chemistry and (D) single-step chemistry.

The data analysis carried out to study the flame structure shows that the link between the flame inner layer (reaction zone) and the reaction rate peak is lost when filtering. Next, a 1D premixed flame was studied to verify that this link is ensured with the thickened flame model. The results of these premixed 1D flame calculations allow to observe the effects of the thickened flame model on the flame structure for various parameters. It is shown that (i) the thickened flame model allows to keep the link peak heat release (but of reduced amplitude) and temperature in the flame, (ii) the flame speed computed based on the flame front heat release and temperature profiles is accurate for a limited range of

thickening factors and mesh sizes, and (iii) the no-model (laminar chemistry) mechanism with single-step chemistry allows to capture the flame structure and the flame speed throughout the flame correctly when using between 10 to 15 points through the flame front. This work can be applied to improve (i) our understanding of combustion dynamics where the flame location has been shown to be important and (ii) model assessment and development. The impact of the present results on turbulent combustion modeling is that LES, if not resolving the flame thickness with a sufficient number of grid points, cannot simultaneously capture the reaction rate maximum amplitude and the flame speed.

7 Fuel vaporization physics and modeling

Future combustors operating in a partially premixed regime or a fully premixed regime such as presented in the next chapter will require the modeling and physical understanding of fuel boiling and vaporization processes. They will also require to include two-phase flows and phase change physics. The present section describes some of the current modeling approaches. In addition, recent LES calculations undertaken for aeronautical combustors are discussed.

The fuel vaporization process have been initially investigated for single droplets in the context of spray combustion. The review article of Sirignano [193] identified four major research areas: (i) droplet/gas stream boundary conditions, (ii) transient heating of the droplets, (iii) multi-component fuel vaporization (different fuel components have different vaporization rates, which can vary significantly during the droplet lifetime), and (iv) combustion and vaporization of sprays. The review article of Law [567] focused on the fundamental mechanisms governing droplet vaporization and combustion. Since these pioneering reviews, the description of spray and its modeling have been extended. Particularly, prior to combustion, the single-droplet stage is indeed preceded by a succession of transformations of the liquid fuel jet from the injection. Wu and Faeth [568] performed an experimental study to investigate the aerodynamic effects on the primary breakup of turbulent liquids. The article of Faeth et al. [569] further described the structure and breakup properties of sprays for multi-phase flow phenomena relevant to spray combustion. The passage from injection in liquid fuel form to spray follows the following steps. The primary breakup consists of the transformation from the liquid sheet to ligaments, i.e., large aggregates of fuel of various shapes. These ligaments are then transformed into spray through the secondary breakup stage. Various flow processes and

flow instabilities are responsible for these transformations. The injector plays a key role in these transformations due to the impact of the fluid mechanic processes on the transformations. Consequently, the flow dynamics of cross-flow in jets have also received significant attention, see the article of Smith and Mungal [570] and the review by Karagozian [571].

The modeling of nonreacting and reacting spray with numerical simulations is out of the scope of the present section. The focus here is on the state of the art for the application of such modeling tools to realistic combustor geometries relevant to commercial aircraft combustors. The article of Hannebique et al. [572] listed in their LES modeling study specific relevant subgrid-scale challenges: the modeling of the atomization of the liquid jet fuel, the modeling of the dispersion of fuel droplets, interaction of fuel with walls, evaporation, and combustion. The article of Franzelli et al. [573] documented the structure and dynamics of a swirled spray flame modeled with tabulated chemistry adapted to spray combustion. In Li et al. [574], simulations were performed to investigate spray atomization and subsequent droplet transport in a swirling air stream generated by a complex multi-nozzle/swirler combination. The level-set method coupled to the volume of fluid method was employed to model isothermal flow.

The complete direct tracking of gaseous flow and liquid fluid with phase change within swirl injectors for combustion applications is currently out of reach, and no such capabilities exist. It will be a critical multi-physics capability for injector design optimization such as presented in the next chapter of this book. In addition, the processes of fuel vaporization under high pressure and high temperature (supercritical fluid) conditions require additional physical descriptions, which are discussed in the next section.

8 Supercritical combustion regime at take-off conditions

Future combustors operating in a partially premixed regime or a fully premixed regime such as presented in the next chapter will require to operate at high overall pressure ratios. For those engines, at take-off conditions, it is likely that the fluid is in the supercritical state. The modeling and physical understanding of the supercritical state of the fluid will be more and more important. The present section summarizes some of the relevant aspects in this context.

Rocket propulsion and combustion studies have been pioneering in the field of supercritical combustion because of the high operating pressures in rockets. The major review articles of Oefelein and Yang [27] and Yang [575] focused on the modeling of supercritical vaporization, mixing, and combustion processes in liquid-fueled propulsion systems. These articles provided overviews of theoretical modeling and numerical simulation and included multiple liquid propellants, including hydrocarbon and cryogenic fluids. Experimental work and detailed characterization of flame stabilization for these propulsion systems were documented by Singla et al. [576] and Candel et al. [577]. The articles of Hickey and Ihme [578] and Schmitt et al. [579] focused on the modeling of transcritical and supercritical mixing and combustion for rocket combustion simulations.

The investigation of the supercritical state for mixing and supercritical combustion (chemistry) for high pressure and high temperature aeroengines is weakly documented in the literature and should be addressed in future work.

7

Lean fully premixed injector design

Rising awareness of the consequences of global warming has prompted several countries to sign multiple international treaties with the ultimate goal of reducing greenhouse gas (GHG) emissions, including CO_2. The Kyoto Protocol is the international reference agreement that sets targets in terms of reducing GHG emissions. Since going into effect in 2005, signatory countries have ratified the text committing to reduce their emissions by 5% from 1990 levels during the period 2008 to 2012. The 2015 United Nations Climate Change Conference COP21, held in Paris, has led to the Paris Agreement. This agreement states an overall objective for keeping the global temperature increase less than 2°C above preindustrial levels. One of the major consequences of the Paris Agreement is the reduction of emissions in order to achieve a balance between anthropogenic emission by sources and removal by sinks of GHGs in the second half of the 21st century. Consequently, the development and use of technologies aiming at reducing or suppressing pollutant emissions will have a strong impact and will help to reach the targeted COP21 goals. In this context, it is imperative to improve the combustion technologies and significantly reduce emissions to minimize the environmental impact of jet engines. It is known that conversion of hydrocarbon fuels into burned products generates GHGs like CO_2 and pollutants like unburned hydrocarbons HC, nitric oxides NO_x, and carbon monoxide CO. Among other harmful consequences, nitric oxides NO_x and unburned hydrocarbons are major contributors to the formation of smog and near-ground level ozone. There are two ways to reduce those emissions: modify their generation or eliminate their emission. It is also important to distinguish between emissions from ground gas turbines and from jet engines, as the emission from the former can be sequestrated or go through post-treatment, while the emissions from the latter cannot. In addition, space and weight constraints of ground gas turbines and jet engines are different so that technologies for emission reductions or for static and dynamic stability are different. Finally, the emissions from jet engines, while being a small contribution to the worldwide overall emissions, are emitted at high altitudes and the

Stabilization and Dynamic of Premixed Swirling Flames
https://doi.org/10.1016/B978-0-12-819996-1.00015-9

subsequent effects are not known. The International Civil Aviation Organization through its Committee on Aviation Environmental Protection has established international certification limits for nitrogen oxide (NO_x) emissions for jet engines. The Federal Aviation Administration, in turn, enforces these standards in the USA through engine certification.

As pointed out by the NASA Aeronautics Research Mission Directorate, achieving low emissions and the requirements of cleaner power and propulsion systems constitute a constraint for the research, development, and design process of future ground gas turbines and aircraft engines. Vehicles for subsonic and supersonic flight regimes will be required to operate on a variety of certified aircraft fuels and emit extremely low amounts of gaseous and particulate emissions. Future aircraft will be designed with smaller engine cores operating at higher pressures to increase overall efficiency. Future combustors will also likely employ lean-burn concepts to reduce harmful emissions. Fundamental combustion research coupled with associated physics-based model development of combustion processes will provide the foundation for technology development critical for these vehicles. Combustion involves multi-phase, multi-component fuel, turbulent, unsteady, 3D, reacting flows where much of the physics of the processes is not completely understood. In that context, low emission combustor concepts for small high pressure engine cores relevant to the next generation of turbofans are required and this chapter focuses on such injector development.

There are three main combustor architectures used among the leading jet engine manufacturers, which as presented in Tacina [580] and Lefebvre [34] are: the lean direct injection (LDI), see Tacina et al. [116]; the lean premixed/prevaporized (LPP), see Lefebvre [581]; and the rich-burn quick-quench lean-burn (RQL) combustion systems, see Lefebvre [34]. The LDI concept injects the fuel (liquid or gaseous) directly into the reaction zones. The LPP combustor consists of a regime where liquid fuel is mixed and prevaporized prior to combustion. The RQL has three distinct combustor regions. In the front region, the rich combustion zone is expected to limit the formation of NO_x. In the center region, additional air quenches the flame and reduces the overall equivalence ratio allowing an overall leaner combustion zone expected to minimize the thermal NO_x in the downstream location of the combustor. Significant efforts have been made for LPP injectors, but no attempt toward a fully premixed injection for jet engine application is documented in the literature. In order to comply with future engine emission certification, a fully premixed combustion mode could be a potential candidate. While the study of premixed

combustion has received significant attention over the last few decades with tremendous advances in both the physical understanding and the modeling, see for examples the articles of Huang and Yang [22], Palies et al. [396], Candel et al. [582,23], the study and design of combustion injector systems allowing to reach and operate in full lean premixed mode for jet engines has received less or no attention. Premixed swirled combustion of fuel blend (hydrocarbon, natural gas, or hydrogen) could be the combustion mode allowing satisfying the future requirements on emissions.

The single most important difference between the proposed LFP technology and existing injectors is the generation of a sprayless fully premixed gas injected into the combustion chamber. Some of the advantages of LFP over LPP and other existing technologies are also noteworthy. LFP injectors are able to reach lower NO_x emissions, as demonstrated for example by the low swirl injector, see Cheng et al. [583] developed for ground-based gas turbine applications. Another advantage is that there is no spray modeling required within the combustor. Finally, there would be potentially no soot emitted and combustion efficiency will be nearly 100%.

This chapter is dedicated to the feasibility study of an LFP injector for high overall pressure ratio small core engines at take-off conditions, as future turbofan gas turbine engine combustors are expected to operate at high overall pressure ratio and have smaller cores than their predecessors. In order to perform this feasibility study, some of the related constraints are introduced and discussed. Then, in order to achieve the major objective of the LFP design, a three-unit fully premixed injector is defined and selected aspects are described. Computational modeling analyses are used to design the units of the LFP injector and are presented in the next sections.

1 Design procedure

The design space for the LFP injector is at the intersection of combustion physics, combustor constraints, and jet engine operating conditions. Each of these aspects is briefly discussed in this section to describe the current design space. This chapter presents the first iteration of a design loop. Future efforts should be undertaken in addition to this initial work. Combustion physics is one component of the design space and broadly encompasses many aspects such as autoignition, chemical kinetics, vaporization, flammability limits, flame propagation, turbulent mixing, combustion instability, flashback, blowout, turbulent combustion, and radiation. One of the most important aspects

for premixed combustion is the balance between the flame surface speed, the flow speed, and the burning velocity, see Markstein [124] and Matalon and Matkowsky [545]. Indeed, this balance drives the flame surface position within the combustor and subsequently determines static stability. In addition, this balance includes implicitly most physical processes at work. The balance is written as $\mathbf{w} = \mathbf{v} + S_d\mathbf{n}$, where $\mathbf{v}$ is the flow velocity vector, S_d is the flame displacement speed, and $\mathbf{n}$ is the normal vector on the flame front. The flame speed contains two terms, i.e., the thermal diffusion term and the reacting term, and can be written as $S_d = (\nabla \cdot [\lambda/c_p \nabla T] + \dot{\omega}_T/c_p)/\rho|\nabla T|$, see Palies [29]. It is also worthwhile to recall that the flame speed decreases with increasing operating pressure and increases with increasing upstream unburned gas temperature, see Acharya and Kuo [123]. Recently, the flame speed link to the flow speed has been studied by Palies [29], and the results indicate that the instantaneous flame surface speed is controlled by flow effects. It was discussed in Chapter 3 of this book that the flame stabilizes in regions of balance between flow and flame speeds or regions of approximate balance between flow fluctuations and flame speeds. For these reasons, particular attention has to be paid to the resolution of the quantities of the flame surface speed, flow speed, and burning velocity budget in the numerical simulations.

Another important aspect of combustion physics relevant to the design of LFP is the autoignition phenomenon. This phenomenon occurs when the following three necessary (but not sufficient for premixed combustion) elements are at work together: the presence of heat, the presence of an oxidizer, and the presence of fuel, with appropriate levels to trigger autoignition. Autoignition requires to have a mixture of oxidizer and fuel within the flammability limits and within a temperature range above a threshold. The lower and upper flammability limits also have to be considered. In addition, there is a time delay for ignition which in the presence of flow is reflected as an ignition distance delay. In other words, there are multiple approaches to prevent autoignition: maximize regions where the temperature of the local mixture is below the threshold, foster regions where the local mixture is not in the flammability range, and make use of the ignition time delay with respect to the convective time. This has been documented in the literature. In Lefebvre et al. [148], the authors studied the autoignition of lean hydrocarbon mixtures with a temperature range between 670 K and 1020 K at various pressures. For gaseous mixtures, the autoignition time is made up of the time for the fuel vapor to mix with air and the time of the chemical kinetics. The mixture then autoignites at some distance downstream, depend-

ing on the air velocity. Similar studies have been undertaken on jet flames by Cabra et al. [149,150], where the coflowing hot vitiated flow provides the heat to the fuel central jet stream, leading to a distance where the flame stabilizes. This has been further studied by Schulz et al. [151], where limited reactions were observed immediately downstream of the injection prior to the autoignition and flame stabilization of the methane–air jet in the 1350 K vitiated coflow occurring far downstream. The LFP parameters that should be optimized in a second step of the injector design will be the injection stream locations (air and fuel) and their diameters for temperature and species distributions.

The second component of the design space consists of the combustor requirements. Pollutant generation is strongly related to the combustion mode (premixed, nonpremixed, partially premixed, etc.) and the fuel used in the combustor. Static and dynamic stability are also closely linked to the combustor through the boundary conditions, the flowfield, and the flame region, which are highly dependent on the injector design.

The role of the combustor is to provide chemical energy, converted first into thermal energy to rise the temperature from the compressor outlet, which is then converted into kinetic energy to raise the velocity to the inlet of the turbine. This conversion of the chemical energy to the thermal energy can be achieved through multiple different combustion modes (premixed, stratified premixed, partially premixed, and nonpremixed combustion mode occurring in the gas phase). The premixed mode involves the perfect mixing of the fuel and the air so that each given fluid control volume upstream of the flame has the same equivalence ratio, see the reviews on premixed combustion by Huang and Yang [22], Candel et al. [23] for swirling flames. In practice, the equivalence ratio can slightly vary due to effects of convection and diffusion of the species. The stratified premixed regime consists of a flow where the equivalence ratio is not constant as in the premixed case and where multiple homogeneous zones of equivalence ratio are seen by the flame front. The partially premixed case is characterized by regimes where the mixture is not fully premixed. The nonpremixed combustion or diffusion flame regime is observed when the flame is generated by two distinct streams of fuel and air so that a given fluid control volume upstream of the flame is located either in the fuel or the air streams until these streams mix up to the stoichiometric line. Laboratory-scale and jet engine combustors operate in these regimes, depending upon the injector/combustor configurations.

As pointed out in this section, the combustor must also satisfy multiple requirements. The relevant constraints to the present

Table 7.1 Operating conditions at take-off.

Altitude h	Sea level
Pressure P_0 [atm]	1
Pressure P_3 [atm]	55
Temperature T_0 [K]	288
Temperature T_3 [K]	950
Gaseous air 1 [kg s^{-1}]	0.0271 (10%)
Gaseous air 2 [kg s^{-1}]	0.0542 (20%)
Gaseous air 3 [kg s^{-1}]	0.1897 (70%)
Primary air [kg s^{-1}]	0.271
Fuel mass flow [kg s^{-1}]	0.0275
Stoichiometric ratio	9.7[a]
Stoichiometric fuel/air ratio	0.1035[a]
Primary equivalence ratio	1
Primary/secondary air ratio	10% vs 90%
Global equivalence ratio	0.1

[a] Based on the first reaction of the mechanism considered here; based on the reaction releasing heat.

initial design are: (i) sustain static stability, the flame must be sustained over the flight envelope; (ii) avoid blowout, the combustor must be able to function in the lean combustion regimes; (iii) allow reignition, ignition must be enabled in case of flameout; (iv) limit pollutant emissions; (v) mitigate dynamic stability, combustion instabilities have to be suppressed; and (vi) prevent injector coking. To summarize this section, the combustor has to satisfy a set of requirements to ensure a safe functioning while minimizing the environmental impact and optimizing efficiencies of the jet engine.

The third component of the design space consists of the jet engine operating conditions. They are intrinsically linked to the performance requirements for a given aircraft at the considered operating point. In the present study, the operating point corresponds to take-off conditions. Take-off has been selected to evaluate static stability challenges (flashback, flame stabilization) at this critical condition on the flight envelope of commercial aircraft. It is also assumed here that any lean fully premixed (LFP) system operating at cruise conditions will have reduced pollutant emissions with respect to nonpremixed flames. The jet engine design procedure is

not taken into account here. Indeed, aircraft and engine characteristics from the literature are instead used, allowing to develop the main steps of a methodology for injector design. The International Standard Atmosphere (ISA) is the reference model for the evolution of pressure, temperature, and density of the Earth's atmosphere and it is used in aeronautics to determine the jet engine upstream conditions along the flight path. The take-off conditions with respect to the ISA are summarized in Tab. 7.1. The index 0 marks the station upstream of the fan, while the index 3 refers to the upstream conditions of the combustor (or compressor outlet without taking into account the diffuser effect). The conditions are given for the stagnation variables and not the static ones. As the stagnation values are higher than the static ones, they are selected for design purposes in the present study, providing design margins. In addition, by assuming the thrust and the thrust-specific fuel consumption of existing engines from public domain literature data, one can estimate the mass flow of fuel. A value of 0.0275 $\mathrm{kg\,s^{-1}}$ per injector was used for take-off. Other relevant conditions are summarized in Tab. 7.1.

2 Innovation and concept definition

The LFP injector concept is now described. The overall goal of this injector is to generate a perfectly lean (at cruise conditions) premixed swirling flame inside the combustion chamber with an inlet liquid fuel entering the first unit of the injector. To do so, three units respectively achieve liquid-fuel vaporization (unit 1), fresh gas premixing (unit 2), and flame stabilization (unit 3). In the present feasibility study, the fuel considered for the design is a surrogate of kerosene at take-off conditions. Each unit is designed as compact as possible in order to fit into a small core engine. The initial design concept is illustrated in Fig. 7.1 (the figure is not to scale). Relevant conditions are summarized in Tab. 7.1. Part of the nearly 950 K air exiting the last stage of the high pressure compressor enters the vaporizing unit and ensures the exchange of heat to the nearly 280 K liquid fuel. The exchange of heat is accomplished through a heat exchanger consisting of a spiral rectangular channel inside which the liquid fuel begins vaporizing at a distance where the temperature of vaporization of the liquid fuel is reached. The spiral channel structure allows to fit the heat exchanger into a given diameter. The expected gaseous fuel stream exiting the vaporizing unit then enters into the cross-flow of air upstream of the swirler of the premixing unit. The combination of cross-flow and swirl imparted to the flow induces the premixing between the gaseous air and the fuel vapor. Finally, the pre-

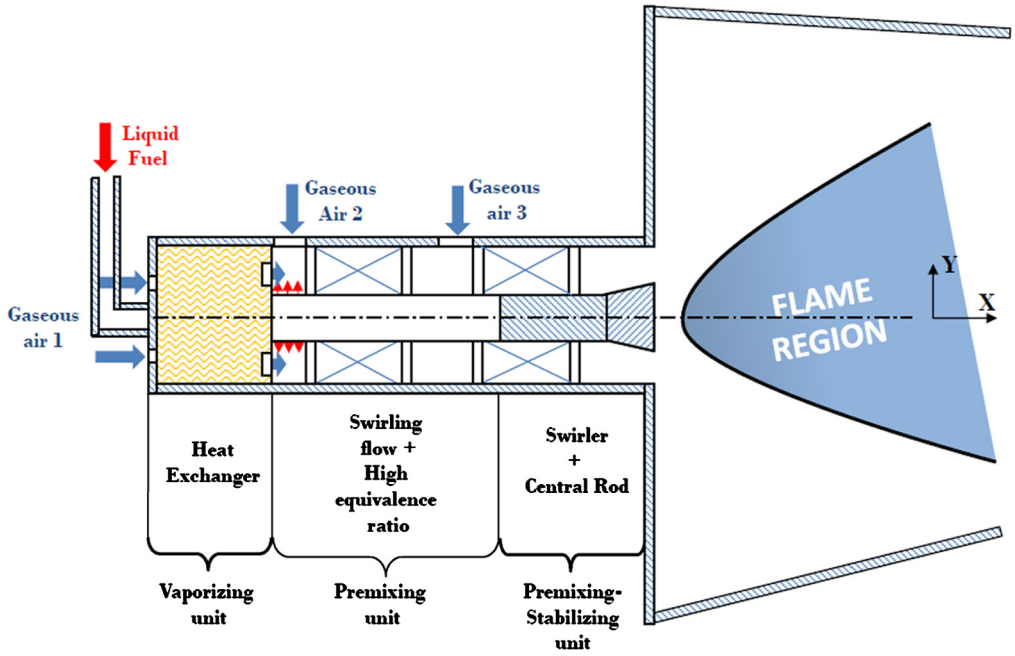

Figure 7.1 Lean fully premixed concept. Schematic of the lean fully premixed injector concept. Source: Image taken from Palies et al. [584].

mixed stream enters the stabilizing unit, where a second swirler ensures additional premixing and swirling flame stabilization. The LFP injector concept design intent is to be sprayless and the injection location is shielded from direct radiation of the flame by the swirler vanes. The coking issue is expected to occur at temperatures above the temperature of the vaporized fuel within the injector. The coking issue will be prevented by limiting the temperature of the vaporized fuel within the vaporizing unit. The next three sections present the methodology and associated results of the initial design procedure where the dilutions and cooling jets are not modeled.

3 Modeling and sizing

3.1 Vaporizing unit

The vaporizing unit is made up of three layers rolled into a spiral shape for compactness. A schematic is given in Fig. 7.2. The front view of this unit is also given in Fig. 7.1. The side view depicts the spiral rolled layered structure. The bottom sketch rep-

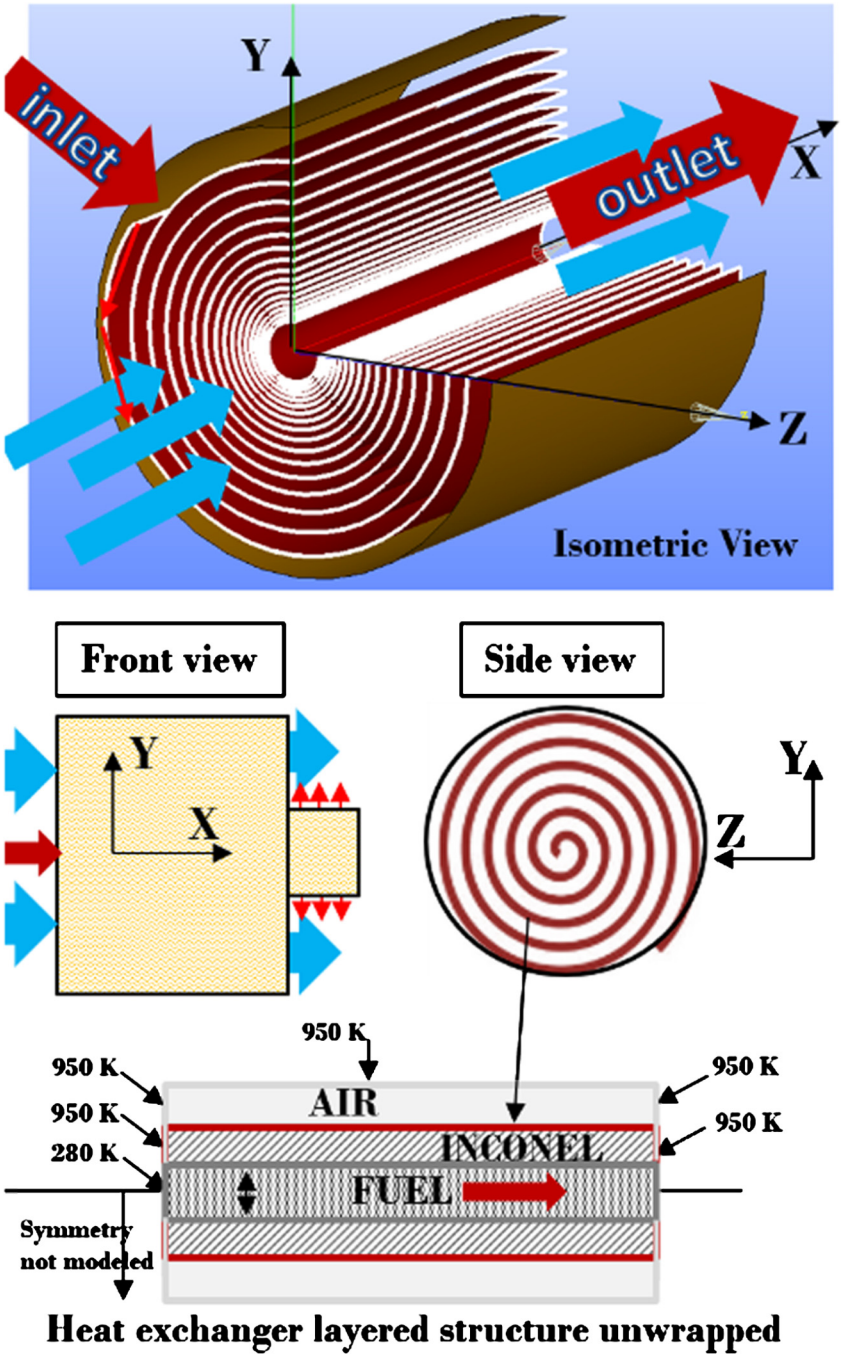

Figure 7.2 Vaporizing unit. Vaporizing unit zoom on heat exchanger design. Source: Image taken from Palies et al. [584].

Table 7.2 Data used for the design of the vaporization unit at take-off conditions.

Parameter/layer	Air	Inconel	Fuel
ρ [kg m^{-3}]	21.1	800	600
λ [W m^{-1} K^{-1}]	0.069	20.0	0.070
c_p [J K^{-1} kg^{-1}]	1371	542	6500

resents the unwrapped layered structure made up of an air layer (0.0005 m), a central inconel layer (0.0005 m), and a fuel layer (thickness h). The heat exchanger is $l = 0.2$ m in length when unwrapped. The materials and fluid properties determined at take-off operating conditions are obtained from the literature and are listed in Tab. 7.2. The modeling of the thermal heat transfer inside the first injector unit (heat exchanger) layers is as follows. A transient 2D and 3D heat transfer code solves heat conduction in the air and inconel layers, and coupled heat conduction/convection for laminar regimes in the fuel channel is implemented. A Poiseuille flow profile is used inside the fuel channel. The equation solved by this code in each layer of the geometry is

$$\rho c_p \left(\frac{\partial T}{\partial t} + u \frac{\partial T}{\partial x} + v \frac{\partial T}{\partial y} + w \frac{\partial T}{\partial z} \right) = \lambda \left(\frac{\partial^2 T}{\partial x^2} + \frac{\partial^2 T}{\partial y^2} + \frac{\partial^2 T}{\partial z^2} \right), \quad (7.1)$$

where ρ is the density, c_p is the specific heat at constant pressure, and λ is the thermal conductivity. The velocities (u, v, w) were determined based on the mass flows and section areas of the air and the fuel layers, and were modeled with a laminar velocity profile. While initially the modeling was in 2D, the model has been extended to 3D in order to capture both coflow and transverse flow of air scenarios inside the vaporization unit. This code allows to estimate the temperature distribution inside the injector vaporizing unit's layers. The fluid is taken at rest inside the air layer and turbulence is not taken into account within the fuel channel for the 2D cases. Extension of the code to 3D has been carried out, taking into account a uniform flow within the air layer. Compared with 2D cases, the results show a temperature reduction in the air layer and a slightly reduced temperature inside the fuel channel. Two-phase flow and phase change modeling were not taken account in this initial study. Half of the through thickness layered structure is modeled. Selected results are plotted in Fig. 7.3A to F.

Fig. 7.3A and B depict respectively the temperature distribution at distances $d = 0.1$ mm and $d = 0.2$ mm below the inconel–

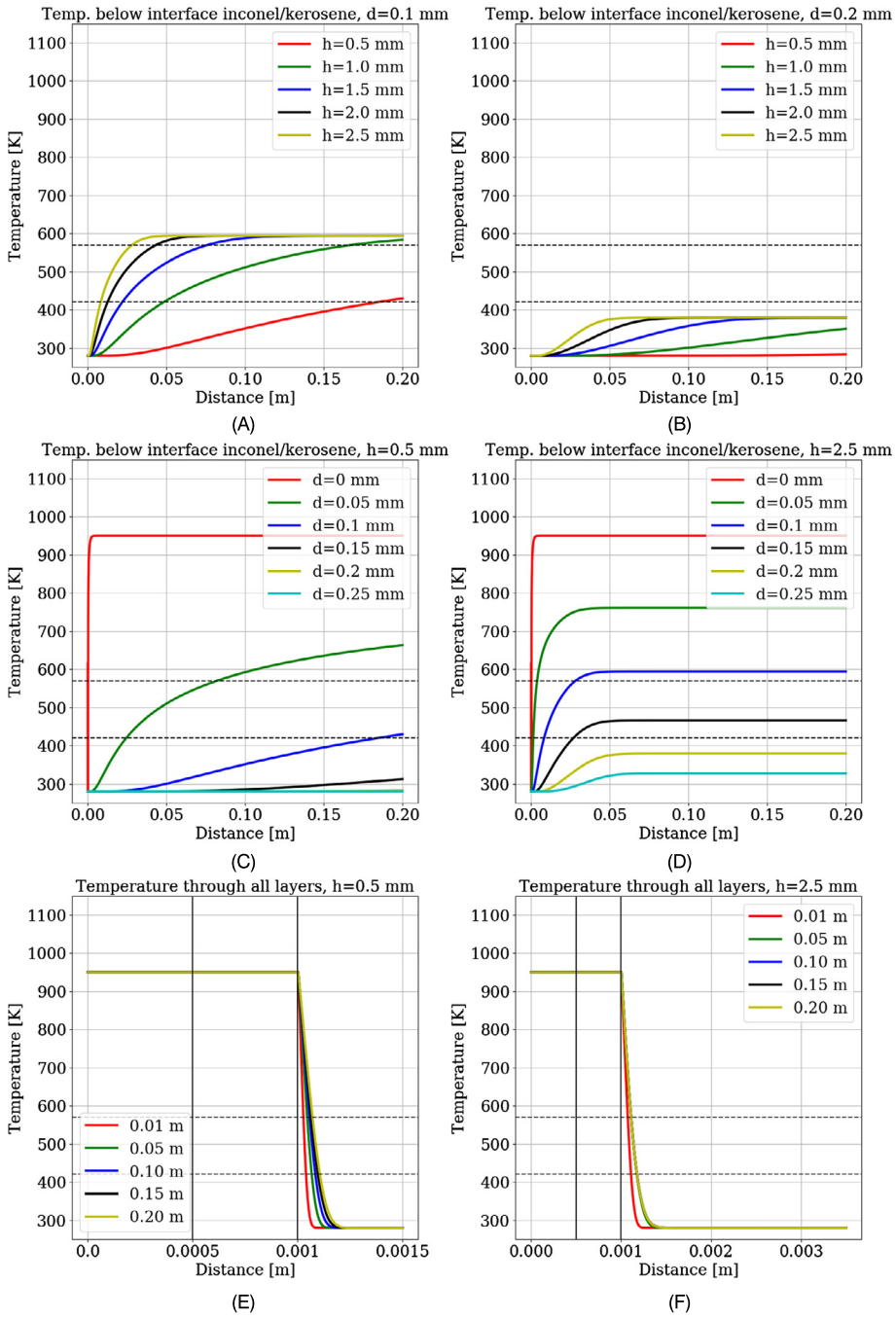

Figure 7.3 Temperature distributions. Temperature distributions inside the vaporizing unit. Source: Image taken from Palies et al. [584].

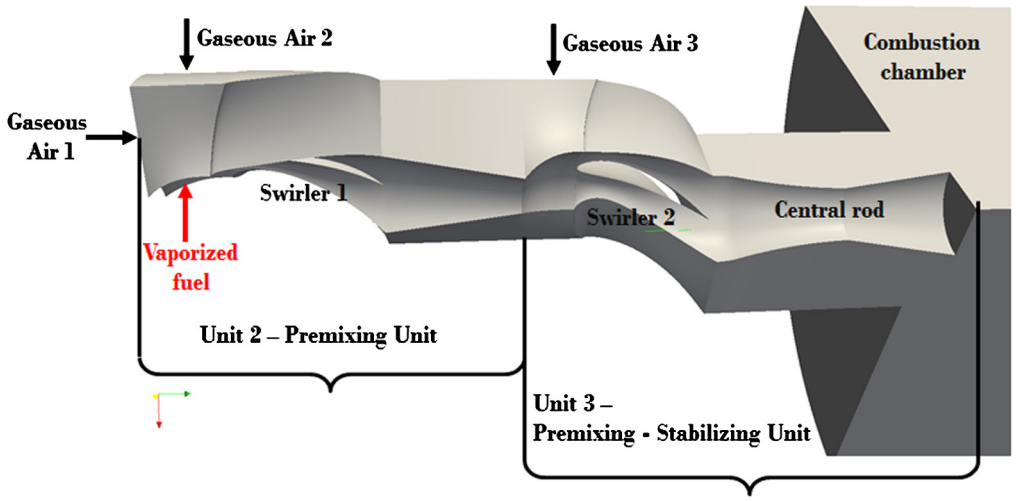

Figure 7.4 Numerical model. Modeling of the coupled units 2 and 3. Source: Image taken from Palies et al. [584].

fuel interface in the fuel channel for various thicknesses h of the channel. The dotted superimposed horizontal lines represent a range for fuel vaporization (420 K and 570 K) to occur depending on the pressure inside the fuel channel. It is worthwhile to recall that the critical thermodynamic conditions for kerosene are $P_{cr} = 21.4$ atm and $T_{cr} = 663$ K, see Wang and Yang [585]. One can conclude from these two sets of curves that the thicker the fuel channel layer h is, the higher the temperatures are. Also, as the distance from the inconel–fuel channel interface increases, the temperature drops. This is attributed to the low thermal diffusivity of the fuel at those operating conditions. Fig. 7.3C and D present also the temperature distribution inside the fuel channel of thicknesses $h = 0.5$ mm and $h = 2.5$ mm respectively at multiple distances d from the inconel–fuel interface. This set of curves confirms the role of the thickness h and that for $h = 2.5$ mm, the maximum distance d inside the fuel channel where vaporization will occur is between 0.3 and 0.4 mm. Fig. 7.3E and F display the through thickness temperature distributions at multiple axial locations. These plots show the rapid decrease of the temperature within the fuel layer so that the vaporization of the fuel is concentrated within the low velocity region of the boundary layer of the inconel–channel interface. It is expected that vaporization of the fuel will be strongly enhanced by unsteady mixing effects associated with the transition of the fuel from liquid to gas within the channel and the addition of dedicated obstacles enhancing mix-

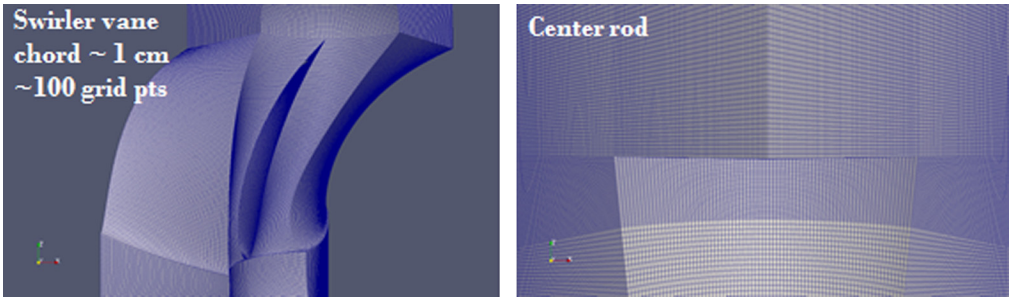

Figure 7.5 Mesh views. Left: Swirler view ($\Delta x = 100$ μm). Right: Central rod view ($\Delta x = 60$ μm). Source: Image taken from Palies et al. [584].

ing of the vaporized gases and liquid fuel in order to get full fuel vaporization prior to the premixing unit.

In addition, it is expected that the volume expansion will increase the velocity of the gaseous vaporized stream within the fuel channel, possibly triggering turbulence and enhancing heat transfer. The effects on the heat transfer should be investigated in future work with a two-phase flow model including phase changes. The spiral-shaped heat exchanger should be modeled with other tools in a future work to capture more accurately the heat transfer behavior. The spiral shape will induce/foster inner or outer radial vaporization regions, instead of the perfect symmetry of the 2D transient model. While the present model is an initial study showing that some vaporization temperature will be reached, further analyses with additional tools for multiple configurations are required to model and capture the processes of this important engineering challenge to the LFP concept.

Figs. 7.6 and 7.7 present the heat exchanger unit. The air stream flows inside the dark gray space in between the spiral (top left figure), the liquid fuel enters the heat exchanger via the light gray-colored spiral channel, starting near the outer diameter of the heat exchanger and exiting near the center on the other side of the heat exchanger tube. A cross-section of the isometric view on the right side shows the inlet and exit of fuel and air more clearly. For the first design iteration, the vaporizing unit operates such that the air flows axially (blue arrows) through the compact spiral heat exchanger (x axis as indicated in the figure) and the fuel flows through the channel azimuthally (red arrows). The fuel will enter from the outer spiral location and exit from the center of the spiral, as shown by red arrows. The fuel pipe and connectors linking the fuel pump to the fuel inlet of the heat exchanger are not shown on this schematic. The air exiting from the heat exchanger will be annularly distributed to exit as shown in Fig. 7.1. The fuel exiting the

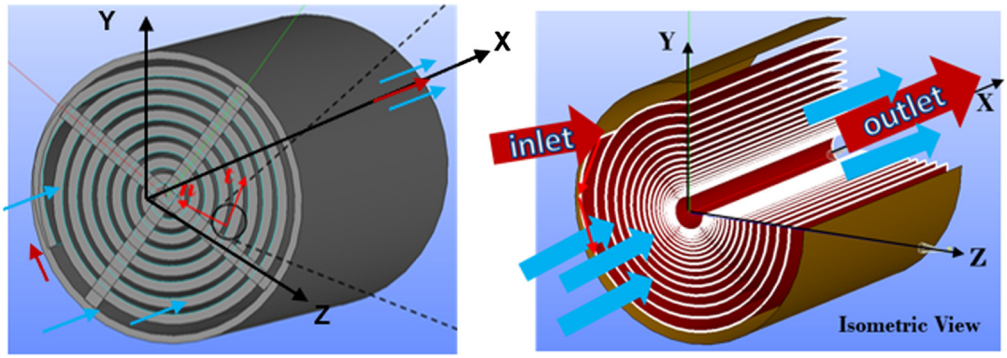

Figure 7.6 Heat exchanger isometric views. Description of the spiral heat exchanger constituting the vaporizing unit. Blue arrows indicate air entry and exit, and red arrows indicate fuel entry and exit. Source: Image taken from Palies et al. [586].

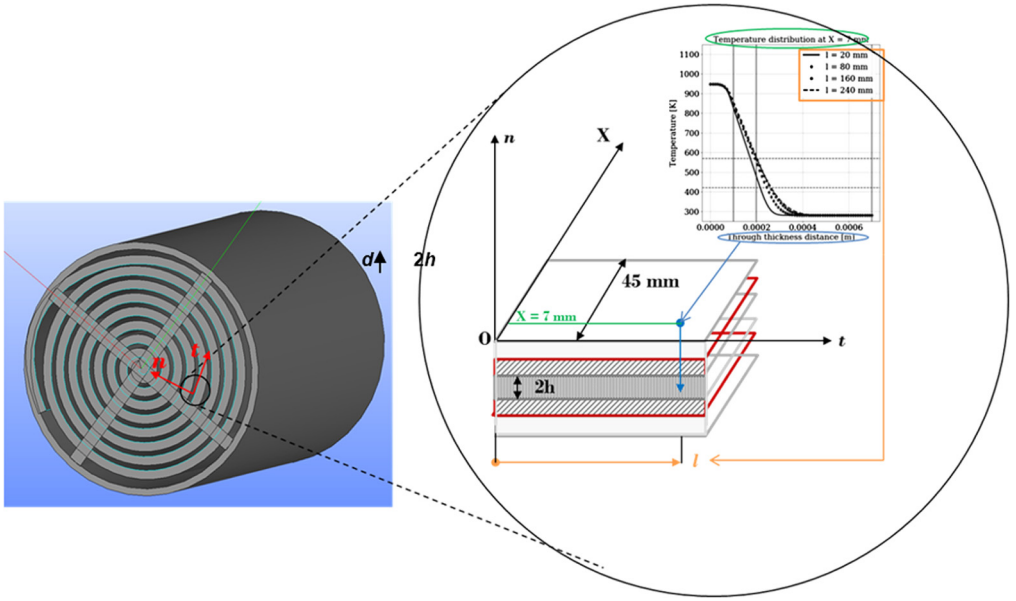

Figure 7.7 Heat exchanger view. Illustration of the heat exchanger unit and dimensions relevant to temperature distribution plots. On the left figure, the coordinate system is colored in red. Source: Image taken from Palies et al. [586].

heat exchanger will be converged toward the central rod and will exit as sketched in Fig. 7.1. The right sketch of Fig. 7.7 represents the unwrapped structure consisting of an air channel, an inconel wall between air and fuel channels, and a kerosene fuel channel layer, where the half-width of the fuel channel is h, the width of

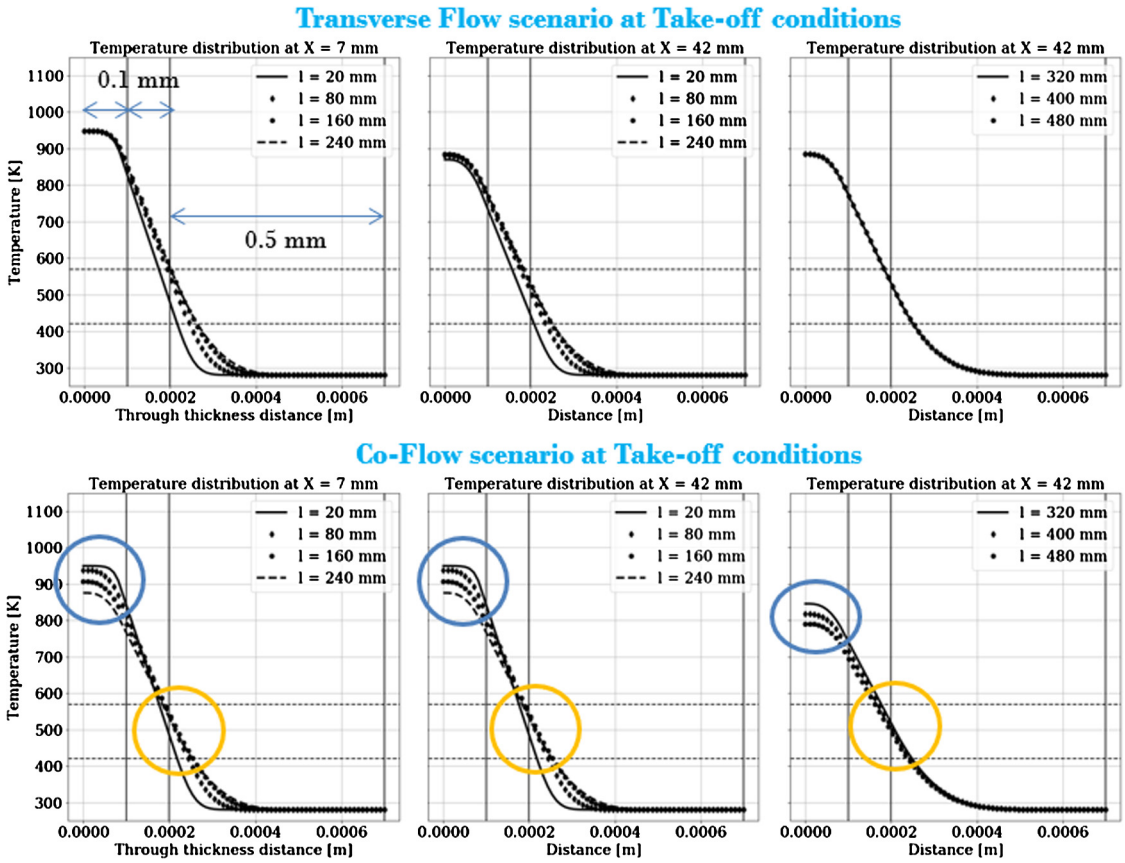

Figure 7.8 Modeling temperature results. Effects of fuel thicknesses and air flow scenarios on heat transfer. Source: Image taken from Palies et al. [586].

the air channel is h_{air}, and the inconel thickness between air and fuel channels is t_{metal}. The material and fluid properties were determined at take-off operating conditions based on literature data.

Results of simulations at take-off conditions for the transverse flow (top figures) and coflow scenarios (bottom figures) for air and inconel layers of both 0.1 mm and fuel layer thicknesses of 1 and 0.5 mm are plotted in Fig. 7.8. This combination of thicknesses shows that the temperatures reached will enable vaporization of the fuel inside the channel layer. Furthermore, the coflow scenario shows a reduction of inlet air temperature, as expected. Further modeling refinement and thickness optimization should be considered next.

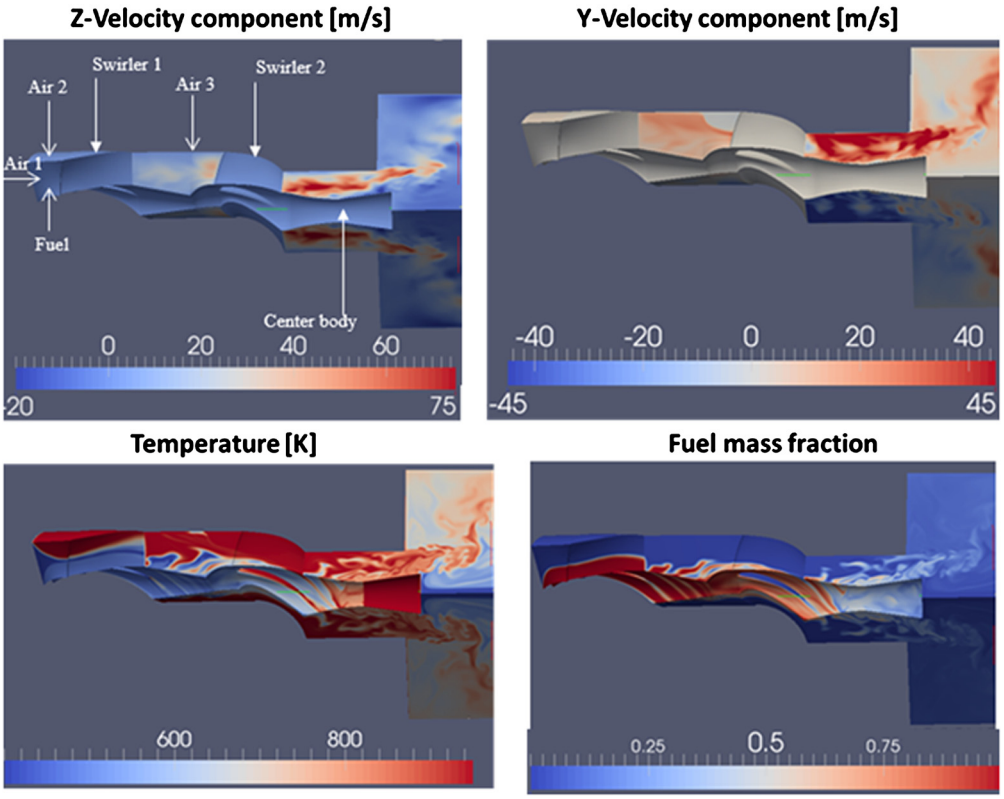

Figure 7.9 Zoom on injector flowfield. Top left: Axial velocity z component. Top right: Transverse velocity y component. Bottom left: Temperature. Bottom right: Fuel mass fraction. Source: Image taken from Palies et al. [586].

3.2 Premixing and premixing-stabilizing units

The results of the nonreacting LES numerical simulations in the injection system (units 1 and 2) are presented in Fig. 7.9. Each figure represents respectively the axial velocity, the y component of velocity, the temperature, and the mass fraction of kerosene surrogate. The total structured grid count is nearly nine million cells and the time step was set to 1.0×10^{-8} s. Only a quarter of the geometry was modeled using periodicity. The results shown in the figure were obtained without activating the chemical mechanism. This flowfield did not reach the fully established flow state inside the combustor chamber. The calculations with two-step chemistry were also performed; they are discussed later in this chapter. These simulations used that initial input flowfield for initialization. Fig. 7.9 allows observing the diffusion of temperature and species respectively within the domain along with the leaning of

the mixture by the main air flow stream (gaseous air stream 3). Periodic and isothermal/adiabatic walls no-slip boundary conditions were used.

The modeling methodology is now presented for the coupled premixing and premixing-stabilizing units. Reacting large eddy simulations (LESs) were performed to initiate the design of the coupled units with the Loci-CHEM code, a finite volume code for 3D chemically reacting turbulent flows, see Luke et al. [215], Luke and George [216]. The geometry and the close-up views of the mesh are respectively depicted in Figs. 7.4 and 7.5. The geometry is an extension of the configuration of Palies et al. [253]. The methodology consists of multiple steps, including mesh size determination and generation, boundary condition selection, and combustion and turbulence modeling. The mesh size has been determined according to two main criteria: the Kolmogorov scale and the thermal flame thickness. The simulations are also used to verify that no combustion occurs within the premixing unit.

The complete reacting formulation of the code is used including the following two-step chemical mechanism. The first reaction of the mechanism writes

$$C_{10}H_{20} + 10O_2 \longrightarrow 10CO + 10H_2O, \tag{7.2}$$

and the associated volumetric reaction rate is

$$\dot{\omega}_1 = A_1 \left[\frac{\rho Y_{C_{10}H_{20}}}{W_{C_{10}H_{20}}}\right]^{0.5} \left[\frac{\rho Y_{O_2}}{W_{O_2}}\right]^{0.5} T^{a_1} \exp\left(-Ea_1/RT\right), \tag{7.3}$$

where $A_1 = 4.5\text{E}7\ \text{s}^{-1}$, $a_1 = 0.1$, and $Ea_1 = 30\,000\ \text{cal mol}^{-1}$. The second reaction, for the equilibrium, writes

$$2CO + O_2 \longleftrightarrow 2CO_2, \tag{7.4}$$

and its volumetric reaction rate is

$$\dot{\omega}_2 = A_2 \left(\left[\frac{\rho Y_{CO}}{W_{CO}}\right] \left[\frac{\rho Y_{O_2}}{W_{O_2}}\right]^{0.5} - \frac{1}{K} \left[\frac{\rho Y_{CO_2}}{W_{CO_2}}\right] \right) \exp\left(-Ea_2/RT\right), \tag{7.5}$$

where $A_1 = 4.5\text{E}10\ \text{s}^{-1}$ and $Ea_2 = 20\,000\ \text{cal mol}^{-1}$.

The NASA five-coefficient polynomials for the thermodynamic and transport properties were used. An equivalence ratio of unity is set for the present study at take-off conditions considering the air flowing through the injector only (primary air). The flame speed and adiabatic flame temperature quantities were determined first at conditions corresponding to take-off, see Tab. 7.1,

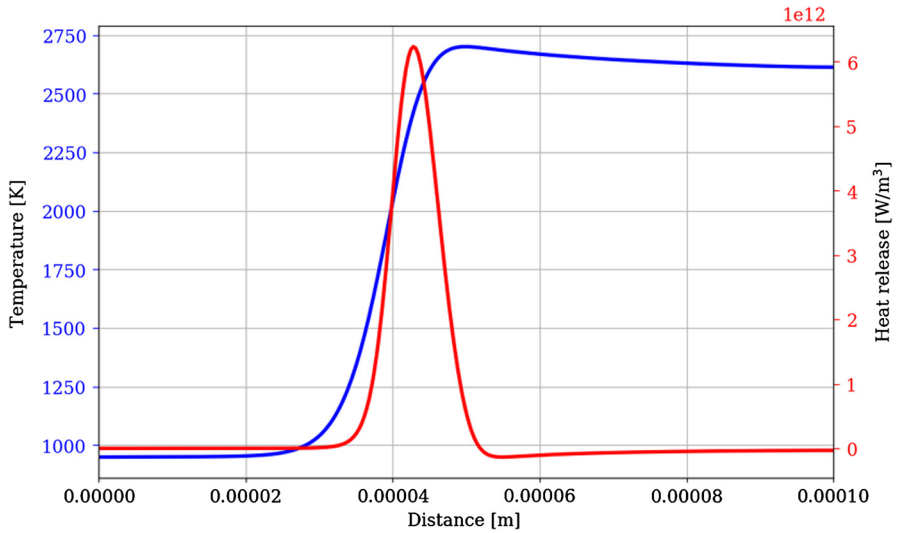

Figure 7.10 Flame structure. 1D laminar premixed flame structure for the global two-step mechanism considered. Source: Image taken from Palies et al. [584].

with a complex chemical mechanism (209 species and 1673 reactions) of Dagaut [587] using 1D laminar premixed flames in Cantera. Next, the global two-step mechanism was obtained to first retrieve the flame speed and get close to the adiabatic flame temperature. The values obtained with the complex chemical mechanisms of Dagaut [587] are a flame speed of 0.82 m s^{-1} and an adiabatic flame temperature of 2470 K. The obtained 1D premixed flame structure with the presently determined two-step mechanism is given in Fig. 7.10, where the flame speed is 0.83 m s^{-1} and the adiabatic flame temperature is 2610 K. The computed values of temperature (blue curve) and heat release (red curve) of the premixed laminar flame, as obtained by Cantera, are displayed. The calculated ignition delay time yields a value of 3.5 ms with the complex mechanism and 0.75 ms with the global mechanism. This discrepancy was retained as a safety factor for the design of the injector. The Blint thickness (close to the flame thermal thickness) was determined as 15 µm. The nonuniform mesh resolution was taken as 60 µm in the finest region, near the injector, and simulations were carried out on a quarter periodic configuration taking into account directly two swirler vanes.

The Kolmogorov scale is determined in the fresh gases. The turbulent Reynolds number is equal to $Re_t = \rho u' l_0/\mu$, where ρ is the density of the fluid, u' is the turbulent velocity fluctuation, l_0 is the integral length scale assumed here to be equal to 0.022 m (the in-

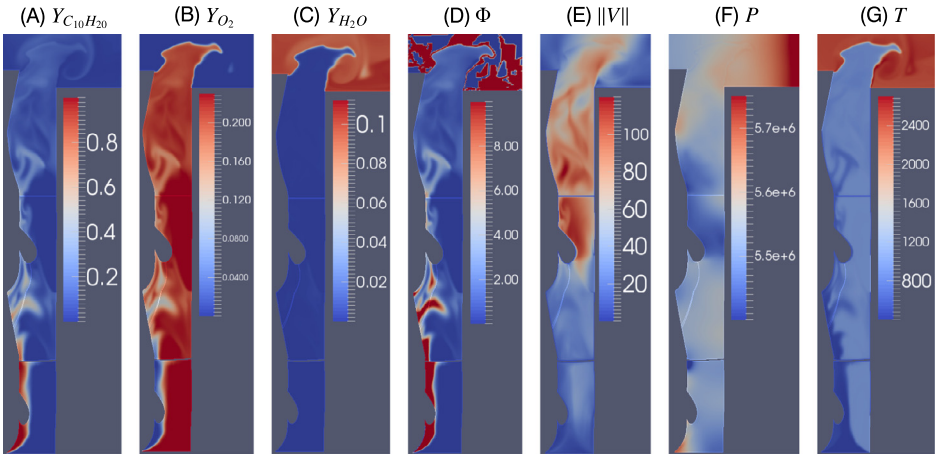

Figure 7.11 Injector flowfield. Coupled premixing and stabilizing unit LES results inside the LFP injector. Source: Image taken from Palies et al. [584].

jector diameter), and the dynamic viscosity μ is 4×10^{-5} Pa s, leading to a value of the turbulent Reynolds number of nearly 60 000. In addition, the Kolmogorov scale η can be written as $\eta = l_0 Re_t^{-3/4}$, which leads to a value of 15 µm. The total grid count is nearly ten million cells. The equivalent unstructured tetrahedron mesh of the full geometry would be above 200 millions cells with respect to these two scales. The Smagorinsky model was used in all simulations. The thickened flame model of Colin et al. [319] was used with the dynamic thickening method of Wang et al. [588].

Instantaneous flowfield results of the reacting LESs are given in Fig. 7.11A to G. The results are taken from a longitudinal slice through the injector upstream of the combustion chamber. It is possible to distinguish the fuel and air inlets and the two modeled units (second and third) of the injector, along with the statically steady stable flame. In Fig. 7.11A to C, the mass fractions of fuel, Y_{O_2}, and Y_{H_2O} are given along with the equivalence ratio Φ field in Fig. 7.11D. Fig. 7.11E to G depict the fluid velocity vector magnitude, the static pressure, and the static temperature. One observes the distribution of the equivalence ratio field in three distinct zones. In the upstream zone, the fuel stream (assumed at 475 K once vaporized), gaseous air stream 1 (at 400 K due to the expected temperature reduction within the heat exchanger), and gaseous air stream 2 (950 K) are injected. There is no noticeable reaction in that zone. The second zone, located between the outlet of the first swirler and the outlet of the second swirler (materialized by horizontal lines where the swirler mesh and the longitudinal slice

Table 7.3 Radially averaged or integrated values.

Variable	Back plane	Swirler 2 outlet	Swirler 1 outlet
$\overline{P}$	5 570 560	5 471 000	5 517 900
$\overline{T}$	890	872	815
$\overline{\Phi}$	0.924	0.864	3.35
S	0.414	0.262	0.303

intersect), is a high equivalence ratio region to prevent autoignition. Limited reaction occurs, as shown by the Y_{H_2O} mass fraction level. A complex chemical mechanism should be used in a second step of the design to characterize accurately this limited reaction event. Beyond swirler 2 and gaseous air stream 3, this limited reaction is stopped. This could be the consequence of high local levels of vorticity and flow strain. The third zone is located downstream of the swirler 2 outlet up to the back plane of the combustor. The flow speed increases significantly, and the species and temperature fields homogenize as the mixture is leaned out by gaseous air stream 3 prior to stabilization of the swirling flame, see Fig. 7.11G for the temperature. Pressure oscillations can be observed from Fig. 7.11F and occur in the azimuthal direction of the flame tube. It reflects the end of the statistically stable regime. The dynamic stability of this configuration being out of the scope of the present study, this is not further discussed in this chapter.

Similar observations can be deduced from the transversal slices through the injector given in Fig. 7.12A to C. The color scale maximum of the H_2O mass fraction (0.003 maximum) and static temperature (950 K maximum) highlights the limited reaction occurring and the complete reduction of that reaction after the outlet of the second swirler.

The extracted profiles (at that time step) at three axial locations (swirler 1 outlet, swirler 2 outlet, and back plane of the combustor) are plotted in Fig. 7.13A for axial and azimuthal velocities, B for mass fraction of fuel and oxygen, and C for static temperature and pressure. Radially spatial averages of static pressure, temperature, and equivalence ratio along with estimated swirl numbers are documented in Tab. 7.3 and obtained from these instantaneous profiles. The profiles taken at the back plane of the combustor distinctly show the uniformity reached for the temperature, pressure, and species, prior to the combustion region contributing to static stability.

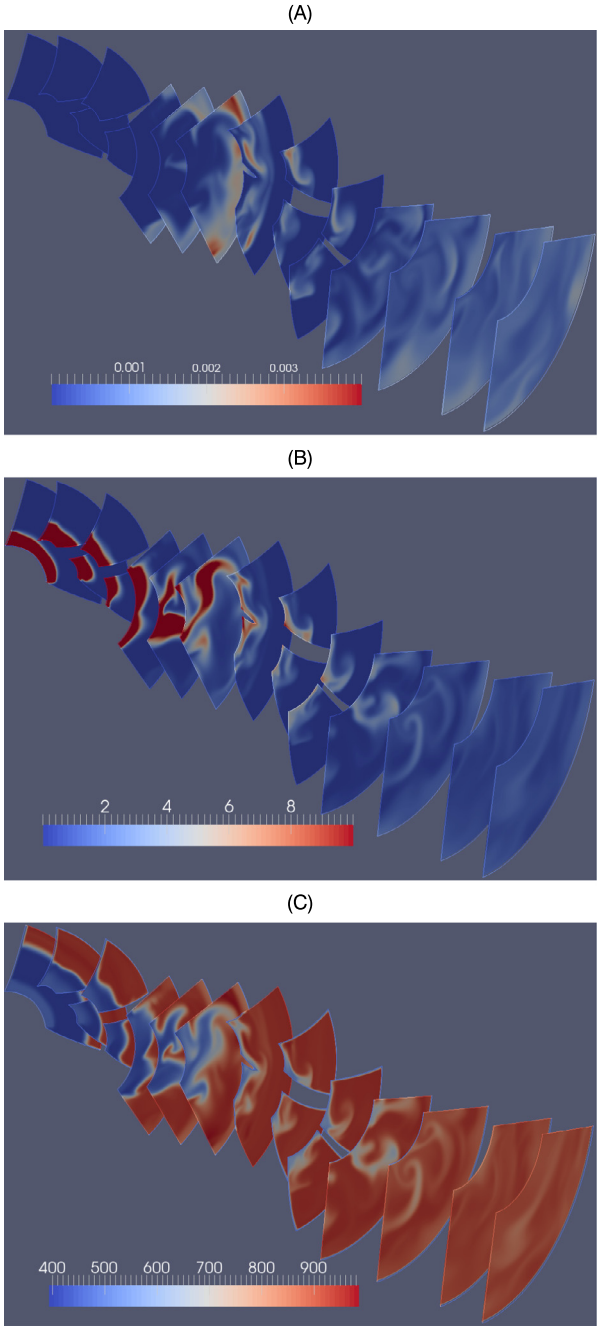

Figure 7.12 Zoom on injector flowfield. Coupled premixing and stabilizing unit LES results inside the LFP injector. Transversal slice. (A) Mass fraction Y_{H_2O}. (B) Equivalence ratio Φ. (C) Temperature T. Source: Image taken from Palies et al. [584].

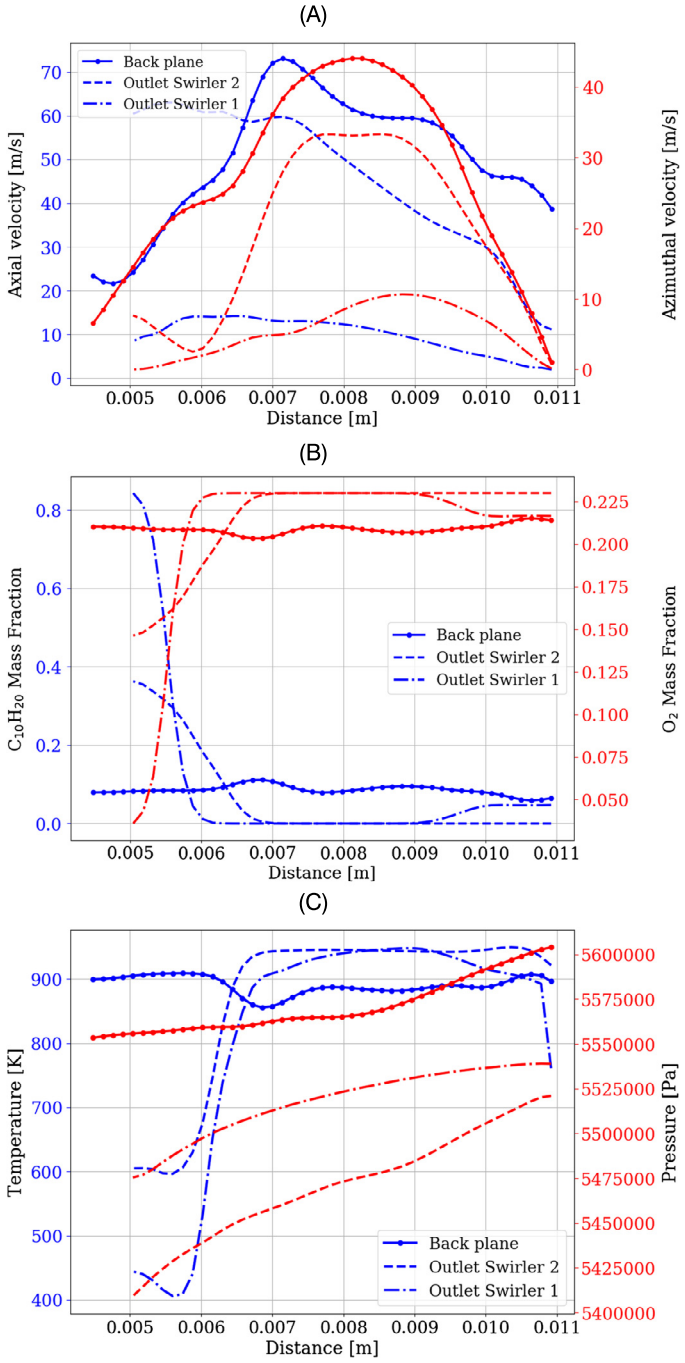

Figure 7.13 Results profiles. Coupled premixing and stabilizing unit LES results inside the LFP injector. Profiles. (A) Velocities. (B) Mass fractions Y. (C) Temperature T and pressure P. Source: Image taken from Palies et al. [584].

One of the key aspects of the design of the LFP injector is to generate a fully premixed stabilized swirling flame without autoignition within the injector. The present reacting numerical simulations indicate that at the take-off conditions selected, there is no autoignition within the injector but only limited reaction that does not trigger ignition in this statically stable regime. The autoignition temperature of kerosene fuel is between 500 K and 600 K. It is important to discuss the multiple mechanisms that can participate to limit autoignition in the present case:

- Mixing of species versus mixing of heat: Autoignition can be triggered when the local fluid properties are within the flammability limits for a premixed flame or on the stoichiometric line for a diffusion flame if local heat is available. This gives a condition on species and temperature for autoignition for the local fluid. Mixing of species and heat is controlled by multiple processes and phenomena, including for example the gradients of species, temperature, aerodynamic effects, and turbulence. These processes have different effects on heat and species. As a consequence, these fields evolve differently, and it is important to compare each field with each other to detect possible conditions for autoignition. For example in Fig. 7.11A to D and G, one can compare the distributions of species (and equivalence ratio) and temperature. In the most upstream regions, prior to the end of the first swirler outlet, the stoichiometric region is either located where the temperature is below 600 K, preventing autoignition, or in a region where autoignition of the gaseous fuel could occur because the local temperature is higher. But other mechanisms prevent that latter autoignition.
- High flammability limit: By design, the present injector makes use of high flammability region mixtures to avoid autoignition in the premixing unit. Indeed, a premixed flame cannot be generated nor propagate if the local fluid properties are outside the lean or rich flammability limits. As a consequence, when the local equivalence ratio is high, there cannot be local autoignition because the mixture is too rich. The second zone of the injector (between the swirlers) reflects that aspect with some overall high equivalence ratio regions.
- High flow strain and vorticity: Another phenomenon preventing autoignition is the presence of strong flow strain and vorticity, which cause direct extinction or hinder autoignition as observed on the present results. The limited reaction observed is rapidly extinguished by the flowfield itself.
- Ignition delay time versus interaction time: A previous section has shown that the time delay was of the order of 0.75 ms. In the

present injector, the flowfield is highly turbulent and the local conditions of appropriate species and heat conditions are not maintained for a sufficient duration, allowing ignition to occur within the injector.

It is also important to remember that the equivalence ratio and temperature distributions will be modified if the geometry of the injector changes. The species and temperature distributions upstream of the flame will indeed depend on the geometry and swirl rates. A reduced-order model should be developed to investigate these aspects and to guide the use of full reacting CFD on selected cases in future work.

4 Conclusion

This chapter presented an initial design study for an LFP injector system for commercial aircraft engines. The injector is made of three units: a vaporizing unit, a premixing unit, and a premixing-stabilizing unit. The design of the present injector is at the intersection of combustion physics, combustor requirements, and jet engine operating conditions. Elements of these fields are used to determine the appropriate boundary conditions, including operating pressure and inlet temperature, and the required physical model parameters, such as the chemical mechanism parameters. This work is motivated by future high pressure, high temperature small core engines aiming at higher efficiencies and reduced NO_x emissions. The chapter described results of the design process with numerical simulations. The first unit, the vaporization unit, is initially modeled with a transient 2D (and then 3D) finite difference code to capture heat transfer from conduction and convection inside the vaporizing unit fuel channel. The vaporization of the inlet liquid fuel is captured in the immediate vicinity of the inconel layer–fuel channel interface. The second and third units (premixing and premixing-stabilizing) are studied in a coupled fashion where the inlet boundary conditions are computed based on the take-off operating conditions considered. The coupled unit is studied with numerical LESs. The results indicate that: (i) there is potential to design an injector with fully premixed stream when using a heat exchanger to enable premixed combustion for gas turbine engines; (ii) the LFP injector does not present autoignition but limited reaction only during the statically stable regime studied, (iii) the LFP injector allows to form a premixture of appropriate equivalence ratio; and (iv) preliminary results show the potential in terms of static stability.

The perspectives of the present work are: (i) to continue the refinement of the injector design with detailed numerical simula-

tions at relevant operating conditions, (ii) to make direct comparisons with existing injectors in terms of design requirements, (iii) to enhance the models and parameters used in the study (such as BC, chemistry mechanisms, mesh resolution, etc.), (iv) to reduce the overall injector size, and finally (v) to carry out experimental testing and measurements for demonstration and model validation.

Conclusion and perspectives

Energy and transport industries face many outstanding technical, economical, geopolitical, and environmental challenges. Recently the 2015 United Nations Climate Change Conference, COP21, has led to the Paris Agreement. This Agreement states an overall objective to maintain global temperatures well below 2°C above preindustrial levels and to pursue efforts to limit the temperature increase to 1.5°C. The design and use of technologies aiming at reducing or suppressing emission of pollutants such as NO_x and CO_2 will thus have a strong impact and will help to reach the COP21 goals. The idea of the hydrogen economy in that perspective has been the subject of several reports, such as from the USA National Academy of Engineering in 2004. This economy is based on hydrogen for energy generation and transport (automotive, boats, aircraft, etc.). In June 2018, France initiated a pioneering deployment plan of hydrogen for energy transition which aims at tending towards such a hydrogen economy. Furthermore, in 2018, the European Commission presented its strategic long-term vision for a climate-neutral economy by 2050. The European Commission wrote in the companion report of this strategic vision: "...hydrogen-based technologies (such as electric vehicles and vessels based on fuel cells) may become competitive in the medium to long-term. Liquefied natural gas with high blends of bio-methane could also be a short-term alternative for long-distance haul. Aviation must see a shift to advanced biofuels and carbon-free e-fuels, with hybridisation and other improvement in aircraft technology having a role in improving efficiency. In long distance shipping and heavy-duty vehicles, not only bio-fuels and bio-gas but also e-fuels can have a role provided that they are carbon-free throughout their production chain. E-fuels can be used in conventional vehicle engines, relying on the existing refuelling infrastructure. Further significant steps in research and development are needed in production of decarbonised fuels as well as the vehicle technologies such as batteries fuel cells and hydrogen gas engines..."

In this general worldwide context, it is important to improve and adapt combustion technologies to reduce their environmental impact in terms of emissions and to increase engine efficiencies, for example, for the engine thermal efficiency, by enabling the optimum gas turbine engine combustor outlet temperature.

Regarding the reduction of the pollutants emission, there are two possible ways: reduce their formation or eliminate their emission. There are two ways to do so in aviation: the fuel selection and the combustion regime/combustor configuration selection. One method for nitric oxide NO_x emission reduction consists in burning in the lean premixed mode, where fuel and air are premixed before they react. One possible method for complete suppression of the emission of pollutants, including NO_x and CO_2, is hydrogen combustion, which generates water vapor and releases heat. The suppression of the formation of pollutants is a major argument in favor of hydrogen–oxygen combustion, but it is a long-term goal requiring many intermediate steps. Tremendous research and design are required to reach this long-term goal. As a step toward this goal, research should focus on premixed combustion modes with a mixture of natural gas and hydrogen. In addition, in this context, technologies and systems enabling onboard separation of oxygen from air should be researched.

Another critical aspect of future work will be the use of current and future knowledge of premixed combustion and combustors to reduce the fuel burn. The links between the flame speed, flame surface area, heat release, and kinetic energy generation should be investigated for this goal. The link between flame stabilization and pollutant emission reduction has to be researched also in a more comprehensive manner. Finally, the perspectives for theoretical and data mining/analyses, numerical modeling, and testing/experiments are significant.

References

1. G. D. Brewer, The Outlook for Hydrogen: a Summary, in: Hydrogen Aircraft Technology, CRC Press, 399–409, 1991.
2. M. D. Guynn, E. D. Olson, Evaluation of an aircraft concept with over-wing, hydrogen-fueled engines for reduced noise and emissions.
3. N. R. Council, et al., The hydrogen economy: opportunities, costs, barriers, and R&D needs, National Academies Press, 2004.
4. B. Khandelwal, A. Karakurt, P. R. Sekaran, V. Sethi, R. Singh, Hydrogen powered aircraft: The future of air transport, Progress in Aerospace Sciences 60 (2013) 45–59.
5. REN21, Renewable 2005 Global Status Report, Worldwatch Institute, Washington, DC, 2005, renewable Energy Policy Network for the 21^{st} Century.
6. ICAO, ICAO Annex 16: Environmental Protection, Volume II - Aircraft Engine Emissions, Tech. Rep. 40CFR 87.89, international Civil Aviation Organization, 2008.
7. C. Chang, C. Lee, J. Herbon, S. Kramer, NASA environmentally responsible aviation project develops next-generation low-emissions combustor technologies (Phase I), J. Aeronaut. Aerosp. Eng 2 (4) (2013) 116.
8. H. Hubbard, Aeroacoustics of Flight Vehicles: Theory and Practice. Volume 1: Noise Sources, vols. 1-2, Scientific and Techn. Information Office, Nat. Aeronautics and Space Administration, 1991.
9. O. Zaporozhets, V. Tokarev, K. Attenborouh, Aircraft Noise. Assessment, prediction and control, Spon Press, 2011.
10. A. P. Dowling, Y. Mahmoudi, Combustion noise, Proceedings of the Combustion Institute 35 (1) (2015) 65–100.
11. M. Ihme, Combustion and Engine-Core Noise, Annual Review of Fluid Mechanics 49 (1) (2017) 277–310.
12. I. C. A. Organization, Data Definition Standard. Events Phases, Tech. Rep. ECCAIRS 4.2.8, 2010.
13. J. Penner, D. Lister, D. Griggs, M. McFarland, D. Dokken, Aviation and the Global Atmosphere: A Special Report of the Intergovernmental Panel on Climate Change, Cambridge University Press, 1999.
14. A. F. El-Sayed, Aircraft Propulsion and Gas Turbine Engines, CRC Press, 2008.
15. R.-R. PLC, The Jet Engine, Rolls-Royce, 1996.
16. E. T. Vincent, The theory and design of gas turbines and jet engines, McGraw-Hill, 1950.
17. S. Candel, Mécanique des Fluides - Cours, Dunod, 2001.
18. P. Hill, C. Peterson, Mechanics and Thermodynamics of Propulsion, Pearson, 2010.
19. G. C. Oates, The aerothermodynamics of aircraft gas turbine engines, Tech. Rep., Washington University Seattle, 1978.
20. J. D. Anderson, Modern Compressible Flow: With Historical Perspective (McGraw-Hill series in mechanical engineering), McGraw-Hill, New York, 1982.
21. K. Kuo, R. Acharya, Fundamentals of turbulent and multi-phase combustion, John Wiley & Sons, 2012.
22. Y. Huang, V. Yang, Dynamics and stability of lean-premixed swirl-stabilized combustion, Progress in Energy and Combustion Sciences 35 (2009) 293–384.
23. S. Candel, D. Durox, T. Schuller, J. Bourgouin, J. Moeck, Dynamics of swirling flames, Annual review of fluid mechanics 46 (2014) 147–173.
24. S. Taamallah, K. Vogiatzaki, F. Alzahrani, E. Mokheimer, M. Habib, A. Ghoniem, Fuel flexibility, stability and emissions in premixed hydrogen-rich gas turbine combustion: Technology, fundamentals, and numerical simulations, Applied energy 154 (2015) 1020–1047.
25. S. S. Rashwan, M. A. Nemitallah, M. A. Habib, Review on premixed combustion technology: stability, emission control, applications, and numerical case study, Energy & Fuels 30 (12) (2016) 9981–10014.
26. D. Dunn-Rankin, P. Therkelsen (Eds.), Lean Combustion, Second Edition, Academic Press, Boston, 2016.
27. J. C. Oefelein, V. Yang, Modeling high-pressure mixing and combustion processes in liquid rocket engines, Journal of Propulsion and Power 14 (5) (1998) 843–857.
28. P. Ma, L. Bravo, M. Ihme, Supercritical and transcritical real-fluid mixing in diesel engine applications, Tech. Rep., ARL, 2015.
29. P. Palies, Mechanisms of premixed turbulent swirling flame stabilization, Bulletin of the American Physical Society (2018).
30. R. Tacina, Low NO_x Potential of Gas Turbine Engines, Tech. Rep., NASA, Lewis Research Center, Cleveland, Ohio, 1990.

31. P. Buelow, B. Williams, D. Bretz, M. Spooner, C. Mohamed, H. Gill, Lean direct injection atomizer for gas turbine engines, uS Patent 7,779,636, 2010.
32. S. Dhanuka, J. Temme, J. Driscoll, Unsteady Aspects of Lean Premixed Prevaporized Gas Turbine Combustors: Flame-Flame Interactions, Journal of Propulsion and Power 27 (3) (2011) 631–641.
33. B. Sen, Y. Guo, R. McKinney, F. Montanari, F. Bedford, Pratt and Whitney Gas Turbine Combustor Design Using ANSYS Fluent and User Defined Functions, in: ASME. Turbo Expo: Power for Land, Sea, and Air, Volume 2: Combustion, Fuels and Emissions, Parts A and B, 1547–1556, 2012, GT2012-70145.
34. A. Lefebvre, Gas turbine combustion, Taylor and Francis, 1998.
35. T. C. Lieuwen, Unsteady Combustor Physics, Cambridge University Press, 2012.
36. T. C. Williams, R. W. Schefer, J. C. Oefelein, C. R. Shaddix, Idealized gas turbine combustor for performance research and validation of large eddy simulations, Review of Scientific Instruments 78 (3) (2007) 035114.
37. E. Caffo, C. Padovani, Flashback in premixed air flames, Combustion and Flame 7 (1963) 331–337.
38. S. Plee, A. Mellor, Review of flashback reported in prevaporizing/premixing combustors, Combustion and Flame 32 (1978) 193–203.
39. Y. Sommerer, D. Galley, T. Poinsot, S. Ducruix, F. Lacas, D. Veynante, Large eddy simulation and experimental study of flashback and blow-off in a lean partially premixed swirled burner, Journal of Turbulence 5 (37) (2004) 1–3.
40. A. C. Benim, K. J. Syed, Flashback mechanisms in lean premixed gas turbine combustion, Academic press, 2014.
41. M. Konle, F. Kiesewetter, T. Sattelmayer, Simultaneous high repetition rate PIV-LIF-measurements of CIVB driven flashback, Experiments in Fluids 44 (4) (2008) 529–538.
42. M. Konle, T. Sattelmayer, Interaction of heat release and vortex breakdown during flame flashback driven by combustion induced vortex breakdown, Experiments in fluids 47 (4–5) (2009) 627.
43. C. Heeger, R. Gordon, M. Tummers, T. Sattelmayer, A. Dreizler, Experimental analysis of flashback in lean premixed swirling flames: upstream flame propagation, Experiments in fluids 49 (4) (2010) 853–863.
44. V. Kurdyumov, E. Fernández, A. Linan, Flame flashback and propagation of premixed flames near a wall, Proceedings of the Combustion Institute 28 (2) (2000) 1883–1889.
45. V. Kurdyumov, E. Fernandez-Tarrazo, J.-M. Truffaut, J. Quinard, A. Wangher, G. Searby, Experimental and numerical study of premixed flame flashback, Proceedings of the Combustion Institute 31 (1) (2007) 1275–1282.
46. C. Eichler, T. Sattelmayer, Experiments on flame flashback in a quasi-2D turbulent wall boundary layer for premixed methane-hydrogen-air mixtures, Journal of Engineering for Gas Turbines and Power 133 (1) (2011) 011503.
47. D. Ebi, N. T. Clemens, Experimental investigation of upstream flame propagation during boundary layer flashback of swirl flames, Combustion and Flame 168 (2016) 39–52.
48. S. Plee, A. Mellor, Characteristic time correlation for lean blowoff of bluff-body-stabilized flames, Combustion and Flame 35 (1979) 61–80.
49. S. Shanbhogue, S. Husain, T. Lieuwen, Lean blowoff of bluff body stabilized flames: Scaling and dynamics, Progress in Energy and Combustion Science 35 (1) (2009) 98–120, ISSN 0360-1285.
50. T. M. Muruganandam, S. Nair, R. Olsen, Y. Neumeier, A. Meyers, J. Jagoda, T. Lieuwen, J. Seitzman, B. Zinn, Blowout control in turbine engine combustors, in: AIAA 2004-0637, 42^{th} Aerospace Sciences meeting & Exhibit, Reno, NV, 2004.
51. T. M. Muruganandam, J. Seitzman, Origin of Lean Blow Out Precursors in Swirled Gas Turbine Combustors, in: AIAA 2005-1163, 43^{th} Aerospace Sciences meeting & Exhibit, Reno, NV, 2005.
52. M. Stöhr, I. Boxx, C. Carter, W. Meier, Dynamics of lean blowout of a swirl-stabilized flame in a gas turbine model combustor, Proceedings of the Combustion Institute 33 (2) (2011) 2953–2960, ISSN 1540-7489.
53. D. E. Cavaliere, K. James, E. Mastorakos, A Comparison of the Blow-Off Behaviour of Swirl-Stabilized Premixed, Non-Premixed and Spray Flames, Flow, Turbulence and Combustion 91 (2) (2013) 347–372.
54. M. De Giorgi, A. Sciolti, S. Campilongo, A. Ficarella, Image processing for the characterization of flame stability in a non-premixed liquid fuel burner near lean blowout, Aerospace Science and Technology 49 (2016) 41–51.
55. H. Ganji, R. Ebrahimi, Numerical estimation of blowout, flashback, and flame position in MIT micro gas-turbine chamber, Chemical Engineering Science 104 (2013) 857–867.
56. I. Sigfrid, R. Whiddon, R. Collin, J. Klingmann, Influence of reactive species on the lean blowout

limit of an industrial DLE gas turbine burner 161 (5) (2014) 1365–1373.
57. R. Santhosh, S. Basu, Transitions and blowoff of unconfined non-premixed swirling flame, Combustion and Flame 164 (2016) 35–52, ISSN 0010-2180.
58. T. M. Muruganandam, J. Seitzman, Fluid Mechanics of Lean Blowout Precursors in Gas Turbine Combustors, International Journal of Spray and Combustion Dynamics 4 (1) (2012) 29–60.
59. L. Esclapez, P. Ma, M. Ihme, Large-eddy simulation of fuel effect on lean blowout in gas turbines, in: Center for Turbulence Research, Annual Rsearch Briefs, 2015.
60. L. Esclapez, P. Ma, E. Mayhew, R. Xu, S. Stouffer, T. Lee, H. Wang, M. Ihme, Fuel effects on lean blow-out in a realistic gas turbine combustor, Combustion and Flame 181 (2017) 82–99.
61. A. Tyliszczak, D. E. Cavaliere, E. Mastorakos, LES/CMC of Blow-off in a Liquid Fueled Swirl Burner, Flow, Turbulence and Combustion 92 (1) (2014) 237–267.
62. H. Zhang, E. Mastorakos, Prediction of Global Extinction Conditions and Dynamics in Swirling Non-premixed Flames Using LES/CMC, Modelling, Flow, Turbulence and Combustion 96 (4) (2016) 863–889.
63. A. Giusti, M. Kotzagianni, E. Mastorakos, LES/CMC simulations of swirl-stabilised ethanol spray flames approaching blow-off, Flow, Turbulence and Combustion 97 (4) (2016) 1165–1184.
64. A. Giusti, E. Mastorakos, Detailed chemistry LES/CMC simulation of a swirling ethanol spray flame approaching blow-off, Proceedings of the Combustion Institute 36 (2) (2017) 2625–2632, ISSN 1540-7489.
65. S. Shanbhogue, S. Husain, T. Lieuwen, Lean blowoff of bluff body stabilized flames: scaling and dynamics, Progress in Energy and Combustion Science 35 (1) (2008) 98–120.
66. G. Lacaze, B. Cuenot, T. Poinsot, M. Oschwald, Large eddy simulation of laser ignition and compressible reacting flow in a rocket-like configuration, Combustion and Flame 156 (6) (2009) 1166–1180.
67. R. Maly, M. Vogel, Initiation and propagation of flame fronts in lean CH4-air mixtures by the three modes of the ignition spark, in: Symposium (International) on Combustion, vol. 17, Elsevier, 821–831, 1979.
68. C. C. Swett Jr, Spark ignition of flowing gases using long-duration discharges, in: Symposium (International) on Combustion, vol. 6, Elsevier, 523–532, 1957.
69. T. Kravchik, E. Sher, Numerical modeling of spark ignition and flame initiation in a quiescent methane-air mixture, Combustion and Flame 99 (3–4) (1994) 635–643.
70. F. Grisch, G.-A. Grandin, D. Messina, B. Attal-Trétout, Laser-based measurements of gas-phase chemistry in non-equilibrium pulsed nanosecond discharges, Comptes Rendus Mécanique 337 (6–7) (2009) 504–516.
71. Y. Ju, W. Sun, Plasma assisted combustion: Dynamics and chemistry, Progress in Energy and Combustion Science 48 (2015) 21–83.
72. A. Starikovskiy, N. Aleksandrov, Plasma-assisted ignition and combustion, Progress in Energy and Combustion Science 39 (1) (2013) 61–110.
73. J.-F. Bourgouin, D. Durox, T. Schuller, J. Beaunier, S. Candel, Ignition dynamics of an annular combustor equipped with multiple swirling injectors, Combustion and Flame 160 (8) (2013) 1398–1413.
74. T. Poinsot, Flame ignition and propagation, Combustion Energy Frontier Resaerch Center.
75. G. Von Elbe, B. Lewis, Theory of ignition, quenching and stabilization of flames of nonturbulent gas mixtures, in: Symposium on Combustion and Flame, and Explosion Phenomena, vol. 3, Elsevier, 68–79, 1948.
76. G. Stancu, F. Kaddouri, D. Lacoste, C. Laux, Atmospheric pressure plasma diagnostics by OES, CRDS and TALIF, Journal of Physics D: Applied Physics 43 (12) (2010) 124002.
77. Q. Liu, Y. Zhang, Shock wave generated by high-energy electric spark discharge, Journal of Applied Physics 116 (15) (2014) 153302.
78. R. Freeman, J. Craggs, Shock waves from spark discharges, Journal of Physics D: Applied Physics 2 (3) (1969) 421.
79. J. E. Shepherd, J. C. Krok, J. J. Lee, Jet A explosion experiments: Laboratory testing.
80. G. Lacaze, Simulation aux Grandes Echelles de l'allumage de moteurs fusées cryotechniques, Ph.D. thesis, Institut National Polytechnique de Toulouse-INPT, 2009.
81. C. Ternel, Contribution au développement de l'allumage par laser pour les moteurs à combustion interne, Ph.D. thesis, Rouen, 2006.
82. K. Hünecke, Jet engines. Fundamentals of therory, design and operation, Motorbooks International, 1997.
83. N. Cumpsty (Ed.), Jet Propulsion. A simple guide to the aerodynamics and thermodynamics design and performance of jet engines, Second Edition, Cambridge University Press, 2003.

84. A. H. Lefebvre, D. R. Ballal, Gas turbine combustion: alternative fuels and emissions, CRC press, 2010.
85. W. Anderson, V. Yang (Eds.), Liquid Rocket Engine Combustion Instability, Progress in Astronautics and Aeronautics, American Institute of Aeronautics and Astronautics, Inc., 1995.
86. M. Dranovsky (Ed.), Combustion Instabilities in Liquid Rocket Engines: Testing and Development Practices in Russia, Progress in Astronautics and Aeronautics, American Institute of Aeronautics and Astronautics, Inc., 2007.
87. T. C. Lieuwen, V. Yang (Eds.), Combustion instabilities in gas turbines, Operational experience, Fundamental mechanisms, and Modeling, vol. 210 of *Progress in Astronautics and Aeronautics*, American Institute of Aeronautics and Astronautics, Inc., 2005.
88. M. S. Natanzon, F. E. C. Culick (Eds.), Combustion Instability, Progress in Astronautics and Aeronautics, American Institute of Aeronautics and Astronautics, Inc., 1999.
89. F. Culick, M. Heitor, J. Whitelaw, Unsteady Combustion, NATO Science Series E, Springer Netherlands, 1996.
90. M. Anand, J. Zhu, C. Connor, M. Razdan, Combustor flow analysis using an advanced finite-volume design system, in: ASME 1999 International Gas Turbine and Aeroengine Congress and Exhibition, American Society of Mechanical Engineers, 1999.
91. S. James, J. Zhu, M. Anand, Large-eddy simulations as a design tool for gas turbine combustion systems, AIAA journal 44 (4) (2006) 674–686.
92. H. Mongia, T. Held, G. Hsiao, R. Pandalai, Incorporation of combustion instability issues into design process: GE aeroderivative and aero engines experience, Progress in astronautics and aeronautics 210 (2005) 43.
93. H. C. Mongia, GE Aviation low emissions combustion technology evolution, Tech. Rep., SAE Technical Paper, 2007.
94. R. McKinney, A. Cheung, W. Sowa, D. Sepulveda, The Pratt and Whitney TALON X low emissions combustor: Revolutionary results with evolutionary technology, in: 45th AIAA Aerospace Sciences Meeting and Exhibit, 386, 2007.
95. F. Ma, W. Proscia, V. Ivanov, F. Montanari, Large eddy simulation of self-excited combustion dynamics in a bluff-body combustor, in: 51st AIAA/SAE/ASEE Joint Propulsion Conference, 3968, 2015.
96. G. Boudier, L. Gicquel, T. Poinsot, D. Bissieres, C. Bérat, Comparison of LES, RANS and experiments in an aeronautical gas turbine combustion chamber, Proceedings of the Combustion Institute 31 (2) (2007) 3075–3082.
97. H. Musaefendic, Y. Méry, T. Noel, An Uncertainty Quantification Framework Coupled With a 1D Physics-Based Model for the Prediction of NOx Emissions in a RQL Combustion Chamber, in: ASME Turbo Expo 2015: Turbine Technical Conference and Exposition, American Society of Mechanical Engineers, 2015.
98. F. Lacombe, Y. Méry, Mixed Acoustic-Entropy Combustion Instabilities in a Model Aeronautical Combustor: Large Eddy Simulation and Reduced Order Modeling, Journal of Engineering for Gas Turbines and Power 140 (3) (2018) 031506.
99. H. C. Mongia, Future Trends in Commercial Aviation Engines Combustion, in: Novel Combustion Concepts for Sustainable Energy Development, Springer, 113–176, 2014.
100. Y. Liu, X. Sun, V. Sethi, D. Nalianda, Y.-G. Li, L. Wang, Review of modern low emissions combustion technologies for aero gas turbine engines, Progress in Aerospace Sciences (2017).
101. P. Palies, D. Durox, T. Schuller, S. Candel, Experimental study on the effect of swirler geometry and swirl number on flame describing functions, Combustion Science and Technology 183 (7) (2011) 704–717.
102. X. Han, X. Hui, C. Zhang, Y. Lin, P. He, C. Sung, Combustion Instabilities in a Lean Premixed Pre-Vaporized Combustor at High-Pressure High-Temperature, ASME Proceedings 177 (GT2017-65190) (2017) 2349–2371.
103. R. Tacina, C. Wey, K. Choi, Flame tube NOx emissions using a lean-direct-wall-injection combustor concept, in: 37th Joint Propulsion Conference and Exhibit, 3271, 2001.
104. R. Palm, S. Grundmann, M. Weismüller, S. Saric, S. Jakirlic, C. Tropea, Experimental characterization and modelling of inflow conditions for a gas turbine swirl combustor, International Journal of Heat and Fluid Flow 27 (2006) 924–936.
105. R. Cheng, D. Yegian, M. Miyasato, G. Samuelsen, C. Benson, R. Pellizzari, P. Loftus, Scaling and development of low-swirl burners for low-emission furnaces and boilers, Proceedings of the Combustion Institute 28 (2000) 1305–1313.
106. A. Gupta, D. Lilley, N. Syred, Swirl flows, Abaqus Press, 1984.
107. J.-F. Bourgouin, J. Moeck, D. Durox, T. Schuller, S. Candel, Sensitivity of swirling flows to small changes in the swirler geometry, Comptes Rendus Mécanique 341 (1–2) (2013) 211–219.

108. C. T. Chang, J. D. Holdeman, Low Emissions RQL flametube combustor test results, Tech. Rep. TM-2001-211107, NASA, 2001.
109. R. R. Tacina, Combustor technology for future aircraft, Tech. Rep. 103268, NASA, 1990.
110. K. J. Low, Fuel nozzle guide plate mistake proofing, uS Patent 8,689,563, 2014.
111. K. M. Tacina, Swirl-Venturi Lean Direct Injection Combustion Technology for Low-NOx Aero Gas Turbine Engines.
112. Y. R. Hicks, K. M. Tacina, R. C. Anderson, Effect of Air Swirler Configuration on Lean Direct Injector Flow Structure and Combustion Performance with a 7-point Lean Direct Injector Array.
113. R. Tacina, P. Lee, C. Wey, A lean-direct-injection combustor using a 9 point swirl-venturi fuel injector, ISABE 1106 (2005) 2005.
114. Y. R. Hicks, C. M. Heath, R. C. Anderson, K. M. Tacina, Investigations of a combustor using a 9-point swirl-venturi fuel injector: recent experimental results.
115. K. M. Tacina, C. Chang, Z. J. He, P. Lee, H. C. Mongia, B. K. Dam, A second generation swirl-venturi lean direct injection combustion concept, in: 50th AIAA/ASME/SAE/ASEE Joint Propulsion Conference, 3434, 2014.
116. R. Tacina, C. Wey, P. Laing, A. Mansour, A low NO_x lean-direct injection, multipoint integrated module combuster concept for advanced aircraft gas turbines.
117. A. Lefebvre, Lean Premixed/Prevaporized Combustion, CP-2016, NASA, 1977.
118. A. Mancini, H. Mongia, Mixer assembly for gas turbine engine combustor, US Patent 8,171,735, 2012.
119. R. Cheng, D. Littlejohn, W. A. Nazeer, K. O. Smith, Laboratory studies of the flow field characteristics of low-swirl injectors for adaptation to fuel-flexible turbines, Journal of Engineering for Gas Turbines and Power 130 (2) (2008) 021501.
120. R. Cheng, Velocity and scalar characteristics of premixed turbulent flames stabilized by weak swirl, Combustion and Flame 101 (1–2) (1995) 1–14.
121. C. Chan, K. Lau, W. Chin, R. Cheng, Freely propagating open premixed turbulent flames stabilized by swirl, in: Symposium (International) on Combustion, vol. 24, Elsevier, 511–518, 1992.
122. D. Littlejohn, R. Cheng, W. Nazeer, K. Smith, Development of the Low Swirl Injector for Fuel-Flexible GasTurbines, Tech. Rep., Ernest OrlandoLawrence Berkeley NationalLaboratory, Berkeley, CA (US), 2007.
123. R. Acharya, K. Kuo, Fundamentals of Turbulent and Multiphase Combustion, Wiley, 2012.
124. G. Markstein, Nonsteady flame propagation, Pergamon Press, 1964.
125. F. Williams, Combustion theory, The Benjamin/Cummings Publishing Company, Inc., California, 1985.
126. A. Kerstein, W. Ashurst, F. Williams, Field equation for interface propagation in an unsteady homogeneous flow field, Phys. Rev. A 37 (7) (1988) 2728–2731.
127. F. Baillot, D. Durox, R. Prud'homme, Experimental and theoretical study of a premixed vibrating flame, Combust. Flame 88 (2) (1992) 149–152.
128. S. Ducruix, D. Durox, S. Candel, Theoretical and experimental determination of the transfer function of a laminar premixed flame, Proceedings of the Combustion Institute 28 (2000) 765–773.
129. T. Schuller, D. Durox, S. Candel, A unified model for the prediction of laminar flame transfer functions: comparisons between conical and V-flame dynamics, Combustion and Flame 134 (2003) 21–34.
130. S. Ducruix, T. Schuller, D. Durox, S. Candel, Combustion dynamics and instabilities: Elementary coupling and driving mechanisms, Journal of propulsion and power 19 (5) (2003) 722–734.
131. T. Lieuwen, Modeling premixed combustion-acoustic wave interactions: A review, Journal of propulsion and power 19 (5) (2003) 765–781.
132. T. Lieuwen, Modeling premixed combustion-acoustic wave interactions: a review, J. Propuls. Power 19 (5) (2003) 765–781.
133. T. Lieuwen, Analysis of acoustic wave interactions with turbulent premixed flames, Proceedings of the Combustion Institute 29 (2) (2002) 1817–1824.
134. P. Palies, D. Durox, T. Schuller, S. Candel, Acoustic-convective mode conversion in an aerofoil cascade, Journal of Fluid Mechanics 672 (2011) 545–569.
135. S. Candel, D. Durox, S. Ducruix, A.-L. Birbaud, N. Noiray, T. Schuller, Flame dynamics and combustion noise: progress and challenges, International Journal of Aeroacoustics 8 (1) (2009) 1–56.
136. D. Durox, T. Schuller, S. Candel, Combustion dynamics of inverted conical flames, Proceedings of the Combustion Institute 30 (2005) 1717–1724.
137. D. Durox, T. Schuller, N. Noiray, S. Candel, Experimental analysis of nonlinear flame transfer functions for different flame geometries, Proceedings of the Combustion Institute 32 (2009) 1391–1398.

138. T. Schuller, A. Cuquel, P. Palies, J. Moeck, D. Durox, S. Candel, Modeling the response of premixed flame transfer functions-Key elements and experimental proofs, in: 50th AIAA Aerospace Sciences Meeting including the New Horizons Forum and Aerospace Exposition, 985, 2012.
139. A. Cuquel, D. Durox, T. Schuller, Scaling the flame transfer function of confined premixed conical flames, Proceedings of the Combustion Institute 34 (1) (2013) 1007–1014.
140. S. H. Preetham, T. C. Lieuwen, Response of turbulent premixed flames to harmonic acoustic forcing, Proceedings of the Combustion Institute 31 (1) (2007) 1427–1434.
141. R. Balachandran, B. O. Ayoola, C. F. Kaminski, A. P. Dowling, E. Mastorakos, Experimental investigation of the nonlinear response of turbulent premixed flames to imposed inlet velocity oscillations, Combustion and Flame 143 (2005) 37–55.
142. R. Balachandran, A. P. Dowling, E. Mastorakos, Non-linear response of turbulent premixed flames to imposed inlet velocity oscillations of two frequencies, Flow, turbulence and combustion 80 (2008) 455–487.
143. C. A. Armitage, R. Balachandran, E. Mastorakos, R. S. Cant, Investigation of the nonlinear response of turbulent premixed flames to imposed inlet velocity oscillations, Combustion and Flame 146 (2006) 419–436.
144. A. Chapparro, E. Landry, B. Cetegen, Transfer function characteristics of bluff-body stabilized, conical V-shaped premixed turbulent propane-air flames conical V-shaped premixed turbulent propane–air flames, Combustion and Flame 145 (2006) 290–299.
145. R. Rajaram, T. Lieuwen, Acoustic radiation from turbulent premixed flames, Journal of Fluid Mechanics 637 (2009) 357–385.
146. M. Blanchard, P. J. Schmid, D. Sipp, T. Schuller, Pressure wave generation from perturbed premixed flames, Journal of Fluid Mechanics 797 (2016) 231–246.
147. A. Haghiri, M. Talei, M. J. Brear, E. R. Hawkes, Sound generation by turbulent premixed flames, Journal of Fluid Mechanics 843 (2018) 29–52.
148. A. H. Lefebvre, W. G. Freeman, L. H. Cowell, Spontaneous ignition delay characteristics of hydrocarbon fuel-air mixtures.
149. R. Cabra, T. Myhrvold, J. Chen, R. Dibble, A. Karpetis, R. Barlow, Simultaneous laser Raman-Rayleigh-LIF measurements and numerical modeling results of a lifted turbulent H_2/N_2 jet flame in a vitiated coflow, Proceedings of the Combustion Institute 29 (2) (2002) 1881–1888.
150. R. Cabra, J.-Y. Chen, R. Dibble, A. Karpetis, R. Barlow, Lifted methane–air jet flames in a vitiated coflow, Combustion and Flame 143 (4) (2005) 491–506.
151. O. Schulz, T. Jaravel, T. Poinsot, B. Cuenot, N. Noiray, A criterion to distinguish autoignition and propagation applied to a lifted methane–air jet flame, Proceedings of the Combustion Institute 36 (2) (2017) 1637–1644.
152. E. Mastorakos, T. Baritaud, T. Poinsot, Numerical simulations of autoignition in turbulent mixing flows, Combustion and Flame 109 (1–2) (1997) 198–223.
153. B. Zinn, Real-Time Control of Lean Blowout in a Turbine Engine for Minimizing No (x) Emissions.
154. H. Chiu, M. Summerfield, Theory of combustion noise, Acta Astronautica 1 (7–8) (1974) 967–984.
155. W. Strahle, A review of combustion generated noise, in: Aeroacoustics Conference, 1023, 1975.
156. W. Strahle, Combustion noise, Progress in Energy and Combustion Science 4 (3) (1978) 157–176.
157. A. Putnam, L. Faulkner, Overview of combustion noise, Journal of energy 7 (6) (1983) 458–469.
158. I. Duran, S. Moreau, F. Nicoud, T. Livebardon, E. Bouty, T. Poinsot, Combustion noise in modern aero-engines, AerospaceLab (7) (2014).
159. A. Schwarz, J. Janicka, Combustion Noise, Fluid mechanics and its applications, Springer Berlin Heidelberg, 2009.
160. F. Greiffenhagen, J. Peterleithner, J. Woisetschläger, Prediction of Combustion Noise of a Swirl-Stabilized Flame Using Laser Interferometric Vibrometry Validated by Acoustic Measurements, in: ASME Turbo Expo 2017: Turbomachinery Technical Conference and Exposition, American Society of Mechanical Engineers, 2017.
161. M. Merk, W. Polifke, R. Gaudron, M. Gatti, C. Mirat, T. Schuller, Measurement and Simulation of Combustion Noise and Dynamics of a Confined Swirl Flame, AIAA Journal (2018) 1–13.
162. F. Grimm, J. Dierke, R. Ewert, B. Noll, M. Aigner, Modelling of combustion acoustics sources and their dynamics in the PRECCINSTA burner test case, International Journal of Spray and Combustion Dynamics 9 (4) (2017) 330–348.
163. Y. Liu, A. Dowling, N. Swaminathan, R. Morvant, M. Macquisten, L. Caracciolo, Prediction of combustion noise for an aeroengine combustor, Journal of Propulsion and Power 30 (1) (2013) 114–122.
164. J. O'Brien, J. Kim, M. Ihme, Investigation of the mechanisms of jet-engine core noise using

large-eddy simulation, in: 54th AIAA Aerospace Sciences Meeting, 2016.
165. A. S. Morgans, I. Duran, Entropy noise: A review of theory, progress and challenges, International Journal of Spray and Combustion Dynamics 8 (4) (2016) 285–298.
166. T. Livebardon, S. Moreau, L. Gicquel, T. Poinsot, E. Bouty, Combining LES of combustion chamber and an actuator disk theory to predict combustion noise in a helicopter engine, Combustion and Flame 165 (2016) 272–287.
167. C. Silva, M. Leyko, F. Nicoud, S. Moreau, Assessment of combustion noise in a premixed swirled combustor via large-eddy simulation, Computers & Fluids 78 (2013) 1–9.
168. C. Silva, M. Merk, T. Komarek, W. Polifke, The contribution of intrinsic thermoacoustic feedback to combustion noise and resonances of a confined turbulent premixed flame, Combustion and Flame 182 (2017) 269–278.
169. M. Leyko, F. Nicoud, T. Poinsot, Comparison of direct and indirect combustion noise mechanisms in a model combustor, AIAA journal 47 (11) (2009) 2709–2716.
170. C. K. Tam, S. A. Parrish, J. Xu, B. Schuster, Indirect combustion noise of auxiliary power units, Journal of Sound and Vibration 332 (17) (2013) 4004–4020.
171. S. Candel, Combustion Dynamics and Control: Progress and Challenges, Proceedings of the Combustion Institute 29 (2002) 1–28.
172. T. Poinsot, D. Veynante, Theoretical and Numerical Combustion, 2nd Edition, Edwards, 2005.
173. L. Crocco, Research on combustion instability in liquid propellant rockets, Proceedings of the Combustion Institute 12 (1968) 85–99.
174. A. Putnam, Combustion driven oscillations in industry, Elsevier, New-York, 1971.
175. F. Culick, Dynamics of combustion systems: fundamentals, acoustics and control, in: RTO AVT Course on "Active control of engine dynamics", Brussels, Belgium, 2001.
176. J. O'Connor, V. Acharya, T. Lieuwen, Transverse combustion instabilities: Acoustic, fluid mechanic, and flame processes, Progress in Energy and Combustion Science 49 (Supplement C) (2015) 1–39.
177. C. J. Lawn, G. Penelet, Common features in the thermoacoustics of flames and engines, International Journal of Spray and Combustion Dynamics (2018).
178. M. P. Juniper, R. Sujith, Sensitivity and nonlinearity of thermoacoustic oscillations, Annual Review of Fluid Mechanics 50 (1) (2018) 661–689.
179. T. Poinsot, Prediction and control of combustion instabilities in real engines, Proceedings of the Combustion Institute 36 (1) (2017) 1–28.
180. P. Palies, Dynamique et Instabilités de Combustion des Flammes Swirlées, Ph.D. thesis, Ecole Centrale Paris, 2010.
181. T. Lieuwen, B. Zinn, The role of equivalence ratio fluctuations in driving combustion instabilities in low NO_x gas turbines, Proceedings of the Combustion Institute 27 (1998) 1809–1816.
182. A. Lipatnikov, J. Chomiak, Turbulent flame speed and thickness: phenomenology, evaluation, and application in multi-dimensional simulations, Progress in Energy and Combustion Science 28 (1) (2002) 1–74.
183. L. Lovach Ev, Flammability limits—a review, Combustion Science and Technology 20 (5–6) (1979) 209–224.
184. N. Peters, Laminar flamelet concepts in turbulent combustion, in: Symposium (International) on Combustion, vol. 21, Elsevier, 1231–1250, 1988.
185. E. Mularz, Lean, premixed, prevaporized combustion for aircraft gas turbine engines, in: 15^{th} Joint Propulsion Conference, 1318, 1979.
186. R. Dickman, W. Dodds, E. Ekstedt Lean, Lean, Premixed-Prevaporized (LPP) combustor conceptual design study, NASA CR-159629.
187. P. Leonard, A. Mellor, Correlation of lean blowoff of gas turbine combustors using alternative fuels, Journal of energy 7 (6) (1983) 729–732.
188. J. Blust, D. Ballal, G. Sturgess, Fuel effects on lean blowout and emissions from a well-stirred reactor, Journal of propulsion and power 15 (2) (1999) 216–223.
189. F. Xie, Y. Huang, B. Hu, F. Wang, Improved semiempirical correlation to predict lean blowout limits for gas turbine combustors, Journal of Propulsion and Power 28 (1) (2012) 197–203.
190. P. C. Ma, H. Wu, J. W. Labahn, T. Jaravel, M. Ihme, Analysis of transient blow-out dynamics in a swirl-stabilized combustor using large-eddy simulations, Proceedings of the Combustion Institute 37 (4) (2019) 5073–5082.
191. D. Galley, A. Pubill Melsio, S. Ducruix, F. Lacas, D. Veynante, Experimental study of the dynamics of a LPP injection system, in: 40th AIAA/ASME/SAE/ASEE Joint Propulsion Conference and Exhibit, 4032, 2004.
192. D. Galley, S. Ducruix, F. Lacas, D. Veynante, Mixing and stabilization study of a partially premixed swirling flame using laser induced fluorescence, Combustion and Flame 158 (2011) 155–171.
193. W. A. Sirignano, Fuel droplet vaporization and spray combustion theory, Progress in Energy and Combustion Science 9 (4) (1983) 291–322.

194. T. Lieuwen, K. McManus, Combustion Dynamics in Lean-Premixed Prevaporized (LPP) Gas Turbines, J. Propuls Power 19 (5) (2003) 721.
195. A. Masri, Partial premixing and stratification in turbulent flames, Proceedings of the Combustion institute 35 (2) (2015) 1115–1136.
196. D. Galley, Etude de la stabilisation de flammes turbulentes prévaporisées prémélangées pauvres, Ph.D. thesis, Laboratoire EM2C, Ecole Centrale Paris, 2006.
197. M. Stöhr, R. Sadanandan, W. Meier, Experimental study of unsteady flame structures of an oscillating swirl flame in a gas turbine model combustor, Proceedings of the Combustion Institute 32 (2) (2009) 2925–2932.
198. I. Boxx, M. Stöhr, C. Carter, W. Meier, Temporally resolved planar measurements of transient phenomena in a partially pre-mixed swirl flame in a gas turbine model combustor, Combustion and Flame 157 (8) (2010) 1510–1525.
199. B. Franzelli, E. Riber, L. Y. Gicquel, T. Poinsot, Large eddy simulation of combustion instabilities in a lean partially premixed swirled flame, Combustion and flame 159 (2) (2012) 621–637.
200. M. Stöhr, Z. Yin, W. Meier, Interaction between velocity fluctuations and equivalence ratio fluctuations during thermoacoustic oscillations in a partially premixed swirl combustor, Proceedings of the Combustion Institute 36 (3) (2017) 3907–3915.
201. C. Dem, M. Stöhr, C. M. Arndt, A. M. Steinberg, W. Meier, Experimental study of turbulence-chemistry interactions in perfectly and partially premixed confined swirl flames, Zeitschrift für Physikalische Chemie 229 (4) (2015) 569–595.
202. M. Stöhr, C. Arndt, W. Meier, Transient effects of fuel–air mixing in a partially-premixed turbulent swirl flame, Proceedings of the Combustion Institute 35 (3) (2015) 3327–3335.
203. M. S. Sweeney, S. Hochgreb, M. J. Dunn, R. S. Barlow, The structure of turbulent stratified and premixed methane/air flames I: Non-swirling flows, Combustion and flame 159 (9) (2012) 2896–2911.
204. M. S. Sweeney, S. Hochgreb, M. J. Dunn, R. S. Barlow, The structure of turbulent stratified and premixed methane/air flames II: Swirling flows, Combustion and Flame 159 (9) (2012) 2912–2929.
205. R. S. Barlow, G.-H. Wang, P. Anselmo-Filho, M. Sweeney, S. Hochgreb, Application of Raman/Rayleigh/LIF diagnostics in turbulent stratified flames, Proceedings of the Combustion Institute 32 (1) (2009) 945–953.
206. F. Proch, A. M. Kempf, Numerical analysis of the Cambridge stratified flame series using artificial thickened flame LES with tabulated premixed flame chemistry, Combustion and Flame 161 (10) (2014) 2627–2646.
207. H. Turkeri, X. Zhao, S. B. Pope, M. Muradoglu, Large eddy simulation/probability density function simulations of the Cambridge turbulent stratified flame series, Combustion and Flame 199 (2019) 24–45.
208. F. Seffrin, F. Fuest, D. Geyer, A. Dreizler, Flow field studies of a new series of turbulent premixed stratified flames, Combustion and Flame 157 (2) (2010) 384–396.
209. K.-J. Nogenmyr, P. Petersson, X.-S. Bai, A. Nauert, J. Olofsson, C. Brackman, H. Seyfried, J. Zetterberg, Z. Li, M. Richter, et al., Large eddy simulation and experiments of stratified lean premixed methane/air turbulent flames, Proceedings of the Combustion Institute 31 (1) (2007) 1467–1475.
210. K.-J. Nogenmyr, C. Fureby, X.-S. Bai, P. Petersson, R. Collin, M. Linne, Large eddy simulation and laser diagnostic studies on a low swirl stratified premixed flame, Combustion and Flame 156 (1) (2009) 25–36.
211. K.-J. Nogenmyr, P. Petersson, X.-S. Bai, C. Fureby, R. Collin, A. Lantz, M. Linne, M. Alden, Structure and stabilization mechanism of a stratified premixed low swirl flame, Proceedings of the Combustion Institute 33 (1) (2011) 1567–1574.
212. E. Fooladgar, C. Chan, Effects of stratification on flame structure and pollutants of a swirl stabilized premixed combustor, Applied Thermal Engineering 124 (2017) 45–61.
213. P. Palies, M. Ilak, R. Cheng, Transient and limit cycle combustion dynamics analysis of turbulent premixed swirling flame, Journal of Fluid Mechanics 830 (2017) 681–707.
214. D. Yegian, R. Cheng, Development of a lean premixed low-swirl burner for low NOx practical applications, Combustion Science and Technology 139 (1) (1998) 207–227.
215. E. A. Luke, X.-L. Tong, J. Wu, L. Tang, P. Cinnella, A chemically reacting flow solver for generalized grids, AIAA Journal (2003).
216. E. A. Luke, T. George, Loci: A rule-based framework for parallel multi-disciplinary simulation synthesis, Journal of Functional Programming 15 (3) (2005) 477–502.
217. S. M. Candel, T. J. Poinsot, Flame stretch and the balance equation for the flame area, Combustion Science and Technology 70 (1–3) (1990) 1–15.
218. M. Matalon, On flame stretch, Combustion Science and Technology 31 (3–4) (1983) 169–181.

219. C. Law, Dynamics of stretched flames, in: Symposium (International) on Combustion, vol. 22, Elsevier, 1381–1402, 1989.
220. C. Law, C. Sung, Structure, aerodynamics, and geometry of premixed flamelets, Progress in Energy and Combustion Science 26 (4–6) (2000) 459–505.
221. S. Chung, D. Chung, C. Fu, P. Cho, Local extinction Karlovitz number for premixed flames, Combustion and flame 106 (4) (1996) 515–520.
222. E.-S. Cho, S. Chung, T. Oh, Local Karlovitz numbers at extinction for various fuels in counterflow premixed flames, Combustion science and technology 178 (9) (2006) 1559–1584.
223. C. Law, D. Zhu, G. Yu, Propagation and extinction of stretched premixed flames, in: Symposium (International) on Combustion, vol. 21, Elsevier, 1419–1426, 1988.
224. C. Wu, C. K. Law, On the determination of laminar flame speeds from stretched flames, in: Symposium (International) on Combustion, vol. 20, Elsevier, 1941–1949, 1985.
225. A. Fayoux, K. Zähringer, O. Gicquel, J.-C. Rolon, Experimental and numerical determination of heat release in counterflow premixed laminar flames, Proceedings of the Combustion Institute 30 (1) (2005) 251–257.
226. P.-H. Renard, D. Thevenin, J.-C. Rolon, S. Candel, Dynamics of flame/vortex interactions, Progress in energy and combustion science 26 (3) (2000) 225–282.
227. F. Egolfopoulos, P. Cho, C. Law, Laminar flame speeds of methane-air mixtures under reduced and elevated pressures, Combustion and flame 76 (3–4) (1989) 375–391.
228. C. Vagelopoulos, F. Egolfopoulos, C. Law, Further considerations on the determination of laminar flame speeds with the counterflow twin-flame technique, in: Symposium (international) on combustion, vol. 25, Elsevier, 1341–1347, 1994.
229. G. Andrews, D. Bradley, Determination of burning velocities: a critical review, Combustion and Flame 18 (1) (1972) 133–153.
230. H. Lee, L. Jiang, A. Mohamad, A review on the laminar flame speed and ignition delay time of Syngas mixtures, International Journal of Hydrogen Energy 39 (2) (2014) 1105–1121.
231. J. Botha, D. Spalding, The laminar flame speed of propane/air mixtures with heat extraction from the flame, in: Proc. R. Soc. Lond. A, vol. 225, The Royal Society, 71–96, 1954.
232. J. Tien, M. Matalon, On the burning velocity of stretched flames, Combustion and Flame 84 (3–4) (1991) 238–248.
233. S. Daniele, P. Jansohn, J. Mantzaras, K. Boulouchos, Turbulent flame speed for syngas at gas turbine relevant conditions, Proceedings of the Combustion Institute 33 (2) (2011) 2937–2944.
234. D. B. Spalding, Mathematical models of turbulent flames; a review, Combustion Science and Technology 13 (1–6) (1976) 3–25.
235. T. Mitani, Propagation velocities of two-reactant flames, Combustion Science and Technology 21 (3–4) (1980) 175–177.
236. P. Renard, J. Rolon, D. Thévenin, S. Candel, Investigation of heat release, extinction, and time evolution of the flame surface, for a nonpremixed flame interacting with a vortex, Comb. Flame 117 (1999) 189–205.
237. A. Brockhinke, A. Bülter, J. C. Rolon, K. Kohse-Höinghaus, ps-LIF measurements of minor species concentration in a counterflow diffusion flame interacting with a vortex, Applied Physics B 72 (4) (2001) 491–496.
238. P. Renard, D. Thévenin, J. Rolon, S. Candel, Dynamics of flame-vortex interactions, Prog. Energ. Combust. Sci. 26 (2000) 225–282.
239. M. Metghalchi, J. C. Keck, Laminar burning velocity of propane-air mixtures at high temperature and pressure, Combustion and flame 38 (1980) 143–154.
240. X. J. Gu, M. Z. Haq, M. Lawes, R. Woolley, Laminar burning velocity and Markstein lengths of methane–air mixtures, Combustion and flame 121 (1–2) (2000) 41–58.
241. N. Syred, J. Beer, Combustion in swirling flows: a review, Combustion and flame 23 (2) (1974) 143–201.
242. N. Peters, F. Williams, Coherent structures in turbulent combustion, in: The role of coherent structures in modelling turbulence and mixing, Springer, 364–393, 1981.
243. C. Coats, Coherent structures in combustion, Progress in Energy and Combustion Science 22 (5) (1996) 427–509.
244. C. Paschereit, E. Gutmark, W. Weisenstein, Coherent structures in swirling flows and their role in acoustic combustion control, Physics of fluids 11 (1999) 2667–2678.
245. L. Y. Gicquel, G. Staffelbach, T. Poinsot, Large eddy simulations of gaseous flames in gas turbine combustion chambers, Progress in Energy and Combustion Science 38 (6) (2012) 782–817.
246. J. Beer, N. Chigier, Combustion Aerodynamics, Elsevier Science, 1972.
247. N. Syred, A review of oscillation mechanisms and the role of the precessing vortex core (PVC) in swirl combustion systems, Progress in Energy and Combustion Science 32 (2006) 93–161.

248. J. O'Connor, Visualization of shear layer dynamics in a transversely forced flow and flame, Journal of Propulsion and Power 31 (4) (2015) 1127–1136.
249. C. Foley, I. Chterev, B. Noble, J. Seitzman, T. Lieuwen, Shear layer flame stabilization sensitivities in a swirling flow, International Journal of Spray and Combustion Dynamics 9 (1) (2017) 3–18.
250. J. Chen, H. Im, Correlation of flame speed with stretch in turbulent premixed methane/air flames, in: Symposium (International) on Combustion, vol. 27, Elsevier, 819–826, 1998.
251. P. Schmid, Dynamic mode decomposition of numerical and experimental data, Journal of Fluid Mechanics 656 (2010) 5–28.
252. P. Palies, T. Schuller, D. Durox, S. Candel, Modeling of premixed swirling flames transfer functions, Proceedings of the Combustion Institute 33 (2) (2011) 2967–2974.
253. P. Palies, D. Durox, T. Schuller, P. Morenton, S. Candel, Dynamics of premixed confined swirling flames, Comptes Rendus Mecanique 337 (6–7) (2009) 395–405.
254. B. Janus, A. Dreizler, J. Janicka, Experimental study on stabilization of lifted swirl flames in a model GT combustor, Flow, turbulence and combustion 75 (1–4) (2005) 293–315.
255. R. W. Schefer, D. Wicksall, A. Agrawal, Combustion of hydrogen-enriched methane in a lean premixed swirl-stabilized burner, Proceedings of the combustion institute 29 (1) (2002) 843–851.
256. H. S. Kim, V. K. Arghode, M. B. Linck, A. K. Gupta, Hydrogen addition effects in a confined swirl-stabilized methane-air flame, International Journal of Hydrogen Energy 34 (2) (2009) 1054–1062.
257. S. Taamallah, S. J. Shanbhogue, A. F. Ghoniem, Turbulent flame stabilization modes in premixed swirl combustion: Physical mechanism and Karlovitz number-based criterion, Combustion and Flame 166 (2016) 19–33.
258. S. Shanbhogue, Y. Sanusi, S. Taamallah, M. Habib, E. Mokheimer, A. Ghoniem, Flame macrostructures, combustion instability and extinction strain scaling in swirl-stabilized premixed CH4/H2 combustion, Combustion and Flame 163 (2016) 494–507.
259. L. Chong, T. Komarek, R. Kaess, S. Foller, W. Polifke, Identification of flame transfer functions from LES of a premixed swirl burner, in: ASME Paper GT2010-22769, ASME Turbo Expo 2010, Glasgow, Scotland, 2010.
260. P. Benard, G. Lartigue, V. Moureau, R. Mercier, Large-Eddy Simulation of the lean-premixed PRECCINSTA burner with wall heat loss, Proceedings of the Combustion Institute 37 (4) (2019) 5233–5243.
261. K. Kim, S. Hochgreb, The nonlinear heat release response of stratified lean-premixed flames to acoustic velocity oscillations, Combustion and Flame 158 (12) (2011) 2482–2499.
262. K.-J. Nogenmyr, H. Cao, C. Chan, R. Cheng, Effects of confinement on premixed turbulent swirling flame using large eddy simulation, Combustion Theory and Modelling 17 (6) (2013) 1003–1019.
263. T. Guiberti, L. Zimmer, D. Durox, T. Schuller, Experimental analysis of V-to M-shape transition of premixed CH4/H2/air swirling flames, in: ASME Turbo Expo 2013: Turbine Technical Conference and Exposition, American Society of Mechanical Engineers, 2013.
264. T. Guiberti, D. Durox, P. Scouflaire, T. Schuller, Impact of heat loss and hydrogen enrichment on the shape of confined swirling flames, Proceedings of the Combustion Institute 35 (2) (2015) 1385–1392.
265. H. S. Kim, V. K. Arghode, A. K. Gupta, Flame characteristics of hydrogen-enriched methane–air premixed swirling flames, International journal of hydrogen energy 34 (2) (2009) 1063–1073.
266. J. Burguburu, G. Cabot, B. Renou, A. M. Boukhalfa, M. Cazalens, Effects of H2 enrichment on flame stability and pollutant emissions for a kerosene/air swirled flame with an aeronautical fuel injector, Proceedings of the Combustion Institute 33 (2) (2011) 2927–2935.
267. M. Malanoski, M. Aguilar, D.-H. Shin, T. Lieuwen, Flame leading edge and flow dynamics in a swirling, lifted flame, Combustion Science and Technology 186 (12) (2014) 1816–1843.
268. P. Iudiciani, C. Duwig, Large eddy simulation of the sensitivity of vortex breakdown and flame stabilisation to axial forcing, Flow, Turbulence and Combustion 86 (3–4) (2011) 639–666.
269. D. Lacoste, J. Moeck, D. Durox, C. Laux, T. Schuller, Effect of nanosecond repetitively pulsed discharges on the dynamics of a swirl-stabilized lean premixed flame, Journal of Engineering for Gas Turbines and Power 135 (10) (2013) 101501.
270. S. Barbosa, G. Pilla, D. Lacoste, P. Scouflaire, S. Ducruix, C. O. Laux, D. Veynante, Influence of nanosecond repetitively pulsed discharges on the stability of a swirled propane/air burner representative of an aeronautical combustor, Phil. Trans. R. Soc. A 373 (2048) (2015) 20140335.
271. J. Nichols, Aeroacoustic post-processing with MapReduce, in: Center for Turbulence Research, Annual Research Briefs 2013, Stanford, USA, 2013.

272. L. Crocco, Aspects of Combustion Instability in Liquid Propellant Rocket Motors, J. Am. Rocket Soc. 21 (1951) 163–178.
273. A. P. Dowling, A kinematic model of ducted flame, Journal of Fluid Mechanics 394 (1999) 51–72.
274. N. Noiray, D. Durox, T. Schuller, S. Candel, A unified framework for nonlinear combustion instability analysis based on the flame describing function, Journal of Fluid Mechanics 615 (2008) 139–167.
275. W. Pun, S. Palm, F. Culick, Combustion dynamics of an acoustically forced flame, Combustion Science and Technology 175 (3) (2003) 499–521.
276. D. M. Kang, F. E. C. Culick, A. Ratner, Combustion dynamics of a low-swirl combustor, Combustion and Flame 151 (2007) 412–425.
277. J. Cooley, J. Tukey, An algorithm for the machine calculation of complex Fourier series, Mathematics of Computation 19 (90) (1965) 297–301.
278. J. Samaniego, B. Yip, T. Poinsot, S. Candel, Low-frequency combustion instability mechanisms in a side-dump combustor, Combustion and Flame 94 (4) (1993) 363–380, ISSN 0010-2180.
279. S. Wang, S. Hsieh, V. Yang, Unsteady flow evolution in swirl injector with radial entry. I. Stationnary conditions, Physics of Fluids 17 (045106) (2005).
280. D. Davis, P. Therkelsen, D. Littlejohn, R. Cheng, Effects of hydrogen on the thermo-acoustics coupling mechanisms of low-swirl injector flames in a model gas turbine combustor, Proceedings of the Combustion Institute 34 (2) (2013) 3135–3143, ISSN 1540-7489.
281. E. Motheau, F. Nicoud, T. Poinsot, Mixed acoustic-entropy combustion instabilities in gas turbines, Journal of Fluid Mechanics 749 (2014) 542–576.
282. G. Settles, Schlieren and Shadowgraph Techniques: Visualizing Phenomena in Transparent Media, Experimental Fluid Mechanics, Springer Berlin Heidelberg, ISBN 9783642566400, 2012.
283. M. Van Dyke, An Album of Fluid Motion, Parabolic Press, 1982.
284. G. Toker, Holographic Interferometry: A Mach–Zehnder Approach, CRC Press, 2016.
285. C. Lomas, Fundamentals of hot wire anemometry, Cambridge University Press, 2011.
286. R. Goldstein, Fluid Mechanics Measurements, Hemisphere Publishing Corporation, 1983.
287. A. Boutier, J.-M. Most, Laser Doppler Velocimetry, John Wiley & Sons, Inc., 33–138, 2012.
288. M. Riethmuller, L. David, B. Lecordier, Particle Image Velocimetry, John Wiley & Sons, Inc., 159–281, 2012.
289. H. G. Maas, A. Gruen, D. Papantoniou, Particle tracking velocimetry in three-dimensional flows, Experiments in Fluids 15 (2) (1993) 133–146.
290. J. Gregory, H. Sakaue, T. Liu, J. Sullivan, Fast Pressure-Sensitive Paint for Flow and Acoustic Diagnostics, Annual Review of Fluid Mechanics 46 (1) (2014) 303–330.
291. H. Iams, B. Salzberg, The Secondary Emission Phototube, Proceedings of the Institute of Radio Engineers 23 (1) (1935) 55–64.
292. J. W. Daily, Laser induced fluorescence spectroscopy in flames, Progress in Energy and Combustion Science 23 (2) (1997) 133–199, ISSN 0360-1285.
293. A. Lozano, B. Yip, R. K. Hanson, Acetone: a tracer for concentration measurements in gaseous flows by planar laser-induced fluorescence, Experiments in Fluids 13 (6) (1992) 369–376.
294. N. Chigier, Combustion Measurements, Combustion (Hemisphere Publishing Corporation), Taylor & Francis, 1991.
295. H. Albrecht, N. Damaschke, M. Borys, C. Tropea, Laser Doppler and Phase Doppler Measurement Techniques, Experimental Fluid Mechanics, Springer Berlin Heidelberg, ISBN 9783662051658, 2013.
296. C. Law, Dynamics of stretched flames, Proceedings of the Combustion Institute 22 (1988) 1381–1402.
297. C. Law, Combustion Physics, Cambridge University Press, 2010.
298. F. Egolfopoulos, Geometric and radiation effects on steady and unsteady strained laminar flames, in: Symposium (International) on Combustion, vol. 25, Elsevier, 1375–1381, 1994.
299. C. Rutland, J. Ferziger, Unsteady strained premixed laminar flames, Combustion science and technology 73 (1–3) (1990) 305–326.
300. C. A. Petrov, A. F. Ghoniem, The transient response of strained laminar-premixed flames, Combustion and flame 102 (3) (1995) 401–417.
301. F. Baillot, A. Bourehla, D. Durox, The characteristics method and cusped flame fronts, Combustion Science and Technology 112 (1) (1996) 327–350.
302. A. Bourehla, F. Baillot, Appearance and stability of a laminar conical premixed flame subjected to an acoustic perturbation, Combustion and flame 114 (3–4) (1998) 303–318.
303. D. Durox, F. Baillot, G. Searby, L. Boyer, On the shape of flames under strong acoustic forcing: a mean flow controlled by an oscillating flow, Journal of fluid mechanics 350 (1997) 295–310.

304. A. Birbaud, D. Durox, S. Candel, Upstream flow dynamics of a laminar premixed conical flame submitted to acoustic modulations, Combustion and Flame 146 (3) (2006) 541–552.
305. D. Durox, T. Schuller, N. Noiray, A. Birbaud, S. Candel, Rayleigh criterion and acoustic energy balance in unconfined self-sustained oscillating flames, Combustion and Flame 156 (2009) 106–119.
306. A.-L. Birbaud, S. Ducruix, D. Durox, S. Candel, The nonlinear response of inverted "V" flames to equivalence ratio nonuniformities, Combustion and flame 154 (3) (2008) 356–367.
307. Y. Marzouk, A. Ghoniem, H. Najm, Dynamic response of strained premixed flames to equivalence ratio gradients, Proceedings of the combustion institute 28 (2) (2000) 1859–1866.
308. P. Clavin, Dynamic behavior of premixed flame fronts in laminar and turbulent flows, Prog. Energy Combust. Sci. 11 (1985) 1–59.
309. T. Echekki, J. Chen, Unsteady strain rate and curvature effects in turbulent premixed methane-air flames, Combustion and Flame 106 (1–2) (1996) 184–202.
310. E. Hawkes, J. Chen, Comparison of direct numerical simulation of lean premixed methane–air flames with strained laminar flame calculations, Combustion and Flame 144 (1–2) (2006) 112–125.
311. H. Pitsch, Large-Eddy Simulation of turbulent combustion, Annual Review of Fluid Mechanics 38 (1) (2006) 453–482.
312. R. Mercier, Turbulent combustion modeling for Large Eddy Simulation of non-adiabatic stratified flames, Ph.D. thesis, Ecole Centrale Paris, 2015.
313. B. Fiorina, D. Veynante, S. Candel, Modeling Combustion Chemistry in Large Eddy Simulation of Turbulent Flames, Flow, Turbulence and Combustion 94 (1) (2015) 3–42.
314. K. Bray, Laminar Flamelets in Turbulent Combustion Modeling, Combustion Science and Technology 188 (9) (2016) 1372–1375.
315. D. G. Lilley, Turbulent swirling flame prediction, AIAA Journal 12 (2) (1974) 219–223.
316. D. G. Lilley, Modeling of combustor swirl flows, Acta Astronautica 1 (9–10) (1974) 1129–1147.
317. D. G. Lilley, Combustor swirl flow modeling, AIAA Journal 13 (4) (1975) 419–420.
318. D. Haworth, Progress in probability density function methods for turbulent reacting flows, Progress in Energy and Combustion Science 36 (2) (2010) 168–259.
319. O. Colin, F. Ducros, D. Veynante, T. Poinsot, A thickened flame model for large eddy simulations of turbulent premixed combustion, Physics of Fluids 12 (7) (2000) 1843–1863.
320. F. Charlette, C. Meneveau, D. Veynante, A power-law flame wrinkling model for LES of premixed turbulent combustion Part I: non-dynamic formulation and initial tests, Combustion and Flame 131 (1–2) (2002) 159–180.
321. F. Charlette, C. Meneveau, D. Veynante, A power-law flame wrinkling model for LES of premixed turbulent combustion Part II: dynamic formulation, Combustion and Flame 131 (1–2) (2002) 181–197.
322. V. Moureau, D. Domingo, L. Vervisch, From Large-Eddy Simulation to Direct Numerical Simulation of a lean premixed swirl flame: Filtered laminar flame-PDF modeling, Combustion and Flame 158 (7) (2011) 1340–1357.
323. B. Fiorina, R. Vicquelin, P. Auzillon, N. Darabiha, O. Gicquel, D. Veynante, A filtered tabulated chemistry model for LES of premixed combustion, Combustion and Flame 157 (3) (2010) 465–475.
324. P. Auzillon, R. Vicquelin, O. Gicquel, N. Darabiha, D. Veynante, B. Fiorina, A filtered tabulated chemistry model for large eddy simulation of reactive flows, in: 48th AIAA Aerospace Sciences Meeting Including the New Horizons Forum and Aerospace Exposition, 205, 2010.
325. D. Veynante, T. Schmitt, M. Boileau, V. Moureau, Analysis of dynamic models for turbulent premixed combustion, in: Proceedings of the Summer Program, vol. 387, Center for Turbulence Research, Stanford Univ./NASA-Ames, 2012.
326. B. Franzelli, E. Riber, B. Cuenot, Impact of the chemical description on a Large Eddy Simulation of a lean partially premixed swirled flame, Comptes Rendus Mécanique 341 (1–2) (2013) 247–256.
327. P. Wang, N. Platova, J. Fröhlich, U. Maas, Large eddy simulation of the PRECCINSTA burner, International Journal of Heat and Mass Transfer 70 (2014) 486–495.
328. N. Ansari, P. Strakey, G. Goldin, P. Givi, Filtered density function simulation of a realistic swirled combustor, Proceedings of the Combustion Institute 35 (2) (2015) 1433–1442.
329. J. Anker, D. Wunsch, L. Romagnosi, K. Claramunt, C. Hirsch, Development and Assessment of Combustion Models for Gas Turbine and Aero-Engine Applications, in: ASME Turbo Expo 2015: Turbine Technical Conference and Exposition, American Society of Mechanical Engineers, 2015.
330. R. Mercier, V. Moureau, D. Veynante, B. Fiorina, LES of turbulent combustion: on the consistency

between flame and flow filter scales, Proceedings of the Combustion Institute 35 (2) (2015) 1359–1366.
331. P. Wang, J. Fröhlich, U. Maas, Z.-x. He, C.-j. Wang, A detailed comparison of two sub-grid scale combustion models via large eddy simulation of the PRECCINSTA gas turbine model combustor, Combustion and Flame 164 (2016) 329–345.
332. P. S. Volpiani, T. Schmitt, D. Veynante, Large Eddy Simulation of a turbulent swirling premixed flame coupling the TFLES model with a dynamic wrinkling formulation, Combustion and Flame 180 (2017).
333. J.-M. Lourier, C. Eberle, B. Noll, M. Aigner, Influence of turbulence-chemistry interaction modeling on the structure and the stability of a swirl-stabilized flame, in: ASME Turbo Expo 2015: Turbine Technical Conference and Exposition, American Society of Mechanical Engineers, 2015.
334. J. Bell, M. Day, M. Lijewski, Simulation of nitrogen emissions in a premixed hydrogen flame stabilized on a low swirl burner, Proceedings of the Combustion Institute 34 (1) (2013) 1173–1182.
335. T. Plessing, C. Kortschik, N. Peters, M. Mansour, R. Cheng, Measurements of the turbulent burning velocity and the structure of premixed flames on a low-swirl burner, Proceedings of the Combustion Institute 28 (1) (2000) 359–366.
336. J. Bell, M. Day, A. Almgren, R. Cheng, I. Shepherd, Numerical simulation of premixed turbulent methane combustion, in: Computational Fluid and Solid Mechanics 2003, Elsevier, 1247–1250, 2003.
337. P. Petersson, J. Olofsson, C. Brackman, H. Seyfried, J. Zetterberg, M. Richter, M. Aldén, M. A. Linne, R. K. Cheng, A. Nauert, D. Geyer, A. Dreizler, Simultaneous PIV/OH-PLIF, Rayleigh thermometry/OH-PLIF and stereo PIV measurements in a low-swirl flame, Applied optics 46 (19) (2007) 3928–3936.
338. R. Cheng, D. Littlejohn, P. Strakey, T. Sidwell, Laboratory investigations of a low-swirl injector with H2 and CH4 at gas turbine conditions, Proceedings of the Combustion Institute 32 (2) (2009) 3001–3009.
339. M. Day, S. Tachibana, J. Bell, M. Lijewski, V. Beckner, R. Cheng, A combined computational and experimental characterization of lean premixed turbulent low swirl laboratory flames: I. Methane flames, Combustion and Flame 159 (1) (2012) 275–290.
340. M. Day, S. Tachibana, J. Bell, M. Lijewski, V. Beckner, R. Cheng, A combined computational and experimental characterization of lean premixed turbulent low swirl laboratory flames II. Hydrogen flames, Combustion and Flame 162 (5) (2015) 2148–2165.
341. Y. Minamoto, K. Aoki, M. Tanahashi, N. Swaminathan, DNS of swirling hydrogen-air premixed flames, International Journal of Hydrogen Energy 40 (39) (2015) 13604–13620.
342. D. Peitsch, Modelling the transient behaviour of jet engines, in: ASME Turbo Expo 2000: Power for Land, Sea, and Air, American Society of Mechanical Engineers Digital Collection, 2000.
343. C. Wang, Y.-G. Li, B.-Y. Yang, Transient performance simulation of aircraft engine integrated with fuel and control systems, Applied Thermal Engineering 114 (2017) 1029–1037.
344. T. J. Rosfjord, J. M. Cohen, Evaluation of the transient operation of advanced gas turbine combustors, Journal of Propulsion and Power 11 (3) (1995) 497–504.
345. A. Chaparro, B. Cetegen, Blowoff characteristics of bluff-body stabilized conical premixed flames under upstream velocity modulation, Combustion and Flame 144 (1) (2006) 318–335.
346. S. Chaudhuri, B. Cetegen, Blowoff characteristics of bluff-body stabilized conical premixed flames with upstream spatial mixture gradients and velocity oscillations, Combustion and Flame 153 (4) (2008) 616–633.
347. S. Kostka, A. Lynch, B. Huelskamp, B. Kiel, J. Gord, S. Roy, Characterization of flame-shedding behavior behind a bluff-body using proper orthogonal decomposition, Combustion and Flame 159 (9) (2012) 2872–2882.
348. S. Tuttle, S. Chaudhuri, S. Kostka, K. Kopp-Vaughan, T. Jensen, B. Cetegen, M. Renfro, Time-resolved blowoff transition measurements for two-dimensional bluff body-stabilized flames in vitiated flow, Combustion and Flame 159 (1) (2012) 291–305.
349. K. Kopp-Vaughan, T. Jensen, B. Cetegen, M. Renfro, Analysis of blowoff dynamics from flames with stratified fueling, Proceedings of the Combustion Institute 34 (1) (2013) 1491–1498, ISSN 1540-7489.
350. H. B. Ganji, R. Ebrahimi, Numerical estimation of blowout, flashback, and flame position in MIT micro gas-turbine chamber, Chemical Engineering Science 104 (2013) 857–867.
351. I. R. Sigfrid, R. Whiddon, R. Collin, J. Klingmann, Influence of reactive species on the lean blowout limit of an industrial DLE gas turbine burner, Combustion and Flame 161 (5) (2014) 1365–1373.
352. Q. An, W. Y. Kwong, B. D. Geraedts, A. M. Steinberg, Coupled dynamics of lift-off and precessing vortex

core formation in swirl flames, Combustion and Flame 168 (2016) 228–239.
353. P. C. Nassini, D. Pampaloni, A. Andreini, R. Meloni, Large-Eddy Simulation of Lean Blowoff in a premixed swirl-stabilized flame, GT2019-90856, Arizona, USA, 2019.
354. S. Chaudhuri, S. Kostka, S. Tuttle, M. Renfro, B. Cetegen, Blowoff mechanism of two dimensional bluff-body stabilized turbulent premixed flames in a prototypical combustor, Combustion and Flame 158 (7) (2011) 1358–1371.
355. K. Prieur, D. Durox, T. Schuller, S. Candel, Strong azimuthal combustion instabilities in a spray annular chamber with intermittent partial blow-off, Journal of Engineering for Gas Turbines and Power 140 (3) (2018) 031503.
356. S. Nair, T. Lieuwen, Near-Blowoff dynamics of a bluff-body stabilized flame, Journal of Propulsion and Power 23 (2) (2007) 421–427.
357. J. C. Broda, S. Seo, R. J. Santoro, G. Shirhattikar, V. Yang, An experimental study of combustion dynamics of a premixed swirl injector, Proceedings of the Combustion Institute 27 (1998) 1849–1856.
358. S. Seo, Parametric study of lean-premixed combustion instability in a pressurized model gas turbine combustor, Ph.D. thesis, The Pennsylvania State University, 1999.
359. Y. Huang, V. Yang, Bifurcation of flame structure in a lean-premixed swirl-stabilized combustor: transition from stable to unstable flame, Combustion and Flame 136 (2004) 383–389.
360. H. Gotoda, H. Nikimoto, T. Miyano, S. Tachibana, Dynamic properties of combustion instability in a lean premixed gas-turbine combustor, Chaos 21 (1) (2011).
361. P. Therkelsen, J. Enrique Portillo, D. Littlejohn, S. Martin, R. Cheng, Self-induced unstable behaviors of CH_4 and H_2/CH_4 flames in a model combustor with a low-swirl injector, Combustion and Flame 160 (2013) 307–321.
362. S. Taamallah, Z. LaBry, Shanbhogue, A. Ghoniem, Thermo-acoustic instabilities in lean premixed swirl-stabilized combustion and their link to acoustically coupled and decoupled flame macrostructures, Proceedings of the Combustion Institute 35 (2015) 3273–3282.
363. S. Nagaraja, K. Kedia, R. Sujith, Characterizing energy growth during combustion instabilities: Singularvalues or eigenvalues?, Proceedings of the Combustion Institute 32 (2009) 2933–2940.
364. P. Palies, D. Davis, R. Cheng, M. Ilak, Dynamic Mode Decomposition (DMD) Application to Premixed Low Swirl Injector Flames, in: 68^{th} Annual Meeting of the APS Division of Fluid Dynamics 60, 2015.
365. J.-F. Bourgouin, D. Durox, J. Moeck, T. Schuller, S. Candel, Self-Sustained Instabilities in an Annular Combustor Coupled by Azimuthal and Longitudinal Acoustic Modes, in: ASME Turbo Expo GT2013-95010, San Antonio, Texas, USA, 2013.
366. T. Sayadi, P. Schmid, F. Richecoeur, D. Durox, Parametrized data-driven decomposition for bifurcation analysis, with application to thermo-acoustically unstable systems, Physics of Fluids (2015) 037102.
367. Z. Labry, S. Taamallah, G. Kewlani, S. Shanbhogue, A. Ghoniem, Intermittency and Mode Transition in an Acoustically Uncoupled Lean Premixed Swirl-Stabilized Combustor, in: ASME Turbo Expo, GT2014-27266, 2014.
368. G. Bonciolini, D. Ebi, U. Doll, M. Weilenmann, N. Noiray, Effect of wall thermal inertia upon transient thermoacoustic dynamics of a swirl-stabilized flame, Proceedings of the Combustion Institute 37 (4) (2019) 5351–5358.
369. P. Palies, D. Durox, T. Schuller, S. Candel, Nonlinear combustion instability analysis based on the flame describing function applied to turbulent premixed swirling flames, Combustion and Flame 158 (2011) 1980–1991.
370. S. Taamallah, Z. LaBry, S. Shanbhogue, M. Habib, A. Ghoniem, Correspondence Between Stable Flame Macrostructure and Thermo-acoustic Instability in Premixed Swirl-Stabilized Turbulent Combustion, Journal of Engineering for Gas Turbines and Power 137 (7) (2015) 071505.
371. G. Richards, M. Yip, Oscillation combustion from a premix fuel nozzle, in: Combustion Institute/American Flame Research Committee Meeting, San Antonio, Texas, USA, 1995.
372. D. Straub, G. Richards, Effect of axial swirl vane location on combustion dynamics, in: ASME Turbo Expo, vol. 99-GT-109, Indianapolis, USA, 1999.
373. T. Komarek, W. Polifke, Impact of swirl fluctuations on the flame response of a perfectly premixed swirl burner, Journal of Engineering for Gas Turbine and Power 132 (061053) (2010).
374. C. M. Vagelopoulos, F. N. Egolfopoulos, Direct experimental determination of laminar flame speeds, in: Symposium (international) on combustion, vol. 27, Elsevier, 513–519, 1998.
375. N. Bouvet, C. Chauveau, I. Gökalp, S.-Y. Lee, R. J. Santoro, Characterization of syngas laminar flames using the Bunsen burner configuration, International Journal of Hydrogen Energy 36 (1) (2011) 992–1005.

376. B. Bédat, R. K. Cheng, Effects of buoyancy on premixed flame stabilization, Combustion and flame 107 (1–2) (1996) 13–26.
377. N. Karimi, M. J. Brear, S.-H. Jin, J. P. Monty, Linear and non-linear forced response of a conical, ducted, laminar premixed flame, Combustion and flame 156 (11) (2009) 2201–2212.
378. N. Noiray, D. Durox, T. Schuller, S. Candel, Passive control of combustion instabilities involving premixed flames anchored on perforated plates, Proceedings of the Combustion Institute 31 (1) (2007) 1283–1290.
379. K. M. Lyons, Toward an understanding of the stabilization mechanisms of lifted turbulent jet flames: experiments, Progress in Energy and Combustion Science 33 (2) (2007) 211–231.
380. M. S. Mansour, Stability characteristics of lifted turbulent partially premixed jet flames, Combustion and flame 133 (3) (2003) 263–274.
381. G. J. Smallwood, Ö. Gülder, D. R. Snelling, B. Deschamps, I. Gökalp, Characterization of flame front surfaces in turbulent premixed methane/air combustion, Combustion and Flame 101 (4) (1995) 461–470.
382. Ö. Gülder, G. J. Smallwood, R. Wong, D. Snelling, R. Smith, B. Deschamps, J.-C. Sautet, Flame front surface characteristics in turbulent premixed propane/air combustion, Combustion and Flame 120 (4) (2000) 407–416.
383. A. Boukhalfa, I. Gökalp, Influence of the Damköhler number on the average thickness of conical turbulent premixed methane/air flames, Combustion and flame 73 (1) (1988) 75–87.
384. R. Cheng, I. Shepherd, The influence of burner geometry on premixed turbulent flame propagation, Combustion and Flame 85 (1–2) (1991) 7–26.
385. E. E. Zukoski, Flame stabilization on bluff bodies at low and intermediate Reynolds numbers, Ph.D. thesis, California Institute of Technology, 1954.
386. K. Kundu, D. Banerjee, D. Bhaduri, Theoretical analysis on flame stabilization by a bluff-body, Combustion Science and Technology 17 (3–4) (1977) 153–162.
387. D. Michaels, A. F. Ghoniem, Impact of the bluff-body material on the flame leading edge structure and flame–flow interaction of premixed CH4/air flames, Combustion and Flame 172 (2016) 62–78.
388. S. Chaudhuri, S. Kostka, M. W. Renfro, B. M. Cetegen, Blowoff dynamics of bluff body stabilized turbulent premixed flames, Combustion and flame 157 (4) (2010) 790–802.
389. J. Kariuki, J. R. Dawson, E. Mastorakos, Measurements in turbulent premixed bluff body flames close to blow-off, Combustion and flame 159 (8) (2012) 2589–2607.
390. A. Chaparro, E. Landry, B. M. Cetegen, Transfer function characteristics of bluff-body stabilized, conical V-shaped premixed turbulent propane–air flames, Combustion and flame 145 (1–2) (2006) 290–299.
391. W. Kim, M. G. Mungal, M. A. Cappelli, The role of in situ reforming in plasma enhanced ultra lean premixed methane/air flames, Combustion and Flame 157 (2) (2010) 374–383.
392. H. El-Rabii, K. Zähringer, J.-C. Rolon, F. Lacas, Laser ignition in a lean premixed prevaporized injector, Combustion science and technology 176 (9) (2004) 1391–1417.
393. M. Cordier, A. Vandel, G. Cabot, B. Renou, A. Boukhalfa, Laser-induced spark ignition of premixed confined swirled flames, Combustion Science and Technology 185 (3) (2013) 379–407.
394. T. Komarek, W. Polifke, Impact of swirl fluctuations on the flame response of a perfectly premixed swirl burner, Journal of Engineering for Gas Turbine and Power 132 (061053).
395. P. Palies, T. Schuller, D. Durox, L. Gicquel, S. Candel, Acoustically perturbed turbulent swirling flames, Physics of Fluids 23 (3) (2011) 037101.
396. P. Palies, D. Durox, T. Schuller, S. Candel, The combined dynamics of swirler and turbulent premixed swirling flames, Combustion and Flame 157 (9) (2010) 1698–1717.
397. T. Schuller, D. Durox, P. Palies, S. Candel, Acoustic decoupling of longitudinal modes in generic combustion systems, Combustion and Flame 159 (5) (2012) 1921–1931.
398. X. Han, J. Li, A. Morgans, Prediction of combustion instability limit cycle oscillations by combining flame describing function simulations with a thermoacoustic network model, Combustion and Flame 162 (10) (2015) 3632–3647.
399. P. Wolf, G. Staffelbach, L. Gicquel, J.-D. Müller, T. Poinsot, Acoustic and large eddy simulation studies of azimuthal modes in annular combustion chambers, Combustion and Flame 159 (11) (2012) 3398–3413.
400. S. Roux, G. Lartigue, T. Poinsot, T. Bérat, Studies of mean and unsteady flow in a swirled combustor using experiments, acoustic analysis and large eddy simulations, Combust. & Flame 141 (1–2) (2005) 40–54.
401. A. Ghani, L. Gicquel, T. Poinsot, Acoustic analysis of a liquid fuel swirl combustor using dynamic mode decomposition, in: ASME Turbo Expo 2015:

Turbine Technical Conference and Exposition, American Society of Mechanical Engineers, 2015.
402. E. Motheau, Y. Méry, F. Nicoud, T. Poinsot, Analysis and modeling of entropy modes in a realistic aeronautical gas turbine, Journal of Engineering for Gas Turbines and Power 135 (9) (2013) 092602.
403. C. F. Silva, F. Nicoud, T. Schuller, D. Durox, S. Candel, Combining a Helmholtz solver with the flame describing function to assess combustion instability in a premixed swirled combustor, Combustion and Flame 160 (9) (2013) 1743–1754.
404. C. Kraus, S. Harth, H. Bockhorn, Experimental investigation of combustion instabilities in lean swirl-stabilized partially-premixed flames in single-and multiple-burner setup, International Journal of Spray and Combustion Dynamics 8 (1) (2016) 4–26.
405. J. Blimbaum, M. Zanchetta, T. Akin, V. Acharya, J. O'Connor, D. Noble, T. Lieuwen, Transverse to longitudinal acoustic coupling processes in annular combustion chambers, International Journal of Spray and Combustion Dynamics 4 (4) (2012) 275–297.
406. A. Saurabh, C. O. Paschereit, Combustion instability in a swirl flow combustor with transverse extensions, in: ASME Turbo Expo 2013: Turbine Technical Conference and Exposition, American Society of Mechanical Engineers, 2013.
407. K. Thomson, Time dependent boundary conditions for hyperbolic systems, J. Comput. Phys. 68 (1987) 1–24.
408. T. Poinsot, S. Lele, Boundary conditions for direct numerical simulations of compressible viscous flows, J. Comp. Phys. 101 (1992) 104–129.
409. A. Kaufmann, F. Nicoud, T. Poinsot, Flow forcing techniques for numerical simulation of combustion instabilities, Combustion and Flame 131 (2002) 371–385.
410. S. Ducruix, S. Candel, External Flow Modulation in Computational Fluid Dynamics, AIAA Journal 42 (8) (2004) 1550–1558.
411. L. Selle, F. Nicoud, T. Poinsot, Actual Impedance for Nonreflecting Boundary Conditions: Implications for Computation of Resonators, AIAA Journal 42 (5) (2004) 958–964.
412. B. D. Bellows, M. K. Bobba, A. Forte, J. M. Seitzman, T. Lieuwen, Flame transfer function saturation mechanisms in a swirl-stabilized combustor, Proceedings of the Combustion Institute 31 (2007) 3181–3188.
413. B. D. Bellows, M. K. Bobba, J. M. Seitzman, T. Lieuwen, Nonlinear flame transfer function characteristics in a swirl-stabilized combustor, Journal of Engineering for Gas Turbines and Power 129 (4) (2007) 954–961.
414. C. Külsheimer, H. Büchner, Combustion dynamics of turbulent swirling flames, Combustion and Flame 131 (2002) 70–84.
415. D. Kim, J. G. Lee, B. D. Quay, D. Santavicca, K. Kim, S. Srinivasan, Effect of flame structure on the flame transfer function in a premixed gas turbine combustor, Journal of Engineering for Gas Turbines and Power 132 (2) (2010) 757–765.
416. S. Thumuluru, H. Ma, T. Lieuwen, Measurements of the flame response to harmonic excitation in a swirl combustor, AIAA Journal (2012).
417. G. Borghesi, F. Biagioli, B. Schuermans, Dynamic response of turbulent swirling flames to acoustic perturbations, Combustion Theory and Modelling 13 (3) (2009) 487–512.
418. B. D. Bellows, Q. Zhang, Y. Neumeier, T. Lieuwen, B. Zinn, Forced response studies of a premixed flame to flow disturbances in a gas turbine combustor, in: AIAA-2003-824, Aerospace Sciences Meeting and Exhibit, Reno, NV, 2003.
419. K. Kim, H. Lee, J. Lee, B. Quay, D. Santavicca, Flame transfer function measurements and instability frequency prediction using a thermoacoustic model, in: ASME Paper GT2009-60026, Proceedings of ASME Turbo Expo 2009, Orlando, USA, 2009.
420. K. Kim, J. Lee, H. Lee, B. Quay, D. Santavicca, Characterization of forced flame response of swirl-stabilized turbulent lean-premixed flames in a gas turbine combustor, Journal of Engineering Gas Turbines and Power 132 (2010) 4.
421. K. T. Kim, D. Santavicca, Generalization of turbulent swirl flame transfer functions in gas turbine combustors, Combustion Science and Technology 185 (7) (2013) 999–1015.
422. A. Gentemann, C. Hirsch, K. Kunze, F. Kiesewetter, T. Sattelmayer, W. Polifke, Validation of flame transfer function reconstruction for perfectly premixed swirl flames, in: ASME Paper GT2004-53776, ASME Turbo Expo 2004, Vienna, Austria, 2004.
423. C. Hirsch, D. Fanaca, P. Reddy, W. Polifke, T. Sattelmayer, Influence of the swirler design on the flame transfer function of premixed flames, in: ASME Paper GT2005-68195, ASME Turbo Expo 2005, Nevada, USA, 2005.
424. P. Palies, D. Durox, T. Schuller, S. Candel, Experimental study on effects of swirler geometry and swirl number on flame describing functions, Combustion Science and Technology 183 (2011) 704–717.
425. S. Terhaar, B. Cosic, C. Pashereit, K. Oberleithner, Impact of Shear Flow Instabilities on the Magnitude and Saturation of the Flame Response,

Journal of Engineering for Gas Turbines and Power 136 (071502) (2014).
426. B. D. Bellows, Y. Neumeier, T. Lieuwen, Forced response of a swirling, premixed flame to flow disturbances, Journal of Propulsion and Power 22 (5) (2006) 1075–1084.
427. I. Yilmaz, A. Ratner, M. Ilbas, Y. Huang, Experimental investigation of thermoacoustic coupling using blended hydrogen-methane fuels in a low swirl burner, International Journal of Hydrogen Energy 35 (1) (2010) 329–336.
428. K. Kim, S. Hochgreb, Measurements of triggering and transient growth in a model lean-premixed gas turbine combustor, Combustion and Flame 159 (3) (2012) 1215–1227.
429. C. Stone, S. Menon, Swirl control of combustion instabilities in a gas turbine combustor, Proceedings of the Combustion Institute 29 (2002) 155–160.
430. S. Schimek, J. Moeck, C. Paschereit, An experimental investigation of the nonlinear response of an atmospheric swirl-stabilized premixed flame, in: ASME Paper GT2010-22827, ASME Turbo Expo 2010, Glasgow, Scotland, 2010.
431. N. A. Bunce, Flame transfer function measurements and mechanisms in a single-nozzle combustor, Ph.D. thesis, 2013.
432. N. Bunce, J. G. Lee, B. D. Quay, D. A. Santavicca, Mixture-forced flame transfer function measurements and mechanisms in a single-nozzle combustor at elevated pressure, in: ASME 2011 Turbo Expo: Turbine Technical Conference and Exposition, American Society of Mechanical Engineers, 1317–1326, 2011.
433. Z. Han, S. Hochgreb, The response of stratified swirling flames to acoustic forcing: Experiments and comparison to model, Proceedings of the Combustion Institute 35 (3) (2015) 3309–3315.
434. M. Gatti, R. Gaudron, C. Mirat, T. Schuller, Effects of the Injector Design on the Transfer Function of Premixed Swirling Flames, in: ASME Turbo Expo 2017: Turbomachinery Technical Conference and Exposition, American Society of Mechanical Engineers, 2017.
435. F. Di Sabatino, T. Guiberti, W. Boyette, W. Roberts, J. Moeck, D. Lacoste, Effect of pressure on the transfer functions of premixed methane and propane swirl flames, Combustion and Flame 193 (2018) 272–282.
436. F. Di Sabatino, T. Guiberti, J. Moeck, W. Roberts, D. Lacoste, Influence of the laminar burning velocity on the transfer function of premixed methane and propane swirl flames, in: ASME Turbo Expo 2019 GT2019-90870, 2019.
437. J. A. Ranalli, C. R. Martin, P. R. Black, U. Vandsburger, R. West, Measurement of Flame Transfer Functions in Swirl-Stabilized, Lean-Premixed Combustion, Journal of Propulsion and Power 25 (6) (2009) 1350–1354.
438. B. Ćosić, S. Terhaar, J. Moeck, C. Paschereit, Response of a swirl-stabilized flame to simultaneous perturbations in equivalence ratio and velocity at high oscillation amplitudes, Combustion and Flame 162 (4) (2015) 1046–1062.
439. K. Kim, J. Lee, B. Quay, D. Santavicca, Response of partially premixed flames to acoustic velocity and equivalence ratio perturbations, Combustion and Flame 157 (9) (2010) 1731–1744.
440. B. Schuermans, F. Guethe, D. Pennell, D. Guyot, C. Paschereit, Thermoacoustic modeling of a gas turbine using transfer functions measured under full engine pressure, Journal of Engineering for Gas Turbines and Power 132 (11) (2010) 111503.
441. J. O'Connor, V. Acharya, Development of a flame transfer function framework for transversely forced flames, in: ASME Turbo Expo 2013: Turbine Technical Conference and Exposition, American Society of Mechanical Engineers, 2013.
442. M. Malanoski, M. Aguilar, V. Acharya, T. Lieuwen, Dynamics of a transversely excited swirling, lifted flame: Part I-Experiments and data analysis, in: ASME Turbo Expo 2013: Turbine Technical Conference and Exposition, American Society of Mechanical Engineers, 2013.
443. M. Hauser, M. Wagner, T. Sattelmayer, Transformation of transverse acoustic velocity of the burner approach flow into flame dynamics, in: ASME Turbo Expo 2012: Turbine Technical Conference and Exposition, American Society of Mechanical Engineers, 803–814, 2012.
444. M. Aguilar, M. Malanoski, G. Adhitya, B. Emerson, V. Acharya, D. Noble, T. Lieuwen, Helical flow disturbances in a multinozzle combustor, Journal of Engineering for Gas Turbines and Power 137 (9) (2015).
445. T. E. Smith, I. P. Chterev, B. L. Emerson, D. R. Noble, T. C. Lieuwen, Comparison of single and multinozzle reacting swirl flow dynamics, Journal of Propulsion and Power 34 (2) (2017) 384–394.
446. A. Saurabh, J. P. Moeck, C. O. Paschereit, Swirl flame response to simultaneous axial and transverse velocity fluctuations, Journal of Engineering for Gas Turbines and Power 139 (6) (2017) 061502.
447. C. Mirat, D. Durox, T. Schuller, Analysis of the spray and transfer function of swirling spray flames from a multi-jet steam assisted liquid fuel injector, in: ASME Turbo Expo 2014: Turbine

Technical Conference and Exposition, American Society of Mechanical Engineers, 2014.
448. M. T. Szedlmayer, B. D. Quay, J. Samarasinghe, A. De Rosa, J. G. Lee, D. A. Santavicca, Forced flame response of a lean premixed multi-nozzle can combustor, in: ASME Paper No. GT2011-46080, 2011.
449. C. Smith, CFD assessment of passive and active control strategies for lean, premixed combustors, in: 37th Aerospace Sciences Meeting and Exhibit, 714, 1999.
450. S. Hermeth, Mechanisms affecting the dynamic response of swirled flames in gas turbines, Ph.D. thesis, INPT, 2012.
451. S. Hermeth, G. Staffelbach, L. Gicquel, T. Poinsot, LES evaluation of the effects of equivalence ratio fluctuations on the dynamic flame response in a real gas turbine combustion chamber, Proceedings of the Combustion Institute 34 (2) (2013) 3165–3173.
452. H. Krediet, C. Beck, W. Krebs, S. Schimek, C. Paschereit, J. Kok, Identification of the flame describing function of a premixed swirl flame from LES, Combustion Science and Technology 184 (7–8) (2012) 888–900.
453. H. Krediet, C. Beck, W. Krebs, J. Kok, Saturation mechanism of the heat release response of a premixed swirl flame using LES, Proceedings of the Combustion Institute 34 (1) (2013) 1223–1230.
454. V. Acharya, T. Lieuwen, Effect of azimuthal flow fluctuations on flow and flame dynamics of axisymmetric swirling flames, Physics of Fluids 27 (3) (2015) 105106.
455. L. Rofi, G. Campa, V. Anisimov, F. Daccá, E. Bertolotto, E. Gottardo, F. Bonzani, Numerical procedure for the investigation of combustion dynamics in industrial gas turbines: LES, RANS and thermoacoustics, in: ASME Turbo Expo 2015: Turbine Technical Conference and Exposition, American Society of Mechanical Engineers, 2015.
456. A. Andreini, B. Facchini, A. Innocenti, M. Cerutti, Flame transfer function identification and thermoacoustic analysis of an annular heavy-duty gas turbine combustor, in: 22nd International Congress on Sound and Vibrations, 2015.
457. A. Ghani, T. Poinsot, L. Gicquel, J.-D. Müller, LES study of transverse acoustic instabilities in a swirled kerosene/air combustion chamber, Flow, Turbulence and Combustion 96 (1) (2016) 207–226.
458. F. Biagioli, A. Scarpato, K. Syed, Dynamic response of swirl stabilized turbulent premixed flames based on the Helmholtz-Hodge velocity decomposition, Flow, Turbulence and Combustion 96 (4) (2016) 1005–1022.
459. A. Innocenti, A. Andreini, B. Facchini, A. Peschiulli, Numerical analysis of the dynamic flame response of a spray flame for aero-engine applications, International Journal of Spray and Combustion Dynamics 9 (4) (2017) 310–329.
460. L. Tay-Wo-Chong, A. Scarpato, W. Polifke, LES Combustion Model With Stretch and Heat Loss Effects for Prediction of Premix Flame Characteristics and Dynamics, in: ASME Turbo Expo 2017: Turbomachinery Technical Conference and Exposition, American Society of Mechanical Engineers, 2017.
461. D. Laera, A. Morgans, Large Eddy Simulations for the flame describing function of a premixed turbulent swirling flame.
462. N. Worth, J. Dawson, Modal dynamics of self-excited azimuthal instabilities in an annular combustion chamber, Combustion and Flame 160 (11) (2013) 2476–2489.
463. M. Bauerheim, G. Staffelbach, N. A. Worth, J. Dawson, L. Y. Gicquel, T. Poinsot, Sensitivity of LES-based harmonic flame response model for turbulent swirled flames and impact on the stability of azimuthal modes, Proceedings of the Combustion Institute 35 (3) (2015) 3355–3363.
464. Y. Xia, A. Morgans, W. Jones, Simulating flame response to acoustic excitation for an industrial gas turbine combustor, in: 24th International Congress on Sound and Vibration, ICSV 2017, 2017.
465. D. Pampaloni, A. Andreini, B. Facchini, C. O. Paschereit, Large-Eddy-Simulation Modeling of the Flame Describing Function of a Lean-Premixed Swirl-Stabilized Flame, Journal of Propulsion and Power (2019) 1–11.
466. D. You, Y. Huang, V. Yang, A generalized model of acoustic response of turbulent premixed flame and its application to gas-turbine combustion instability analysis, Combustion Science and Technology 177 (2005) 1109–1150.
467. G. H. Markstein, Nonsteady flame propagation: AGARDograph, vol. 75, Elsevier, 1964.
468. V. Acharya, D.-H. Shin, T. Lieuwen, Premixed flames excited by helical disturbances: Flame wrinkling and heat release oscillations, Journal of Propulsion and Power 29 (6) (2013) 1282–1291.
469. V. Acharya, T. Lieuwen, Response of non-axisymmetric premixed, swirl flames to helical disturbances, in: ASME Turbo Expo 2014: Turbine Technical Conference and Exposition, American Society of Mechanical Engineers, 2014.
470. V. Acharya, M. Malanoski, M. Aguilar, T. Lieuwen, Dynamics of a transversely excited swirling, lifted flame: flame response modeling and comparison

with experiments, Journal of Engineering for Gas Turbines and Power 136 (5) (2014) 051503.
471. V. Acharya, D.-H. Shin, T. Lieuwen, et al., Swirl effects on harmonically excited, premixed flame kinematics, Combustion and Flame 159 (3) (2012) 1139–1150.
472. S. Wang, V. Yang, Unsteady flow evolution in swirl injector with radial entry. II. External excitations, Physics of Fluids 17 (045107) (2005).
473. N. Cumpsty, F. Marble, The interaction of entropy fluctuations with turbine blade rows; a mechanism of turbojet engine noise, Proceedings of the Royal Society London Series A 357 (1977) 323–344.
474. T. Poinsot, A. Trouve, D. Veynante, S. Candel, E. Esposito, Vortex-driven acoustically coupled combustion instabilities, Journal of Fluid Mechanics 177 (1987) 265–292.
475. K. Yu, A. Trouvé, J. Daily, Low-frequency pressure oscillations in a model ramjet combustor, Journal of Fluid Mechanics 232 (1991) 47–72.
476. C. Paschereit, E. Gutmark, W. Weisenstein, Excitation of thermoacoustic instabilities by interaction of acoustics and unstable swirling flow, AIAA Journal 38 (6) (2000) 1025–1034.
477. J. Keller, Thermoacoustic oscillations in combustion chambers of gas turbines, AIAA Journal 33 (12) (1995) 2280–2287.
478. A. Sengissen, J. Van Kampen, R. Huls, G. Stoffels, J. Kok, T. Poinsot, LES and experimental studies of cold and reacting flow in a swirled partially premixed burner with and without fuel modulation, Combustion and Flame 150 (2007) 40–53.
479. P. Weigand, W. Meier, X. Duan, W. Stricker, M. Aigner, Investigations of swirl flames in a gas turbine model combustor I. Flow field, structures, temperature, and species distributions, Combustion and Flame 144 (2006) 205–224.
480. S. Lee, S. Seo, J. Broda, S. Pal, R. Santoro, An experimental estimation of mean rate and flame structure during combustion instability in a lean premixed gas turbine combustor, Proceedings of the Combustion Institute 28 (2000) 775–782.
481. S. Ishizuka, T. Murakami, T. Hamasaki, K. Koumura, R. Hasegawa, Flame speeds in combustible vortex rings, Combustion and Flame 113 (1998) 542–553.
482. G. Haller, An objective definition of a vortex, J. Fluid. Mech. 525 (2005) 1–26.
483. K. Kim, D. Santavicca, Interference mechanisms of acoustic/convective disturbances in a swirl-stabilized lean-premixed combustor, Combustion and Flame 160 (8) (2013) 1441–1457.
484. V. Caux-Brisebois, A. Steinberg, C. Arndt, W. Meier, Thermo-acoustic velocity coupling in a swirl stabilized gas turbine model combustor, Combustion and Flame 161 (2014) 3166–3180.
485. K. Kim, D. Santavicca, Interference mechanisms of acoustic-convective disturbances in a swirl-stabilized lean premixed combustor, Combustion and Flame 160 (8) (2013) 1441–1457.
486. A. De Rosa, S. Peluso, B. Quay, D. Santavicca, The effect of confinement on the structure and dynamic response of lean-premixed, swirl-stabilized flames, Journal of Engineering for Gas Turbines and Power 138 (6) (2016) 061507.
487. J. P. Moeck, J.-F. Bourgouin, D. Durox, T. Schuller, S. Candel, Nonlinear interaction between a precessing vortex core and acoustic oscillations in a turbulent swirling flame, Combustion and Flame 159 (8) (2012) 2650–2668.
488. J. O'Connor, T. Lieuwen, Recirculation zone dynamics of a transversely excited swirl flow and flame, Physics of fluids 24 (7) (2012) 2893–2900.
489. S. Alekseenko, V. Dulin, Y. Kozorezov, D. Markovich, Effect of high-amplitude forcing on turbulent combustion intensity and vortex core precession in a strongly swirling lifted propane/air flame, Combustion Science and Technology 184 (10–11) (2012) 1862–1890.
490. S. Wang, X. Liu, G. Wang, L. Xu, L. Li, Y. Liu, Z. Huang, F. Qi, High-repetition-rate burst-mode-laser diagnostics of an unconfined lean premixed swirling flame under external acoustic excitation, Applied Optics 58 (10) (2019).
491. M. L. Munjal, Acoustics of Ducts and Mufflers, John Wiley & Sons, Inc., New York, 1987.
492. S. Stow, A. Dowling, Thermoacoustic oscillations in an annular combustor, in: ASME paper GT2001-0037, 2001.
493. F. Nicoud, L. Benoit, C. Sensiau, T. Poinsot, Acoustic Modes in Combustors with Complex Impedances and Multidimensionnal Active Flames, AIAA Journal 45 (2) (2007).
494. B. Schuermans, F. Guethe, D. Pennel, D. Guyot, C. Paschereit, Thermoacoustic modeling of a gas turbine using transfer functions measured at full engine pressure, in: ASME paper GT2009-59605, ASME Turbo Expo 2009, Florida, USA, 2009.
495. L. Selle, G. Lartigue, T. Poinsot, R. Koch, K. Schildmacher, W. Krebs, B. Prade, P. Kaufmann, D. Veynante, Compressible large eddy simulation of turbulent combustion in complex geometry on unstructured meshes, Combustion and Flame 137 (2004) 489–505.
496. M. Bauerheim, F. Nicoud, T. Poinsot, Progress in analytical methods to predict and control

azimuthal combustion instability modes in annular chambers, Physics of Fluids 28 (2) (2016) 021303.

497. D. Durox, J. P. Moeck, J.-F. Bourgouin, P. Morenton, M. Viallon, T. Schuller, S. Candel, Flame dynamics of a variable swirl number system and instability control, Combustion and Flame 160 (9) (2013) 1729–1742.
498. R. Kulkarni, F. Nicoud, Predicting the amplitude of limit cycles by using a Helmholtz solver, in: International Summer School and Workshop on Non-Normal and Nonlinear Effects in Aero and Thermoacoustics, Technische Universitat Munchen, Munchen, Germany, 17-20 May 2010.
499. D. Laera, S. Camporeale, A Weakly Nonlinear Approach Based on a Distributed Flame Describing Function to Study the Combustion Dynamics of a Full-Scale Lean-Premixed Swirled Burner, Journal of Engineering for Gas Turbines and Power 139 (0742-4795) (2017).
500. F. Nicoud, T. Poinsot, Thermoacoustic instabilities: Should the Rayliegh criterion be extended to include entropy changes, Comb. & Flame 142 (2005) 153–159.
501. F. E. C. Culick, Unsteady motions in combustion chambers for propulsion systems, AGARDograph, NATO/RTO-AG-AVT-039, 2006.
502. M. Zellhuber, J. Schwing, B. Schuermans, T. Sattelmayer, W. Polifke, Experimental and Numerical Investigation of Thermoacoustic Sources Related to High-Frequency Instabilities, International Journal of Spray and Combustion Dynamics 6 (1) (2014) 1–34.
503. J. Apeloig, F. d'Herbigny, F. Simon, P. Gajan, M. Orain, S. Roux, Liquid-Fuel Behavior in an Aeronautical Injector Submitted to Thermoacoustic Instabilities, Journal of Propulsion and Power (2015).
504. M. Bauerheim, P. Salas, F. Nicoud, T. Poinsot, Symmetry breaking of azimuthal thermo-acoustic modes in annular cavities: a theoretical study, Journal of Fluid Mechanics 760 (2014) 431–465.
505. G. Lartigue, U. Meier, C. Bérat, Experimental and numerical investigation of self-excited combustion oscillations in a scaled gas turbine combustor, Applied Thermal Engineering 24 (11) (2004) 1583–1592, industrial Gas Turbine Technologies.
506. P. M. Allison, Y. Chen, M. Ihme, J. F. Driscoll, Coupling of flame geometry and combustion instabilities based on kilohertz formaldehyde PLIF measurements, Proceedings of the Combustion Institute 35 (3) (2015) 3255–3262.
507. K.-U. Schildmacher, A. Hoffmann, L. Selle, R. Koch, C. Schulz, H.-J. Bauer, T. Poinsot, W. Krebs, B. Prade, Unsteady flame and flow field interaction of a premixed model gas turbine burner, Proceedings of the Combustion Institute 31 (2) (2007) 3197–3205.
508. A. Cochet, V. Bodoc, C. Brossard, D. O., C. Guin, M. Lecourt, R. Orain, A. Vincent-Randonnier, ONERA test Facilities for Combustion in Aero Gas Turbine Engines, and Associated Optical Diagnostics, Journal Aerospace Lab (AL11-01), challenges in combustion for aerospace propulsion.
509. N. Fdida, C. Brossard, A. Vincent-Randonnier, D. Gaffié, Characterization of the kerosene spray in a swirl-stabilized flame, in: 16^{th} Int Symp on Applications of Laser Techniques to Fluid Mechanics, lisbon, Portugal, July 09–12, 2012, 2012.
510. F. Richecoeur, T. Schuller, A. Lamraoui, S. Ducruix, Analytical and experimental investigations of gas turbine model combustor acoustics operated at atmospheric pressure, Comptes Rendus Mécanique 341 (1) (2013) 141–151.
511. C. Huang, R. Gejji, W. Anderson, C. Yoon, V. Sankaran, Combustion Dynamics Behavior in a Single-Element Lean Direct Injection (LDI) Gas Turbine Combustor, in: AIAA Propulsion and Energy (AIAA 2014-3433), 2014.
512. C. Kraus, S. Harth, H. Bockhorn, Experimental investigation of combustion instabilities in lean swirl-stabilized partially-premixed flames in single- and multiple-burner setup, International Journal of Spray and Combustion Dynamics 8 (1) (2016) 4–26.
513. C. Kraus, L. Selle, T. Poinsot, C. Arndt, H. Bockhorn, Influence of heat transfer and material temperature on combustion instabilities in a swirl burner, Journal of Engineering for Gas Turbines and Power 139 (5) (2017) 051503.
514. J. Samarasinghe, W. Culler, B. D. Quay, D. A. Santavicca, J. O'Connor, The Effect of Fuel Staging on the Structure and Instability Characteristics of Swirl-Stabilized Flames in a Lean Premixed Multinozzle Can Combustor, Journal of Engineering for Gas Turbines and Power 139 (12) (2017) 121504.
515. S. Roy, T. Yi, N. Jiang, G. Gunaratne, I. Chterev, B. Emerson, T. Lieuwen, A. Caswell, J. Gord, Dynamics of robust structures in turbulent swirling reacting flows, Journal of Fluid Mechanics 816 (2017) 554–585.
516. E. Karlis, Y. Hardalupas, A. M. Taylor, J. Rogerson, S. Sadasivuni, M. Stöhr, U. Stopper, Thermoacoustic phenomena in an industrial gas

turbine combustor at two different mean pressures, in: AIAA Scitech 2019 Forum, 0675, 2019.
517. E. Karlis, Y. Liu, Y. Hardalupas, A. M. Taylor, H_2 enrichment of CH_4 blends in lean premixed gas turbine combustion: An experimental study on effects on flame shape and thermoacoustic oscillation dynamics, Fuel 254 (2019) 115524.
518. S. Tachibana, K. Saito, T. Yamamoto, M. Makida, T. Kitano, R. Kurose, Experimental and numerical investigation of thermo-acoustic instability in a liquid-fuel aero-engine combustor at elevated pressure: Validity of large-eddy simulation of spray combustion, Combustion and Flame 162 (6) (2015) 2621–2637.
519. T. Providakis, L. Zimmer, P. Scouflaire, D. Ducruix, Characterization of the Acoustic Interactions in a Two Stage Multi Injection Combustor Fed with Liquid Fuel, Journal of Engineering for Gas Turbines and Power 134 (11) (2012).
520. C. M. Arndt, M. Severin, C. Dem, M. Stöhr, A. M. Steinberg, W. Meier, Experimental analysis of thermo-acoustic instabilities in a generic gas turbine combustor by phase-correlated PIV, chemiluminescence, and laser Raman scattering measurements, Experiments in Fluids 56 (4) (2015) 69.
521. A. Giusti, Advances in the modeling of dispersion and diffusion of entropy waves in gas turbine combustors, in: 24th International Congress on Sound and Vibration, ICSV 2017, 2017.
522. N. A. Worth, J. R. Dawson, Self-excited circumferential instabilities in a model annular gas turbine combustor: Global flame dynamics, Proceedings of the Combustion Institute 34 (2) (2013) 3127–3134.
523. P. Wolf, G. Staffelbach, A. Roux, L. Gicquel, T. Poinsot, V. Moureau, Massively parallel LES of azimuthal thermo-acoustic instabilities in annular gas turbines, Comptes Rendus Mecanique 337 (6–7) (2009) 385–394.
524. P. Wolf, R. Balakrishnan, G. Staffelbach, L. Y. Gicquel, T. Poinsot, Using LES to study reacting flows and instabilities in annular combustion chambers, Flow, turbulence and combustion 88 (1–2) (2012) 191–206.
525. G. Staffelbach, L. Gicquel, G. Boudier, T. Poinsot, Large Eddy Simulation of self excited azimuthal modes in annular combustors, Proceedings of the Combustion Institute 32 (2009) 2909–2916.
526. J.-F. Parmentier, P. Salas, P. Wolf, G. Staffelbach, F. Nicoud, T. Poinsot, A simple analytical model to study and control azimuthal instabilities in annular combustion chambers, Combustion and Flame 159 (7) (2012) 2374–2387.
527. N. Noiray, M. Bothien, B. Schuermans, Investigation of azimuthal staging concepts in annular gas turbines, Combustion Theory and Modelling 15 (5) (2011) 585–606.
528. G. Ghirardo, M. Juniper, Azimuthal instabilities in annular combustors: standing and spinning modes, Proc. R. Soc. A 469 (2157) (2013) 20130232.
529. M. Bauerheim, J. Parmentier, P. Salas, F. Nicoud, T. Poinsot, An analytical model for azimuthal thermoacoustic modes in an annular chamber fed by an annular plenum, Combustion and Flame 161 (5) (2014) 1374–1389.
530. L. Li, X. Sun, Effect of vorticity waves on azimuthal instabilities in annular chambers, Combustion and Flame 162 (3) (2015) 628–641.
531. G. Ghirardo, M. P. Juniper, J. P. Moeck, Weakly nonlinear analysis of thermoacoustic instabilities in annular combustors, Journal of Fluid Mechanics 805 (2016) 52–87.
532. S. Menon, V. Sankaran, C. Stone, Subgrid combustion modeling for the next generation national combustion code, NASA Report CR—2003-212202.
533. S. Menon, Simulation of Combustion Dynamics in Gas Turbine Engines, in: Parallel Computational Fluid Dynamics 2002, Elsevier, 33–42, 2003.
534. A. Kauffmann, F. Nicoud, T. Poinsot, Flow forcing techniques for numerical simulations of combustion instabilities, Combustion and Flame 131 (4) (2002) 371–385.
535. K. W. Thompson, Time-dependent boundary conditions for hyperbolic systems, II, Journal of computational physics 89 (2) (1990) 439–461.
536. F. Nicoud, Defining Wave Amplitude in Characteristic Boundary Conditions, Journal of Computational Physics 149 (2) (1999) 418–422.
537. D. H. Rudy, J. C. Strikwerda, A nonreflecting outflow boundary condition for subsonic navier-stokes calculations, Journal of Computational Physics 36 (1) (1980) 55–70, ISSN 0021-9991.
538. J.-P. Legier, T. Poinsot, D. Veynante, Dynamically thickened flame LES model for premixed and non-premixed turbulent combustion, in: Proceedings of the summer program, vol. 12, Center for Turbulence Research, Stanford, CA, 2000.
539. C. D. Pierce, P. Moin, Progress-variable approach for large-eddy simulation of non-premixed turbulent combustion, Journal of fluid Mechanics 504 (2004) 73–97.
540. H. Pitsch, Large-eddy simulation of turbulent combustion, Annu. Rev. Fluid Mech. 38 (2006) 453–482.

541. S. Candel, D. Veynante, F. Lacas, E. Maistret, N. Darabiha, T. Poinsot, Coherent flamelet model: applications and recent extensions, in: Recent advances in combustion modelling, World Scientific, 19–64, 1991.
542. F. E. Marble, J. E. Broadwell, The coherent flame model for turbulent chemical reactions, Tech. Rep., Purdue University Lafayette, 1977.
543. S. Candel, T. Poinsot, Flame stretch and the balance equation for flame surface area, Combustion Science and Technology 70 (1990) 1–15.
544. T. Poinsot, D. Veynante, Theoretical and Numerical Combustion, Edwards, Philadelphia, 2001.
545. M. Matalon, B. J. Matkowsky, Flames as gasdynamic discontinuities, Journal of Fluid Mechanics 124 (1982) 239–259.
546. D. Veynante, V. Moureau, Analysis of dynamic models for large eddy simulations of turbulent premixed combustion, Combustion and Flame 162 (2015).
547. H. Pitsch, P. Trisjono, Can combustion models be developed from DNS data?, in: 19th Australasian Fluid Mechanics Conference, 2014.
548. H. Pitsch, P. Trisjono, A systematic approach for combustion models development, in: Euopean Combustion Meeting, 2015.
549. G. Borghesi, J. Bellan, A priori and a posteriori investigations for developing large eddy simulations of multi-species turbulent mixing under high-pressure conditions, Physics of Fluids 27 (3) (2015) 035117.
550. P. Trisjono, H. Pitsch, Systematic Analysis Strategies for the Development of Combustion Models from DNS: A Review, Flow, Turbulence and Combustion 95 (2) (2015) 231–259.
551. P. Sagaut, Large eddy simulation for incompressible flows: an introduction, 2006.
552. V. Moureau, P. Domingo, L. Vervisch, From large-eddy simulation to direct numerical simulation of a lean premixed swirl flame: Filtered laminar flame-pdf modeling, Combustion and Flame 158 (7) (2011) 1340–1357.
553. J. Ludwig, Image convolution, 2006.
554. E. Hawkes, O. Chatakonda, H. Kolla, A. Kerstein, J. Chen, A petascale direct numerical simulation study of the modelling of flame wrinkling for large-eddy simulations in intense turbulence, Combustion and flame 159 (8) (2012) 2690–2703.
555. D. Veynante, V. Moureau, M. Boileau, T. Schmitt, A priori analysis of dynamic models for large eddy simulations of turbulent premixed combustion, in: Direct and Large-Eddy Simulation IX, Springer, 497–502, 2015.
556. F. Charlette, C. Meneveau, D. Veynante, A power-law flame wrinkling model for LES of premixed turbulent combustion Part II: dynamic formulation, Combustion and Flame 131 (1) (2002) 181–197.
557. R. Knikker, D. Veynante, C. Meneveau, A priori testing of a similarity model for large eddysimulations of turbulent premixed combustion, Proceedings of the Combustion Institute 29 (2) (2002) 2105–2111.
558. P. Volpiani, T. Schmitt, D. Veynante, A posteriori tests of a dynamic thickened flame model for large eddy simulations of turbulent premixed combustion, Combustion and Flame 174 (2016) 166–178.
559. F. Proch, P. Domingo, L. Vervisch, A. M. Kempf, Flame resolved simulation of a turbulent premixed bluff-body burner experiment. Part II: A-priori and a-posteriori investigation of sub-grid scale wrinkling closures in the context of artificially thickened flame modeling, Combustion and Flame 180 (2017) 340–350.
560. M. Boger, D. Veynante, H. Boughanem, A. Trouvé, Direct numerical simulation analysis of flame surface density concept for large eddy simulation of turbulent premixed combustion, in: Symposium (International) on Combustion, vol. 27, Elsevier, 917–925, 1998.
561. N. Chakraborty, R. Cant, A priori analysis of the curvature and propagation terms of the flame surface density transport equation for large eddy simulation, Physics of Fluids 19 (10) (2007) 105101.
562. N. Chakraborty, M. Klein, A priori direct numerical simulation assessment of algebraic flame surface density models for turbulent premixed flames in the context of large eddy simulation, Physics of Fluids 20 (8) (2008) 085108.
563. Y. Gao, N. Chakraborty, N. Swaminathan, Algebraic closure of scalar dissipation rate for large eddy simulations of turbulent premixed combustion, Combustion Science and Technology 186 (10–11) (2014) 1309–1337.
564. U. Allauddin, M. Klein, M. Pfitzner, N. Chakraborty, A priori and a posteriori analyses of algebraic flame surface density modeling in the context of Large Eddy Simulation of turbulent premixed combustion, Numerical Heat Transfer, Part A: Applications 71 (2) (2017) 153–171.
565. J. Galpin, A. Naudin, L. Vervisch, C. Angelberger, O. Colin, P. Domingo, Large-eddy simulation of a fuel-lean premixed turbulent swirl-burner, Combustion and Flame 30 (2008) 1775–1782.
566. W. Meier, P. Weigand, X. R. Duan, R. Giezendanner-Thoben, Detailed characterization

of the dynamics of thermoacoustic pulsations in a lean premixed swirl flame, Combustion and Flame 150 (2007) 2–26.
567. C. K. Law, Recent advances in droplet vaporization and combustion, Progress in energy and combustion science 8 (3) (1982) 171–201.
568. P.-K. Wu, G. Faeth, Aerodynamic effects on primary breakup of turbulent liquids, Atomization and Sprays 3 (3) (1993).
569. G. Faeth, L.-P. Hsiang, P.-K. Wu, Structure and breakup properties of sprays, International Journal of Multiphase Flow 21 (1995) 99–127.
570. S. Smith, M. Mungal, Mixing, structure and scaling of the jet in crossflow, Journal of fluid mechanics 357 (1998) 83–122.
571. A. R. Karagozian, Transverse jets and their control, Progress in energy and combustion science 36 (5) (2010) 531–553.
572. G. Hannebique, P. Sierra, E. Riber, B. Cuenot, Large eddy simulation of reactive two-phase flow in an aeronautical multipoint burner, Flow, turbulence and combustion 90 (2) (2013) 449–469.
573. B. Franzelli, A. Vié, M. Boileau, B. Fiorina, N. Darabiha, Large eddy simulation of swirled spray flame using detailed and tabulated chemical descriptions, Flow, Turbulence and Combustion 98 (2) (2017) 633–661.
574. X. Li, M. C. Soteriou, W. Kim, J. M. Cohen, High fidelity simulation of the spray generated by a realistic swirling flow injector, Journal of Engineering for Gas Turbines and Power 136 (7) (2014) 071503.
575. V. Yang, Modeling of supercritical vaporization, mixing, and combustion processes in liquid-fueled propulsion systems, Proceedings of the Combustion Institute 28 (1) (2000) 925–942.
576. G. Singla, P. Scouflaire, C. Rolon, S. Candel, Transcritical oxygen/transcritical or supercritical methane combustion, Proceedings of the combustion institute 30 (2) (2005) 2921–2928.
577. S. Candel, M. Juniper, G. Singla, P. Scouflaire, C. Rolon, Structure and dynamics of cryogenic flames at supercritical pressure, Combustion Science and Technology 178 (1–3) (2006) 161–192.
578. J. Hickey, M. Ihme, Supercritical mixing and combustion in rocket propulsion, Annual Research Briefs (2013) 21–36.
579. T. Schmitt, L. Selle, A. Ruiz, B. Cuenot, Large-eddy simulation of supercritical-pressure round jets, AIAA journal 48 (9) (2010) 2133–2144.
580. R. Tacina, Low NO_x potential of gas turbine engines, in: 28th AIAA Aerospace Sciences Meeting, 1990.
581. A. H. Lefebvre, Lean premixed/prevaporized combustion.
582. S. Candel, D. Durox, T. Schuller, P. Palies, J.-F. Bourgouin, J. P. Moeck, Progress and challenges in swirling flame dynamics, Comptes rendus mecanique 340 (11–12) (2012) 758–768.
583. R. K. Cheng, S. A. Fable, D. Schmidt, L. Arellano, K. Smith, Development of a low swirl injector concept for gas turbines, in: Proceedings of IJPGC 2001, 2001 International Joint Power Conference.
584. P. Palies, R. Acharya, A. Hoffie, M. Thomas, Lean Fully Premixed Injection for Commercial Jet Engines: An Initial Design Study, in: ASME Turbo Expo 2019 GT2019-91653, 2019.
585. X. Wang, V. Yang, Supercritical mixing and combustion of liquid-oxygen/kerosene bi-swirl injectors, Journal of Propulsion and Power 33 (2) (2016) 316–322.
586. P. P. Palies, R. Acharya, A. Hoffie, Design and Challenges of Lean Fully Premixed Injectors for Gas Turbine Engines, in: AIAA Propulsion and Energy 2019 Forum, 2019.
587. P. Dagaut, On the kinetics of hydrocarbons oxidation from natural gas to kerosene and diesel fuel, Physical Chemistry Chemical Physics 4 (11) (2002) 2079–2094.
588. G. Wang, M. Boileau, D. Veynante, Implementation of a dynamic thickened flame model for large eddy simulations of turbulent premixed combustion, Combustion and Flame 158 (11) (2011) 2199–2213.

Index

S

T

U

V

W

STABILIZATION AND DYNAMIC OF PREMIXED SWIRLING FLAMES

Prevaporized, Stratified, Partially, and Fully Premixed Regimes

PAUL PALIES

Stabilization and Dynamic of Premixed Swirling Flames focuses on swirling flames in various premixed modes (prevaporized, stratified, partially, and fully premixed) for the combustor, and the development and design of current and future swirl-stabilized combustion systems. This includes predicting capabilities, modelling of turbulent combustion, and a complete overview of the topic of stabilization and combustion dynamics of these flames in aeroengines. The book discusses the effects of the operating envelope on upstream fresh gases and the subsequent impact on flame speed/combustion/mixing. It also presents a theoretical framework for flame stabilization. The last chapter covers the design of a fully premixed injector for future jet engine applications.

Key Features

- Describes the phenomenology of premixed combustion, driving mechanisms of combustion instability, and various investigation approaches.
- Features a complete overview of the current challenges of swirling flames and combustors and the requirements and physics of fluids at work, both enabling the development of future gas turbine engine combustors.
- Includes the latest numerical results and analyses of flashback, lean blowout, and combustion instabilities.

About the author

Paul Palies is a Principal Scientist at CFDRC. He is a dedicated aeronautical research scientist and a specialist in propulsion including all aspects of combustion dynamics. He graduated from Ecole Centrale Paris in aerospace and from University of Paris XI in mechanics-physics. He holds a doctorate in combustion from Ecole Centrale Paris. He previously was a senior research scientist at the research center of United Technologies Corporation and worked with Pratt and Whitney's main combustor team. He has a demonstrated experience in acoustics, combustion and fluid dynamics and is an expert in combustion dynamics applied to laboratory scale combustor and jet engines.

ELSEVIER

ACADEMIC PRESS
An imprint of Elsevier
elsevier.com/books-and-journals

ISBN 978-0-12-819996-1